Triazole-Pyridine Derivatives: Versatile Building Blocks for Metallosupramolecular Assemblies and Materials

Isabel N. Hegarty, BSc

January 2020

Trinity College Dublin
The University of Dublin

Based on research carried out under the direction of
Prof. Thorfinnur Gunnlaugsson

A thesis submitted to the School of Chemistry,
Trinity College Dublin, The University of Dublin, for the degree of
Doctor of Philosophy

Declaration

This thesis is submitted for the degree of Doctor of Philosophy to the University of Dublin, Trinity College and has not been submitted before for any degree or examination to this or any other university. Other than where acknowledged, all work described herein is original and carried out by the author alone. Permission is granted so that the Library may lend or copy this thesis upon request. This permission covers only single copies made for study purposes, subject to normal conditions of acknowledgment.

_____

Isabel N. Hegarty

Abstract

This thesis, entitled "Triazole-Pyridine Derivatives: Versatile Building Blocks for Metallosupramolecular Assemblies and Materials", describes the design, synthesis and characterisation of a series of 1,2,3-triazol-4-yl-picolinamide (**tzpa**) and 2,3-bis(1,2,3-triazol-4-yl)picolinamide (**btp**) derivatives. The ligands are explored in the context of their coordination chemistry with *d*-metals Cu(I), Cu(II), and Ag(I), as well as their capacity to coordinate and sensitise the emission of lanthanide (Ln(III)) ions, in particular, Tb(III) and Eu(III).

Chapter 1 provides an introduction to symmetrical terdentate ligand motifs, with a particular focus on dipicolinic acid (**dpa**) and **btp**. This section will provide a review of the literature, describing recent advances in the coordination chemistry of these ligands with various *d*- and *f*-metals both in solution and in soft-materials. This is followed by a review of pyridine-centred, asymmetric ligand motifs and their self-assembly with *d*- and *f*-metals as well. The chapter is concluded by highlighting work from the Gunnlaugsson group, which serves as a platform from which the research explored in the following chapters has been based.

Chapter 2 describes the design and synthesis of a pair of chiral enantiomeric **tzpa** ligands, and their self-assembly with Cu(I) and Cu(II) salts in the solid state and in solution is studied. Single crystals of X-ray diffraction quality were grown and the resultant [2 × 2] tetrameric M$_4$L$_4$ grid structures are described. Oxidation of Cu(I) to Cu(II) upon complexation is observed as well as single deprotonation of each ditopic ligand under mild conditions. The effects of both reaction solvent and counterion on the assemblies formed is evident in this chapter. The self-assembly of these ligands with various Cu(I) and Cu(II) salts in solution is investigated through the use of UV-visible absorption and fluorescence spectroscopy, as well as circular dichroism. Speciation and global stability constants (β) related to each species are determined by non-linear regression analysis and indicate the formation of multiple species in solution at various metal:ligand stoichiometries. This chapter concludes by employing cyclic voltammetry (CV) to examine the Cu(I)/(II) redox behaviour of the complexes in order to probe the spontaneous oxidation of Cu(I) observed upon complexation.

Chapter 3 describes the design and synthesis of a series of monotopic and ditopic **tzpa** derivatives, functionalised with coordinating pyridyl groups. These ligands coordination chemistry with Cu(I), Cu(II) and Ag(I) salts is described. A ditopic **tzpa** ligand

functionalised with 3-pyridyl "arms" generates a Ag(I) organogel, while its 2-pyridyl derivative forms a tetrameric [2 × 2] grid structure analogous to that described in Chapter 2. A monotopic **tzpa** ligand, functionalised with one pyridyl "arm" generates a Ag(I) 1D polymer structure, while a 2D polymer with Cu(II) is formed from a monotopic **tzpa** derivative with two pyridyl "arms". It will be shown that altering the linker moiety between the terdentate binding sites can significantly affect the solubility of the ligands and thus their coordination chemistry. The self-assembly these ligands with Cu(I) and Cu(II) salts is also investigated through UV-visible absorption and fluorescence spectroscopy and, as in Chapter 2, the speciation and stability constants are determined by non-linear regression analysis.

Chapter 4 describes the functionalisation of the **tzpa** ligand motif with amino acid residues as the first step towards generating Ln(III)-**tzpa** complexes which would be stable in aqueous media. Firstly, these **tzpa** ligands are examined in the context of their capacity to sensitise Tb(III) and Eu(III) emission. The self-assembly of an L-phenylalanine functionalised ligand with Tb(III) and Eu(III) is investigated by UV-visible absorption, fluorescence and time-gated emission spectroscopy. The self-assembly of an L-tryptophan functionalised ligand with Tb(III) is also examined, and the fully saturated ML_3 assemblies of each of these ligands with Tb(III) are studied in H_2O to determine their stability. A monotopic **tzpa** ligand, not functionalised with an amino acid residue, is also synthesised and its self-assembly with Tb(III) is examined. The self-assembly of chiral ditopic **tzpa** ligand described in Chapter 2 will also be investigated.

Chapter 5 focuses on incorporating the **btp** coordination motif into a polymer material in order to generate a Tb(III)-sensitised material which is stable in an aqueous environment and responsive to external stimuli. A **btp** compound, functionalised at the 4-pyridyl position is synthesised and this compound itself forms an organogel in CH_3CN. The incorporation of the compound into a p(HEMA-*co*-MMA-*co*-EGDMA) polymer matrix is then described and the uptake of Tb(III) and Eu(III) ions into the hard polymer through swelling in aqueous media is investigated. The material is shown to exhibit red/green emission upon Eu(III)/Tb(III) uptake, respectively; however, the system exhibits some limitations that are also discussed. The **btp** compound will also be utilised to functionalise a polymer backbone, polyethylene-alt-maleic anhydride (p(E-alt-MA)), through covalent attachment, and the introduction of Tb(III)-based supramolecular crosslinks of this polymer is explored. The photophysical properties of this polymer are characterised by UV-visible absorption, fluorescence and time-gated emission spectroscopy, and the self-assembly of the

polymer with Tb(III) is also described. Finally, luminescent hydrogels are demonstrated, before concluding this chapter by describing approaches to exploit these preliminary results.

Finally, Chapter 6 outlines the experimental and synthetic procedures used for the studies described in this thesis as well as the compound characterisation for the compounds prepared. This is followed by literature references and appendices to support the preceding chapters.

Acknowledgements

Shauna and Thomas, best of luck with the rest of your studies! It will really fly by and before you know it you will be sitting here like me writing this thesis.

To the past TG members who have made the last four years so much fun! Amy, Betramy Lynch, Dr. Parallel Lynes, you kept me going with mugs of tea and chats. And our dinner dates in Maynooth of late have really kept me from going crazy working from home! Can't believe the #lovelylongford is going to be discontinued but delighted for and your new adventure in Cork! Dermy, our renditions of Gaudete will ring through the streets of Dublin again soon I hope. Sandra,"salsa, tequila, corazón"…mucho gracias mi amor! Joe, I would say thanks for those samples I inherited, but….I guess the lab shanty made up for it 😉 Thanks for making me feel so welcome to the group as a fellow Maynoothian when I was just starting out and Trinity was an intimidating prospect! Also thank you to Eoin, my **btp** buddy, Sachi, Bjorn, Esther, Fergus, Anna, Emma and Raju.

Bruno, my basketball buddy, you have been a great friend and I was so sorry we didn't get to finish this together the way we started! You have kept me laughing from day one and we have truly missed you over the last few months. I'm definitely coming to visit Catania to play basketball by the sea!

Hannah, I was tempted to just copy your acknowledgements and see if anyone noticed! You have been my other half since day one, teaching me all the Trinity ways. We have cemented our friendship through ripped jeans, forgotten nights, my horrible crystal structures and almost four years of being side by side. You have been such an amazing PhD partner in crime and I really couldn't have asked for anyone better to share the last four years of ups and downs with. Your strength is inspiring and whoever gets to sit beside you in your next adventure is one luck person!

Adriana, the Princess, TBSI hasn't been the same since you left and our donut dates have come to an end! Thank you for popping into Maynooth over the last few months…now for cocktails!

Granny, you are an amazing woman and an inspiration to all of your children and grandchildren. You have supported me since day one, even when you thought another four years in college was probably a bit mad! You are always interested in how the work is going and your mantra "education is no load" is certainly one I've taken to heart.

Paul, thank you so so much for all of your patience and support! You helped me to focus on the positive and gave me perspective when I couldn't see the finish line. The constant supply of Lindt and bloopers helped too! 😊 The ups and downs of this year have

been many both in and out of the lab and I couldn't have gotten through it without you. You can finally stop pretending you know what my project is about now!

And finally, to my amazing family, would you believe, I'm finally finished! Shane, thanks for indulging my urge to escape PhD life with our trip to Cuba and all the encouragement you have given me. I never get to feel too sorry for myself for the long hours with you and dad around 😉 Mum and Dad, I cannot begin to express how grateful I am for your continuous love and support. You are never without advice, encouragement and food. It is because of you both that I have gotten this far and I certainly wouldn't have gotten through the past four years without you both cheering me on. Of all the many teachers I have had in my life you have been the very best!

Abbreviations

-co-	copolymer
1D	one dimensional
2D	two dimensional
3D	three dimensional
^3T	triplet excited state
Å	angstrom
AIBN	azobissisobutyronitrile
ar	aromatic
atm.	atmosphere(s)
bbpy	2,6-bis(benzimidazol-2-yl)pyridine
bipy	bipyridine
Boc_2O	di-*tert*-butyl dicarbonate
btp	2,6-bis(1,2,3-triazol-4-yl)pyridine
CD	circular dichroism
CPL	circularly polarised luminescence
CuAAC	copper(I)-catalysed alkyne-azide 'click'
cyclen	1,4,5,10-tetraazacyclododecane
d	doublet
DMF	*N,N*-dimethylformamide
DMSO	dimethylsulfoxide
dpa	pyridine-2,6-dicarboxamide
DSC	differential scattering calorimetry
E	energy
EDCI	1-ethyl-3-(3-dimethylaminopropyl)carbodiimide
EDTA	ethylenediamine tetra acetate
EGDMA	ethylene glycol dimethacrylate
equiv.	equivalent(s)
ES	excited state
ESI	electrospray ionisation
Et_2O	diethyl ether
EtOAc	ethyl acetate
fluor	fluorescence

FT-IR	fourier-transform infrared spectroscopy
GS	ground state
HEMA	(2-hydroxylethyl)methacrylate
HMBC	heteronuclear multiple-bond correlation spectrscopy
HOBt	1-hydroxybenzotriazole hydrate
HOMO	highest occupied molecular orbital
HPLC	high-performance liquid chromatography
HRMS	high resolution mass specrometry
IR	infrared
ISC	inter-system crossing
J	NMR coupling constant
J	total angular momentum quantum number
K	kelvin
L	total orbital angular momentum quantum number
L	ligand
Ln	lanthanide
LUMO	lowest unoccupied molecular orbital
M	molar (mol.dm^{-3})
MD	magnetic dipole
m$_l$	orbital angular momentum quantum number
ML	complex with metal-to-ligand ratio of 1:1
ML$_2$	complex with metal-to-ligand ratio of 1:2
ML$_3$	complex with metal-to-ligand ratio of 1:3
MLCT	metal-to-ligand charge transfer
MMA	methyl methacrylate
MOF	metal organic framework
MR	magnetic resonance
MRI	magnetic resonance imaging
m$_s$	spin angular momentum quantum number
NEt$_3$	triethylamine
NMR	nuclear magnetic resonance
OLED	organic light emitting diodes
p-	para

p( )	poly( )
PE	polyethylene
PEG	polyethylene glycol
PET	photo-induced electron transfer
pH	$-\log_{10}[H^+]$
phosph	phosphorescence
pybox	2,6-Bis[2-oxazolinyl]pyridine
q	number of bound water molecules (to a Ln^{III} on)
q_{Tb}, q_{Eu}	hydration state of Tb^{III}, hydration state of Eu^{III}
RT	room temperature
S	total spin angular momentum quantum number
S_0	singlet ground state
S_1	singlet excited state
SEM	scanning electron microscopy
SOMO	singularly occupied molecular orbital
T_1	triplet excited state
TBA	tetrabutyl ammonium
tBu	*tert*-butyl
TFA	trifluoroacetic acid
T_g	transition temperature
THF	tetrahydrofuran
tzpa	(1,2,3-triazol-4-yl)picolinamide
TRD	time resolved detection
UV	ultra-violet
UV-Vis	ultra-violet and visible
v/v	volume/volume
wt%	weight percent
XNOR	exclusive NOT OR
α	proportional to
β	global stability constant
β-CD	beta cyclodextrin
δ	chemical shift (NMR)
ΔH	enthalpy

ΔS	change in entropy
ε	molar extinction coefficient
η_{sens}	efficiency of sensitisation of lanthanide luminescence
η_{sens}	sensitisation efficiency (%)
λ	wavelength
λ_{abs}	absorbance wavelength
λ_{em}	emission wavelength
λ_{exc}	excitation wavelength
λ_{max}	absorbance maxima wavelength
ν	frequency (cm^{-1})
τ	luminescence lifetime
τ_1	luminescence lifetime 1
τ_2	luminescence lifetime 2
τ_{em}	emission lifetime
τ_{obs}	observed luminescence lfetime
τ_{OD}	luminescence lifetime in D_2O
τ_{OH}	luminescence lifetime in H_2O
τ_R	radiative lifetime
ϕ	quantum yield (%)
ϕ_{tot}	total quantum yield

Note on publications

Chapter 2 was mostly described in the article "Unexpected linkage isomerism in chiral tetranuclear bis-terdentate (1,2,3-triazol-4-yl)-picolinamide (tzpa) grids" co-authored with Dr. Hannah L. Dalton, Dr. Adam F. Henwood, Dr. Chris S. Hawes, and Prof. Thorfinnur Gunnlaugsson in *Chemical Communications* (*Chem. Comm.* **2019**, 55, 9523 - 9526)

Table of Contents

"Research is formalised curiosity. It is poking and prying with a purpose"

Zora Neale Hurston

1. Introduction

1 Introduction

Supramolecular chemistry, a term first used by Lehn in 1978[1] – describes "chemistry beyond the molecule".[2] It refers to the use of non-covalent interactions such as hydrogen bonding, metal-coordination interactions, electrostatic interactions, and π-π interactions *etc.* to generate a range of large, higher order entities from small, simple molecular components.[3–5] As such, individual molecular components require specific, considered design in order to induce spontaneous and controlled self-assembly using such interactions. Molecular recognition is achieved through a process of molecular complementarity, whereby host ligands are designed with the geometry, size and charge of the guest in mind, not unlike the "lock and key" hypothesis for the formation of enzyme-substrate complexes.[2] The range of supramolecular architectures which have been achieved to date is truly impressive, while considering the weak interactions which control the assembly and hold these systems in place. The labile nature of the interactions that underpin supramolecular chemistry mean that it is intrinsically dynamic in nature, which is advantageous due to the possibility of reversibility, internal rearrangement and exchange of components to generate a structure which represents a thermodynamic minimum.[5,6] Examples of supramolecular chemistry included a plethora of different structures including cryptands,[7] podands[8] and crown ethers,[9] and more recently, interlocked systems,[10–14] supramolecular materials,[15–18] metal-organic frameworks (MOFs)[17,19–21] and functional devices.[22,23] Such systems are often the result of carefully designed metal-ligand interactions. In particular transition metal ions in the 2+ oxidation state are of interest in designing supramolecular architectures due to the largely predictable nature of their coordination chemistry and their favourable magnetic, spectroscopic and electronic properties which cannot be accessed using purely organic assemblies. Due to ligand field effects, *d*-metal ions, typically comprising coordination numbers of two to six, have highly defined geometries around the coordination sphere which dictate the subsequent geometry of the supramolecular self-assembly.[12,24–26] Their ability to achieve a balance between a relatively strong M-L dative bond which is also labile enough to facilitate reversible coordination processes facilitates the self-assembly reaching a thermodynamic equilibrium.

On the other hand, lanthanide ions typically possess higher coordination numbers, ranging from six to twelve. Each of the lanthanide ions possess a similar size and reactive profile due to a phenomenon known as the "lanthanide contraction" whereby as the nuclear charge increases as the ionic radii decreases across the series due to poor shielding of the

nuclear charge by the electrons in the 4*f* orbitals.[27] Lanthanides have been explored in the context of a variety of applications, including imaging, medical diagnostics,[23,28,29] and in electronic devices,[30] which stems from their unique magnetic and photophysical properties. These properties make lanthanide ions an attractive motif for the formation of supramolecular self-assemblies and a more detailed description of lanthanide photophysics will be conducted in Chapter 4.

       Much work in the Gunnlaugsson group has focused on metal-directed self-assembly, the results of which have led to the formation of elegant supramolecular architectures, conferred with attractive photophysical properties which have also served to give insights into the mechanism of formation. The work presented in this PhD thesis aims to build upon the insights previously obtained within the Gunnlaugsson group, and from others, investigating the metal-directed self-assembly of systems based on the pyridine-2,6-dcarboxamide (**H₂dpa**) and 2,6-bis(1,2,3-triazol-4-yl)pyridine (**btp**) ligand frameworks. By combining these two coordination motifs, forming an asymmetrical metal coordination site, we have generated a new class of terdentate coordination compounds – (1,2,3-triazol-4-yl)picolinamide (**tzpa**) ligands – which we have applied to fundamental investigations of their metal-driven self-assembly. The following sections will explore the coordination chemistry of these systems and will equip us with the knowledge to successfully engineer increasingly complex higher order metallosupramolecular assemblies.

1.1 Symmetrical terdentate ligands

A wide variety of ligands with a terdentate binding motif have been developed over the last few decades, with a variety of coordination modes.[31] Pyridine-centred, symmetrical terdentate ligands are widespread in the literature and include but are not limited to: derivatives of pyridine-2,6-dicarboxylic acid (**H₂dpa**),[32,33] 2,6-bis(oxazoline)pyridine (**pybox**),[34] 2,6-di(pyrazolyl)pyridine (**bpp**)[35], 2,2';6,2"-terpyridine (**terpy**) [36–39,] and 2,6-bis(1,2,3-triazol-4-yl)pyridine (**btp**)[40] with each of these coordination motifs implicated in a host of applications, such as catalysis,[41,42], anion binding,[43] sensing and imaging.[25] In the following sections a selection of these coordination motifs, their coordination chemistry and numerous applications will be discussed in detail.

1.1.2 Dipicolinic acid

Pyridine-2,6-dicarboxylic acid (dipicolinic acid (**H₂dpa**)) is a commercially available, water soluble O,N,O-chelator which has been utilised as the building block for the formation of
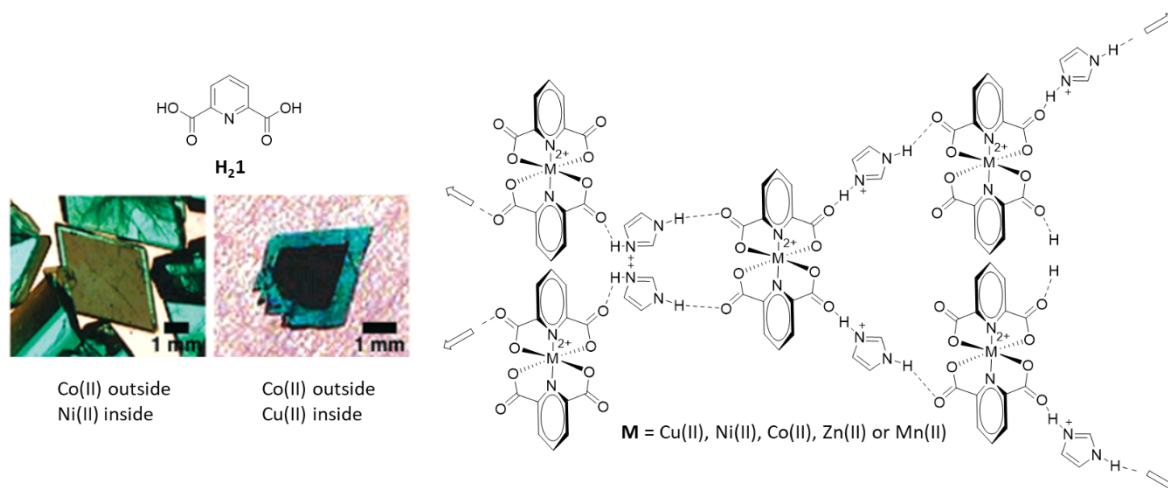
Figure 1.1 *Compound **H₂1** (**H₂dpa**) and a schematic representation of hydrogen bonding network generated with ligand **H₂1**, imidazolium cations and metal ions as well as a photograph of composite crystals generated from **H₂1** and Cu(II), Ni(II) or Co(II) metal. ions. Reproduced from Ref. 56.*

polymeric metal-organic frameworks and supramolecular assemblies.[21,44–46] The rigid 120°angle between the central pyridine and the carboxylate groups allows for coordination to both *d*- and *f*-metals.[47] Its coordination chemistry with many transition metals has been widely studied; however, for the purpose of relevance to this thesis, examples containing copper, silver and lanthanide ions will be the primary focus of discussion here. Cu(II) based systems have proven particularly interesting with applications spanning from molecular magnetism and crystal engineering to bioinorganic chemistry.[48–53] The usual coordination mode of **H₂1** with Cu(II) is through the *N,O*-binding site; however, examples have also been reported of **H₂1** acting as a monoatomic bridging ligand.[54,55] The affinity of **H₂1** to participate in hydrogen bonding, in addition to its metal chelation abilities, has seen it extensively employed in the formation of crystalline materials. For example, MacDonald *et al.* reported Cu(II) 2D networks based on these interactions.[56] The network design relied on hydrogen bonding interactions between the deprotonated carboxylate groups of ligand **1** and imidazolium cations to generate the well-ordered layers. Single crystal X-ray diffraction confirmed the structure and connectivity, with each Cu(II) ion coordinated to two **H₂dpa** ligands in a typical octahedral fashion and hydrogen bonding interactions acting to link the imidazolium cations to **1** in an infinite network (see Figure 1.1). As the four carboxylate groups of **1** are in a planar tetrahedral arrangement, perpendicular layers are formed. The structure was found to be remarkably similar for Mn(II), Co(II), Ni(II) and Zn(II) and the authors were able to show that the metal ions could be interchanged within the hydrogen-bonded network without causing a collapse of the network. They also demonstrated that composite crystals, composed of two different metal complexes, could be achieved. For
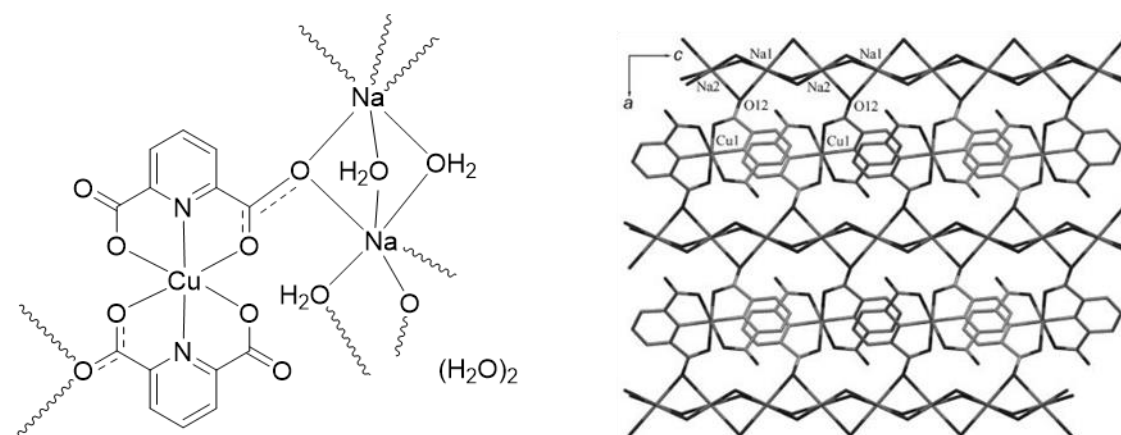
Figure 1.2 *Schematic representation of **dpa** assembly [Cu(μ-**1**)$_2${Na$_2$(μ-H$_2$O)$_4$}]$_n$·2nH$_2$O and fragment of the crystal packing diagram along the b axis showing a front view of the 2D metal-organic layer. Reproduced from Ref. 57.*

example, crystals of the Co(II) complex were placed in a DMSO solution containing crystals of the Cu(II) complex. An epitaxial film of the Cu(II) crystals were observed to grow over the Co(II) crystals and was shown by optical polarizing microscopy to behave as a single crystal.

Aqua complexes of transition metals continue to be explored due to their myriad possible applications such as catalysis, biochemistry, pharmaceutical products and magnetic materials.[45,50,52] Kirillova *et al.* reported the first highly soluble Cu(II) coordination polymer based on the **H₂dpa** binding motif with a view to examining its efficacy as a bioinspired catalyst precursor for peroxide oxidation of cycloalkanes.[57] The 2D Na/Cu coordination network [Cu(μ-**1**)$_2${Na$_2$(μ-H$_2$O)$_4$}]n·2nH2O was synthesised from the dissolution of Cu(NO$_3$)$_2$, sodium hydroxide, **H₂1** and triethanolamine. While no triethanolamine was found to be present in the structure of the complex, its absence during complexation resulted in the formation of a different structure. X-ray quality single crystals were obtained and revealed the [Cu(μ-**1**)$_2${Na$_2$(μ-H$_2$O)$_4$}]$_n$·2nH$_2$O structure shown in Figure 1.2, with each **H₂1** deprotonated to facilitate coordination through the carboxylate ions. The Cu(II) atoms sits in a distorted octahedral environment with ligands **1** almost perpendicular to each other around the metal centre. One carboxylate of the **dpa** bridges two Na atoms, while both inter- and intramolecular hydrogen bonding further reinforces the 2D metal-organic network. Preliminary studies on the efficiency of the complex to act as a catalyst for peroxidative oxidation have shown some promise.

Particularly relevant to work described in this thesis are pyridine-2,6-dicarboxamide (**pdc**) based ligands which have been studied extensively with both transition metals and lanthanide ions alike. The amide derivative of **H₂dpa** facilitates the introduction of
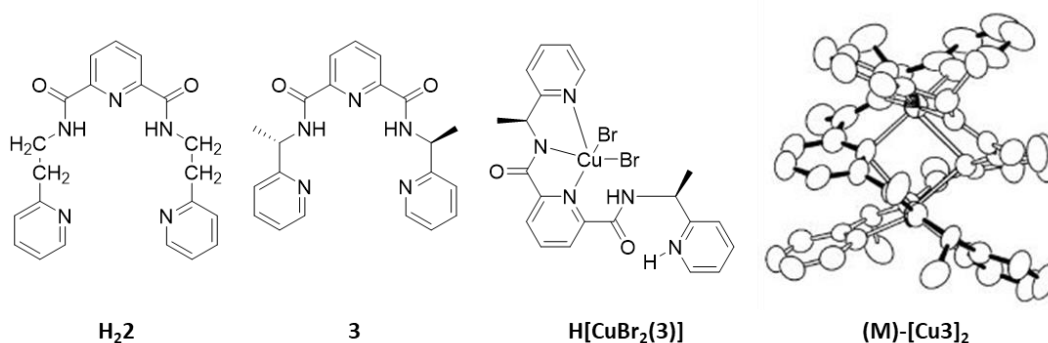
Figure 1.3 *Compounds **H₂2**, **3** and H[CuBr₂(**3**)] along with thermal ellipsoid plot of double stranded helicate structure (M)-[Cu**3**]₂. Reproduced from Ref. 61.*

additional functional groups to the chelating core, giving the ligand increased versatility over the simple **H₂dpa** motif. Two five-membered chelate rings can form an N_3 pincer cavity between the amide and pyridyl N donors of these pyridine-2,6-dicarboxamide systems with the σ-donating amide N contributing towards stabilisation of metal ions in higher oxidation states.[58] Chavez and co-workers reported the formation of the first dipeptide complex of copper involving a CuN_5 motif, using pyridine-2,6-dicarboxamide derivatives.[59] In the presence of base ligand **H₂2** is doubly deprotonated, which facilitates coordination of the amide nitrogens to the metal ion. In this case, copper(II) acetate in CH_3OH is sufficient to deprotonate the amido nitrogens and reaction of **H₂2** under these conditions yielded [Cu(**2**)]; however, in the absence of a basic counterion, the addition of two equivalents of sodium acetate is required to form the desired [Cu(**2**)] complex. X-ray quality crystals were obtained of the structure, with the Cu(II) ion adopting a distorted square-pyramidal geometry coordinated to five N atoms, two of which are deprotonated amido groups and three of which are pyridyl groups. The absorption spectrum of the complex features a broad band at 613 nm and an additional shoulder at 750 nm, which are bands characteristic of tetragonally coordinated Cu(II) complexes.[60]

Higher order structures have also been reported based on the pyridine-2,6-dicarboxamide motif. Yano *et al.* have detailed the formation of a mononuclear complex and a dicopper helicate from the reaction of compound **3** and CuBr₂.[61] Interconversion between the discrete complex and its double stranded helical structure can be observed upon the addition of triethylamine (NEt₃) under reflux conditions, and the process can subsequently be reversed upon addition of HBr. The structures of both the discrete complex and the helicate were confirmed by, among other techniques, X-ray crystallography (see Figure 1.3). In the case of the mononuclear complex, the Cu(II) ion is coordinated through the central pyridyl N, the deprotonated amide N and the terminal pyridyl N, with two bromine ions
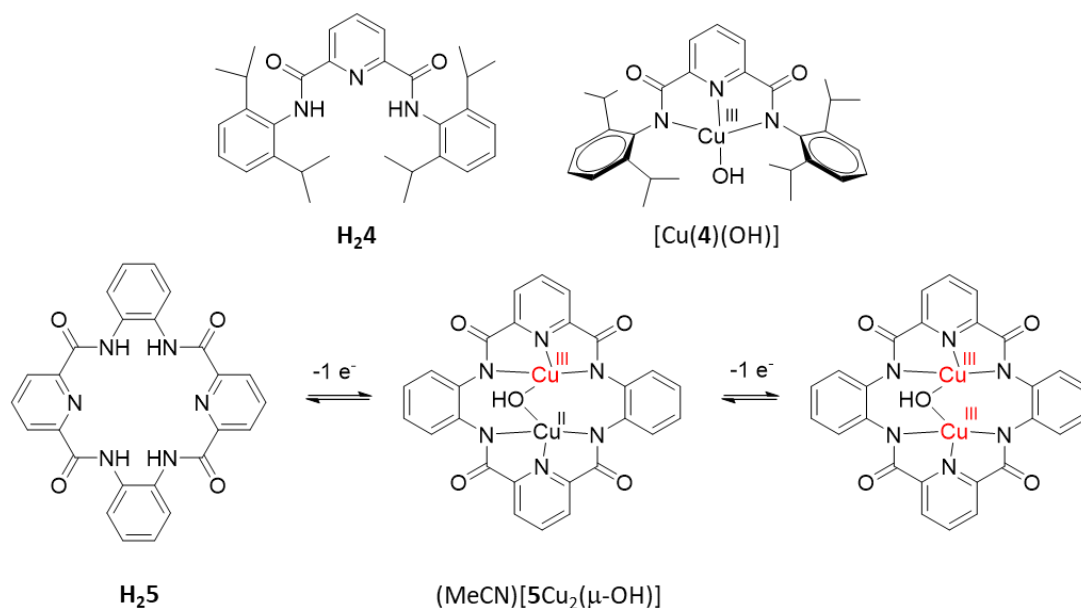
Figure 1.4 *Compound **H₂4** and [Cu(**4**)(OH)]reactive complex along with compound **H₂5** and hydroxo-bridged dicopper complexes (MeCN)[**5**Cu₂(μ-OH)].*

completing the coordination sphere. The second terminal pyridyl N is protonated, leaving the overall charge on the complex as neutral. The helicate structure is composed of two Cu(II) ions and two doubly deprotonated ligands. Each copper ion is coordinated to one deprotonated amide N from each ligand and one terminal pyridyl N, while both the central pyridyl N atoms bridge the two Cu(II) atoms. Heating a 1:1 mixture of *S-* and *R-*(**3**) under reflux with CuBr₂ in the presence of NEt₃ resulted in the formation of a racemic mixture of helicates (*M*)-[Cu(*S*)-**3**]₂ and (*P*)-[Cu(*R*)-**3**)]₂ indicating the system is capable of self-recognition.

Metal-bound oxygen-based species have been reported as intermediates for a range of oxidation reactions.[62,63] Preparation of complexes which have a similar structure to these proposed intermediates has frequently been undertaken in order to provide insights into the mechanisms of such reactions, and provide evidence for the feasibility or stability of proposed intermediates. One class of these complexes are metal hydroxo species, which are important intermediates in metal-promoted aerobic oxidation reactions. In particular, compounds containing the pyridine-2,6-dicarboxamide motif have been reported to stabilise the protonated version of the elusive [Cu(III)-O]⁺ ion, – a mononuclear copper hydroxo Cu(III)-OH.[64,65] Tolman and co-workers conducted both electrochemical and chemical oxidation of Cu(II) complexes of **H₂4** to generate the species [Cu(**4**)(OH)] with a Cu(III)-OH core, and used both DFT calculations and single crystal X-ray diffraction to unequivocally confirm the structure. The reactive species [Cu(**4**)(OH)] was observed to react

7
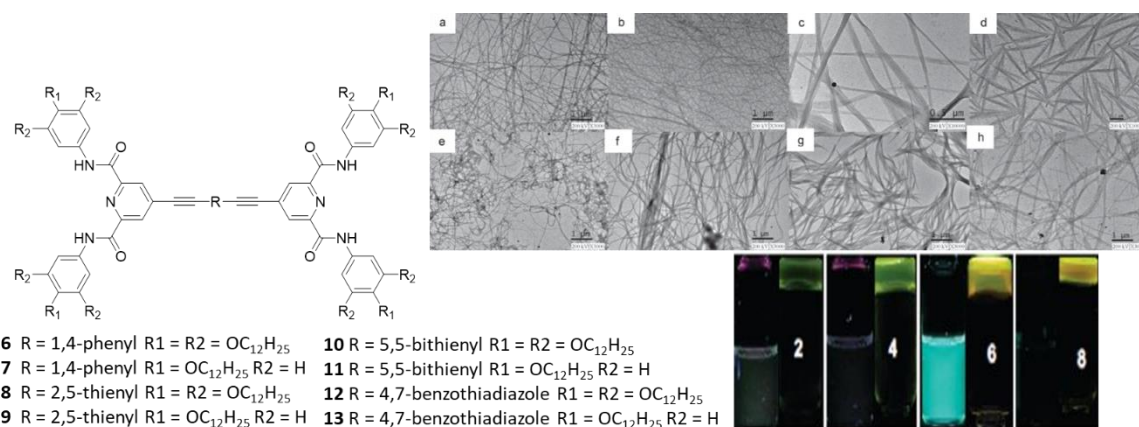
Figure 1.5 *Back-to-back compounds **6** – **13** synthesised for the formation of soft-materials and liquid crystals. (a,b) TEM images of xerogels of **7** from p-xylene and toluene, (c,d) **9** from DCM and toluene, (e,f) **11** from 1-heptanol and toluene and (g,h) **13** from 1-heptanol and toluene. Gels 2, 4, 6, and 8 generated from compounds **7, 9, 11,** and **13**, respectively. Pictures reproduced from Ref. 70.*

with dihydroanthracene (DHA) to yield anthracene and the aqua complex [Cu(**4**)(H$_2$O)] as the products. Due to the high rate of hydrogen atom abstraction displayed by [Cu(**4**)(OH)] from DHA and phenols, it was surmised that the reactive Cu(III)-OH species is a viable intermediate in the catalytic oxidation.

Following on from this work, the authors reported the synthesis of a pyridine-2,6-dicarboxamide macrocyclic ligand for the formation of a μ-hydroxo-bridged dicopper complex [(**5**)Cu$_2$(μ-OH)](Me$_4$N).[66] The complex was reported to undergo one-electron oxidations resulting in reactive Cu(II)Cu(III) and Cu(III)Cu(III) mixed-valent compounds which were characterised by spectroscopic investigations, theoretical calculations and low temperature chemical reactions. Evidence for the hydroxo bridge was gleaned from modelling the electrochemical and UV-visible absorption data.

Exploiting the affinity of pyridine-2,6-dicarboxylate for hydrogen bond formation in addition to its metal chelation abilities, derivatives of the ligand have been designed for the generation of soft-materials and liquid crystals.[67–69] For example, Shen and co-workers have developed several fluorescent soft-materials from back-to-back pyridine-2,6-dicarboxamide units functionalised with long carbon chains.[70] The soft-materials were described as thermoreversible and solution studies indicated that at elevated temperature, weakening of the intermolecular interactions such as hydrogen bonding and π-π stacking interactions led to increased conformational freedom. Interestingly, upon cooling again to gelation temperature, increased aggregation occurred resulting in an increase in the fluorescence emission and quantum yield inhibiting nonradiative decay processes. TEM imaging showed
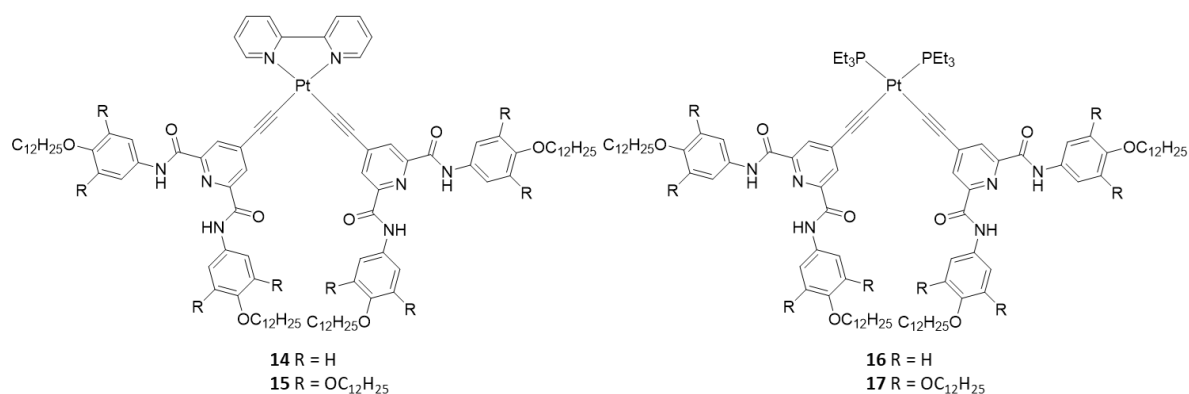
Figure 1.6 *Compounds **14–17** synthesised for the formation of fluorescent soft-materials with tuneable emission.*

a network of fibres with dimensions between 50 and 100 nm. Compounds **6, 8, 9** and **13** were found to demonstrate liquid crystal-like behaviour, which was confirmed by differential scanning calorimetry (DSC) and polarised optical microscopy.

The authors have also described the formation of Pt(II)-**pdc** soft-materials using complexes **14-17**, with a view to introducing interesting photophysical properties to the system.[69] The morphologies of these materials were similar to those reported for their corresponding organogel systems above; however, unusual photophysical properties were observed upon undergoing the gel-sol transition. Upon heating to elevated temperatures, an increase in the fluorescence response was observed, which was found to be due to increased degrees of freedom. This results in the formation of low energy, metal-metal-ligand charge transfer (MMLCT) excimers, which exhibit enhanced emission at long wavelengths due to increased π-π and Pt(II)-Pt(II) interactions.

The design of coordination polymers and supramolecular structures with Ag(I) is an area of continued interest in supramolecular chemistry due to the labile nature of silver ions and their capability of forming complexes with a variety of different coordination numbers. They have also been shown to have use in biological applications such as antimicrobial activities.[71] The capacity of silver ions to form tight silver-silver interactions is also appealing, and has been used to influence the formation of supramolecular coordination polymers.[72] Because of this, in addition to the knowledge that pyridine-2,6-carboxamide is structurally related to the biologically relevant pyridine-3- and -4-carboxamide, it is no surprise that exploring the coordination chemistry of these ligands with Ag(I) has been of interest to many researchers. For example, Cheng *et al.*,[73] while attempting to obtain single crystals of the pyridine-2,6-dicarboxamide compound **H₂1** with various Ag(I) salts, observed that conducting a hydrothermal reaction between 2,6-dicyanopyridine and a Ag(I) salt
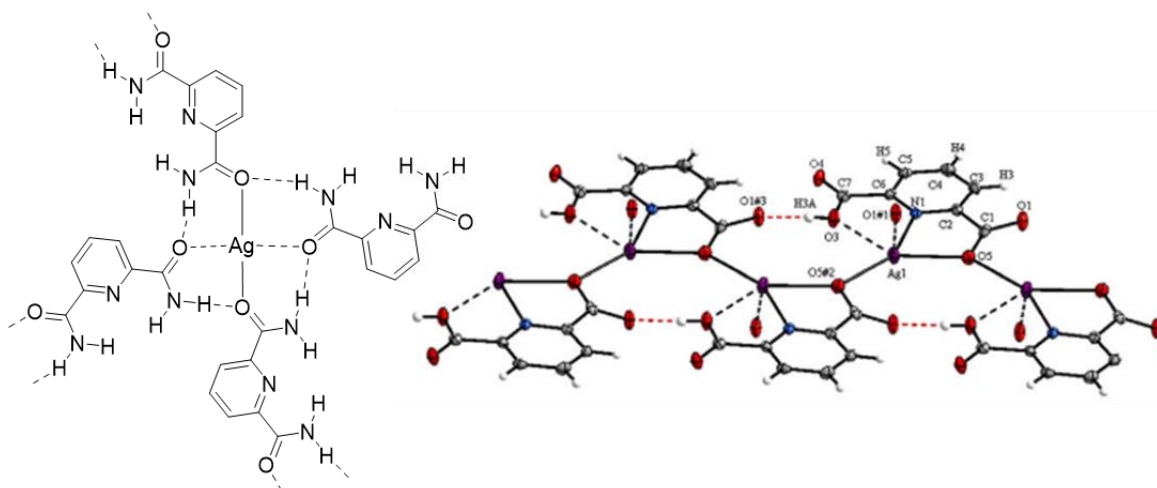
Figure 1.7 *Structure of [Ag(**1**)₂NO₃]ₙ framework along c-axis showing hydrogen bonding interactions along with coordination environment of Ag(I) in [Ag(**H1**)]ₙ.*

yielded superior crystals of the desired product $[Ag(\mathbf{1})_2NO_3]_n$ caused by slow hydrolysis of the dicyanopyridine and coordination to the silver atom. Reaction with $AgBF_4$ and $AgNO_3$ yielded crystals which were isostructural. The structure $[Ag(\mathbf{1})_2NO_3]_n$ shows each silver atom coordinating to two oxygen atoms from two distinct ligands, as well as four weak Ag-O interactions with four other ligands, generating a 3D network with 1D open-channels. To compensate for the weak Ag-O interactions, the structure is further stabilised by stronger π-π and hydrogen bonding interactions. Upon reaction of $AgNO_3$ with **pdc** and 2,6-dicyanopyridine under the same conditions as before, the authors yielded crystals of $[Ag(\mathbf{H1})]_n$. Each silver atom here coordinates a pyridyl nitrogen atom and three oxygen atoms of three distinct ligands, with each ligand being singly deprotonated, which generates a charge neutral 2D coordination polymer. This demonstrates the versatile coordinating nature of Ag(I) ions.

Other frameworks such as mixed-metal metal organic frameworks (MOFs) have also been developed from **dpa.** Zhao and co-workers reported the generation of a heterometallic
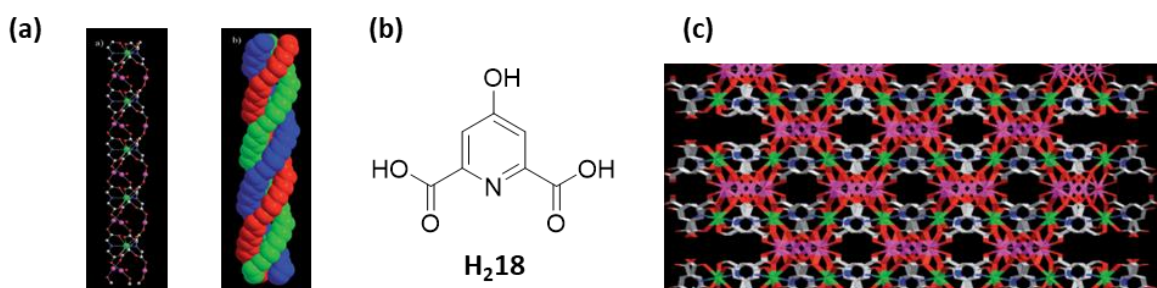
Figure 1.8 *(a)Triple stranded helical structures of {[ErAg₃(**1**)₃(H₂O)]}ₙ and space fill diagram of right-hand triple-stranded helical structures and L and R type triple stranded helices. (b) Ligand **H₂18** (c) 2D layer motif constructed by Er(III) ions, of {[ErAg₃(**H₂18**)₂(H₂O)]}ₙ.. Reproduced from Ref. 74.*

organic framework (HMOF) containing Ag(I) and Er(III) metal centres. Each repeating unit consisted of three ligand **1** molecules, three silver atoms, and one erbium atom.[74] Each Er(III) is coordinated by three ligands in an O,N,O fashion, fulfilling the high coordination requirements of the lanthanide ion, while there are two distinct silver environments present in the structure. The first silver atom is coordinated by two carboxylate oxygen atoms and one water oxygen atom while the second silver environment consists of only two COO^- oxygen atoms. Each carbonyl group in the structure, therefore, coordinates through one oxygen to a silver atom, and by the other oxygen to an Er(III) atom, to generate the triple stranded helicate. Introducing a hydroxy group at the 4-position of the ligand, forming ligand **H₂18**, resulted in a significantly different framework. In this case, each Er(III) is coordinated by two tridentate ligands, as well as two hydroxy groups from two other ligands, leaving the Er(III) in an eight-coordinate environment and generating a 2D array. There are also two distinct silver coordination geometries in which the silver coordinates through the carboxylic group to generate a 3D porous polymer. Examination of the NIR luminescence of both systems reveals that both effectively sensitise the Er(III) luminescence.

The dipicolinic acid binding motif and its derivatives have been extensively studied by researchers such as Bünzli, Piguet, Chauvin, and their co-workers, for the purposes of forming highly luminescent supramolecular self-assemblies with Ln(III) ions through the *O-N-O* binding site. Lanthanide ions are chiefly employed in supramolecular chemistry, to exploit their unique photophysical properties. Their narrow emission bands, long luminescence lifetimes and large Stokes' shifts make them excellent probes for applications in biological media.[75–77] However, the low molar absorptivity of the formally forbidden *f-f* electronic transition means that direct excitation of the lanthanide ion is highly inefficient. Thus, the lanthanide excited states are typically accessed *via* indirect population by an energy transfer mechanism from a donor species, known as the "antenna effect", which has been shown to produce bright lanthanide luminescence. Bünzli and co-workers have thoroughly investigated this phenomenon, correlating the relationship between the molecular structure of lanthanide containing assemblies with their resulting photophysical properties. This work has widely featured the pyridine-2,6-dicarboxamide motif and its derivatives, due to its ability to form nine-coordinate complexes, which eliminate deleterious quenching solvent molecules from completing the lanthanide coordination sphere. Their investigations have shown that the donor ligand **dpa** efficiently sensitises Eu(III) and Tb(III) emission, and have subsequently adopted saturated complexes of $Cs_3[Eu.(\mathbf{1})_3]$ and $Cs_3[Tb.(\mathbf{1})_3]$ as
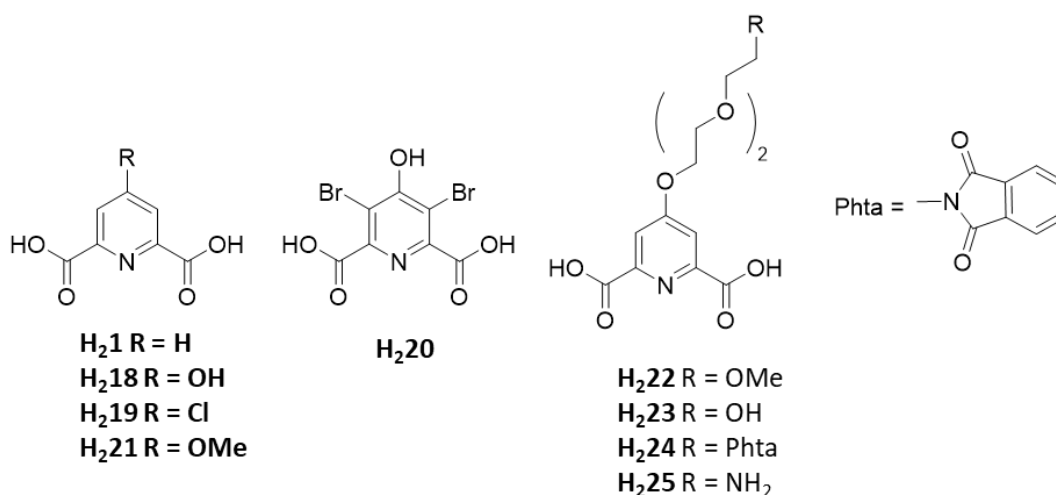
Figure 1.9 Dpa *derivatives, compounds **H₂1** and **H₂18-25***

$H_2$1 R = H
$H_2$18 R = OH
$H_2$19 R = Cl
$H_2$21 R = OMe

$H_2$20

$H_2$22 R = OMe
$H_2$23 R = OH
$H_2$24 R = Phta
$H_2$25 R = NH₂

Phta =

convenient standards for quantum yield determination of Tb(III) and Eu(III) containing lanthanide complexes.[78,79]

George and co-workers have effectively demonstrated the impact functionalisation of the pyridyl ring of the **dpa** can have on its capacity to sensitise Eu(L)₃ (L = **H₂1**, **H₂18**, **H₂19**, **H₂20**) complexes, and subsequently induce emission.[80] Substituents -H, -OH and -Cl were introduced at the 4-pyridyl position and the authors reported lanthanide sensitisation was highest in the case of -Cl, and least with -OH. This was in contrast to a previously reported study with Tb(III) which found the opposite to be the case.[81] Long luminescence lifetimes were observed for Eu(**H₂18**)₃, in the range of 1.2 ms in H_2O to 2.9 ms, in CH_3OH making this system attractive for the development of biological probes.

Gassner has shown that derivatising these simple **dpa** molecules provides the potential for coupling of these systems onto biological molecules. For example, grafting polyoxyethylenyl groups onto the back of the pyridine ring with various different terminal groups generates ligands **H₂22–25**.[24] These ligands were observed to sensitise Eu(III) and, to a lesser extent Tb(III), with luminescence and quantum yield tuning found to be dependent on the terminal substituent; in the case of Eu(III), complexes exhibited quantum yields ranging from 13 and 30% in H_2O.

One area of interest for lanthanide chelates is that of molecular imaging. Of these lanthanides, gadolinium complexes are particularly attractive for use as magnetic resonance imaging (MRI) contrast agents. Muller and Parac-Vogt have reported a novel synthetic strategy for the incorporation of two different lanthanide ions into one heterometallic complex, with a view to combining the luminescence properties from Eu(III) with the MRI active properties of Gd(III).[82] A second binding motif diethylenetriaminepentaacetic acid
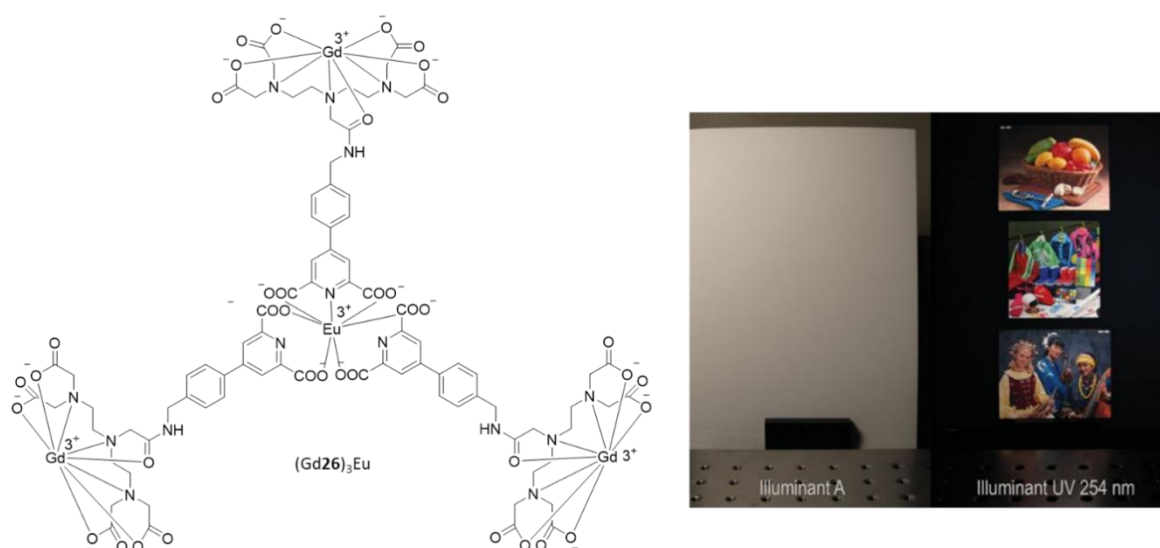
Figure 1.10 *Structure of (Gd**26**)₃Eu synthesised for use as MRI agent and photographs printed with Eu**1**₃ and Tb**1**₃ luminescent ink under ambient light (left) and under UV light (right). Reproduced from Ref. 82.*

(DTPA) was introduced to the **dpa** ligand in order to facilitate this. Sequential deprotection of the ditopic ligand allows for site selective coordination of the distinct lanthanide ions, resulting in the bimetallic complex (Gd**26**)₃Eu which could be considered as a bimodal imaging/MRI agent in the future.

Recently, Chauvin and co-workers reported the use of these europium and terbium trisdipicolinate complexes along with a commercially available blue ink Firefly™ (Vermont Photoinkjet, LLC) for inkjet printing onto paper.[83] Compounds Eu**1**₃ and Tb**1**₃ act as anti-counterfeit ink which are invisible under ambient light but appear luminescent under 254 nm UV irradiation producing full colour images (Figure 1.10).

The extraction of heavy metal cations is a challenge which is currently under investigation by many research groups due to the limitations of current techniques for radioactive waste management of radiopharmaceuticals. Chauvin, in collaboration with Bochud and Froidevaux, have responded to this deficit, developing **dpa** ligands **H27** and **28**
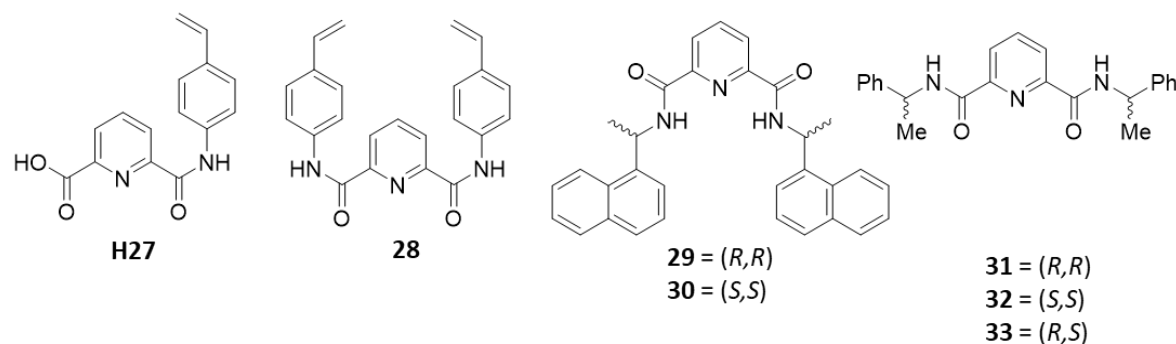
Figure 1.11 *Compounds **H27** and **28** synthesised for the generation of ion-imprinted polystyrene resins for Y(III) extraction and compounds **29**–**33**, chiral dpa derivatives.*

13

functionalised with a styrene moiety which was complexed with yttrium (Y(III)) to form complexes Y(**27**)$_3$ and Y(**28**)$_3$(ClO$_4$)$_3$.[84] These were incorporated into polymers produced from reactions in the presence of divinylbenzene, allyl alcohol and azobis(isobutyronitrile). The yttrium ions could then be extracted after polymerisation, giving an ion-imprinted resin. Eu(III) luminescence was employed to investigate the local lanthanide coordination environment within the polymer, with the $^5D_0 \rightarrow {}^7F_{1,2,3}$ transitions used to identify D$_2$ and D$_3$ symmetry of the model complexes [Eu.(**27**)$_3$] and [Eu.(**28**)$_3$]$^{3+}$, respectively. The resin exhibited selectivity for Y(III) and heavy Ln(III) ions over Ca^{2+}, Sr^{2+} and K$^+$.

In solution, 3:1 **dpa**:Ln assemblies exist as racemic mixtures of Λ and Δ helices, and this inherent chirality has proved to be an advantageous property for selective molecular recognition of chiral biological substrates.[85] Optically active molecules, such as amino acids or sugar derivatives,[28,86] induce chirality in the racemic **dpa** mixture, influencing the optical rotation in a phenomenon known as the "Pfeiffer effect".[87] With this in mind, Gunnlaugsson and co-workers in parallel with Muller and co-workers, have modified the **dpa** motif with chiral chromophores, synthesising ligands **29**, **30** and **31**–**33** respectively.[88,89] These ligands were reported to efficiently sensitise visible and NIR emitting lanthanides, and all exhibited circularly polarised luminescence (CPL). Monitoring the $^5D_0 \rightarrow {}^7F_{1,2,3}$ transitions for the Eu(III) complexes by CPL revealed mirror image CPL spectra for each set of enantiomers, indicating that the metal ion is residing in a chiral environment. Mullers discovery that [Eu(**L**)$_3$]$^{3+}$ (L = **31**, **32**) generated stable optical isomers, with CPL activity which remained constant over time has led to this system being proposed as a CPL calibration standard.[25,89] X-ray crystal structures obtained for these tris complexes with [Ln(**29**)$_3$]$^{3+}$ (Ln = Eu(III),

34 (*R,R*) R = a   **41** (*S,S*) R = c
35 (*S,S*) R = a   **42** (*R,R*) R = d
38 (*R,R*) R = b   **43** (*S,S*) R = d
39 (*S,S*) R = b   **44** (*R,R*) R = e
40 (*R,R*) R = c   **45** (*S,S*) R = e

36 (*R,R,R*)
37 (*S,S,S*)
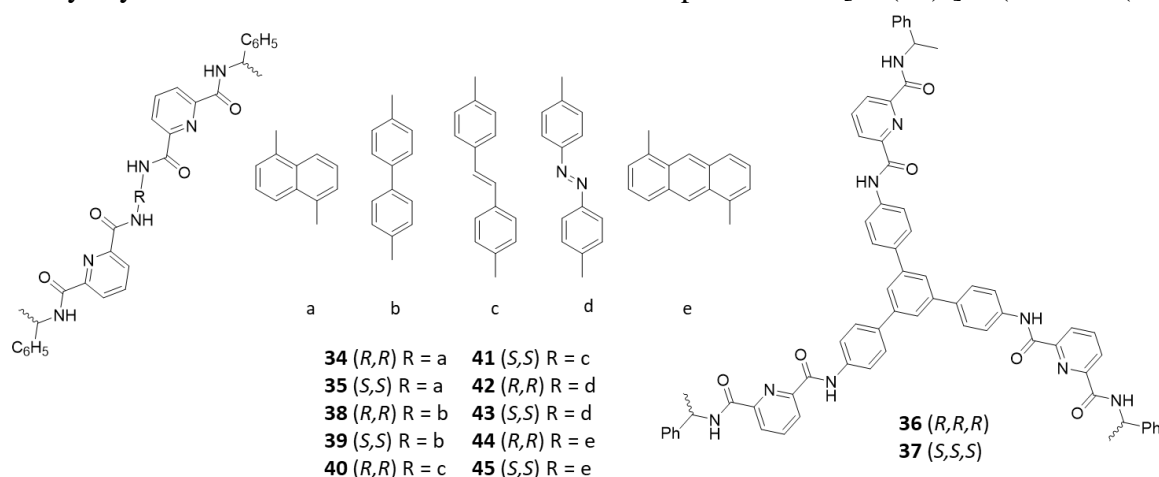
***Figure 1.12** Compounds **34**–**45** synthesised for the formation of cages, helicates and other higher order supramolecular structures.*

14

Tb(III), Sm(III)) and [Nd(**30**)$_3$]$^{3+}$ were all isostructural. The **dpa** motif has been extensively studied by the Gunnlaugsson group and will be discussed further in Section 1.3 below.

The bis(terdendate) and tris(terdendate) compounds **34, 35** and **36, 37** have been developed by Bünzli and Sun for the formation of luminescent lanthanide tetrahedral cages.[90] Eu$_4$(**34**)$_6$, Eu$_4$(**35**)$_6$, Eu$_4$(**36**)$_4$, and Eu$_4$(**37**)$_4$ formed edge and face-capped assemblies respectively with the ligand chirality transferred to the complexes, yielding ΛΛΛΛ or ΔΔΔΔ stereochemical centre at the metal site. X-ray crystallography, NMR spectroscopy and circular dichroism spectrometry (CD) confirmed this homochirality. Furthermore, upon addition of a 1:1 mixture of **34** and **36** to Eu(III) in solution, self-sorting behaviour was observed; the two ligands could discriminate each other, and thus, over time the only complexes generated were Eu$_4$(**34**)$_6$ and Eu$_4$(**36**)$_4$. Moreover, discrimination occurs between *R* and *S* enantiomers **36** and **37**, which also lead to the formation of homoligand chiral cages ΔΔΔΔ–Eu$_4$(**36**)$_4$ and ΛΛΛΛ–Eu$_4$(**37**)$_4$ as a racemic mixture. Following on from this work, the authors reported a study on the effect of altering the length of the chelating arms of ligand **34**. Their results show that this distance is crucial to the final outcome of the lanthanide assembly, with the alterations resulting in structures ranging from Ln$_2$L$_3$ helicates and Ln$_4$L$_6$ tetrahedra to Ln$_8$L$_{12}$ cubes (L = **38–45**).[91] Compound **42**, with an extended central linker, formed the triple-stranded helicate Eu$_2$(**42**)$_3$ upon reaction with Eu(III), while changing only one atom in the spacer sequence, yielding compound **40**, resulted in a mixture of the tetrahedral complex Eu$_4$(**40**)$_6$ and the helicate Eu$_2$(**40**)$_3$. Altering the central spacer to an anthracene moiety resulted in the formation of the triple stranded helicate Eu$_2$(**45**)$_3$, which subsequently transformed to the cubic assembly Eu$_8$(**45**)$_{12}$ during crystallisation. More recently, the authors have shown that these tetrahedral cages can be generated with other metal ions such as Ca(II), Cd(II) and other lanthanide metal ions.[92] All of the cages were found to be stable in the presence of excess metal ions, and self-sorting behaviour was observed in mixed metal environments. Finally, these cages have shown promise for lanthanide separation using liquid-liquid extraction techniques.

With regard to the pyridine-2,6-dicarboxylic acid ligands and their derivatives discussed in this section, it is clear that a wide range of supramolecular self-assemblies are possible. Careful design of these systems, considering ligand functionalisation, chirality, metal coordination geometry, solvent, and metal:ligand stoichiometry allows for precise control over the supramolecular self-assembly process and the subsequent architectures generated. In particular, the choice of metal centre greatly influences not only the

coordination geometry, but also the photophysical properties of the systems, and thus allows for the design of functional supramolecular assemblies with specific desirable properties. While pyridine-2,6-dicarboxamide benefits from ease of functionalisation *via* substitution at the amide group, a frequently employed alternative method of introduce functionalities to these systems has focused on introducing functional triazoles using "click" chemistry. This will be discussed in the following section.

1.1.3 The 1,2,3-triazole

While the synthesis of 1,2,3-triazoles from the azide-alkyne 1,3-dipolar cycloaddition reaction has been known since the early 1890s, it was only in 2002, with the report of the highly efficient copper (I)-catalysed 1,3-dipolar azide-alkyne cycloaddition (CuAAC)[93,94] reaction, that the synthesis and use of 1,2,3-triazoles for a vast array of applications has been explored. The 1,3-Huisgen reaction was previously described as the "cream of the crop" of "click" reactions; however, this reaction was inhibited by non-selective formation of both the 1,4- and 1,5-substituted 1,2,3-triazoles. This deleterious drawback has since been overcome by the CuAAC reaction which is high yielding, requires only mild reaction conditions, and crucially, is regioselective.[95,96] Of particular advantage to the CuAAC reaction is the ease with which the requisite azides and alkynes, with a vast array of functionalities, can be introduced into organic compounds; the azide precursors are easily synthesised by reaction of organic halides with sodium azide, or from primary amines with the use of a simple catalyst (imidazole-1-sulfonyl azide hydrochloride), while the alkyne
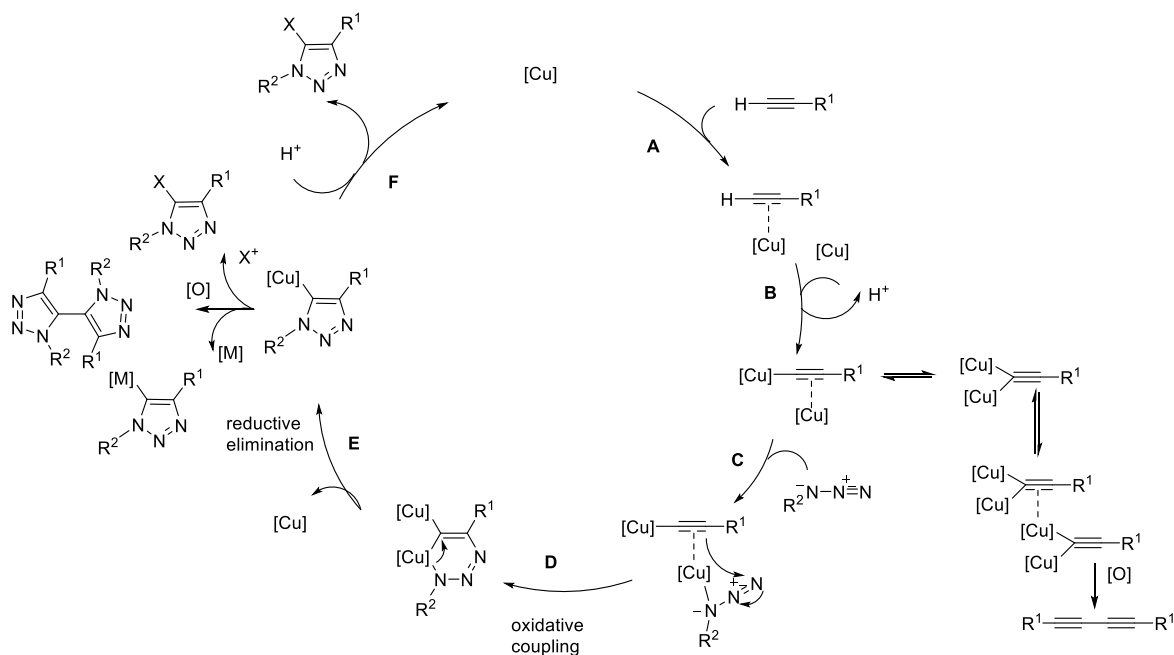
Figure 1.3 *Proposed mechanism for the formation of the 1,2,3-triazole proposed by Schulze and Schubert.*

16

precursors are readily generated using palladium-catalysed Sonogashira coupling reactions. Another advantage of the CuAAC reaction is that is can be conducted in aqueous media, which is cheap and environmentally benign.

A mechanism for the reaction was proposed in 2005 by Sharpless *et al.* with the use of computational studies,[97] and was further developed by Schulze and Schubert in 2014.[98] The rate limiting step may provide evidence for the regioselectivity of the 1,4-isomer, where the nucleophilic attack of the β-carbon to the terminal electrophilic nitrogen is believed to be directed by the Cu(I)-π coordination at the α-carbon.

While the 1,2,3-triazole has been widely used as a versatile synthetic linker, to join building blocks, it has also been explored in a wide array of applications which are continuing to be developed and go beyond the use of click chemistry as a functionalisation method including anion binding,[43] metal coordination,[40,95] and catalysis.[41,42] It bears a physiochemical resemblance to the amide functional group due to the relative planarity of triazoles, and their strong dipole moments, which favour its involvement as a linker in biological, biochemical and carbohydrate research.[99] The 1,2,3-triazole can also be utilised for its coordinating properties for a wide range of applications, from metal ion sensing and catalysis, to biochemical and medicinal chemistry applications. However, until work by Schibli and co-workers, which described the installation of a triazole metal chelation site into molecules using a single step CuAAC reaction, there were surprisingly few examples of click chemistry being used to generate ligands based on 1,2,3-triazoles.[100] Since this work, research efforts utilising 1,2,3-triazoles as chelating moieties have garnered significant interest. Among these, pyridyl-triazoles, the archetype of which is 2,6-bis(1,2,3-triazol-4-yl)pyridine (**btp**), are among the most widely explored. These will be the focus of the following section.

1.1.4 2,6-Bis(1,2,3-triazol-4-yl)pyridine

The **btp** motif was first synthesised and reported by Fokin and co-workers in 2004 using the CuAAC reaction. They synthesised **btp** as one of a series of triazole containing ligands, in order to stabilise the thermodynamically unstable Cu(I) species of the same reaction, thus enhancing the rate of the reaction.[101] While tris-(benzyltriazolylmethyl)amine (TBTA) proved the most efficient at stabilising the Cu(I) species when compared to the library of other triazole containing compounds, **btp** has been employed since then for a wide range of applications which will be discussed in detail below. However, as the **btp** motif and its

17
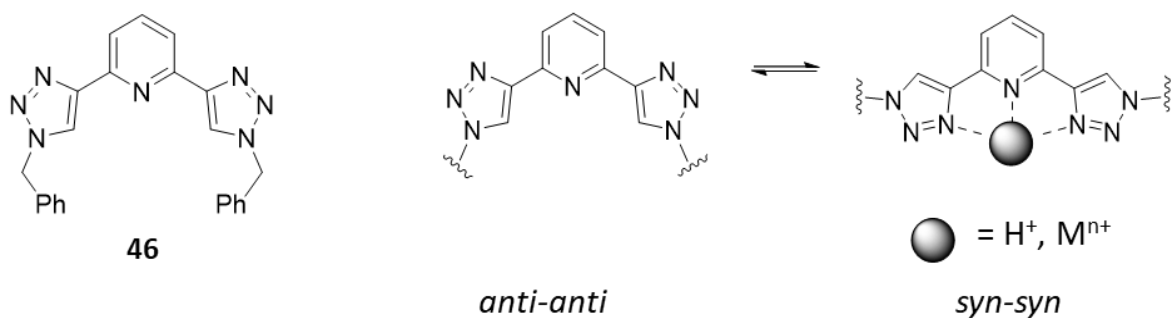
Figure 1.14 Compound **46** and a schematic representation of the conformational switching of the **btp** triazoles.

coordination chemistry has been recently reviewed at length in 2014 by Byrne and Gunnlaugsson,[40] in the interest of conciseness a review of the most relevant and more recent **btp** advances will be detailed here.

It has been widely reported that **btp** can adopt various conformations due to the free rotation about the C-C bond between the pyridine and the triazole moieties. The free ligand has been shown through X-ray crystallography to adopt an *anti-anti* conformation with respect to the pyridyl nitrogen.[102–105] This is believed to be the dominant conformation as it minimises repulsion between the nitrogen lone pairs. Nuclear Overhauser effect (NOE) NMR measurements were used to demonstrate this conformation was also prevalent in solution, with no interaction observed between the triazole and pyridyl protons. Upon protonation, however, medium strength intramolecular hydrogen bonding interactions are observed, indicating a conformational switching to the *syn-syn* form. This is also observed upon the introduction of other cations or metal ions.[95] This has been repeatedly confirmed by single crystal X-ray diffraction of various **btp** metal complexes.[40]

Flood and co-workers were the first to report *d-* and *f-*metal complexes of the **btp** motif. They reported the synthesis of **btp** ligands **47** and **48**, and investigated their interactions with Fe(II), Ru(II) and Eu(III).[106] The [Fe(**47**)$_2$]·2PF$_6$, [Ru(**47**)$_2$]·2PF$_6$ and [Eu(**48**)$_3$]·3ClO$_4$ metal complexes were isolated in high yields and X-ray quality crystals
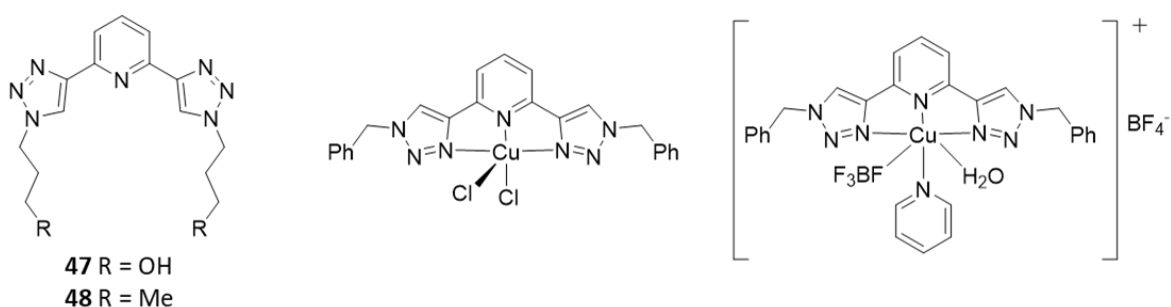
Figure 1.15 Compounds **47** and **48** as well as Cu(II) complexes [Cu(**46**)Cl$_2$] and [Cu(**46**)$_2$(BF$_4$)(py)(H$_2$O)]BF$_4$
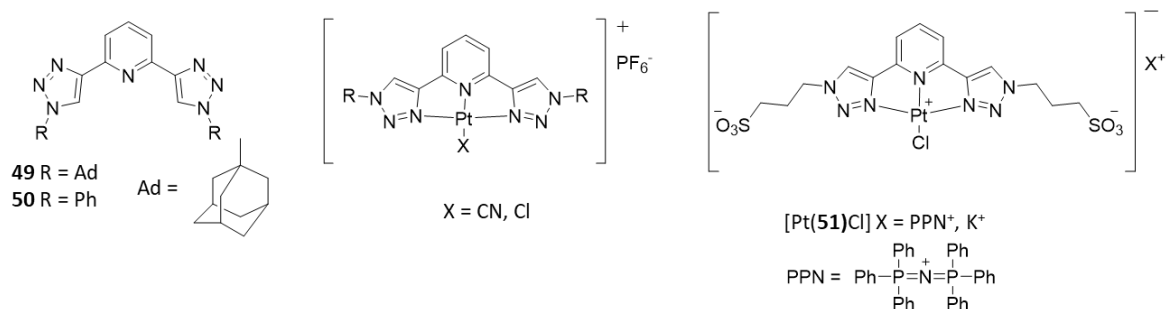
*Figure 1.16 Compounds **49**–**51** synthesised for the generation of luminescent Pt(II) complexes.*

obtained, with coordination to each metal occurring in a terdentate fashion through the two triazole N atoms and one pyridine N of each ligand.

Due to the d^{10} electronic configuration of Ag(I), silver complexes tend to be labile and can exhibit a wide range of coordination numbers, from two to six, can be accommodated, resulting in a large variety of coordination geometries.[107] This makes it an attractive metal for the formation of metallosupramolecular architectures. Efforts by Crowley and co-workers to isolate **btp** complexes coordinated to Ag(I) have been fruitful, with the structure of an intertwined tetrameric architecture reported, where each ligand **46** is coordinated to three of the four available Ag(I) ions.[102] The Ag(I) ions adopt a distorted tetrahedral coordination geometry, with each metal coordinating to various pyridyl and triazole nitrogen atoms. This species was confirmed to be present in solution through ^{1}H NMR studies, although the X-ray crystallographic data was not sufficient for more than the connectivity to be determined. The authors also reported the synthesis of the **btp** Cu(II) complex [Cu(**46**)Cl$_2$], where the metal centre adopts a distorted square pyramidal geometry.[102] The coordination sphere is composed of three N atoms, two N donors from the triazole rings and one pyridyl N, and is completed by two chloride ligands.

Other Cu(II) complexes of **46** include a report by Danielraj *et al.* of the X-ray crystal structure of the complex [Cu(**46**)$_2$(BF$_4$)(py)(H$_2$O)]BF$_4$ in which the triazole rings adopt the *syn-syn* conformation to accommodate the distorted octahedral geometry about the Cu(II) ion, as well as the free ligand **46** where the triazole rings were in the *anti-anti* conformation.[108] H$_2$O–BF$_4$ hydrogen bonds stabilise the overall structure. The authors reported a quenching of the ligand fluorescence upon complexation to the metal ion.

De Cola and co-workers reported the synthesis of two **btp** derivatives functionalised with a bulky adamantyl group (ligand **49**) and planar phenyl groups (ligand **50**).[109] They synthesised Pt(II) complexes from these ligands in good to moderate yields and single crystals suitable for X-ray diffraction studies of [**49**(Pt)(CN)], [**49**(Pt)(Cl)], and [**50**(Pt)(Cl)]

were obtained, unequivocally determining the molecular structure. The authors observed that, due to its much stronger ligand field effect, that upon changing the ancillary ligand from chloride to cyanide, the luminescence is switched on at room temperature. When the ancillary ligand is Cl⁻ changing from the bulky adamantyl group [**49**(Pt)(Cl)], to the planar phenyl group [**50**(Pt)(Cl)] gives rise to changes in the crystal packing. The bulky nature of the adamantyl groups results in no Pt(II)-Pt(II) interactions, while in the case of the phenyl substituents, coupling between neighbouring complexes was seen. However, when the CN⁻ ligand is employed, Pt(II)-Pt(II) interactions are induced irrespective of the bulky nature of the ligand functionalisation due to the π-accepting nature of the CN⁻ ancillary ligand.

Btp–Pt(II) complexes have been further explored by Yam *et al.* who reported supramolecular architectures stemming from a combination of π-π stacking and Pt(II)-Pt(II) interactions.[110] The self-assembly of the complex bearing the amphiphilic ligand **51** can be controlled by altering the solvent composition, promoting aggregation and disaggregation which lead to both significant morphological and spectroscopic changes, driven by the variation in platinum-platinum intermolecular distance. This results in interesting vapochromic and vapoluminescent properties exhibited by these complexes. Exposure, in the solid state, of complex [Pt(**51**)Cl]PPN to methanol results in a drastic colour change from orange to violet with a concomitant red shift observed in the visible absorption spectrum and a red-shift in the emission spectrum from 614 to 672 nm. Surprisingly, removal of the
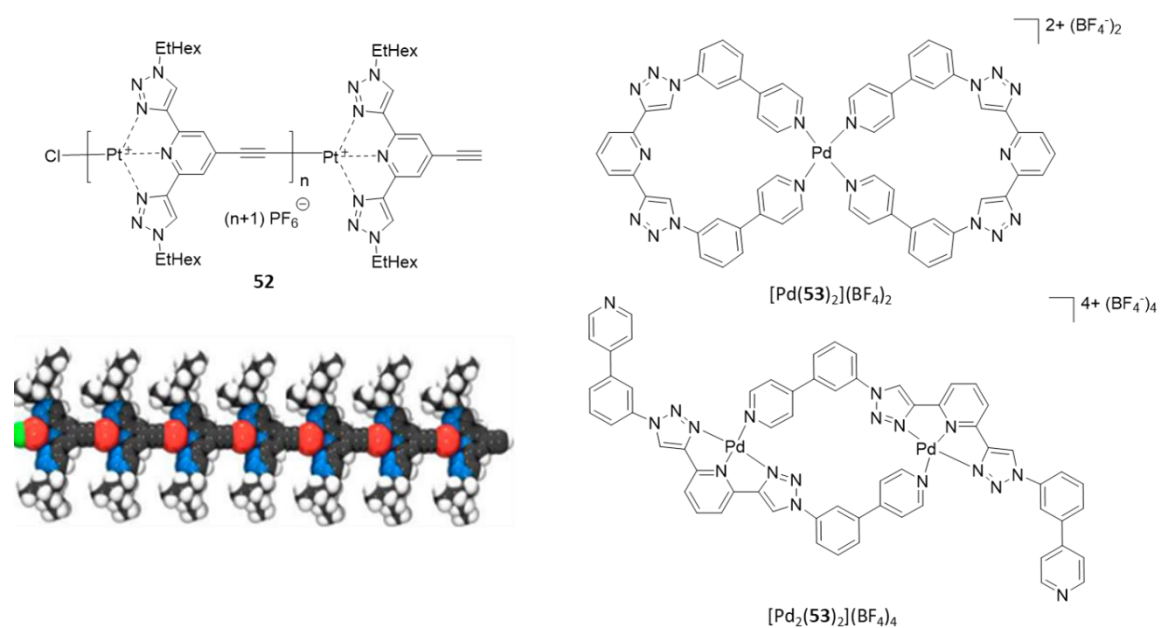
Figure 1.17 *Pt(II)-Polymer **52** and compound **53** for the self-assembly of Pd(II)monomer [Pd(**53**)$_2$](BF$_4$)$_2$ and dimer [Pd$_2$(**53**)$_2$](BF$_4$)$_4$. Reproduced from Ref 112.*

methanol vapor induced a further change in colour to blue-violet and shift in the emission to 700 nm which could then be converted back to orange upon exposure to water vapor. A thin film was prepared on a quartz slide and rapid colour change from orange to violet was again observed and could be returned to the blue-violet state upon purging with dry nitrogen or under vacuum. The authors expect this system to have potential in areas such as chemo sensing, logic gates and volatile organic compound (VOC) monitoring. A memory device was also generated using [Pt(**51**)Cl]PPN as the active material which exhibited stable binary memory performance with long retention times of over 10^4 seconds.

A Pt(II)-**btp** supramolecular polymer **52** which is soluble in common organic solvents was generated by Schulze and co-workers.[111] Previous examples in the area of Pt(II) polymers have suffered from low solubility due to the propensity of such complexes to stack, which complicates the synthesis. This system, by contrast, was highly soluble and thus suitable for thin film deposition by spin-coating. Its solid-state emission properties made it a favourable candidate for using in optoelectronic devices.

Recently Preston and Kruger reported a new **btp**-ligand **53** with two pendant monodentate pyridyl arms.[112] The two potential binding sites were exploited in order to generate both a "figure-of-eight" complex [Pd(**53**)$_2$](BF$_4$)$_2$, and a [Pd$_2$(**53**)$_2$](BF$_4$)$_4$ dimer, which were both characterised by NMR spectroscopies and electrospray ionisation mass spectrometry (ESI-MS). At a 2:1 ratio of **53**:Pd(II), the ^{1}H NMR and ^{1}H DOSY NMR spectra indicated the formation of the symmetrical [Pd(**53**)$_2$](BF$_4$)$_2$ assembly. In this case, the central terdentate binding pocket is unoccupied, while the Pd centre is coordinated by four pendant pyridyl N atoms. The addition of a further equivalent of Pd(II) however, lead to the formation of a dimeric complex where the central terdentate pocket is coordinated to the metal centre. NOESY revealed site-specific self-recognition between dimers in solution which can be turned on and off by altering the Pd(II) to ligand stociometry in solution.

Schmollinger *et al.* reported the glycosylation of **btp** to produce, among other ligands, **54** and **55**,[113] which they have used to synthesise a variety of Ru(II) and Pd(II) complexes.[114] The authors speculate that these complexes have promise as chiral catalysts which could be used for enantioselective synthesis.
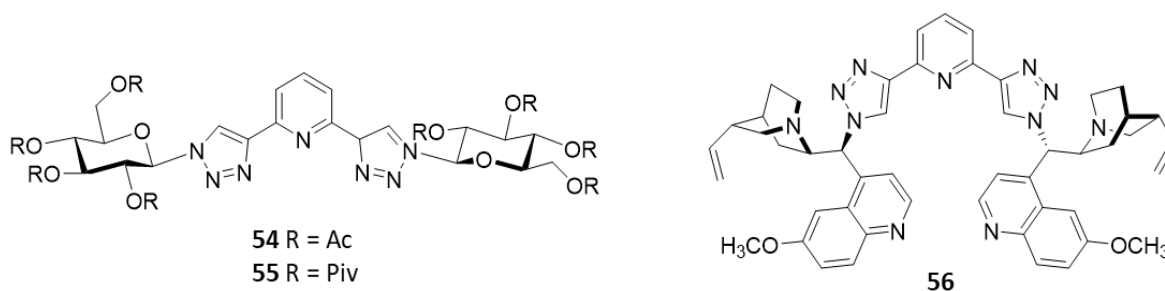
Figure 1.18 *Compounds **54**, **55** and **56** synthesised to investigate their efficacy as chiral catalysts.*

The CuAAC reaction has also been utilised to synthesis a **btp** ligand derived from cinchona alkaloids. The authors investigated whether the chirality of this ligand enabled it to act as an effective ligand for asymmetric copper-catalysed Michael additions.[115] However, it was shown that compounds with a bi-triazole linker were more effective in transfer of chirality than the **btp** derivative **56**. This same ligand was reported to form a Cu(II) complex which was confirmed by high resolution mass spectrometry (HRMS).[116] However, it was not demonstrated whether metal coordination occurred at the terdentate **btp** binding site or the quinoline cinchona ligand component..

As mentioned in Section 1.1 above, lanthanides have been widely explored in the area of supramolecular chemistry due to their unique photophysical and magnetic properties,[23,28,117–119] making them attractive candidates for biological imaging and sensing applications.[23,28,29] In addition, their long-lived excited states, line-like emission bands, and high coordination numbers make them candidates of interest for the formation of supramolecular metallostructures. Flood *et al.* were the first to demonstrate that **btp** ligand **48** could form a stable coordination complex with Eu(III) using X-ray crystallography. It was observed that three ligands were employed to fulfil the high coordination requirement of Eu(III) giving the complex [Eu(**48**)$_3$](ClO$_4$)$_3$. The ligand was shown to sensitise Eu(III), with the complex exhibiting the characteristic Eu(III) red emission upon excitation of the ligand with UV-light. Hecht and co-workers have reported similar **btp**-Eu(III) crystal structures [Eu(**57**)$_3$](CF$_3$SO$_3$)$_3$ and [Eu(**58**)$_3$](CF$_3$SO$_3$)$_3$ where the **btp** is functionalised at the 4-pyridyl position.[95]

The 4-pyridyl position of the **btp** has also been functionalised by Chandrassekar *et al.* who have reported the synthesis of a series of dimeric bis-**btp** systems (**59**-**61**) as well as their self-assembly with Eu(III).[120] The π-conjugated **btp** systems, upon complexation with Eu(III), precipitated as white powders and the appearance of the characteristic *f-f* transitions

22
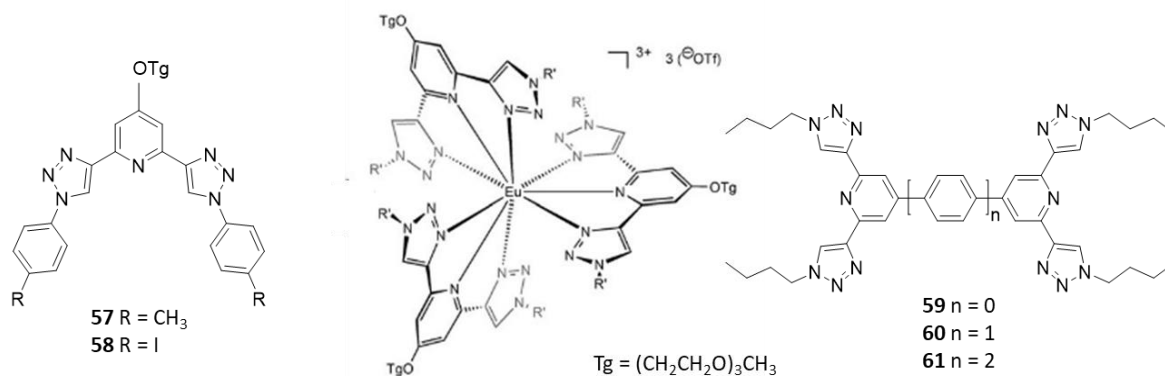
Figure 1.19 *Compounds **57** and **58**, structure of [Eu(**57**)$_3$](CF$_3$SO$_3$)$_3$ or [Eu(**58**)$_3$](CF$_3$SO$_3$)$_3$ and back-to-back compounds **59**–**61**.*

of Eu(III) in the emission spectrum indicated successful sensitisation of the metal centre by the ligand antenna.

Non-covalent, supramolecular interactions such as hydrogen bonding, π-π stacking and metal-ligand interactions have increasingly been of interest for use in the formation of soft-materials due to the labile nature of these interactions. In particular, metallo-supramolecular gels have garnered interest as they can exhibit the properties of the metal ion and may also lead to gels of a more robust nature. Weng and co-workers have reported the construction of a number of **btp** polymers,[121] such as **62** and **63**, which form metallo-supramolecular gels upon coordination with Zn(II) and Eu(III). Macromolecule **62** was synthesised *via* incorporating a bis-propene functionalised **btp** ligand into a bis-isocyanate prepolymer resulting in approximately 12 **btp** molecules per single polymer backbone. The gel properties can be tuned by altering the stoichiometric ratio of the metal ions, solvent or concentration. The gels showed repeatable self-healing as well as thermo- and chemo-responsiveness. A combination of gels of different metal ions were also found to be self-healing when placed together. This provides evidence for the dynamic nature of the self-healing of these metallo-supramolecular polymers.
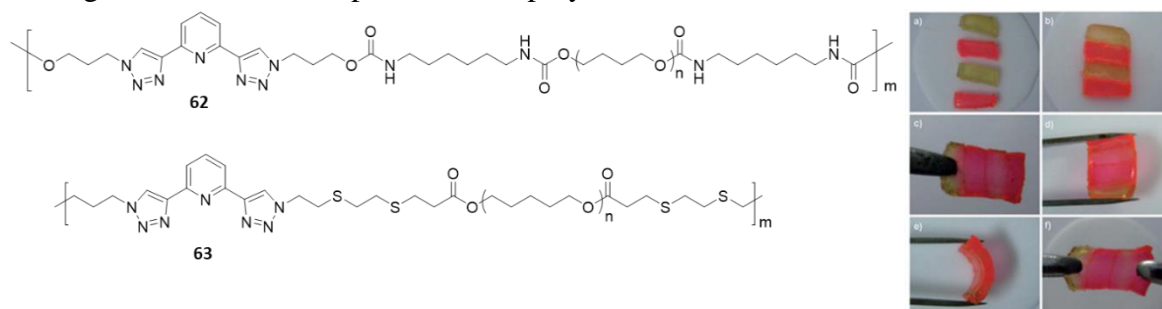
Figure 1.20 *Structure of polymers **62** and **63** as well as images to demonstrate the self-healing nature of the metallo-supramolecular polymers. Reproduced from Ref 121.*

More recently the authors have extended this work to a similar system that utilises more robust thiol-ene chemistry, eliminating the moisture sensitivity of the polyurethane reaction.[16] Using Zn(II), Eu(III) and Tb(III) metals, gels could be readily formed from polymer **63** as before, and solid films can also be obtained by casting the gel in Teflon casters and drying. The mechanical properties of the films could be tuned by modulating the stoichiometric ratio of the three metal ions, with the Zn(II) containing films unfolding the largest tensile modulus at small strain, the Eu(III) containing film can be extended further than the other samples, and the Tb(III) films display the highest tensile strength values at larger strain. Similarly to their previous reports, these systems were capable of fast self-healing and the gel demonstrated thermodynamic stability but was kinetically labile which makes a suitable system for where a fast response is required.

Gunnlaugsson[122,123] has also reported the formation of both polymer films and metallogels with **btp** derivatives incorporating Eu(III) and Tb(III) for sensing and materials applications. These as well as other contributions by Gunnlaugsson to this area of **btp**-lanthanide self-assembly will be discussed in Section 1.3 below.

A particular area of interest in recent years is in the design of ligands which discriminate lanthanides and actinides for solvent extraction processes used in the removal of actinides (An). Actinides like neptunium, plutonium, americium and, curium are of particular interest due to their production during nuclear reactor operation from neutron

47   **64**   **65**   **66**

67 R = C$_8$H$_{17}$
68 R = C$_{12}$H$_{25}$
70 R = C$_7$H$_{14}$COOH

69
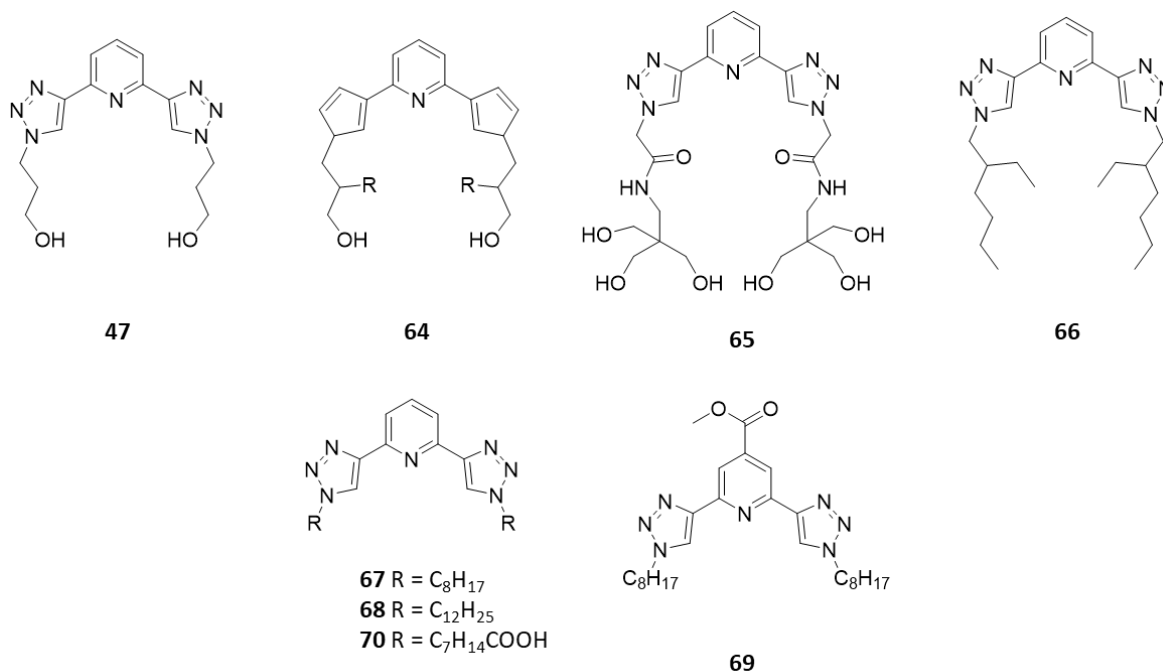
Figure 1.21 *Compounds **47** and **64**–**70** synthesised for the separation of actinides and lanthanides by liquid-liquid extraction methods.*

capture by uranium-235/238. Recycling of nuclear fuel, and ultimately closing the nuclear fuel cycle, is considered one of the most promising ways to reduce nuclear waste into the future but this requires reliable actinide separation processes.[124,125] The specific challenge is separating americium and curium from fission lanthanides as both are present as trivalent cations and have similar size. Some progress has been made in the use of soft N-donor ligands which have been shown to have a stronger binding affinity for actinides over the lanthanides leading to good selectivity.[126] However, their binding affinity is often hindered under acidic conditions due to the basic nature of the nitrogen atoms.

Wagner and Macerata have reported the use of a **btp** ligand functionalised at the N1 nitrogen of the triazole with various hydrophilic groups for the selective extraction of actinides from an actinide/lanthanide mixture. Investigation of the efficiency of ligands **47**, **64**, and **65** in liquid-liquid extraction conditions revealed the higher binding affinity of each of the ligands for Am(III) over Eu(III). In the case of ligand **47**, the concentration of Am(III) was reduced in the organic phase to 14% from 94% while Eu(III) only saw a 2% decrease.[127] Selectivity was also observed for Cm(III) and Pu(IV), indicating that the ligands are capable of selective extraction of actinides in multiple oxidation states. The process was found to be reversible where cations were released from the ligands by re-extraction. Ligand **47** outperformed ligands **64** and **65** despite ligand **65**'s higher water solubility and so ligand **47** was selected to progress by the authors to the next study. Am(III) was replaced by Cm(III) in this report due to its excellent photophysical properties which allowed for the examination of the system using time resolved laser fluorescence spectroscopy (TRLFS).[128] Investigation to determine the optimal extraction conditions were carried out and both the ionic strength and H^+ concentration were found to play large roles in determining the stability constants of Cm(III) with ligand **47**. Increasing the ionic strength while decreasing the H^+ concentration, were found to stabilise the $[Cm(47)_3]^{3+}$ species, facilitating the extraction process. Moving towards the conditions required for extraction experiments, results in a decrease in the stability by four orders of magnitude. Following on from this work, the authors have shown that this **btp**-diol **47** is the first carbon, hydrogen, oxygen, nitrogen (CHON) compliant coordinating ligand suitable for industrial processes since it can achieve An/Ln separation in a centrifugal contactor device.[129]

Having explored the hydrophilic derivatives of **btp** the authors then functionalised the **btp** core with lipophilic chains of different lengths and polarities yielding ligands **66-70**.[130] Ligand **66** was found to have the highest extraction efficiency and selectivity, in some cases reaching 80% due to its higher solubility when compared to **67-70**. The promising
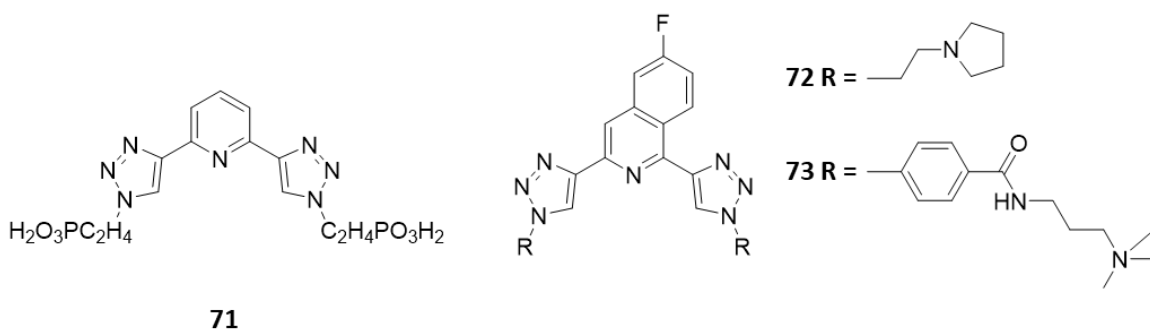
Figure 1.22 *Compound **71** synthesised for solid phase separation of lanthanides and actinides and compounds **72** and **73**, fluoroisoquioline derivatives of **btp**.*

extraction properties of **66** make it a compound worth investigating for possible industrial applications.

The use of solid phase materials for the purpose of separating actinides and lanthanides is also an area which is gaining interest stemming from the need to reduce the use of organic solvents.[126] Taking inspiration from the work of Macerata *et al.* described above,[127] where they successfully separated transuranium elements (TRUs) from lanthanides using a propan-1-ol-funcationalised-**btp**, Veliseck-Carolan and Rawal utilised the **btp** ligand for functionalisation of a solid phase material, reacting phosphonate derived **btp 71** with ZrCl$_4$ to form a Zr-**btp** phosphonate material.[131] This material was characterised, and its separating efficiency analysed. Even in a competitive environment where excess Eu(III) was present, selective Am(III) sorption was seen. While this system was not as efficient as some solvent-extraction methods which have been reported, it was the first instance of a solid phase sorbent material which was capable of selective Am(III) extraction in the presence of excess Ln(III).

Other interesting applications of the **btp** motif include work by Maiti and Dash to selectively target human telomeric G-quadruplex and inhibit telomerase activity, arresting cancer cell growth.[132] New **btp**-based ligands **72** and **73** were designed as an isoquinoline derivative, with the CuAAC reaction conditions allowing for ease of functionalisation of the fluoro-isoquinoline.

While much work has been conducted examining the metal-coordination of **btp** derivatives, the compound has also been shown to be an effective motif for binding anions. For example, Flood *et al.* have utilised this property to generate higher order structures: incorporating the **btp** binding motif into an aryl-triazole foldamer in the presence of chloride ions stabilises the anions.[133] The assembly exhibits CH-Cl⁻ hydrogen bonding interactions, as well as π-π stacking and ion-dipole interactions which combine to stabilise a 1:1 single

helix which can be transformed to a 2:2 double helix (see Figure 1.23) by changes in solvent polarity and temperature. The triazoles within the structure serve as both linkers between the aryl substituents and also act as the principal hydrogen bonding residues to stabilise the chloride ions. The authors expect this 2:2 double helix to aid in the understanding of how, by designing the primary sequence of abiological polymers, we can control the structure and resultant functions of the secondary structure.

Byrne, Gunnlaugsson and co-workers have also demonstrated the **btp** motifs anion binding capabilities.[13] They reported the synthesis of a **btp**-catenane **75** which shows pronounced selectively for the phosphate anion through triazole hydrogen-bonding interactions. This was the first example reported in literature of a selective [2]catenane host for phosphate. X-ray crystallography provides the structure for both the [2]catenane and the macrocycle, demonstrating that these self-templated systems are driven by hydrogen bonding interactions that are not amide based.

Other interlocked systems in which **btp** has been implicated have been developed by Goldup *et al.* They reported the formation of 2,2'-bipyridine macrocycles which were converted into rotaxanes with the use of the CuAAC conditions and finally extended to the production of Sauvage-type molecular shuttles (Figure 1.24).[134] The macrocycle was observed to alternate between binding sites, preferentially binding at the bidentate monotriazolepyridine site upon addition of Cu(I), and upon addition of Zn(II), the macrocycle occupied the **btp** terdentate binding site. More recently the authors reported the synthesis of a series of catenanes *via* the active template approach in high yields (71-72%), two of which were based on the **btp** motif.[14] Both structures were confirmed by single crystal X-ray diffraction.

74   **75**
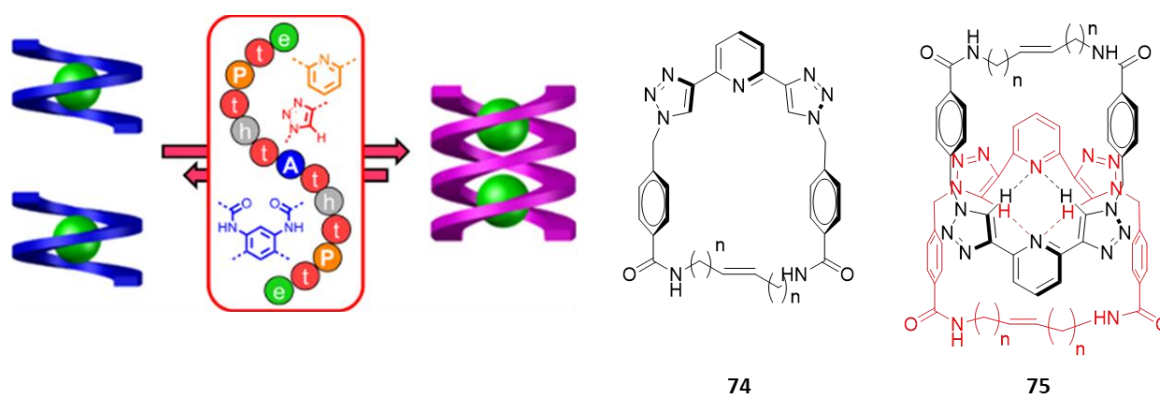
Figure 1.23 Schematic representation of 1:1 and 2:2 helices generated by Flood and co-workers and macrocycle 74 and [2]catenane 75 reported by Gunnlaugsson which shows selectivity for phosphate anions. Reproduced from Ref 133.
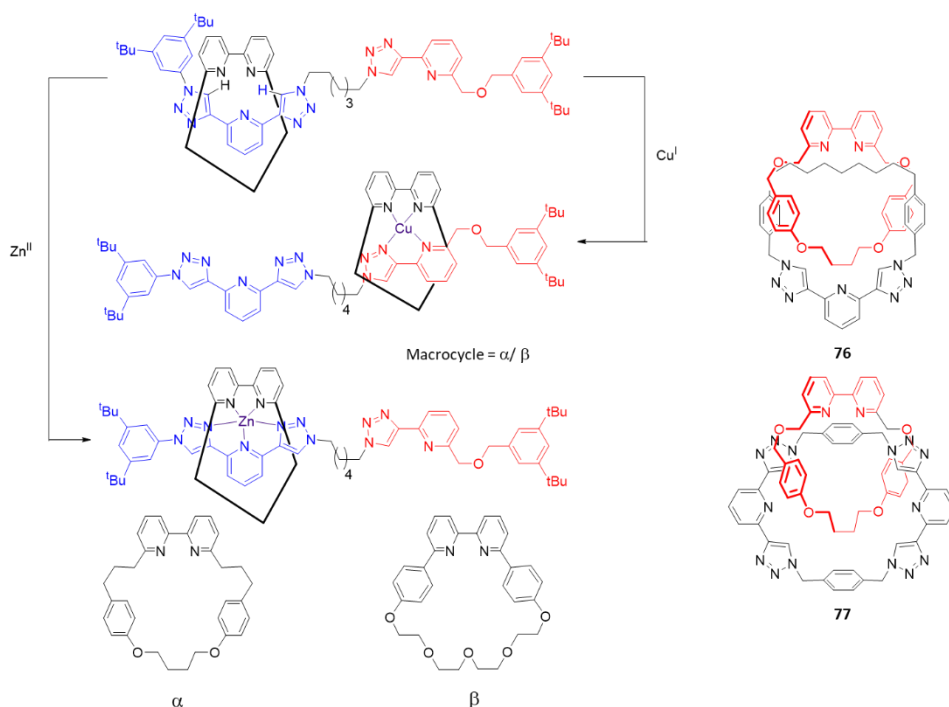
Figure 1.24 *Schematic representation of molecular shuttle rotaxane developed by Goldup and structures of catenanes **76** and **77** based on the **btp** motif also by Goldup.*

As described in Section,1.1.4 the **btp** motif and its derivatives have been utilised in a wide range of areas. Its facile synthesis and functionalisation through the CuAAC click reaction makes this an attractive system for the generation of supramolecular self-assemblies. Its ability to sensitise lanthanide ions can lead to systems with interesting photophysical properties and the selective binding affinity for actinides over the lanthanides makes **btp** derivatives excellent candidates for An/Ln separation. In a similar fashion to the **dpa** systems discussed in Section 1.1.2, thoughtful design of **btp** derivatives can lead to many different outcomes and applications for these ligands. Control of the ligand functionality, metal geometry, stoichiometry or the introduction of anions, can all influence the resultant self-assembly of these systems and the structures generated. Much focus has been placed on symmetric terdentate ligands in the literature; however, asymmetric ligands can provide many interesting properties and a selection of these will be discussed in Section 1.2.

Asymmetrical terdentate ligands

Pyridine-based ligands are ubiquitous in the literature due to the σ-donating nature of the pyridyl N and facile functionalisation of the pyridine ring.[135,136] The introduction of two independent binding motifs to the pyridine centre creates an asymmetric terdentate

coordination site and further expands the range of supramolecular architectures achievable. The combination of pyridine, tetrazole, triazole, carboxylate or pyrazole coordination motifs, among others provides scope for new coordination compounds with a host of applications. In the following section a variety of these compounds will be examined.

1.2.1 Monotopic self-assemblies

Asymmetric binding sites must first be considered in their simplest form, gaining insight into their metal ion coordination behaviour and photophysical properties. This section will detail the self-assembly of a selection of asymmetric, pyridine-centred, terdentate motifs with various *d*- and *f*-metals beginning with 2,2'-bipyridine (**bpy**) derivatives.

Since its inception, a vast array of metal complexes have been reported with the **bpy** motif as a bidentate chelator for the generation of supramolecular scaffolds. This stems from its relative ease of functionalisation and ability to form stable complexes with transition metals and lanthanides. Functionalisation of each of the two rings in all available positions have been explored, introducing groups that can perform a variety of different roles such as coordinating the metal ion and/or participating in additional bonding interactions. Chen and co-workers have reported the formation of six Cu(I) clusters with terdentate **bpy** ligands **78– 81**, as well as two phosphine ligands (triphenylphosphine, PPh$_3$, or bis(diphenylphosphino)methane, dppm).[137] By introducing functionality to the 2,2'-bipyridyl and tetrazole moieties, the various coordination modes which are possible for these ligands were explored. Reacting ligands **78** to **81** with Cu(I) and PPh$_3$ in similar conditions,
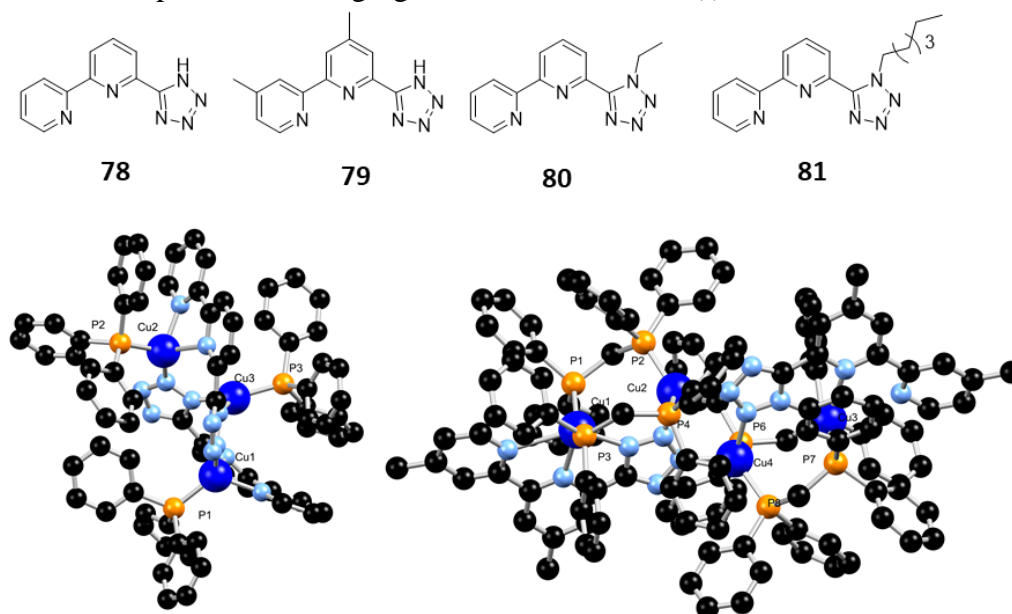
Figure 1.25 *Compounds **78-81** synthesised for the formation of Cu(I) clusters and [Cu$_3$(**78**)$_2$(PPh$_3$)$_3$)] along with [Cu$_4$(**79**)$_2$(dppm)$_4$].*

four distinct Cu(I) clusters were formed. Complexes [Cu$_3$(**78**)$_2$(PPh$_3$)$_3$)](ClO$_4$)·H$_2$O·ClCH$_2$CH$_2$Cl, and [Cu$_3$(**79**)$_2$(PPh$_3$)$_3$)](ClO$_4$)· CH$_3$OCH$_3$·CH$_3$COCH$_3$ are analogous and only differ by methylation of the bipyridine ring. Both form trinuclear clusters consisting of two tetrahedral four-coordinate Cu(I) ions. The cluster is completed by the third Cu(I) ion which is three coordinate, and in a formally trigonal planar coordination geometry, coordinating to one P from a PPh$_3$ ligand and two N atoms from the tetrazole moieties. Bridging from the tetrazolate and pyridyl groups connect the Cu(I) atoms in the cluster. Ligands **80** and **81** in which an NH alkyl chain is appended to the tetrazole were reacted under the same conditions giving dinuclear clusters [Cu$_2$(**80**)$_2$(PPh$_3$)$_2$] and [Cu$_2$(**81**)$_2$(PPh$_3$)$_2$]. Despite occupying different space groups, in the extended packing these complexes are structurally similar to each other with each Cu(I) present in a distorted tetrahedral environment, coordinating to one PPh$_3$ ligand and three N donors, two of which come from the 2,2'-bipyridyl ring of one ligand, and the last one of which comes from the tetrazole ring of another ligand. Replacing the PPh$_3$ ligands with one dppm chelate, two distinct tetranuclear clusters [Cu$_4$(**78**)$_2$(dppm)$_4$] and [Cu$_4$(**79**)$_2$(dppm)$_4$] were formed instead. It can be concluded that both the NH-alkylation and variation of the phosphine ligand have a remarkable impact on the structures of the Cu(I) clusters, while methylation of the 2,2-bipyridyl ring has little effect on the system.
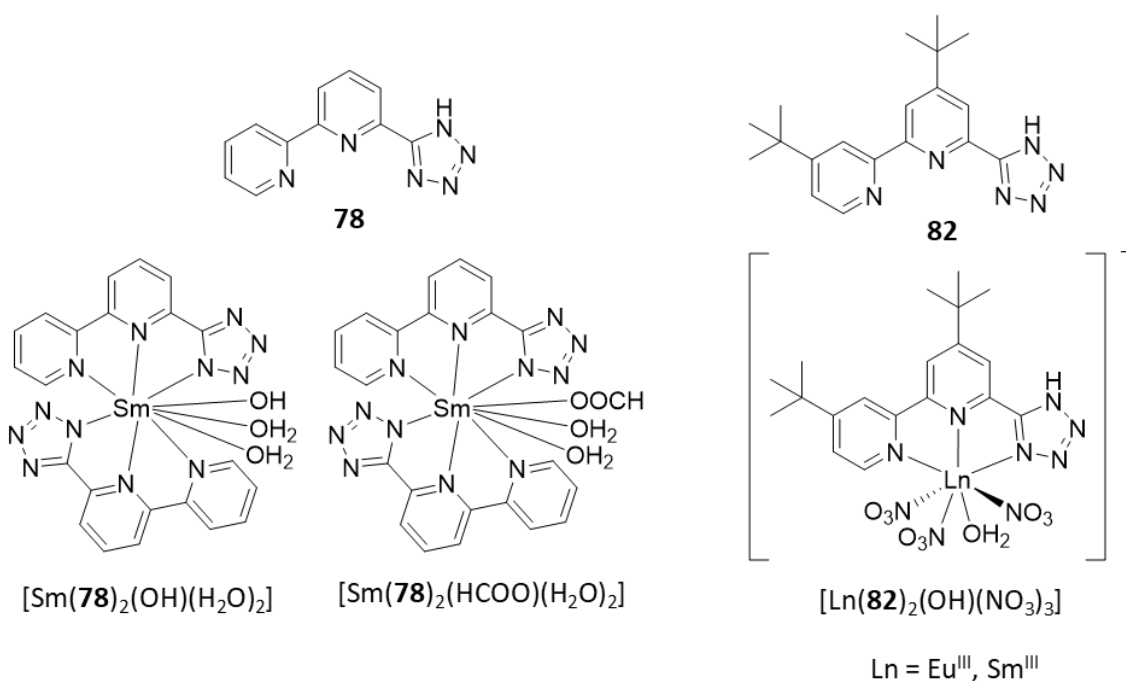
Figure 1.26 *Compound **78** and its complexes with Sm(III) [Sm(**78**)$_2$(OH)(H$_2$O)$_2$] and [Sm(**78**)$_2$(HCOO)(H$_2$O)$_2$] and compound **82** and its complexes with Eu(III) and Sm(III) [Eu(**82**)$_2$(OH)(NO$_3$)$_3$ and [Sm(**82**)$_2$(OH)(NO$_3$)$_3$].*

Like **btp** in Section 1.1.4 above, the **bpy**-tetrazolate ligand `6-(tetrazol-5-yl)-2,2'-bipyridine,**78**, has been investigated as a potential soft N-donor ligand for the separation of actinides and lanthanides. Kratsch *et al.* reported two different 1:2 metal:ligand complexes, the structures of which were confirmed by single crystal X-ray diffraction, upon reaction of Sm(III) with ligand **78** in isopropyl alcohol followed by suspension in DMF.[138] The assembly [Sm(**78**)$_2$(OH)(H$_2$O)$_2$] was formed after two weeks, while allowing the solution to stand for twelve weeks afforded a second structure [Sm(**82**)$_2$(HCOO)(H$_2$O)$_2$]. Decomposition of the DMF to formic acid and dimethylamine accounted for the presence of the formate anion. Time-resolved laser-induced spectroscopy (TRLFS) titration experiments revealed the formation of 1:2 and 1:3 Cm(III) chelates in solution, while only 1:1 and 1:3 species with Eu(III) were observed. Conditional stability constants indicated that ligand **78** formed more stable 1:3 complexes with Cm(III) than Eu(III) with a theoretical separation factor determined to be approximately 500. While these initial results appear promising, the low solubility of ligand **78** in non-polar solvents required for industrial separation prevented successful liquid-liquid extraction. Thus the authors have, more recently, reported ligand **82**, functionalised with *tert*-butyl moieties with a view to improving the solubility of the system.[139] Solubility studies revealed that while the ligand was soluble in CH$_3$OH, increasing the lipophilicity of the solvent resulted in decreased solubility of the ligand. The theoretical separation factor indicates that due to the introduction of the *tert*-butyl groups, the selectivity for Cm(III) observed in the previous system was lost. A change in the complexation mechanism due to the steric demands imposed by the *tert*-butyl groups, was attributed to the cause of this observation. It is interesting to note how a small change to the ligand structure can fundamentally change the binding affinity of the ligand.

Wen and co-workers have also demonstrated the effect of a small change to a ligand structure and its impact on the photophysical properties of a lanthanide system.[140] Addition of three equivalents of Tb(III) or Eu(III) to ligand **78**, followed by recrystallisation, led to the formation of single crystals of X-ray diffraction quality. The mononuclear complexes consist of a Eu(III) or Tb(III) ion coordinated by six N atoms from two **78** ligands, with three O atoms from two water molecules and one DMF completing the coordination spheres. However, upon introducing a methyl group to the 2,2'-bipyridyl ring, forming ligand **79**, the lanthanide complex generated under the same conditions no longer contains water in the coordination sphere. Instead the H$_2$O molecules have been replaced with a nitrate anion. As expected, photophysical solution studies indicated that the absence of H$_2$O molecules in the coordination sphere of the complex resulted in enhanced luminescence quantum yields due
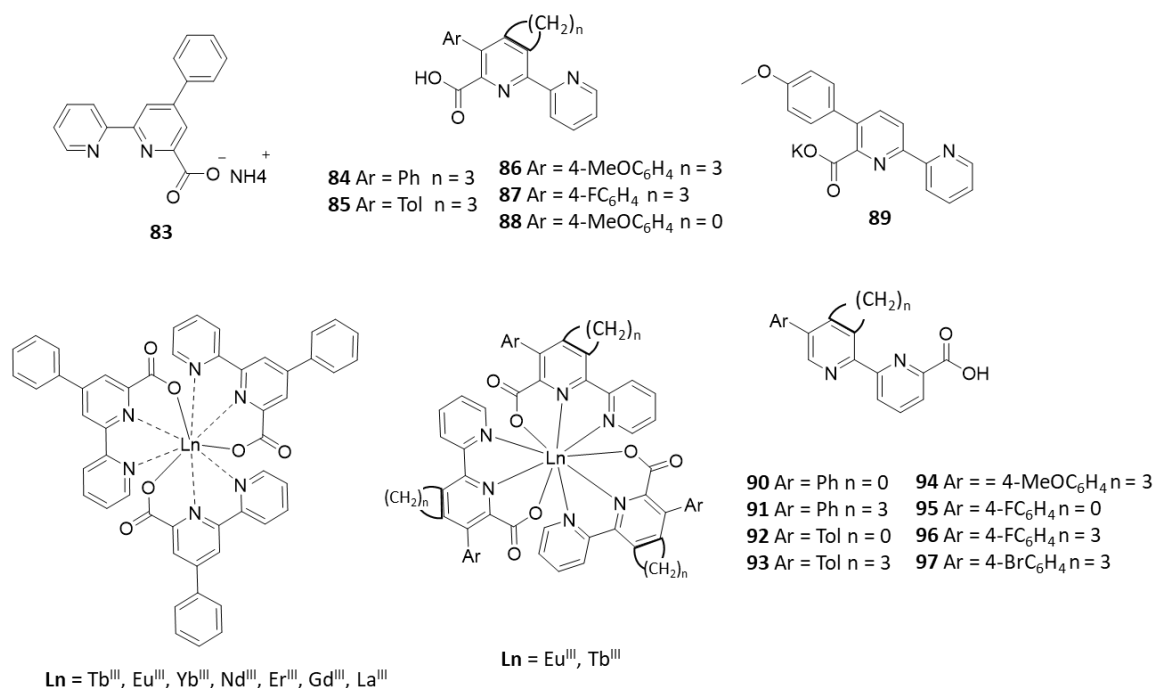
Figure 1.27 Compounds 83, 84–88 and 89–97 and schematic representations of their lanthanide complexes.

to the absence of O-H vibrations which typically quench the emission of the lanthanide complexes.

2,2'-Bipyridine has been subject to many derivatisations, generating a vast array of coordination sites and geometries. One such derivative is 6-carboxy-2,2'-bipyridine. A neutral derivative **83** was synthesised and its photophysical properties with a range of lanthanide ions were reported by Kottas and co-workers.[141] Single crystals suitable for X-ray diffraction were obtained of both a europium and lanthanum complex, showing the ligands fully saturating the inner coordination sphere of the lanthanide ions in a nine coordinate fashion. The typical narrow emission spectra, characteristic of the lanthanide ions, was observed when Tb(III) and Eu(III) were added to the ligand in solution, as well as relatively long lifetimes (0.2 – 2.2 ms). Intense emission in the NIR region was also observed for the infrared emitting lanthanide ions with high emission quantum yields of 60% for Eu(III), 7% for Tb(III) and 0.7% for Yb(III) in CH_2Cl_2.

Neutral lanthanide complexes are of interest as they have potential applications in light emitting devices. However, solubility of such systems in non-polar organic solvent was a concern of Krinochkin and co-workers when they synthesised a new class of 6-carboxy-2,2'-bipyridine ligands **84-88**, derivatised with various aromatic substituents on the 5-position of the 2,2'-bipyridine ring.[142] While the quantum yields of the 1:3 Ln:L Eu(III) complexes of these systems were up to 11% lower than previously reported for similar

neutral lanthanide complexes, the improved solubility of these systems in non-polar organic solvents reduces the constrain on the practical uses of these systems. More recently the authors have reported ligands **90-97**, in which the carboxyl group is instead located on the other pyridine ring of the 2,2'-bipyridine ring system, in order to allow the aromatic substituent and the 2,2-bipyridine ring to sit coplanar with respect to each other, improving the photophysical properties of the corresponding Eu(III) system. The new ligand system was found to be unsuitable for sensitisation of Tb(III) but the 1:3 Ln:L Eu(III) assembly requires much less energy for excitation due to longer absorption wavelength and exhibits higher Eu(III) luminescence efficiency than the previously reported system.[143]

Achieving a high emission quantum yield through the careful design of lanthanide coordinating ligands is an extensive area of research due to the restricted availability of lanthanide metals in recent years and as a result, increasing prices.[144–146] Attempts to increase the quantum yield of a carboxy-bipyridine based system were conducted by Botelho *et al.* by considered ligand design.[147] Terdentate ligand **98** was shown to coordinate to Eu(III) in a 1:3 stoichiometry such that the coordination number of the metal centre was nine, thus eliminating any possible non-radiative deactivation by coordinating water molecules. This was combined with a large energy difference between the excited state of the ligand and the
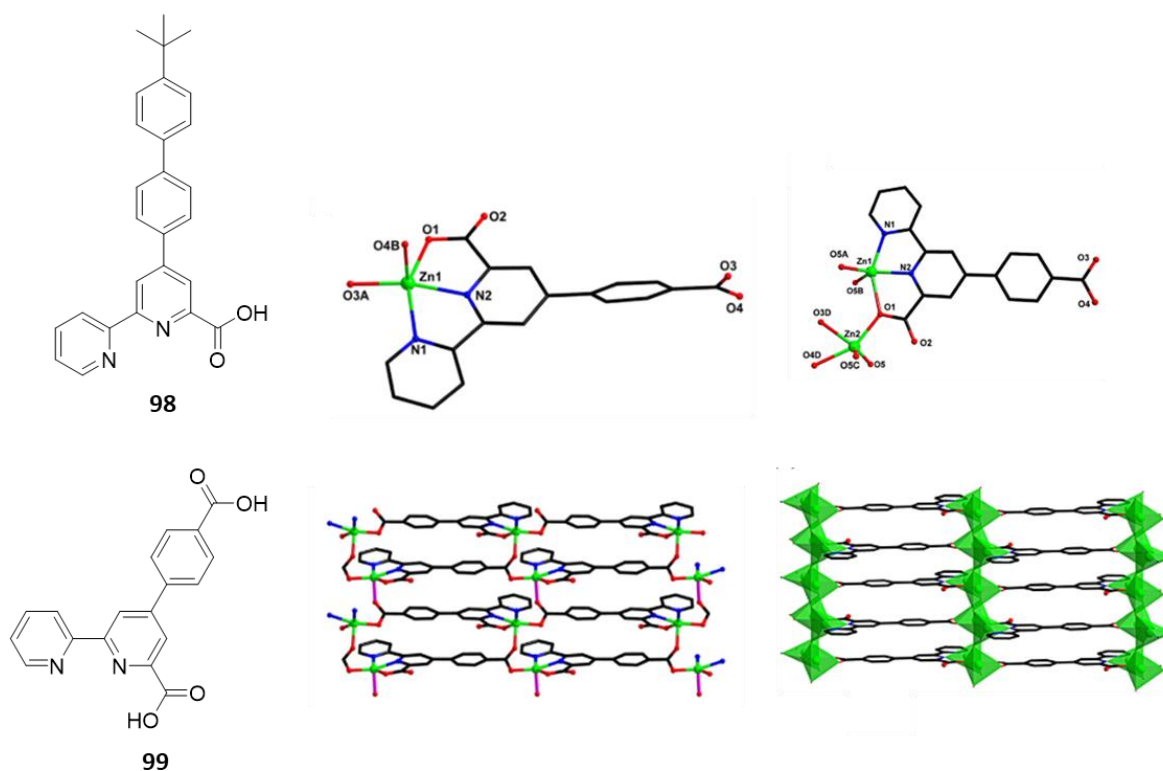

Figure 1.28 *Compound **98** and compound **99** with Zn(II) complexes [Zn(**99**)]$_n$·2n(H$_2$O) and [Zn$_2$(**99**)(µ-OH)$_2$]$_n$·1.5n(H$_2$O) along with 2D and 3D structures. Reproduced from Ref 147.*

Eu(III) centre, which prohibited back energy transfer, resulting in a quantum yield for the system of 85% in CH_2Cl_2. Introduction of the phenyl-*tert*-butyl substituent to the bipyridine unit had the effect of lowering the excited state energy of the ligand when compared to ligand **83** discussed above, as reported by Kottas *et al.* Due to the high quantum yield reported for this system, the authors then investigated the incorporation of this complex into a solid host to prevent leakage of the complex for applications such as bioanalytical devices.[148] Wet impregnation of a mesoporous silica and phenyl-modified silica in the form of powders and xerogels with a Eu(III) complex of **98,** [Eu(**98**)$_3$] was successful and phenyl-modified silica was found to have higher levels of retention of guest molecules. High quantum yields of 65%, and long lifetimes suggest further investigation of the applications of this system would be worthwhile for bioanalytical applications.

While 6-carboxy-2,2'-bipyridine derivatives have been utilised as a terdentate binding motif for the lanthanide ions, they also have applications in *d*-metal coordination chemistry. For example, a carboxy-phenyl derivative of 6-carboxy-2,2'-bipyridine, **99**, has been reported, which upon reaction with zinc could form 2D and 3D coordination polymers.[149] Complexes [Zn(**99**)]$_n$·2n(H_2O) and [Zn$_2$(**99**)(μ-OH)$_2$]$_n$·1.5n(H_2O) were synthesised under similar conditions, varying only the pH of the solution. At pH = 2 ligands coordinate to the Zn atom however, at pH = 6 both hydroxyl groups and ligands coordinate to the Zn centre giving two distinct 2D coordination polymers. The final structure, a 3D two-fold self-interpenetrated network is generated when an auxiliary ligand glutaric acid is involved in the coordination. Coordination polymers [Zn(**99**)]$_n$·2n(H_2O) and [Zn$_2$(**99**)(μ-OH)$_2$]$_n$·1.5n(H_2O) were shown to possess high thermal stability and excellent luminescence properties.

The coordination of 2,2'-bipyridine derivatives with *d*-metals has also been a fruitful area of research within the Gunnlaugsson group in recent years. 2,2′-Bipyridine-6-carboxylate derivatives **100** and **102** have been synthesised and their coordination chemistry and structural properties investigated.[150] Solvothermal synthesis techniques were employed, including *in situ* ester hydrolysis. Reaction of cadmium nitrate with ligands **100** and **102** while varying reaction time, temperature and stoichiometry resulted in the formation of two distinct mononuclear Cd(II) complexes [Cd(**100**)$_2$]H_2O and [Cd(**102**)$_2$]and two trinuclear Cd(II) clusters [Cd$_3$(**100**)$_3$(NO$_3$)$_2$(DMF)$_4$]NO$_3$ and [Cd$_3$(**102**)$_3$(NO$_3$)$_2$(DMF)$_4$]NO$_3$·DMF. Upon reaction of the ligands **100, 101** and **102** with Co(II)/(III) only mononuclear divalent
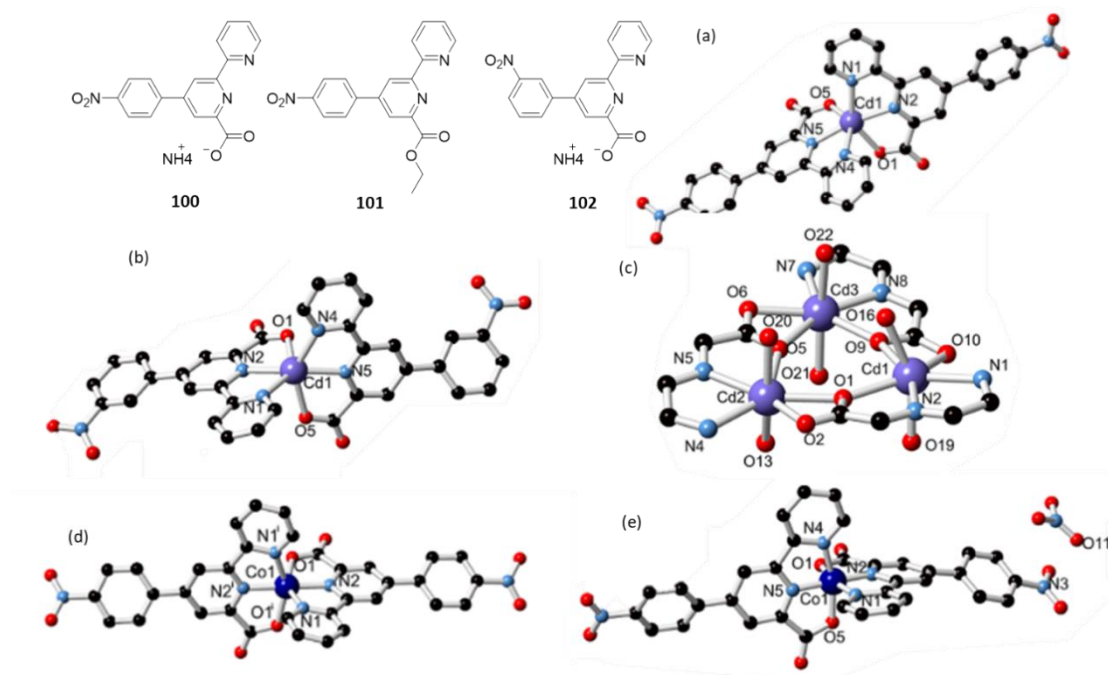
Figure 1.29 *Compounds **100**, **101** and **102** and crystal structures of (a) [Cd(**100**)$_2$]H$_2$O (b) [Cd(**102**)$_2$] (c) [Cd$_3$(**100**)$_3$(NO$_3$)$_2$(DMF)$_4$]NO$_3$ (d) [Co(**100**)$_2$] (e) [Co(**100**)$_2$]NO$_3$. Reproduced from Ref 150.*

complexes were observed with the formation of a trivalent impurity in each case. Modification of the reaction solvent resulted in the generation of a single-phase product.

Tetrazole analogues of the aforementioned pyridine-2,6-dicarboxylic acid binding motif have also been explored as asymmetric binding motifs for the lanthanide ions. Work by Andreiadis *et al.* reports the synthesis and photophysical characterisation of lanthanide complexes of **H$_2$103** as well as their solid state structure which was determined by single crystal X-ray diffraction.[151] The nine coordinate europium centre of [Eu(**103**)$_3$](NHEt$_3$)$_3$ is coordinated by three carboxylate oxygen atoms, three tetrazole nitrogen atoms, and three pyridine nitrogen atoms with the charge balanced by three triethylammonium ions. Similarly to the complex [Ln(**dpa**)$_3$]$^{3+}$, the ligands wrap around the metal centre, generating a Λ or Δ helical chiral complex at the metal centre.[152] Upon examination of the photophysical characteristics of the system it was reported that replacing one carboxylate of the **dpa** ligand with a tetrazolate in ligand **H$_2$103** resulted in a red shift in the absorbance profile of the Eu(III) complex, as well as a large increase in intensity. This extension of the excitation window towards the visible region may prove useful for future biological applications. Upon examination of the emission spectra of the ligand with non-luminescent gadolinium, a direct comparison of the singlet and triplet excited states of the ligand **H$_2$103** and **dpa** could be
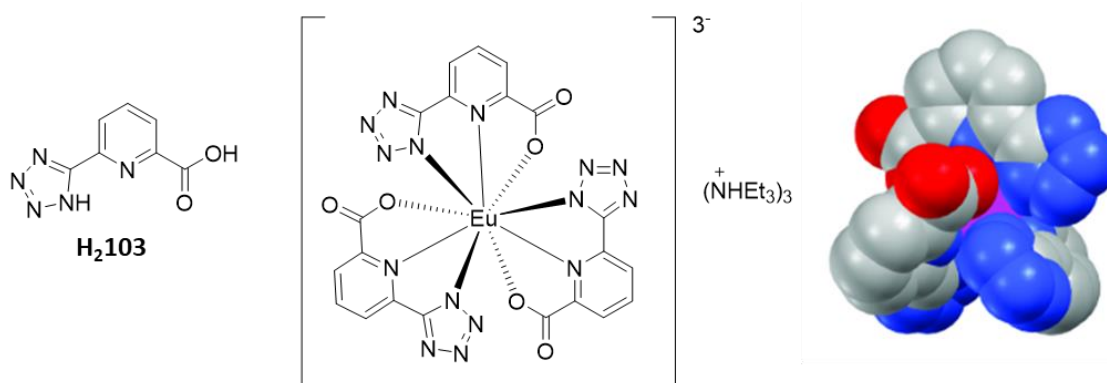
Figure 1.30 *Compound **H₂103**, schematic representation of [Eu(**103**)₃](NHEt₃)₃ and space fill model of [Eu(**103**)₃]³⁻ anion (right). Reproduced from Ref 153.*

drawn. The tetrazolate moiety has the effect of decreasing the energy levels of the ligand, leaving the energies of **H₂103** slightly lower than the previously reported **dpa**.[153]

While only a small selection of the reported asymmetric binding motifs are described above it is clear that their self-assembly with a variety of metal ions generates of a wide variety of interesting structures. Inclusion of two binding sites in one ligand structure increases the complexity of the self-assemblies and offers the potential to generate more complex, higher order structures. Examples of these more complex structures will be described in the following section.

1.2.2 Ditopic self-assemblies

Ligands with the ability to coordinate metal ions at two distinct binding sites allows for the possibility of forming higher order structures such as helicates, grids and cages. Manipulating ligand design in order to accommodate the coordination number and geometry of the metal ion facilitates the formation of supramolecular architectures and functional materials. One strategy in which this can be achieved is by varying the central spacer between the two chelating sites. Al-Rasbi *et al.* investigated this effect with a series of bis-pyrazolyl-bipyridyl ligands **104-106**.[154] Upon reaction of **104** with Ni(II) and Cu(II), two dinuclear double stranded helicates were obtained and their structures confirmed by single crystal X-ray diffraction. Each metal ion was six-coordinate, coordinating to two pyridyl N atoms and one pyrazole N of each ligand. Addition of Ag(I) to the ligand **104** resulted in a single stranded helicate while a mesohelicate was observed upon reaction of ligand **105** with Ni(II). Addition of Ag(I) and Cd(II) to ligand **106** yielded a discrete M₃:L₂ complex and a circular helicate, respectively, indicating that the choice of metal, as well as small changes to the structure of the ligand, have profound consequence for the assemblies formed. While inferences could be made about the influence of structural variations in the ligand on the
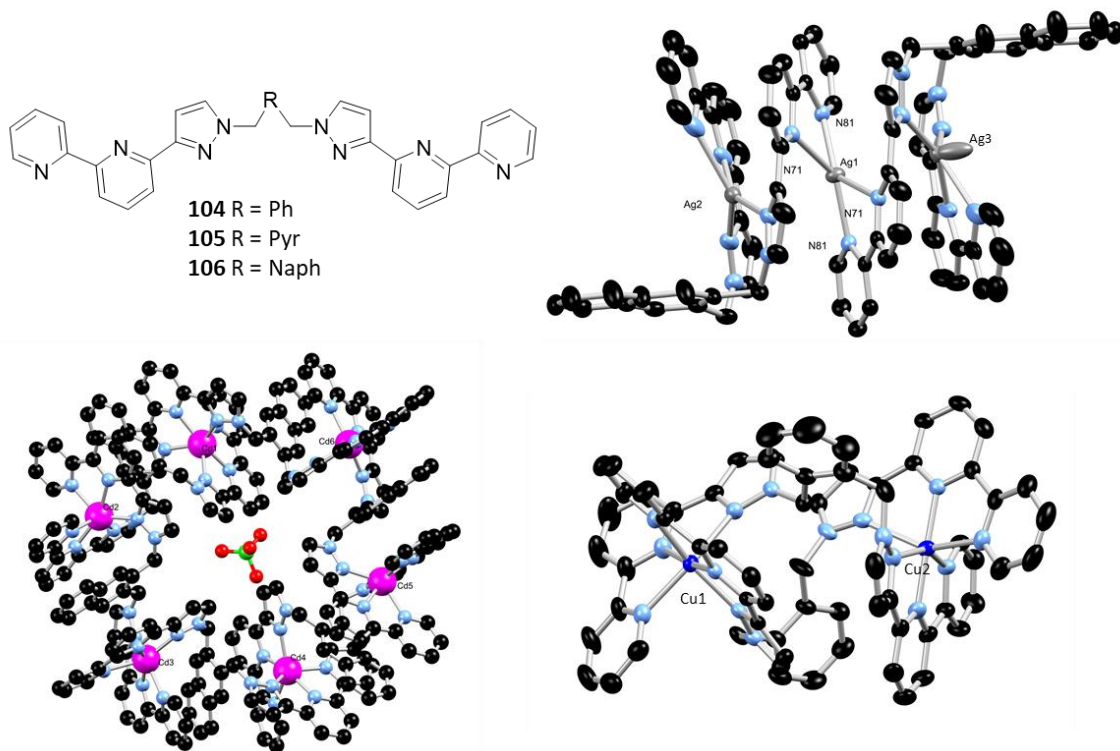
Figure 1.31 *Compounds **104**–**106** and crystal structures of helicate [Ag₃(**106**)₂](BF₄)₃·2CH₃CN, circular helicate [Cd₆(**106**)₆](ClO₄)₁₂ and [Cu₂(**104**)₂][ClO₄]₄.*

complexes formed, it is difficult to do so with any predictive power. This is because the number of variables in these systems are large and the solid-state structures obtained may not represent the thermodynamically most stable species but a kinetically trapped, stable intermediate assembly, which can nevertheless crystallise. In solution a more complicated process occurs, indicating that the solid-state structure may not be representative of the system. Another example of a dinuclear system taking advantage of the excellent metal binding properties of bipyridine is ligand **H107**, which is a **bpy** dimer bridged by a pyrazole ring. Deprotonation of ligand **H107**, and addition of Co(II), Mn(II), Fe(II) or Cu(II) lead to the formation of highly stable [2 × 2] grid structures with an octahedral coordination spheres for Co(II), Fe(II) and Mn(II).[155] However, only a penta-coordinate binding mode was observed for the Cu(II) ion, with one of the pyridyl groups of each ligand non-coordinating and the overall [2 × 2] grid structure is retained. There is no evidence of dissociation of any of the structures in solution. The authors suspected that due to the non-coordinating nature of the two pyridyl groups in the assembly, it may be possible to generate further coordination compounds with **H107** and Cu(II) by altering the synthesis conditions.[156] Deprotonation of **H107**, and reaction with copper nitrate leads to the formation of a discrete dinuclear complex

{**107**Cu$_2$(OMe)(MeOH){κ1-O-(NO$_3$)}} while increasing the chelating ring size to ligand **H108** significantly alters the metal-metal distances. Variable temperature magnetic susceptibility measurements were also conducted on the complexes of ligand **H108**, [**108**Cu$_2$(μ-OH)(ClO$_4$)(MeCN)]-(ClO$_4$), [**108**Cu$_2$(dmf)$_2$(μ3-OH)]$_2$(ClO$_4$)$_4$·4dmf and [**108**Cu$_2$](ClO$_4$)$_2$. Substantial antiferromagnetic coupling was observed between the two Cu(II) ions.

In related work, the deprotonated ligand **107** has been utilised for the development of an Fe$_4$ [2 × 2] grid which was shown to exhibit spin-crossover (SCO) behaviour.[157] Deprotonation of ligand **H107** followed by treatment with Fe(BF$_4$)$_2$·6H$_2$O yields [Fe$_4$(**107**)$_4$](BF$_4$)$_4$ the structure of which was confirmed by ESI mass spectrometry, elemental analysis and single crystal X-ray diffraction. Each iron atom sits in a distorted octahedral environment, coordinated by two independent ligands in an N,N,N terdentate binding mode. From the bond lengths measured in the crystal structure, as well as using Mössbauer spectroscopy, the spin state of the Fe(II) atom adopts a low-spin configuration. At room temperature all four Fe(II) atoms were found to be in a high-spin state, but upon cooling to 133K one Fe(II) atom adopts a low-spin configuration. The redox properties of the complex were investigated by cyclic voltammetry (CV). Four reversible oxidations could be assigned to individual one-electron Fe(II)/(III) processes of each iron centre, to yield **1**$^{8+}$. The intermediate **1**$^{6+}$ species appeared to be somewhat thermodynamically stable, due to the larger gap in the redox couples between the second and third oxidations than for the
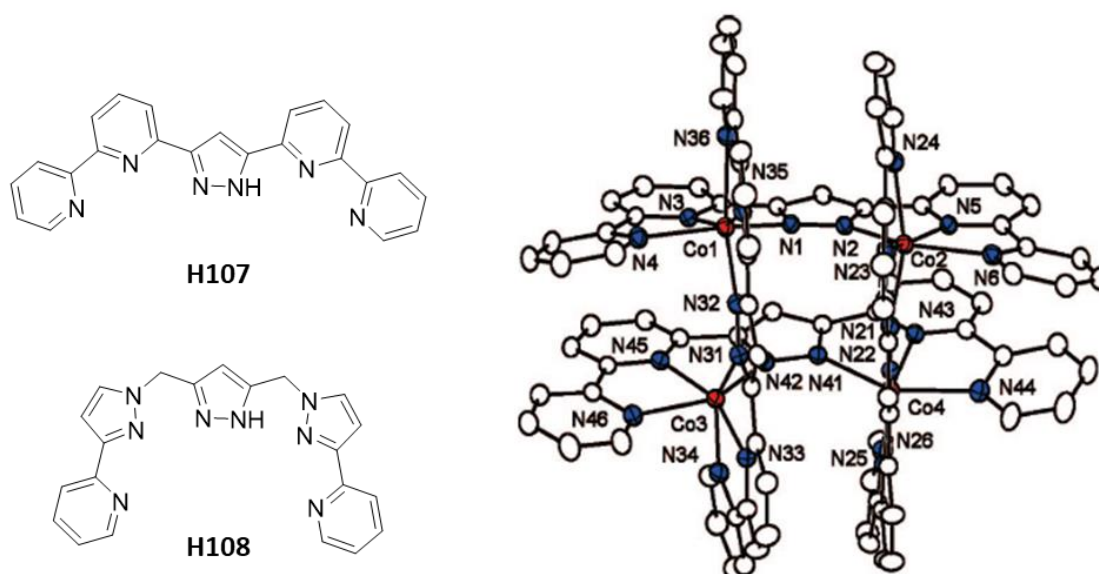
Figure 1.32 *Compound **H107** and crystal structure of [2×2] Co grid [Co$_4$(**107**)$_4$][NaNO$_3$]$_4$(NO$_3$) and compound **H108**. Reproduced from Ref 157.*
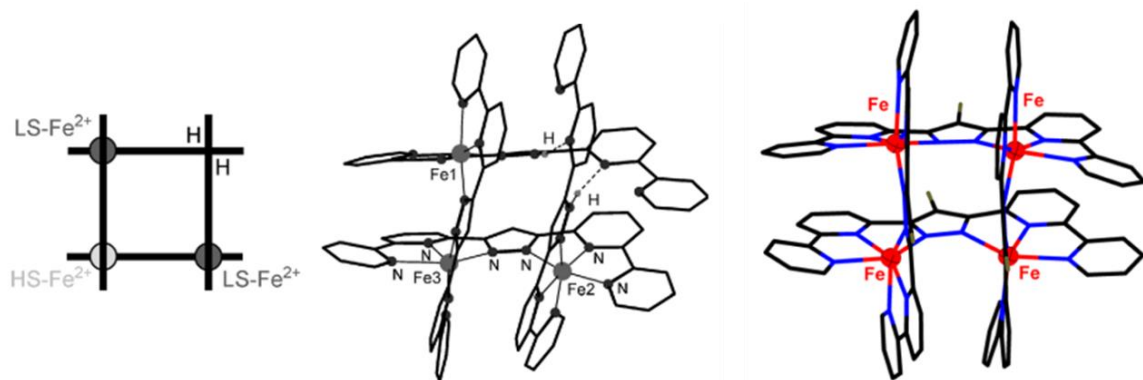
Figure 1.33 *Molecular structures of [Fe₄(**107**)₄]⁴⁺ and [Fe₃(**107**)₂(**H107**)₂]⁴⁺. Reproduced from Ref 158.*

corresponding redox gaps between the first and second waves, and the third and fourth. Indeed, the doubly oxidised species could be crystallised, and its structure unequivocally determined by single crystal X-ray diffraction.

While attempting to synthesise [Fe₄(**107**)₄](BF₄)₄, the authors generated a side-product [Fe₃(**107**)₂(**H107**)₂](BF₄)₄.[158] Optimising the synthesis of this product and examination of its spin crossover (SCO) behaviour lead to some excellent results. The [2 × 2] grid complex was devoid of a metal at one vertex, with two of the four ligands deprotonated and two remaining in the protonated state. The two NH protons were located in the position devoid of a metal ion, stabilised by two interligand hydrogen bonds to give the analogous [2 × 2] structure, as confirmed by single crystal X-ray diffraction. A complete spin-crossover (SCO) transition was observed slightly above room temperature with a large thermal hysteresis recorded. The SCO could be inhibited by the addition of various solvents, with those capable of strong hydrogen bonding being the most effective. This process was both fast and highly reversible.

While only a select few examples of ligands with asymmetric binding pockets are described above, substantial effort is nevertheless ongoing to develop more effective ligand scaffolds and widen the scope of the subsequent monometallic and multimetallic systems. These reports have provided a greater insight into the self-assembly of a variety of systems, and allowed for the generation of functional, complex extended structures with fine-tuned physical, photophysical, magnetic, and other properties.

The Gunnlaugsson group has developed a large array of symmetric and asymmetric supramolecular coordination motifs and examined their *d-* and *f*-metal directed self-assembly. The following sections will discuss derivatives of the **dpa** and **btp** motifs for the generation of soft-materials, helicates, clusters, MOFs and responsive polymer materials.

1.3 Recent Examples from the Gunnlaugsson Group

In recent years, the Gunnlaugsson group has developed a variety of **dpa** antennas for use in generating self-assemblies with lanthanide ions. Generation of self-assemblies such as helicates and bundles have led to simultaneously elegant and functional systems, which offer the potential for utilisation as luminescent probes for imaging and sensing.

A chiral luminescent self-assembly from naphthalene derived **pdc** ligand dubbed "The Trinity Sliotar" was developed, in which three chiral pyridylamide tridentate ligands coordinate to a lanthanide metal centre (Ln(III) = Eu(III), Tb(III), Sm(III), Nd(III) and Yb(III)).[88] Ligands **29** (*R,R*) and **30** (*S,S*) were shown to influence the chirality of the metal centre during the self-assembly, with **29** inducing Λ chirality and **30**, Δ chirality at the metal ion. Circular dichroism and X-ray crystallography were used to confirm these results. Spectroscopic investigations of the self-assembly process in solution were carried out and indicate the presence of 1:1,1:2 and, 1:3 Ln(III):**29** species in solution. As expected the tris complex was the most luminescent due to the absence of solvent molecules in the inner coordination sphere. Coordination to the Ln(III) metal centre occurs through the central pyridyl N and two carboxamide O atoms of the **pdc** motif, while π-π stacking interactions between the central pyridine and the two naphthalene units serve to stabilise the 3D bundle.

In order to probe the effect changes to the ligand structure might have on the overall photophysical performance of the system, isomers of the naphthyl ethylamine were installed to give ligands, **109** and **110**.[159] The luminescence quantum yields for the 2-naphthyl system, were EuL$_3$ L = **109** and **110**, saw a reduction in quantum yields reported for the 1-naphthyl system, reducing from 4% to 1% in both CH$_3$CN and CH$_3$OH. Excited state lifetimes remained similar for both complexes, indicating that it is likely inefficient energy transfer from the ligand antenna to the metal centre which is the cause of the reduction in quantum yield and not a quenching effect caused by solvent molecules. Single crystal X-ray diffraction provided evidence for a less tightly packed and more flattened structure with the same O,N,O coordination mode. A lack of π-π stacking interactions, which were present in the 1-naphthyl structure, are responsible for this.

Building on this work, ligands **111**-**118** were synthesised, introducing further functionality at the 4-pyridyl position, ranging from PEG, ethoxy and propargyl chains to crown ethers and carbohydrates (not shown). It was found that in each case the 4-pyridy functionality was oriented away from the central metal ion, resulting in no interruption of the π-π stacking interactions between the naphthyl and pyridyl groups. Self-assembly in each case was found to produce the ML_3 species in solution with the 4-pyridyl functionality exerting the most effective control on solubility.[160] Dr. Samuel Bradberry synthesised a further derivative with a possessing propane sulfonate functionality in order to solubilise this system in water using 3-propanesultone and caesium carbonate.[161] Eu(III) complexes of both enantiomers Eu·**119**$_3$ and Eu·**120**$_3$ formed in a 1:3 M:L stoichiometry and quantum yields of 12% in H_2O were reported which is significantly higher than that reported for compound Eu·**29**$_3$ and Eu·**30**$_3$ in organic solvent. CD and CPL spectroscopies were utilised in order to examine the self-assembly of the system in solution and obtain binding constants for the major species in H_2O or buffer solution. It was also observed that **119** and **120** form hydrogels in the presence of Cs_2CO_3 upon heating. The addition of Eu(III) to these gels caused a gel-to-sol phase transition as the Eu(III) complexes were not stable within the gel matrix.
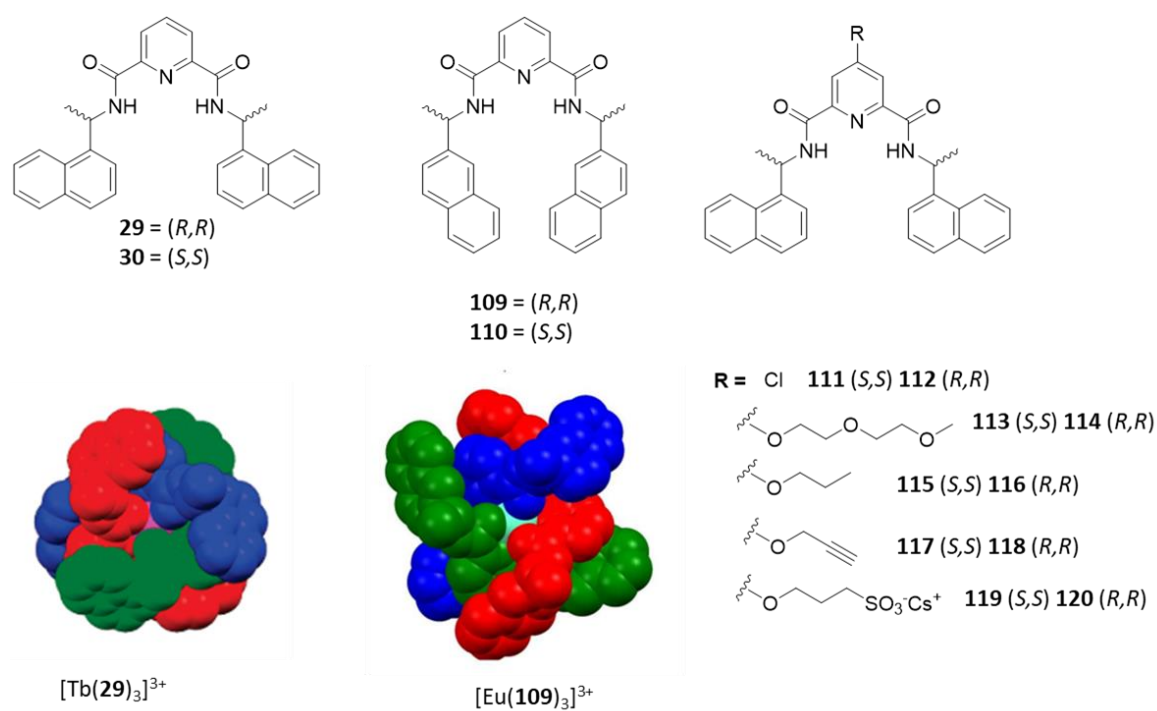
Figure 1.34 Compounds 29, 30 and 109–120 synthesised for the development of lanthanide directed helical assemblies and space fill X-ray crystal structure of [Tb(29)₃]³⁺ and [Eu(109)₃]³⁺. Reproduced from Ref 88.

Extending these mononuclear structures, two **pdc** chelates were linked with various spacer groups to generate a dinuclear ligand capable of forming larger, more complex supramolecular structures. Self-assembly of compounds **121-128,** altering only the xylene spacer, resulted in a series of bimetallic, triple-stranded helicates in solution [Ln$_2$**L**$_3$] L = **121**–**128**.[162–164] All helicates were formed in high yields (*ca.* 90%) with the same O,N,O coordination mode seen for the mononuclear systems above, generating a fully saturated coordination environment around the Ln(III) ions (for **121** and **122** Ln(III) = Tb(III), Eu(III), Lu(III), Sm(III) and **123-128** Ln(III) = Eu(III)) with strong luminescence. Each bimetallic triple stranded species forms as a single homochiral species, adopting either ΔΔ or ΛΛ stereochemistry, confirmed by CPL spectroscopy and X-ray diffraction. More recently, the introduction of a 4,4′-(cyclohexane-1,1-diyl)bis(2,6-dimethylaniline) spacer to this system, generating ligands **129** and **130**, was reported and a decrease in the quantum yields for the corresponding complexes was observed. The reduction in quantum yield was attributed to the increased flexibility compared to the previously reported xylylene linkers.[165]

In order to examine the self-assembly of these systems further, asymmetric mononuclear **pdc** ligands, **131** and **132** were synthesised. These "half-ligands" were the precursors to several ligands employed in the formation of the aforementioned triple stranded dimetallic helicates. The result of self-assembly studies with Eu(III) in solution

121-130

121 (S,S)   **123** (S,S)   **125** (S,S)   **127** (S,S)
122 (R,R)   **124** (R,R)   **126** (R,R)   **128** (R,R)

129 (S,S)
130 (R,R)
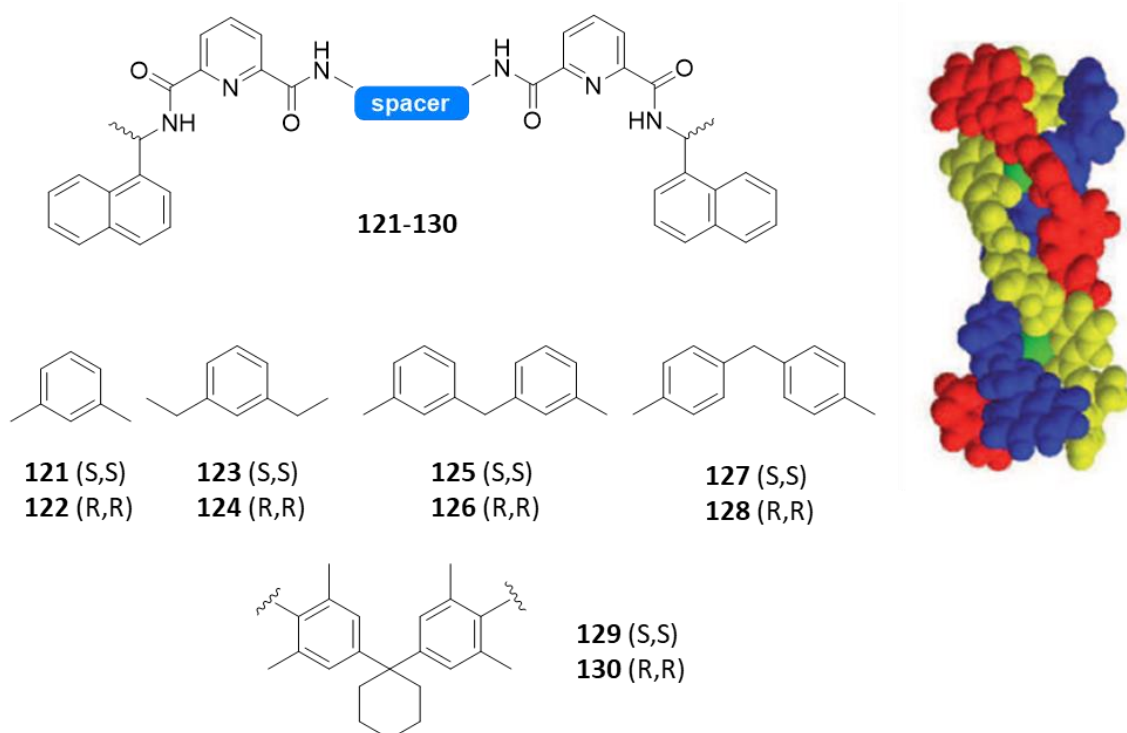
Figure 1.35 *Compounds **121**–**130** synthesised for the formation of triple stranded helicates with Ln ions and molecular model of [Eu$_2$(**126**)$_3$]. Reproduced from Ref 162.*
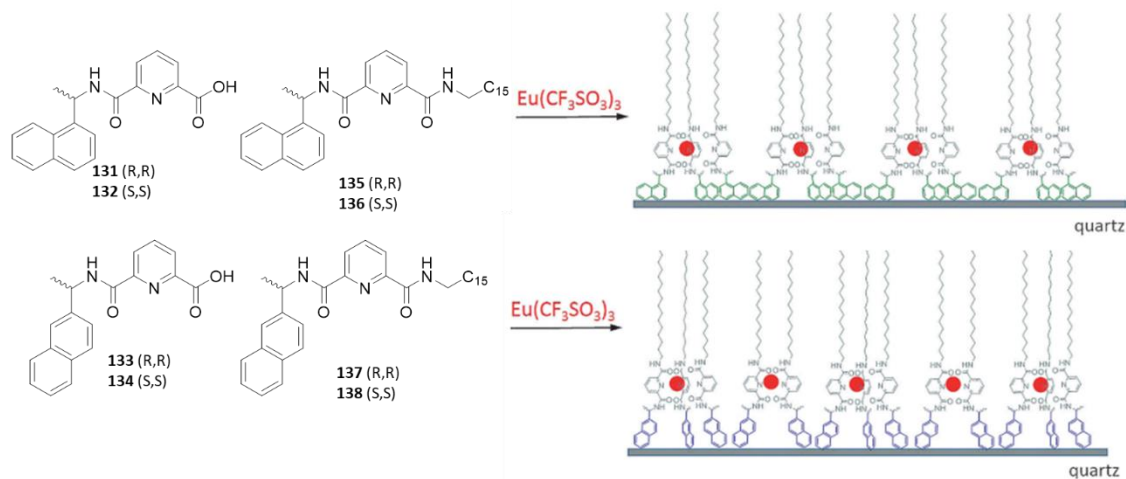
Figure 1.36 *Compounds **131**–**138** and ligands forming Langmuir-Blodgett films of Eu(L)₃]³⁺. Reproduced from Ref 158.*

showed that Ln:**131**₃ and Ln:**132**₃ geometries are formed preferentially, with only a single chiral geometrical isomer formed in solution which is influenced, as before, by the chirality of the ligand. Stability constants were estimated by spectroscopic titrations and found to be similar to the symmetrical ligand systems **131** and **132**. Eu(III) self-assemblies using ligands **133** and **134** were also examined in solution, and as with the analogous dinuclear system, the naphthalene moiety influences the photophysical performance and solution stability.[166] The Eu(**133**)₃ system again experienced a four-fold reduction in quantum yield when compared to Eu(**131**)₃, and the 1:3 stoichiometry was formed in only 80% abundance when compared to 100% for Eu(**131**)₃. The self-assembly of Eu(III) with **133** and **134** was the first report of the use of a CD titration to examine the self-assembly of a system in solution and establish their stability constants.

Both ligands have been functionalised further for the generation of Langmuir-Blodgett (LB) films. Introduction of long lipophilic chains to the structures generated ligands **135-138** which were immobilised onto solid supports following complexation in a 1:3 stoichiometry with Nd(III) Eu(III) or Sm(III) ions and the chiral emission of the films was probed.[167–170] Other approaches for the generation of soft-materials based on the **dpa** ligand scaffold include the formation of a luminescent metallogel from the lanthanide-directed self-assembly of **139** with Eu(III) or Tb(III). Luminescent supramolecular gels were formed in CH₃OH where ligands coordinate Ln(III) ions through the terminal carboxylates to generate a self-healing metallogel.[68] Mixed Eu(III)/Tb(III) gels were also generated and tuning of the luminescence colour was possible based on the ratio of the two lanthanide ions (See Figure
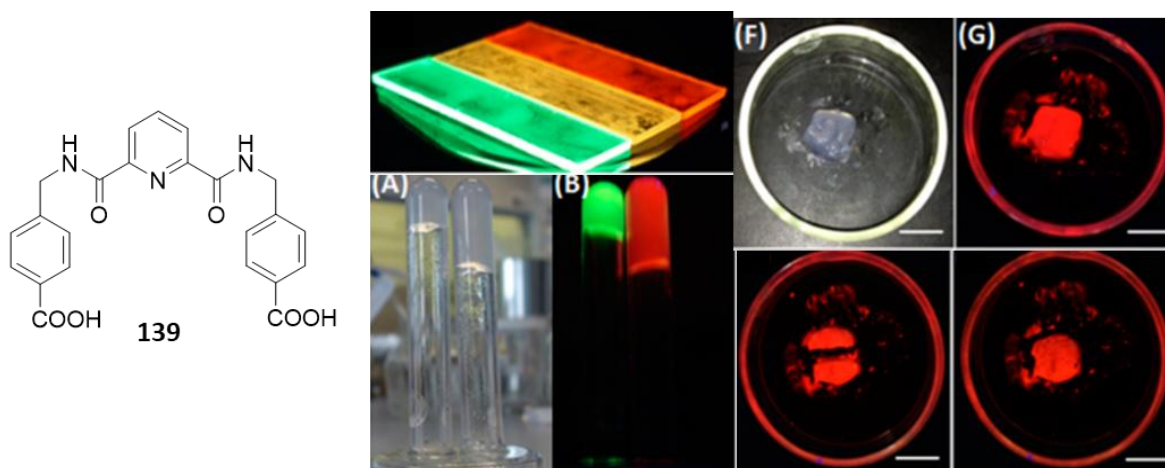
Figure 1.37 *Organogelator **139** and lanthanide gels deposited on a film showing red and green emission from the Eu(III) and Tb(III) based gels, respectively, as well as a Eu(III):Tb(III) gel generating yellow emission. Self-healing nature of Eu(III) doped gel also shown. Reproduced from Ref 68.*

1.37). Altering the Ln(III) ion also has a large impact on the system with different rheological properties observed for Eu(III), Tb(III), and mixed Eu(III)/Tb(III) metal gels.

The area of supramolecular metallogel formation has been one of particular interest to the Gunnlaugsson group. While molecular gels rely on weak self-assembly processes such as hydrogen bonding interactions, π-π stacking interactions, and host-guest recognition, metallogels also employ strong metal-ligand coordination interactions which may improve the stability of the subsequent gels as well as contributing to their complexity and function.[171–174] Success has been achieved in the formation of supramolecular metallogels based on derivatives of the **btp** motif. Ligand **140** formed a soft-material upon complexation with RuCl$_2$ following the addition of NH$_4$PF$_4$ which was stable to the "inversion test".[175] Compound **143** formed a stable metallogel with Eu(III) in CH$_3$OH solution which was highly luminescent to the naked eye. A ligand hydrogel was also generated through pH changes and rheological studies were conducted to probe the mechanical properties of both gels. As anticipated, the metallogel exhibited a more robust nature than the hydrogel, evidenced by the self-healing nature of the Eu(III) gel Eu.**143** which was seen to recover its solid-like behaviour upon repeated strain cycles. Bridging of the carboxylate terminals between ligands *via* the metal ion is likely to be the source of this healable nature.[123]Investigation of the coordination chemistry of ligand **140** and **141** with a series of transition metals was also conducted. In the cases of ligand **141** as well as [Ru·**140**$_2$](PF$_6$)Cl [Ir·**141**Cl$_3$] and [Ni·**141**$_2$](PF$_6$)Cl, single crystals of X-ray quality were obtained.[175] As expected, the ligand was orientated in the *anti-anti* conformation in keeping with structures reported for similar **btp** ligands and adopts a "horseshoe" configuration while when coordinated to the metal
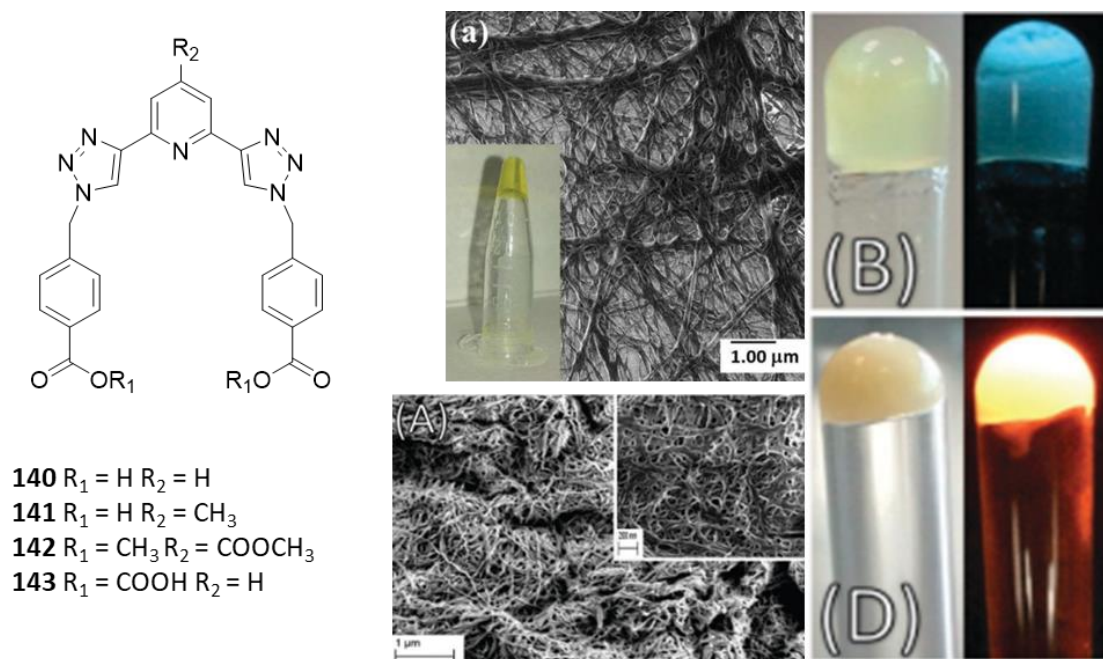
Figure 1.38 Compounds **140-143**. (a) SEM image of Ru gel generated from ligand **138** showing fibrous nature. (A) SEM image of hydrogel of ligand **143** and (B&D) showing hydrogel under ambient light and under UV-irradiation as well as Eu(III) gel showing red emission under UV-light. Reproduced from Ref 175.

140 R$_1$ = H R$_2$ = H
141 R$_1$ = H R$_2$ = CH$_3$
142 R$_1$ = CH$_3$ R$_2$ = COOCH$_3$
143 R$_1$ = COOH R$_2$ = H

ions the ligand adopts a *syn-syn* conformation.[102–105] Each metal in the complexes adopt a distorted octahedral geometry with the triazole rings and the central pyridyl nitrogen coordinating the metal ion.

The introduction of chirality to these **btp** self-assemblies was recently explored as systems which exhibit interesting chiroptical properties have potential sensing and imaging applications.[25] A new method for introducing chirality in a one-pot synthesis from chiral amines was achieved by Dr. Joseph Byrne and subsequently the formation of optically active luminescent self-assemblies with Eu(III) and Tb(III) was monitored by CD spectroscopy and CPL.[176] The synthetic strategy involved firstly converting the relevant chiral amine into an azide *in situ* with the diazo-transfer reagent ImSO$_2$N$_3$·H$_2$SO$_4$, catalysed by Cu(II) with a concomitant colour change from cyan to lilac. The CuAAC reaction was then conducted by adding sodium ascorbate to reduce Cu(II) to Cu(I), and then adding the relevant alkyne. Yields of approximately 50% were achieved, and crucially the amine stereochemistry was retained. Eu(III) and Tb(III) complexes of **144** and **145** were subsequently synthesised. Quantum yields were found to be higher for the Tb(III) analogue (56-67 %) than the Eu(III) species (0.5-0.8%) measured in CH$_3$CN, which is consistent with previous studies.[123] Hydration states of these complexes were found to be zero indicating that the coordination sphere is fully saturated for both pairs of enantiomers. Self-assembly with Eu(III) and Tb(III)
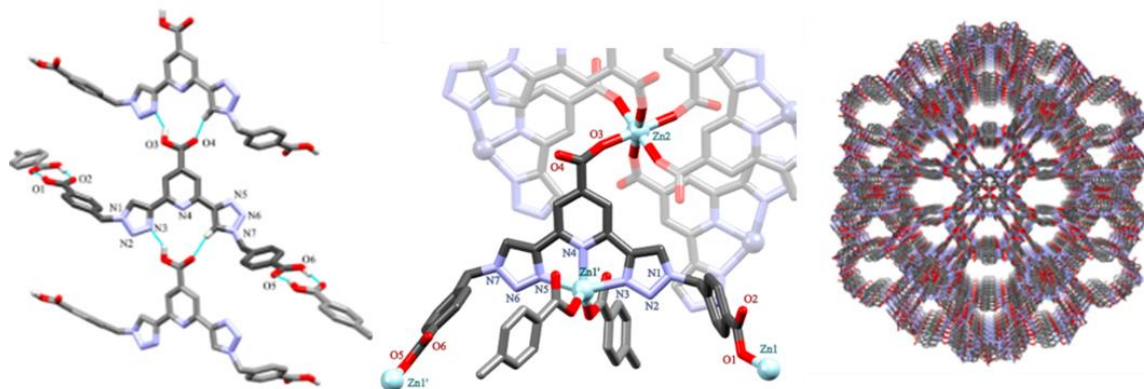
Figure 1.40 *X-ray crystal structure of ligand **143** displaying 3D hydrogen bonding network. Fragment of crystal structure of Poly-[Zn₇(**141**)₆] showing Zn connectivity and view of solvent channels in the crystal structure of the MOF. Reproduced from Ref 19.*

was monitored by UV-visible spectroscopy, time-delayed lanthanide luminescence and CD spectroscopy. Relatively high global stability constants were observed for 1:1(log β_{11} = 6.7), 1:2 (log β_{12} = 13.4) and 1:3 (log β_{13} = 20.9) metal:ligand species in solution with the 1:3 species being the most emissive species due to the fully saturated coordination sphere.

The introduction of biologically relevant moieties to the **btp** motif by appending amino acids to the structure was also conducted.[177] It was thought that this would be a facile way to introduce chirality to the ligand system. While the self-assembly of the ligands **146**–**152** could be monitored by UV-visible spectroscopy and lanthanide luminescence spectra, the CD spectra of the ligands were poorly resolved and showed only small differences between enantiomers indicating that the distance between the chiral amino acid centre and the metal ion was too large to induce a chiral response from the metal centre. Tb(III) and Eu(III) complexes were prepared and quantum yields of 46-70% in CH_3CN were obtained for the Tb(III) complexes, except the tryptophan derivatives which were much lower Eu(III) complexes, by contrast, exhibited drastically lower quantum yields in the range of 0.3-3%, In all cases the coordination spheres of the complex were found to be fully saturated. More recently, McCarney and Gunnlaugsson reported the first example of a 3D MOF [Zn₇**143**₆]·(H₂NMe₂)₄·(H₂O)₄₅ based on the **btp** motif.[19] The ligand **143** was obtained in single crystal form and X-ray diffraction analysis showed the **btp** adopted a *syn-anti* conformation. This is the first time this orientation has been observed for a **btp** derivative and is in contrast to the common *anti-anti* orientation typically observed for the free ligand. Reaction of ligand **143** with Zn(II) nitrate afforded yellow crystals which were characterised by X-ray diffraction. The resulting coordination polymer was comprised of two distinct

146	Gly	R = H
147	L-Ala	CH$_3$
148	D-Ala	CH$_3$
149	L-Phe	CH$_2$Ph
150	D-Phe	CH$_2$Ph
151	L-Trp	
152	D-Trp	
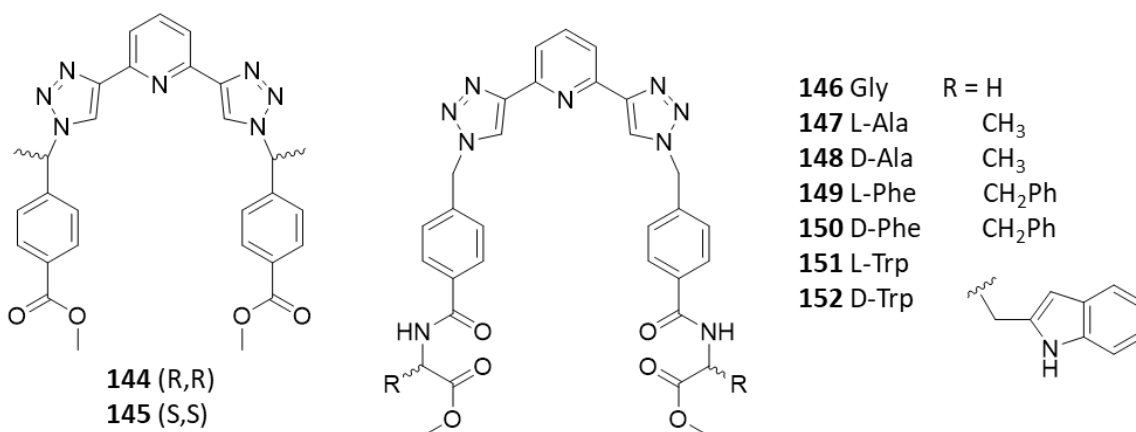
Figure 1.39 *Compounds **144–152** chiral derivatives of **btp***

coordination environments with one Zn(II) atom exhibiting trigonal bipyramidal geometry coordinating to a *syn-syn* oriented **btp**, and two carboxylate oxygen atoms from two adjacent ligands. The second Zn(II) is coordinated to six carboxylate oxygen atoms in an octahedral environment. Complete evacuation of the coordination polymer caused a reduction in void volume; however, guest exchange was still observed in solution with dimethylammonium cations being exchanged for cationic guest molecules such as luminescent Ln(III) ions and dyes. Upon cation exchange, sensitisation of Eu(III) and Tb(III) within the network was also observed.

While a large body of work has been conducted on **btp** and **pdc** systems independently, Dr. Samuel Bradberry and Dr. Joseph Byrne realised an opportunity to exploit the two systems with Eu(III) and Tb(III) to generate a luminescent polymer gel logic system. Complexation of **dpa** derivative **153** with Eu(III) and **btp** derivative **140** with Tb(III) generated two independent 1:3 metal:ligand systems which had previously been characterised.[178] The Eu(III) complex of **153** (Eu.**153**$_3$) was responsive to the presence of [H$^+$] caused by protonation of the pendant amine which resulted in reduced photoinduced electron transfer (PET) and a subsequent increase in the emission intensity. The Tb(III) complex of **140** [Tb(**140**)$_3$] was found to be responsive to F$^-$, where addition of TBAF resulted in a quenching of the Tb(III) emission and enhancement of the ligand fluorescence. The complexes were encapsulated into a poly(HEMA-*co*-MMA) matrix and then polymerised, resulting in a hard and brittle film. The film was then swelled in CH$_3$OH to give a flexible soft-material. Acidification of the CH$_3$OH solution lead to an increase in the Eu(III) centred emission, while the Tb(III) emission was quenched due to dissociation of the Tb(III) complex. Addition of TBAF to the neutral system caused a switching off of the Tb(III) emission again due to dissociation. Lastly, fluoridation followed by acidification

Eu **153**   Tb **140**
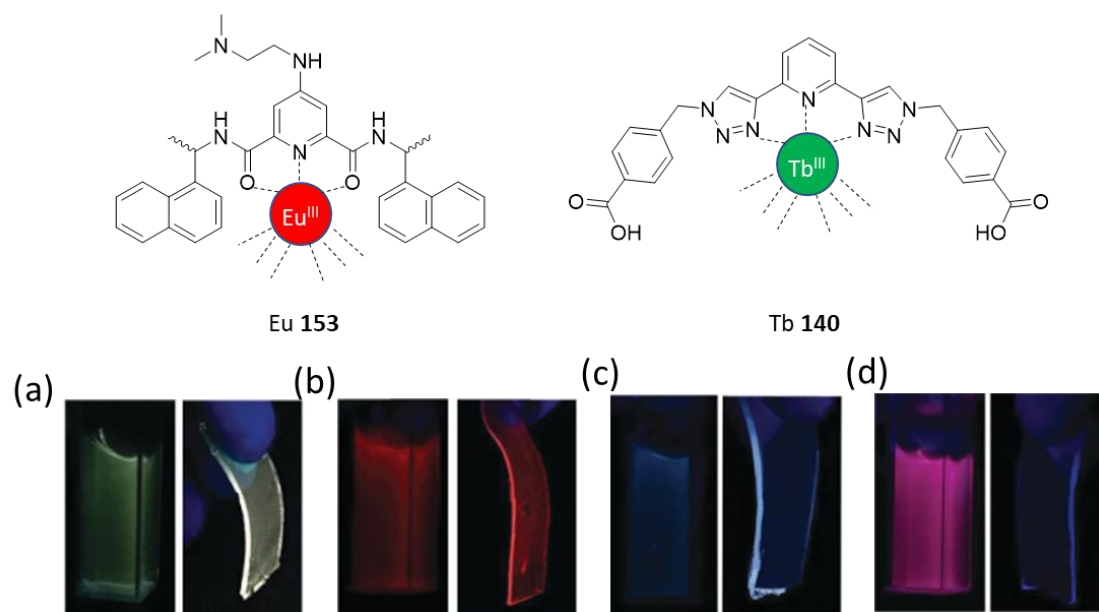
*Figure 1.41 Schematic representation of Eu(III) and Tb(III) complexes of **153** and **140** respectively (a) Input state (0,0) green emission from solution and solid state film (b) Input state (1,0) red emission from solution and solid state film (c) Input state (0,1) blue emission from solution and solid state film (d) Input state (1,1) purple emission from solution and solid state film. Reproduced from Ref 178.*

caused a quenching of Tb(III) emission and concomitant enhancement of Eu(III) emission. Reversing of these switches was not possible due to the dissociation of the Tb(III) complex.

The area of metallo-supramolecular soft materials is one which is has garnered significant interest in recent years due to the tuneable functional properties and reversible nature of the coordination interactions, which can allow for the generation of materials with self-healing properties or chemical responses to mechanical stimuli.[18] Another advantage is the metal based emission which can be achieved from these soft materials. An interesting approach is to graft these ligand monomers, capable of coordinating to metals, to an organic polymer backbone to generate a robust polymer system with rich spectroscopic properties. Bradberry and co-workers have reported a naphthyl-**dpa** ligand **154** functionalised with a methacrylamide moiety which they co-polymerised with
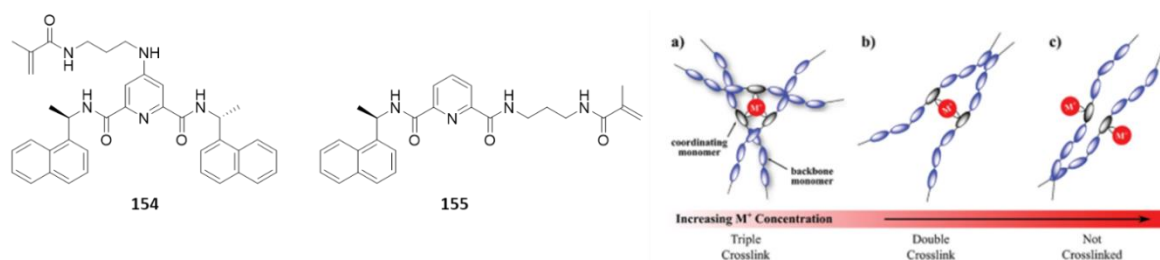
*Figure 1.42 Compounds **154** and **155** synthesised for the preparation of (HEMA-co-EGDMA)co-polymer and schematic representation of the crosslinks formed between copolymer chains by metal coordination at different metal stoichiometries.*
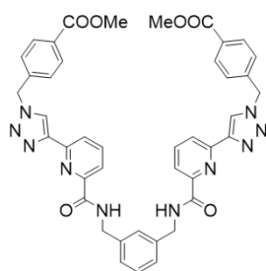
156
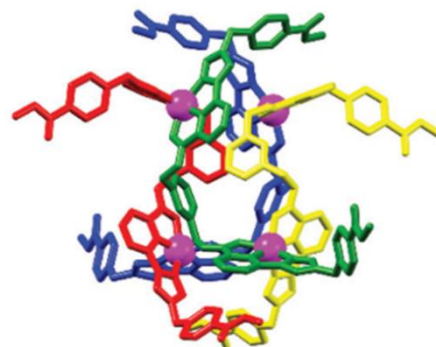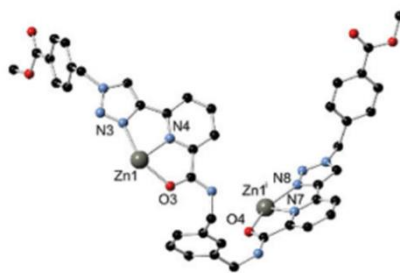
Figure 1.43 *Compound **156** and X-ray crystal structures of [Zn₄(**156**)₄](ClO₄)₈ showing geometry and coordination of one fragment of the [2 × 2] grid and simplified connectivity of the folded grid with each ligand coloured separately. Hydrogen atoms and anions omitted for clarity. Reproduced from Ref 180.*

p(HEMA-*co*-EGDMA) to yield a cross-linked metallo-hydrogel.[179] Asymmetric ligand **155** was also prepared as a co-polymer to study the effects of symmetry on the cross-linked system. The successful co-polymerisation of the ligands was confirmed by thermogravimetric analysis (T_g). Swelling of the materials in Eu(III) solution (0.33 equivalents) resulted in strong red Eu(III) centred emission from p(HEMA-*co*-EGDMA-*co*-**154**) but a much less intense response from the asymmetric co-polymer **155** was observed. The ratios of emission bands in the **154**-co-polymer matched those observed in solution for the [Eu·(**154**)₃]³⁺ species indicating that co-polymerisation did not restrict the coordination geometry of the Eu(III) centre. Hydration states were determined to be $q = 0$ and $q = 3$ for the symmetric and asymmetric systems respectively. Clearly the unsaturated coordination sphere of Eu(III) in the case of the **155** co-polymer results in quenching of the Eu(III) luminescence and a less emissive material.

A ligand designed by combining both the **dpa** and **btp** binding motifs within a single terdentate coordination site was developed by Dr. Dawn Barry in 2017.[180] This bis-terdentate (1,2,3-triazol-4-yl)-picolinamide (**tzpa**) ligand **156** was synthesised with an *m*-xylylene linker moiety and upon reaction with various *d*-metal ions, a folded [2 × 2] grid structure was formed which was confirmed by single crystal X-ray diffraction as well as UV-visible absorption and NMR spectroscopy studies in solution. These results will be discussed in more detail in the introduction to Chapter 2.

1.4 Work described within this thesis

The work presented in this thesis will address a range of derivatives of the aforementioned **dpa** and **btp** ligands, while also combining these two motifs and expanding on the recently

developed ditopic **tzpa** ligand. Their self-assembly with the lanthanide ions Tb(III) and Eu(III) will be explored with potential applications being of particular interest in the case of Tb(III) due to their strong emission properties. The coordination chemistry of these systems with *d*-metals, Cu(II) and Ag(I) in particular, will also be discussed in detail.

Chapter 2 will address the synthesis of a new chiral **tzpa** ligand and explore its coordination chemistry with Cu(II). It will become apparent how small changes to the reaction conditions can lead to significant structural differences in the resultant Cu(II) complexes. It will aim to determine the effects which introducing chirality to the **tzpa** ligand will have on the self-assembly of these ligands with Cu(II) ions. Previous work in the Gunnlaugsson group has shown that the self-assembly of an achiral ditopic **tzpa** ligand with *d*-metals led to the formation of 2×2 tetranuclear grid structure. In this Chapter, the effect of introducing a chiral functionality to this ditopic tzpa self-assembly will be explored. As discussed above, the introduction of chirality to the dpa system has been shown to influence the self-assembly of metallosupramolecular compelxes and also induce chirality at the metal centre, leading to the formation of helical structures.

Chapter 3 will be concerned with the synthesis of further **tzpa** derivatives to facilitate the formation of higher order assemblies. It will aim to explore the effect which introducing coordinating pyridyl motifs to the **tzpa** ligand design will have on the self-assembly of these systems with Cu(I)/(II) and also Ag(I) ions. These ligands are designed to generate soft-materials and higher-order coordination polymers as the introduction of pyridyl substituents will increase the opportunity for metal coordination interactions and could promote the formation of complex networks of non-covalent interactions.

Chapter 4 will describe the synthesis of a new class of amino acid functionalised (1,2,3-triazol-4-yl)-picolinamide (**tzpa**) ligands and will detail their self-assembly with lanthanide ions in solution and in the solid state. The **tzpa** ligands described in Chapters 1 and 2 are designed to be soluble in organic media. This allows for the formation of *d*-metal complexes and crystals of X-ray diffraction quality of these assemblies. The objective of Chapter 4 is to design and synthesise water soluble **tzpa** ligands and to generate lanthanide complexes with these ligands which are stable in aqueous media. The introduction of amino acid residues to the tzpa ligand design is the first step towards exploring the water solubility of these systems and the self-assembly of these novel ligands with Tb(III) and Eu(III) ions will be explored.

Chapter 5 will detail the synthesis of a 4-pyridyl-functionalised **btp** ligand and its self-assembly with lanthanide ions. The objective of this chapter is to functionalise the **btp**

ligand at the 4-pyridyl position with a moiety know to cause gelation, such as BTA, in order to generate a soft-material which has the capacity to coordinate *d-* or *f*-metal ions through the triazole-pyridyl functionality of the **btp** moiety. A preliminary study on the incorporation of this system into covalent polymer systems to take advantage of its photophysical applications will also be described. Finally, this chapter will aim to generate a robust polymer system incorporating emissive **btp**-Ln(III) complexes and examine the photophysical properties of this system.

Chapter 6 will describe experimental procedures and techniques for the work described herein followed by references and additional information.

"Sometimes the bravest and most important thing you can do is just show up"

Brené Brown

2. Unexpected Linkage Isomerism in Chiral Tetranuclear Bis-terdentate (1,2,3-triaozol-4-yl)picolinamide Grids

2.1 Introduction

As was mentioned in Chapter 1, the **dpa** terdentate ligand **H₂1** is a widely reported ligand which has commonly been employed in *d*-metal coordination chemistry.[47,56] Due to the ease of functionalisation and the ligand's propensity to form highly stable transition metal complexes, it has been utilised as a coordination motif in myriad applications, such as the formation of MOFs and large supramolecular assemblies.[74] In particular, coordination complexes formed with **H₂1** and Cu(II) have shown applications from bioinorganic chemistry to molecular magnetism.[48–52] Derivatisation of this coordination motif is easily achieved through amide coupling reactions to generate the 2,6-pyridine dicarboxamide ligand. Crucially, deprotonation of the amide nitrogen atoms can take place under basic conditions, resulting in metal coordination through these anionic amide N atoms. Introducing further substituents provides the opportunity to tune the structural properties of the resulting metal complexes leading to the formation of self-assemblies such as helicates and cages.[61,90] Alternatively, soft-materials can be generated by introducing long, aliphatic carbon chains, while the introduction of chirality to the **pdc** motif can influence the self-assembly of higher order structures with metal ions leading to self-sorting behaviour.[67–70] Recently it has been shown that homochiral, porous MOFs could be generated by enantioselective resolution of racemic mixtures.[181]

The **btp** motif has also been shown to form discrete coordination complexes with various first row transition metals and lanthanide ions.[40] The triazole "arms" can be easily functionalised through the CuAAC reaction, yielding a wide range of possible **btp** ligands suitably modified for the appropriate application. Like **pdc**, examples include the derivatisation of the **btp** motif with long aliphatic carbon chains, leading to the formation of soft-materials as well as the design and synthesis of compounds for the extraction of actinides from mixtures of *f*-metals and **btp** ligands capable of anion binding studies.[13,121–123,128,182]

With this in mind, a ligand designed by combining both the **dpa** and **btp** binding motifs within a single terdentate coordination site was first explored by Barry, Gunnlaugsson and co-workers in 2017.[183] The bis-terdentate (1,2,3-triazol-4-yl)-picolinamide (**tzpa**) ligand, **156**, which they reported, was a ditopic compound, which incorporated a *m*-xylylene central linker between two terdentate **tzpa** moieties. The *m*-xylylene linker was introduced in order to influence the self-assembly of the ditopic ligand with a view to forming helical structures upon complexation with various *d*- and *f*-metals. However, it was found that this ligand, **156**, favours the formation of tetranuclear [2 × 2] grid species with Zn(II) and

Fe(II) metal ions under mild reaction conditions. Reaction of the ligand with zinc perchlorate hexahydrate yielded colourless crystals which were shown by single crystal X-ray diffraction to exhibit the $[Zn_4(\textbf{156})_4](ClO_4)_8$ structure. The Zn(II) atoms occupy an octahedral geometry, wherein each metal ion is coordinated by the carbonyl oxygens, pyridyl nitrogens and triazole nitrogens of two distinct ligands, leaving each ligand bridging two Zn(II) atoms. The binding pockets of the ligands adopt a *syn* orientation which influences the overall topology of the complex, to generate a [2 × 2] grid. The coordination chemistry of the ligand was also explored with Fe(II); however, the crystals obtained displayed poor diffraction characteristics. Nonetheless, it was possible to determine the unit cell of the crystals and equivalent cell parameters to the tetranuclear Zn(II) complex were obtained, indicating that the Fe(II) species was isostructural with the $[Zn_4(\textbf{156})_4](ClO_4)_8$ complex. By contrast, reaction of the ligand with copper nitrate trihydrate under similar reaction conditions yielded crystals which, upon examination single crystal X-ray diffraction were found to be a dinuclear complex of the form $[Cu_2(NO_3)_4(\textbf{156})]\cdot5CH_3CN$. The process to generate this M_2L species is likely to be solubility driven, as the dinuclear complex was the only isolable product regardless of reaction stoichiometry. Each Cu(II) ion adopts a square pyramidal geometry, with the two coordination sites adopting *anti*-orientations, leading to each Cu atom being crystallographically unique. Each ligand molecule is coordinated to two metal ions in a bis terdentate fashion with two nitrato ligands completing the coordination sphere.

The self-assembly of these complexes was also probed in solution by analysing the changes in the UV-visible absorption and fluorescence spectra of **156** upon addition of Zn(II). Changes in the spectra were only observed up to the addition of 1 equivalent of Zn(II). The changes in absorbance could be fit using non-linear regression analysis to generate estimates of the solution state speciation and stability constants. The two species estimated to exist in solution were the ligand species **156**, and a 4:4 metal:ligand species $[Zn_4(\textbf{156})_4]^{8+}$ while the stability constant was determined to be $\log\beta_{44} = 48.8 \pm 1.0$. ^{1}H NMR titration studies were carried out to confirm this speciation observed by UV-visible absorption spectroscopy.

Other examples of [2 × 2] grid structures generated from dinuclear ligands have been reported by Meyer and co. workers, who reported the formation of tetranuclear complexes using Co(II), Mn(II), or Cu(II) under basic conditions.[155] Nitschke *et al.* have reported the formation of a [2 × 2] Cu(I) grid, which assembles only in aqueous solution.[184] The reaction of diaminobenzamide and pyridinedicarboxaldehyde with $[Cu(CH_3CN)_4](BF_4)$ precipitated

the complex as a tetrameric grid structure in the solid state. Hydrophobic effects were attributed to be the likely agent for the formation of this self-assembly, as organic solvents appeared to solvate the ligand molecules and prohibit the formation of this Cu(I) templated structure under such conditions. Bis-terdentate diamide ligands have also been shown to form two tetranuclear Cu(II) square grid complexes.[185]

Modular ligands upon which a family of analogues can be easily synthesised are vital for establishing structure-function relationships in complex polynuclear systems. The CuAAC reaction discussed in Chapter 1 is particularly useful in this regard, as modular derivatisation of the alkyne and/or azide precursor is facile, making the synthesis of a series of derivatives based on modified 1,2,3-triazole moieties highly feasible.[176,186] Furthermore, the heterocyclic triazole species can be readily conjugated to other coordinating functionalities such as pyridine to generate a series of multi-dentate ligand structures. Given that even small structural changes to the ligand motifs can have a large impact on their subsequent self-assembly in the presence of different metal ions (due to solubility, metal coordination geometry, and influence of non-covalent interactions), it is thus important to conduct structure-function studies with a series of ligand derivatives.

With this in mind and inspired by the metallosupramolecular [2 × 2] grids generated from ligand **156**, we set out to prepare a new **tzpa** ligand derivative, introducing chirality to the triazole "arms" through the CuAAC "click" reaction. Ligands **H₂157** and **H₂158** were synthesised in order to explore the effect of chirality on the self-assembly of the ditopic **tzpa** ligand system. As discussed in Chapter 1, introducing chirality to **dpa** systems has been shown to influence the self-assembly of metallosupramolecular complexes and the chirality of the metal centre, forming helical structures.[88] These chiral **tzpa** ligands, **H₂157** and **H₂158**, were designed to investigate the possible influences of chirality on the self-assembly of this asymmetric coordination motif. It was also of interest to examine the self-assembly behaviour of the **tzpa** ligand structure with Cu(I)/(II) salts due to the interesting solubility driven process with the achiral tzpa ligand **156** which resulted in the formation of an M₂L species.

This chapter describes the synthesis of chiral enantiomeric ligands **H₂157** and **H₂158** and their self-assembly with copper salts in the solid state and in solution. Single crystals of X-ray diffraction quality were obtained with various copper salts and the solution state assembly of these systems was monitored by UV-visible absorption spectroscopy. Along with the formation of isostructural tetrameric grid structures, unexpected linkage isomerism,

where an *in-situ* amide deprotonation promotes an asymmetric binding mode, under remarkably mild conditions is demonstrated.

2.2 Design and synthesis of ligand H₂157 and H₂158

As discussed above, the **tzpa** ligand motif has been reported only once in the literature, by Gunnlaugsson and Barry.[183] The enantiomeric ligand derivatives, **H₂157** and **H₂158**, were designed to introduce a chiral methyl group to the triazole "arms" of the **tzpa** ligand structure. The synthetic route shown in Scheme 2.1 afforded compounds **H₂157 and H₂158** from commercially available starting materials in a three-step synthetic procedure in moderate yield.

The first two steps in the synthesis of ligands **H₂157** (*S,S*) and **H₂158** (*R,R*), were conducted using the procedure as reported by Barry for the synthesis of compound **156**.[180] 6-Bromopyridine-2-carboxylic acid (2.1 equivalents) was reacted with 1 equivalent of *m*-xylylenediamine in a peptide-coupling reaction conducted in a CH₂Cl₂:DMF mixture at room temperature, using HOBt and EDC·HCl. After 48 hours, the crude product was isolated as a yellow oil which was dissolved in CH₂Cl₂, washed with 1.0 M HCl and saturated
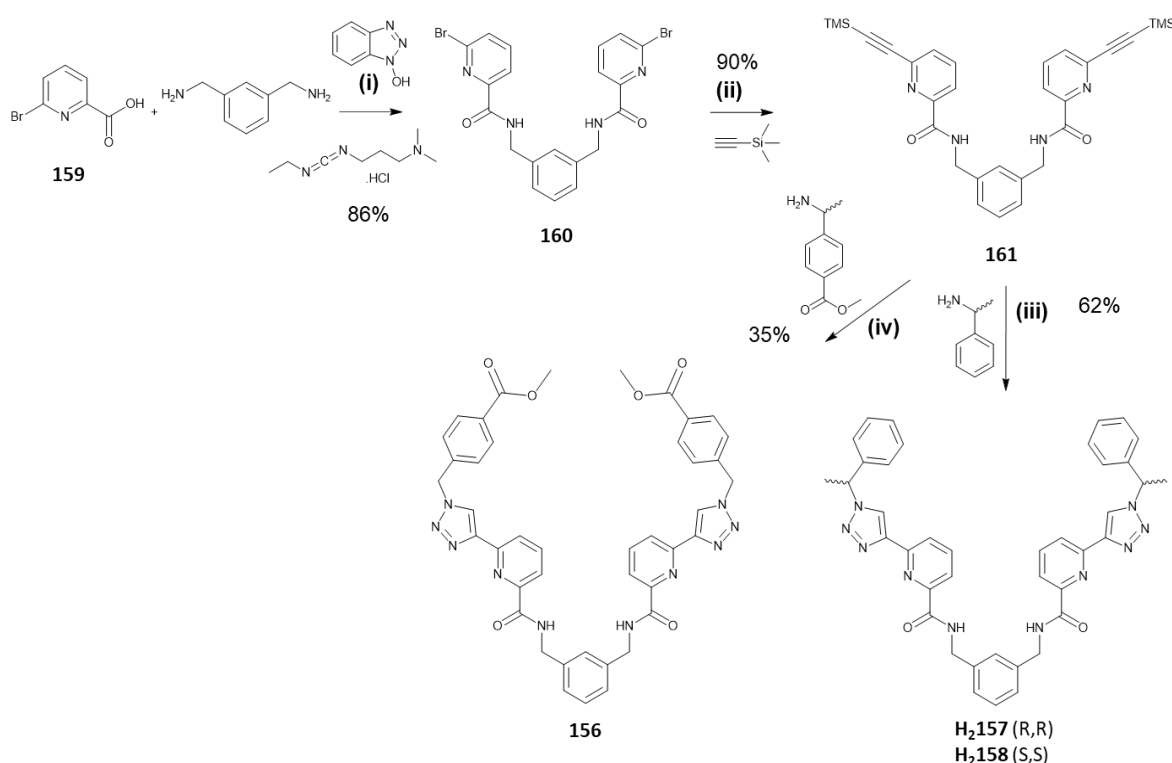
Scheme 2.1 *Synthesis and structure of **156**, **H₂157** and **H₂158**. Reagents and conditions: (i), NEt₃, 4:1 DCM:DMF (ii) CuI, Pd(PPh₃)₄, THF:NEt₃, (iii) (a) ImSO₂N₃.H₂SO₄, K₂CO₃, CuSO₄·5H₂O, MeOH, (b) Na ascorbate, K₂CO₃, H₂O: ᵗBuOH, **161**, DMF (ivNaN₃ CuSO₄·5H₂O, K₂CO₃, sodium ascorbate.*

aqueous NaHCO$_3$, dried over magnesium sulfate, then filtered and the solvent removed to yield **160** as a while solid. The di-bromo product **160** was then subjected to a Sonogashira coupling with ethynyltrimethylsilane using Pd(PPh$_3$)$_3$ as the catalyst, under an argon atmosphere at room temperature. After two days the crude product was isolated as a brown oil and purified by column chromatography to yield compound **161** as a brown solid. ^{1}H and ^{13}C{^{1}H} NMR spectroscopies, high-resolution mass spectrometry (HRMS) and IR spectroscopy were employed to verify the formation of the product. In addition, the solid-state crystal structure of the compound **161** was determined by X-ray diffraction analysis, the details of which will be discussed in Section 2.3. In order to introduce the chiral methyl group to the ligand, (S)-α-methylbenzylamine or (R)-α-methylbenzylamine were used in CuAAC reactions with the diazo transfer reagent imidazole-1-sulfonyl azide sulfuric acid (ImSO$_2$N$_3$·H$_2$SO$_4$) which generates the corresponding azide *in situ. via* a Cu(II) catalysed diazo transfer reaction while retaining the chirality of the methyl-benzylamine. The progress of this reaction is easily monitored by observing changes in the colour of the reaction mixture. In the first step, the reaction mixture changed from green to a lilac colour after five hours, indicating the formation of the azide. The second step of the reaction involved the addition of sodium ascorbate, to generate the Cu(I) species required for catalysis of the click reaction, and K$_2$CO$_3$ to deprotect the alkyne moiety. The suspension then turned a yellow colour and a DMF solution of the TMS-protected alkyne was added. After 48 hours the reaction mixture had turned an orange colour. The product was isolated by washing with a solution of EDTA in aqueous ammonia to scavenge the remaining Cu(II)/(I) ions, before
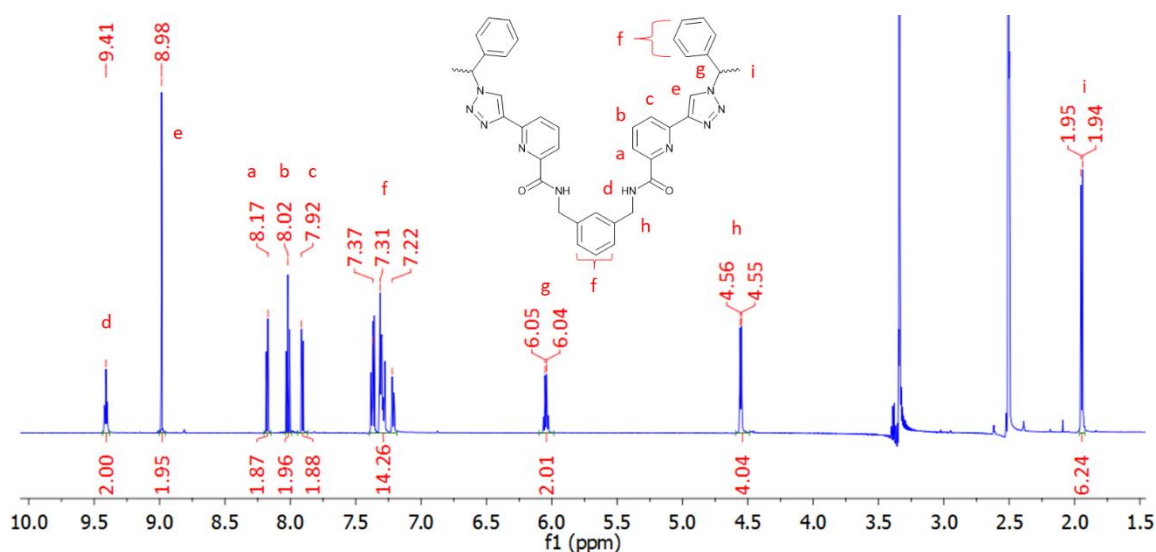

Figure 2.1 ^{1}H NMR spectrum (600 MHz, DMSO-d$_6$) of **H$_2$157** (S,S)

59

extracting into CH$_2$Cl$_2$. The crude product was purified by flash column chromatography to yield a white solid in 62% yield for **H$_2$157** (*S,S*) and 76% in the case of **H$_2$158** (*R,R*).

As shown in the ^{1}H NMR spectrum (600 MHz, DMSO-*d$_6$*) of **H$_2$157** (*S,S*) in Figure 2.1, resonances corresponding to the pyridyl protons reside at 8.18, 8.02 and 7.91 ppm. The amide proton can be found downfield at 9.41 ppm, and the triazole proton also resides downfield as a singlet at a resonance of 8.98 ppm. The chiral methyl groups, integrating to six protons appear upfield at 1.95 ppm and the peak at 6.05 ppm corresponds to the CH proton adjacent to these methy groups. Aromatic protons corresponding to the central *m*-xylylene ring and the phenyl arms are located at 7.45–7.09 ppm, integrating to fourteen protons. Finally, the CH$_2$ protons next to the central aromatic linker reside at 4.55 ppm as a doublet. ^{13}C\{^{1}H\} NMR, HRMS and IR spectroscopy were also employed to verify the formation of the desired chiral product **H$_2$157** (*S,S*) (See Appendix Figure A2.2 for ^{1}H NMR spectrum of **H$_2$158** (*R,R*)).

2.3 X-ray crystal structure of compound 161

Single crystals of X-ray diffraction quality of **161** were obtained by slow evaporation of a solution of **161** in hexane. Compound **161** crystallised in the triclinic space group *P*-1 and contained two complete molecules of the compound in the asymmetric unit with no solvent or guest species present. The two molecules adopt slightly different conformations of the amide groups about the central xylyl bridge but as a whole they both adopt quite similar U-shaped conformations. Intermolecular hydrogen bonding from the four amide N-H groups serve to bind the two residues in a tight dimer with two hydrogen bonding modes evident in the structure. Amide nitrogen atoms N4 and N6 were observed to donate hydrogen bonds to
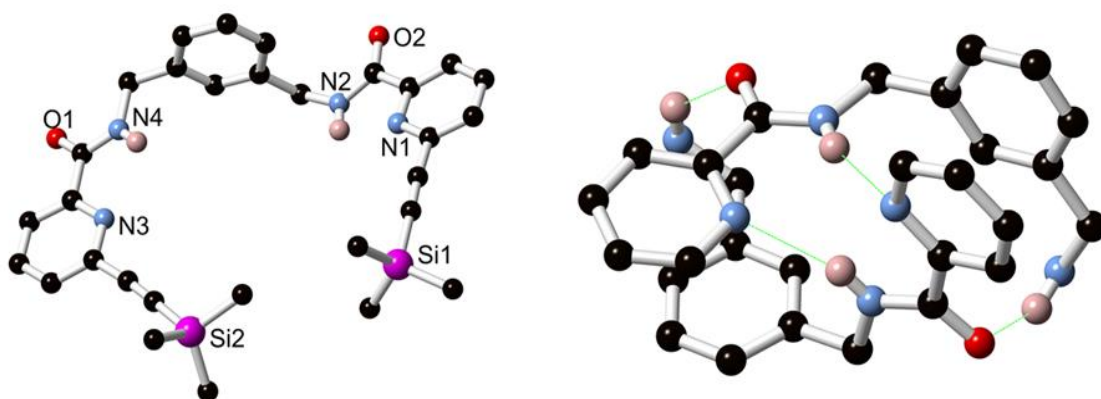

Figure 2.2 *(Left) Structure of one unique molecule of compound **161** with heteroatom labelling scheme. Selected hydrogen atoms are omitted for clarity. (Right) Primary mode of interaction between the two species in the solid-**161** dimer. Terminal trimethylsilyl-alkynylpyridine groups and selected hydrogen atoms are omitted for clarity.*

60

the pyridine nitrogen atom of their opposite residue with $N{\cdots}N$ distances of 3.162(2) and 3.249(2) Å, and N-H$\cdots$N angles of 160.6° and 163.13°, respectively. Intermolecular amide-amide hydrogen bonding interactions from nitrogen atoms N2 and N8 display O$\cdots$N-H distances of 2.957(2) and 2.930(2) Å, respectively, and N-H$\cdots$O angles of 134.5° and 137.0°, respectively. More linear association is interrupted by the steric clashes between the folded molecules. Further interactions, between the xylyl and pyridyl rings of the molecules are also observed. Typical heterotopic π-π interactions are evident with a minimum interatomic distance of 3.373(2) Å for the C5$\cdots$N5 interaction. Due to the dimerization of the two molecules accounting for all the strong hydrogen bond donors, the remaining intermolecular interactions between adjacent dimers consists largely of π-π, C-H$\cdots$π and C-H$\cdots$O interactions. The structure and primary hydrogen bonding interactions in **161** are shown in Figure 2.2 (see also Appendix Table A2.1). This solid-state structure was analysed by Dr. Hannah Dalton.

## 2.4 Formation of $[Cu_2(H_2157)](NO_3)_8$ and $[Cu_4(H_2157)_4](NO_3)_8$

Armed with the knowledge that a [2 × 2] tetrameric grid results from the reaction of ligand **156** with zinc perchlorate or iron perchlorate, the self-assembly of ligands **H_2157** and **H_2158** with these same salts under similar reaction conditions was investigated. Reaction of ligand **H_2157** with $Fe(ClO_4)_2{\cdot}6H_2O$ in CH_3CN, followed by toluene diffusion, resulted in the formation of red crystals. These crystals were analysed by single crystal X-ray diffraction, and a structural model was constructed. However, the quality of the single crystals generated was poor with only a low-resolution single crystal diffraction dataset being obtained. The connectivity model presented in Figure 2.3 indicates that the structure is similar to that reported by Dr. Dawn Barry for the $[Zn_4(156)_4](ClO_4)_8$ complex,[180] with four equivalent
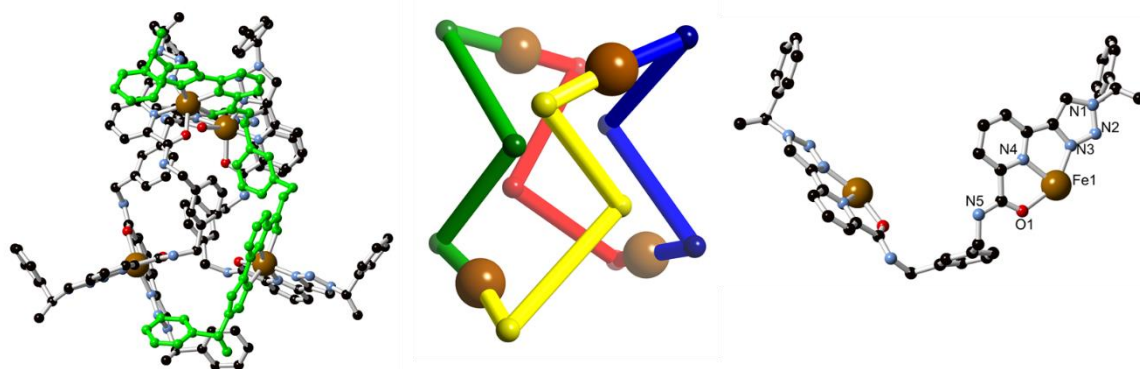
Figure 2.3 *Structural model of $[Fe_4(H_2157)_4](ClO_4)_8$ with a single ligand strand highlighted in green; connectivity model of $[Fe_4(H_2157)_4](ClO_4)_8$ and representative coordination geometry in the structure of $[Fe_4(H_2157)_4](ClO_4)_8$ with ligand molecule truncated for clarity.*

Fe(II) atoms, each coordinating to two ligands in a bis-terdentate fashion. Coordination to the metal ion occurs through two pyridyl nitrogen atoms, two triazolyl nitrogen atoms and two amide oxygen atoms, with the overall structure resembling a [2 × 2] square grid. Unfortunately, no crystals of X-ray diffraction quality were obtained from the 1:1 mixture of ligand **H₂157** with $Zn(ClO_4)_2 \cdot 6H_2O$.

To build upon this result the coordination chemistry of **H₂157** was investigated with a variety of other transition metal ions. Cu(II) was initially chosen due to its capability to exhibit several different coordination modes, which would potentially differentiate it from the Zn(II) analogues, and allow the ligand to more readily influence the structure and topology of the final assembly. Reaction of **H₂157** with $Cu(NO_3)_2 \cdot 3H_2O$ in CH_3OH solution in a 1:1 metal:ligand stoichiometric ratio yielded a blue solution. Upon concentration by slow evaporation, single crystals of X-ray diffraction quality were observed. The structure, determined by single crystal X-ray diffraction, revealed a tetranuclear supramolecular M_4L_4 assembly with a stoichiometry of $[Cu_4(\mathbf{H_2157})_4](NO_3)_8$. This structure was found to be structurally analogous to the [2 × 2] Zn(II) grid formed from the achiral tzpa ligand **156**. However, in keeping with the homochiral pendant groups the diffraction data were solved in the tetragonal space group $P4_3$, while in the case of the Zn(II) grid the data were solved in the tetragonal space group $I4_1/a$. The entire complex resides within the asymmetric unit. The tetrameric assembly consists of four equivalent six-coordinate Cu(II) atoms, each in a distorted octahedral environment. Each metal ion is bound in a bis-terdentate fashion by two non-equivalent ends of **H₂157** ligands, coordinating to two pyridyl nitrogen atoms, two triazolyl nitrogen atoms, and two amide oxygen atoms. As expected, a prominent Jahn-Teller axis is observed along one $N_{triazolyl}$-Cu-O_{amide} vector in each metal. The axial bonds all lie in
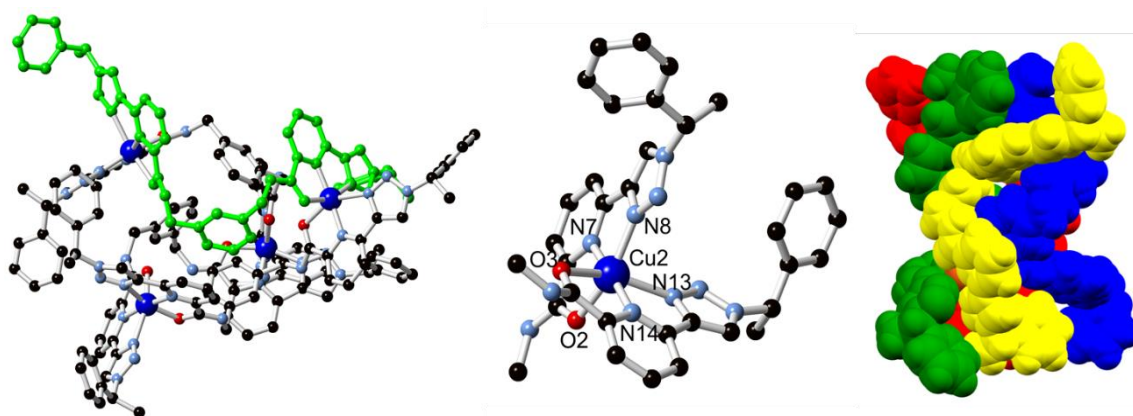
***Figure 2.4*** *Complete structure of $[Cu_4(\mathbf{H_2157})_4](NO_3)_8$ with a single ligand strand highlighted in green; representative coordination geometry in the structure of $[Cu_4(\mathbf{H_2157})_4](NO_3)_8$ with ligand molecule truncated for clarity and space fill model of $[Cu_4(\mathbf{H_2157})_4](NO_3)_8$*

a distance range of 2.26–2.45 Å while the equatorial M-L bonds lie in a distance range of 1.92–2.10 Å. As was the case for the achiral Zn(II) complex $[Zn_4(156)_4](ClO_4)_8$ the overall assembly of the $[Cu_4(H_2157)_4](NO_3)_8$ complex is a $[2 \times 2]$ square grid, rather than the possible circular helicate topology. Somewhat surprisingly, despite the inherently chiral nature of the ligand H_2157, the inner structure of the tetranuclear assembly is in fact achiral, with S_4 symmetry similar to that of the achiral $[Zn_4(156)_4](ClO_4)_8$ assembly. The structure of the metal binding sites thus does not appear to be influenced by the chirality of the ligand which is likely due to the distance of the chiral centre from the metal centres. The Cu-Cu distance of 10.7960(2) Å is similar to that observed for the Zn(II) structure which exhibits a Zn-Zn distance of 10.7493(7) Å. The assembly acts as an eight-connected hydrogen bond donor with each amide N-H donating a hydrogen bond to one NO_3^-. This results in four localised NO_3^- anions accepting two hydrogen bonds each and bridging two complexes. Only the four NO_3^- ions involved in hydrogen bonding, and one involved in a localised hydrogen bonding interaction with a lattice water molecule, could be crystallographically resolved. The remaining three anions overlap crystallographic symmetry elements among diffuse pockets of electron density. Their electron density contribution was accounted for using SQUEEZE, which is a tool for calculating disordered solvent or ion contributions, and their presence was confirmed with supporting bulk-phase characterisation methods. Elemental analysis on the air-dried sample confirmed the structure to be $[Cu_4(H_2157)_4](NO_3)_8] \cdot 2CH_3OH$. Phase purity was confirmed using powder X-ray diffraction at 100K (see Figure 2.6). This structure and the following crystal structures in
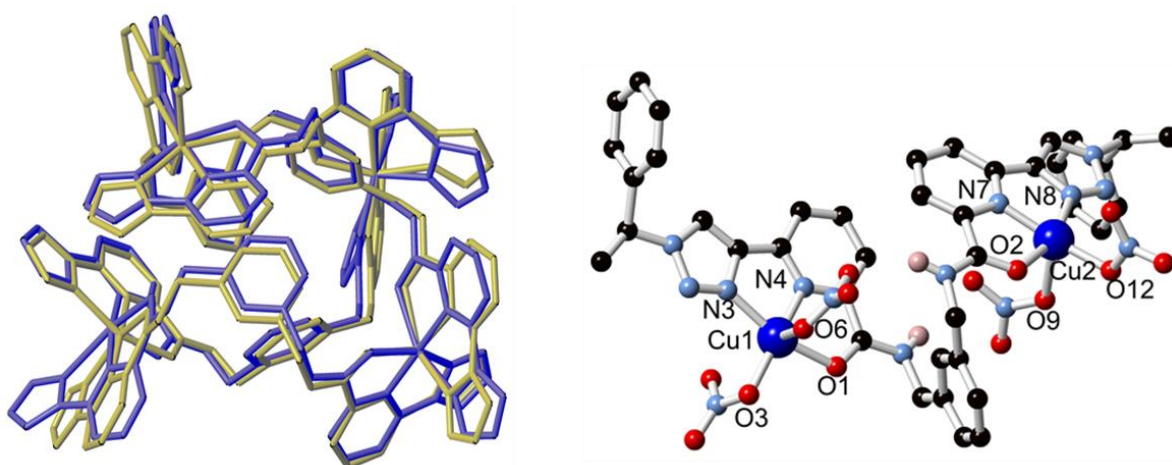
Figure 2.5 *Overlay of complex $[Cu_4(H_2157)_4](NO_3)_8$ (blue) with the tetranuclear zinc complex $[Zn_4(156)_4](ClO_4)_8$ reported by Barry et al.[S6] (grey), showing the overlap of the four metal sites (used as anchor points). Side arms, lattice solvents, anions and hydrogen atoms are omitted for clarity Also Structure of $[Cu_2(H_2157)(NO_3)_4] \cdot 1.5CH_3CN$.*

63
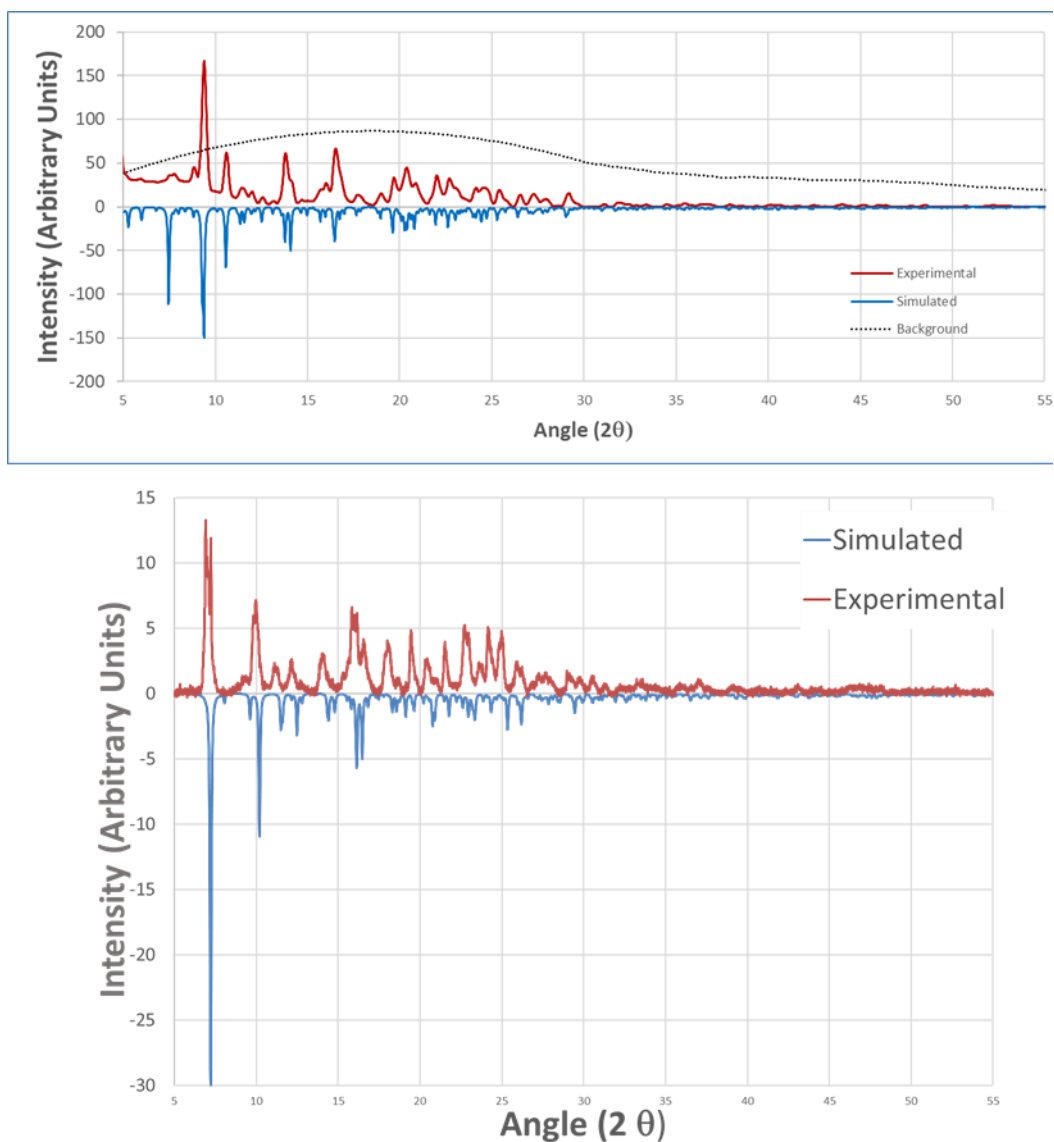
Figure 2.6 *X-ray diffraction pattern for (top) Cu₄(**H₂157**)₄(NO₃)₈ and (bottom) [Cu₂(**H₂157**)(NO₃)₄]·1.5CH₃CN measured at (100 K) (red) compared to the pattern simulated from the single crystal X-ray data obtained at (100K) (blue).*

Chapter 2, were solved by Dr. Chris Hawes. The M_4L_4 complex was not detectable by HRMS, and this was attributed to fragility of the complex which likely underwent fragmentation in the MALDI experiment. Reaction of ligand **H₂158** with $Cu(NO_3)_2·3H_2O$ under the same conditions as described above yielded an oily precipitate and unfortunately, the structure could not be determined by X-ray crystal diffraction.

Upon reaction of the ligand **H₂157** with $Cu(NO_3)_2·3H_2O$ in the same 1:1 molar ratio as above, changing only the reaction solvent from CH_3OH to CH_3CN, a blue solution was obtained. This solution yielded blue crystals after sitting for several weeks at 2 ˚C. These crystals were analysed by single crystal X-ray diffraction. They showed poor diffraction characteristics; however, a connectivity model of [Cu₂(**H₂157**)(NO₃)₄]CH₃CN could be

elucidated (Figure 2.5). The model suggests the formation of a dinuclear complex analogous to the dinuclear complex [$Cu_2(NO_3)_4$**156**]·$5CH_3CN$ discussed in Section 2.2, which was prepared with the achiral **tzpa** ligand **156**. The complex was found to be the sole isolable product from the reaction, regardless of reaction stoichiometry, with no evidence for the formation of an analogous M_4L_4 structure in the solid state with CH_3CN, suggesting that this is a solubility driven process. The connectivity model was refined in the monoclinic space group $P2_1/c$. The asymmetric unit was observed to contain the discrete complex in its entirety and one lattice acetonitrile molecule. One molecule of the ligand **H$_2$157** coordinates to two crystallographically unique Cu(II) ions in a bis-terdentate fashion. The two copper ions adopt similar coordination geometries, with both displaying square pyramidal environments coordinating to the terdentate (N,N,O) ligand. The coordination sphere of each copper is completed by two monodentate nitrato ligands. The axial nitrato ligands show extended Cu-O bond lengths of 2.2–2.3 Å compared to those in the equatorial plane which are approximately 1.9–2.0 Å. This was also the case upon analysis of the [$Cu_2(NO_3)_4$**156**]·$5CH_3CN$ structure. The Cu-Cu distance was measured to be 8.567(2) Å, compared with that of 8.5981(9) Å for the achiral complex. The ligand is folded about the central *m*-xylyl group and this conformation is supported by intramolecular hydrogen bonding interactions from the amide groups of the ligand to the non-coordinating nitrato oxygen atoms from the adjacent binding pocket. The terminal chiral arms are not involved in any specific or directional intermolecular interactions with nearby molecules. Phase purity was confirmed using powder X-ray diffraction at 100K (see Figure 2.6) and elemental analysis on an air dried sample confirmed a formula of [$Cu_2(NO_3)_4$(**H$_2$157**)]·$1.5CH_3CN$. Again, the complex was not detectable by HRMS.

Reaction of the ligand enantiomer, **H$_2$158** with $Cu(NO_3)_2$·$3H_2O$ in a 1:1 molar ratio under the same reaction conditions yielded blue crystals upon standing in CH_3CN for five days. The crystals were analysed by single crystal X-ray diffraction, but the complex displayed poor diffraction characteristics and there was significant disorder. However, a connectivity model could be elucidated, and indicated the structure was similar to that of the complex [$Cu_2(NO_3)_4$(**H$_2$157**)]·CH_3CN, with the unit cell containing two full molecules of the complex in this case as well as one acetonitrile molecule. The connectivity model was refined in the triclinic space group P-1. Again, a single ligand molecule **H$_2$158** coordinates two crystallographically unique Cu(II) ions in a bis-terdentate fashion. The coordination environment of the two copper ions is the same as for the other enantiomeric complex

$[Cu_2(NO_3)_4(\mathbf{H_2157})]\cdot CH_3CN$, with two nitrato ligands completing the coordination sphere. The axial nitrato ligands again show extended Cu-O bond lengths compared to those in the equatorial plane. This was also the case for the $[Cu_2(NO_3)_4(\mathbf{H_2157})]\cdot CH_3CN$ complex (see appendix Table A2.1), and both complexes exhibited similar Cu-Cu distance. Thus in conclusion, it is evident that enantiomers $\mathbf{H_2157}$ and $\mathbf{H_2158}$ generate isostructural M_2L complexes when reacted with $Cu(NO_3)_2$ and the ligand chirality has little influence on the extended crystal structure.

2.5 Formation of $[Cu_4(\mathbf{H157})_4](PF_6)_4$

Having examined the coordination chemistry of ligands $\mathbf{H_2157}$ and $\mathbf{H_2158}$ with Cu(II), it was interesting to determine if there there would be any structural variability upon reaction with Cu(I) salts. It was expected that the Cu(I) species would undergo immediate oxidation to form the analogous $[Cu_4(\mathbf{H_2157})_4](NO_3)_8$ structure, or a bis-bidentate analogue of the above complexes, with the usual N_4 tetrahedral coordination of many Cu(I) species. However, upon reaction in CH_3OH and diffusion of toluene vapor, blue crystals of $[Cu_4(\mathbf{H157})_4](PF_6)_4$ were obtained. The structure, as determined by X-ray diffraction, revealed a tetranuclear supramolecular M_4L_4 assembly with similar connectivity to $[Cu_4(\mathbf{H_2157})_4](NO_3)_8$, but exhibiting linkage isomerism at the metal site. The diffraction data were solved in the monoclinic $C2$ space group with two halves of two unique complexes residing within the asymmetric unit. The $[2 \times 2]$ grid consists of four metal ions coordinating in a six-coordinate N_5O coordination sphere. One amide oxygen atom has been replaced by a deprotonated amide nitrogen atom in each ligand and each ligand is singly deprotonated such that each Cu ion is coordinated with one of each of *N,N,N* and *N,N,O* coordination modes. Unsurprisingly, given the increase in ligand field strength of the deprotonated amide, the desymmetrisation of the coordination sphere also switches the Jahn-Teller axis of elongation to be fixed along the single $N_{triazolyl}$-Cu-O_{amide} axis at each coordination site. This mixed N,O-donation from a pyridylamide group is a rare observation with single linkage isomers coordinating through anionic nitrogen or neutral oxygen donors being far more common. While the metal coordination is significantly altered in the complex, the overall connectivity and topology is surprisingly unchanged. The reduced symmetry of the ligand, following deprotonation, results in a complex with a reduced C_2 symmetry element as well. The tetrameric assembly assumes a more compact arrangement than its $[Cu_4(\mathbf{H_2157})_4]^{8+}$ counterpart, caused by four intermolecular hydrogen bonding interactions which are formed between the remaining deprotonated amide nitrogen atoms and the non-coordinated amide
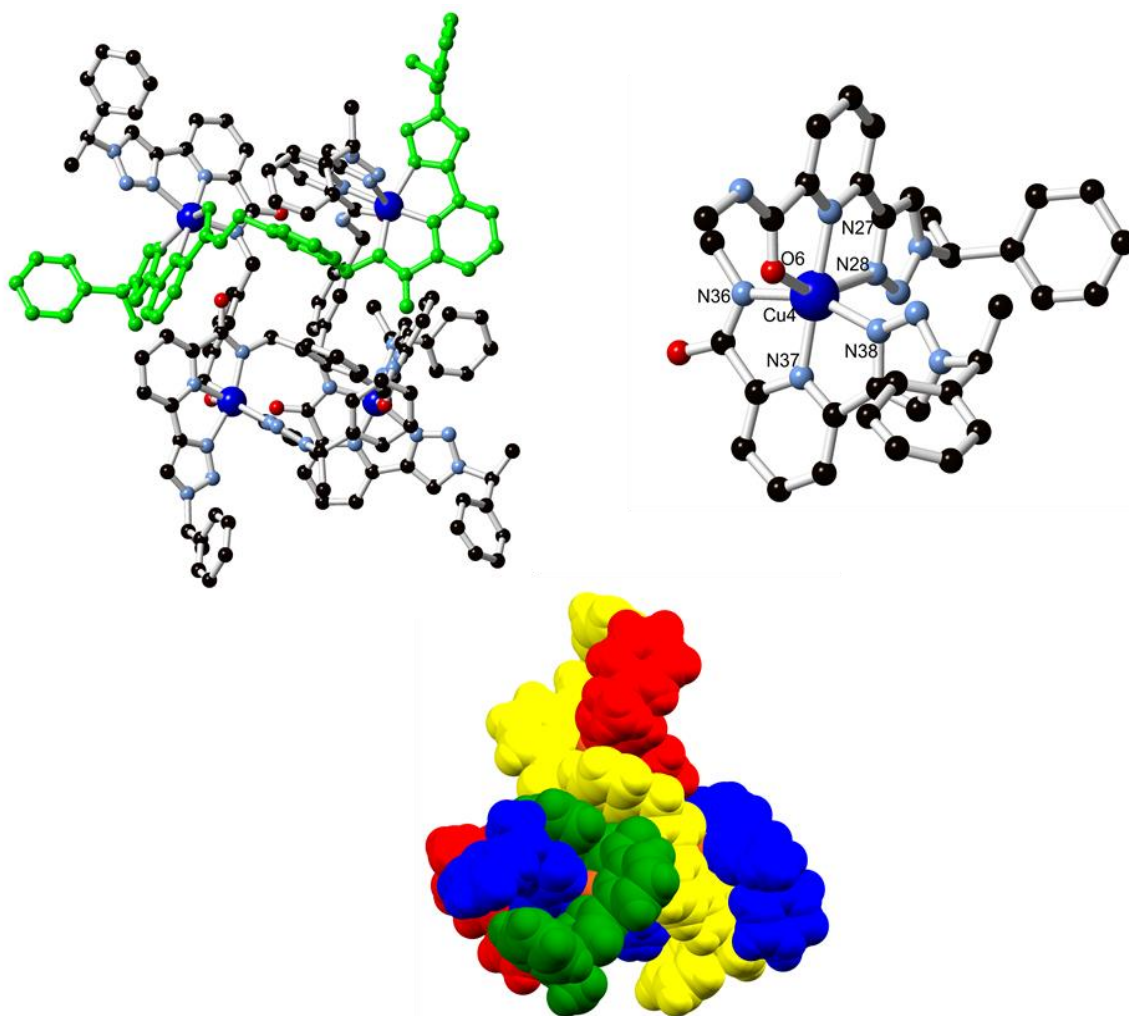
Figure 2.7 *Complete structure of [Cu₄(**H157**)₄](PF₆)₄ with a single ligand strand highlighted in green; Representative coordination geometry in the structure of [Cu₄(**H157**)₄](PF₆)₄ with ligand molecules truncated for clarity showing both modes of amide coordination through oxygen atom O6 and nitrogen atom N36 and space fill model of [Cu₄(**H157**)₄](PF₆)₄.*

oxygen atoms from adjacent strands. The Cu_4 tetrahedral volume was reduced by 16%; however, the total molecular volume remains essentially unaffected. Due to the intermolecular interactions accounting for all the hydrogen bond donors, the extended structure contains only π-π stacking and C-H···X hydrogen bonding interactions. Four toluene molecules more were located from the Fourier residuals and show C-H···F interactions stemming from the triazolyl C-H groups. Electron density pockets which were diffuse and could not be suitably modelled were accounted for using the SQUEEZE[187] routine with supporting methods showing $[Cu_4(\textbf{H157})_4(PF_6)_4]$ ·4PhMe·12H₂O as the formula for the bulk material. Elemental analysis determined the solvent content to be four toluene molecules and twelve water molecules. Thermogravimetric analysis was then employed to confirm this formula, showing a loss in mass of 14.4%, which is in good

agreement with the elemental analysis which indicates a solvent mass of 14.0%. (See Appendix Figure A2.1). Phase purity was confirmed by powder X-ray diffraction at 100K. Upon reaction of enantiomeric ligand **H₂158** with [Cu(CH₃CN)₄](PF₆) under the same reaction conditions a semi-crystalline material was obtained which, unfortunately, was not suitable for X-ray diffraction.

Attempts were made to obtain crystalline material from other cuprous salts [Cu(CH₃CN)₄](BF₄) and [Cu(CH₃CN)₄](CF₃SO₃); however, no crystalline material was obtained due to the high solubility of the resulting assemblies in CH₃CN. As we rely on crystallisation in these systems it is likely that the different steric requirements of these salts can result in different outcomes.

Following on from the study of these solid-state assemblies, the systems were studied in solution under mild conditions at lower concentration using spectroscopic techniques to elucidate the species present in solution along with their stability constants.

2.6 Solution studies of H_2157 with $Cu(NO_3)_2$ and $[Cu(CH_3CN)_4]PF_6$ in CH_3OH and CH_3CN

Having successfully analysed the solid-state structures, the complexes [Cu₄(**H₂L**)₄](NO₃)₈ [Cu₂(**H₂L**)(NO₃)₄]CH₃CN and [Cu₄(**HL**)₄](PF₆)₄ (L = **157** or **158**) were characterised spectroscopically in CH₃OH and CH₃CN, at 298 K, by dissolution of the crystalline material in the chosen solvent.

The UV-visible absorption spectra for complexes [Cu₄(**H₂157**)₄](NO₃)₈ and [Cu₄(**H₂158**)₄](NO₃)₈ recorded in CH₃OH, were dominated by two main bands (Figure 2.8).
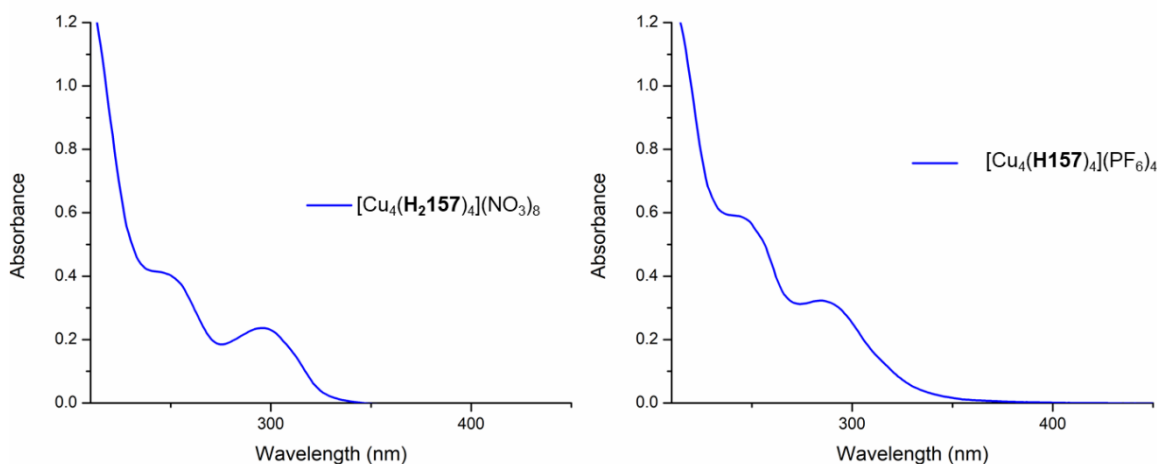
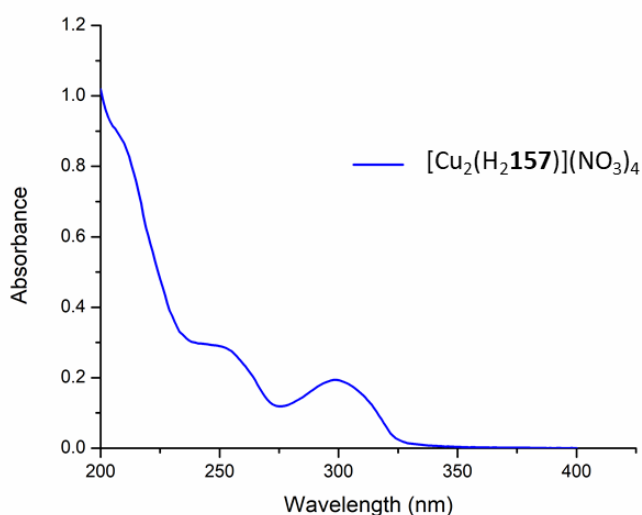***Figure 2.8*** *The UV-vis absorption spectra of (left) [Cu₄(**H₂157**)₄](NO₃)₈ and (right) [Cu₄(**H157**)₄](PF₆)₄ (1.2 × 10⁻⁵ M) in CH₃OH.*

68

A high energy band, observed at $\lambda_{max} = 248$ nm, and a lower energy band at $\lambda_{max} = 295$ nm were observed in the UV-visible absorption spectrum. The emission spectra displayed an emission band at 350 nm with very low intensity. The photophysical properties of $[Cu_4(\textbf{H157})_4](PF_6)_4$ and $[Cu_4(\textbf{H158})_4](PF_6)_4$ complexes were also examined in CH_3OH and their UV-visible absorption spectra are shown in Figure 2.8. The main bands associated with the copper complexes occur at $\lambda_{max} = 245$ nm and $\lambda_{max} = 285$ nm. The luminescence spectra show a low intensity band at 353 nm, indicating that upon complexation to the metal ion, the ligand fluorescence is almost completely quenched. Finally, the $[Cu_2(\textbf{H}_2\textbf{157})](NO_3)_4$ and $[Cu_2(\textbf{H}_2\textbf{158})](NO_3)_4$ complexes were analysed in CH_3CN solution and display a band centred at $\lambda_{max} = 252$ nm as well as a broad band at $\lambda_{max} = 300$ nm. All the complexes were stable in solution over several hours with no evidence of dissociation observed from the UV-visible absorption or fluorescence spectra.

Analysis of the $[Cu_4(\textbf{H157})_4](PF_6)_4$ system by MALDI mass spectrometry showed various M+L fragments, including [4M+3L+PF$_6$] (*m/z* 2459.55, calc. 2459.57). Unfortunately, neither the parent tetracation or octacation were detected, suggesting that the higher-order assemblies are unstable under the harsh MALDI fragmentation conditions.

Having examined the absorption spectra and HRMS of the complexes the self-assembly of these ligands with Cu(I) and Cu(II) *in situ* was examined with a series of UV-visible absorption titrations.


Figure 2.9 *The UV-vis absorption spectrum of $[Cu_2(\textbf{H}_2\textbf{157})](NO_3)_4$ (1.1×10^{-5} M) in CH_3CN.*

2.7 Solution studies of the self-assembly of H₂157 with Cu(NO₃)₂ and [Cu(CH₃CN)₄]PF₆

The self-assembly of ligand **H₂157** with $Cu(NO_3)_2$, $[Cu(MeCN)_4](PF_6)$, $Fe(ClO_4)_2 \cdot 6H_2O$ and additionally $Cu(ClO_4)_2 \cdot 6H_2O$ was investigated in solution. The formation of multiple metal:ligand species in solution was monitored *in situ* by analysing the changes in the UV-visible absorption and luminescence spectra. The data was fit using non-linear regression analysis in order to elucidate the stoichiometric species in solution and determine their stability constants. All measurement were repeated three times to ensure reproducibility.

Solution studies of compound **H₂157** titrated with a metal $Cu(NO_3)_2$ stock solution were examined under mild conditions. A solution of **H₂157** at a concentration of 1×10^{-5} M, in CH_3OH, was analysed by absorbance and fluorescence spectroscopy upon addition of aliquots of a CH_3OH solution of $Cu(NO_3)_2$ at room temperature. Changes in the UV-visible absorption and luminescence spectra of the ligand were monitored in order to investigate the kinetic self-assembly of compound **H₂157** with $Cu(NO_3)_2$ in solution, see Figure 2.10. The absorption spectrum of **H₂157** displayed two main bands, centred at $\lambda_{max} = 291$ nm and $\lambda_{max} = 250$ nm attributed to $\pi \rightarrow \pi^*$ transitions. Upon addition of the metal solution, a decrease in the absorbance of the band centred around 250 nm up to the addition of 1 equivalent of $Cu(NO_3)_2$ was observed. However, thereafter a hyperchromic effect was seen. Meanwhile the band at $\lambda = 290$ nm saw an increase in absorbance and a concomitant redshift upon addition of $Cu(NO_3)_2$ which continued beyond 1 equivalent. No plateau was reached up to the addition of 3.0 equivalents of metal solution.
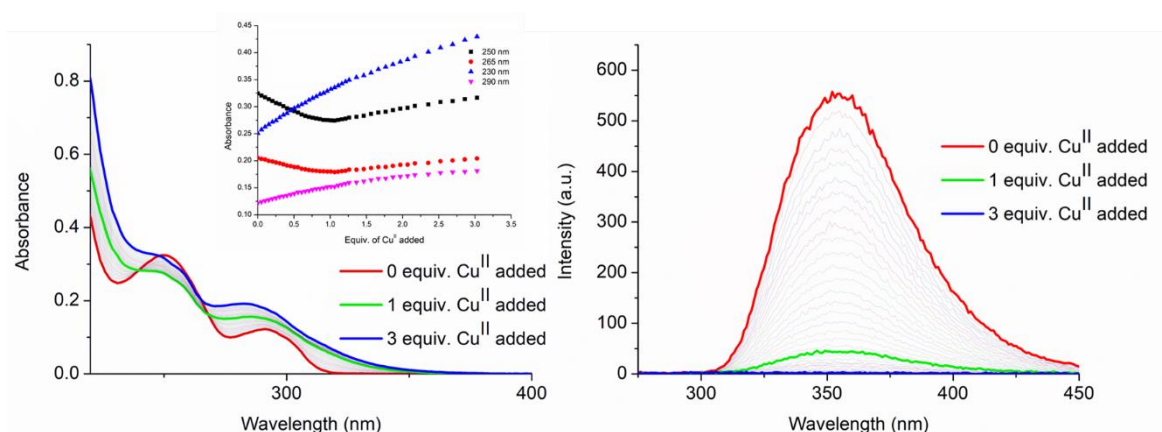
***Figure 2.10** The overall changes in the (left) UV-vis absorption spectra and (right) fluorescence emission spectra upon titrating **H₂157** (1×10^{-5} M) against $Cu(NO_3)_2$ ($0 \rightarrow 3$ equiv.) in CH_3OH at RT. **Inset**: corresponding experimental binding isotherms of absorbance at $\lambda = 250, 265, 230$ and 290 nm.*

The ligand centred fluorescence spectrum displayed an emission band centred at $\lambda = 354$ nm upon excitation at $\lambda_{exc} = 250$ nm. The intensity of this band decreased upon the addition of the Cu(NO$_3$)$_2$ stock solution. The fluorescence decreased significantly up to the addition of 1.0 equivalent of Cu(NO$_3$)$_2$, and the addition of excess metal up to 1.5 equivalents of the Cu(II) resulted in complete quenching of the ligand fluorescence.

Having observed how the reaction solvent plays a vital role in the outcome of the solid-state self-assembly of ligand **H$_2$157** with Cu(NO$_3$)$_2$, this effect was examined *in situ*. As discussed above, changing the reaction solvent from CH$_3$OH to CH$_3$CN favours the formation of an M$_2$L species rather than the anticipated M$_4$L$_4$ tetrameric grid assembly in the solid state. Changes in the UV-visible absorption and fluorescence spectra of **H$_2$157** (1 $\times$ 10^{-5} M) were monitored upon the addition of aliquots of Cu(NO$_3$)$_2$ in CH$_3$CN solution at room temperature. The ligand absorption spectrum remained unchanged from the spectrum recorded in CH$_3$OH with two main bands observed at $\lambda_{max} = 250$ nm and $\lambda_{max} = 291$ nm. Upon addition of 1 equivalent of Cu(NO$_3$)$_3$, a small decrease in the high energy absorption band at $\lambda = 250$ nm was observed, along with broadening of the peak. No further changes were observed up to the addition of 4.0 equivalents of metal ion. The longer wavelength absorption band at $\lambda = 291$ nm increased in intensity upon the addition of Cu(II) and a concomitant red-shift was observed. No plateau was reached up to the addition of 4 equivalents of metal solution. The ligand fluorescence was also monitored and a similar
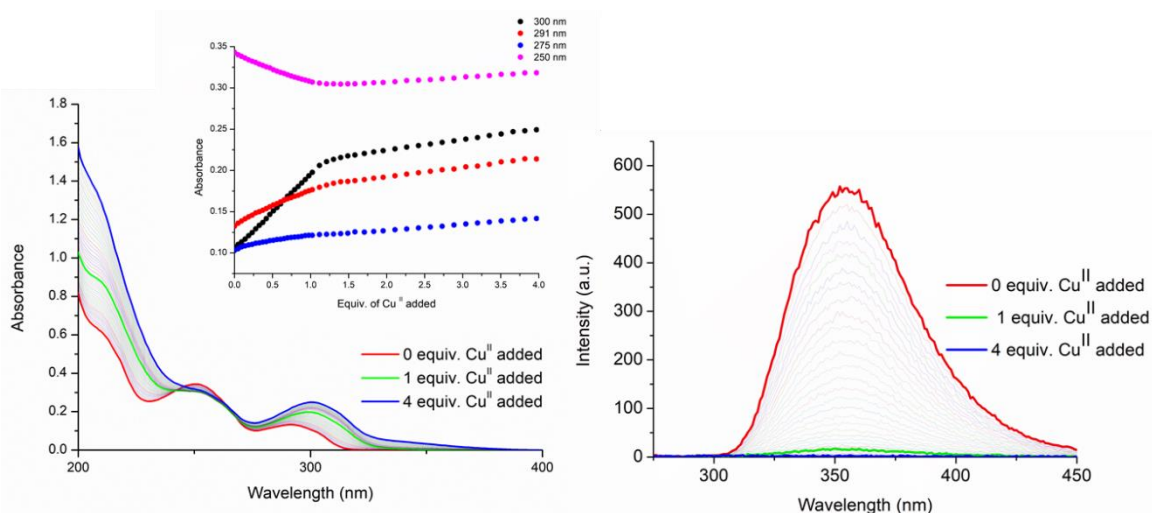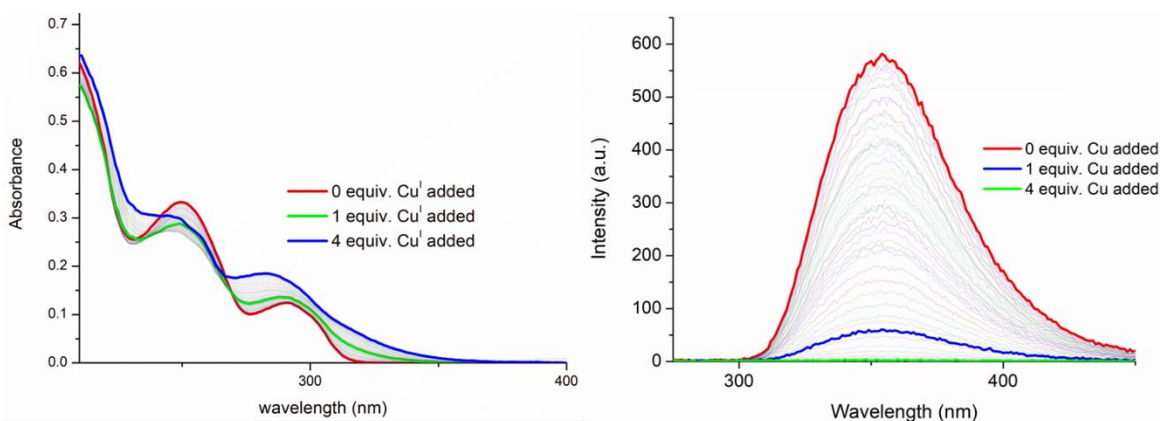

Figure 2.11 *The overall changes in the (left) UV-vis absorption spectra and (right) fluorescence emission spectra upon titrating* ***H$_2$157*** *(1$\times$10^{-5} M) against Cu(NO$_3$)$_2$ (0→4 equiv.) in CH$_3$CN at RT.* ***Inset****: corresponding experimental binding isotherms of absorbance at $\lambda = 300$, 291, 275 and 250 nm.*

trend was observed in CH$_3$CN as for CH$_3$OH previously: ligand fluorescence was quenched upon the addition of 1.0 equivalent of Cu(II).

Having evaluated the self-assembly of **H$_2$157** with Cu(NO$_3$)$_2$, attention was turned to the ligands interaction with [Cu(CH$_3$CN)$_4$](PF$_6$) *in situ*. The metal-directed self-assembly was evaluated spectroscopically in CH$_3$OH. As described above, specific aliquots of [Cu(CH$_3$CN)$_4$](PF$_6$) stock solution were added to a solution of ligand **H$_2$157** (1×10^{-5} M) in CH$_3$OH and changes to the UV-visible and fluorescence spectra were monitored in order to analyse this dynamic process. The initial absorption spectrum of ligand **H$_2$157** again displayed two main bands at λ_{max} = 250 and λ_{max} = 291 nm. Addition of the [Cu(CH$_3$CN)$_4$]PF$_6$ metal solution, up to 2 equivalents of the metal stock, resulted in a decrease in the absorbance of the high energy band at λ_{max} = 250 nm. Thereafter, the absorbance increased in intensity where even up to the addition of 4 equivalents of [Cu(CH$_3$CN)$_4$](PF$_6$) these changes had not reached a plateau. The lower energy band located at λ_{max} = 291 nm experienced only a slight increase in absorbance up to the addition of 2 equivalents of metal solution, with a concomitant broadening of the band observed. Subsequently, upon addition of a further 2.0 equivalents of metal solution, a more substantial hyperchromic shift was observed along with a blueshift and a concomitant broadening of this band. A plateau was not reached by the addition of 4.0 equivalents of metal solution. Again, the fluorescence emission spectrum of the ligand was measured, and the emission band was centred at λ = 354 nm upon excitation of the ligand at 250 nm. The fluorescence emission was reduced significantly with the addition of the [Cu(CH$_3$CN)$_4$](PF$_6$) solution, up
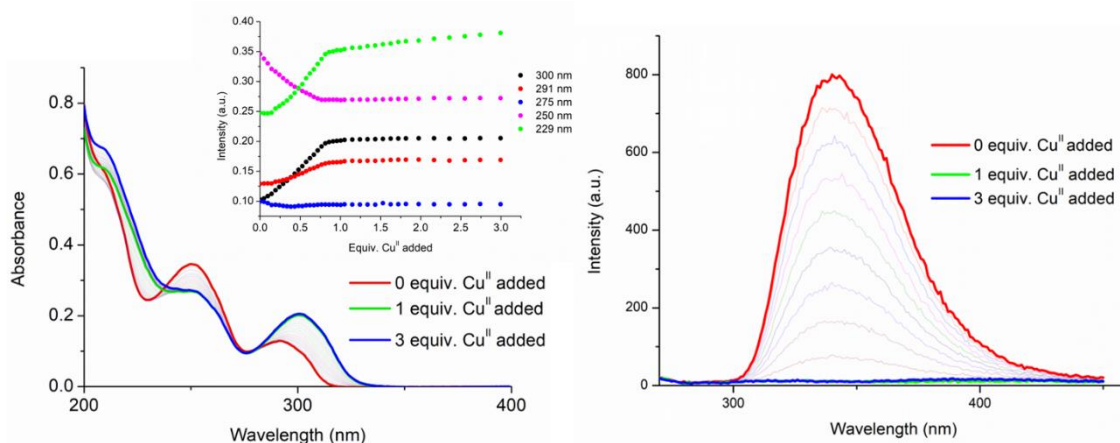
Figure 2.12 *The overall changes in the (left) UV-vis absorption spectra and (right) fluorescence emission spectra upon titrating **H$_2$157** (1×10^{-5} M) against [Cu(CH$_3$CN)$_4$](PF$_6$) ($0\rightarrow4$ equiv.) in CH$_3$OH at RT.*

Figure 2.13 *The overall changes in the (left) UV-vis absorption spectra and (right) fluorescence emission spectra upon titrating **H₂157** (1×10⁻⁵ M) against Cu(ClO₄)₂ (0→3 equiv.) in CH₃CN at RT.* ***Inset****: corresponding experimental binding isotherms of absorbance at λ = 300, 291, 275, 250 and 229 nm.*

to 1 equivalent of the metal solution, and upon addition of 2 equivalents the emission was completely quenched.

Finally, having examined the effects of solvent and metal oxidation state on the self-assembly of the ligand **H₂157** with copper ions, it was of interest to establish the effect of the copper counterion on the assembly of this system. Thus the changes in the UV-visible absorption spectrum of **H₂157**, upon addition of $Cu(ClO_4)_2$ in CH_3CN solution under the same conditions as described above, were studied. Changes to the high energy band centred at λ_{max} = 250 nm occurred in the form of a decrease in intensity, up to the addition of 1 equivalent of Cu(II), after which a plateau was reached. The lower energy band, occurring at λ_{max} = 291 nm, experienced an increase in intensity up to the addition of 1 equivalent of the metal solution with a concomitant red-shift. Subsequent additions of excess Cu(II) did not result in any change to the spectrum indicating the formation of a stable 1:1 (or possibly 4:4) assembly. The ligand centred emission was completely quenched upon the addition of 1 equivalent of the metal solution, with no further changes observed after this point. A titration was also carried out with another perchlorate metal salt, $Fe(ClO_4)_2 \cdot 6H_2O$, under the same conditions and the changes in the UV-visible and fluorescence spectra were very similar to those shown for the $Cu(ClO_4)_2$ titration (see appendix Figure A2.x) which indicates the self-assembly behaviour of **H₂157** with $Fe(ClO_4)_2$ and $Cu(ClO_4)_2$ is similar and likely influenced by the counterion.

In order to evaluate the changes to the UV-visible absorption spectra during each titration described above, and assess the self-assembly mechanism, the measurements were

analysed by non-linear regression analysis. From this analysis the binding model and stability constants could be estimated.

2.8 Fitting of titration data and calculation of complex stability constants

The changes observed in the absorption spectra were analysed and the species estimated to exist in solution described below are considered valid based upon solid-state structures obtained as well as the typical coordination requirements of the metal ion. In order to provide a robust estimation of the formation of complex species, a global analysis method was used wherein all the spectra were regressed together to determine a value for the stability constants. During this refinement, concentration profiles were established for each stoichiometric species in solution. This analysis was completed with ReactLab EQUILIBRIA software.

Analysis of the UV-visible absorption data for **H₂157** with Cu(NO₃)₂ in CH₃OH solution pointed to the presence of three main species, (**H₂157**, 2:1 metal:ligand assembly and 4:4 metal:ligand assembly) with the distribution of these species estimated from this analysis. The dominant species in solution was determined to be the 4:4 species, up to the addition of 1.0 equivalent of metal solution, with approximately 90% abundance at 1 equivalent of metal ion. Upon addition of excess Cu(NO₃)₂, a decrease in the abundance of the 4:4 species was observed, with the 2:1 species becoming more prominent in solution. It is likely that addition of excess Cu(II) induced dissociation of the M_4L_4 species, demonstrating the assemblies' unstable nature at low concentrations, and in the presence of excess Cu(II). The 2:1 species observed here is expected to be related to the crystallised
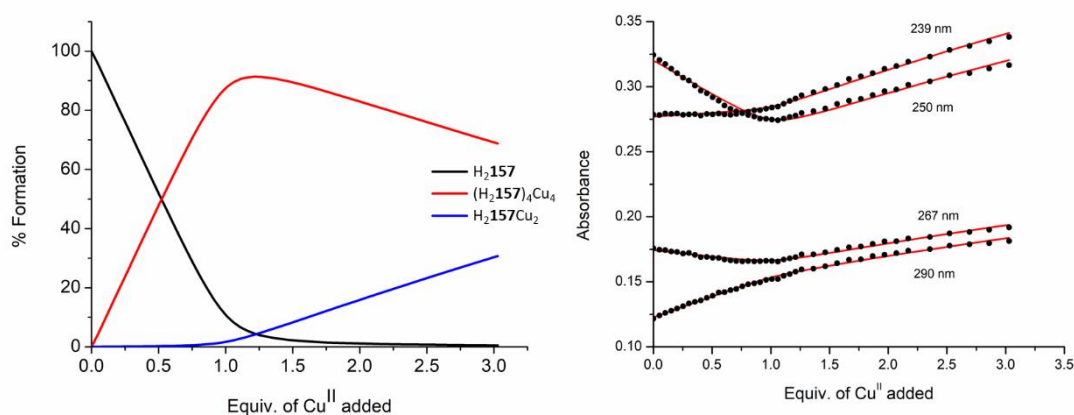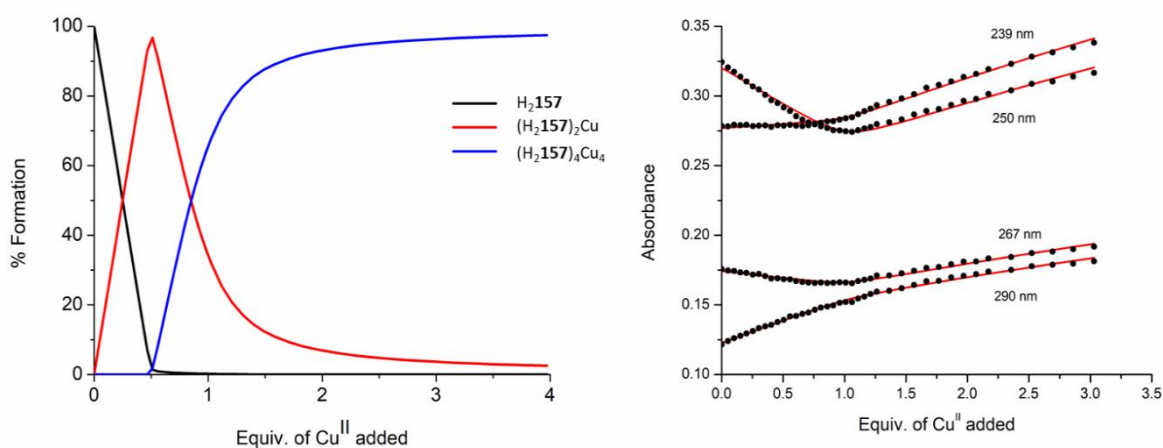

Figure 2.14 *(left) The speciation distribution diagram obtained from the fit of the UV-vis absorption titration data of ligand **H₂157** against Cu(NO₃)₂ in CH₃OH. (right) the fit of the experimental binding isotherms using non-linear regression analysis software ReactLab.*

[Cu$_2$(**H$_2$157**)(NO$_3$)$_4$]CH$_3$CN complex described in Section 2.4, with each terdentate *N,N,O,* binding pocket coordinating one Cu(II) ion, and solvent or nitrato ligands completing the Cu(II) coordination sphere. From the changes observed in the UV-visible absorption spectra throughout the titration, binding constants were estimated for each species. The 4:4 metal:ligand assembly formed with $\log\beta_{44} = 42.3 \pm 0.3$, which is comparable to that seen for the achiral compound **156** with Zn(ClO$_4$)$_2$. The second species (2:1 metal:ligand) had a calculated binding constant of $\log\beta_{21} = 11.3 \pm 0.1$.

Analysis of the UV-visible absorption data of **H$_2$157** with Cu(NO$_3$)$_2$ in CH$_3$CN solution indicated the presence of three main species in solution (**H$_2$157**, 1:2 metal:ligand and 4:4 metal:ligand). The distributions of these species were estimated and shown in Figure 2.15. The dominant species in solution, up to the addition of 0.5 equivalents of metal, was found to be the ML$_2$ species with up to 97% abundance. Upon the addition of further Cu(NO$_3$)$_2$ the abundance of the 1:2 species decreased, and the 4:4 metal:ligand species reached an abundance of 95% by the addition of 2 equivalents of Cu(II). This 4:4 species is likely analogous to the [Cu$_4$(**H$_2$157**)$_4$](NO$_3$)$_8$ complex described in Section 2.4. From the changes in the absorption spectra, binding constants were determined, with the 1:2 species found to be $\log\beta_{12} = 15.4 \pm 0.1$, and the second species binding constant calculated as $\log\beta_{44}$ = 48.0. The higher stability constant for the M$_4$L$_4$ species when compared to the same species formed in CH$_3$OH above is consistent with the speciation distribution which demonstrates that the 4:4 species in CH$_3$CN is highly stable even upon addition of excess Cu(NO$_3$)$_2$, which was not the case in CH$_3$OH.

Figure 2.15 *(left) The speciation distribution diagram obtained from the fit of the UV-vis absorption titration data of ligand **H$_2$157** against Cu(NO$_3$)$_2$ in CH$_3$CN. (right) the fit of the experimental binding isotherms using non-linear regression analysis software ReactLab.*
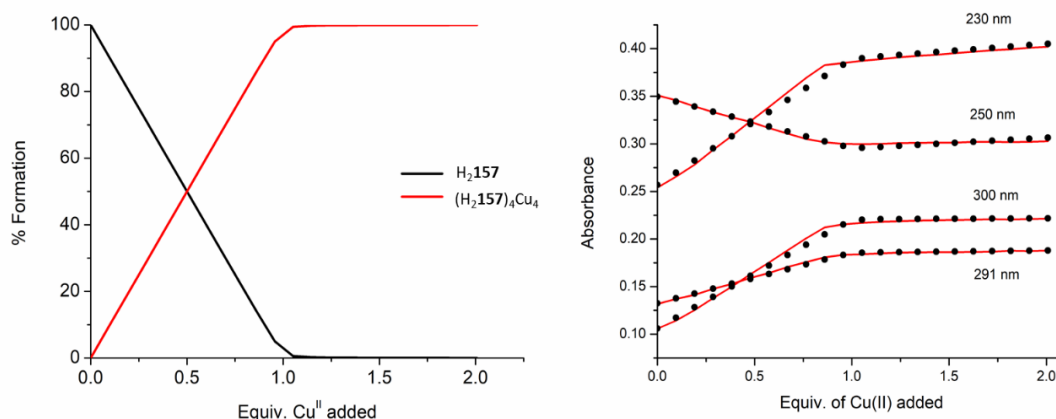
Figure 2.16 *(left) The speciation distribution diagram obtained from the fit of the UV-vis absorption titration data of ligand **H₂157** against Cu(ClO₄)₂ in CH₃CN. (right) the fit of the experimental binding isotherms using non-linear regression analysis software ReactLab.*

Upon analysis of the UV-visible absorption titration data for **H₂157** with [Cu(CH₃CN)₄](PF₆) in CH₃OH, multiple species were observed in solution. Unfortunately, due to the complexity of the speciation data, it could not be fit to a one or two species model. Finally, the changes to the UV-visible absorption titration data for **H₂157** and Cu(ClO₄)₂ was analysed using ReactLab. The speciation distribution and fit of the binding isotherms are shown in Figure 2.16. The analysis indicated the presence of only two species in solution (**H₂157** and 4:4 metal:ligand), with the M_4L_4 species reaching 100% abundance upon the addition of 1 equivalent of the Cu(ClO₄)₂ solution. The stability constant was determined as $\log\beta_{44} = 47.8 \pm 0.6$. These results likely indicate the formation of a [2 × 2] grid structure in solution, analogous to [Cu₄(**H₂157**)₄](NO₃)₈ which appears to be stable even in the presence of excess metal ions in solution. The stability constant is very close to the related stability constant for Cu(NO₃)₂ in CH₃CN and slightly higher than that of the same species in CH₃OH. Analysis of the changes in the UV-visible absorption spectra of **H₂157** with Fe(ClO₄)₂ yielded similar results to those described for Cu(ClO₄)₂. Only two species were observed to be present in solution (**H₂157** and 4:4 metal:ligand), with the stability constant for the assembly determined to be $\log\beta_{44} = 36.2 \pm 0.2$. While the stability constant was lower than the stability constants obtained in the Cu(ClO₄)₂ titration, the speciation was similar, suggesting the counterion influences the self-assembly of these systems.

From the analysis of these results, we can conclude that the solvent in which the self-assembly occurs plays a large role in determining the speciation. Changing only the solvent, from protic (CH₃OH) to aprotic (CH₃CN), alters the assemblies formed, as well as their corresponding stabilities. These observations are in agreement with the observations made

for the solid state studies in Sections 2.4 and 2.5. It is also interesting to consider the effect of the counterion on the assemblies. The $Cu(ClO_4)_2$ salt appears to form more stable M_4L_4 structures than the $Cu(NO_3)_2$ salt, with no evidence of intermediate assemblies, or dissociation of the structures in solution; however, crystalline material suitable for X-ray diffraction analysis of this species could not be obtained.

2.9 Chiroptical properties of Cu(II) complexes – Circular Dichrosim

Circular dichroism (CD) is an experimental technique which differentiates absorption of right- and left-circularly polarised light caused by an optically active asymmetric chromophore (or a symmetric chromophore in an asymmetric environment). Measurements are carried out in the visible and ultra-violet region of the electromagnetic spectrum, monitoring electronic transitions.[188] Circularly polarised light interacts differently with chiral molecules, with the right and left-handed components of electromagnetic radiation interacting with the electrons residing in a chiral environment to different extents. This results in a CD signal which is given by:

$$\textbf{Equation 1: } \Delta A = A_L - A_R$$

where A_L represents the absorbance of left-handed circularly polarised light and A_R is the absorbance of right-handed circularly polarised light. The circular dichroism spectrum of a chiral compound, therefore, may possess both positive and negative signals. This technique was employed in this section to probe the chiral nature of both the ligand and the metal-complexes which were formed.

The CD spectra of enantiomers **H₂157** and **H₂158** were recorded in CH_3CN in order to probe the chiral nature of the ligands. The enantiomeric compounds gave rise to CD absorption bands which are mirror images of each other. The CD spectra are dominated by the appearance of a high energy band at $\lambda = 215$ nm, and a band of lower intensity at $\lambda = 290$ nm, with a very small band appearing at $\lambda = 255$ nm. Bands at 255 nm and 290 nm correspond to bands observed in the UV-visible absorption spectra of the ligands **H₂157** and **H₂158**, while the band observed at 215 nm is unique to the CD spectra of the ligands.
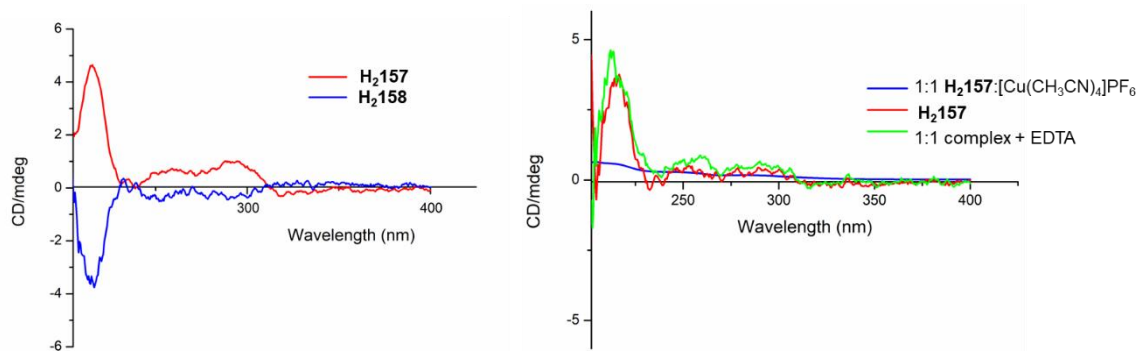
Figure 2.17 *CD spectra of (left) ligands **H₂157** and **H₂158** and (right) ligand **H₂157**, 1:1 **H₂157**:[Cu₄(CH₃CN)](PF₆) and 1:1 complex + EDTA showing elimination of signal upon self-assembly with metal ion.*

The CD spectrum of the ligand **H₂157** with [Cu(CH₃CN)₄]PF₆ in a 4:4 metal:ligand stoichiometry recorded in CH₃OH is shown in Figure 2.17. This was recorded in order to probe the chirality of the ligand, as well as the effects of the ligand chirality on the M₄L₄ assembly, with the latter being formed in solution adding 1 equivalent of [Cu(CH₃CN)₄]PF₆ to a solution of the ligand **H₂157**. The ligand trace exhibits the main bands described above at 215, 255 and 290 nm. Upon addition of 1 equivalent of the metal solution, the main bands observed for the chiral ligand are supressed. No evidence of chirality transfer from the ligand to the metal centre was observed. Thus, the self-assembly of the M₄L₄ complex in solution appears to negate the chirality of the ligand **H₂157** in this case. In order to confirm that the ligand had not undergone racemisation in solution, a solution of EDTA was added to the 4:4 complex to scavenge the Cu(II) ions. Upon addition of 1 equivalent of the EDTA solution, recovery of the bands associated with the ligand chirality was observed.

2.10 Cyclic Voltammetry

The transfer of electrons between an electrode surface and molecules in solution is the fundamental process in electrochemical reactions. Voltammetry refers to a technique that measures a current response upon applying a given voltage or series of voltages from the electrode. Three electrodes are required for voltammetric measurements (working, counter, and reference). A cyclic voltammogram is obtained when the voltage is swept between two values at a fixed rate, and upon reaching the maximum/minimum voltage, the scan direction is reversed, returning the voltage back to its initial state. The voltage sweeps can be cycled multiple times. The voltage output from the electrode to the solution, and back to the electrode, either oxidises or reduces the analyte, and this is measured experimentally from
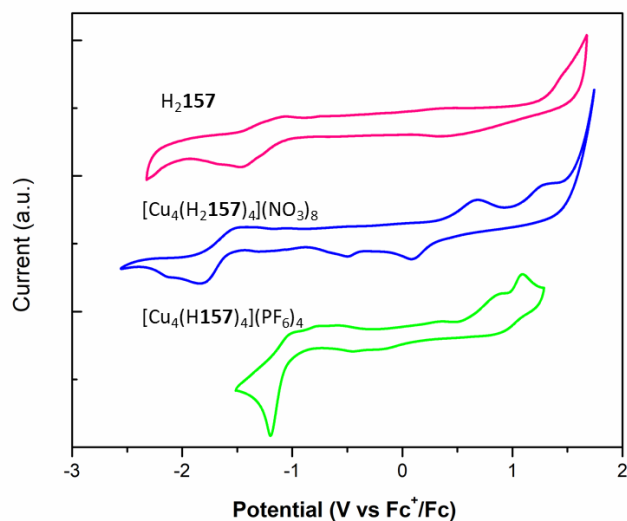
Figure 2.18 *Cyclic voltammetry for **H₂157**, [Cu₄(**H₂157**)₄](NO₃)₈ and [Cu₄(**H157**)₄](PF₆)₄ recorded in deaerated acetonitrile; supporting electrolyte TBAPF₆ 0.1 M. The Fc⁺/Fc couple was used as an internal standard. Scan rates were at 100 mV s⁻¹ and were in the negative scan direction.*

the resultant current response. Cyclic voltammetry (CV) is thus an excellent tool for characterising the reduction and oxidation processes of molecular species.

Due to the interesting behaviour of ligand **H₂157** in the complex [Cu₄(**H157**)₄](PF₆)₄ where each ligand in the complex is singly deprotonated, coupled with the spontaneous oxidation of Cu(I) to Cu(II) under very mild reaction conditions, it was decided to probe the electrochemical properties of the two complexes [Cu₄(**H₂157**)₄](NO₃)₈, and [Cu₄(**H157**)₄](PF₆)₄ as well as the ligand **H₂157** using CV. Studies were carried out at an approximate concentration of 1×10^{-2} M in CH₃CN. The ferrocene/ferrocenium redox couple was used as the internal standard. As expected, the CV traces of the ligand and the [Cu₄(**H₂157**)₄](NO₃)₈ complex are distinctly different from that of the [Cu₄(**H157**)₄](PF₆)₄ complex (Figure 2.18). The ligand exhibits an irreversible reduction at an electrochemical onset of -1.15 V which can be seen in Figure 2.18 and a second irreversible reduction, the onset of which occurs at approximately -2.50 V. Upon examination of the CV trace scanned from -2.8 to +1.8 major return waves are observed, the onset of which occur at -1.49 V and -1.20 V. However, when the window is cut to -2.2 V they disappear, indicating that these are electrochemical side-products arising from the major irreversible reduction at -2.50 V. No discernible oxidation was detected for the ligand in the observable solvent window.

The [Cu₄(**H₂157**)₄](NO₃)₈ CV trace exhibits a small cathodic shift in the reduction wave, with an onset of -1.61 V which is similar to the reduction process observed for the

ligand. However, in contrast to the ligand, an oxidation process is observed for $[Cu_4(\textbf{H}_2\textbf{157})_4](NO_3)_8$ at +1.13 V. It is difficult to definitively discern whether this is a Cu(II)/(III) or ligand-based process, but it is worth noting the lack of any oxidation for the ligand at similar potentials. The irreversible oxidation at +0.45 V in the CV of the $[Cu_4(\textbf{H}_2\textbf{157})_4](NO_3)_8$ complex is observed to disappear when the window is cut to 0.0 V indicating that this is an electrochemical side-product generated from scanning the reduction. (See Appendix Figure A2.6 for anodic trace).

By contrast, the reduction of $[Cu_4(\textbf{H157})_4](PF_6)_4$ is significantly anodically shifted, with an onset of reduction of -0.91 V that can tentatively be ascribed to a Cu(II)/(I) process, based on similar systems reported by Sauvage *et al.* for octahedral Cu(II)/(I) catenane systems.[189,190] This irreversible Cu(II)/(I), which is not observed for the ligand or for $[Cu_4(\textbf{H}_2\textbf{157})_4](NO_3)_8$, points towards the unstable nature of the Cu(I) species and is indicative of its spontaneous oxidation to Cu(II) in the reaction of $[Cu(CH_3CN)_4]PF_6$ with $\textbf{H}_2\textbf{157}$ to form $[Cu_4(\textbf{H157})_4](PF_6)_4$. The oxidation observed at +0.64 V is found to be the electrochemical side-product generated from the reduction at -0.91 V. When the electrochemical window is cut to 0.0 V the oxidation at +0.64 V disappears providing evidence for this observation. (See Appendix Figure A2.7 for anodic trace).

2.11 Conclusions and future work

In this chapter, two novel enantiomeric ligands, $\textbf{H}_2\textbf{157}$ and $\textbf{H}_2\textbf{158}$, based on the **tzpa** motif were designed, synthesised, and characterised. Their ability to form supramolecular assemblies with *d*-metals was explored, from the formation of solid-state structures, to monitoring their self-assembly in solution using UV-visible absorption spectroscopy and CD spectroscopy. The self-assembly of this chiral system was compared to a previously reported achiral system, to determine the effects of the introduction of a chiral methyl group on the overall solid-state and solution-state structures obtained.

The compounds $\textbf{H}_2\textbf{157}$ and $\textbf{H}_2\textbf{158}$ were designed with a view to introducing chirality to the bis-terdentate binding scaffold, by functionalising the triazole "arms" of the motif with chiral methyl groups. This represents the first example of a chiral **tzpa** ligand and also the first derivative of this novel bis-terdentate binding motif. Synthesis of these enantiomers was achieved by a linear synthetic pathway, involving only three steps, with their formation verified by ^{1}H NMR, ^{13}C{^{1}H} NMR, IR spectroscopy and HRMS.

Reaction of ligand $\textbf{H}_2\textbf{157}$ with $Fe(ClO_4)_2$ in CH_3CN in a 1:1 molar ratio resulted in the formation of a tetranuclear supramolecular M_4L_4 assembly with the overall topology

resembling a [2 × 2] square grid. Unfortunately, the crystals were of poor quality and only a structural model of the complex could be constructed. However, it can be concluded that this structure is similar to that reported by Barry *et al.* for the achiral ligand **156** in [Zn_4(**156**)$_4$](ClO_4)$_8$.[180]

Further studies were conducted to explore the coordination chemistry of ligand **H₂157** with Cu(II), due to the labile nature of the copper ion. Reaction of **H₂157** with Cu(NO_3)$_2$ at high concentration in CH_3OH in a 1:1 molar ratio resulted in the formation of a M_4L_4 tetrameric [2 × 2] grid structure. The [Cu_4(**H₂157**)$_4$](NO_3)$_8$ complex consists of four, six-coordinate Cu(II) ions. Despite the chiral nature of the ligands the metal coordination sites do not appear to be influenced by this chirality. Examination of the self-assembly of this system at lower concentration by UV-visible absorbance spectroscopy revealed the formation of two major species in solution (4:4 metal:ligand and 2:1 metal:ligand) with relatively high stability constants. In solution, the 4:4 metal:ligand species, analogous to the [Cu_4(**H₂157**)$_4$](NO_3)$_8$ structure, is formed; however, in the presence of excess metal ions, the complex is unstable and dissociates to the 2:1 metal:ligand assembly.

To probe the effects of solvent on this system, the reaction of **H₂157** with Cu(NO_3)$_2$ was repeated in CH_3CN in the same molar ratio. This time the species which crystallised was identified as [Cu_2(**H₂157**)(NO_3)$_4$]CH_3CN. In this case the 4:4 metal:ligand species was not observed in the solid state under any reaction conditions examined. Reaction of the ligand **H₂158** with Cu(NO_3)$_2$ under the same conditions yielded a solid-state structure with the same stoichiometry and connectivity as **H₂157**, generating [Cu_2(**H₂158**)(NO_3)$_4$]CH_3CN an M_2L assembly. With both enantiomers generating two isostructural complexes, it can be concluded that the chiral nature of the ligand does not exert significant influence on the Cu(II) metal centre or the overall structure.

Finally, the self-assembly of ligand **H₂157** with Cu(ClO_4)$_2$ in solution was examined in order to determine the effect of the counterion on the speciation. In this case, only the ligand, **H₂157**, and the M_4L_4 species were present as determined from fitting of the UV-visible titration data using global analysis. Total conversion of the ligand species to the M_4L_4 species was estimated from the data, and no evidence of dissociation of the tetrameric assembly upon addition of excess Cu(ClO_4)$_2$ was observed. By contrast, dissociation of the M_4L_4 species to the M_2L complex was observed in the Cu(NO_3)$_2$ titration. This indicates that the perchlorate counterion stabilises the M_4L_4 tetrameric assembly, while in the case of the nitro counterion, multiple species co-exist in solution. Unfortunately, no solid-state structure

of the 4:4 metal:ligand species generated with $Cu(ClO_4)_2$ could be obtained, likely due to the high solubility and stability of the assembly in solution.

CD spectroscopy was employed to probe the chiral nature of the ligands. As expected, the spectra of the enantiomers were mirror images of one another, confirming structural isomerism. Upon addition of 1 equivalent of a Cu(I) solution, the bands demonstrating the ligand's chirality were lost, and the complex which forms does not appear to be influenced by the chiral nature of the ligand. It was also demonstrated that the ligand had not racemised in solution by addition of 1 equivalent of EDTA to scavenge the Cu(I) ions and release the free ligand.

Future prospects for this work include design and synthesis of a ligand in which its chiral nature has a larger influence on the self-assembly with *d*-metals. For ligand **H₂157** and **H₂158**, the chirality showed little effect on the self-assembly process as the methyl group is small and unable to influence the larger tetrameric grids which formed here. The derivatives of **tzpa** possible are limitless and a series of novel structures will be discussed in chapter 3.

"You have brains in your head. You have feet in your shoes. You can steer yourself in any direction you choose. You're on your own. And you know what you know. You are the guy who'll decide where to go"

<div align="right">Dr. Seuss, Oh, The Places You'll Go</div>

3. Metallosupramolecular Polymers and Materials Generated from Bis-tridentate and Mono-tridentate (1,2,3-triazol-4-yl)-Picolinamide (tzpa) Systems

3.1 Introduction

The coordination chemistry of the chiral **tzpa** ligands **H₂157** and **H₂158** with Cu(I) and Cu(II) salts has been discussed in Chapter 2, demonstrating the ligands ability to generate discrete metallo-supramolecular architectures such as [2 × 2] square grid assemblies and also an M₂L complex. In this chapter, the design and synthesis of a series of achiral derivatives of the **tzpa** ligand motif are described, and the ability of these novel ligands to form higher-order assemblies and soft materials through careful ligand design and metal-ligand interactions is examined.

Gels are commonplace in our everyday lives. They can be described as having a continuous structure that is solid-like in its rheological behavior.[191] Gels have myriad applications, from hair gels to contact lenses. These gels are typically generated from two-component mixtures of a polymer in water, which immobilizes the liquid within the polymeric strands to give a soft material. However, in recent years, interest has grown in forming gels from low molecular weight gelators (LMWGs), notable examples of which include supramolecular metallogels.[192] These gels are formed primarily through non-covalent interactions between small molecules, which generates a fibrous network within which the solvent molecules can be immobilized. These interactions include hydrogen bonding, π-π stacking, van der Waals forces, and/or metal coordination interactions and, due to the highly labile and reversible nature of these interactions, can often lead to the formation of reversible gel-to-sol phase transitions.[193] Interest in supramolecular gels has been particularly driven by their potential to exhibit responsivity to a variety of different external stimuli, including light, temperature, and pH.[194–197] Thus potential applications for these supramolecular gels include sensors, drug delivery and release, tissue engineering, and molecular electronics.[192,194,197–199] The use of metals in the formation of supramolecular metallogels is of particular interest as the properties of the metal, such as their electronic, magnetic, and optical properties, can be imparted to the gel and the coordination bond strength can also be tuned.[200] Gelation is often referred to as incomplete crystallization and therefore many gels are discovered serendipitously. However, more recently, research has focused on the considered design of LMWGs, where specific hydrogen bonding groups, metal chelation motifs, and aromatic units capable of assembling *via* π-π stacking interactions are incorporated into the LMWG in order to exert control over the gelation process. An example of a supramolecular metallogel generated by Zhao and co-workers has

demonstrated the close relationship between gelation and crystallisation.[201] They have shown that a coordination complex can be generated from 4,4'-bipyridine and AgNO$_3$; however, the system can be driven towards the formation of a supramolecular metallogel by addition of excess ligand, which suppresses the growth of the coordination polymer. This example gives a valuable insight into the subtle interactions in this system which prompt gelation and demonstrates the effects which changes to the metal:ligand stoichiometry can have on the subsequent formation of gels or coordination complexes.

Metal-organic coordination polymers can also be designed and constructed through self-assembly interactions. Design of these systems considers the coordination geometry of the metal ion, denticity of the ligand, counterion, solvent, and metal:ligand ratio. Thoughtful design of rigid coordinating ligands, coupled with a suitable metal ion, can reliably generate cage architectures[202–204] or continuous MOFs.[181,205] However, by contrast, ligands incorporating more flexibility in their design, exert less control over the self-assembly processes and can thus tend toward coordination polymers or mixtures of products. Similarly, ligands incorporating dissimilar coordination sites can also generate coordination polymers. Metal-organic coordination polymers have been examined for a wide range of applications including gas storage, luminescence applications and catalysis.[206] An example demonstrating the effects subtle alterations of the ligand structure can have on the resulting networks was reported by Burchell and co-workers.[207] Changing only the position of the pendant pyridyl nitrogen atoms in a ligand based on the **pdc** motif, resulted in significant changes to the interchain hydrogen bonding interactions, demonstrating that combining metal coordinating capabilities with hydrogen bonding interactions to generate supramolecular architectures has excellent potential for the design of coordination polymers. Similarly, the **btp** motif has also been functionalised with pyridyl groups for the formation of coordination polymers. They have been used to show that heterometallic assemblies can be generated through ligands which incorporate coordination sites of different denticities.[208] This allowed the authors to generate a heterometallic Fe(II)/Ag(I) linear coordination polymer. The **btp** motif is an excellent candidate for the design of coordination polymers as the triazole arms can be easily functionalised using the CuAAC reaction to install further metal coordination sites or other possible functionalities.

With this in mind, this chapter describes the design of a series of new **tzpa** ligands, functionalised with pyridyl moieties. The pyridyl substituent was selected to increase the opportunity for metal coordination interactions to promote the formation of complex networks of non-covalent interactions which might result in gel formation or higher-order

coordination polymers.[201,209–211] The coordination chemistry of these new **tzpa** derivatives were studied with Cu(I) and Cu(II) ions for direct comparison to the chiral **tzpa** system described in Chapter 2. Furthermore, Ag(I) salts were investigated as coordinating ions for these new ligands due to the widely reported affinity of Ag(I) for pyridyl donor ligands. Ag(I) is a highly labile metal ion, which can adopt coordination numbers ranging from two to six and, due to its d^{10} electronic configuration, gives complexes that are diamagnetic in nature. Its ability to form d^{10}-d^{10} argentophilic bonding interactions between Ag(I) ions also provides increased opportunity for the formation of silver coordination polymers.[72] In this chapter, subtle changes to the new pyridyl-**tzpa** ligand design to generate ligands **162**, **166**, **H169** and **H₂172** are described. Subsequently, larger changes to the central linker of the ditopic ligand to generate ligands **173** and **176** are also described. These more significant changes to the structure, alter the flexibility and solubility of the ligand, leading to significant changes in the coordination chemistry behaviour.

## 3.2 Design and synthesis of ligands 162 and 166

The following sections describe the synthesis and characterisation of compounds **162**, **166**, **H169**, **H₂172**, **173**, and **176**, and their self-assembly behaviours with Cu(I), Cu(II) and Ag(I) salts in the solid state and solution. Single crystals were obtained for a number of these systems providing the structures of a [2 × 2] tetrameric grid similar to that described in Chapter 2, as well as 1D, and 2D polymeric structures. A silver-based supramolecular metallogel is also described and characterised. Following on from the work described in Chapter 2, derivatives of the **tzpa** motif was synthesised and their self-assembly with Cu(I), Cu(II) and Ag(I) ions were examined. Having concluded in Chapter 2 that the chiral methyl groups installed on the **tzpa** ligand **H₂157** had little influence on the self-assembly of this system, a coordinating pyridyl functionality was introduced in place of the chiral methylbenzyl group. As discussed above, the pyridine motif is an excellent metal
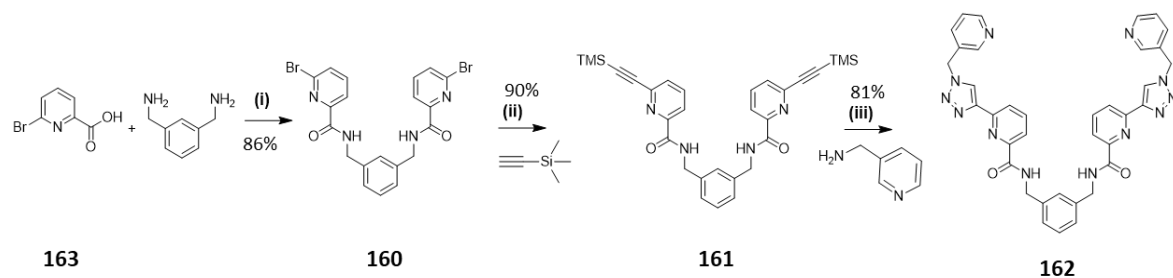
Scheme 3.1 *Synthesis and structure of **162**. Reagents and conditions: (i) hydroxybenzotriazole, EDC·HCl, NEt₃, 4:1 CH₂Cl₂:DMF (ii) CuI, Pd(PPh₃)₄, THF:NEt₃, (iii) (a) ImSO₂N₃.H₂SO₄, K₂CO₃, CuSO₄·5H₂O, CH₃OH, (b) Na ascorbate, K₂CO₃, H₂O: ᵗBuOH, **161**, DMF.*

coordinating motif due to the σ-donating nature of the pyridyl nitrogen and can be easily installed via the CuAAC reaction. It was anticipated that replacing the inert phenyl group with a coordinating motif such as pyridine would provide an excellent opportunity to develop extended networks.

Two 3-pyridyl-functionalised **tzpa** ligands, **162** and **166**, were designed and their synthesis is described herein, beginning with the functionalisation of the **tzpa** "arms" with 3-methypyridine to generate ligand **162**. Synthesis of ditopic ligand **162** involved a three-step synthetic pathway, depicted in Scheme 3.1. Steps one and two were identical to those reported by Dr. Dawn Barry, and also described in Chapter 2 for the synthesis of compound **H₂157**, and thus will not be discussed in detail here.[183] Step three involved a CuAAC reaction in which 3-(aminomethyl)pyridine was converted into the corresponding azide *via* a diazotransfer reagent imidazole-1-sulfonyl azide sulfuric acid ($ImSO_2N_3 \cdot H_2SO_4$) over eight hours. The reaction mixture turned from orange to teal green upon completion. The "click" reaction was then carried out *in situ* with the addition of sodium ascorbate, K_2CO_3, and TMS-
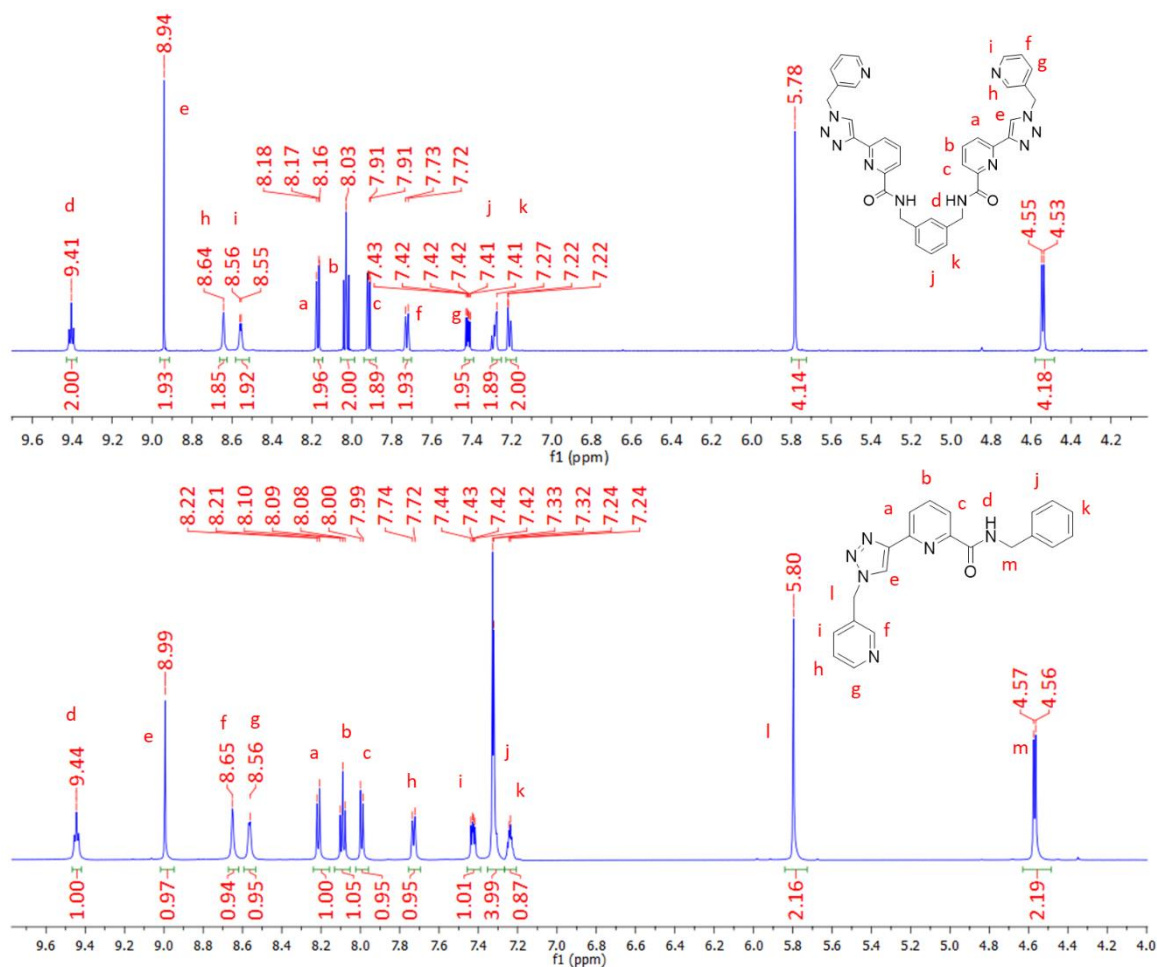

Figure 3.1 ^1H NMR spectrum (600 MHz, DMSO-d_6) of (top) **162** and (bottom) **166**.

90

protected alkyne **161** solubilised in DMF. The reaction proceeded over two days, before the product was extracted into CH_2Cl_2, washed with a solution of EDTA in aqueous ammonia, and then dried under vacuum to yield a white solid in a yield of 81%. ^1H NMR spectroscopy was employed to verify the formation of the product. (see Figure 3.1)

As seen in the ^1H NMR spectrum (600 MHz, DMSO-d_6) of compound **162** in Figure 3.1, resonances corresponding to the central pyridyl protons occur at 8.17, 8.03 and 7.91 ppm, appearing as two doublets, and a triplet. The singlet assigned to the triazole protons appears downfield at 8.94 ppm, while the amide protons occur further downfield at 9.41 ppm and as a triplet due to coupling with the adjacent CH_2 protons. These CH_2 protons occur at a resonance of 4.54 ppm. The *m*-xylyl protons reside at 7.27 and 7.22 ppm. Finally, the protons associated with the pyridyl "arms" are located at 8.64, 8.56, 7.72, and 7.45 ppm with the adjacent CH_2 signal appearing at 5.78 ppm. $^{13}C\{^1H\}$ NMR, HRMS and IR spectroscopy were also employed to verify the formation of the desired product **162** (Appendix Figure A3.1).

In order to probe the self-assembly of a simple monotopic **tzpa** system, ligand **166** was synthesised. This ligand was designed to examine the self-assembly of the terdentate binding site in a simpler monotopic ligand structure compared to the previously explored ditopic derivatives which have a propensity to form complex, multi-metallic structures. Ligand **166** was synthesized *via* a three-step synthetic pathway from commercially available starting materials. Step one involved a peptide-coupling reaction between 6-bromopyridine-2-carboxylic acid and benzylamine to generate compound **167**, which was followed by a Sonogashira coupling reaction with 1 equivalent of ethynyltrimentylsilane to generate the crude product **168** as a brown solid. The compound was purified by column chromatography to give the pure product in moderate yield and was characterised by ^1H and $^{13}C\{^1H\}$ NMR spectroscopies, HRMS, and IR spectroscopy (Appendix Figure A3.3-3.4). In addition, the crystal structure of the compound **168** was obtained from single crystal X-ray diffraction analysis. This will be discussed in further detail in Section 3.2. In order to introduce the 3-
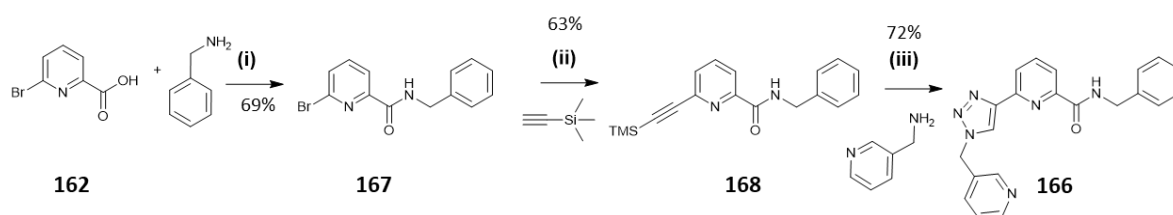

Scheme 3.2 *Synthesis and structure of **166**. Reagents and conditions: (i) hydroxybenzotriazole (HOBt), EDC·HCl, NEt₃, 4:1 CH₂Cl₂:DMF (ii) CuI, Pd(PPh₃)₄, THF:NEt₃, (iii) (a) ImSO₂N₃.H₂SO₄, K₂CO₃, CuSO₄·5H₂O, CH₃OH, (b) sodium ascorbate, K₂CO₃, H₂O: ᵗBuOH, **168**, DMF.*

methylpyridine functionality to compound **168**, 3-(aminomethyl)pyridine was employed in a click reaction, using the method described above for compound **162**, to give a white solid in 72% yield. As before, the compound was fully characterised and the ^{1}H NMR spectrum can be seen in Figure 3.1.

As expected, the resonances in the ^{1}H NMR spectrum of **166** occur at very similar resonances to that of compound **162**. The peaks at 7.32 and 7.24 ppm, corresponding to the phenyl arm now integrate to five protons overall. Furthermore, ^{13}C{^{1}H} NMR, HRMS and IR spectroscopy were also employed to verify the formation of the desired product **166** (Appendix Figure A3.2). The crystal structure of compound **166** was also obtained by single crystal X-ray diffraction and will be discussed in Section 3.3.

3.3 X-ray crystal structure of compound 168

Single crystals of X-ray diffraction quality of compound **168**, were obtained by evaporation of a solution of **168** from DMF. This structure was solved by Dr. Hannah Dalton. Compound **168** was analysed in the triclinic *P*-1 space group and the asymmetric unit contains only one complete molecule, with no solvent or guest species present. Surprisingly, there are no hydrogen bonding interactions between the amide N-H donor and the carbonyl oxygen atom, which is likely inhibited due to a steric clash. Intermolecular hydrogen bonding CH···O interactions exist between the oxygen atom O1 and the C12 of an adjacent molecule, with an O1··· C12 distance of 3.6396(17) Å and a C-H···O angle of 159.65(7)˚.
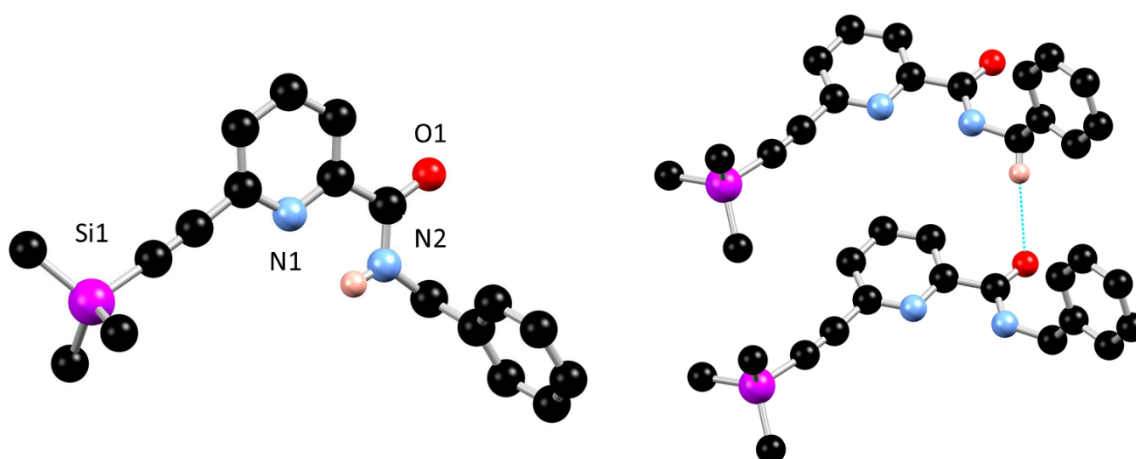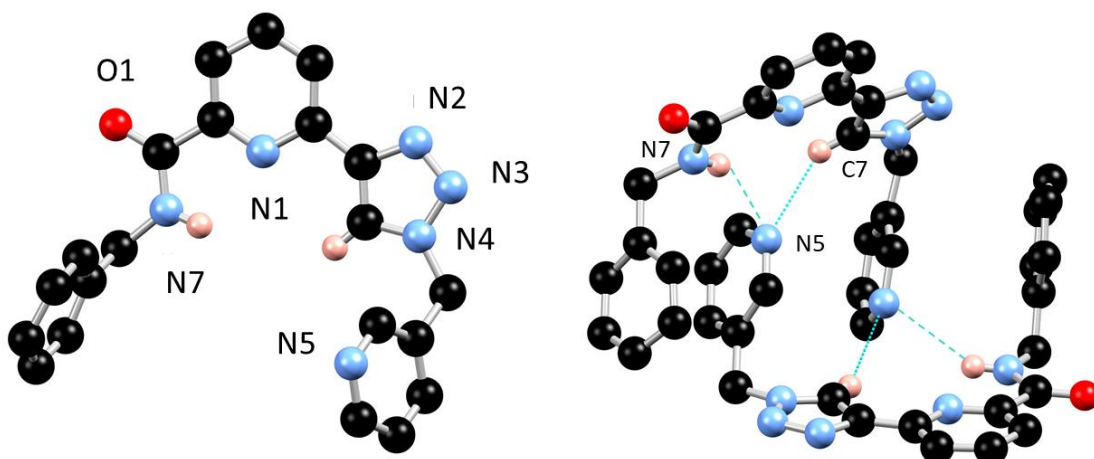

Figure 3.2 *(Left) Structure of one unique molecule of compound **168** with heteroatom labelling scheme. Selected hydrogen atoms are omitted for clarity. (Right) Primary mode of interaction between the two species in **168**. Selected hydrogen atoms are omitted for clarity.*

3.4 X-ray crystal structure of compound 166

Yellow crystals of compound **166** were obtained by slow evaporation of **166** from hexane. This structure was solved by Dr. Hannah Dalton. These single crystals were subjected to X-ray diffraction analysis and the data was found to solve in the orthorhombic $P2_12_12$ space group, modelled as a two-component inversion twin. The unit cell contains only one ligand molecule and there are no guest species or solvent molecules present. The pendant phenyl and pyridyl rings are both disordered over two orientations due to the flexibility of the ligand "arms". The

ligand adopts a U-shaped conformation in which the triazole, pyridine, and carboxamide groups are coplanar, and the pyridyl and phenyl arms are near-perpendicular to this plane, both extending in the same direction. Two ligands are held in a tight dimer by intermolecular hydrogen bonding interactions between an amide NH group and a pyridyl N atom. The amide nitrogen N7 is observed to donate a hydrogen bond to the pyridine nitrogen of the adjacent molecule in the dimer, with an N···N distance of 3.54(3) Å, and an NH···N angle of 146.4(6)°. There is an additional CH···N interaction observed between the pyridyl N5 and the CH of the triazole ring of an adjacent molecule with N5···C7 distance 3.41(3) Å and CH···N angle 146.0(7)°.

Figure 3.3 *(Left) Structure of one unique molecule of compound **166** with heteroatom labelling scheme. Selected hydrogen atoms are omitted for clarity. (Right) Primary modes of interaction between the two species in the solid-**166** dimer. Selected hydrogen atoms are omitted for clarity.*

3.5 Formation of coordination polymer *poly*-{[Ag$_2$(166)$_2$](CF$_3$SO$_3$)$_2$}$_n$

Having explored the coordination chemistry of the chiral **tzpa** ligand **H$_2$157** in Chapter 2 with Cu(I) and Cu(II) salts, ligand **166** was examined under the same conditions. However, reaction of ligand **166** with Cu(NO$_3$)$_2$ or [Cu(CH$_3$CN)$_4$](PF$_6$) did not yield any single crystals suitable for X-ray diffraction analysis. Unable to elucidate a solid-state structure for this system with Cu(I) or Cu(II), Ag(I) was investigated due to the propensity of pyridyl nitrogen donors to coordinate Ag(I) ions.

Reaction of ligand **166** with AgCF$_3$SO$_3$ in a 1:1 molar ratio in THF resulted in the formation of yellow crystals. Analysis by single crystal X-ray diffraction revealed a 1D polymeric structure *poly*-{[Ag$_2$(166)$_2$](CF$_3$SO$_3$)$_2$}$_n$ where the diffraction data were solved in the monoclinic *P*2$_1$/*n* space group. This structure was solved by Dr. Chris Hawes. The asymmetric unit contains two whole ligand molecules with two silver atoms and two triflate ions completing the unit cell. Each silver ion is coordinated in a bidentate fashion by the N4 and N5 atoms of the pyridyl-triazole binding site, and the pyridyl nitrogen N7 of an adjacent pendant ligand arm completes a trigonal planar coordination geometry about the silver centre. There is an Ag···O contact between the amide oxygen and the coordinating Ag of each ligand, with distances for Ag2···O1 and Ag1···O2 of 2.730(4) and 2.647(4) Å, respectively. An argentophilic interaction exists between two symmetry equivalent Ag2 atoms, at an Ag-Ag distance of 3.0364(10) Å which is below the van der Waals diameter of Ag(I) of 3.44 Å. Ag-Ag interactions have been shown to play a crucial role in the formation of silver coordination polymers and the control of supramolecular structures, forming 1D and 2D architectures.[72,205] Each ligand molecule adopts a z-shaped conformation, with the
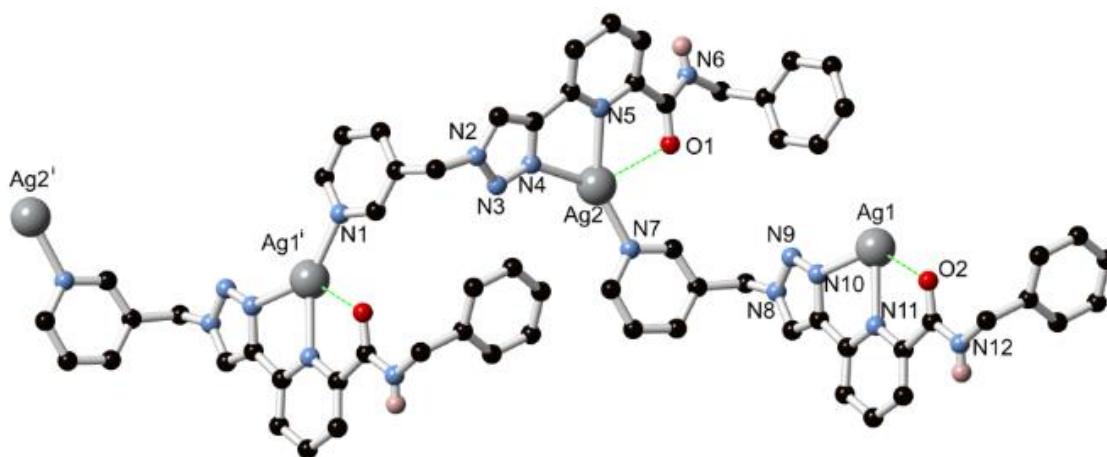
Figure 3.4 *Structure of the coordination polymer poly-{[Ag$_2$(166)$_2$](CF$_3$SO$_3$)$_2$} with labelling scheme for unique heteroatoms. Hydrogen atoms omitted for clarity.*
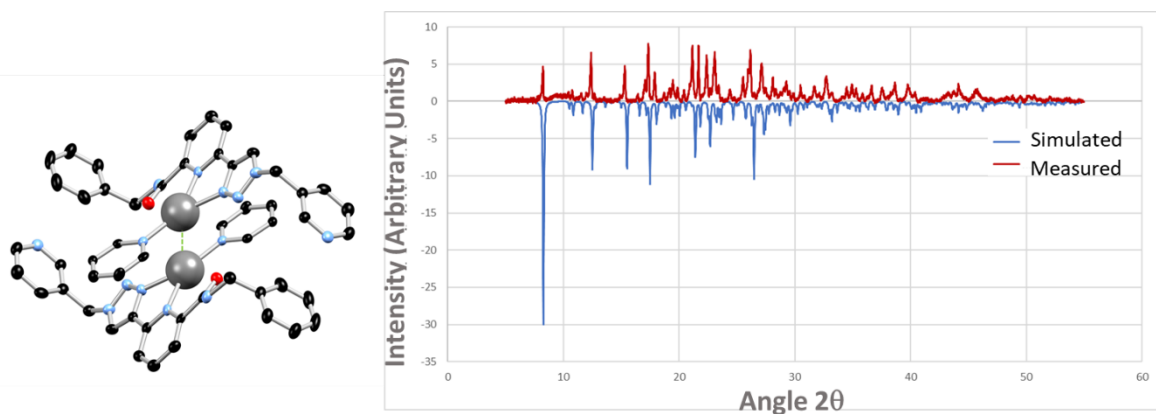
Figure 3.5 *(Left) Argentophilic interaction between Ag2 atoms. (Right) X-ray diffraction pattern for **166** 1D polymer measured at (100 K) (red) compared to the pattern simulated from the single crystal X-ray data obtained at (100K) (blue).*

pyridine and triazole coplanar, and the pyridyl and phenyl arms orientated at angles of 110.9(5) and 106.1(4)° to the plane, respectively. There are hydrogen bonding interactions between the amide N12 and the carbonyl O7 of the triflate anion with an N···O distance of 2.860(7) Å. Phase purity was confirmed by using powder X-ray diffraction analysis at 100K. (See Figure 3.5) Elemental analysis on the air-dried sample confirmed the structure of $\{[Ag_2(\mathbf{166})_2](CF_3SO_3)_2\}_n$. IR spectroscopy revealed a C-F stretch at 1250 cm^{-1} as well as an N-H stretch at 3344 cm^{-1} and C=O at 1650 cm^{-1}.

### 3.6 Formation of Ag(I) metallogel with compound 162

Having been successful in the formation of a silver 1D coordination polymer from compound **166**, the possibility of forming a more complex coordination polymer structure with bis-terdentate compound **162** was explored. Reaction of ligand **162** with AgCF$_3$SO$_3$ under the same conditions as described for compound **166** above, however, resulted in an amorphous solid. Subsequently, ligand **162** was investigated with a series of other Ag(I) salts under various solvent conditions. Upon reacting ligand **162** with AgBF$_4$ in CH$_3$CN in a 1:1 molar ratio at high concentration, an opaque gel formed overnight. The ligand itself was not capable of gelation under these conditions, indicating that the metal-ligand interactions play a key role in the soft material formation. A crude test of the gelation behaviour is the "inversion test", whereby the potential gel sample is inverted for longer than one hour. If the soft material can support its own weight this indicates it is more viscous than a liquid, and suggests the material is worth subjecting to further rigorous rheological testing to gain
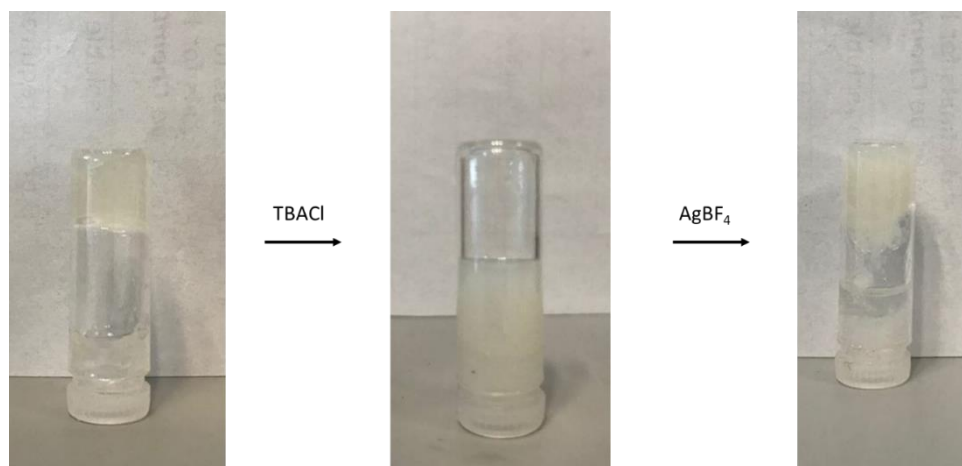
Figure 3.6 *(Left) Inversion test of AgBF₄ gel of **162** in CH₃CN in 1:1 molar ratio. (Middle) Addition of TBACl resulting in destruction of the gel network. (Right) Addition of AgBF₄ to re-form the AgBF₄ gel of **162** demonstrating chemoreversibility of the system.*

insight into the physical properties of the soft material. The sample, as seen in Figure 3.6, was capable of supporting its own weight overnight. Various gelation concentrations were examined, and at 0.1 wt% the gel which formed, appeared robust to the naked eye. The gel was stable in a sealed vial for several months with little discolouration observed.

The chemoreversibility of the gel was also investigated. Addition of 1 equivalent of tetrabutylammonium chloride (TBACl) to the soft material resulted in the deformation of the gel, returning the material to a liquid state. This was attributed to sequestering of the silver ions by Cl⁻, which results in a gel-sol transition. This process was reversible, with the addition of 1 equivalent of AgBF₄ regenerating the gel, demonstrating the dynamic nature
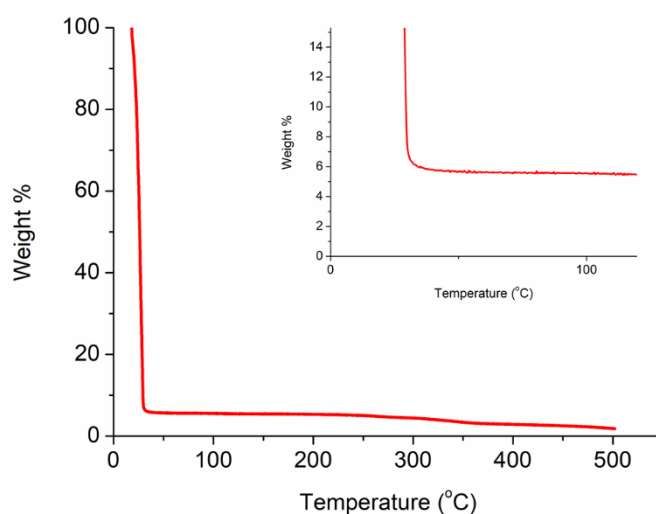
***Figure 3.7*** *TGA thermograph of **162** AgBF₄ gel showing weight loss of 5.5% before 50 °C.*

of the system, and confirming the key role of the metal-ligand interactions in controlling the formation of the supramolecular metallogel (Figure 3.6).

In order to investigate the wt% of the gel, thermogravimetric analysis (TGA) was carried out on the material. TGA was carried out from 15 to 500 ˚C and showed a loss in mass of 94.5 % at 50 ˚C, which indicates that the gel was formed at 5.5 wt%. This is consistent with the preparation of the gel. (See Figure 3.7)
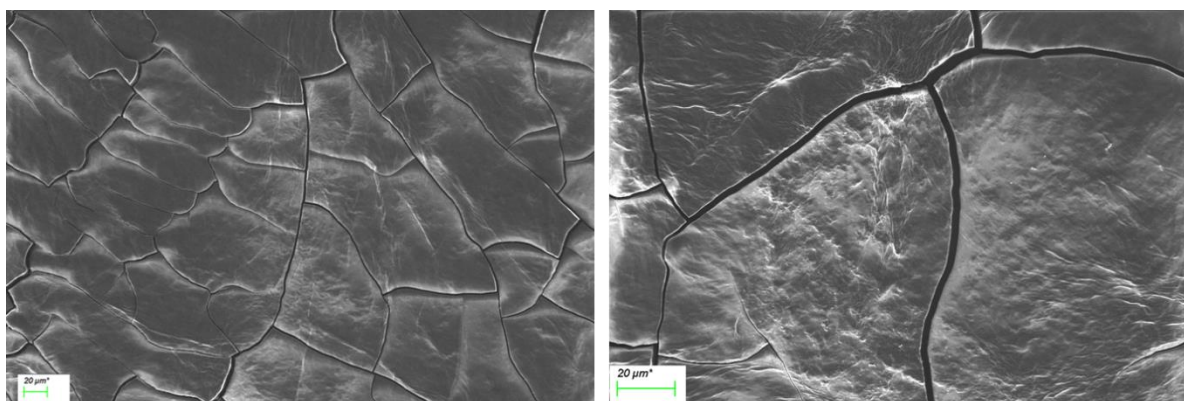
Figure 3.8 *SEM images of **162** gel with AgBF₄ (scale bar 20 μm) showing sheet-like structure of the material. Sample coated with Au to prevent charging the specimen.*

A xerogel of compound **162** with AgBF₄ was also generated by drying the gel sample under vacuum in order to study the morphology of the system using scanning electron microscopy (SEM). The SEM operates under a vacuum and thus xerogels must be used as the sample is required to be completely dry before imaging can commence. Therefore, the sample concentration cannot be obtained by this method. The SEM images show a sheet-like structure with no evidence of the fibrous morphology often seen in supramolecular gels. The gel appears like a dried fibrous film and it is possible that drying the sample resulted in a collapse of the fibrous cross-linking morphology which generated the gel. Cryo SEM was
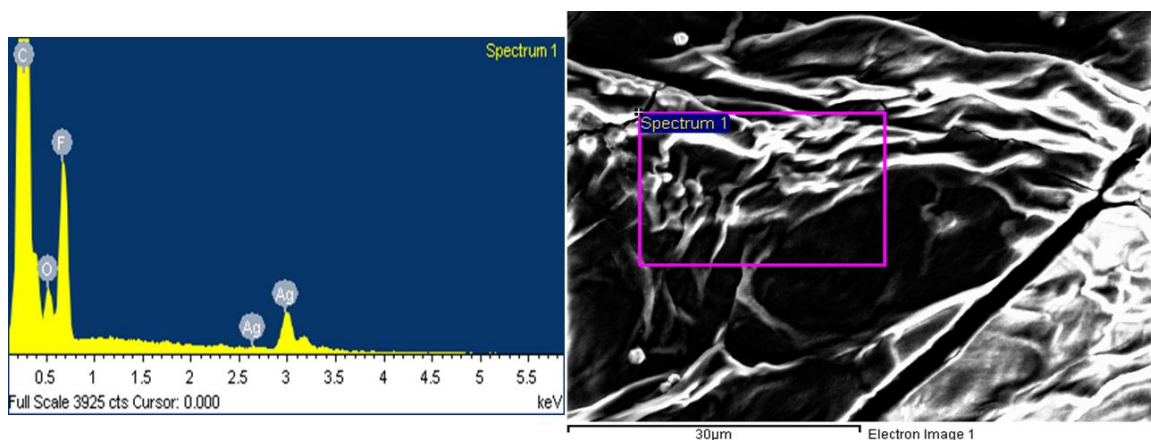

Figure 3.9 *(Left) EDX energy dispersive spectrum for the gel of **162** with AgBF₄ showing the presence of carbon, oxygen, fluorine and silver. (Right) Area of the spectrum under SEM which was examined by EDX.*

97

unfortunately not available for use at the time of this study and future work would re-examine this morphology without collapse of the gel network during drying which is possible in cryo SEM.

Energy-dispersive X-ray (EDX) spectroscopy was employed to examine the metal species present in the xerogel sample. EDX spectroscopy is a technique used to determine the elemental composition of a sample under SEM analysis. Bombardment with an electron beam causes the sample to emit X-rays due to electron vacancies created by the electron beam being filled by electrons from higher energy orbitals. This X-ray is characteristic of the element from which it is emitted and thus can be used to determine the elements which are present in the sample.[212] The EDX spectrum for the Ag(I) gel sample is shown in Figure 3.9. The elements observed to be present in the sample were carbon, oxygen, fluorine and silver. The fluorine likely originates from the BF_4^- anion used to generate the soft material.

In order to examine the physical properties of the gel, rheological experiments were conducted in collaboration with Dr. Benjamin Haffner and Dr. Matthias Möbius. Rheology is defined as the study of the deformation and flow of matter under the influence of an applied stress.[213] A material can be ascribed as a solid if, under the application of a continuous weak stress, the material resists further deformation overall. By contrast, a material is defined as a liquid if, following the application of stress, flow of the material is observed. A gel displays both liquid-like and solid-like behaviours, and thus exhibits both elastic and viscoelastic responses to an applied stress. The elastic storage modulus, G', describes the energy stored in the elastic structure of the sample while the elastic loss modulus, G'', describes the energy dissipated as heat or the viscous behaviour of the sample.
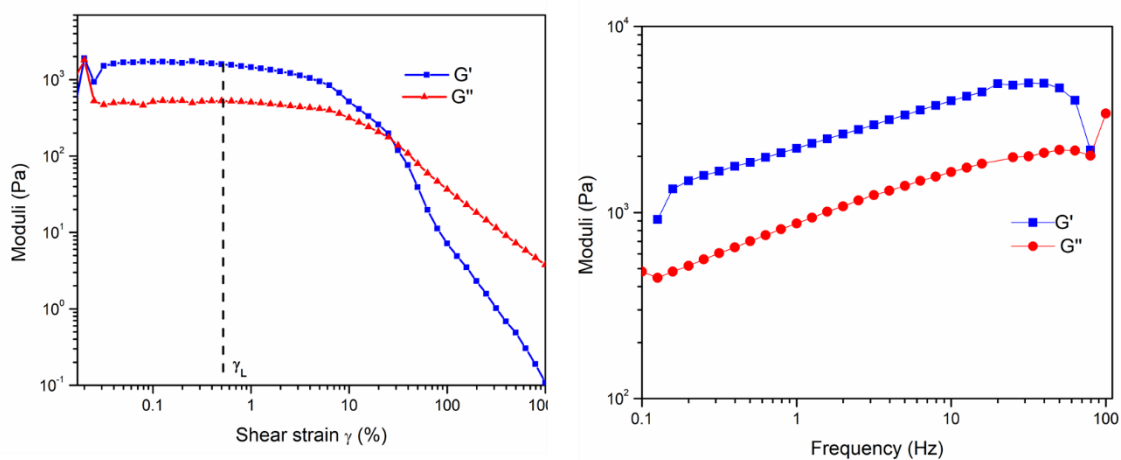
Figure 3.10 *(Left) Amplitude (strain) sweep experiment of **162**-AgBF₄ gel showing the linear viscoelastic region (γ_L) and confirming the behaviour of the material as a gel. (Right) Frequency sweep experiment demonstrating that G' increases with increased frequency.*
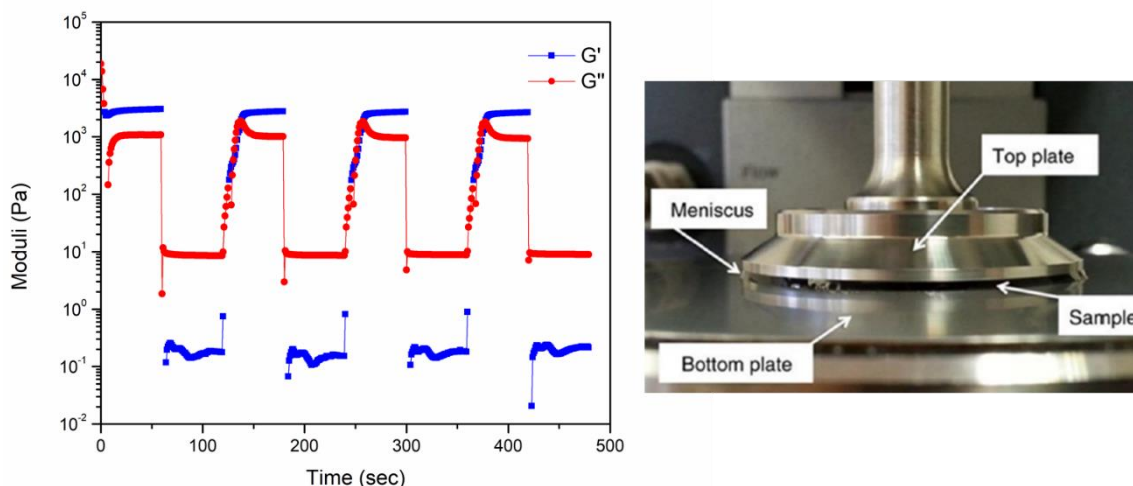
Figure 3.11 (Left) Oscillatory recovery test revealing the mechanical reversibility of the gel with strain amplitude oscillated between γ = 0.1 % and 500% over four cycles. (Right) Image of the rheometer plates.

A typical example of a rheological experiment conducted to confirm gel-like behaviour of soft materials is an amplitude sweep experiment. This experiment aims to determine the deformation behaviour of the sample in the non-destructive deformation range, and also to determine the upper limits of deformation of the sample. In this experiment, the strain on the sample is increased in a stepwise manner while a constant frequency is maintained. In Figure 3.10 it can be seen that the storage modulus G′ is larger than the loss modulus G″, (G′ = 1.62 × 10^3 and G″ = 4.93 × 10^2 Pa) indicating that the material behaves like a gel and thus fits the definition of a viscoelastic solid material. The linear viscoelastic region (LVE) can also be determined. The LVE is defined as the range in which further tests can be carried out on the material without destruction of the sample. The limit of the LVE region for this sample is 0.5% and is labelled as γ_L in Figure 3.10. After this point, the values of G′ and G″ begin to converge, and the material begins to flow. The convergence point is termed the yield point. A frequency sweep experiment serves the purpose of examining the time-dependent behaviour of the material within the linear viscoelastic region to gain insight into the long-term stability of the gel. The amplitude is kept constant while the frequency is increased in steps. Having determined that the limit of the LVE region is 0.5% the frequency sweep was measured at γ = 0.1 %. As seen in Figure 3.10, G′ > G″ over the entire frequency range which indicates that the material has a crosslinked structure. An oscillatory recovery test was also conducted in order to examine the mechanical reversibility of the gel. In this test the effect on the storage and loss moduli is examined while shearing beyond the yield stress at low strain amplitude in a linear viscoelastic regime. The results show that the gel rapidly returns

99

to its original strength after shearing, and this behaviour was found to repeat over multiple cycles. This is a common feature of supramolecular gels, due to the reversible nature of the supramolecular interactions which generate the gel material. This behaviour can be described as 'thixotropic'. Silver-based coordination LMWGs have been reported in the literature as attractive metallogels due to the labile nature of coordination interactions which can be generated between ligands and the silver ion.[172,214] Sun and co-workers have reported the formation of a metallogel based on Schiff base ligands and their coordination interaction with AgNO$_3$. These gels also demonstrate thixotropic properties and the authors demonstrate the coordination interaction between the silver ion and nitrogen atom of the pyridine ring of the ligand during gelation as well as the contribution of hydrogen bonding interactions to the gelation of the solvent system.[215]

A variety of other silver salts and solvent conditions were examined with compound **162**, but unfortunately no other metallogels were obtained with this ligand. In the case of AgNO$_3$, only a solid precipitate formed, while with AgCF$_3$SO$_3$ a flocculent material was observed instead. This points towards the importance of the BF$_4^-$ anion in facilitating the gelation behaviour of the **162**-AgBF$_4$ system. This may be a result of the BF$_4^-$ anion solubilising the resulting **162**-AgBF$_4$ complex sufficiently in order to facilitate the formation of a fibrous network capable of immobilising the CH$_3$CN molecules.

Unfortunately, no single crystals of X-ray diffraction quality were obtained of this system. However, coordination polymer {[Ag$_2$(**166**)$_2$](CF$_3$SO$_3$)$_2$}$_n$ gives an insight into the interactions which could be present in the metallogel system. It is likely that metal-ligand interactions between the pyridyl and triazole nitrogens and the Ag(I) ions, as well as coordination through the 3-pyridyl "arms" of the ligands generate the extended structures. Ag(I) has a propensity to form metallogels due in part to its flexible capacity to adopt a variety of different coordination modes, which can lead to the formation of fibrous aggregates from which gels may be obtained. Interactions through the pyridyl "arms" are further confirmed by treating chiral compound **H$_2$157**, described in Chapter 2 with AgBF$_4$ under the conditions which generated a gel with ligand **162.** No gel was formed in the case of **H$_2$157** indicating that any interactions which occur through the nitrogen atom of the pendant pyridyl arms are essential to the metallogel formation. Therefore, it is clear that the introduction of 3-pyridyl binding sites to the **tzpa** ligand in the cases of ligands **162** and **166**, can result in metal-ligand interactions between Ag(I) and the pendant pyridyl nitrogen. This resulted in the formation of higher order structures than the discrete assemblies described for chiral ligand **H$_2$157** with Cu(II) in Chapter 2. Coordination through the pendant pyridyl

nitrogen in the case of ligand **162** resulted in a 1D polymer and in the case of monotopic derivative **166**, an Ag(I) metallogel resulted.

3.7 Design and synthesis of compounds H169 and H$_2$172

Following on from the design of ligands **162** and **166**, and the successful formation of higher-order assemblies with Ag(I) salts, the monodentate ligand **H169**, based on ligand **166**, was designed with a view to replacing the non-coordinating phenyl arm with a 4-pyridyl substituent. Having demonstrated that compound **166** can generate a coordination polymer network by forming metal-ligand interactions with Ag(I), it was anticipated that the additional coordinating arm would increase the complexity of the self-assembly.

In addition, a derivative of compound **162** was designed in which the position of the pyridyl nitrogen atom was changed from the 3-pyridyl position, to the 2-pyridyl position. Due to the pivotal role which this nitrogen atom plays in the formation of extended structures, its position within the ring was explored to determine how the morphology of the resultant self-assembled structures could be modulated.

Ligand **H169** was synthesized *via* a three-step synthetic pathway, starting from 6-bromopyridine-2-carboxylic acid (Scheme 3.4). The first step involved peptide coupling this starting material with 4-(aminomethyl)pyridine in a CH$_2$Cl$_2$:DMF mixture at room temperature, using HOBt and EDC·HCl. After 48 hours the crude product was isolated as a yellow oil, which was taken up in CH$_2$Cl$_2$, before washing with 1.0 M HCl and saturated aqueous NaHCO$_3$, and then dried under vacuum to yield a while solid. This intermediate **170** was subjected to a Sonogashira coupling using ethynyltrimethylsilane, and Pd(PPh$_3$)$_4$ as the catalyst, under an argon atmosphere at room temperature. The crude product was isolated as a brown oil which was purified by flash column chromatography to yield a brown solid in moderate yield. The compound was characterised by NMR and IR spectroscopies as well as HRMS. Step three involved subjecting **171** to a CuAAC reaction with 3-(aminomethyl)pyridine in analogous conditions to those described for compound **166**. The
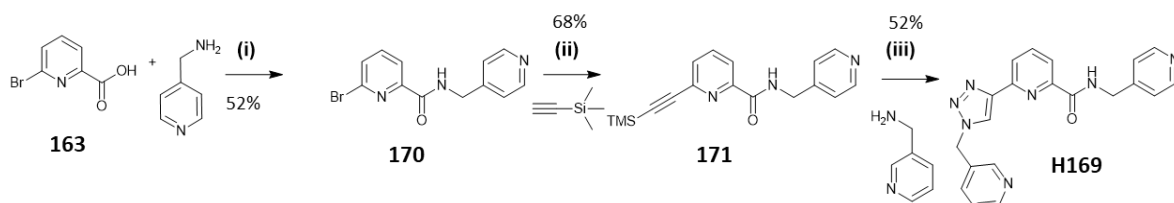
Scheme 3.3 *Synthesis and structure of **H169**. Reagents and conditions: (i) hydroxybenzotriazole (HOBt), EDC·HCl, NEt$_3$, 4:1 CH$_2$Cl$_2$:DMF (ii) CuI, Pd(PPh$_3$)$_4$, THF:NEt$_3$, (iii) (a).H$_2$SO$_4$, K$_2$CO$_3$, CuSO$_4$·5H$_2$O, CH$_3$OH, (b) sodium ascorbate, K$_2$CO$_3$, H$_2$O: ^{t}BuOH, **171**, DMF.*

azide was generated from the 3-(aminomethyl)pyridine *in situ*, using the diazotransfer reagent $ImSO_2N_3.H_2SO_4$. Upon observation of a colour change from orange to green, the click reaction was initiated, where sodium ascorbate, K_2CO_3 and TMS-protected alkyne compound **171**, dissolved in DMF, were added to the reaction mixture under an inert atmosphere. The reaction proceeded over two days at room temperature yielding the crude product. Purification was carried out first by protonating compound **H169** with aqueous 1M HCl, then deprotonated using 1M NaOH, and then extracting into CH_2Cl_2. Removal of the solvent *in vacuo* gave the compound in 52% yield. ^{1}H NMR spectroscopy was employed to verify the formation of the product. (Figure 3.12)

The ^{1}H NMR spectrum (600 MHz, DMSO-d_6, Figure 3.12) of **H169** shows the triazole proton appearing as a singlet downfield at 8.99 ppm, while the amide proton appears as a triplet and is shifted even further downfield at 9.54 ppm. The three central pyridyl protons occur at 8.22, 8.10 and 7.99 ppm, and appear as two doublets and a singlet. The signals at 8.65 and 8.57 ppm were assigned to the protons of the pendant 3-methylpyridine arm with the remaining protons for this pyridine ring, appearing at 7.74 and 7.44 ppm as a
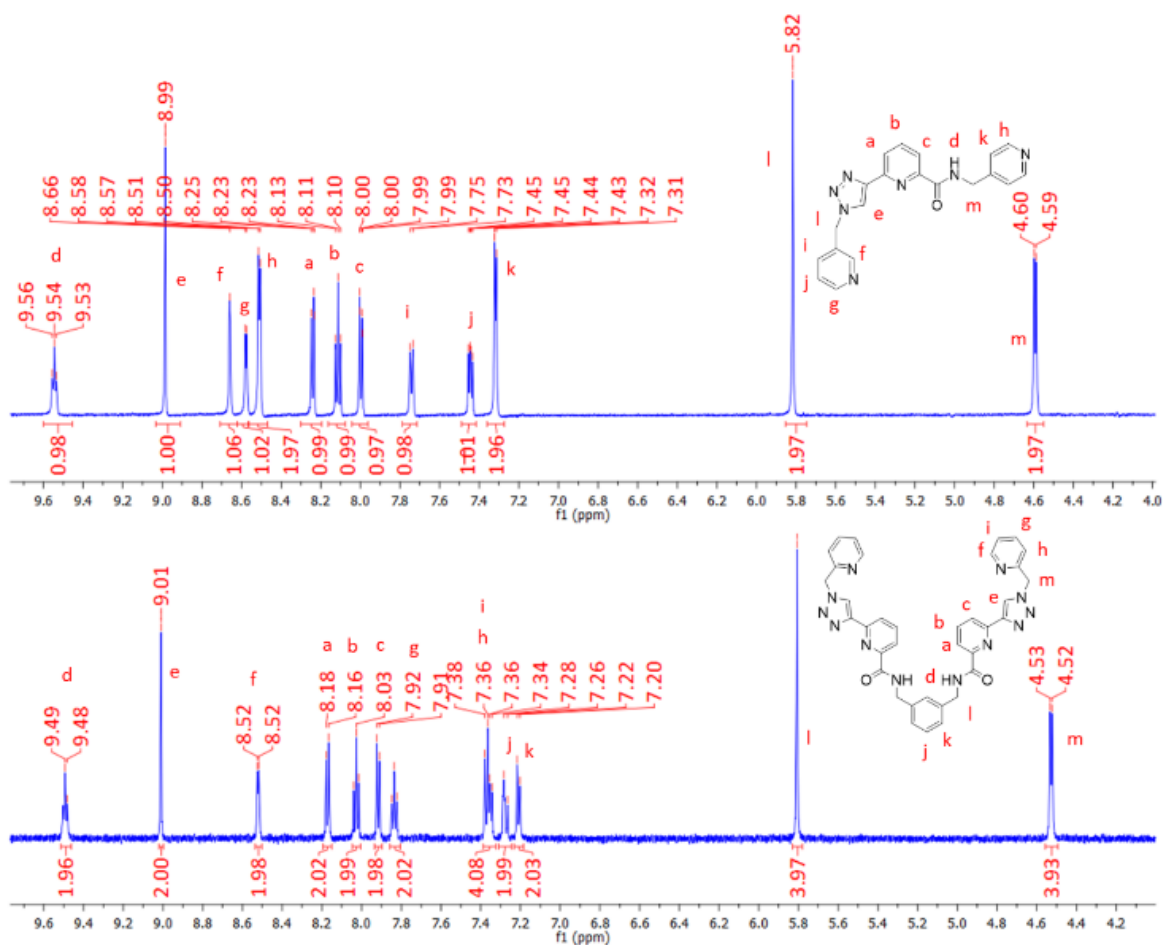
Figure 3.12 [1]*H NMR spectrum (600 MHz, DMSO-d₆) of (top)* **H₂169** *and (bottom)* **H₂172**.

102

doublet and multiplet respectively. The pyridyl protons associated with the 4-methylpyridine arm occur at 8.50 and 7.31 ppm as doublets integrating to two protons each. Finally, the singlet at 5.82 ppm corresponds to the CH_2 protons adjacent to the triazole moiety while the doublet at 4.59 ppm is assigned to the CH_2 protons next to the carboxamide group. $^{13}C\{^1H\}$ NMR, IR spectroscopy and HRMS were also employed to verify the formation of the desired product **H169**. (See details in experimental Chapter 6)

Ditopic ligand **H₂172** was synthesised in a three-step procedure, the first two steps of which are the same as those described for compound **162**. With the bis-TMS protected alkyne **161** in hand, attempts were made to synthesise ligand **H₂172** according to the procedure outlined for **162** using 2-(aminomethyl)pyridine; however, this procedure was unsuccessful. This was likely due to the generation of an intermediate copper complex during the ligand synthesis which resulted in a precipitate which was insoluble in most organic solvents. Instead, the product was successfully synthesised using 2-(bromomethyl)pyridine hydrobromide, which was converted to the relevant azide in the presence of sodium azide in a DMF/H_2O mixture. After formation of the azide *in situ,* tris[(1-benzyl-1*H*-1,2,3-triazol-4-yl)methyl]amine (TBTA), [Cu(CH_3CN)₄]PF₆, and K_2CO_3 were added, and the resultant mixture turned a red colour. The addition of TBTA stabilises the Cu(I) intermediate, thereby increasing the overall yield of the reaction. The TMS protected alkyne **161** was then added and after 48 hours the product was isolated as a crude oil. The product was purified by an acid/base wash, from which the pure product precipitated as a white solid in 63% yield. The compound was fully characterised by NMR and IR spectroscopies, as well as HRMS. As expected, the ^1H NMR spectrum of **H₂172** was similar to the spectrum of **162**. The amide, triazole and central pyridyl protons are shifted slightly upfield by approximately 0.05 ppm compared to their counterparts in compound **162**. The protons associated with the pyridyl arms appear as a doublet and two multiplets at 8.52, 7.83,
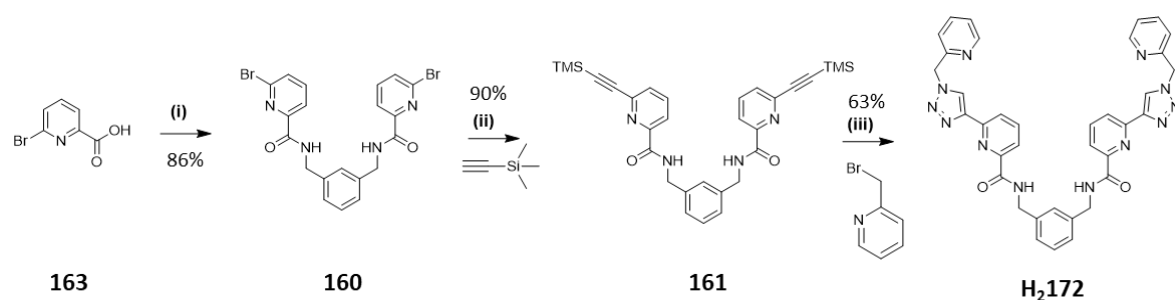

Scheme 3.4 *Synthesis and structure of* **H₂172**. *Reagents and conditions: (i)m-xylylenediamine, hydroxybenzotriazole (HOBt), EDCI·HCl, NEt₃, 4:1 CH_2Cl_2:DMF (ii) CuI, Pd(PPh₃)₄, THF:NEt₃, (iii) (a) NaN₃, K_2CO_3, TBTA, [Cu(CH_3CN)₄]PF₆, K_2CO_3, CH_3OH, **161**.*

and 7.36-7.39 ppm corresponding to eight protons overall. As expected, the CH_2 and *m*-xylyl protons appear at the same resonances as compound **162**. $^{13}C\{^1H\}$ NMR, HRMS and IR spectroscopy were also employed to verify the formation of the desired product **H$_2$172** (Appendix Figure A3.8).

3.8 Exploration of the coordination chemistry of H169

Reaction of ligand **H169** with various silver salts under a variety of reaction conditions, unfortunately, did not yield any crystals suitable for X-ray diffraction. However, upon reaction of **H169** in a 1:1 M:L stoichiometric ratio with $[Cu(CH_3CN)_4](CF_3SO_3)$ in CH_3OH, blue single crystals were formed upon standing for several weeks at room temperature. These crystals were analysed, and the structure was determined by X-ray diffraction to be a 2D polymer of the form $[Cu_3(\mathbf{169})_2(CF_3SO_3)(OCH_3)_2)]CF_3SO_3 \cdot H_2O$. This structure was solved by Dr. Chris Hawes. The diffraction data were solved in the triclinic *P*-1 space group. The asymmetric unit contains two complete ligand molecules, three unique copper ions, one coordinating triflate, two methoxide ligands and one aqua ligand. The unit cell is completed by one triflate molecule, and 0.75 of a water molecule. Each copper ion is oxidised to Cu(II) and each ligand **H169** is deprotonated at the amide nitrogen, which enables the two unique ligands to coordinate through the terdentate triazolyl-pyridyl-amide N_3 binding site to a Cu(II) ion. Two L2 ligands and two Cu3 ions generate a loop by coordinating the Cu3 through the terminal pyridyl nitrogen atoms, N8 and N14, of L2. The ligands are inverted
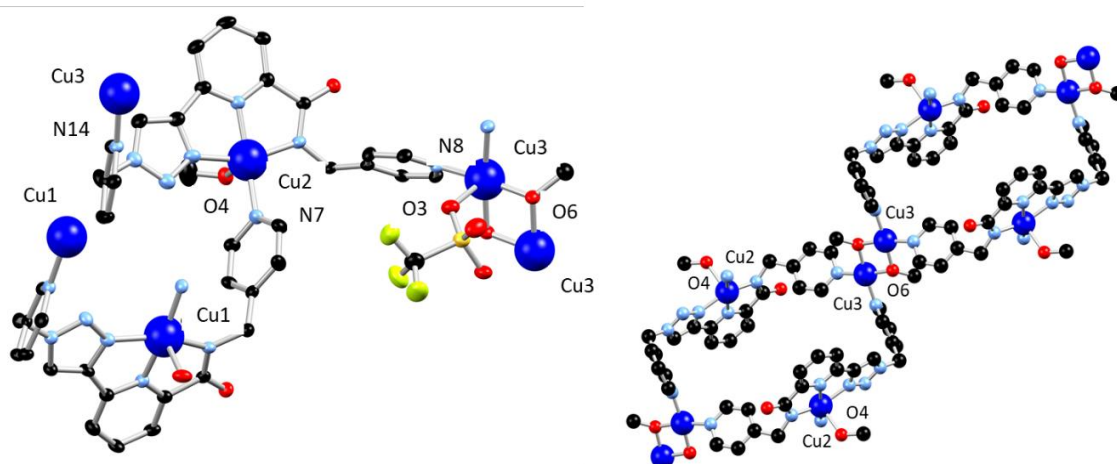

Figure 3.13 *(Left) Structure of one unique molecule of compound* $[Cu_3(\mathbf{169})_2(CF_3SO_3)(OCH_3)_2)]CF_3SO_3 \cdot H_2O$ *and additional Cu ions to demonstrate connectivity with heteroatom labelling scheme. Hydrogen atoms are omitted for clarity. (Right) Loop structure of L2 and Cu3 with Cu1 and additional ligands omitted for clarity.*
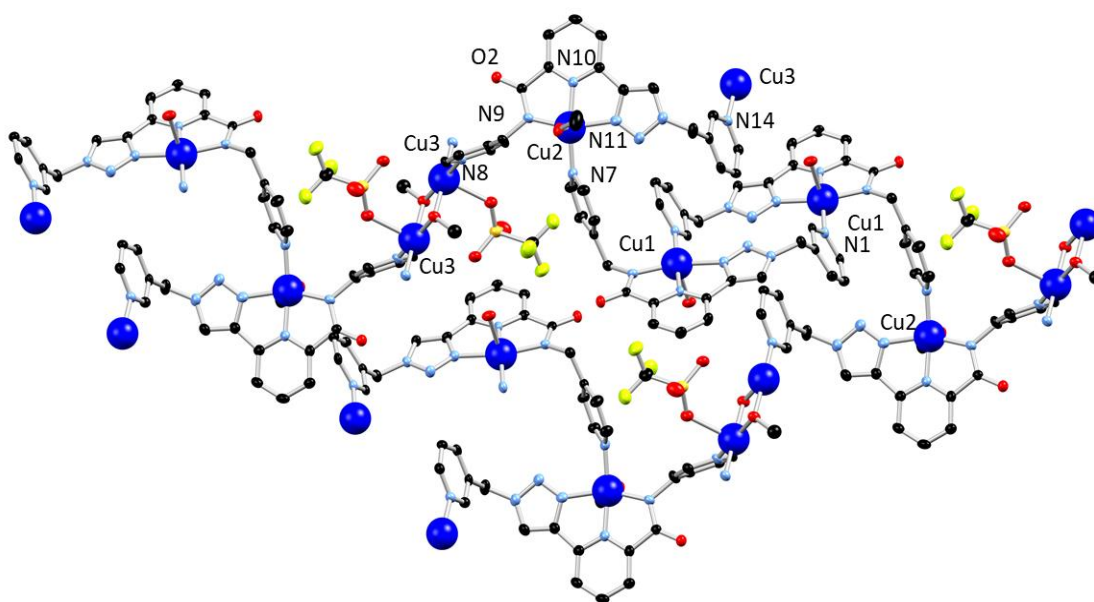
Figure 3.14 *Showing the extended structure of [Cu$_3$(**169**)$_2$(CF$_3$SO$_3$)(OCH$_3$)$_2$)]CF$_3$SO$_3$·H$_2$O showing the loop structure generated by ligand L2 and Cu3 as well as the loop generated by L1 and Cu1. Hydrogen atoms and methoxide ligands omitted for clarity.*

relative to each other with a mean plane distance of 10.548 Å, and a triflate ion occupies the cavity of the loop. Two L1 ligands and two Cu1 sites also generate a loop through coordinating terminal pyridyl nitrogen atoms, N1, and these two loops are linked by coordinating to Cu2. The (L2-Cu3)$_2$ loops are also directly bridged through two methoxide ligands. Cu3 coordinates a methoxide ligand, a triflate ligand, and the pyridyl nitrogen atoms N8 and N14. Angles of 171.4(2)° for N8-Cu3-O6 and 95.06(19)° for N8-Cu3-O3, and an average angle of 95.57° for Cu3-N14, suggests a distorted tetrahedral geometry for Cu3. Both Cu1 and Cu2 adopt a distorted square pyramidal geometry, coordinating through the *N$_3$* binding site of the ligand as well as a pyridyl nitrogen of an adjacent ligand and an aqua ligand or methoxide ligand respectively. Two Cu3 centres are bridged by two methoxy groups leading to a planar Cu$_2$O$_2$ bridge with a Cu-Cu distance of 2.930(2) Å, a Cu2-O6 distance of 1.943(5) and 1.923(6) Å and O6-Cu-O6 angle of 81.44(15)° and the methoxide ligand coordinates Cu2 at a distance of 2.275(4) Å. The metal-ligand bond lengths for a range of Cu(II)-OCH$_2$ bridges have been retrieved from the Cambridge Structural Database, CSD (version 5.40 February 2019). A plot of the bond lengths of 937 compounds are shown in Figure 3.15 and shows a narrow distribution of distances from 1.9-1.95 Å which correspond to the bridging alkoxide structures while the distribution around 2.2-2.6 Å correspond to the more weakly bound bridging alcohols. This indicates that the Cu2-O6 bridge in this structure involves a deprotonated methanol ligand. The deprotonation of the
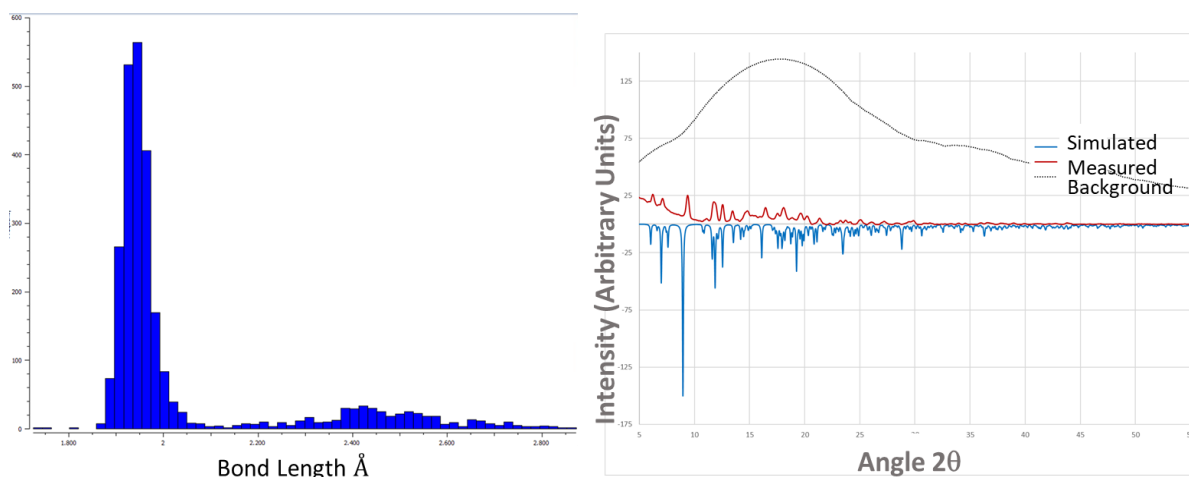
Figure 3.15 *(Left) Plot of Cu(II)-OCH$_2$ bond lengths obtained from Cambridge Structural Database, CSD (version 5.40 February 2019). (Right) X-ray diffraction pattern for **169** 2D polymer measured at (100 K) (red) compared to the pattern simulated from the single crystal X-ray data obtained at (100K) (blue).*

amide nitrogen in CH$_3$OH under extremely mild conditions, in the absence of base, is highly unusual, but was also observed in Chapter 2 in the reaction of ligand **H$_2$157** with [Cu(CH$_3$CN)$_4$]PF$_6$, which also underwent oxidation to Cu(II) upon complexation. The generation of methoxide ligands which coordinate to the Cu(II) centre is also highly unusual under these mild reaction conditions.[216] It is possible that the copper oxidation process could simultaneously cause deprotonation of the methanol, generating methoxide which, in turn, may deprotonate the amide nitrogen. It is worth noting that unlike in the structure of [Cu$_4$(**H157**)$_4$](PF$_6$)$_4$ in Chapter 2, there are no protonated amides in this structure. The complex engages in hydrogen bonding interactions with triflate anions *via* the coordinating water molecule and further hydrogen bonding interactions occur between the carboxamide O3 and a water molecule. Powder X-ray diffraction at 100K was used to confirm phase purity. Unfortunately, no single crystals were obtained from reaction of ligand **H169** with other Cu(I) or Cu(II) salts.

3.9 Formation of [Cu$_4$(H172)$_4$](PF$_6$)$_4$

As compound **H$_2$172** is similar in structure to compound **162**, differing only by the position of the pendant pyridyl nitrogen atom, attempts were made to obtain a structure of this ligand with Ag(I) salts. However, these attempts were unsuccessful, and thus indicates the important role played by the regiochemistry of the nitrogen atom within the pyridyl ring. However, reacting **H$_2$172** with [Cu(CH$_3$CN)$_4$](PF$_6$) in CH$_3$OH solution in a 1:1 metal:ligand stoichiometry, yielded blue crystals after several weeks. The single crystals obtained were solved and refined in the triclinic *P*-1 space group and revealed a tetranuclear M$_4$L$_4$ assembly

106
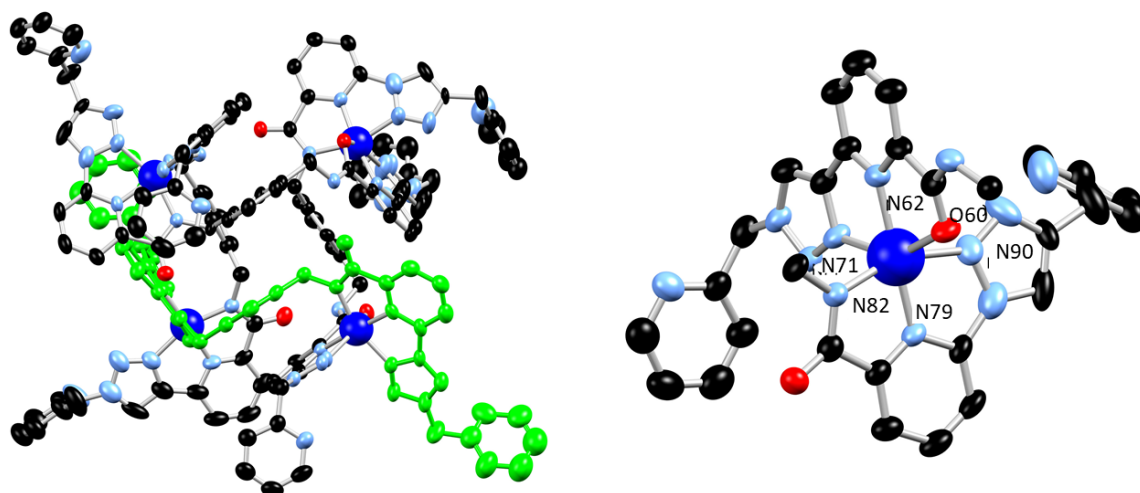
Figure 3.16 *(Right) Complete structure of [Cu$_4$(**H172**)$_4$](PF$_6$)$_4$ with a single ligand strand highlighted in green. (Left) Representative coordination geometry in the structure of [Cu$_4$(**H172**)$_4$](PF$_6$) with ligand molecules truncated for clarity showing both modes of amide coordination through oxygen atom O60 and nitrogen atom N82. Thermal ellipsoids shown at 50% probability.*

[Cu$_4$(**H172**)$_4$](PF$_6$)$_4$ with the same connectivity as the discrete tetranuclear structure [Cu$_4$(**H157**)$_4$](PF$_6$)$_4$ in Chapter 2. This structure was solved by June Lovitt. The asymmetric unit contains two unique complexes which differ only by the positioning of the flexible pendant pyridyl arms. As before, the [2 × 2] grid consists of four metal ions coordinated in a six-coordinate, N$_5$O coordination sphere. Each ligand has been singly deprotonated at an amide nitrogen and coordination occurs such that each Cu ion is coordinated by one of each *N,N,N* and *N,N,O* coordination modes. The overall connectivity and topology of the complex is unchanged when compared to its [Cu$_4$(**H157**)$_4$](PF$_6$)$_4$ counterpart. Internuclear distances such as the intrastrand Cu-Cu distance, decreased from an average of 8.77 to 8.54 Å when compared to the [Cu$_4$(**H157**)$_4$](PF$_6$)$_4$ system. The C$_4$ tetrahedral volume also decreases by 8% in this case; however, the total molecular volume is not affected. The four remaining protonated nitrogen atoms are involved in intermolecular hydrogen bonding interactions with the non-coordinated carboxamide oxygen atoms from an adjacent molecule. The extended structure contains π-π stacking and C-H⋯X hydrogen bonding interactions only, as the hydrogen bond donors in each ligand are involved in metal coordination. It is interesting to note that the pendant pyridyl nitrogen arms are not involved in the metal coordination and exert no influence on the structure obtained. Having obtained this M$_4$L$_4$ assembly in the solid state, the self-assembly of ligand **H$_2$172** with [Cu(CH$_3$CN)$_4$]PF$_6$ in solution was also examined.

3.10 Study of formation of [Cu₄(H172)₄](PF₆)₄ assembly in solution

The self-assembly of **H₂172** with [Cu(CH₃CN)₄]PF₆ *in situ* was investigated by a series of spectroscopic measurements. This procedure entailed the titration of a 1×10^{-5} M solution of **H₂172** against specific aliquots of [Cu(CH₃CN)₄]PF₆ and analysing the changes which occur in the UV-visible absorption and fluorescence spectra. The study was performed in CH₃OH as this was the solvent from which the crystals of [Cu₄(**H172**)₄](PF₆)₄ were grown. The titration was repeated three times to ensure reproducibility.

Upon examination of the UV-visible absorption spectrum of the ligand **H₂172** in CH₃OH, two characteristic bands were identified at λ_{max} = 250 nm and λ_{max} = 290 nm (ε = 31×10^3 cm⁻¹ M⁻¹ at λ_{abs} = 251 nm) which are ascribed to classical π-π* transitions, due to their high absorptivities and near-UV absorption regime. The overall changes in the UV-visible absorption spectrum of **H₂172** as a function of the addition of [Cu(CH₃CN)₄]PF₆ are displayed in Figure 3.17. As shown by binding isotherms in Figure 3.16, upon the addition of the metal solution, the high energy band located at λ = 250 nm undergoes a hypochromic effect, up to the addition of approximately 1 equivalent of the metal solution. Subsequent additions of Cu(I) solution resulted in an enhancement of the absorption intensity, and even up to the addition of 3.0 equivalents of the metal salt had not reached a plateau. This is likely due to a build-up of unreacted Cu(I). These changes suggest the formation of a 1:1, or most likely in this particular system, a 4:4 metal:ligand assembly in solution upon reaching the
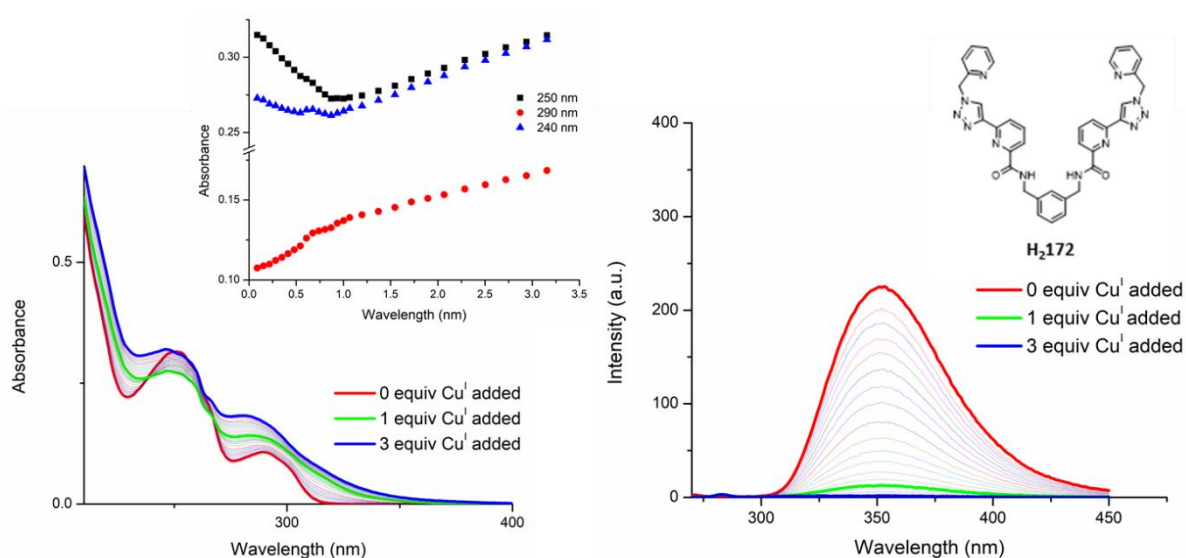

Figure 3.17 *The overall changes in the (left) UV-vis absorption spectra and (right) fluorescence emission spectra (excitation wavelength λ = 260 nm) upon titrating* ***H₂172*** *(1×10⁻⁵ M) against [Cu(CH₃CN)₄]PF₆ (0→3 equiv.) in CH₃OH at RT.* ***Inset***: *corresponding experimental binding isotherms of absorbance at λ = 250, 290, and 240 nm.*

stoichiometric 1:1 ratio of metal:ligand. Two isosbestic points at 267 nm and 263 nm were also observed, indicating the presence of multiple correlated species in solution. The lower energy band centred at $\lambda = 290$ nm, underwent a blue shift and a concomitant hyperchromic effect where the band was shifted to $\lambda = 284$ nm at the addition of 1.0 equivalents of Cu(I) salt. A broadening of the absorbance band was also observed. Subsequent additions of the metal solution resulted in a further increase in intensity and broadening of the absorbance band. Upon excitation of the assembly at $\lambda = 260$ nm, a ligand centred fluorescence band was observed at an emission maximum of $\lambda = 352$ nm. The luminescence signal was weak but was affected by the self-assembly process. As shown in Figure 3.17, quenching of the ligand fluorescence was seen upon addition of [Cu(CH$_3$CN)$_4$]PF$_6$, with a 95% reduction in the emission intensity observed after the addition of 1.0 equivalents of metal solution.

Interestingly, the changes observed in the UV-visible absorption and fluorescence spectra of **H$_2$172** upon addition of [Cu(CH$_3$CN)$_4$]PF$_6$ are very similar to the changes observed for the chiral ligand **H$_2$157** with the same metal salt, described in Chapter 2. These results are consistent with the observations that the crystal structures of the two systems are highly similar, and thus provides further evidence that they are also forming isostructural self-assembled systems in solution. This is despite the differences in the ligand structures, which thus suggests, as with the solid-state structures, that the pyridyl or chiral arms of the ligands do not exert any significant influence over the resulting self-assembly with [Cu(CH$_3$CN)$_4$]PF$_6$ in solution.

3.11 Fitting of [Cu$_4$(H172)$_4$](PF$_6$)$_4$

As before, in order to probe the speciation and the stability constants for this system, the UV-visible absorption titration data were analysed with a view to obtaining an insight into the stoichiometry in solution and associated binding constants. A global analysis method was employed to regress the spectra together and provide an estimate for the ratios of the species existing in solution and their concentration profiles. The analysis was completed with ReactLab EQUILIBRIA software.
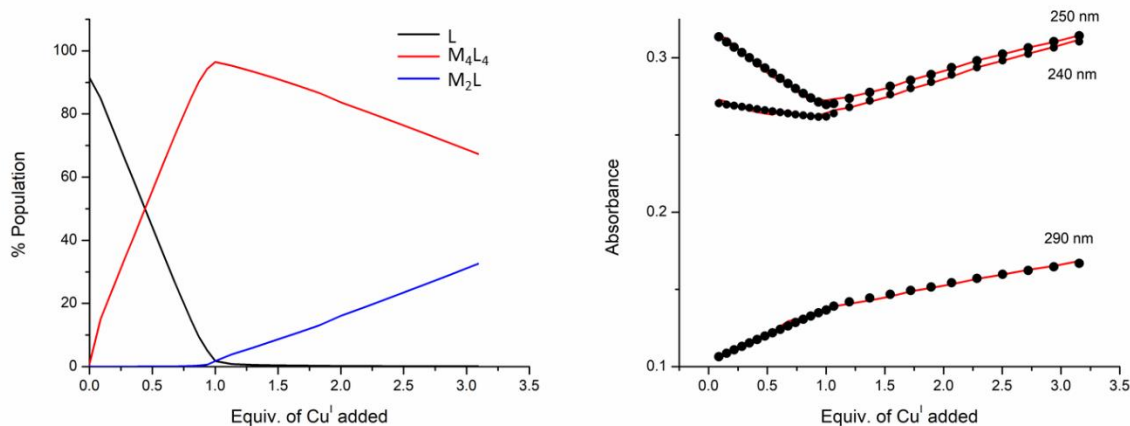
Figure 3.18 *(left) The speciation distribution diagram obtained from the fit of the UV-vis absorption titration data of ligand* **H₂172** *against [Cu(CH₃CN)₄]PF₆ in CH₃OH. (Right) The fit of the experimental binding isotherms using non-linear regression analysis software ReactLab.*

Analysis of the UV-visible absorption data for **H₂172** with [Cu(CH₃CN)₄]PF₆ in CH₃OH solution pointed to the formation of three independently absorbing species in solution (**H₂172**, 2:1 metal:ligand species and 4:4 metal:ligand species). Between the addition of 0.5 and 1.0 equivalents of metal ion, the M_4L_4 species was the most predominant in solution, and is likely to resemble the [2 × 2] grid species observed in the solid state as discussed above. This species attains 95% abundance at its maximum and subsequently, upon the addition of excess Cu(I) to the system, its abundance decreased with a concomitant increase in the presence of the M_2L species. Thus it appears that excess Cu(I) in the system causes dissociation of the M_4L_4 species, demonstrating the sensitivity of the assembly to the metal:ligand stoichiometry in solution at low concentration. The 2:1 metal:ligand species here may be related to the crystallised [Cu₂(**H₂157**)(NO₃)₄]·CH₃CN complex described in Chapter 2 in which each terdentate *N,N,O,* binding pocket coordinates one Cu(II) ion and a solvent ligand completes the Cu(II) coordination sphere. However, it is also possible that coordination through the terminal pyridyl nitrogen atoms results in a new self-assembly. From the changes observed in the UV-visible absorption spectra, stability constants were estimated for each species. The 4:4 metal:ligand assembly formed with $\log\beta_{44} = 45.25\pm0.50$ and the second species (2:1 metal:ligand) had a calculated binding constant of $\log\beta_{21} = 12.22\pm0.14$ These values are comparable to that seen for the self-assembly studies carried out with the chiral ligand **H₂157** and Cu(NO₃)₂, which generates a similar tetranuclear grid structure.

110

3.12 Design and synthesis of compounds 172 and 176

Having synthesised a series of **tzpa** derivatives, changing only the pendant pyridyl arms, a new series of ligands were designed and synthesised with a view to exploring the effects of modifying the central linker moiety and building on the structure-function relationships of this series of compounds. The self-assembly of the new ligands **173** and **176** was studied using Cu(I), Cu(II) and Ag(I). Ligand **173** was designed as an analogue of ligand **162** but with the *m*-xylylene ring modified to a *p*-xylylene linker. It was anticipated that changing the regiochemistry of the *m*-xylylene linker to *p*-xylylene would result in changes to the metallosupramolecular structures.

Ligand **173** was synthesised *via* a three-step synthetic pathway, starting from *p*-xylylene diamine. This was coupled with 6-bromopyridine-2-carboxylic acid in a peptide coupling reaction, using the same procedure as described for compounds **162** and **166** in Section 3.2. The resulting di-bromo compound **174** was then subjected to a Sonogashira coupling using the standard reaction conditions described above, before purifying by flash column chromatography to yield compound **175** as a brown solid. The 3-pyridyl arms were then installed *via* the standard CuAAC reaction conditions using 3-(aminomethyl)pyridine and the diazotransfer reagent $ImSO_2N_3.H_2SO_4$ to generate the azide moiety *in situ* and reaction with compound **174** in the presence of a copper catalyst resulted in the formation of compound **173**. The product was isolated and purified by an acid-base wash with 1M HCl and 1M NaOH to precipitate the product as a pure white solid in 42 % yield.
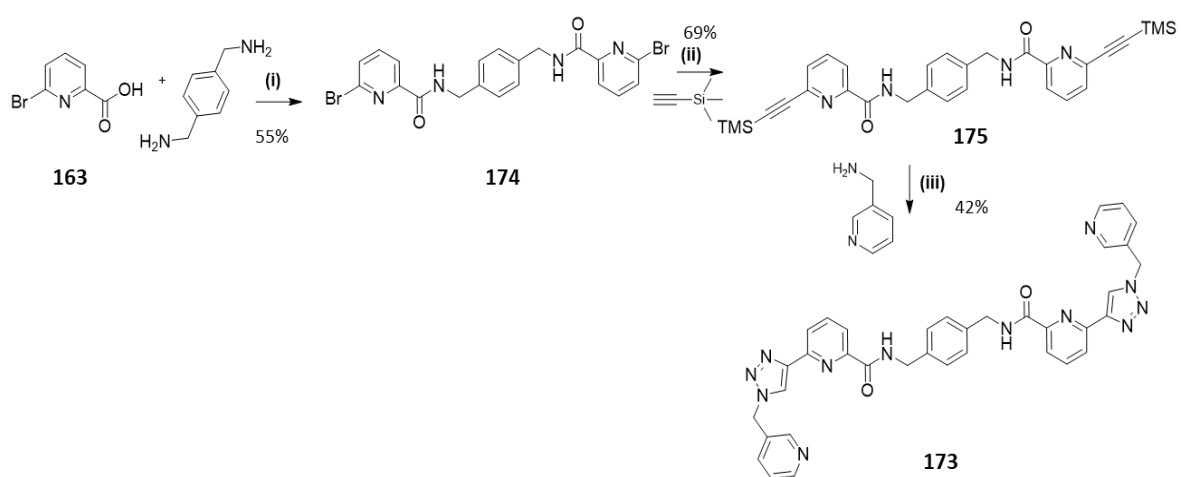
Scheme 3.5 *Synthesis and structure of **173**. Reagents and conditions: (i) hydroxybenzotriazole (HOBt), EDCI·HCl, NEt₃, 4:1 CH2Cl2:DMF (ii) CuI, Pd(PPh₃)₄, THF:NEt₃, (iii) (a) ImSO₂N₃.H₂SO₄, K₂CO₃, CuSO₄·5H₂O, CH₃OH, (b) sodium ascorbate, K₂CO₃, H₂O: ᵗBuOH, **174**, DMF.*
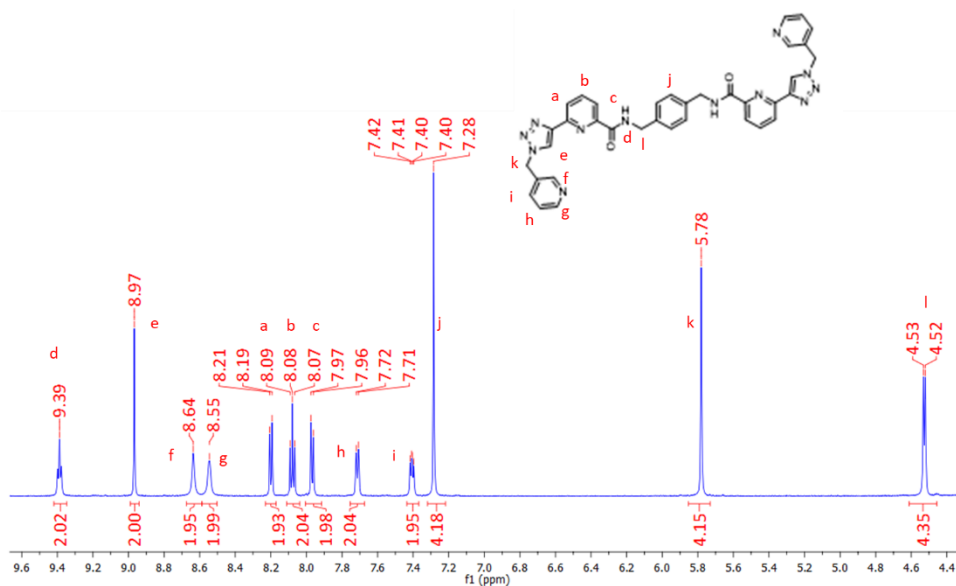
Figure 3.19 *¹H NMR spectrum (600 MHz, DMSO-d₆) of **173**.*

As shown in the ¹H NMR spectrum (600 MHz, DMSO-*d₆*) of **173** in Figure 3.19, resonances corresponding to the amide NH protons can be found downfield at 9.39 ppm with the triazole protons also shifted downfield at 8.97 ppm. The central pyridyl protons appear as two doublets and a triplet at 8.20, 8.08 and 7.96 ppm, respectively, while the pyridyl protons associated with the "arms" of the ligand are located at 8.64, 8.55, 7.72 and 7.41 ppm, integrating to eight protons in total. The *p*-xylyl protons lie at 7.28 ppm and appear as a singlet integrating to four protons due to the C2v symmetry of the system. Finally, the signal corresponding to the CH₂ protons adjacent to the *m*-xylyl linker lie upfield at 4.53 ppm and appears as a doublet while the CH₂ protons associated with the peripheral pyridyl arm resonate at 5.78 ppm. ¹³C{¹H} NMR, HRMS and IR spectroscopy were also employed to verify the formation of the desired product **173** (Figure A3.9).

While the linker moiety introduced in compound **173** differs by the substitution pattern of the xylyl linker, the design of compound **176** goes one step further. In this instance, compound **176** contains a flexible ethylene linker moiety which departs from the rigid aromatic central units employed previously. While the xylylene linker is relatively rigid, it was anticipated that the flexibility of the ethylene moiety would significantly alter the self-assembly of the ditopic ligand with Cu(I)/(II) or Ag(I) as they generate higher-order metallosupramolecular complexes.

Ligand **176** was synthesised according to a three-step synthetic procedure starting from ethylenediamine and 6-bromopyridine-2-carboxylic acid in a peptide coupling reaction conducted in a CH₂Cl₂:DMF (1:4) mixture. The product, compound **177**, was isolated as a white solid following triturating in CH₃OH. Compound **177** was then subjected to a
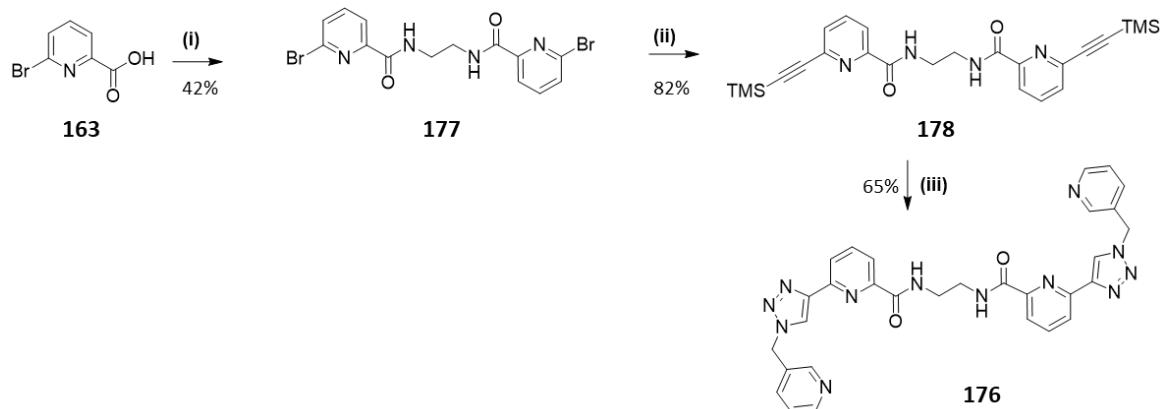
Scheme 3.6 *Synthesis and structure of* **176***. Reagents and conditions: (i) ethylenediamine, hydroxybenzotriazole (HOBt), EDCI·HCl, NEt₃, 4:1 CH₂Cl₂:DMF (ii) CuI, Pd(PPh₃)₄, TMS-acetylene, DMF:NEt₃, (iii) (a) 3-(aminomethyl)pyridine, ImSO₂N₃.H₂SO₄, K₂CO₃, CuSO₄·5H₂O, CH₃OH, (b) sodium ascorbate, K₂CO₃, H₂O: ᵗBuOH,* **178***, DMF.*

Sonogashira coupling reaction in order to install the TMS protected alkyne "arms" of the ligand. The reaction was unsuccessful under the reaction conditions described for ligands **162** and **5** (1:1, THF:NEt₃ mixture at room temperature) due to poor solubility of compound **177** in these solvent conditions, and so an alternative solvent system was devised. The reaction was conducted in a 4:1, DMF:NEt₃ mixture, and heated to 40 ˚C . This solvent system solubilised the starting material **177**, helping to generate the desired product as a brown solid in 82% yield. A CuAAC "click" reaction was then carried out with 3-aminomethylpyridine and compound **178** under the conditions described for compound **173**, resulting in precipitation of compound **176** as a pure while solid (65% yield).

In the ¹H NMR spectrum (600 MHz, DMSO-*d₆*) of **176** (Appendix Figure A3.10), the protons appear at similar resonances to those for compound **173**. The formation of the desired product was characterised by the appearance of the NH protons at 9.18 ppm and the CH₂ protons assigned to the ethyl linker found at 3.57 ppm. As before, ¹³C{¹H} NMR, HRMS and IR spectroscopy were also used to confirm the generation of the desired product (Appendix Figure A3.11).

3.13 Investigation of the coordination chemistry of 173

Having synthesised compound **173**, the self-assembly of this ligand with a variety of *d*-metals was examined, with a focus on Cu(I), Cu(II) and Ag(I). However, the ligand was highly insoluble in most organic solvents. The *p*-xylylene linker was likely the source of this insolubility as the *m*-xylylene derivative **162** was found to be readily soluble in many organic solvents. Despite attempts to generate metal complexes of ligand **173** of X-ray diffraction quality, none were obtained.

It is widely known that hydrogen bonding interactions can contribute to the formation of soft materials and it has been demonstrated that by adjusting the pH of a system in aqueous media, gels can be formed through these hydrogen bonding interactions. Basak and co-workers have reported the formation of a hydrogel upon addition of HCl to a pyridine-based ligand. Heating of the pyridine based gelator in the presence of aqueous HCl resulted in solubilisation of the compound, forming a pyridinium hydrochloride which, upon cooling, generates a transparent hydrogel.[217] Other examples of gels which only form in the acidic pH range include hydrogels of terpyridine derivatives.[218] It was noted that compound **173** was soluble in 1M HCl, which was likely due to protonation of the pyridyl nitrogen atoms, which enhanced solubility of the ligand in its cationic form in aqueous media.

With this in mind, the possibility of forming a soft material with compound **173** as a function of its protonation state was investigated. Upon addition of 1.0 equivalents of aqueous 1M HCl to the ligand, and gentle heating to 40 ˚C, a colourless solution resulted. This solution, upon standing at room temperature for one hour, formed an opaque soft material. The soft material was found to support its own weight *via* the inversion test over several hours. The thermoreversibility of the material was then investigated by heating the soft material to 50 ˚C where the material returned to a colourless solution. Upon cooling again a white precipitate was observed, indicating that the formation of this material was not a thermoreversible process.
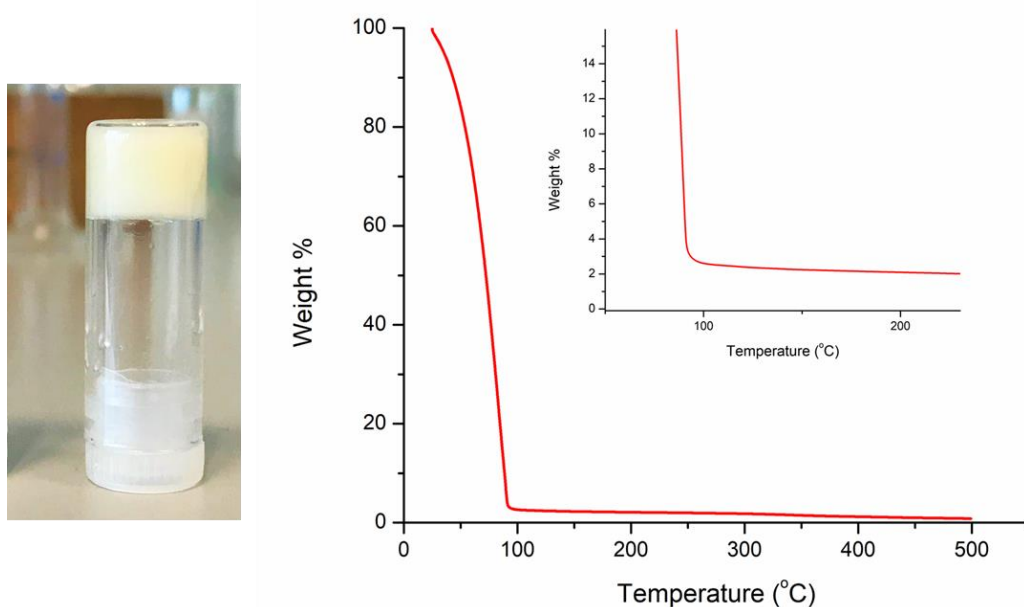
Figure 3.20 *(Left) Inversion test of **173** soft material generated by the addition of 1M HCl. (Right) TGA of the material showing it to be 2.4 wt%.*

A series of other dilute acids were also tested with compound **173** in order to determine the conditions required for soft material formation. HBr, HNO₃, H₂SO₄, CH₃COOH, and TFA were all tested under the same conditions and, in each case, compound **173** was solubilised at 40 ˚C as protonation of the pyridyl nitrogen atoms occurred. However, in each case upon standing at room temperature, compound **173** remained fully solubilised in the acid solution and no soft materials were formed This suggests that the process of soft material formation is selective for HCl, and that formation of the soft material is likely to be induced in part by the counterion Cl⁻. In addition, compound **173** was found to be insoluble in deionised water, or in aqueous salt solutions of NaCl or KCl in water, producing only white suspensions in these cases. This indicates that *both* the protonation state of the pyridyl nitrogen atoms, and the presence of Cl⁻ ions, is required for successful immobilisation of the solvent and subsequent generation of the soft material.

In order to investigate the wt% at which the soft material forms, thermogravimetric analysis was carried out on the material. TGA was carried out from 20 to 500 ˚C showing a loss in mass of 97.6% at 100 ˚C which indicates that the material formed at 2.4 wt%.

A xerogel of the material was generated by drying a sample under vacuum to study the morphology of the system by scanning electron microscopy (SEM). The SEM images (Figure 3.21) show a densely tangled, fibrous structure. The fibrous nature of the material is typical of a supramolecular soft material in which non-covalent interactions such a hydrogen bonding interactions immobilise the solvent.
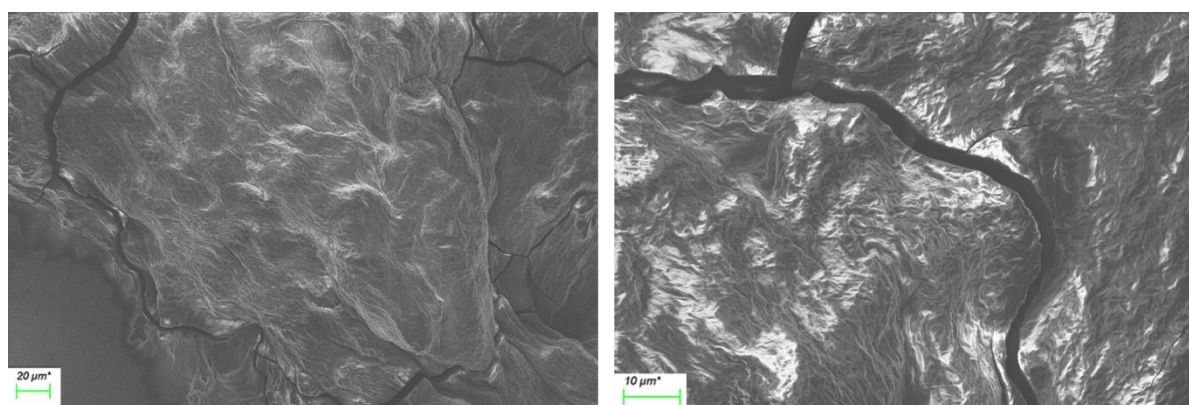
Figure 3.21 *SEM images of soft material generated from compound **173** scale bar 20 μm (left) and 10 μm (right) showing the fibrous nature of the material.*

In order to confirm the site at which protonation occurs in the ligand, compound **173** was resynthesised, but without using an acid/base wash in the work up, which was used previously to purify the compound. In this instance, compound **173** was purified by triturating in toluene. This compound was examined *via* [^1]H NMR spectroscopy as well as compound **173** upon addition of 1 equivalent of 1M HCl (Figure 3.22). A downfield shift in the peaks at 8.63 and 8.53 ppm to 8.71 and 8.61 ppm respectively, was observed along with a downfield shift of approximately 0.15 ppm for the protons resonating at 7.69 and 7.41 ppm. These four resonances which were most affected by the addition of HCl, correspond to the pyridyl protons of the 3-pyridyl "arms" of the ligand, indicating that protonation of these pyridyl nitrogens occur upon addition of 1M HCl. The remaining signals, including those assigned to the central pyridyl protons were not affected by the addition of HCl. No further changes to the [^1]H NMR spectrum, were observed upon addition of excess HCl. From these results it can be concluded that protonation of the 3-pyridyl nitrogen of compound **173**
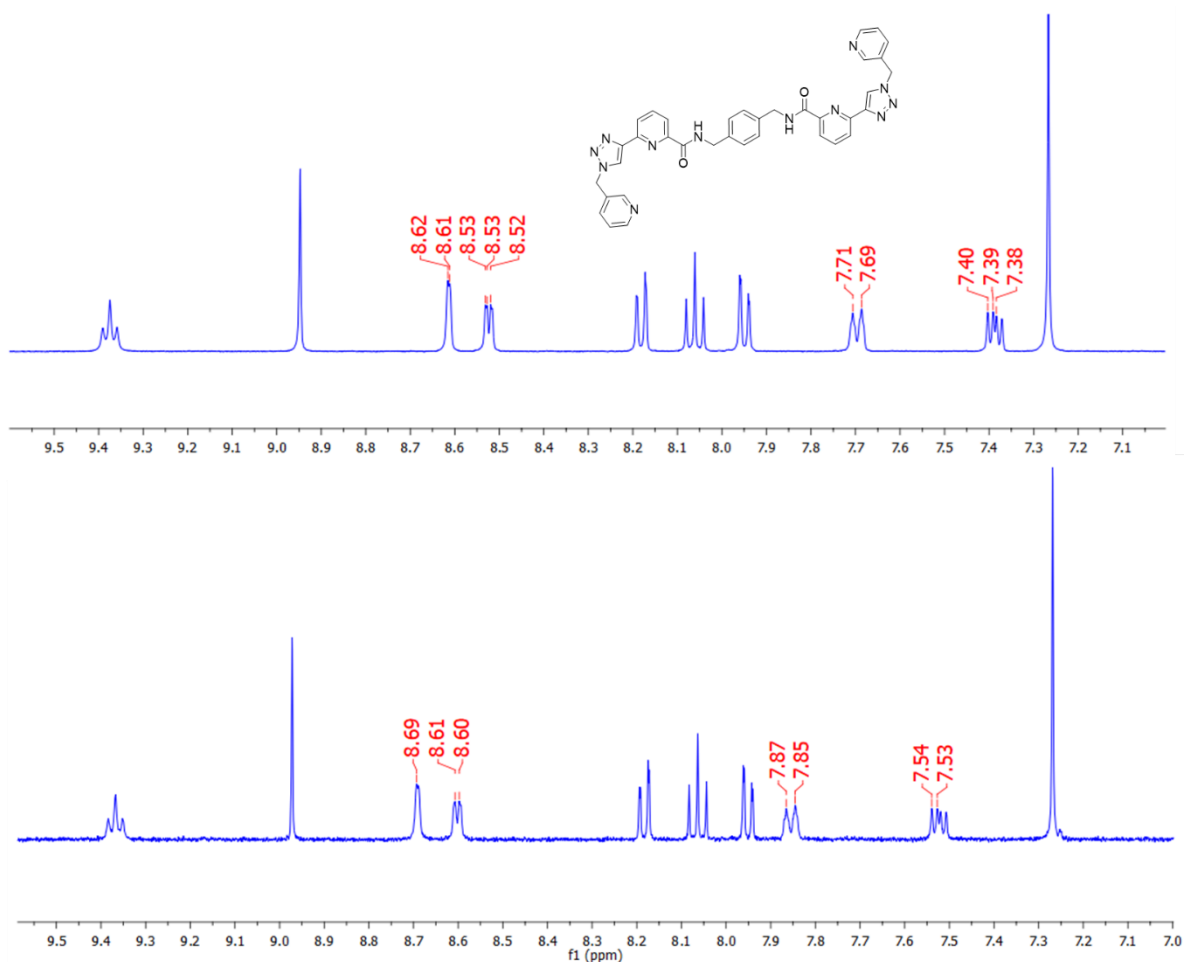
Figure 3.22 *[^1]H NMR spectra (600 MHz, DMSO-d6) of compound **173** (top) and compound **173** upon addition of 1.0 equiv. 1M HCl (bottom) showing a shift in the pyridyl protons associated with the protonated site.*

occurs under the gelation conditions, which facilitates hydrogen bonding interactions that lead to the formation of the fibrous soft material that immobilises the solvent. The soft material was not very robust over a long period of time so no rheological experiments were conducted.

3.14 Examination of the self-assembly of 176 with *d*-metals

Finally, the coordination chemistry of compound **176** with various *d*-metals was investigated. Similar conditions to those which were successful for compounds **162**, **166**, **H169** and **H₂172** were examined in order to determine the effect of changing the linker moiety on the self-assembly of this **tzpa** derivative. Unfortunately, upon reaction of **176** with various Cu(I), Cu(II) an Ag(I) salts, no crystals of X-ray diffraction quality were obtained. However, as this was a novel ligand system and relatively soluble in organic solvents, the self-assembly of the ligand with both [Cu(CH$_3$CN)$_4$]PF$_6$ and Cu(ClO$_4$)$_2$ was monitored in solution using UV-visible absorption and fluorescence spectroscopy. As seen in Section 3.10 and in Chapter 2, analysis of the self-assembly of ligands and *d*-metals *in situ* using these spectroscopic techniques can give valuable insights into the different stoichiometries which exist in solution, and their respective stability constants. This procedure, as before, involved the titration of a 1×10^{-5} M solution of **176** against specific aliquots of, firstly, [Cu(CH$_3$CN)$_4$]PF$_6$ and then analysis of the changes which occur in the UV-visible absorption and fluorescence spectra as a result. This study was performed in CH$_3$OH in order to allow direct comparison with compound **H₂172** described in Section 3.10.

Upon examination of the UV-visible absorption spectrum of the compound **176** in CH$_3$OH, two main bands centred at λ_{max} = 243 nm and λ_{max} = 283 nm, with a shoulder at λ = 293 nm, were observed ($\varepsilon = 44 \times 10^3$ cm^{-1} M^{-1} at λ_{abs} = 245 nm). These bands are attributed to classical π-π* transitions in the ligand structure. The overall changes in the UV-visible absorption spectrum of **176** as a function of the addition of [Cu(CH$_3$CN)$_4$]PF$_6$ are displayed in Figure 3.23. Upon addition of the metal solution, a hypochromic effect was experienced by the low energy band located at λ = 283 nm and this was accompanied by a loss in the hyperfine structure. This hyperchromic effect continued and had not reached a plateau even after the addition of 4.0 equivalents of metal ion. This is likely due to build-up of excess Cu(I) in the system. The high energy band located at λ = 250 nm, also experienced a hypochromic effect, up to the addition of approximately 1.0 equivalents of the metal solution. This was accompanied by a blue shift from λ = 243 nm to 240 nm. Subsequent
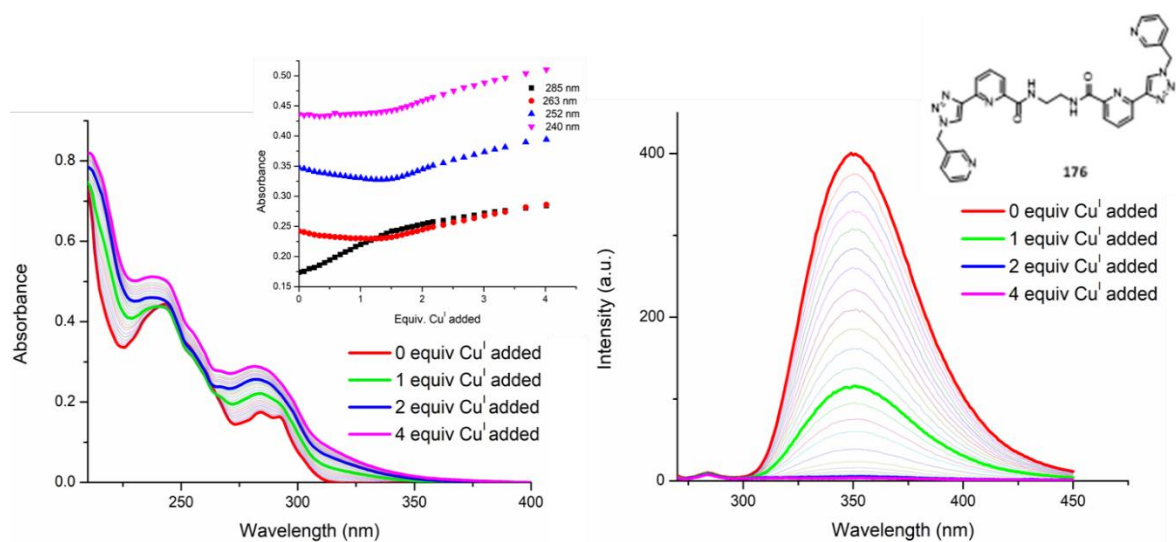
Figure 3.23 *The overall changes in the (left) UV-vis absorption spectra and (right) fluorescence emission spectra upon titrating **176** (1×10⁻⁵ M) against [Cu(CH₃CN)₄]PF₆ (0→3 equiv.) in CH₃OH at RT.* **Inset**: *corresponding experimental binding isotherms of absorbance at λ = 285, 263, 252 and 240 nm.*

additions of Cu(I) resulted in an enhancement in the absorption intensity which again did not reach a plateau even at the addition of 4.0 equivalents of the metal solution. Two isosbestic points occur at 240 nm and 265 nm, indicating the presence of multiple correlated species in solution. Overall, these changes suggest the formation of a 1:1 Cu:**176** assembly in solution at the addition of 1.0 equivalents of Cu(I) during the titration.

Excitation of compound **176** at λ = 260 nm resulted in the appearance of the ligand centred fluorescence band centred at λ = 350 nm. The luminescence was relatively weak but nevertheless observable and, upon addition of the Cu(I) solution, changes in the fluorescence signal were observed, indicating it was affected by the self-assembly process of **176** with Cu(I). As shown in Figure 3.23, quenching of the ligand fluorescence was observed upon addition of [Cu(CH₃CN)₄]PF₆, with a 71% reduction in the emission intensity after the addition of 1.0 equivalents of metal solution. Upon addition of 2.0 equivalents, the fluorescence emission was completely quenched.

The changes observed in the UV-visible and fluorescence spectra of **176** upon addition of [Cu(CH₃CN)₄]PF₆ differ from those observed in the UV-visible absorption and fluorescence spectra when compound **H₂172** was titrated with Cu(I) under the same conditions. This indicates that the self-assembly process is sensitive to the nature of the linker moiety between the two binding sites, with the flexibility of the ethylene linker compared with the. rigid xylylene inducing different speciation in solution. In order to probe

the speciation and stability of these species in solution the titration data were analysed, and will be discussed in the next section.

3.15 Fitting of titration data for 176 and [Cu(CH₃CN)₄]PF₆

As described above, in order to gain insight into the species existing in solution and the stability constants for these species, the UV-visible absorption titration data were analysed using a global analysis method.

Analysis of the UV-visible absorption titration data for **176** with $[Cu(CH_3CN)_4]PF_6$ in CH_3OH solution indicates the presence of three independently absorbing species in solution. These species (**176**, a 2:1 metal:ligand species, and a 1:1 metal:ligand species) co-exist in solution, with the ML species reaching 48% population at the addition of 1.0 equivalents of metal ion. Subsequent additions of Cu(I) result in an increase in both the ML species and the M_2L species.

From the changes observed in the UV-visible absorption spectra, stability constants were estimated for each species. The 1:1 metal:ligand assembly formed with $\log\beta_{11} = 5.43\pm0.02$, while the 2:1 metal:ligand species had a calculated binding constant of $\log\beta_{21} = 10.27$ (fixed manually). The data could also be fit to a model comprising of the species M_4L_4 and M_2L. This speciation distribution is shown in the Appendix Figure A3.12. In this case the binding constants obtained were $\log\beta_{44} = 36.461\pm0.02$ and $\log\beta_{21} = 10.272$ (fixed). No difference in the value of the M_2L binding constants were observed for both models, while the constant for the M_4L_4 species is markedly higher, as expected, than that of the ML species
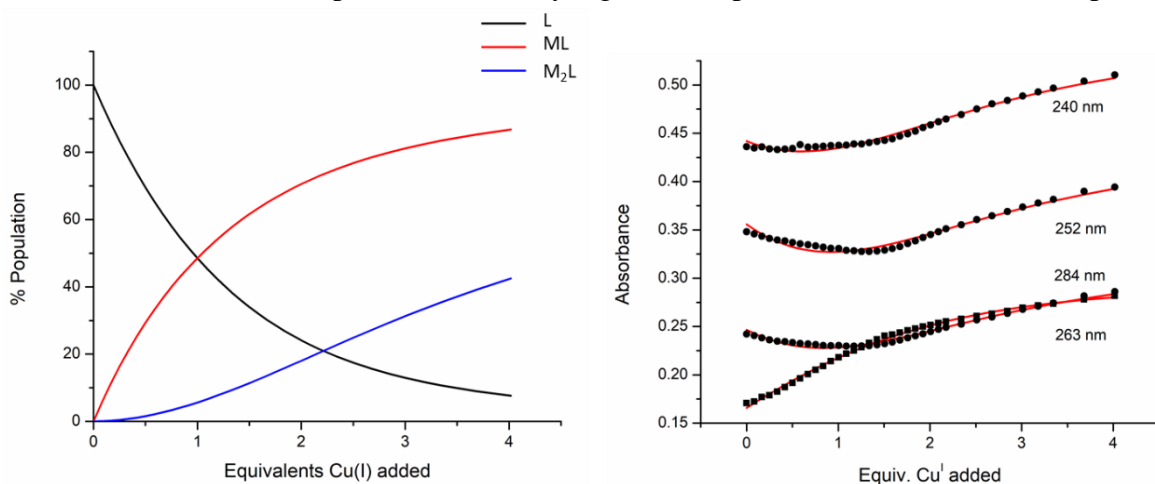
Figure 3.24 *(Left) The speciation distribution diagram obtained from the fit of the UV-vis absorption titration data of ligand **176** against [Cu(CH₃CN)₄]PF₆ in CH₃OH. (Right) The fit of the experimental binding isotherms using non-linear regression analysis software ReactLab.*

Due to the small changes observed in the UV-visible absorption spectrum, an accurate fit was difficult to ascertain. This, combined with the difficulty in obtaining a crystal structure, means that discerning the true speciation in solution is not possible with the current data.

3.16 Titration of compound 176 with Cu(ClO₄)₂

The self-assembly of ligand **176** with a Cu(II) salt was also examined. A 1×10^{-5} M solution of **176** was titrated against specific aliquots of Cu(ClO₄)₂, and the changes to the UV-visible absorption and fluorescence spectra were analysed. The study was conducted in CH_3CN and the spectra can be seen in Figure 3.25.

Two main bands, centred at λ_{max} = 243 nm and λ_{max} = 283 nm, along with a shoulder at λ = 293 nm, were observed in the UV-visible absorption spectrum of the compound **176** (e = 44×10^{-3} cm^{-1} M^{-1} at λ_{abs} = 243 nm). Upon addition of the Cu(II) salt a hyperchromic effect was observed for the band located at λ = 283 nm which was accompanied by a slight broadening of the band. These changes occurred up to the addition of 1.0 equivalents of Cu(II), after which a plateau was reached. The high energy band, located at λ = 250 nm experienced a significant broadening but little change to the absorbance intensity. The most significant changes occurred up to the addition of one equivalent of Cu(II).

Excitation of the ligand at λ = 260 nm resulted in the appearance of ligand centred fluorescence at λ = 338 nm. Upon addition of Cu(II), changes in the fluorescence signal were observed, indicating it was affected by the self-assembly process. As shown in Figure 3.25, quenching of the ligand fluorescence was observed upon addition of Cu(ClO₄)₂, with a 40%
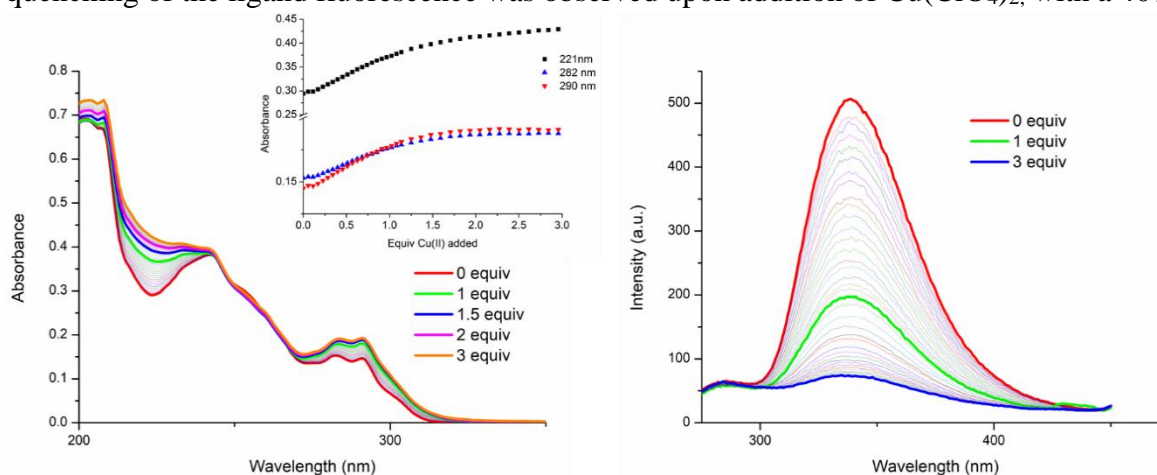
Figure 3.25 *The overall changes in the (left) UV-vis absorption spectra and (right) fluorescence emission spectra upon titrating **176** (1×10⁻⁵ M) against Cu(ClO₄)₂ (0→3 equiv.) in CH₃CN at RT.* ***Inset:*** *corresponding experimental binding isotherms of absorbance at λ = 220, 280 and 290 nm.*

reduction in the emission signal observed after the addition of 1 equivalent of metal solution. Upon addition of 3 equivalents, the fluorescence emission was almost completely quenched.

These changes observed in the UV-visible and fluorescence spectra of **176** upon addition of Cu(ClO$_4$)$_2$ differ to the changes observed in the UV-visible absorption and fluorescence spectra of **176** upon titration with Cu(I) as described in Section 3.10. In order to probe the speciation and stability of the species in solution, the titration data were analysed and will be discussed in the next section

3.17 Fitting of titration data of 176 with Cu(ClO$_4$)$_2$

The UV-visible absorption titration data were analysed using a global analysis method as described above. Analysis of the UV-visible absorption data for **176** with Cu(ClO$_4$)$_2$ in CH$_3$CN solution indicates the presence of three main absorbing species in solution. These species (**176**, 2:1 metal:ligand and 1:1 metal:ligand) co-exist in solution, with the ML species reaching 68% abundance at the addition of 1.0 equivalents of metal. Subsequent additions of the metal solution results in an increase in the abundance of the M$_2$L species, along with a concomitant decrease in the ML species. The ML species, while abundant at 1.0 equivalents of Cu(II), does not appear to be stable in the presence of excess Cu(II), which leads to dissociation of the ML species into the ML$_2$ assembly. From the changes observed in the UV-visible absorption spectra, stability constants were estimated for each species. The 1:1 metal:ligand assembly formed with logβ_{11} = 4.090 (fixed) and the second species (2:1 metal:ligand) had a calculated binding constant of logβ_{21} = 8.80 ± 0.03. The ML species stability constant was fixed manually in order to obtain a fit for the titration data.
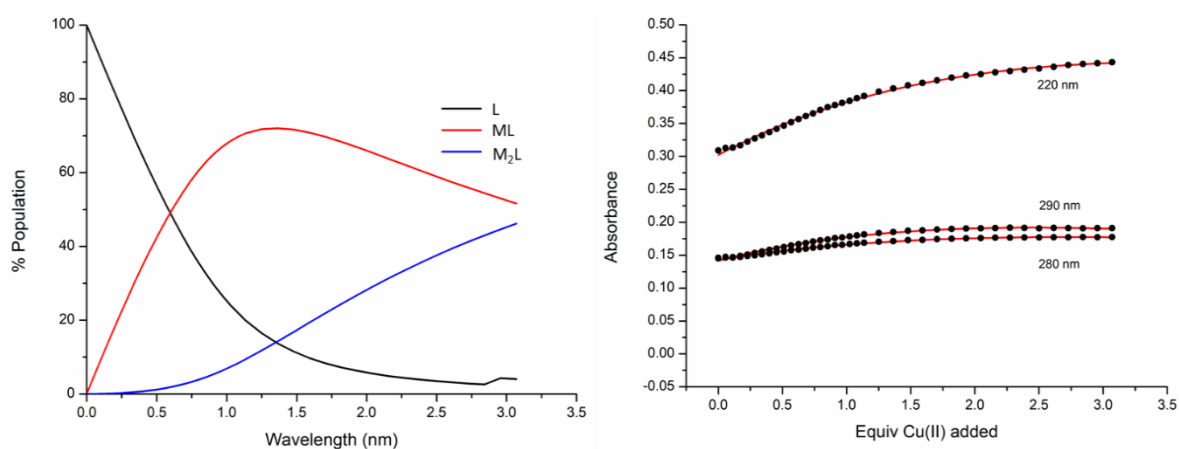
Figure 3.26 *(Left) The speciation distribution diagram obtained from the fit of the UV-vis absorption titration data of ligand **176** against Cu(ClO$_4$)$_2$ in CH$_3$CN. (Right) The fit of the experimental binding isotherms using non-linear regression analysis software ReactLab.*

121

Table 3.1 *Binding constants obtained by fitting spectroscopic data. *Value fixed in order to reach convergence.*

Ligand	Metal	$log\beta_{21}$	$log\beta_{11}$
176	[Cu(CH$_3$CN)$_4$]PF$_6$	10.27*	5.43 ± 0.02
176	Cu(ClO$_4$)$_2$	8.80 ± 0.3	4.09*

3.18 Conclusions and Future Work

In this chapter, six novel ligands **162**, **166**, **H169**, **H₂172**, **162**, and **166**, based on the **tzpa** motif were designed, synthesised and characterised. Their ability to form supramolecular self-assemblies with *d*-metals was explored, from the generation of discrete metal complexes and 1D polymers to the formation of 2D networks. The formation of soft materials was also investigated. The self-assembly of these systems *in situ* was investigated with the use of UV-visible absorption and fluorescence spectroscopy. The objective of increasing the coordination motifs on the **tzpa** ligand, and employing these additional coordination sites to generate higher order metallosupramolecular self-assemblies was achieved.

The design of compound **162** was based on the structure of compound **H₂157** in Chapter 2, changing the chiral phenyl moiety in **H₂157** for a 3-pyridyl substituent, which introduces two additional binding sites. A derivative of compound **162**, compound **166**, was also designed and synthesised with a view to examining the self-assembly of the **tzpa** binding motif in a simple monotopic ligand structure. Ligand **166** formed the 1D polymer {[Ag₂(**5**)₂](CF₃SO₃)₂}ₙ upon reaction with AgCF₃SO₃ in THF . Each Ag centre coordinates two ligands through the pyridyl-triazole N_2 binding site of one ligand, and the pendant pyridyl nitrogen atom of another ligand. In this case, the Ag(I) metal centre is not coordinated by the carbonyl oxygen or amide nitrogen atoms of the ligand in a terdentate fashion, as was the case for the discrete Cu(II) tzpa complexes described in Chapter 2. In the X-ray crystal structure of the free ligand **166**, the triazole moiety is orientated such that the nitrogen atoms point away from the central pyridyl nitrogen due to nitrogen lone pair repulsion while this conformation is reversed in the 1D polymer structure to facilitate

coordination to the Ag(I) ion. The carboxamide also differs in orientation in the free ligand and the polymer structure although the carbonyl oxygen does not coordinate to the Ag(I) ion. The carbonyl oxygen is orientated away from the central pyridyl nitrogen in the free ligand structure, while it is oriented towards the central pyridyl nitrogen in the polymer structure due to an Ag···O interaction.

While no crystal structures of Ag(I) complexes with compound **162** were obtained, the ditopic ligand, upon reaction with $AgBF_4$ in CH_3CN solution, generated a Ag(I) organogel. The gel was found to be chemoreversible but not thermoreversible. The morphology of the xerogel was investigated by SEM and the images showed a sheet-like structure which could be due to collapse of the gel fibres upon drying of the sample. Rheological experiments confirmed the physical properties of the gel and showed that it was thixotropic. Attempts to form a Ag(I) gel from ligand **H₂157** described in Chapter 2 with $AgBF_4$ under the same conditions were unsuccessful and this result, coupled with the coordination modes which occur in the 1D polymer structure of compound **166** with Ag(I) indicate that the pendant pyridyl nitrogen atoms likely play an important role in the generation of this robust gel.

Compound **H169** was then synthesised as a derivative of the monotopic ligand **166**, with two terminal pyridyl groups to facilitate further metal-ligand coordination interactions. While no crystal structures of the ligand with Ag(I) salts were obtained, ligand **H169** generated a 2D polymer $[Cu_3(\mathbf{169})_2(CF_3SO_3)(OCH_3)_2]CF_3SO_3.H_2O$ with $[Cu(CH_3CN)_4]CF_3SO_3$ which formed crystals of X-ray diffraction quality. Each Cu(I) ion was found to oxidise to Cu(II), while each ligand was deprotonated at the coordinating amide nitrogen. Each Cu(II) ion is coordinated through a combination of terminal pyridyl nitrogen atoms and the terdentate triazole-pyridyl-amide N_3 binding site. While deprotonation of the amide nitrogen under such mild conditions in the absence of base is unusual, it was also described in Chapter 2 for another **tzpa** complex generated with $[Cu(CH_3CN)_4]PF_6$ in CH_3OH in the absence of base. Methoxide ligands also take part in metal coordination as an *in situ* deprotonation of the CH_3OH solvent takes place.

The design of compound **H₂172** was based on compound **162**, changing only the position of the pyridyl nitrogen atom. Reaction of this ligand with $[Cu(CH_3CN)_4]PF_6$ in CH_3OH resulted in blue crystals which upon examination by single crystal X-ray diffraction, was determined to be a M_4L_4 [2 × 2] grid structure of the form $[Cu_4(\mathbf{H172})_4](PF_6)_4$, which is isostructural with the complex described in Chapter 2. Again, the Cu(I) ion is oxidised to Cu(II) and each ligand is singly deprotonated, which facilitates coordination through the

amide nitrogen in one of the two binding sites of each ligand while the other site is coordinated to the metal centre through the carbonyl oxygen atom. Each Cu(II) centre, therefore, experiences two different coordination modes. The pendant 2-pyridyl nitrogen atoms were not involved in metal coordination. This, combined with the fact that no crystal structure could be obtained of the self-assembly formed from the reaction of **H₂172** with Ag(I), suggests that the 2-pyridyl positioning of the nitrogen atom was not optimal for metal coordination. The self-assembly of this system was also examined in solution by monitoring the changes to the UV-visible absorption spectrum. Three main species were estimated to exist in solution by global analysis of the changes in the UV-visible absorption data. Stability constants for the three species (**H169**, M_2L and M_4L_4) were estimated and determined to be similar to those described in Chapter 2 for other Cu(II)-**tzpa** systems. From these results it can be concluded that reaction of ditopic **tzpa** ligands with $[Cu(CH_3CN)_4]PF_6$ in CH_3OH can result in oxidation of the Cu(I) ion to Cu(II) and deprotonation of the ditopic ligand to generate a M_4L_4 grid structure when no other coordination sites are geometrically favourable.

Compounds **173** and **176** were designed with more profound changes to the overall structure. Altering the linker between the two binding sites from *m*-xylylene to *p*-xylylene in **173**, and an ethylene in **176**, drastically changed the solubility and behaviour of the compounds. These compounds did not generate metal complexes which could be analysed by X-ray diffraction. Instead, compound **173** was found to form a soft material upon protonation of the pendant pyridyl arms and the self-assembly of compound **176** was investigated with $[Cu(CH_3CN)_4]PF_6$ in order to gain some insight into the possible metal:ligand stoichiometries which are formed in solution.

From this work it can be concluded that the *m*-xylylene linker is key to the crystallisation of these systems. This is likely due to its influence on solubility and coordination geometry. It is also clear that the 3-pyridyl nitrogen position is the most favourable for metal coordination and crystallisation in these **tzpa** systems and the introduction of further coordinating pyridyl sites can in fact generate higher order structures.

"I have not failed. I've just found 10,000 ways that won't work."

Thomas A. Edison

4. Amino-acid Functionalised tzpa Ligands and Their Luminescent Lanthanide Complexes

4.1 Introduction

In Chapters 2 and 3, the coordination chemistry of novel **tzpa** ligands with various *d*-metals was explored. While transition metals such as Ag(I) and Cu(II) generated interesting grid structures and higher order polymers as well as soft-materials through robust metal-ligand interactions, the coordination chemistry of the **tzpa** motif with the more labile lanthanide ions has yet to be explored. Lanthanide ions have long been utilised in supramolecular chemistry to generate photophysically rich materials and self-assembly architectures.[219–221] This chapter will focus on lanthanide self-assembly with a series of **tzpa** ligands, examining the ability of the asymmetric ligand to sensitise Tb(III) and Eu(III) efficiently with a view to generating Ln(III) complexes which are stable to an aqueous environment.

The lanthanides, alongside Sc and Y are known as "rare earth elements" despite their relative abundance in nature and are found in the first row of the *f*-block of the periodic table (elements 57 to 71).[222] The entire series most preferred oxidation state has been found to be 3+ although Ln(II) has been stabilised by Evans and co-workers in organometallic complexes under Schlenk conditions at low temperature.[223,224] The lanthanides differ significantly from the transition metals due to their electronic structure, varying little in oxidation state, coordination behaviour or reactivity across the series.[219]

The electronic configuration of the trivalent lanthanide ions is common to all the lanthanide ions $[Xe]4f^n$ where n = 0, 2-11 except in the case of Ce^{3+} where the configuration is $[Xe]5d^1$. There are seven possible 4*f* wavefunctions, accepting 14 electrons with spin $\pm 1/2$ and are filled following Hund's rule. Therefore, with the exception of La(III) and Lu(III), the lanthanide ions have partially filled *f*-orbitals and are paramagnetic in nature.[225] The 4*f* orbitals are also contracted and therefore are closer to the nucleus than the 5*s* and 5*p* orbitals. This results in poor "shielding" of the electrons within the 4*f* orbitals from the increasing nuclear charge across the series and therefore a decrease in the ionic radius is observed across the series, known as the lanthanide contraction.

Due to the 4*f* electrons lack of participation in coordination interactions, their coordination chemistry across the series is broadly invariant. The lanthanide valence electrons are held close to the nucleus and screened from the surrounding environment by the 5*s* and 5*p* orbitals which results in weaker orbital overlap interactions than the *d*-orbitals. Coordination interactions are therefore mostly electrostatic in nature which is in contrast to the transition metal ions. The valence electronic configuration of the lanthanide ions has been established as $4f^n$ and inter-electron repulsion between electrons in the 4*f* orbitals results in splitting into ground- and excited-states. The angular momentum (L) is derived from the
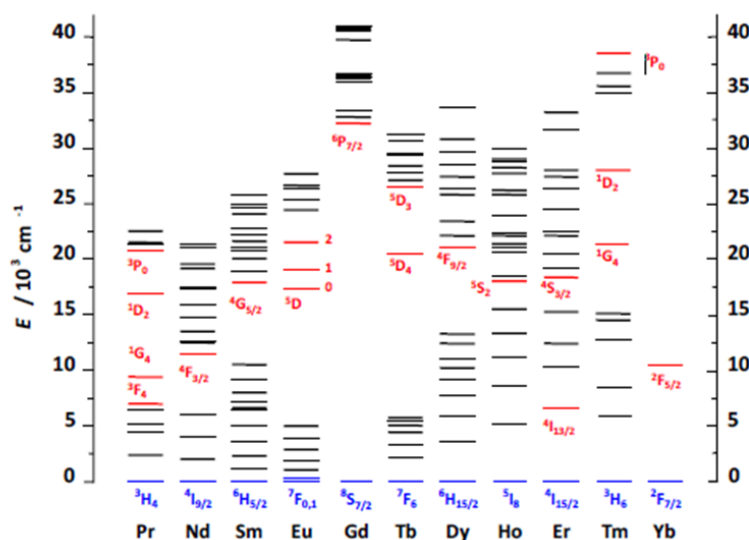
Figure 4.1 *Partial energy diagrams for the lanthanide aquo ions showing the term symbols for key excited states (red) and ground states (blue). Reproduced from ref 219.*

seven orbital angular momentum quantum numbers while the total spin quantum number (S) is combined from the distribution of spins within the orbitals. These two terms combine to give base LS term which is of the form ^{2S+1}L. As both Tb(III) and Eu(III) have 6 unpaired electrons, their ground states are both ^7F. The sub-levels of the ^{2S+1}L configuration are generated by spin-orbit coupling and each level is split by quantum number J with possible values for J between L+S and $|L-S|$. Therefore the ground state of Tb(III) and Eu(III) are determined as being $^7F_6$ and $^7F_0$, respectively.

Electronic transitions between f and d orbitals are rarely observed due to the large energy separation between the two, with an energy separation of 32,000 cm^{-1} between [Xe]$4f^n$ and [Xe]$4f^{n-1}5d^1$. Therefore, the most accessible electronic transitions are f-f transitions, which are parity forbidden as described by the Laporte Rule. This redistribution of electrons within the $4f$ sub-shell results in very weak absorption. The selection rules may become relaxed; however, by mechanisms such as J-mixing or vibronic coupling and the mixing with opposite parity states can result in weak luminescence.[226]

The unique electronic configuration of the lanthanide ions gives rise to luminescence spectra with characteristic features. The varying energy gaps between ground- and excited-state configurations results in emission across the spectrum from UV to NIR. For example, Gd(III) has the largest energy gap with $\Delta E = 32200$ cm^{-1} for $^6P_{7/2} \rightarrow {}^8S_{7/2}$ which corresponds to UV emission while Tb(III) and Eu(III) have energy gaps of $\Delta E = 14800$ cm^{-1} for $^5D_4 \rightarrow {}^7F_6$ and $\Delta E = 12300$ cm^{-1} for $^5D_0 \rightarrow {}^7F_6$ respectively. These emit in the visible region with characteristic green and red light. Nd(III) and Yb(III) on the other hand, emit in the NIR

region as the energy levels of the ground and excited states are significantly closer together. Due to the forbidden nature of the transitions they are line-like and the colour purity is high. Additionally, the lanthanides exhibit long luminescence lifetimes, ranging from the millisecond (ms) range for Eu(III) and Tb(III) to microseconds (µs) for Sm(III) and Dy(III) compared to the nanosecond (ns) range of some organic dyes and biological media.[227] These long-lived excited-states enable their use in time resolved detection (TRD) in biological media. Detection of background autofluorescence can be avoided by imposing a delay time after the excitation and before measurement. Therefore, fluorescence emission with shorter lifetimes in the ns and sub-microsecond ranges decay before measurement commences, resulting in a good signal-to-noise ratio and various small molecules have been designed with this application in mind.[75,76]

While direct excitation of the *f-f* electronic transitions is highly inefficient, emission from Ln(III) ions can be observed through what is known as sensitised emission. This occurs when energy is transferred from a donor species to the metal-centre excited-states rather than absorbed by the metal centre, and radiative deactivation occurs. This is known as the "antenna effect" and the donor species is, known as the sensitising antenna. The process occurs when an emissive lanthanide ion such as Eu(III) or Tb(III) is coordinated by a ligand "antenna" which contains chromophores which absorb in the UV or visible regions. When these ligands are excited the ligand-centred excited-states may deactivate by a number of non-radiative processes or ligand-centred emission. However, when the ligand chromophores are held within the first coordination sphere of the Ln(III) ion, deactivation
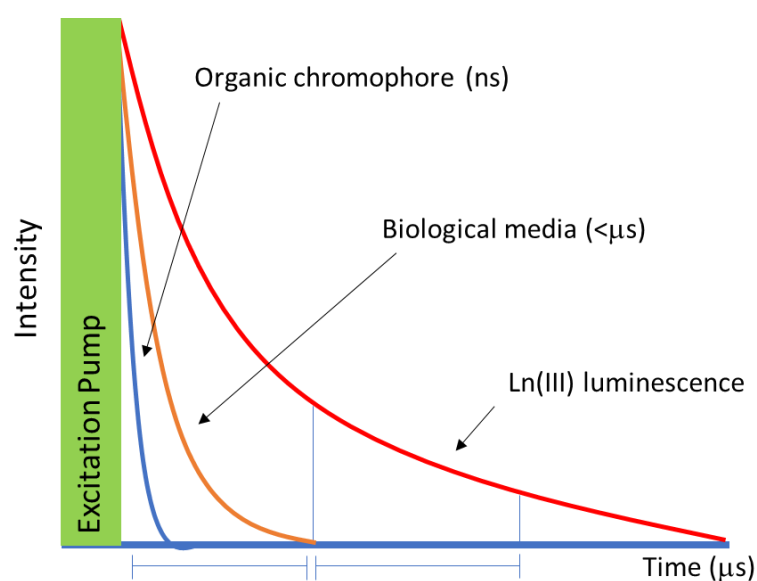
Figure 4.2 *Schematic representation of time-resolved detection (TRD) which allows background fluorescence to decay to negligible levels.*

131

of the ligand-centred excited-state can result in energy transfer to the Ln(III) ion and population of the triplet excited state of the lanthanide. This energy is then either emitted as light (luminescence) or undergoes non-radiative deactivation (quenching). This mechanism has been successfully exploited for a range of Ln(III) systems.[228] The energy transfer from the ligand excited-state to the Ln(III) centre can occur by a number of routes but the most popular for Tb(III) and Eu(III) ions is from the triplet excited state of the ligand (T_1) to the Ln(III) excited state. Triplet-based metal-to-ligand charge transfer mechanisms (^{3}MLCT)[229] have been used as well as direct sensitisation of the Ln(III) emission from the singlet excited states of the ligand *via* the intra-ligand charge transfer (ILCT) singlet excited states;[230] however, the classical triplet (T_1) to Ln(III) excited state remains the most popular approach.

The energy transfer from the chromophore T_1 to the Ln(III) ion is considered to occur by one of two mechanisms known as Dexters and Försters mechanisms.[231,232] The Försters-type involves a dipole coupling mechanism whereby the dipole moment associated with the de-excitation of the ligand T_1 to S_0 is coupled with the acceptor transition dipole associated with the 4*f* orbitals (Ln(III) excited state ← Ln(III) ground state excitation). This results in indirect population of the metal-centred excited-states. This mechanism is distance dependent. The Dexter mechanism also performs more efficiently when the donor antenna is in close proximity to the Ln(III) ion. It involves a two-electron exchange where an electron is transferred from the T_1 excited-state of the ligand to an acceptor sub-orbital of the Ln(III) ion. Simultaneously, an electron is transferred from the HOMO of the metal ion to the gap created by the initial excitation of the ligand.
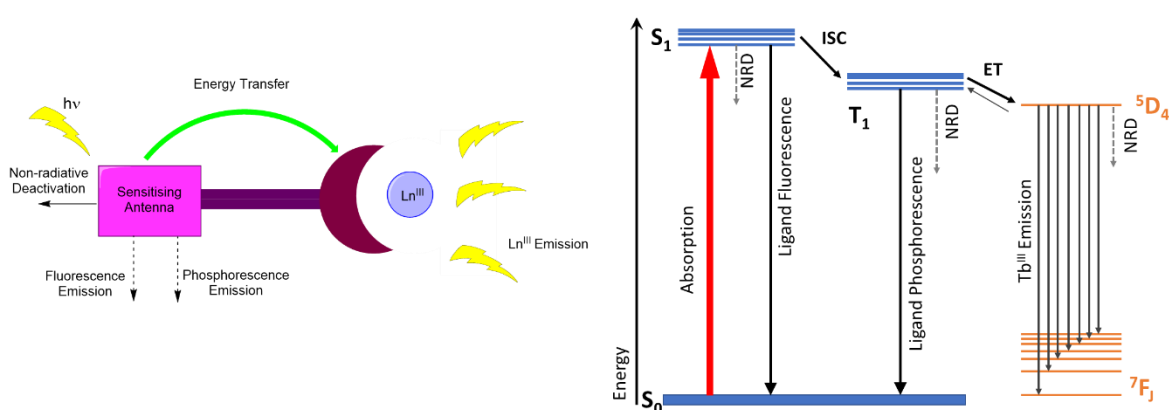
Figure 4.3 *(Left) Schematic representation of the "antenna effect" used to indirectly excite the Ln(III) ion. (Right) Jablonski energy level diagram demonstrating the sensitisation of Tb(III) via excitation of the ligand from the ground state (S_0) to the excited state (S_1), ligand centred ISC to the triplet excited state (T_1) and energy transfer to the Ln(III) ion. Non-radiative deactivation (NRD) pathways are also shown.*

As mentioned above, the proximity of the ligand chromophores to the lanthanide metal centre is crucial to the efficient energy transfer. Due to the hard Lewis acidity of the Ln(III) ions, hard Lewis bases are utilised as ligands to minimise the Ln(III)-ligand distance and generate stronger Ln(III)-ligand interactions.[233] Hard Lewis bases such as carboxylates, amides and N-containing heterocycles compliment the hard Lewis acidity of the Ln(III) ions.

Design of organic chromophores should also take into account the energy difference between the HOMO and LUMO of the chromophore as a high extinction coefficient is required for effective energy absorption. Furthermore, the energy difference between the T_1 excited state and the accepting level of the Ln(III) ion should be between 2500 and 3500 cm^{-1} in order to minimise thermally activated energy back transfer resulting in repopulation of the T_1 state of the ligand while also allowing efficient ligand-to-metal energy transfer to take place.[23] Post sensitisation quenching of the Ln(III) luminescence can also occur through non-radiative deactivation processes. Vibrational collisions with N-H, O-H or C-H oscillators within the Ln(III) coordination sphere quench the Ln(III) excited-states. These oscillators can be part of solvent molecules or in the ligand structure itself; however, their effect can be minimised by fully occupying the inner coordination sphere of the Ln(III) ion with ligand donors, utilising polydentate ligands or macrocyclic ligands.

Macrocyclic ligands are particularly advantageous for coordinating lanthanide ions as they form kinetically stable complexes and provide a large number of donor atoms to fulfil the high coordination requirement of the Ln(III) ion.[234] Macrocyclic derivatives such as cyclen and calixarenes which contain a pre-organised cavity, have been used to encapsulate the Ln(III) ion and generate luminescent sensors as well as imaging agents.[235–238]

In another approach, a number of small acyclic ligands have been developed to promote Ln(III)-directed self-assembly through complex supramolecular systems.[220,239–241] It has been found that small bi- and tri-dentate structures can generate kinetically stable Ln(III) complexes which are in contrast to the macrocyclic ligands due to their dynamic and reversible nature. This approach has led to the formation of systems such as catenanes, rotaxanes,[242] half-helicates,[243] and bundles.[88] Both **dpa** and **btp** ligand motifs have been shown to be suitable ligands for such self-assembly with lanthanide ions and have shown effective sensitisation of the Ln(III) luminescence. In this Chapter the **tzpa** ligand antenna which combines both the **btp** and **dpa** ligand motifs, will be examined for the first time, as a potential sensitising antenna for Tb(III) and Eu(III). Formation of supramolecular self-assemblies with Eu(III) and Tb(III) can be monitored using a variety of techniques such as

NMR spectroscopy, HRMS and by monitoring the UV-visible absorbance and Ln(III)-luminescence *via* spectroscopic techniques. In previous chapters, only UV-visible absorption and ligand fluorescence spectra were used to monitor the self-assembly of **tzpa** ligands with *d*-metals; however, due to the unique photophysical properties of the lanthanide ions described above, time-gated fluorescence spectroscopy can also be used to monitor the self-assembly of these novel ligands with Ln(III) ions in solution.

4.1.1 Introduction of amino acids

As discussed above, the lanthanide ions are uniquely positioned to act as biological probes due to their long-lived excitation-states which enables them to be used for time-resolved detection. However, the solubility of lanthanide complexes in water is crucial to this application as the chemistry of biology is naturally dominated by aqueous systems.[244] While a range of **dpa**-lanthanide complexes and derivatives have been examined for their potential as biological sensors and imaging agents, the aqueous compatibility of **btp**-Ln(III) systems have been explored to a lesser extent. Examples also exist in which asymmetric binding sites have been utilised to generate lanthanide assemblies which are stable in water. Bünzli and co-workers have demonstrated the stability and photophysical properties of a homodinuclear triple stranded helicate in aqueous media with each terdentate binding pocket composed of a carboxamide, central pyridine and benzimidazole unit.[245] This N,N,O binding motif is comparable to the **tzpa** binding motif and it was thought that by grafting water soluble units onto this ligand motif, water soluble Ln(III) assemblies could be accessible.[219]

Previous work in the Gunnlaugsson group has focused on incorporating amino-acid residues into the **btp** ligand scaffold with a view to making this ligand antenna more biologically relevant.[177] The introduction of peptides to Ln(III) probes has been shown to facilitate their uptake into specific cells and the introduction of a single amino acid to the **btp** ligand was considered the first step towards generating biologically compatible **btp** derivatives.[246] Having incorporated the amino acid residues Ala, Gly, Phe and Trp into the **btp** motif to generate ligands **146-152**, the self-assembly of these novel ligands with Tb(III) and Eu(III) was examined and 1:3 metal:ligand complexes were generated. The photophysical properties of these tris complexes were evaluated and low quantum yields of $\Phi = 0.4 - 3.1$ % were observed for the amino acid bundles with Eu(III) while moderate values were observed with Tb(III) of $\Phi = 6.3 - 70$% in CH_3CN. This Tb(III) quantum yield was significantly higher than those previously observed for **dpa** ligands with Tb(III) under similar conditions. This is due to the energy of the triplet excited state of the ligand T_1 being

very close to the energy to the $^5D_4$ excited state of Tb(III), providing a highly efficient energy transfer to the Tb(III)-centre. Investigations to determine the stability of the Tb(III) and Eu(III) complexes of compounds **146-152** in aqueous media were conducted; however, dissociation of the assemblies occurred suggesting that the complexes were not stable in a competitive aqueous environment. It was hypothesised that the **tzpa** ligand, derivatised with amino acid residues, could retain a relatively high quantum yield for Tb(III) ions while possibly resisting dissociation in aqueous media. The design of the **tzpa** ligand allows for further functionalisation at the carboxylate site, providing the opportunity to introduce further water solubilising groups to the ligand motif if required.

With this in mind, preliminary ligands **179-182** were designed and synthesised, based on the **btp** ligands **146-152** and functionalised with a phenylalanine or tryptophan amino acid residue. The self-assembly of these ligands with Tb(III) and Eu(III) was investigated and the quantum yields of both Tb(III) and Eu(III) assemblies were determined. It was expected that 1:3 metal:ligand assemblies would be formed, in this case with ligands **179-182** and Tb(III) or Eu(III) ions, as was found to be the case with the ligands **146-152** which were previously studied. This was due to the high coordination number of the Tb(III) and Eu(III) ions and also previous work with both **btp** and **dpa** and their self-assembly with Ln(III) ions which has shown the favourable formation of tris-complexes.[245, 177, 246] Preliminarily investigations into the stability of these systems in aqueous media were also conducted. Finally, the self-assembly of ditopic **tzpa** ligand **H₂157** described in Chapters 2, along with its monotopic derivative **186** was investigated with Tb(III). It was anticipated that this ditopic ligand could form a circular helicate structure, in contrast with the *d*-metal assemblies formed and described in Chapters 2 and 3.
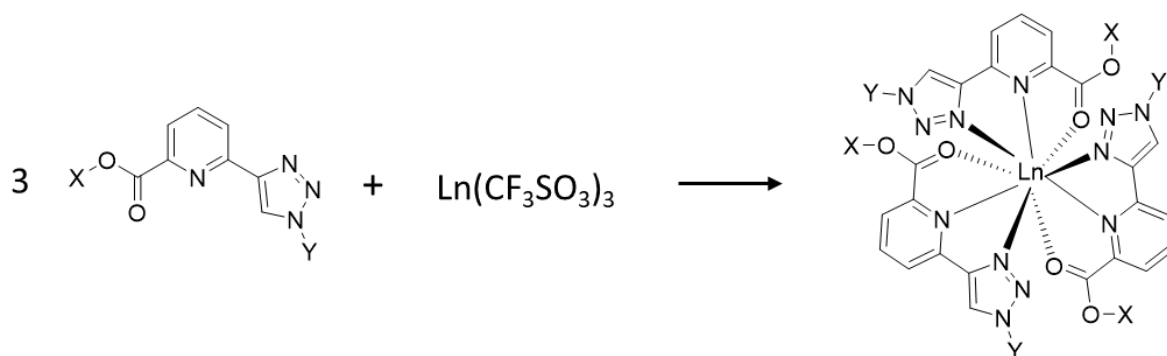
Scheme 4.1 *Schematic representation of possible tris-complex formed upon reaction of **tzpa** ligand derivative (3 equiv.) with Ln(CF₃SO₃)₃.*

4.2 Design and Synthesis of 179-182

Based on the **btp**-amino acid ligands **146-152** developed by Byrne and Gunnlaugsson, two amino acid functionalised **tzpa** ligands were designed and synthesised, as shown in Scheme 4.1. The methyl ester-protected ligands **179** and **180** were synthesised from commercially available starting materials in a four-step synthetic procedure. Methyl-6-bromopicolinate, **183** was synthesised from 6-bromopyridine-2-carboxylic acid in the presence of sulfuric acid and CH$_3$OH under reflux conditions. The resulting compound **183** was subject to Sonogashira coupling with ethynyltrimethylsilane in a THF/NEt$_3$ mixture using Pd(PPh$_3$)$_4$ as a catalyst and the crude compound **184** was isolated as a brown oil. Purification was possible with column chromatography to give **184** as a brown solid in 65% yield. 4-(bromomethyl)benzoic acid was then converted to the relevant azide using sodium azide and employed in a CuAAC reaction *in situ* with compound **184** to generate compound **185**. Compound **185** was isolated by washing with an EDTA solution in aqueous ammonia and upon protonation of the product with 1M HCl the pure product precipitated out as a white solid in 70% yield. Compound **185** was then reacted with L-phenylalanine methyl ester hydrochloride or L-tryptophan methyl ester hydrochloride in a peptide coupling reaction to
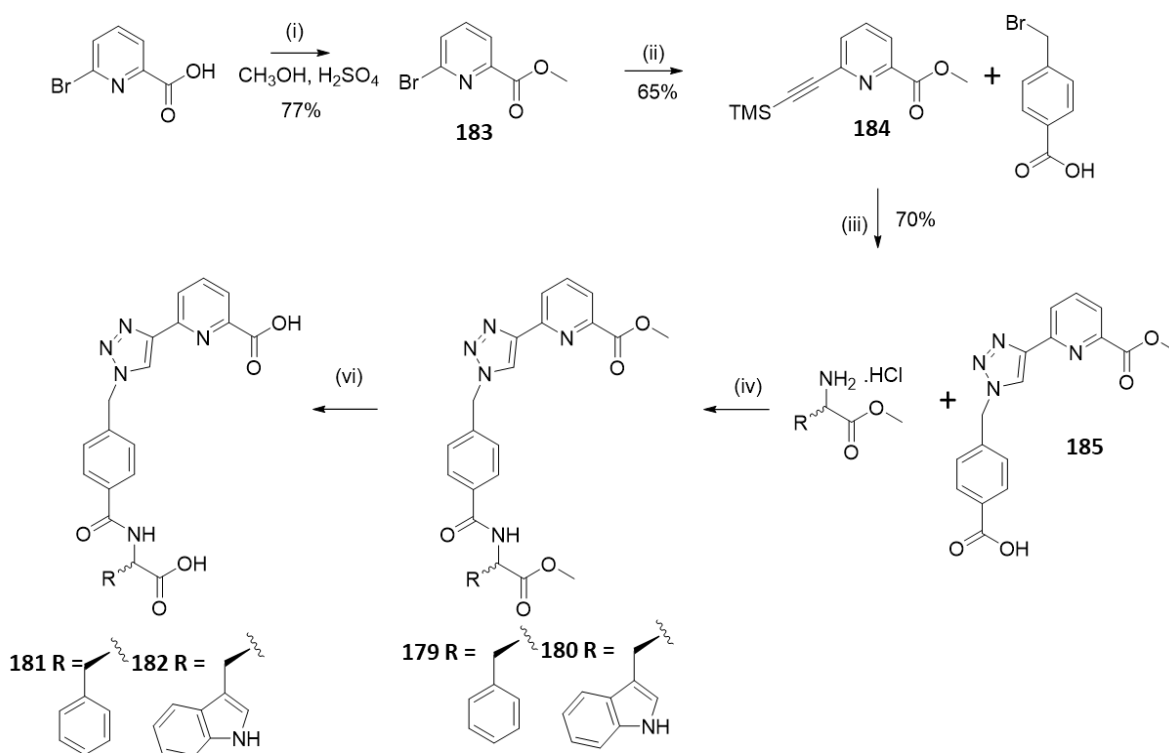
Scheme 4.2 *Structure and synthesis of compound **179** - **182**. Reagents and conditions: (i)CH$_3$OH, H$_2$SO$_4$, (ii) ethyynyltrimethylsilane, THF:NEt$_3$, Pd(PPh$_3$)$_4$, CuI (iii) NaN$_3$, CuSO$_4$·5H$_2$O, sodium ascorbate, K$_2$CO$_3$, DMF/H$_2$O (iv) **179** :hydroxybenzotriazole (HOBt), DMF/CH$_2$Cl$_2$, NEt$_3$, EDC.HCl. (vi) NaOH, 100 °C.*

generate compounds **179** and **180** as white solids in yields of 72% and 63% respectively. Finally, compounds **179** and **180** could be hydrolysed with 1M NaOH under reflux conditions overnight. Upon cooling and subsequent addition of 1M HCl, compounds **181** and **182** precipitated out of solution as pure white solids. All compounds were characterised by NMR spectroscopies, HRMS and IR spectroscopy and the ^{1}H NMR spectra of compounds **179** and **180** are shown below while the ^{13}C{^{1}H} NMR spectra are shown in the Appendix (Figure A4.1 & 4.2). The resonance corresponding to the pyridyl protons of both ligands reside at 8.26, 8.10 and 8.01 ppm while the triazole protons lie downfield at 8.81 ppm. The aromatic protons H_a and H_b resonate at 7.82 and 7.47 ppm as two doublets and the adjacent CH$_2$ protons are located at 5.75 ppm in both compounds. The multiplet upfield at 4.65 ppm corresponds to the proton H_c while the methyl protons associated with the pyridyl ring and the amino acid moiety lie at 3.91 and 3.62 ppm respectively. Finally, the protons at 3.1-3.2 ppm can be assigned to the CH$_2$ protons Hd. The phenylalanine residue generates resonances at 7.28 and 7.19 ppm which correspond to the phenyl ring of the appended amino acid,
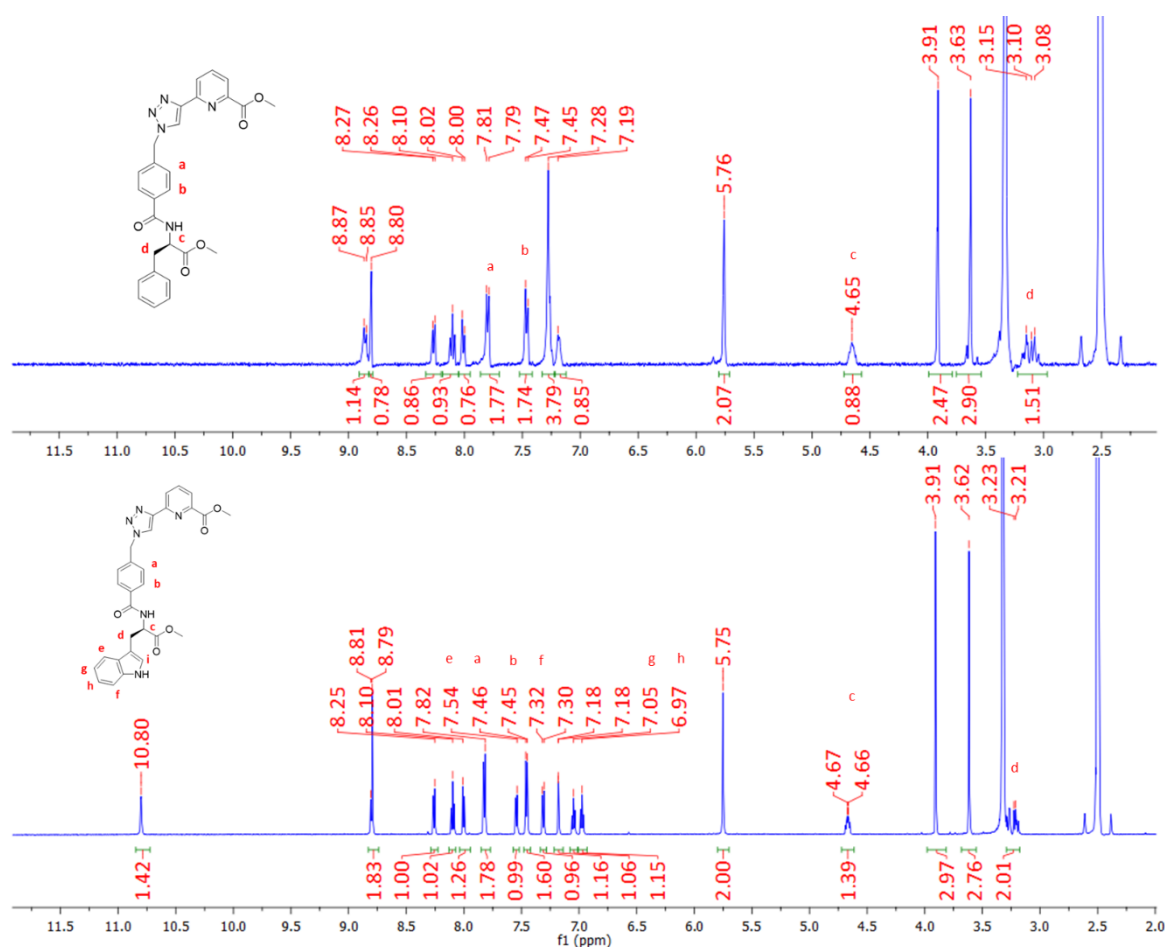
Figure 4.4 ^{1}H NMR spectra of (top) compound **179** and (bottom) **180** (600 MHz, DMSO-d$_6$).

137

integrating to five protons overall. In the case of compound **180** the doublet signals located at 7.54 and 7.31 ppm correspond to the tryptophan protons H_e and H_f while the triplets at 7.05 and 6.97 ppm can be assigned to protons H_g and H_h. The proton H_i resonates at 7.18 ppm and the amide proton of the tryptophan moiety is located downfield at 10.8 ppm. A crystal structure of compound **6** was also obtained and will be described in Section 4.3.

4.3 Crystal structure of 179

Single crystals of X-ray diffraction quality of compound **179** were obtained by evaporation of a solution of **179** from CH_3OH. Compound **179** was analysed in the monoclinic space group $P2_1$ and the asymmetric unit contains only one molecule of the ligand. This structure was solved by Dr. Chris Hawes. The ligand adopts a U-shaped conformation and the packing is dominated by hydrogen bonding interactions. Nitrogen atom N5 is observed to donate a hydrogen bond to the carbonyl oxygen O3 of an adjacent molecule with N5···O3 distance of 3.081(2) Å and NH···O angle of 163.13(12)˚. CH···N interactions are also observed between N1 and the CH_3 of an adjacent molecule with N1···C1 distance of 3.384(3) Å and CH···N angle of 125.43(13)˚. The triazole nitrogens are involved in CH···N interactions with N2···C12 distance of 3.387(4) Å. CH···O interactions between O1 and C20 at a distance of 3.389(3) and O1···C26 distance of 3.362(4) Å also contribute to the overall packing.
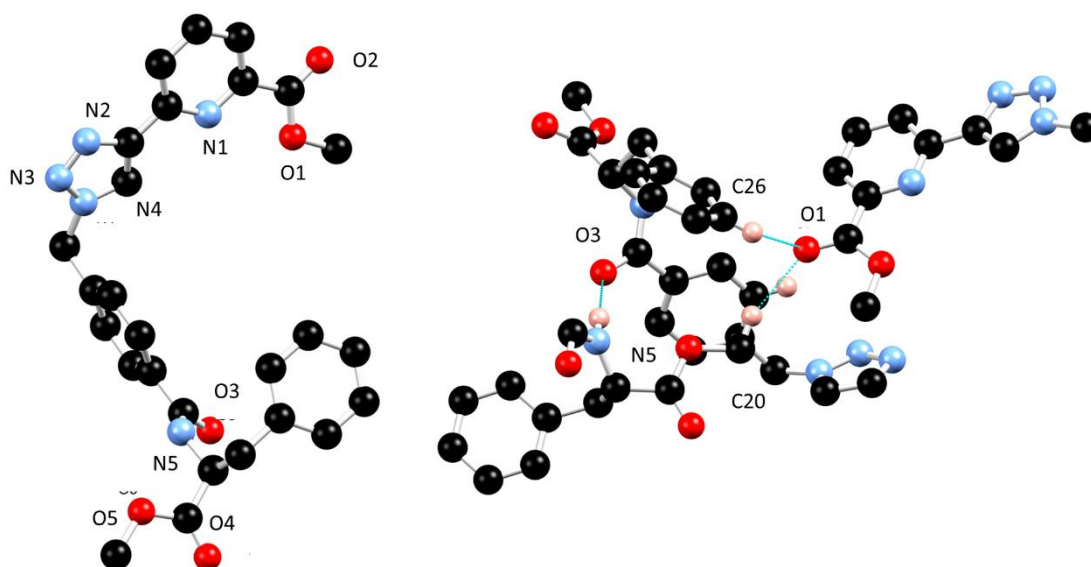
Figure 4.5 *(Left) Structure of one unique molecule of compound **179** with heteroatom labelling scheme. Selected hydrogen atoms are omitted for clarity. (Right) Primary modes of interaction between two molecules of **179**. Selected hydrogen atoms are omitted for clarity.*

4.4 Attempted formation of tris complexes [Tb(179)₃]³⁺, [Eu(179)₃]³⁺ and [Tb(180)₃]³⁺

Following the successful synthesis of compound **179** and **180**, attempts were made to form the tris complexes [Tb(**179**)₃]³⁺, [Eu(**179**)₃]³⁺, and [Tb(**180**)₃]³⁺ by reacting compounds **179** or **180** with Tb(III)/Eu(III) in a 3:1 ligand:metal stoichiometric ratio in CH₃OH. While the methyl ester protected ligands **179** and **180** were unlikely to generate water soluble lanthanide complexes, they were initially examined in order to draw direct comparison to the previously synthesised ligands **146-152** and the photophysical properties of their Tb(III) and Eu(III) complexes.

The complex, [Tb(**179**)₃]³⁺ was prepared by reacting 1 equivalent of Tb(CF₃SO₃)₃ with 3 equivalents of **179** in CH₃OH under microwave irradiation at 70 ˚C for 20 minutes. The resulting colourless solution was concentrated under reduced pressure and dropped slowly into a large excess of cold diethyl ether. The complex was then recovered by centrifugation from the diethyl ether supernatant solution and dried under high vacuum to generate the complex in 56% yield. Complex [Tb(**180**)₃]³⁺ was prepared using the same
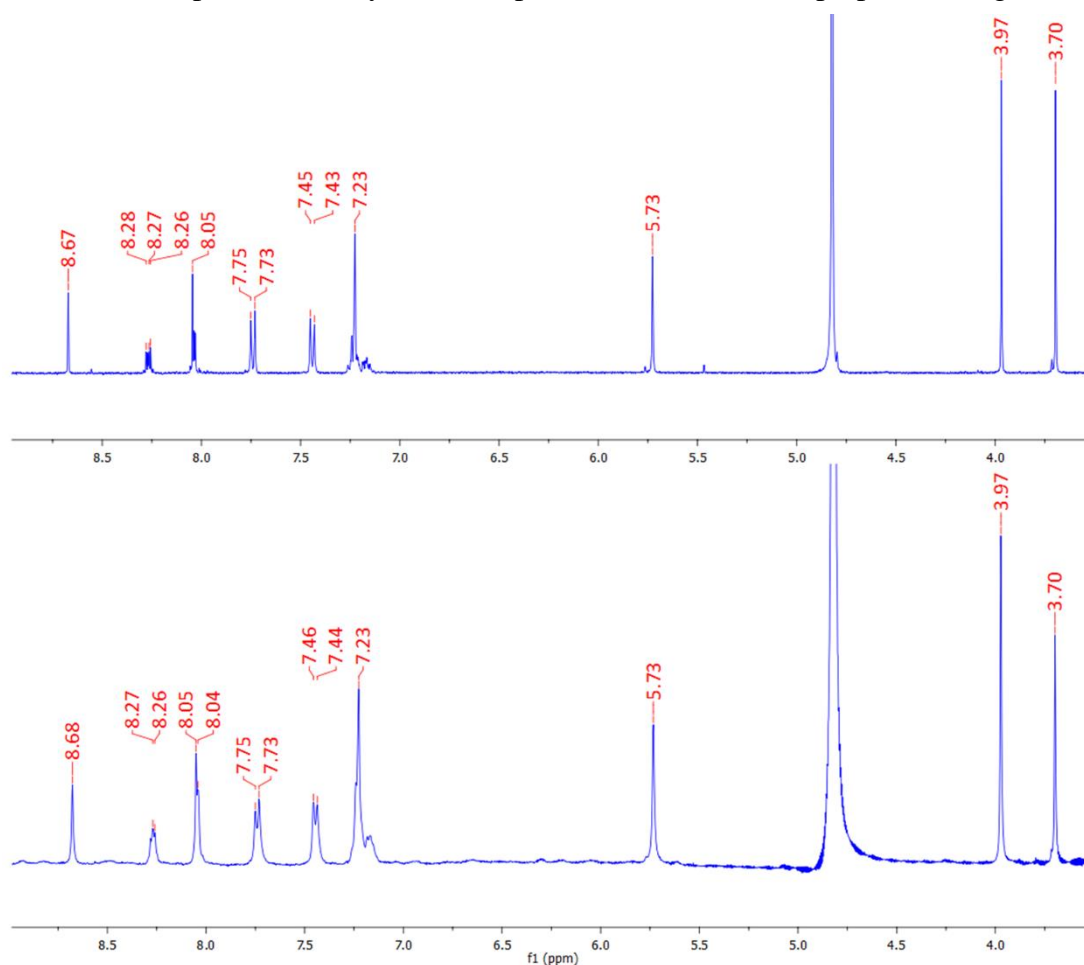
Figure 4.6 *¹H NMR spectra of (top)* ***179*** *and (bottom) [Tb(**179**)₃]³⁺ (400 MHz, CD₃CN).*
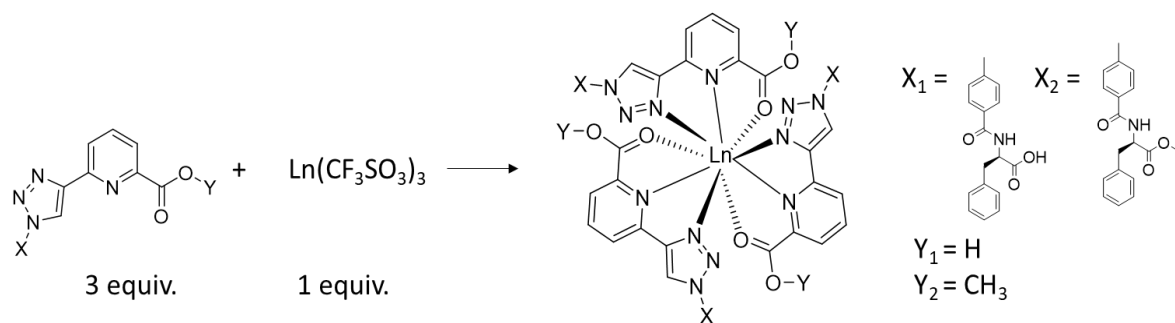
Scheme 4.3 *Schematic representation of possible tris-complex formation upon reaction of ligands 179 - 181 with Ln(CF₃SO₃)₃ showing one possible orientation around the metal centre where wrap Λ or Δ helical chiral complexes are possible.*

procedure and also yielded a while solid in 43% yield while compound $[Eu(\textbf{179})_3]^{3+}$ was prepared with $Eu(CF_3SO_3)_3$ under the same reaction conditions in 69% yield. Scheme 4.2 shows a schematic representation of the desired tris-complex formed from this reaction. Initial visual observations indicated successful Tb(III) complex formation with both the CH_3OH solution and the isolated solids appearing green emissive when irradiated with UV light ($\lambda_{em} = 254$ nm) while the Eu(III) complex was found to be red emissive. Attempts were made to obtain crystals of the Ln(III) complexes under various conditions, unfortunately none were successful. All complexes were characterised by ^1H NMR in CD_3OD and are shown in Figure 4.3 or in Appendix (Figure A4.5-4.6). Due to the paramagnetic nature of the Tb(IIII) ion, a broadening of the signals in $[Tb(\textbf{179})_3]^{3+}$ was observed, however, no significant chemical shift was seen in the ^1H NMR of the complex. This small chemical shift was also observed in previous work by Byrne for the lanthanide peptide bundles discussed in Section 4.1.1.[177] The $[Tb(\textbf{179})_2(CF_3SO_3)_2]^+$ complex was verified by MALDI HRMS but unfortunately no evidence of the $[Tb(\textbf{179})_3]^{3+}$ complex was found (Appendix Figure A4.8). Furthermore, evidence of $[Tb(\textbf{180})_3](CF_3SO_3)_3$ was not obtained by MALDI HRMS but $[Tb(\textbf{180})_2(CF_3SO_3)_2]^+$ was observed (Appendix Figure A4.10). While it is possible that dissociation of the complex occurred during mass analysis, it is also possible that the bis-complex $[Tb(\textbf{179})_2]^{2+}$ was formed despite the reaction stoichiometry used. There is a lack of evidence for the formation of a 1:3 metal:ligand complex in this case. It is unclear from these results, what metal:ligand stoichiometry exists and also if there is a sole product of the complexation or co-existence of multiple species. The IR spectra of the solid complexes were recorded and an increase in the stretching frequency of the carbonyl functional group was observed from 1637 to 1713 cm⁻¹ and a C-F stretch appearing at 1278 cm⁻¹ in the case of $[Tb(\textbf{179})_2]^{2+}$, further indicating the successful complexation of **179** with Tb(III). Similar

changes were observed in the IR spectra of compound **180** and [Tb(**180**)$_2$]$^{2+}$ as well as **179** and [Eu(**179**)$_2$]$^{2+}$.

4.5 Photophysical characterisation of complexes [Tb(179)$_2$]$^{2+}$, [Tb(180)$_2$]$^{2+}$ and [Eu(179)$_2$]$^{2+}$

The photophysical properties of [Tb(**179**)$_2$]$^{2+}$ and [Tb(**180**)$_2$]$^{2+}$ were evaluated in CH$_3$CN solution and are shown in Figure 4.7. The UV-visible absorption spectra of these complexes were dominated by two main absorption bands at $\lambda = 245$ nm and $\lambda = 293$ nm. These bands can be assigned to π-π* transitions in the ligand structure.

Excitation at $\lambda = 255$ nm gave rise to Tb(III)-centred luminescence from both complexes indicating effective population of the $^5D_4$ excited state of the Ln(III) ion and subsequent deactivation of the ^7F_J ($J = 6 - 2$) ground states with line-like emission bands appearing at 490 nm, 545 nm, 584 nm, 622 nm and 645 nm, the latter of which was very weak. The excitation spectra of [Tb(**179**)$_2$]$^{2+}$ and [Tb(**180**)$_2$]$^{2+}$ ($\lambda_{em} = 545$ nm) were also recorded in CH$_3$CN and displayed maximum intensity at approximately 260 nm with a second band located at $\lambda = 290$ nm, indicating successful sensitisation of the Tb(III)-centre by indirect excitation of the antenna moiety.

The [Eu(**179**)$_2$]$^{2+}$ complex was also evaluated in CH$_3$CN by UV-visible absorption and fluorescence spectroscopy. Again, the absorption spectrum was dominated by two main bands located at $\lambda = 250$ nm and $\lambda = 293$ nm. Examination of the fluorescence upon excitation of the complex at $\lambda = 255$ nm resulted in Eu(III)-centred emission resulting from energy transfer from the $^5D_0$ excited states to ^7F_J ($J = 0 - 4$) Eu(III) ground states and generating in line-like emission bands at $\lambda = 579, 590, 619, 650$ and 692 nm.
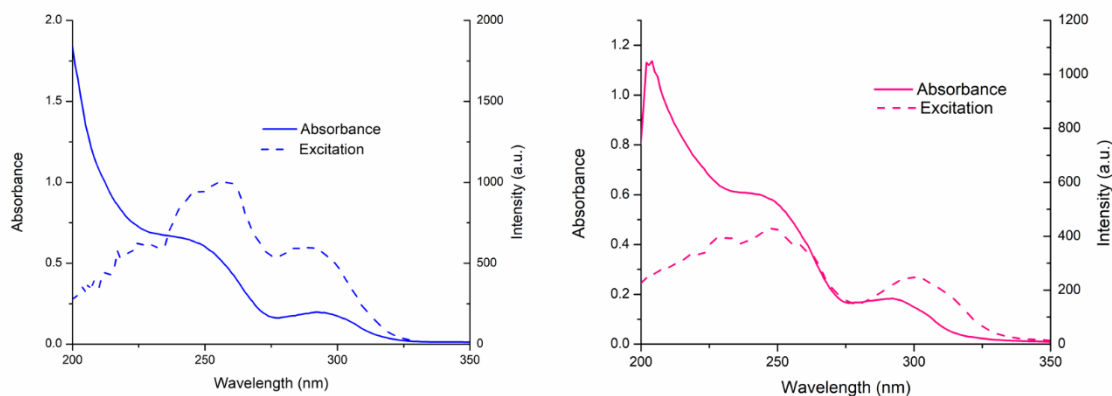
Figure 4.7 *(Left) UV-vis absorbance and excitation ($\lambda_{em} = 545$ nm) spectra of [Tb(**179**)$_2$]$^{2+}$ recorded in CH$_3$CN (2.7 × 10^{-5}M). (Right) UV-vis absorbance and excitation ($\lambda_{em} = 545$ nm) spectra of [Tb(**180**)$_2$]$^{2+}$ recorded in CH$_3$CN (2.5 × 10^{-5}M).*
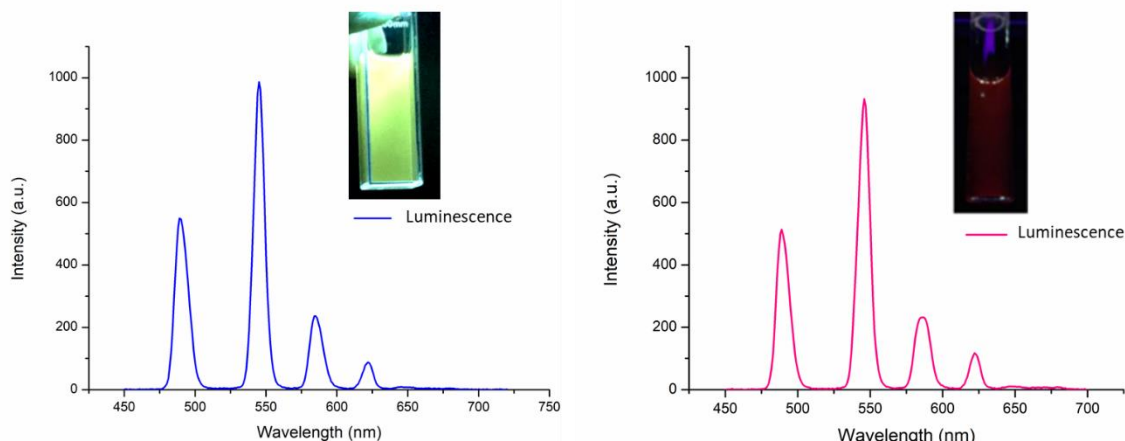
Figure 4.8 *Delayed luminescence spectra of (left) [Tb(**179**)$_2$]$^{2+}$(2.7 × 10^{-5}M) and (right) [Tb(**180**)$_2$]$^{2+}$ (2.5 × 10^{-5}M) recorded in CH$_3$CN showing characteristic Tb(III) transitions $^5D_4 \rightarrow {}^7F_{6,5,4,3,2}$.*

As the ligands **179** and **180** were functionalised with chiral amino acid residues Phe and Trp, attempts were made to obtain CD spectra of the complexes [Tb(**179**)$_2$]$^{2+}$ and [Tb(**179**)$_2$]$^{2+}$; however, no signal was observed in the CD spectrum. This is most likely as the chiral group is remote from the Ln(III) ion and therefore exerts little influence over the self-assembly process with Tb(III) or Eu(III). This was also the case for Tb(III) and Eu(III) complexes of ligands **152-156** previously reported by Byrne and Gunnlaugsson.[177] The CD spectra of the ligands **179** and **180** were very weak and poorly resolved.
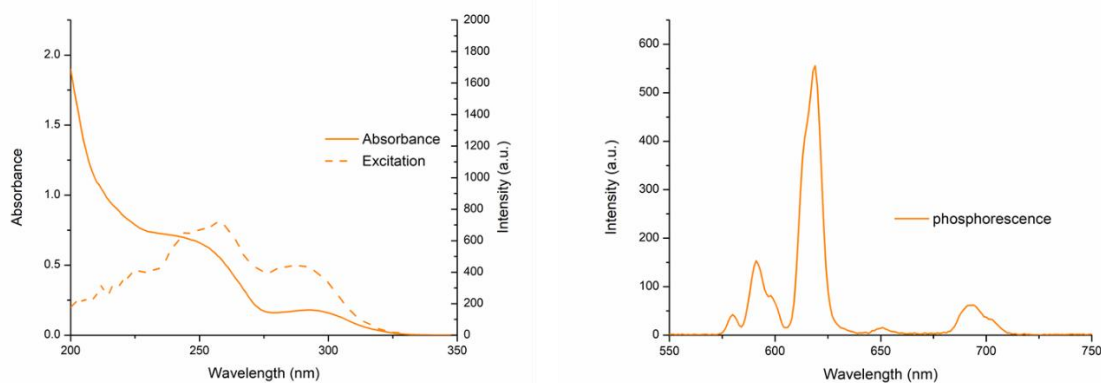
Figure 4.9 *(Left) UV-vis absorbance and excitation (λ = 545 nm) spectra of [Eu(**179**)$_3$]$^{3+}$ recorded in CH$_3$CN. (Right) Delayed luminescence spectra of (left) [Eu(**179**)$_3$]$^{3+}$ (2.9 × 10^{-5}M) showing characteristic Eu(III) transitions $^5D_0 \rightarrow {}^7F_{0,1,2,3,4.}$*

4.6 Luminescence emission lifetimes and Tb(III) hydration states

Luminescence life-time (τ_{obs}) measurements for the Tb(III)-centred emission were recorded for [Tb(**179**)$_2$]$^{2+}$ and [Tb(**180**)$_2$]$^{2+}$ in H$_2$O and D$_2$O in which the complexes were sparingly soluble. The luminescence decay at λ_{em} = 545 nm was measured at various gate times and

the average radiative lifetimes of the phosphorescence emission was calculated. The lifetimes of the $^5D_4$ excited state of Tb(III) were best fitted as a bi-exponential decay for [Tb(**179**)$_2$]$^{2+}$ and [Tb(**180**)$_2$]$^{2+}$ in H_2O and D_2O which indicates that there was more than one emissive species in solution. However, upon repetition of the experiment in CH_3OH and CD_3OD, in which the complexes were fully soluble, the lifetimes were best fit to a mono-exponential decay for [Tb(**179**)$_2$]$^{2+}$ and [Tb(**180**)$_2$]$^{2+}$ indicating that there was a single emissive species in solution. This result likely arises from the improved solubility of the complexes in methanolic solution which likely prevents dissociation of the complex, as occurs in aqueous solution.

From the fitted decay curves, the excited state lifetimes in H_2O and D_2O as well as CH_3OH and CD_3OD are shown in Table 4.1. From this data the hydration state, q, was also determined using Horrocks' equation

$$q^{Tb(III)} = A[(1/\tau_{H2O})-(1/\tau_{D2O})-0.06] \text{ \textbf{Equation 4.1}}$$
$$q^{Eu(III)} = A[(1/\tau_{H2O})-(1/\tau_{D2O})-0.25] \text{ \textbf{Equation 4.2}}$$

A represents the proportionality constant and is specific to Tb(III) systems, determined as 5 in H_2O and 10 in CH_3OH and 1.2 or 2.4 in H_2O or CH_3OH systems respectively for Eu(III). The q value determined for [Tb(**179**)$_2$]$^{2+}$ in an aqueous suspension was ~3 which indicates that three water molecules were bound to the Tb(III)-centre, suggesting the presence of an ML_2 species in the suspension. A second, shorter lifetime was also observed with a calculated q value of approximately 6 which indicates the presence of an ML species. Since the complex was not soluble in aqueous solution, the measurements were repeated in methanolic solution in which the complex was soluble. In this case the hydration state was determined to be approximately zero using Horrocks' equation with modification for methanolic solution. This suggests that the full coordination requirement of the Tb(III) was fulfilled by the ligand **179** under microwave irradiation. The hydration states obtained for [Tb(**179**)$_2$]$^{2+}$ were in agreement with those obtained for [Tb(**179**)$_2$]$^{2+}$ in H_2O with $q = 3$ and $q = 6$ and again in methanolic solution the hydration state was found to be zero. Finally, the hydration state of [Eu(**179**)$_3$]$^{3+}$ was determined to be approximately zero in methanolic solution. Lifetime spectra can be seen in the Appendix (Figures A4.19-4.22).

Table 4.1 *Luminescence lifetimes (τ) recorded from aqueous suspensions and methanolic solutions of $[Tb(179)_2]^{2+}$ and $[Tb(180)_2]^{2+}$ with q-values (hydration states) as determine by Horrocks' equation.*

Complex	$\tau(H_2O)$, ms	$\tau(D_2O)$, ms	$\tau(CH_3OH)$, ms	$\tau(CD_3OD)$, ms	Horrocks' q (± 0.5)
$[Tb(179)_2]^{2+}$			1.905	2.213	0.13
$[Tb(180)_2]^{2+}$			1.943	2.463	0.52
$[Tb(179)_2]^{2+}$ τ_1	0.401	0.751			5.53
$[Tb(179)_2]^{2+}$ τ_2	1.095	2.865			2.52
$[Tb(180)_2]^{2+}$ τ_1	0.376	0.749			6.32
$[Tb(180)_2]^{2+}$ τ_2	1.014	2.424			2.56
$[Tb(181)_2]^{2+}$	1.561	2.203			0.63
$[Tb(182)_2]^{2+}$	1.524	2.145			0.64
$[Eu(179)_2]^{2+}$			0.509	0.682	0.59

4.6.1 Quantum Yields

The photoluminescence quantum yield (Φ_{tot}, %) of each assembly was determined in CH_3CN using a relative method against $Cs_3[Tb(1)_3] \cdot 9H_2O$, a standard developed by Bünzli and co-workers.[78,79] This relative method for quantum yield determination is described in Equation 4.3:

$$\Phi_{REL}^{Tb,L} = \frac{\Phi_S}{\Phi_R} \times \frac{E_S}{E_R} \times \frac{A_R(\lambda R)}{A_S(\lambda S)} \times \frac{I_R(\lambda R)}{I_S(\lambda S)} \times \frac{n_S^2}{n_R^2} \qquad \textbf{Equation 4.3}$$

This equation represents the ratio of the total quantum yield of the sample (Φ_S) and the absolute quantum yield of the known standard (Φ_R) which should be distinguished from the intrinsic quantum yield of lanthanide-centred emission (Φ_{Ln}^{Ln}). This ratio is determined from the absorbance at 279 nm (A_s and A_R), the integration of the luminescence intensities (E_S and E_R), the intensity of the excitation of light (I_S and I_R) and finally the refractive indices of the solution (n_S and n_R). The standard solution of $Cs_3[Tb(1)_3]$ at 6.5×10^{-5} M in tris buffer (0.1 M) was reported to have a quantum yield of 22 ± 2.5 % and $Cs_3[Eu(1)_3]$ at 7.5×10^{-5} M is reported as 24 ± 2.5 % under excitation at 279 nm. The quantum yield was therefore found

to be 84.0(7)% for [Tb($\textbf{179}$)$_2$]$^{2+}$ while [Eu($\textbf{179}$)$_2$]$^{2+}$ has a quantum yield of 5.2(9)%. The quantum yield values for the complexes of compound $\textbf{180}$ were, however, lower than for those complexes of compound $\textbf{179}$ with [Tb($\textbf{180}$)$_2$]$^{2+}$ found to be 15.3(7)%. This is in line with the observation that the tryptophan (Trp) ligand $\textbf{180}$ appears to be a poor sensitizer for Tb(III) when compared to its phenylalanine (Phe) counterpart. This was also previously observed for the peptide bundles reported by Gunnlaugsson and Byrne.[177]

4.7 Examination of self-assembly of 179 with Tb(III) and Eu(III) *in situ*

The Tb(III) and Eu(III) directed self-assembly of $\textbf{179}$ with Tb(CF$_3$SO$_3$)$_3$ or Eu(CF$_3$SO$_3$)$_3$ *in situ* was investigated by a series of spectroscopic measurements. The previous Section 4.5 described the formation and characterisation of [Tb($\textbf{179}$)$_2$]$^{2+}$ and [Eu($\textbf{179}$)$_2$]$^{2+}$ complexes which were the thermodynamic products of a high-temperature synthesis. The self-assembly discussed in this section generates kinetically favourable assemblies under ambient conditions. These assemblies, as seen in previous Chapters, tend to be more dynamic and varied in stoichiometry. Specific aliquots of Tb(III) or Eu(III) solution were added to a solution of $\textbf{179}$ and the changes to the UV-visible absorption and luminescence spectra were monitored after each addition. Again, the experiments were carried out at a ligand concentration of 1×10^{-5} M and repeated three times to ensure reproducibility.

4.7.1 UV-visible absorption titration of 179 with Tb(III)

The UV-visible absorption titration was carried out in CH$_3$CN solution and the compound $\textbf{179}$ showed two main bands in the absorbance spectrum. A high energy band was centred at $\lambda = 245$ nm while a lower energy band was observed at $\lambda = 291$ nm ($\varepsilon = 24057$ cm^{-1} M^{-1} at $\lambda_{abs} = 242$ nm). Upon addition of Tb(III), the band centred at $\lambda = 245$ nm experienced a hypochromic shift and the appearance of a new band at $\lambda = 225$ nm was also observed. These changes reached a maximum at approximately 0.5 equivalents of Tb(III), after which no further significant changes occurred. The low energy band at $\lambda = 291$ nm was subject to a hyperchromic shift and concomitant redshift to $\lambda = 300$ nm upon addition of Tb(III). Again, these changes reached a plateau at the addition of 0.5 equivalents of Tb(III). Two isosbestic points were observed at $\lambda = 236$ nm and $\lambda = 290$ nm, indicating the presence of multiple correlated species in solution. The speciation in solution was elucidated by fitting the data using non-linear regression analysis and will be discussed in Section 4.7.2.
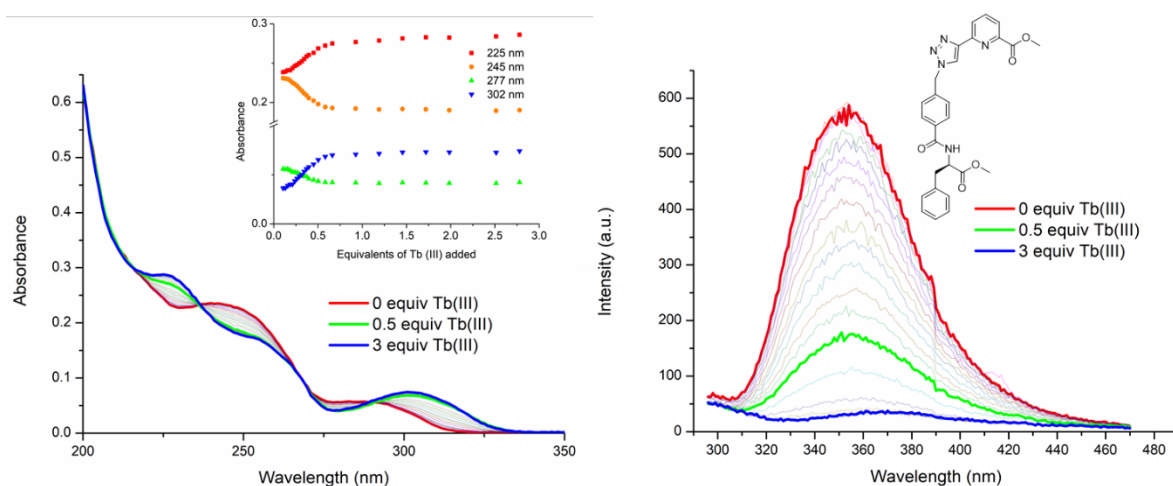
Figure 4.10 *The overall changes in the (left) UV-visible absorption spectra and (right) fluorescence emission spectra (excitation wavelength λ = 255 nm) upon titrating **179** (1×10⁻⁵ M) against Tb(CF₃SO₃)₃ (0→3 equiv.) in CH₃CN at RT.* **Inset:** *corresponding experimental binding isotherms of absorbance at λ = 225, 245, 277 and 300 nm.*

4.7.2 Tb(III)-centred luminescence titrations (emission and time-gated emission)

Upon excitation of ligand **179** at λ = 255 nm, the ligand centred emission was observed at λ = 353 nm and upon addition of Tb(III), the ligand fluorescence was affected by the self-assembly process. The ligand luminescence was gradually quenched upon addition of Tb(III) and a 70% reduction in the luminescence intensity was observed at 0.5 equivalents of metal, as shown in Figure 4.11. The ligand fluorescence was fully quenched by the addition of 0.7 equivalents of Tb(III). As before, this can be attributed to an energy transfer process from
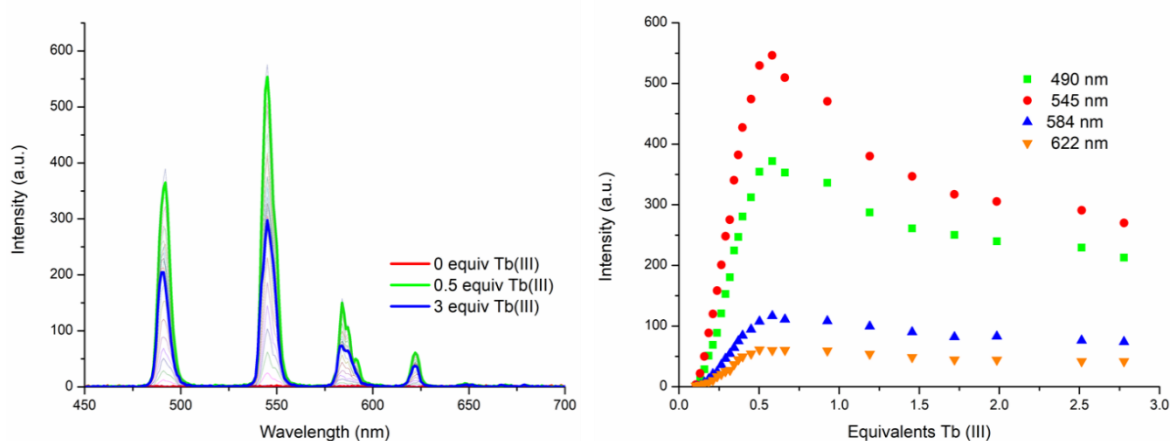
Figure 4.11 *(left) The overall changes to the Tb(III)-centred phosphorescence spectra upon titrating **179** (1×10⁻⁵ M) against Tb(CF₃SO₃)₃ (0→3 equiv.) in CH₃CN at RT. (right) corresponding experimental binding isotherms of phosphorescence at λ = 492, 545, 585 and 623 nm.*

146

the ligand **179** to the Tb(III) metal centre which gives rise to Tb(III)-centred emission, the evolution of which can also be seen during the titration.

The delayed Tb(III)-centred luminescence was also recorded upon excitation of **179** at λ = 255 nm. The spectra and binding isotherms can be seen in Figure 4.11 and show a gradual enhancement in the Tb(III)-centred emission upon addition of the metal solution with the appearance of characteristic Tb(III)-centred transitions at λ = 490, 545 584, 622, 648, 667 and 679 nm. These transitions correspond to deactivation from the $^5D_4$ excited states to the ^7F_J states (where $J = 6 - 0$). This gradual enhancement of the luminescence intensity was observed up to the addition of 0.5 equivalents of Tb(III) and subsequent additions of metal solution resulted in a quenching of the luminescence intensity. Therefore, the most emissive state in solution occurred at the 2:1 ligand:metal stoichiometry, and indicates the formation of a highly emissive 1:3 or 1:2 metal:ligand species in solution at 0.5 equivalents which dissociates into a less emissive species upon addition of excess Tb(III). As an ML species would be more susceptible to solvent quenching effects, its luminescence intensity would be lower. This data were fit using non-linear regression analysis and the speciation in solution was estimated and is discussed in Section 4.7.3.

4.7.3 Fitting of titration data for 179 and Tb(III)

The changes to the UV-visible absorption spectra were analysed using a global analysis method and the speciation in solution was estimated from this analysis as well as the stability constants of these species. Concentration profiles for each species in solution were established and this analysis was all completed with ReactLab EQUILIBRIA software.
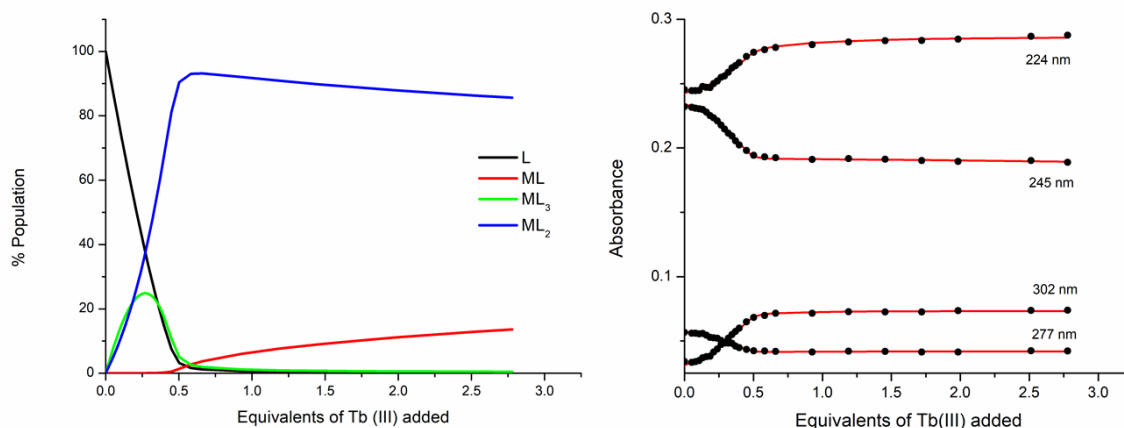
Figure 4.12 *(left) The speciation distribution diagram obtained from the fit of the UV-visible absorption titration data of ligand **179** against Tb(CF₃SO₃)₃ in CH₃CN. (right) the fit of the experimental binding isotherms using non-linear regression analysis software ReactLab.*

147

Analysis of the UV-visible absorption titration data for ligand **179** with $Tb(CF_3SO_3)_3$ pointed to the presence of four main species in solution. (**179**, 1:3 metal:ligand species, 1:2 metal:ligand species and 1:1 metal:ligand species) and the distribution of these species was estimated in the analysis (Figure 4.12). From 0 to 0.25 equivalents of Tb(III), both the 1:2 metal:ligand and 1:3 metal:ligand species co-exist in solution, both reaching approximately 25% abundance. Subsequent additions of Tb(III) resulted in a decrease in the abundance of the ML_3 species while the ML_2 species continued to increase, reaching 92% abundance at 0.5 equivalents of Tb(III). From 0.5 equivalents to 3 equivalents, the ML_2 was subject to gradual dissociation to the ML species due to the presence of excess metal ion in solution. While the ML_3 species is likely the most emissive species in solution due to the exclusion of solvent molecules from the inner coordination sphere of the Tb(III) ion, the ML_2 species is formed more favourably at this low concentration under kinetic control. The formation of the ML_2 species in greater abundance than the ML_3 species in solution is not as seen previously for the self-assembly of **btp** or **dpa** ligands with Ln(III) ions, however, it is not unexpected that this novel asymmetric ligand structure, **tzpa,** behaves differently to symmetrical ligands such as **btp** and **dpa**. Binding constants were estimated for each species from the changes in the UV-visible absorption spectra throughout the titration. The 1:2 metal:ligand species formed with $\log\beta_{12} = 14.4$ and the 1:3 metal:ligand species had a calculated binding constant of $\log\beta_{13} = 19.5$ while the ML species was estimated as $\log\beta_{11} = 6.3\pm0.1$. These values are in excellent agreement with those obtained from Phe-**btp** compound **149** with Tb(III) by Byrne previously.[177] The calculated and experimental binding isotherms are also shown in Figure 4.12 and are in good agreement. Unfortunately, while attempts were made to fit the luminescence titration data, this did not result in data convergence. This is likely due to the complex nature of the Tb(III) sensitisation which can be affected by more than just metal:ligand stoichiometry.

4.7.4 UV-visible absorption titration with Eu(III)

The UV-visible absorption titration of **179** with $Eu(CF_3SO_3)_3$ was also carried out. As before, the ligand **179** showed two main bands in the absorbance spectrum, one at $\lambda = 245$ nm and the second at $\lambda = 291$ nm. Upon addition of Eu(III), the high energy band centred at $\lambda = 245$ nm experienced a hypochromic shift and simultaneously, the appearance of a band at $\lambda = 228$ nm was observed as seen in Figure 4.13. These changes to the absorbance spectrum occurred up to the addition of 0.5 equivalents of Eu(III), after which the changes reached a
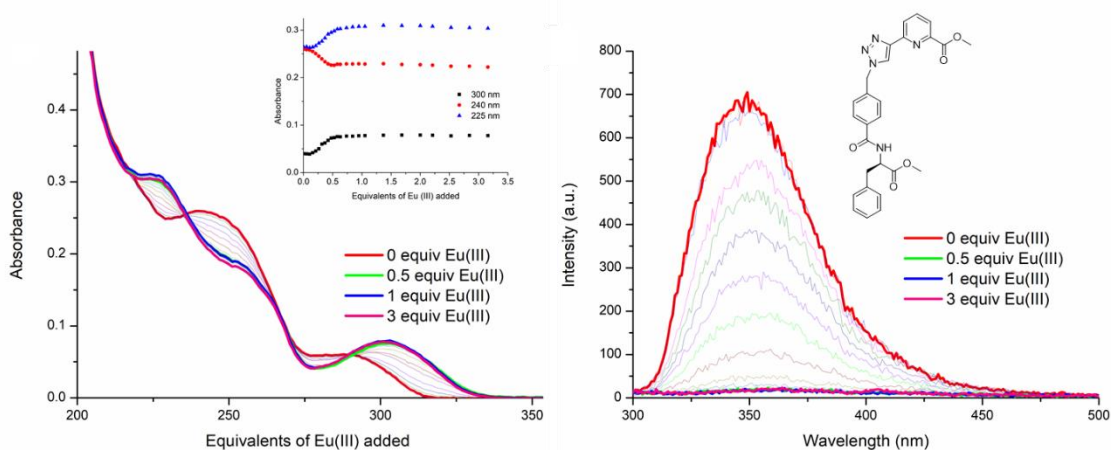
Figure 4.13 *The overall changes in the (left) UV-visible absorption spectra and (right) fluorescence emission spectra (excitation wavelength $\lambda = 255$ nm) upon titrating **179** (1×10^{-5} M) against $Eu(CF_3SO_3)_3$ ($0 \rightarrow 3$ equiv.) in CH_3CN at RT. **Inset**: corresponding experimental binding isotherms of absorbance at $\lambda = 240$ and 225 nm.*

plateau. The lower energy band at $\lambda = 291$ nm experienced a hyperchromic shift and simultaneous redshift to $\lambda = 300$ nm upon addition of Eu(III). These changes also occurred up to the addition of 0.5 equivalents of Eu(III), after which, no significant changes to the absorbance spectrum were observed. Two isosbestic points were also observed at $\lambda = 236$ nm and $\lambda = 290$ nm. These changes were very similar to those described for the self-assembly of compound **179** with Tb(III) and the speciation was determined using non-linear regression analysis as before. This will be discussed in Section 4.7.5.

4.7.5 Eu(III)-centred luminescence titrations (emission and time-gated emission)

Upon excitation of the ligand **179** at $\lambda = 255$ nm, again the ligand centred emission was observed at $\lambda = 353$ nm. Upon addition of Eu(III) this ligand luminescence was gradually quenched due to an energy transfer process from the ligand to the Eu(III) metal centre. This resulted in a complete quenching of the ligand fluorescence upon addition of 0.5 equivalents of Eu(III) (see Figure 4.14). This energy transfer process also resulted in the appearance of Eu(III)-centred emission which gradually increased in intensity over the course of the titration.

The delayed Eu(II)-centred luminescence was also recorded upon excitation of **179** at $\lambda = 255$ nm and the evolution of the characteristic Eu(III)-centred luminescence transitions at $\lambda = 580$, 595, 615, 650 and 695 nm were observed, which correspond to the characteristic Eu(III)-centred $^5D_0 \rightarrow {}^7F_{0,1,2,3,4}$ transitions. This gradual enhancement of the luminescence intensity was observed up to the addition of 0.4 equivalents as a result of sensitisation of the
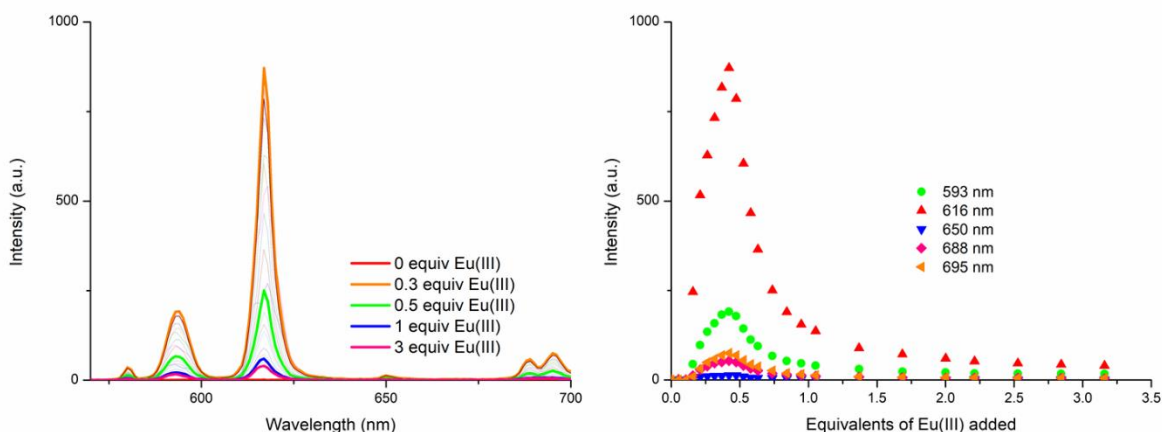
Figure 4.14 *(left) The overall changes to the Eu(III)-centred phosphorescence spectra upon titrating* **179** *(1×10⁻⁵ M) against Eu(CF₃SO₃)₃ (0→3 equiv.) in CH₃CN at RT. (right) corresponding experimental binding isotherms of phosphorescence at λ = 593, 616, 650, 688 and 695 nm.*

Eu(III) emission by the coordinating ligands. Subsequent additions of metal solution resulted in a sharp decrease in the luminescence intensity, which was almost completely quenched after the addition of 1 equivalent of Eu(III). The most emissive state in solution was seen between 0.45 and 0.5 equivalents of Eu(III) which is consistent with the Tb(III) system above and is likely due to the existence of a higher stoichiometric species in solution such as ML_2 or ML_3. The addition of excess Eu(III) resulted in dissociation of this higher stoichiometric species, forming an ML species which is more susceptible to solvent quenching effects. The $^5D_0 \rightarrow {}^7F_0$ transition is not often observed due to its strictly forbidden nature; however, it was observed in this system and indicates that the site symmetry is C_s, C_n, or C_nv. It is interesting to note that the transition occurs for intermediate low symmetry **dpa** complexes such as [Eu(**1**)]⁺ and [Eu(**1**)₂]⁻ but not in the case of high symmetry **dpa** complexes such as $[Eu(H_2O)_9]^{3+}$ or [Eu(**1**)₃]³⁻. This suggests that the assembly in solution is not highly symmetric, allowing the $^5D_0$ transition to gain intensity.[118,247]

4.7.6 Fitting of titration data for 179 and Eu(III)

The changes to the UV-visible absorption spectra and Eu(III)-centred emission spectra were analysed as before using a global analysis method and the speciation as well as their respective stability constants were estimated from the analysis.

Analysis of the UV-visible absorption data pointed to the presence of three main species in solution, the ligand **179**, a 1:2 metal:ligand species and a 1:1 metal:ligand species. The distribution of the species was estimated from the analysis and from 0 to 0.5 equivalents
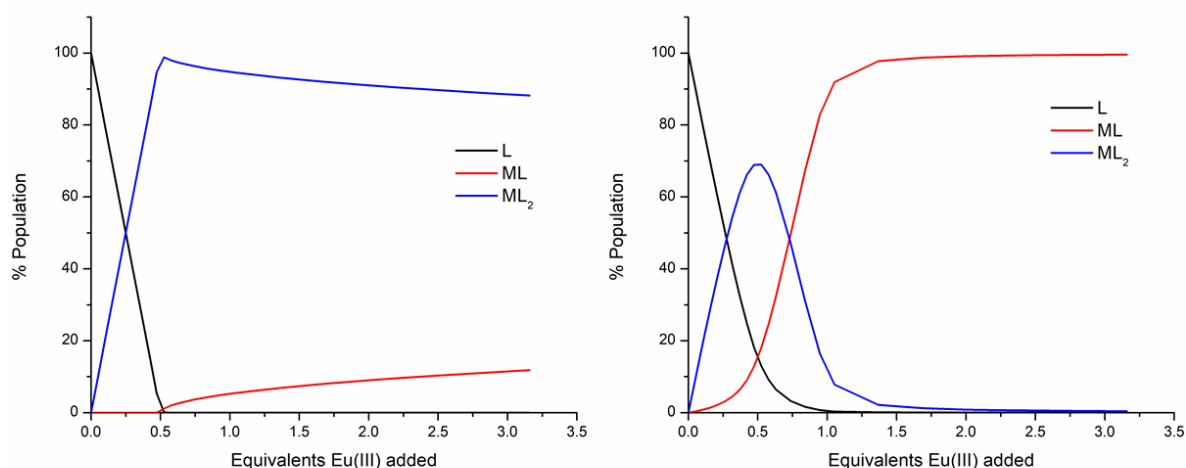
Figure 4.15 *The speciation distribution diagram obtained from (left) the fit of the UV-visible absorption titration data of ligand **179** against Eu(CF₃SO₃)₃ in CH₃CN and (right) the fit of the delayed luminescence titration data of ligand **179** against Eu(CF₃SO₃)₃ in CH₃CN.*

of Eu(III) (see Figure 4.15 for speciation distribution) the ML_2 species was most dominant in solution, reaching 97% abundance at 0.5 equivalents of Eu(III). Subsequent additions of the metal resulted in a slight dissociation of the ML_2 species to a less emissive ML species. While the ML_2 species does not fulfil the coordination requirement of the Eu(III) ion, this is in agreement with the speciation observed for the titration of **179** with Tb(III) also. While the formation of the fully saturated 1:3 metal:ligand species is not observed, this is not unexpected due to the asymmetric nature of the **tzpa** ligand and the labile nature of the interaction between the nitrogen atoms of the ligand and the Tb(III) centre. Binding constants were estimated from the global analysis of the UV-visible absorption data and the 1:2 metal:ligand assembly formed with $\log\beta_{12} = 18.5\pm2.6$ and the second species (1:1 metal:ligand) had a calculated binding constant of $\log\beta_{11} = 8.2\pm1.3$. However, as the error on these values was quite high this was not considered a reliable model. Instead, the time-gated luminescence data was analysed and the speciation was estimated from the analysis. Unfortunately, as the changes to the UV-visible absorption spectra are quite small over the course of the titration, this can cause the fitting of the data to be less accurate than if there were larger changes to the UV-visible absorption spectra observed.

Again, three species were determined to exist in solution, the ligand species **179**, an ML_2 species and an ML species as before. From 0 to 0.5 equivalents of Eu(III) the ML_2 species was most dominant, reaching 69% abundance at 0.5 equivalents of metal solution (see Figure 4.15). From 0.5 equivalents to 2 equivalents of Eu(III), the ML_2 species

151

decreased in abundance and this was accompanied by an increase in the ML species, which reached 100% abundance at 2 equivalents of Eu(III). The binding constants estimated from the analysis of the luminescence data were $\log\beta_{12} = 14.7\pm0.1$ for the ML_2 assembly and $\log\beta_{11} = 8.5\pm0.1$ for the ML species. These values are subject to a much smaller error and can be considered a more accurate representation of the speciation and stability constants for the species in solution.

4.8 UV-visible absorption titration of 180 with Tb(III)

Having examined the self-assembly of ligand **179** with both Tb(III) and Eu(III), the UV-visible absorption and luminescence titrations were carried out with **180** and Tb(III) under the same conditions. Compound **7** showed a sharp band in the absorbance spectrum at $\lambda = 220$ nm with a broad shoulder at $\lambda = 250$ nm. A lower energy band also appeared at $\lambda = 280$ nm with a shoulder at $\lambda = 290$ nm ($\varepsilon = 59442$ cm^{-1} M^{-1} at $\lambda_{abs} = 220$ nm). The bands at $\lambda = 220$ nm and $\lambda = 280$ nm were not observed in the absorbance spectrum of **179** and have previously been assigned to the tryptophan moiety and not the **tzpa** core.[248] Upon addition of Tb(III), the high energy band at $\lambda = 220$ nm experienced a hypochromic shift and concomitant redshift to $\lambda = 222$ nm as seen in Figure 4.16. These changes occurred up to the addition of 0.5 equivalents of the metal solution after which they reached a plateau. The lower energy band also experienced a hypochromic shift up to the addition of 0.5 equivalents and the appearance of a band at $\lambda = 300$ nm was also observed which is characteristic of
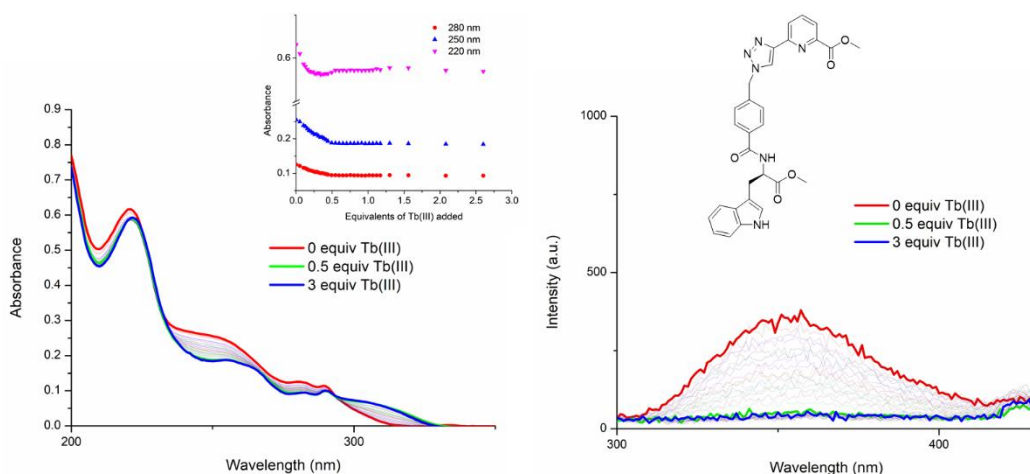
Figure 4.16 *The overall changes in the (left) UV-visible absorption spectra and (right) fluorescence emission spectra (excitation wavelength $\lambda = 230$ nm) upon titrating **180** (1×10^{-5} M) against Tb(CF$_3$SO$_3$)$_3$ ($0\rightarrow3$ equiv.) in CH$_3$CN at RT. **Inset**: corresponding experimental binding isotherms of absorbance at $\lambda = 220$, 250 and 280 nm.*

complexation of the metal to the terdentate binding motif. No further changes were observed upon subsequent additions of Tb(III). The speciation in solution was elucidated by fitting the data using non-linear regression analysis and will be discussed in Section 4.8.2.

4.8.1 Tb(III) centred luminescence titrations (emission and time-gated emission)

Upon excitation of the ligand at $\lambda = 230$ nm, the ligand centred emission was observed at $\lambda = 355$ nm. The intensity was very weak; however, it was apparent that the luminescence was affected by the self-assembly process as the luminescence was gradually quenched upon addition of Tb(III). The fluorescence was completely quenched upon addition of 0.5 equivalents of Tb(III). As the ligand fluorescence was quenched, the evolution of the Tb(III)-centred luminescence was also observed.

The delayed Tb(III)-centred luminescence was recorded upon excitation at $\lambda = 230$ nm and the spectra and binding isotherms can be seen in Figure 4.17. No significant enhancement of the Tb(III)-centred emission was observed up to the addition of 0.5 equivalents of metal solution. However, from 0.5 equivalents the luminescence increased dramatically and continued to increase beyond 5 equivalents of Tb(III) added. The appearance of characteristic transitions at $\lambda = 490, 545, 585, 622, 647, 667$ and 678 nm correspond to the deactivation from the $^5D_4$ excited states to the ^7F_J states of the Tb(III) ion where $J = 6 - 0$. This observation is unusual and suggests that at 1:3 and 1:2 metal:ligand stoichiometries the Tb(III) luminescence is quite weak, while upon addition of excess Tb(III) the Tb(III) luminescence is "switched on". Repeating the titration in degassed solvent or
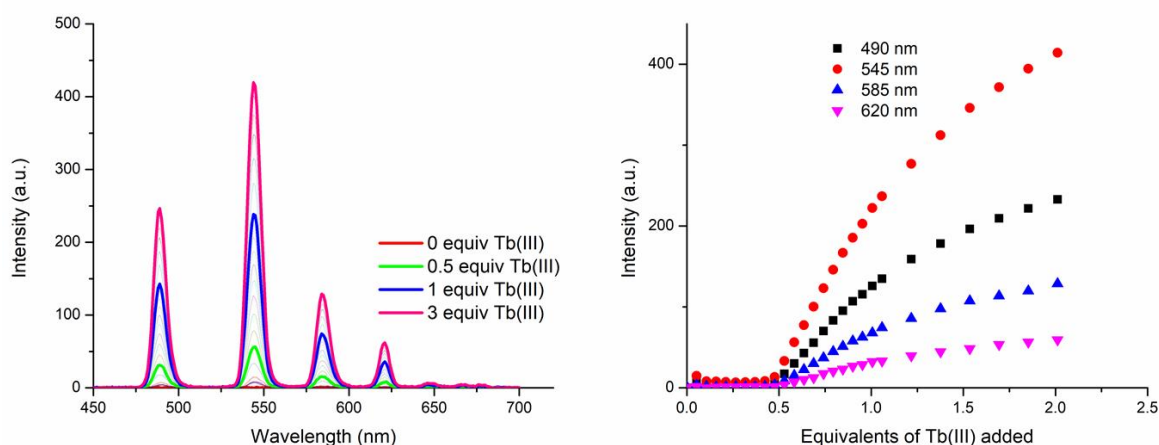
Figure 4.17 *(left) The overall changes to the Tb(III)-centred phosphorescence spectra upon titrating **180** (1×10^{-5} M) against Tb(CF$_3$SO$_3$)$_3$ ($0\rightarrow3$ equiv.) in CH$_3$CN at RT. (right) corresponding experimental binding isotherms of phosphorescence at $\lambda = 492, 545, 583$ and 620 nm.*

excitation at $\lambda = 250$ nm yielded similar results. Tryptophan has been shown to be an naturally-occurring "antenna" for Tb(III).[249,250] Therefore, is possible that excess Tb(III) coordinates the Trp residue from 0.5 equivalents of Tb(III) added and Tb(III) emission results.

4.8.2 Fitting of titration data for 180 and Tb(III)

The changes to the UV-visible absorption spectrum were analysed and the speciation in solution as well as the stability constants were estimated from the global analysis. The analysis pointed to the presence of four main species in solution (**180**, 1:3 metal:ligand species, 1:2 metal:ligand species and 1:1 metal:ligand species). The distribution of these species was also estimated from the analysis and indicates that from 0 to 0.5 equivalents of Tb(III), both the ML_2 and ML_3 species coexist in solution. However, the ML_3 species reaches a maximum abundance of 12% at 0.25 equivalents of Tb(III), while the ML_2 species is significantly more dominant at 94% abundance upon addition of 0.5 equivalents of Tb(III). Subsequent additions of Tb(III) resulted in a gradual dissociation of the ML_2 species into the less emissive ML species. Binding constants were estimated from the analysis and the ML_3 species was found to form with $\log\beta_{13} = 19.2\pm0.2$ while the ML_2 species had a calculated binding constant of $\log\beta_{12} = 14.6\pm0.2$ and finally, the ML species was calculated as $\log\beta_{11} = 6.6\pm0.1$. These values are in good agreement with those seen for compound **179** in Section 4.18, indicating the amino acid moiety does not have a large influence on the self-assembly in solution. These values were also close to the stability constants reported previously for a **btp** tryptophan ligand **151**.[177]
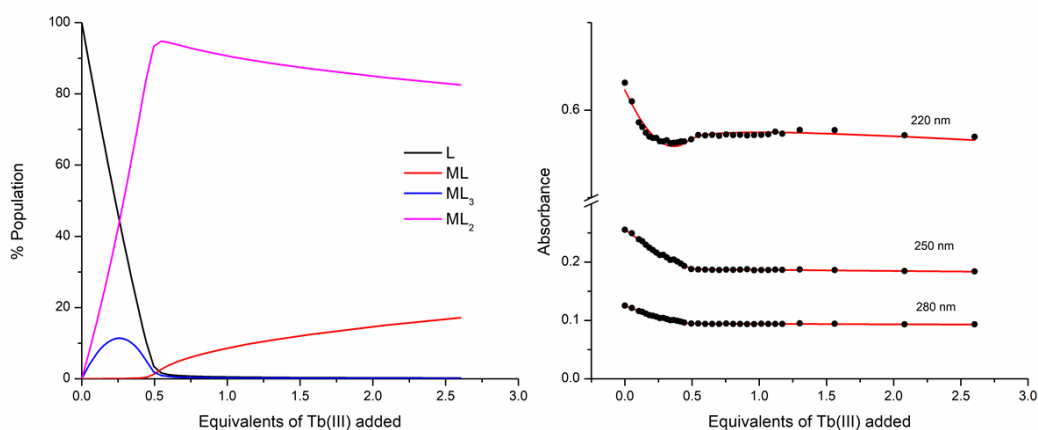
Figure 4.18 *The speciation distribution diagram obtained from (left) the fit of the UV-visible absorption titration data of ligand **180** against Tb(CF₃SO₃)₃ in CH₃CN and the fit of the experimental binding isotherms using non-linear regression analysis software ReactLab.*

It was not possible to fit the changes to the delayed luminescence spectra due to the poor luminescence intensity from 0 to 0.5 equivalents of Tb(III). However, the binding constants and speciation distribution obtained from the UV-visible absorption data are in good agreement with those observed for compound **179** above. This indicates that the ML_3 and ML_2 species, which are most often highly emissive in solution due to the minimisation of solvent quenching effects, are not significantly emissive in this Trp ligand system. However, upon addition of excess Tb(III), more emissive species were generated. Byrne and Gunnlaugsson reported that the **btp**-Trp ligand **151** was a poor sensitizer for both Tb(III) and Eu(III) when compared to other amino acid functionalised ligands and this could also be the case here. However, the tryptophan residue itself has been shown as a highly effective sensitizer for Tb(III).[29,251,252] It is possible, therefore, that at higher metal concentration the lanthanide ion interacts with the Trp residue itself, generating more emissive species in solution.

4.8.3 Titration of 182 in CH$_3$OH and ionic strength

Having determined that compound **180** was a poor sensitizer for Tb(III), the hydrolysed di-acid compound **182** was examined with Tb(CF$_3$SO$_3$)$_3$ in CH$_3$OH solution to determine if the di-acid would generate more emissive ML_2 and ML_3 species for applications in aqueous media. Initial studies suggested that compound **182** generated more emissive 1:3 and 1:2 species in solution than was the case for compound **180**; however, analysis of the data using non-linear regression analysis did not result in data convergence. As self-assembly processes have been shown to be dependent on the solvent and also the ions in solution, ionic strength was introduced into the system. Piguet an co-workers have previously shown that in lanthanide-directed self-assemblies, introducing tetrabutylammonium perchlorate to aprotic systems favours the formation of highly charged species.[253] So in order to gain a better understanding of the self-assembly process in CH$_3$OH, tetraethylammonium chloride (TEACl) ((C$_2$H$_5$)$_4$NCl, 0.05 M) was added to the CH$_3$OH solution and the titration was repeated under the same conditions.

The changes to the UV-visible absorption spectrum were much less significant than those observed for compound **180** in CH$_3$CN solution, however both bands at $\lambda = 220$ nm and $\lambda = 250$ nm experienced a hypochromic shift up to the addition of 0.5 equivalents of Tb(III), after which a plateau was reached. The band centred at $\lambda = 283$ nm was replaced by
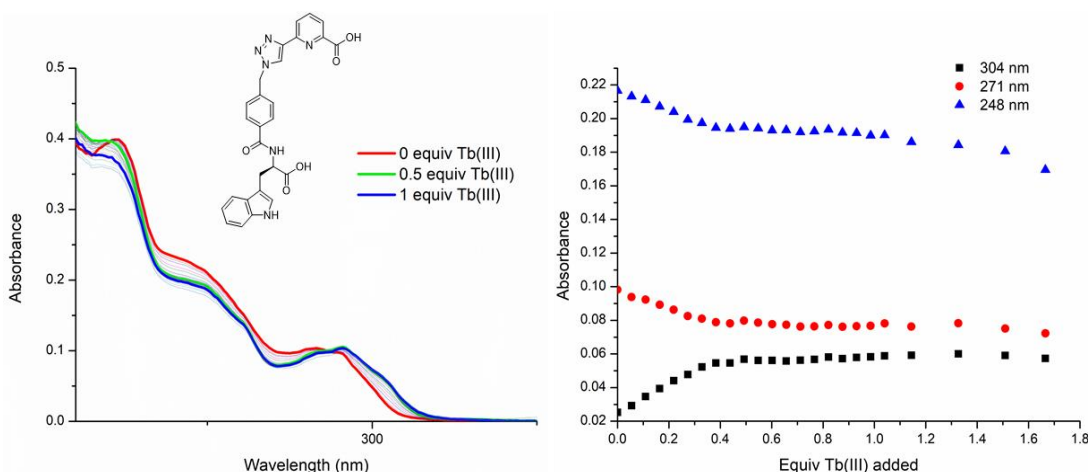
Figure 4.19 *The overall changes in the (left) UV-visible absorption spectra and (right) corresponding experimental binding isotherms of absorbance at λ = 304, 271 and 248 nm upon titrating **182** (1×10^{-5} M) against $Tb(CF_3SO_3)_3$ (0→3 equiv.) in CH_3OH at RT.*

a new band at λ = 291 nm. Again these changes occurred up to the addition of 0.5 equivalents of Tb(III). (ε = 22800 cm^{-1} M^{-1} at $λ_{abs}$ = 244 nm).

Excitation of the ligand at λ = 250 nm resulted in very weak ligand fluorescence, however, upon addition of Tb(III) the evolution of the lanthanide centred luminescence was observed. The luminescence increased in intensity up to the addition of 0.4 – 0.6 equivalents of Tb(III), after which a quenching of the luminescence occurred. The luminescence intensity between 0 and 0.5 equivalents of Tb(III) was significantly higher for compound **182** than seen for compound **180** in Section 4.8.1 above. This suggests that the sensitisation efficiency is greatly improved in the case of the di-acid in CH_3OH solution. Therefore, this
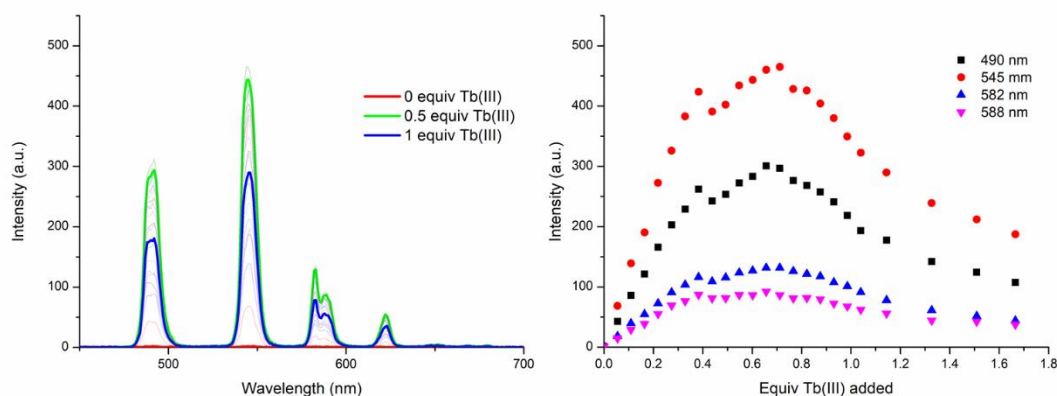
Figure 4.20 *(left) The overall changes to the Tb(III)-centred phosphorescence spectra upon titrating **182** (1×10^{-5} M) against $Tb(CF_3SO_3)_3$ (0→3 equiv.) in CH_3OH (TEACl, 0.05 M) at RT. (right) corresponding experimental binding isotherms of phosphorescence at λ = 490, 545, 582 and 588 nm.*

system may still be suitable for exploiting TRD for the generation of emissive Tb(III) complexes in aqueous solution.

4.8.4 Fitting of data

The changes to the UV-visible absorption spectrum were analysed using ReactLab software but unfortunately due to the small nature of the changes in the UV-visible absorption spectra, the data could be fit to multiple species and no one fit could be determined to be more accurate than the others.

4.9 Stability of [Tb(181)$_2$]$^{2+}$ and Tb[(182)$_2$]$^{2+}$ in aqueous media

In order to determine the stability of complexes [Tb(181)$_2$]$^{2+}$ and [Tb(182)$_2$]$^{2+}$ in aqueous media, 1:2 metal:ligand complexes of **181** or **182** with Tb(CF$_3$SO$_3$)$_3$ were prepared in CH$_3$OH and isolated as described in Section 4.4. The q values obtained in methanolic solution indicate the presence of only one emissive species in solution in each case ([Tb(181)$_2$]$^{2+}$ or [Tb(182)$_2$]$^{2+}$). Each complex was dissolved in CH$_3$CN solution and their stability over 24 hours was monitored by UV-visible and fluorescence spectroscopy. No changes to the spectra were observed over the duration. Luminescence lifetime measurements fit a monoexponential decay indicating the presence of only one species in solution.

Addition of aliquots of H$_2$O to the solution of [Tb(181)$_2$]$^{2+}$ in CH$_3$CN resulted in change to the UV-visible absorption spectrum of the complex with each addition. The absorbance band centred at $\lambda = 302$ nm experienced a hypochromic shift along with a
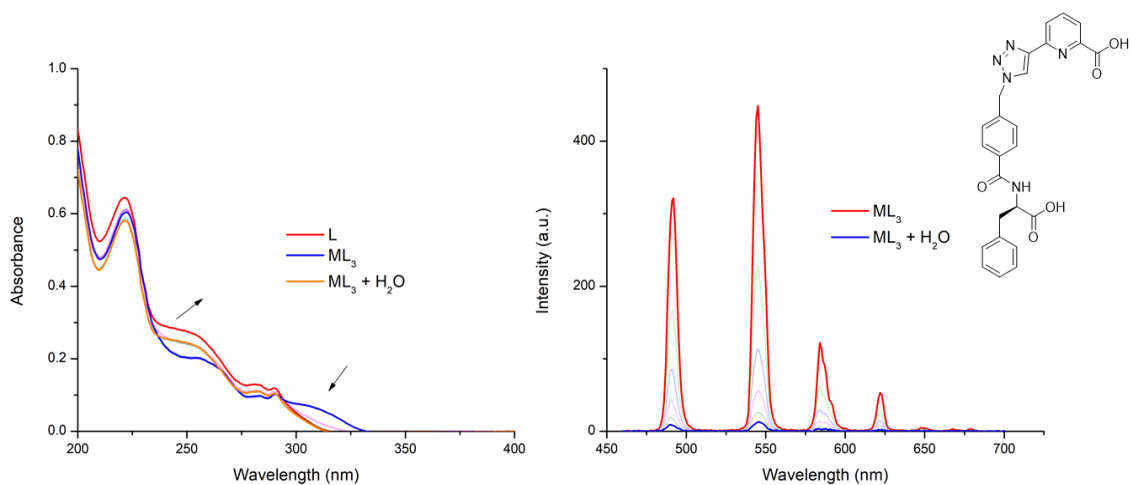
Figure 4.21 *(Left) Absorbance spectra of ligand **181** and [Tb(**181**)$_2$]$^{2+}$ upon addition of H$_2$O showing dissociation of the bis complex. (Right) Time-delayed luminescence spectrum of [Tb(**181**)$_2$]^2 showing decrease in luminescence intensity upon addition of H$_2$O due to dissociation of the bis complex.*

blueshift to 286 nm. The band at λ = 227 nm decreased in intensity while a band characteristic of the free ligand species **181** at λ = 244 nm appeared (see Figure 4.21). Overall the changes in the UV-visible absorption spectrum of $[Tb(\textbf{181})_3]^{3+}$ resulted in a return to the absorbance profile of the free ligand, indicating dissociation of the assembly. The luminescence intensity was also gradually quenched upon addition of H_2O which further indicates the lack of stability of the assembly in a competitive aqueous media. This dissociation was also observed for complex $[Tb(\textbf{182})_3]^{3+}$ and is shown in the Appendix (Figure A4.11). This suggests that these compounds would be unsuitable to act as biological probes due to their instability in a competitive solvent. An alternative strategy is explored in Chapter 5 in order to overcome these challenges.

4.10 Design and synthesis of monotopic ligand 186

Self-assembly studies of ligands **179** and **180** with Tb(III) indicate that the most dominant species in solution was the 1:2 metal:ligand species and not a 1:3 metal:ligand species which would exclude water from the coordination sphere, leading to increased emission intensity and fulfil the coordination requirement of the Tb(III) ion. It was hypothesised that this effect could be caused by steric hinderance, preventing a high yield of the ML_3 species. In order to investigate this possibility, ligand **186** was designed and synthesised. This ligand was expected to be more soluble in organic solvents while also acting as a monotopic derivative of ligands **H₂157** and **162** described in Chapters 2 and 3 whose self-assembly with Tb(III) will be described in Section 4.13 and 4.14. As compound **186** contains no amino acid residue, it was hypothesised that any steric effects which could prevent the formation of the 1:3 metal:ligand species in solution would be eliminated.

Compound **186** was synthesised in a three-step procedure from commercially available starting materials. 6-Bromopyridine-2-carboxylic acid was reacted with benzylamine in a peptide coupling reaction to generate compound **187** in a moderate yield. Compound **187** was subject to Sonogashira coupling using Ph(PPh₃)₄ as a catalyst in a THF:NEt₃ mixture to yield a brown oil which was purified by column chromatography to yield the pure product in 72% yield. Following characterisation by ^1H and $^{13}C\{^1H\}$ NMR spectroscopies as well as IR spectroscopy and HRMS the product was subject to a click reaction in which benzylbromide was converted to the relevant azide *in situ* and reacted with TMS protected alkyne compound **188** in the presence of CuSO₄.5H₂O, K₂CO₃ and sodium ascorbate. The desired product was dissolved in CH_2Cl_2 and isolated by washing with an
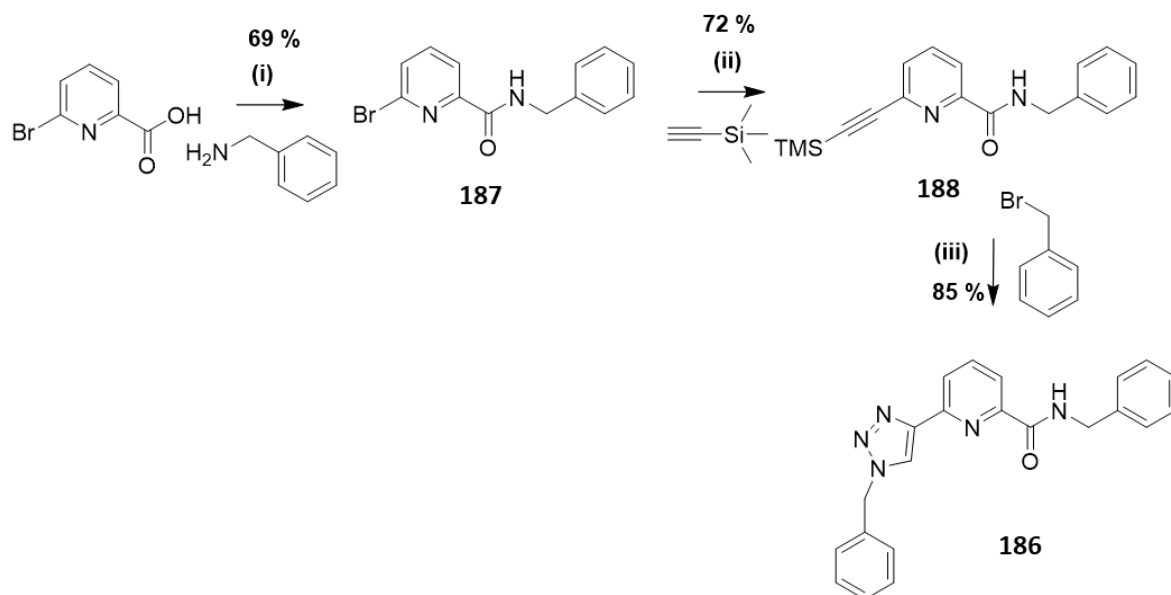
Scheme 4.4 *Synthesis and structure of **186**. Reagents and conditions: (i) hydroxybenzotriazole (HOBt), EDCI, DMF:CH₂Cl₂, NEt₃ (ii) CuI, Pd(PPh₃)₄, DMF:NEt₃ (iii) CuSO₄.5H₂O, K₂CO₃, sodium ascorbate, DMF:H₂O.*

EDTA solution in aqueous ammonia and 1M HCl followed by saturated NaHCO₃ and dried under reduced pressure to yield a colourless oil in 85% yield. The final product was fully characterised by ¹H NMR (600 MHz, DMSO-d_6) and is shown in Figure 4.23.

The resonances corresponding to the triazole proton resides downfield at 8.98 ppm and the three pyridyl protons also occur downfield at 8.21, 8.09 and 7.98 ppm. The phenyl protons of both "arms" of the ligand occur as a multiplet from 7.39 to 7.23 ppm integrating to 10 protons. The signal at 5.73 ppm corresponds to the CH₂ protons nearest to the triazole
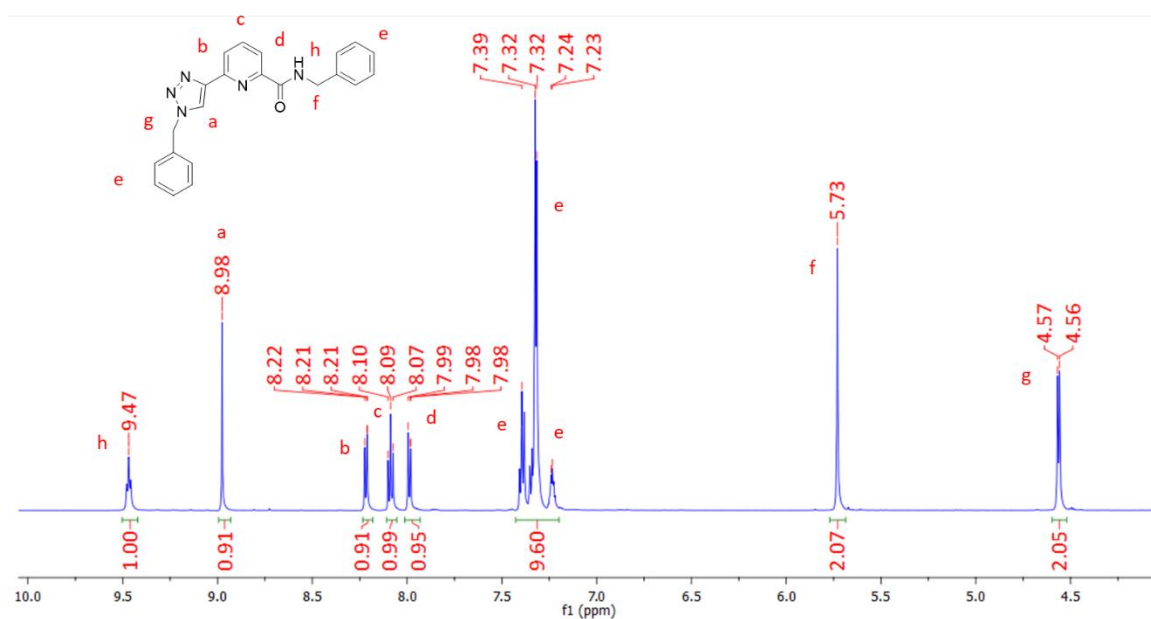
Figure 4.23 *¹H NMR spectrum of **186** (400 MHz, DMSO-d₆).*

159

ring while the CH$_2$ protons adjacent to the amide are located further upfield at 4.57 ppm. Finally, the amide proton is found at 9.47 ppm. [13] C NMR, HRMS and IR spectroscopy were also employed to verify the structure of the final compound.

4.11 Examination of self-assembly of 186 with Tb(III) in solution

The Tb(III)-directed self-assembly of **186** with Tb(CF$_3$SO$_3$)$_3$ *in situ* was investigated by monitoring changes to the UV-visible absorption and luminescence spectra of **186** upon addition of Tb(III). The titrations were again carried out at a ligand concentration of 1×10^{-5} M in CH$_3$CN.

4.11.1 UV-visible absorption titration

In order to monitor the ground state spectroscopic changes, the UV-visible absorption spectra were recorded upon addition of aliquots of Tb(III) to **186**. The UV-visible absorption spectrum of **186** in CH$_3$CN displayed two main bands, a high energy band at λ = 250 nm and a lower energy band located at λ = 290 nm (ε = 17700 cm^{-1} M^{-1} at λ_{abs} = 250 nm).. Significant changes were observed to both of these bands upon addition of Tb(III). The band at λ = 250 nm decreased in absorbance and was significantly broadened up to the addition of 0.5 equivalents of Tb(III) while the lower energy band at λ = 290 nm experienced a hyperchromic shift and concomitant redshift up to 0.5 equivalents of Tb(III). Subsequent additions of the metal solution did not result in any other significant changes to the absorbance profile, suggesting the presence of a 2:1 metal:ligand species in solution which
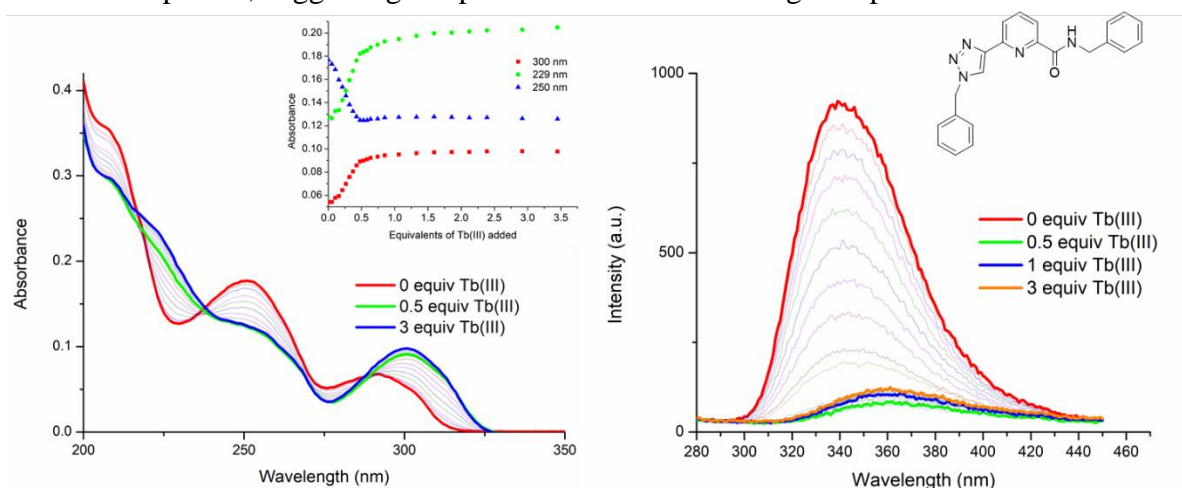
Figure 4.24 *The overall changes in the (left) UV-visible absorption spectra and (right) fluorescence emission spectra (excitation wavelength λ = 250 nm) upon titrating **186** (1×10^{-5} M) against Tb(CF$_3$SO$_3$)$_3$ (0→3 equiv.) in CH$_3$CN at RT. **Inset**: corresponding experimental binding isotherms of absorbance at λ = 300, 230 and 250 nm.*

was stable to the presence of excess Tb(III). Three isosbestic points at $\lambda = 288$, 236 and 217 nm indicate the presence of multiple correlated species in the solution. The speciation was estimated, and stability constants calculated by fitting the data using non-linear regression analysis and will be discussed in Section 4.11.3.

4.11.2 Tb(III)-centred luminescence titrations (emission and time-gated emission)

Upon excitation of the ligand **186** at $\lambda = 250$ nm, ligand centred emission was observed at $\lambda = 340$ nm. This fluorescence was significantly quenched upon addition of Tb(III), indicating that it is affected by the self-assembly of **186** with Tb(CF$_3$SO$_3$)$_3$. A reduction of 91% in the luminescence was observed at 0.5 equivalents of Tb(III) and this can be attributed to the energy transfer process from the ligand "antenna" to the Tb(III) metal centre *via* indirect excitation. This gives rise to characteristic Tb(III)-centred luminescence bands which can be seen both in the fluorescence and the delayed luminescence spectra.

The delayed Tb(III)-luminescence was measured upon excitation at $\lambda = 250$ nm. A large enhancement in the intensity of the luminescence was observed between 0 and 0.5 equivalents of metal solution added. The characteristic Tb(III) emission bands at $\lambda = 490$, 545, 585 and 622 nm as well as significantly weaker bands at 650, 669 and 680 nm were observed due to the "switching on" of the lanthanide luminescence. Subsequent additions of Tb(III) resulted in a gradual reduction in the luminescence intensity which reached a plateau at approximately 2 equivalents of Tb(III). This suggests the formation of a 1:2 metal:ligand species in solution at 0.5 equivalents of Tb(III) which dissociates slowly upon addition of
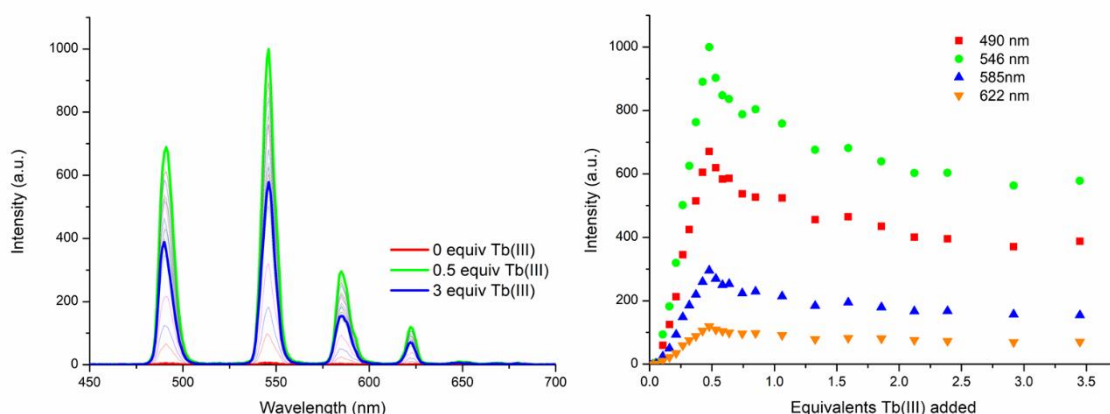
Figure 4.25 *(left) The overall changes to the Tb(III)-centred phosphorescence spectra upon titrating **186** (1×10^{-5} M) against Tb(CF$_3$SO$_3$)$_3$ (0→3 equiv.) in CH$_3$CN at RT. (right) corresponding experimental binding isotherms of phosphorescence at $\lambda = 492$, 545, 585, 623, 650, 669 and 680 nm.*

excess Tb(III) to the system to generate a less emissive species such as a 1:1 metal:ligand species.

4.11.3 Fitting of titration data for 186 and Tb(III)

As shown above, global changes in both the UV-visible absorption and Tb(III)-centred luminescence data were fitted using non-linear regression analysis in order to estimate the speciation in solution as well as their respective stability constants.

Results from the fitting of the UV-visible absorption titration data point to the presence of three absorbing species in solution (**186**, 1:2 metal:ligand species and 1:1 metal:ligand species). As seen in Figure 4.26, it appears that the ML_2 species is most predominant between 0 and 0.5 equivalents of Tb(III), reaching an abundance of 90% at 0.5 equivalents. Subsequent additions of Tb(III) result in a decrease in the ML_2 species with a concomitant increase in the abundance of the less emissive ML species. This indicates that the ML_2 species is not significantly stable at low concentration in the presence of excess Tb(III). Stability constants were calculated and the 1:2 metal:ligand assembly formed with $log\beta_{12} = 13.4\pm0.1$ and the 1:1 metal:ligand species had a calculated binding constant of $log\beta_{11} = 6.5\pm0.1$. These binding constants are very similar to those seen for the amino acid-derived compounds **179** and **180** in Sections 4.7.6 and 4.8.4.

The global changes to the Tb(III)-centred emission spectra were also analysed by the same method. Two species which were estimated to exist in solution from the analysis were the the 1:2 metal:ligand species and 1:1 metal:ligand species. The distribution of these
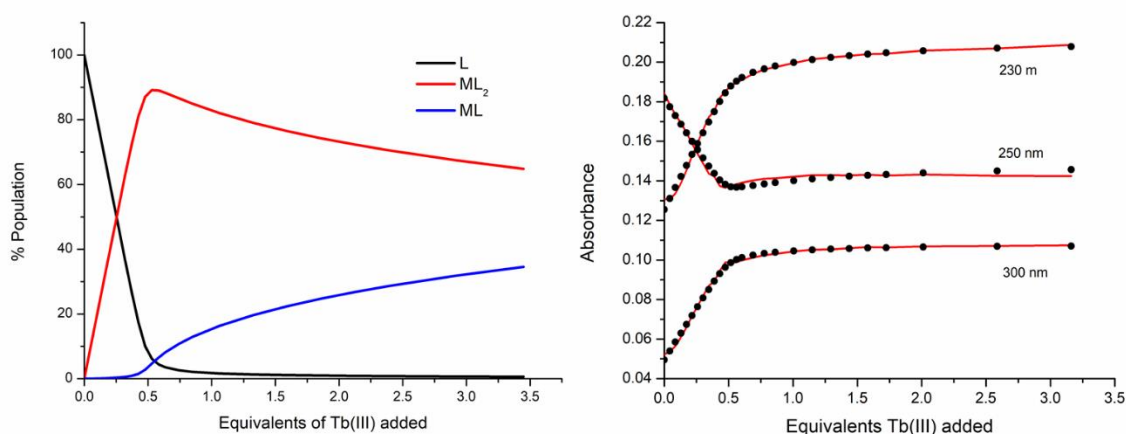
Figure 4.26 *(left) The speciation distribution diagram obtained from the fit of the UV-visible absorption titration data of ligand **186** against Tb(CF₃SO₃)₃ in CH₃CN. (right) the fit of the experimental binding isotherms using non-linear regression analysis software ReactLab.*

species is shown in the appendix (Figure A4.15). Again at 0.5 equivalents of Tb(III), the ML_2 species was the most predominant in solution at 82% abundance and subsequent additions of Tb(III) resulted in a degree of dissociation to the less emissive 1:1 metal:ligand species. The binding constants were estimated for each species and found that the 1:2 metal:ligand assembly formed with $\log\beta_{12} = 14.5\pm0.1$ while the 1:1 metal:ligand species had a binding constant of $\log\beta_{11} = 7.8\pm0.1$ which are in good agreement with the stability constants calculated from the UV-visible absorption data. These results show a preference for the formation of the ML_2 species over the ML_3 species under kinetic control. As compound **186** behaves in a similar fashion to compounds **179** and **180** this indicates that the amino acid residue does not have a significant impact on the self-assembly with Tb(III) in CH_3CN. Under kinetic control at low concentration, little evidence of the fully saturated 1:3 metal:ligand assembly exists while the ML_2 and ML species are formed more favourably as the kinetic products of the reaction. This results is similar to that seen by Gunnlaugsson and Lincheneau for a Tryp-functionalised **dpa** ligand with exclusive formation of the 2:1 metal:ligand assembly and no evidence for the 3:1 metal:ligand complex.[248]

Having examined the self-assembly of monotopic **tzpa** ligands with Ln(III), the possibility of forming higher order structures such as helicates or cages was explored with ditopic ligand **H₂157** will be discussed in Section 4.11.

4.12 Self-assembly of Tb(III) with ditopic ligand H₂157

As the self-assembly of monotopic compound **186** with Tb(III) was explored in Section 4.10, the next step in this study was to examine the self-assembly of ditopic derivative **H₂157** which was synthesised and its coordination chemistry with *d*-metals described in Chapter 2. This ligand formed interesting higher-order structures with Cu(I) and Cu(II), generating a [2 × 2] grid structure and no evidence for the formation of a circular helicate observed in the solid state. However, ditopic ligands such as **38-45** and **121**-**128** described in Chapter 1, have been shown by the Gunnlaugsson group and others to form enantiomerically pure, triple stranded dimetallic helicates with Ln(III) ions.[91,162–164] Supramolecular helicates are of particular interest as they are reminiscent of biomolecules such as the α-helices of polypeptides and the DNA double helix, representing the complex self-organisation found in nature.[254,255] Double and triple helical structures provide an insight into the thermodynamics and kinetics of formation and dissociation of biologically relevant helical macromolecules.[255] It was hypothesised that self-assembly of this chiral ditopic ligand
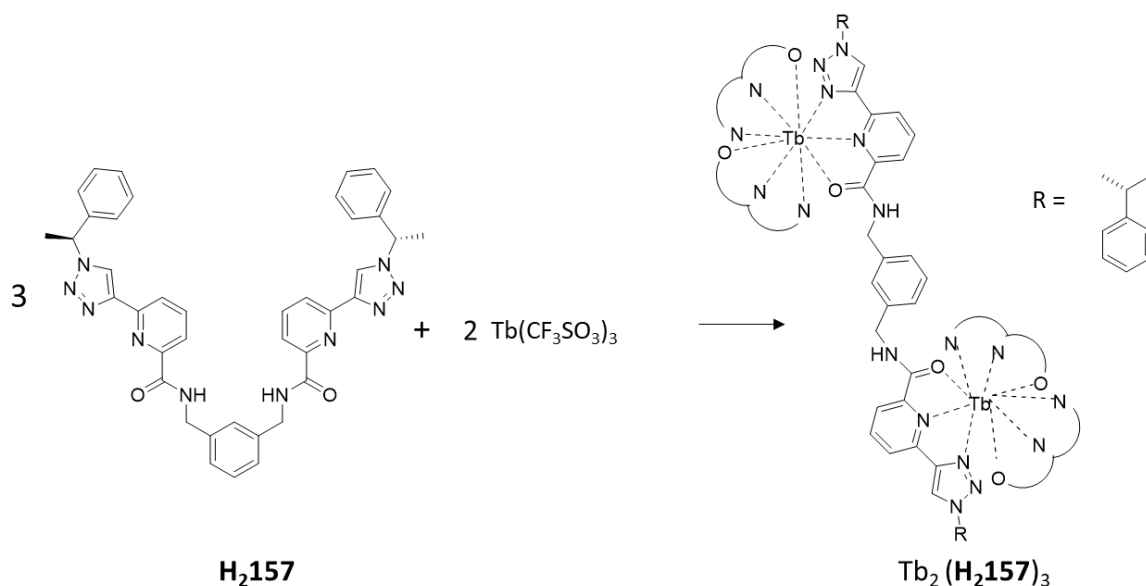
Scheme 4.5 *Schematic representation of reaction of **H₂157** with Tb(CF₃SO₃)₃ showing the possible formation of a triple stranded helicate and possible binding mode.*

H₂157 with Tb(III) could lead to the formation of a circular helicate structure in solution (see Scheme 4.5). While many helicate systems are formed in organic solvents such as CH₃CN, moving towards self-assembly in water based solvent systems is desirable as biological processes occur in an aqueous environment. It is therefore, crucial to move supramolecular chemistry to water. Furthermore, as mentioned in Section 4.1, water solubility of supramolecular assemblies is essential for the function of optical biosensors and cellular imaging agents.[244] While **H₂157** was not water soluble, derivatisation of this ligand would be possible in order to improve its affinity for aqueous media. Initially, the self-assembly of **H₂157** with Tb(III) in CH₃CN solution was investigated in order to determine the speciation in solution and will be discussed in Section 4.13.

4.13 Examination of self-assembly of H₂157 with Tb(III) in solution

The Tb(III) directed self-assembly of ligand **H₂157** with Tb(CF₃SO₃)₃ *in situ* was investigated by a series of spectroscopic measurements. This process involves the addition of known aliquots of Tb(III) solution to **H₂157** and the changes to the UV-visible absorption and luminescence spectra are monitored after each addition. The spectroscopic titrations were carried out at a ligand concentration of 1×10^{-5} M. At this concentration the self-assembly of **H₂157** with Tb(III) was fast and no substantial equilibration period was required after each addition of metal.

4.13.1 UV-visible absorption titration

The speciation of the lanthanide-directed self-assembly was monitored by multiple methods in parallel. The ground state spectroscopic changes were monitored using UV-visible absorption spectroscopy while fluorescence and time-gated luminescence spectroscopy were used to monitor the emission.

The UV-visible absorption spectrum of **H₂157** in CH₃CN displayed two main bands. One band was centred at $\lambda = 251$ nm and the second band was located at $\lambda = 291$ nm ($\varepsilon = 35400$ cm^{-1} M^{-1} at $\lambda_{abs} = 230$ nm).. Significant changes were observed to the UV-visible absorption spectrum upon addition of Tb(III). As shown by the binding isotherms in Figure 4.27, the high energy band at $\lambda = 251$ nm experienced a hypochromic shift and significant broadening of the absorbance band up to the addition of 0.55 equivalents of Tb(III). After this point the changes to this band reached a plateau. Similarly, the lower energy band centred a $\lambda = 291$ nm experienced the most significant changes up to the addition of 0.55 equivalents of metal. The band underwent both a hyperchromic shift and a concomitant redshift by 10 nm. Subsequent addition of Tb(III) did not result in any further significant changes to the spectrum which indicates the formation of stable species in solution. Three isosbestic points at 216 nm, 236 nm and 288 nm were also observed, indicating the presence of multiple correlated species in solution. The speciation in solution was elucidated by fitting this data using non-linear regression analysis and will be discussed in Section 4.12.3.
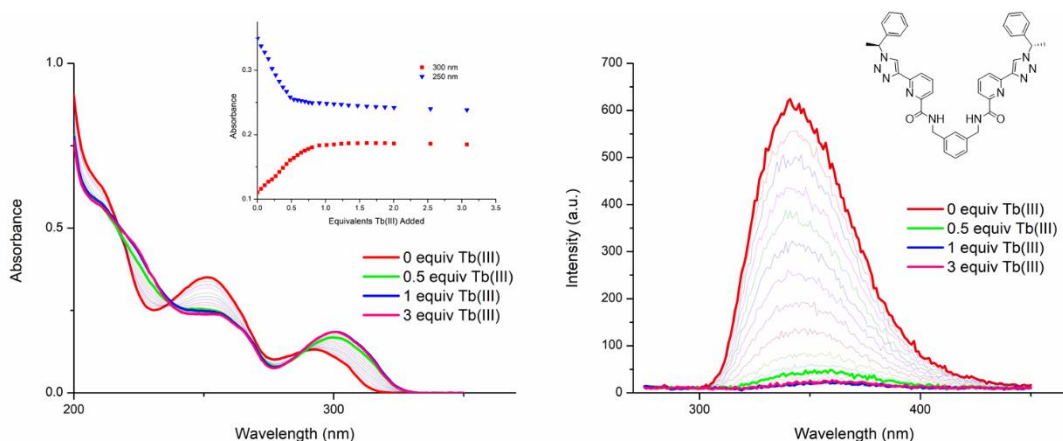
Figure 4.27 *The overall changes in the (left) UV-visible absorption spectra and (right) fluorescence emission spectra (excitation wavelength $\lambda = 260$ nm) upon titrating **H₂157** (1×10^{-5} M) against Tb(CF₃SO₃)₃ ($0\rightarrow3$ equiv.) in CH₃CN at RT. **Inset:** corresponding experimental binding isotherms of absorbance at $\lambda = 300$ and 250 nm.*

4.13.2 Tb(III)-centred luminescence titrations (emission and time-gated emission)

Upon excitation of the ligand **H$_2$157** at $\lambda = 260$ nm, the ligand centred emission was observed at $\lambda = 343$ nm and addition of Tb(III) resulted in a quenching of this luminescence, indicating that it is affected by the self-assembly process. A 93% reduction in the luminescence was observed at the addition of 0.5 equivalents of Tb(III). This can be attributed to an energy transfer process from the ligand **H$_2$157** to the Tb(III) metal centre which gives rise to the characteristic Tb(III)-centred emission *via* indirect excitation.

The delayed Tb(III)-centred luminescence was also recorded upon excitation at $\lambda = 260$ nm. The spectra and binding isotherms can be seen in Figure 4.28. A gradual enhancement was observed in the Tb(III) luminescence from 0 to 0.5 equivalents of metal solution with the characteristic Tb(III)-centred emission transitions appearing at $\lambda = 491$, 545, 583, 622, 649, 668 and 679 nm which correspond to deactivation from the Ln(III) ion $^5D_4$ excited states to the ^7F_J states (where $J = 6 - 0$). Subsequent additions of Tb(III) from 0.5 equivalents to 3 equivalents resulted in a decrease in the phosphorescence intensity. This decrease reached a plateau at the addition of 1 equivalent of metal solution. The most emissive state in solution was therefore at a metal:ligand stoichiometry of 1:2 or 1:3 which likely indicates the formation of an ML$_2$ or ML$_3$ species in solution. A gradual quenching of the Tb(III)-centred luminescence suggests the formation of a less emissive species such as a 1:1 metal:ligand species in solution as a result of the addition of excess Tb(III) to the system causing at least partial dissociation of the highly saturated species. This ML species would be more susceptible to solvent quenching and thus result in lower luminescence intensity.
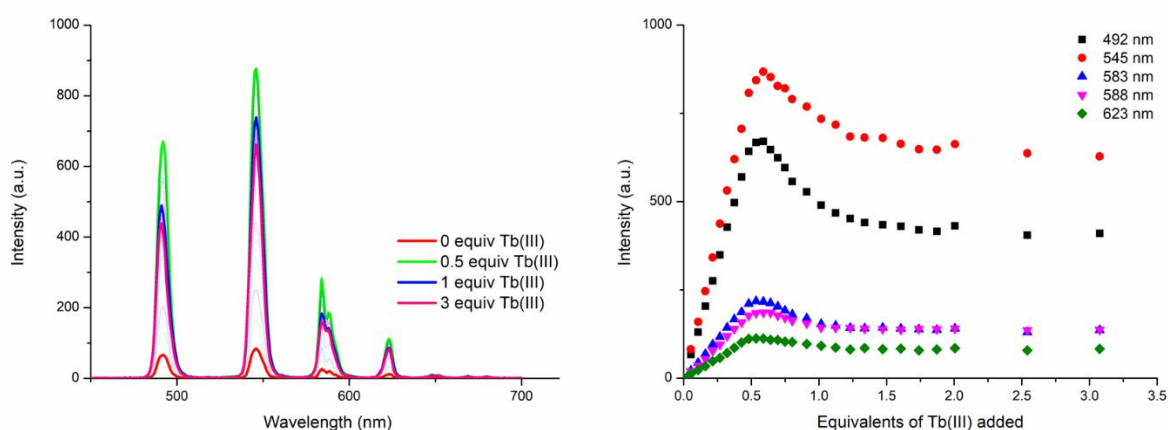
Figure 4.28 *(left) The overall changes to the Tb(III)-centred phosphorescence spectra upon titrating **H$_2$157** (1×10^{-5}M) against Tb(CF$_3$SO$_3$)$_3$ ($0\rightarrow3$ equiv.) in CH$_3$CN at RT. (right) corresponding experimental binding isotherms of phosphorescence at $\lambda = 492$, 545, 583, 588 and 623 nm.*

The data were fit using non-linear regression analysis in order to estimate the speciation in solution and the stability constants of these species and is discussed in Section 4.12.3.

4.13.3 Fitting of titration data for H₂157 and Tb(III)

As discussed in previous chapters, the changes to the UV-visible absorption spectra and Tb(III)-centred emission spectra could be analysed using a global analysis method, and an estimation of the species in solution could be made. The stability constants which correspond to these species was also estimated. Concentration profiles for each species in solution were established and this analysis was all completed with ReactLab EQUILIBRIA software.

Analysis of the UV-visible absorption data for ligand **H₂157** with Tb(CF₃SO₃)₃ in CH₃CN pointed to the presence of three main species in solution (**H₂157**, 2:3 metal:ligand species and 2:2 metal:ligand species) and the distribution of these species were estimated in the analysis. From this estimate, the M_2L_2 species appears most dominant in solution, reaching 100% abundance at 1.2 equivalents of Tb(III). The M_2L_3 species reaches a maximum abundance of 13% at approximately 0.5 equivalents of Tb(III) after which it decreases. This speciation is consistent with the observation that the most emissive stoichiometry in solution was at 0.5 equivalents of Tb(III). While the M_3L_2 species is likely the most emissive species due to exclusion of solvent from the inner coordination sphere of the Ln(III) ion, it does not appear to be the kinetic product of the self-assembly in solution. This observation is in agreement with the self-assembly of compounds **179**, **180**, and **186** described in previous sections. From the changes observed in the UV-visible absorption
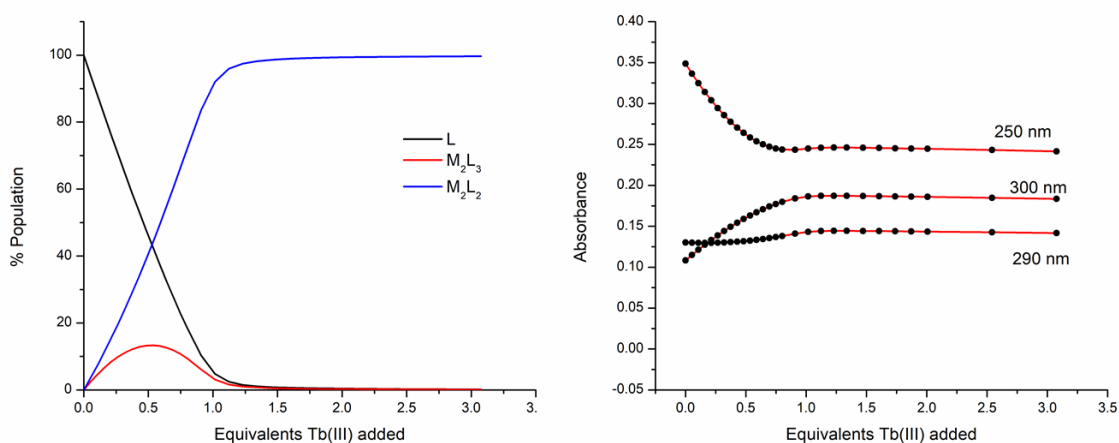
Figure 4.29 *(left) The speciation distribution diagram obtained from the fit of the UV-visible absorption titration data of ligand **H₂157** against Tb(CF₃SO₃)₃ in CH₃CN. (right) the fit of the experimental binding isotherms using non-linear regression analysis software ReactLab.*
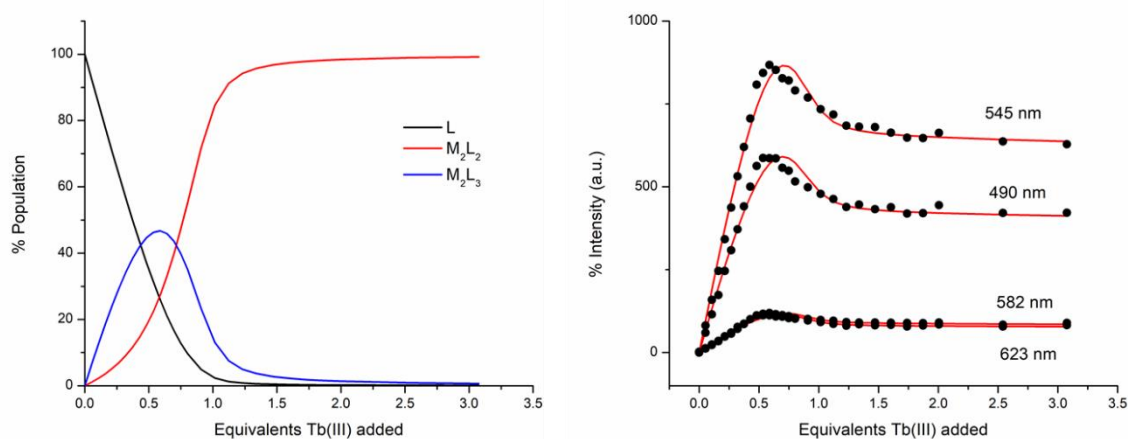
Figure 4.30 (left) The speciation distribution diagram obtained from the fit of the delayed luminescence titration data of ligand **H₂157** against Tb(CF₃SO₃)₃ in CH₃CN. (right) the fit of the experimental binding isotherms using non-linear regression analysis software ReactLab.

spectra throughout the titration, binding constants were estimated for each species. The 2:3 metal:ligand assembly formed with $\log\beta_{23}$ = 24.13±0.1 and the second species (2:2 metal:ligand) had a calculated binding constant of $\log\beta_{22}$ = 19.47±0.1. These stability constants are in excellent agreement with stability constants determined for double and triple stranded helicates reported by the Gunnlaugsson group.[165] The calculated and experimental binding isotherms are shown in Figure 4.29 and are in good agreement indicating a good fit.

In a similar manner, the global changes to the Tb(III)-centred emission were analysed and confirmed the presence of two main species in solution (M_2L_3 and M_2L_2). Again the distribution of the species were estimated from the analysis and from 0 to 0.5 equivalents of Tb(III) the M_2L_3 species most dominant in solution reaching 46% abundance. Subsequently, upon further additions of Tb(III), the abundance of the M_2L_3 species decreased which was likely due to dissociation to the M_2L_2 species in the presence of excess metal. This was is in good agreement with the speciation estimated from the UV-visible absorption data. The binding constants were estimated for each species and the 2:3 metal:ligand assembly formed with $\log\beta_{23}$ = 25.59±0.1 while the second species (2:2 metal:ligand) had a calculated binding constant of $\log\beta_{22}$ = 19.97±0.1. Again, these calculated stability constants are in comparable to those obtained from the changes in the UV-visible absorption data. From these results it can be concluded that a mixture of M_2L_3 and M_2L_2 species exist in solution at low concentration. Attempts were made to examine the self-assembly *via* [1] H NMR studies,

however, significant broadening of the peaks upon addition of even 0.2 equivalents of Tb(III) prevents the use of ^{1}H NMR spectroscopy to monitor the self-assembly.

4.15 Formation of Tb(III) complex

Following examination of the self-assembly of ligand **H₂157**, attempts were made to synthesise an isolate the M₂L₃ complex which was the dominant assembly formed in solution at low concentration. Compound **H₂157** was reacted with Tb(CF₃SO₃)₃ in a 3:2 ligand:metal stoichiometry in CH₃OH solution under microwave irradiation at 70 ˚C for 20 minutes. The resulting colourless solution was concentrated under reduced pressure and dropped into a large excess of cold diethyl ether. The white precipitate generated was isolated by centrifugation from the diethyl ether supernatant solution and dried under high vacuum. The isolated solid was obtained in 32 % yield. Initial visual observations indicated successful Tb(III) complex formation with both the CH₃OH solution and the isolated solid appearing green emissive under UV light (λ_{em} = 254 nm). Attempts were made to characterise the complex by ^{1}H NMR spectroscopy; however, due to the paramagnetic nature of the Tb(III) ion the resonances in the resulting spectrum appeared extremely broad and it was therefore difficult to interpret. No evidence for the M₂L₃ complex was observed by HRMS and the elemental analysis did not confirm the presence of the M₂L₃ species. Attempts were made to crystallise the isolated solid using a variety of solvents and conditions; however, no crystals of X-ray diffraction quality were obtained.

4.16 Conclusions and Future Work

This chapter focused on the synthesis of two new ligands **179** and **180**, incorporating amino acid residues phenylalanine and tryptophan respectively. These compounds with a **tzpa** binding site were designed as a preliminary ligands for the development of water soluble and biologically relevant Ln(III)-assemblies. Bis complexes of these ligands were generated with both Eu(III) and Tb(III) and the quantum yields of these complexes were determined. Quantum yields of the Tb(III) complex was found to be significantly higher (84.0%) than the Eu(III) complex (5.2%) which indicates that the ligand **179** more efficiently sensitises Tb(III) emission than Eu(III) emission. While [Tb(**179**)₂] produced a large quantum yield, [Tb(**180**)₂] was recorded as 15.3%, indicating that functionalisation of the ligand with tryptophan in place of phenylalanine reduced the Tb(III) sensitisation efficiency of the ligand. Investigation of the self-assembly of these ligands with Tb(CF₃SO₃)₃ determined that

under kinetic conditions, a 1:2 metal:ligand species was the more favourable product of the ligand-metal self-assembly and this species is shown to dissociate to the less emissive 1:1 metal:ligand species at higher metal concentration. Self-assembly of compound **180** with Tb(III) further reinforced that compound **180** was a poor sensitizer for Tb(III), with only very weak luminescence observed from 0 to 0.5 equivalents of Tb(III). The self-assembly of compound **182**, the di-acid of compound **180** with Tb(III) (CH_3OH, 0.05 M TEACl) was also examined but unfortunately data convergence was not achieved and therefore the speciation and binding constants could not be determined. It is worth noting that the most significant changes in the UV-visible absorption and luminescence spectra occurred up to the addition of 0.5 equivalents of Tb(III), as was the case for compound **179** where an ML_2 species was the predominant kinetic product of the self-assembly. The stability of the bis complexes [Tb(**181**)$_3$] and [Tb(**182**)$_3$] were examined in aqueous solution; however, dissociation of the complexes to the free ligand was observed even at a low concentration of H_2O. Unfortunately, this indicates that these complexes would not be suitable to act as biological probes. However, future work would introduce water solubilising groups to the picolinic acid of ligand **181**, with a view to generating more stable Tb(III) complexes such a sulfonates or polyoxyethylene chains which have been shown to improve the stability of lanthanide complexes in aqueous media.[245,256,257]

To determine if a steric effect was responsible for the kinetic product of the self-assembly of ligands **179** and **180** with Tb(III) being a 2:1 ligand:metal species and not the anticipated 3:1 assembly, compound **186**, was synthesised an its self-assembly under the same conditions with Tb(III) was examined. However, it was found that compound **186** was also formed in a 1:2 metal:ligand stoichiometry. Ditopic ligand **H₂157** was also titrated with Tb(III) and their speciation was determined using the global analysis method employed previously. It was found to form M_2L_3 species which dissociate to M_2L_2 species at higher metal concentration. Unfortunately, no crystal structure was obtained of this system and so it is difficult to estimate the structure of these assemblies due to the ditopic nature of the ligands. Future work would aim to isolate the M_2L_3 assembly in the solid state and characterise this species in order to understand the structure of the assembly. Future work would also examine the transfer of chirality from the ligand **H₂157** to the metal centre using CD spectroscopy.

"I think we've outgrown full-time education…Time to test our talents in the real world,

d'you reckon?"

Fred Weasley, Harry Potter and the Order of the Phoenix

5. Luminescent Ln(III) Complexes and Doped Polymer Gels as Responsive Polymer Materials

5.1 Introduction

The **btp** motif, as stated in Chapter 1, is a versatile binding motif which can be easily functionalised through the triazole arms using the CuAAC reaction by choosing different azide and/or alkyne starting materials.[40] In addition, the pyridyl ring has been functionalised using standard pyridine chemistry to introduce a variety of substituents.[95,120] This functionalisation has allowed for tuning of the photophysical, electronic and structural properties of the resulting complexes.[24,105] In particular, modification at the 4-pyridy position of the **btp** motif can also provide a synthetic handle for use in the synthesis of higher order supramolecular systems. For example, a supramolecular Pt(II)-**btp** polymer has been reported in which the 4-pyridyl position was functionalised with an acetylide moiety and polymerised in a polycondensation reaction to generate a metallosupramolecular Pt(II) polymer with relatively low synthetic effort. [111] Thin films could be formed from the polymer material, which was subsequently shown to display solid-state emission, and demonstrating the potential of this system for integration into optoelectronic devices. Hecht and co-workers have reported Ru(II)-**btp** complexes, describing their facile functionalisation at the 4-pyridyl position, as well as at the triazolyl N1 position. They showed that the electron withdrawing or donating character of the substituent at the 4-pyryidyl position had a large effect on the resulting redox behaviour of the Ru(II) complex. Stronger electron-donating groups facilitated oxidation of the complexes while electron withdrawing substituents had the opposite effect.[105] A series of 4-pyridyl functionalised **btp** ligands have also been synthesised by the Gunnlaugsson group. A carboxylate functionalised **btp** compound was found to form a metallosupramoecular gel with Eu(III), caused by cross-linking interactions between the carboxylate groups and the Eu(III) metal centre, generating a network of fibres.[123] This same compound also formed a 3D MOF with Zn(II), which was capable of sensitising Eu(III) and Tb(III), and also exhibited cation exchange properties.[19]

While metallosupramolecular gels are highly advantageous due to their dynamic labile interactions which can often lead to self-healing materials, the addition of metal complexes to polymer matrices has also been shown to endow the polymer films with interesting photophysical properties. Non-covalent inclusion of luminescent lanthanide complexes in polymer materials has been widely reported,[258] and Ln(III) complexes have often exhibited enhanced luminescence when homogeneously embedded within a polymer matrix.[259] Doped polymers and blended materials have also been successful in improving the mechanical and thermal properties of the materials, such as their flexibility and thermal stability, while retaining their photoactive properties.[259]

Poly(methyl methacrylate) (p(MMA)) has garnered significant interest as a dopant matrix due to its low cost, facile preparation and optical transparency.[260] Malta and co-workers have shown this by using classical β-diketonate complexes of Eu(III) and Tb(III) as dopants in p(MMA) systems.[261] The complexes exhibited enhanced emission within the polymer matrices, caused by exclusion of water molecules from the inner coordination sphere of the Ln(III) ion. Co-doping the matrices with both Tb(III) and Eu(III) resulted in further enhancement of the Eu(III) emission, which was accounted for by the well-established Tb(III)$\rightarrow$ Eu(III) energy transfer process.[260,262] The emission colour could be tuned across the yellow, red and green areas of the CIE colour space by varying the ratios of Tb(III) and Eu(III), and the complexes within the p(MMA) matrix also showed improved photo-stability under extended UVA (λ_{em} = 254 nm) and UVC (λ_{em} = 330 nm) irradiation.

In recent years, biodegradable and natural polymers have become of significant interest for tissue engineering applications.[263] Chitosan has been reported as a biodegradable polymer matrix in which Eu(III) complexes can be encapsulated. It has been shown that the Eu(III)-centred emission in these chitosan polymer matrices can be fine-tuned and white light can be generated depending on the dopant and excitation wavelength as the host generates a broad emission band in the blue to green.[264] These flexible and transparent films however, were found to exhibit low quantum yields when compared to synthetic polymers such as p(MMA), due to quenching of the Eu(III)-centred emission by -OH oscillators.

Gunnlaugsson and co-workers reported the non-covalent incorporation of a **btp**-Tb(III) complex, [Tb(**140**)$_3$]$^{3+}$, into a gel matrix in combination with a naphthyl-**dpa** complex of Eu(III), [Eu(**153**)$_3$]$^{3+}$.[178] These poly(HEMA-*co*-MMA) (where HEMA is (hydroxyethyl)methacrylate) doped polymers act as a dual-responsive material to [H$^+$] and [F$^-$]. Initially, complexes of [Tb(**140**)$_3$]$^{3+}$ and [Eu(**153**)$_3$]$^{3+}$ were generated and their photophysical properties characterised. Their response to external stimuli was examined, with [Eu(**153**)$_3$]$^{3+}$ showing characteristic Eu(III)-centred luminescence which was significantly enhanced upon protonation of the pendant amine by addition of [H$^+$]. Protonation of this group prohibits the photoinduced electron transfer (PET) process which, in the ligand's neutral form, quenches the ligand excited state. In the case of [Tb(**140**)$_3$]$^{3+}$, the UV-visible absorption spectrum was blue-shifted, and the ligand fluorescence was enhanced upon exposure to [F$^-$], which ultimately resulted in a complete quenching of the Tb(III)-centred emission. This was caused by a F$^-$ induced dissociation of the [Tb(**140**)$_3$]$^{3+}$
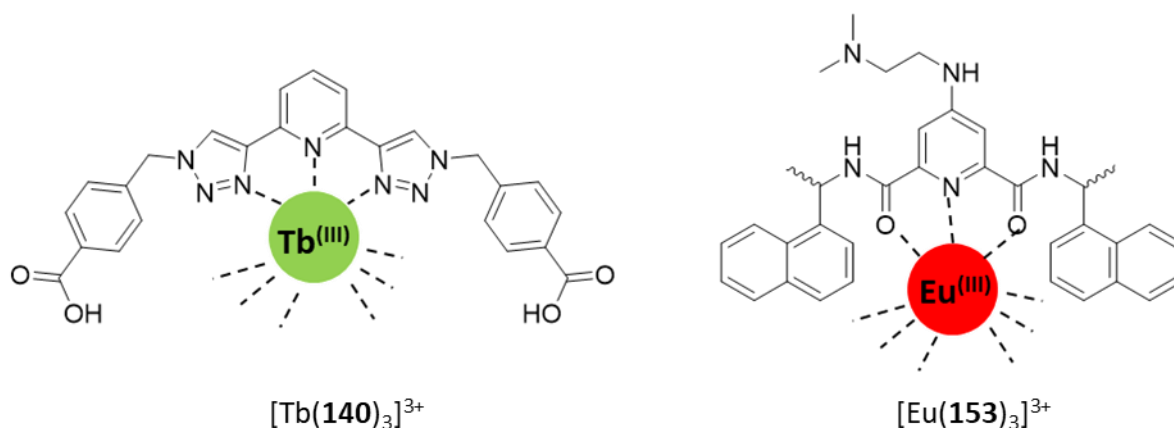
$[Tb(\mathbf{140})_3]^{3+}$ $\qquad\qquad$ $[Eu(\mathbf{153})_3]^{3+}$

Figure 5.1 *Schematic representation of $[Tb(\mathbf{140})_3]^{3+}$ and $[Eu(\mathbf{153})_3]^{3+}$.*

complex. Both complexes $[Tb(\mathbf{140})_3]^{3+}$ and $[Eu(\mathbf{153})_3]^{3+}$ were then incorporated within the poly(HEMA-*co*-MMA) polymer matrix in a non-covalent manner. The unique responses of the Eu(III) and Tb(III) complexes to $[H^+]$ and $[F^-]$, respectively, were retained within the polymer matrix generating a logic-gate mimic. However, leeching of the **btp** ligand **140** from the polymer, following dissociation of the complex $[Tb(\mathbf{140})_3]^{3+}$ upon exposure to $[F^-]$, prevented recycling of the films. Issues surrounding dissociation of the Ln(III)-complexes and subsequent release of the ligand molecules, lack of homogeneity, and concentration quenching, can hamper further development of many non-covalently incorporated systems.[265]

In order to address these issues, a number of systems in which the ligands are covalently attached to the polymer backbone have been developed. Weng and co-workers have developed a functionalised poly(urethane) backbone polymer copolymerised with **btp** sites.[121,266,267] The resulting polymer was soluble in organic solvents and formed an organogel in toluene. Introducing Tb(III) or Eu(III) to the system, and irradiating the gel with UV-light, resulted in green and red emission, respectively. In another case, addition of Zn(II) resulted in blue emission, and the colour could be tuned by varying the metal stoichiometries within the gel. The mechanical properties of the metallogels were particularly interesting, showing self-healing properties and thermoreversibility.

The aim of this Chapter was to synthesise a novel **btp** ligand, functionalising the 4-pyridyl position with a synthetic handle which could be covalently attached to a polymer matrix. Previous work in the group, as described above, explored the non-covalent incorporation of Ln(III)-**btp** complexes into a polymer matrix, and was found to be limited by leeching of the ligand from the polymer material. Thus, covalent attachment of the ligand to the polymer backbone was envisaged to be the next step in this system. The ligand **189**

described below was initially designed with a view forming a tripodal compound functionalised with three **btp** units, as shown in Scheme 5.1. However, while synthesis of this compound was achieved, it was only possible in very small qualities and the resulting material was highly insoluble in most common solvents. Therefore it was decided to utilise compound **189** as a ligand for incorporation into a polymer matrix.

The following sections describe the synthesis of compounds **189** and **190**, and the self-assembly of **190** with Tb(III) in solution. An organogel of compound **189** is formed and finally, the covalent incorporation of compound **189** into a polymer matrix is described and the resulting material characterised.
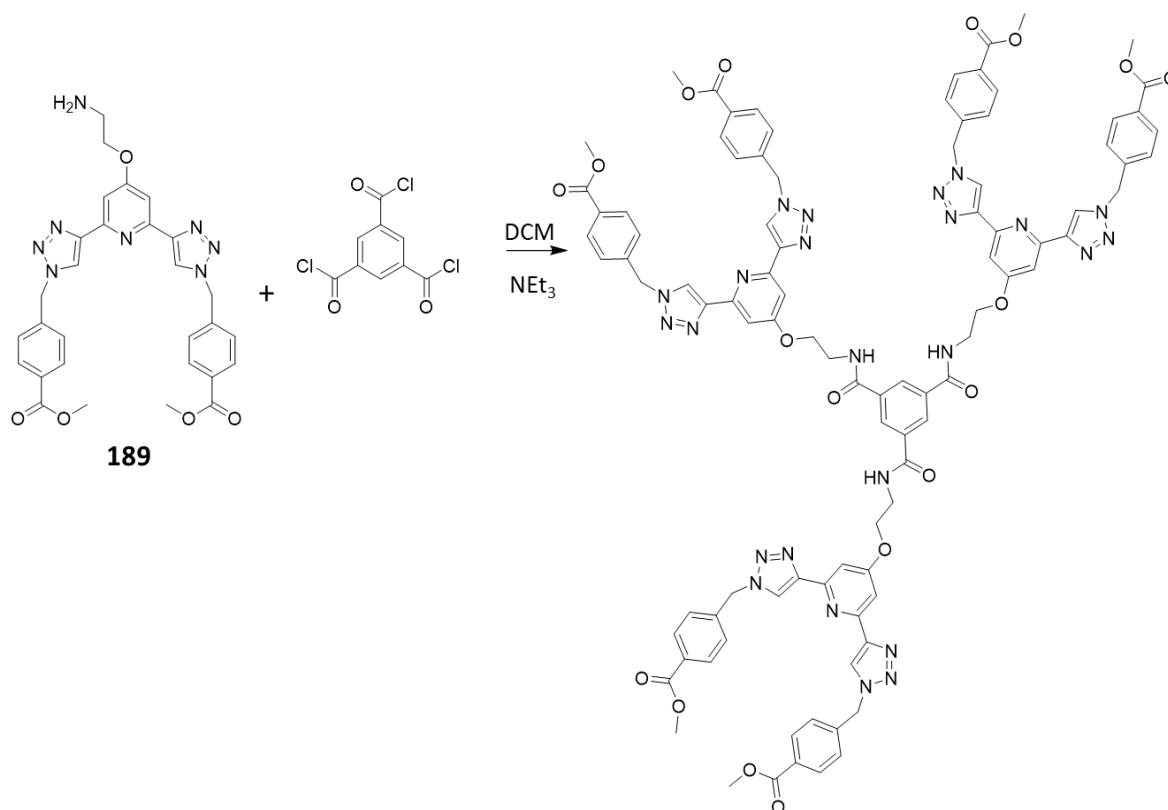
Scheme 5.1 *Attempted synthesis of tripodal compound from ligand **189** (3 equiv.) and benzene-1,3,5-tricarbonyl trichloride*

5.2 Design and synthesis of ligands 189 and 190

Compounds **189** and **190** were designed based on **btp** compound **140** above, functionalised with an amine linker for covalent attachment to a polymer backbone. Synthesis of ligand **189** involved a seven-step synthetic procedure, depicted in Scheme 5.2. Steps one to three have been previously reported, starting from the commercial starting material 2,6-dibromopyridine, from which the *N*-oxide compound **191** is formed. Subsequent nitration at the 4-position of the pyridyl ring with nitric acid resulted in compound **192**, with the *N*-oxide then cleaved using phosphorus tribromide to give compound **193** as a yellow solid in moderate yield (63%). The structure of this compound was further confirmed by X-ray crystallography and will be discussed in Section 5.2. Following on from this, *tert*-butoxycarbonyl (boc) protected ethanolamine, **194** was reacted with sodium metal, generating an alkoxide *in situ*, which was reacted with 2,6-dibromo-4-nitropyridine **193**, to form compound **195**. The product was fully characterised by NMR spectroscopies, IR spectroscopy and HRMS (Appendix Figure A5.1-5.2) with the ^{1}H NMR spectrum showing the characteristic *t*-butyl peak at 1.45 ppm. A large shift in the pyridyl peaks, from 8.19 ppm to 6.98 ppm, was observed when compared to compound **193**. Compound **195** was then
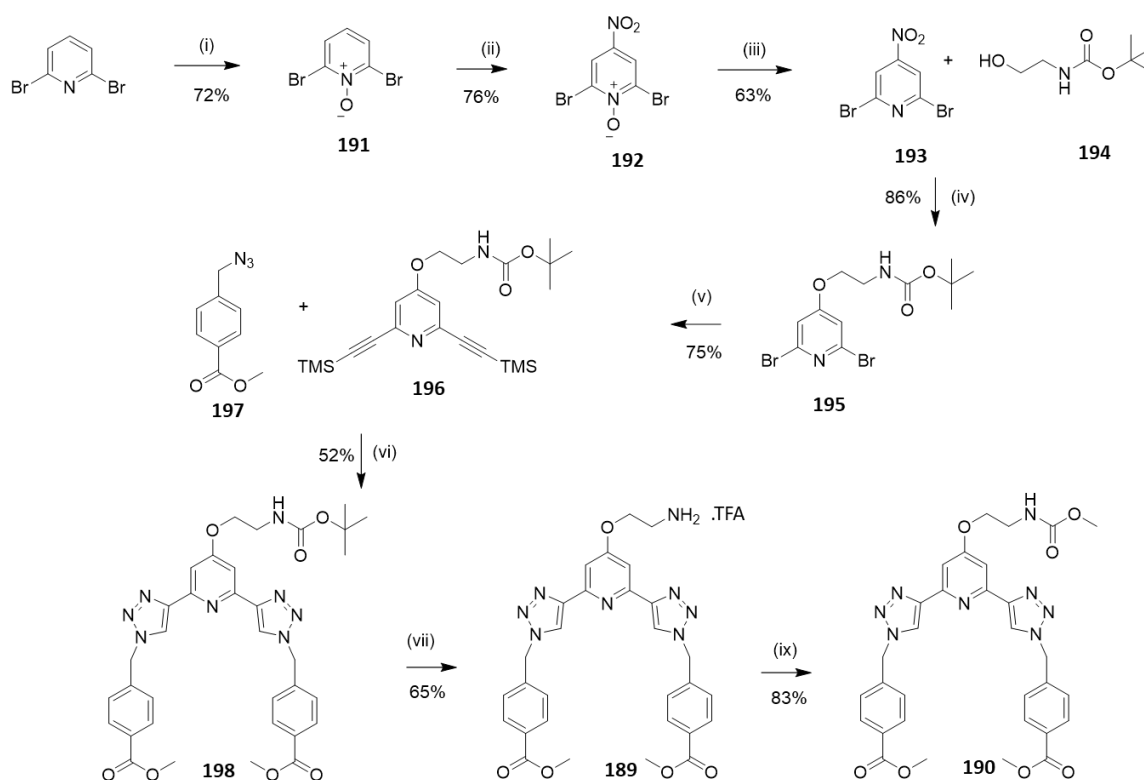
Scheme 5.2 *Synthesis and structure of **189** and **190**. Reagents and conditions: (i) TFA, H$_2$O$_2$, 100 °C (ii) H$_2$SO$_4$, HNO$_3$, 60 °C (iii) PBr$_3$, CHCl$_3$, (iv) Na, THF (v) CuI, Pd(PPh$_3$)$_4$, TMS-acetylene, DMF:NEt$_3$ (vi) CuSO$_4$.5H$_2$O, K$_2$CO$_3$, sodium ascorbate, DMF:H$_2$O (4:1) (vii) TFA (ix) acetic anhydride, NEt$_3$.*

subjected to a Sonogashira coupling reaction with TMS-acetylene to yield the TMS-protected diethynyl compound **196**. The methyl ester "arms" of the compound were installed under CuAAC conditions using $CuSO_4 \cdot 5H_2O$ in a DMF:H_2O mixture, yielding compound **198** in a moderate yield of 52%. Confirmation of the existence of the desired product was obtained from NMR spectroscopies, IR spectroscopy and HRMS. The absence of the TMS protons at 0.25 ppm, along with the appearance of the methylene protons as a singlet at 1.37 ppm, and two doublets corresponding to eight protons of the aromatic rings, confirmed the successful formation of the desired product. The boc protecting group was then removed in neat trifluoroacetic acid (TFA) over 1 hour, and the solution was neutralised with $NaHCO_3$, yielding **189** as a brown precipitate. The final product was fully characterised, and the ^1H NMR spectrum is shown in Figure 5.2. Resonances corresponding to the triazole protons and pyridyl protons reside at 8.68 ppm and 7.51 ppm, respectively. The aromatic protons appear as two sets of doublets at 7.98 ppm and 7.45 ppm, while their neighbouring CH_2 protons occurring as a singlet at 5.80 ppm. The ethyl protons at the 4-position of the pyridyl ring appear as two sets of triplets at 4.15 and 2.93 ppm, and finally the methyl ester protons are found as a singlet at 3.84 ppm. The structure was further confirmed by X-ray crystallography and will be discussed in Section 5.7. With compound **189** in hand, the synthesis of compound **190** could then be carried out. In order to simulate the covalent attachment of compound **189** to a polymer backbone and study the photophysical behaviour of this ligand in this simulated environment, the primary amine of compound **189** was protected with an acetyl group to generate compound **190**. Reaction of **189** with acetic
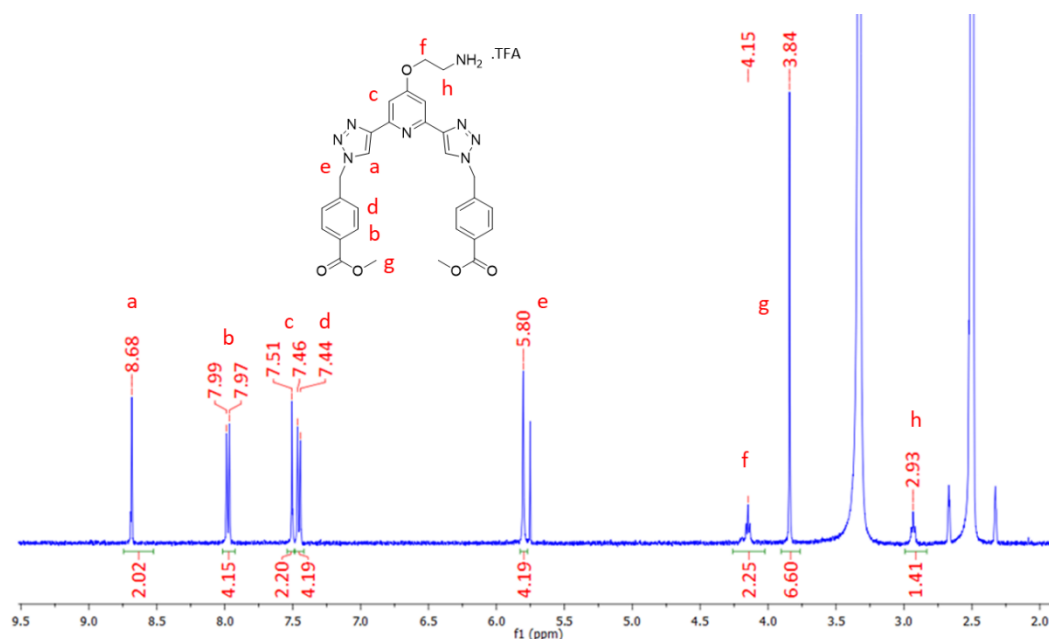
Figure 5.2 *^1H NMR spectrum (600 MHz, DMSO) of compound **189**.*

anhydride in the presence of triethylamine generated compound **190** as a white solid in 83% yield. Again, the compound was fully characterised by NMR spectroscopies, IR spectroscopy and HRMS, and the data is reported in the Appendix (Figures A5.8-A5.9).

5.3 X-ray crystal structure of compound 193

Single crystals of X-ray diffraction quality of compound **193** were obtained by slow evaporation of a solution of **193** in ethyl acetate. This crystal structure was solved by Dr. Chris Hawes. The crystal structure of compound **193** was solved in the chiral orthorhombic space group $P2_12_12_1$ and contains one complete molecule in the asymmetric unit. The extended structure is supported through weak halogen bonding interactions which occur between the bromide and a pyridyl nitrogen of a neighbouring molecule, with a Br2 to N1 distance of 3.784(4) Å and an angle C-Br···N of 95.27(14)˚. These bromines undergo halogen bonding due to the electron deficient nature of the 4-nitropyridine ring which increases the strength and directionality of the halogen bond.[268,269]
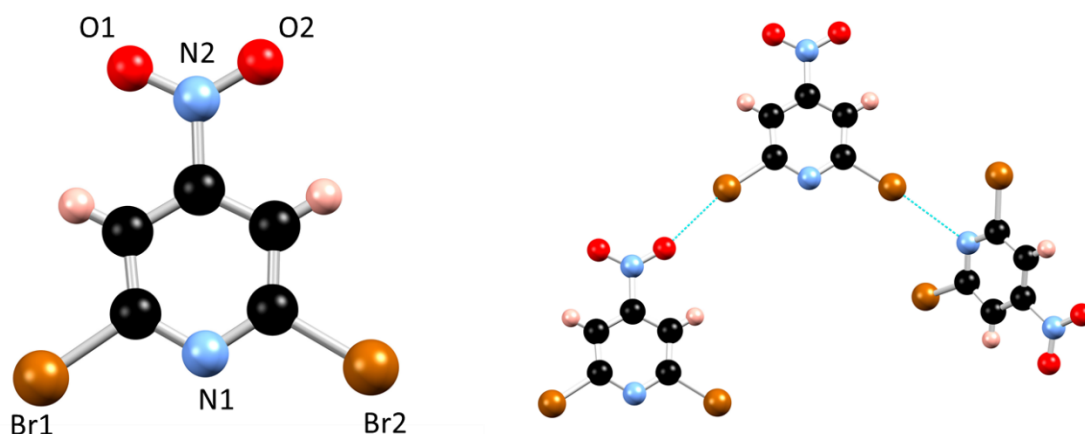
Figure 5.3 *(Left) Structure of one unique molecule of compound **193** with heteroatom labelling scheme, (right) primary mode of interaction between molecules of **193**.*

5.4 Formation of the mononuclear tris chelate complex $[Tb(190)_3]^{3+}$

Preparation of the mononuclear Tb(III) complex was achieved by reacting **190** with $Tb(CF_3SO_3)_3$ in a 1:3 M:L stoichiometric ratio in CH_3OH under microwave irradiation for 15 mins at 70 °C. The solvent was concentrated to 2 mL *in vacuo,* and the pure product was then isolated by vapour diffusion of diethyl ether into the reaction mixture, to yield a white solid in 79% yield. The complex was characterised by ^{1}H NMR spectroscopy, IR spectroscopy and HRMS. The ^{1}H NMR spectrum (400 MHz, CD_3CN-d_3) can be seen in
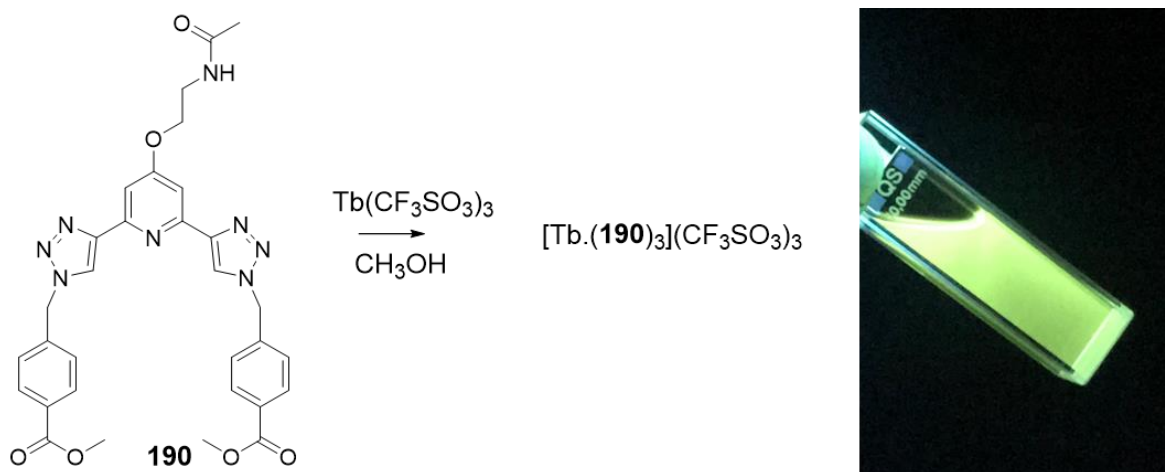
Scheme 5.3 *Preparation of Tb(III) complex [Tb(**190**)₃](CF₃SO₃)₃ carried out under microwave irradiation at 70 °C and green luminescence of the tris complex under UV-light ($\lambda_{em} = 254$ nm)*

Figure 5.4, and shows significant broadening and a large shift in the resonances of the signals when compared to the free ligand **190**, due to the paramagnetic nature of the Tb(III) ion. The complex was subjected to mass spectrometry, but unfortunately the presence of the ML_3 complex was not observed. However, the characteristic isotopic distribution pattern for the $[Tb(190)_3(CF_3SO_3)_2]^+$ complex was observed by MALDI ($m/z = 1677.2877$) see Appendix
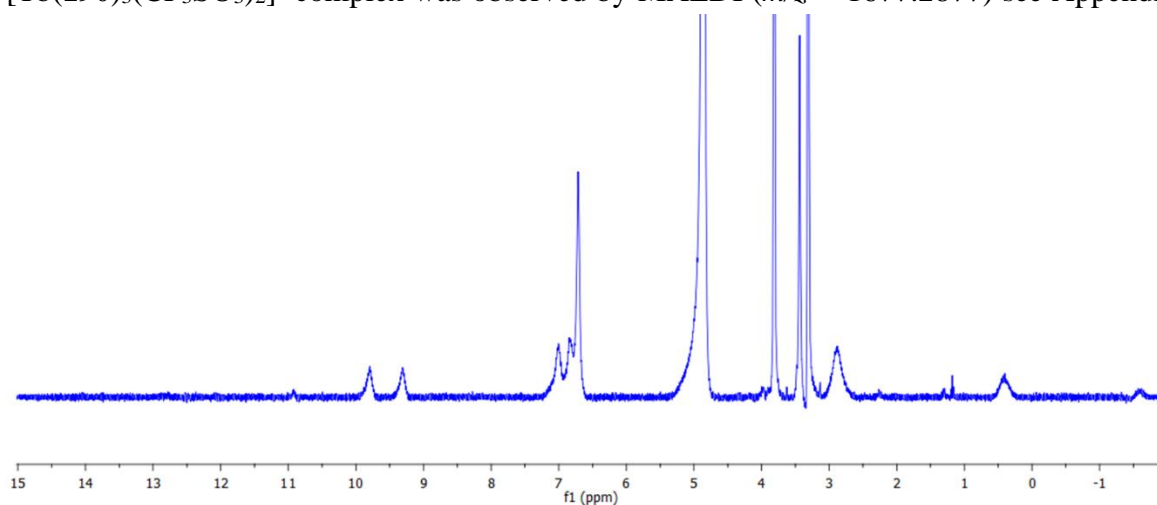
Figure 5.4 *^{1}H NMR spectrum (400 MHz, CD₃CN-$_{d3}$) of [Tb(**190**)₃](CF₃SO₃)₃ showing significant shift and broadening of the signals relative to the free ligand **190**.*

Figure A5.11. The MALDI fragmentation conditions may have caused cleaving of the third ligand from the complex. Elemental analysis was also used to confirm the formation of the tris complex. Following the synthesis of the $[Tb(190)_3]^{3+}$ complex, its photophysical properties were evaluated in solution.

5.5 Photophysical characterisation of complex $[Tb(190)_3](CF_3SO_3)_3$

Having successfully synthesised **190** and its corresponding 1:3 Tb(III) complex, $[Tb(190)_3]^{3+}$ its photophysical properties were then evaluated in CH_3CN and the results are shown in Figure 5.5. The UV-visible absorption spectrum of the terbium complex was dominated by a high energy band at $\lambda_{max} = 236$ nm and a lower energy band at $\lambda = 298$ nm, with a shoulder at $\lambda = 309$ nm. Excitation of the complex at $\lambda = 240$ nm gave rise to Tb(III)-centred emission with characteristic line-like transitions at $\lambda = 490, 545, 585, 622, 648, 667$ and 678 nm. These transitions are indicative of Tb(III)-sensitisation by the ligand antenna **190**, and can be assigned to the $^5D_4 \rightarrow {}^7F_J$ transitions where $J = 6 - 0$. In addition to the phosphorescence spectrum, these transitions can also be observed in the fluorescence emission spectrum, indicating that the energy transfer process from the ligand excited states to the $^5D_4$ excited state of the Tb(III) ion is efficient. The phosphorescence spectrum of $[Tb(190)_3]^{3+}$, recorded with a delay of 0.1 ms, is shown in Figure 5.5. The excitation spectrum, recorded for the Tb(III)-centred luminescence with $\lambda_{em} = 545$ nm, also provided evidence for the sensitisation of the Tb(III) ion from the ligand-centred excited states. The structural features of the excitation spectrum closely resemble the absorption spectrum of **190**, which indicates indirect excitation of the metal centre from the antenna moiety.
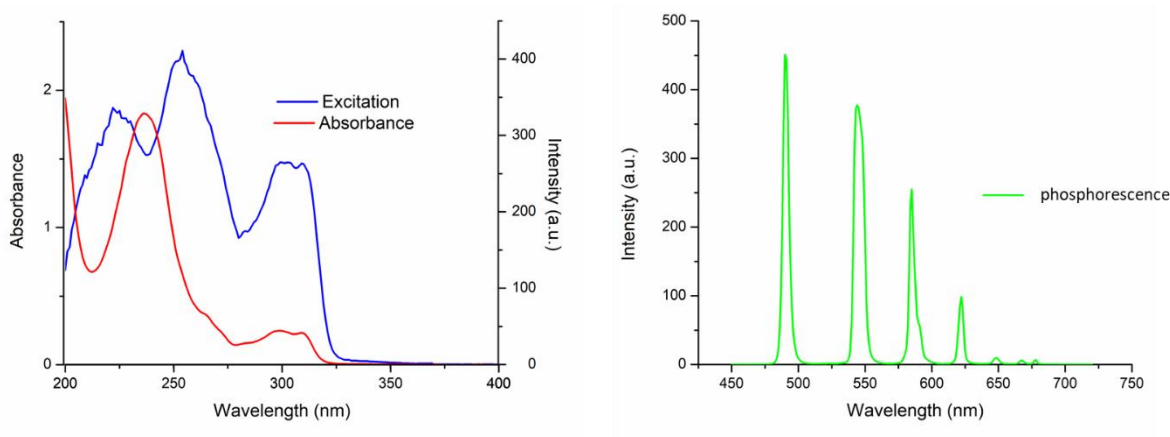
Figure 5.5 *(left) Representative absorption (red) and excitation spectra ($\lambda_{em} = 545$ nm) of* ***btp*** *complex $[Tb(190)_3]^{3+}$ in CH_3CN (1×10^{-3} M) showing sensitisation arising from ligand-centred energy transfer (left), and time-gated emission spectrum of $[Tb(190)_3]^{3+}$ showing characteristic Tb(III) centred-emission (right).*

Furthermore, green emission was also observed from both the solid complex, and the complex dissolved in CH₃CN, upon irradiation with UV light (λ_{exc} = 254 nm).

5.5.1 Luminescence emission lifetimes and Tb(III) hydration states

As discussed in Chapter 4, non-radiative deactivation pathways of the Ln(III excited states which compete with the radiative pathways can detrimentally reduce the luminescence intensity. However, these processes also offer a useful method for probing the number of solvent molecules directly bound to the Ln(III) ion, by using so-called q values or 'hydration states'. By comparing the lifetimes of the lanthanide complexes in CH₃OH and CD₃OD, the number of solvent molecules bound to the metal ion can be determined, due to the fact that O-D oscillators reduce the excited state lifetimes of Tb(III) complexes less than O-H oscillators.[270] The excited state lifetime measurements for [Tb(**190**)₃]³⁺ were measured in CH₃OH and CD₃OD, in which the complex was soluble. The excited state lifetimes in both solvents were best fit to monoexponential decay functions, indicating the presence of only one luminescent species in both CH₃OH and CD₃OD. Lifetime values of τ = 1.88 ± 0.1 ms and 1.98 ± 0.2 ms in CH₃OH and CD₃OD, respectively, were obtained for the [Tb(**2**)₃](CF₃SO₃)₃ complex. Horrocks' equation (Equation 5.1) was used to calculate the hydration state (q value) for each species. A value of $q \approx 0$ was obtained, indicating that the Tb(III) inner coordination sphere was fully saturated by three terdentate ligands, with no bound solvent molecules and is consistent with the ML₃ stoichiometry described in Section 5.4.

$$q^{Tb(III)} = A[(1/\tau_{(CH3OH)}) - (1/\tau_{(CD3OD)}) - 0.06] \qquad \textit{Equation 5.1}$$

5.6 Solution studies of the self-assembly interaction between 190 and Tb(III)

A series of UV-visible absorption and luminescence photophysical titrations were carried out in CH₃CN to investigate the self-assembly of ligand **190** with Tb(CF₃SO₃)₃ *in situ.* The formation of [Tb(**190**)₃]³⁺, described in the previous section, was performed using microwave irradiation to push the reaction towards a thermodynamic minimum as a result of the high temperature at which the synthesis was performed. By contrast, self-assembly in ambient conditions can often result in the formation of kinetically trapped, intermediate assemblies, where these complexes are dynamic in nature and varied in stoichiometry. Here, this process was probed by adding known aliquots of Tb(III) solution to **190** and monitoring

the changes in the UV-visible absorption and luminescence spectra after each addition. The spectroscopic titrations were carried out at a ligand concentration of 1×10^{-5} M. At this concentration the self-assembly was observed to be fast and no substantial equilibration period was required after each addition of Tb(III). The ligand solution was titrated with sequential additions of $Tb(CF_3SO_3)_3$ and the relevant UV-visible, fluorescence and phosphorescence spectra were recorded after each addition. These experiments were repeated three times to ensure reproducibility.

5.6.1 UV-Visible absorption titration

The formation of the lanthanide-directed self-assembly was monitored using multiple methods in parallel. Ground state spectroscopic changes were monitored using UV-visible absorption spectroscopy, while changes in the excitation state were monitored by fluorescence and time-gated luminescence (phosphorescence) spectroscopy.

The UV-visible absorption spectrum of compound **190** consists of two main bands appearing at $\lambda_{max} = 231$ nm and $\lambda_{max} = 300$ nm (Figure 5.6), ($\varepsilon = 54487$ cm^{-1} M^{-1} at $\lambda_{abs} = 230$ nm). Significant changes were observed in the UV-visible absorption spectrum upon addition of Tb(III). As shown by the binding isotherms in Figure 5.6, the high energy band, centred at $\lambda = 231$ nm, underwent a hypochromic shift, up to the addition of 0.15 equivalents of Tb(III). This was followed by a redshift to $\lambda = 236$ nm and a concomitant hyperchromic shift up to the addition of 0.3 equivalents of $Tb(CF_3SO_3)_3$. Subsequent additions of metal
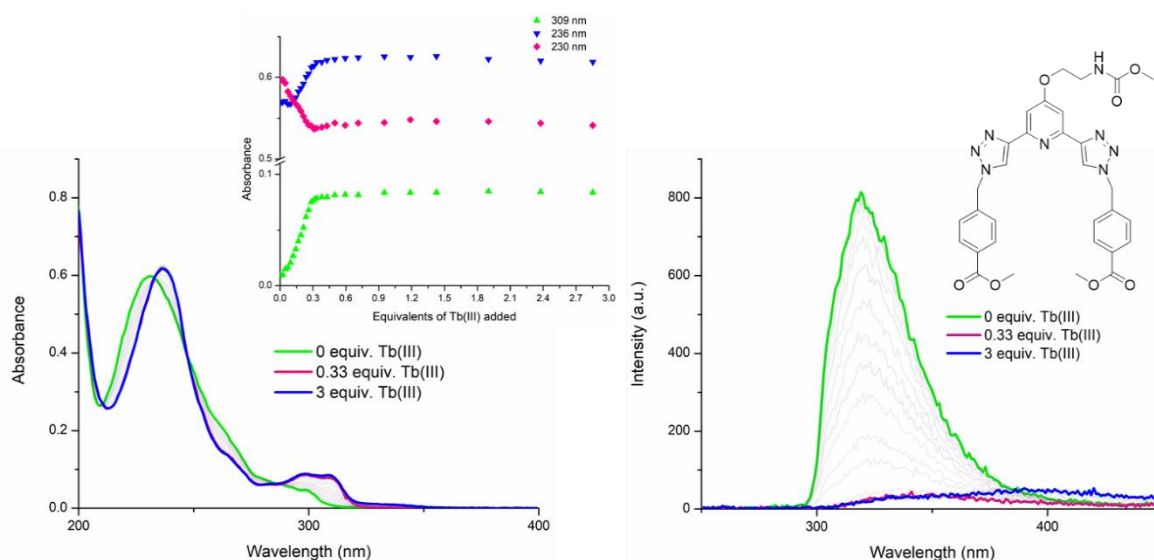
Figure 5.6 *The overall changes in the (left) UV-visible absorption spectra and (right) fluorescence emission spectra (excitation wavelength $\lambda = 237$ nm) upon titrating **190** (1×10^{-5} M) against $Tb(CF_3SO_3)_3$ ($0 \rightarrow 3$ equiv.) in CH_3CN at $22 ^\circ C$. **Inset**: Corresponding experimental binding isotherms of absorbance at $\lambda = 309$, 236, and 230 nm.*

solution did not result in any further changes to the band at 236 nm. The lower energy band at $\lambda = 298$ nm also experienced a hyperchromic shift up to the addition of 0.3 equivalents of Tb(III). These changes were accompanied by a deconvolution of this absorption band into two separate maxima at $\lambda = 308$ nm and 298 nm. Subsequent additions of the metal salt did not result in any further changes to the absorption band at 298 nm after the addition of 0.3 equivalents of Tb(III), which points towards the stability of the species generated in solution at a 1:3 metal:ligand stoichiometry. Three isosbestic points at 232nm, 247 nm and 286 nm were also observed, indicating the presence of two species in solution: likely, the free ligand the and 1:3 metal:ligand species. This speciation in solution was elucidated further by fitting the data using non-linear regression analysis, described in Section 5.5.3; however, the major changes occur in the UV-visible absorption spectrum up to the addition of 0.3 equivalents of Tb(III), and no significant changes were observed after this equivalency, indicating indeed that the likely complex formation is the 1:3 metal:ligand species in solution.

5.6.2 Tb(III)-centred luminescence titrations (fluorescence and time-gated emission)

Upon excitation of the ligand **190** at $\lambda = 237$ nm, ligand centred emission was observed, with a band centred at $\lambda = 319$ nm (Figure 5.7). This ligand luminescence was affected by the self-assembly process, which was evidenced by a quenching of the ligand fluorescence upon addition of Tb(III). Upon addition of 0.3 equivalents of Tb(III), a 96% reduction in the emission was observed. This can be attributed to energy transfer from the ligand **190**, to the Tb(III) metal centre upon self-assembly, giving rise to the characteristic Tb(III)-centred emission *via* indirect excitation. Simultaneously, the evolution of the Tb(III)-centred
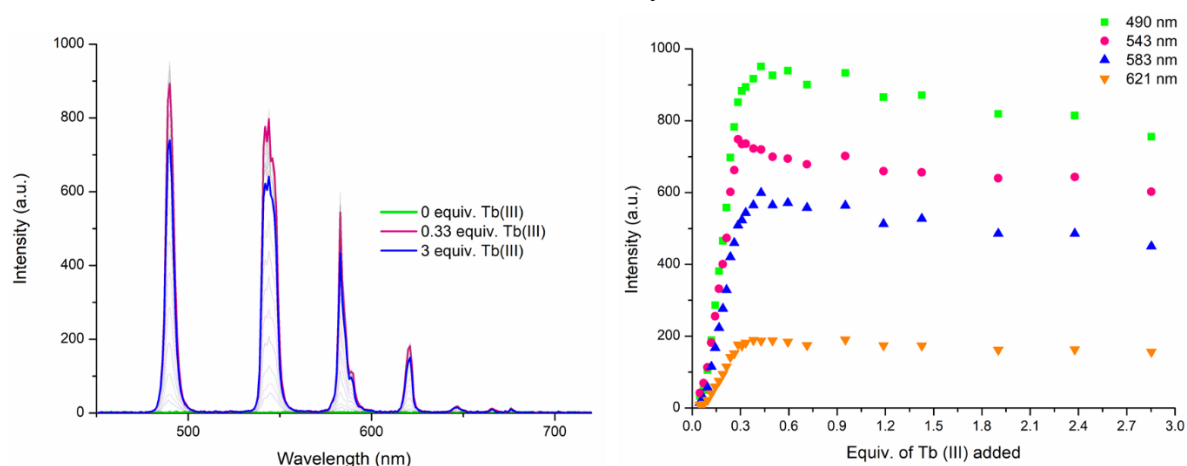
Figure 5.7 *(Left) The overall changes to the Tb(III)-centred phosphorescence spectra upon titrating* ***190*** *(1×10^{-5} M) against Tb(CF$_3$SO$_3$)$_3$ (0→3 equiv.) in CH$_3$CN at 22˚C. (right) corresponding experimental binding isotherms of phosphorescence at $\lambda = 490, 545, 583$ and 621 nm.*

emission was observed in the fluorescence spectra further demonstrating the capability of ligand **190** to sensitise the Tb(III)-centred emission.

The delayed Tb(III)-centred luminescence was also recorded upon excitation at 237 nm, and the resulting spectra and binding isotherms can be seen in Figure 5.7. A gradual enhancement in the Tb(III) luminescence was observed from 0 to 0.3 equivalents of Tb(III), with characteristic Tb(III)-centred emission bands appearing at $\lambda = 490, 545, 583, 620, 646,$ 665, and 675 nm which correspond to deactivation from the $^5D_4$ excited states to the ^7F_J states (where J = 6 – 0). The $^5D_4{\rightarrow}^7F_{2-0}$ bands are typically weak and not always seen in titrations, but they can be clearly observed in this system. Subsequent additions of Tb(III), from 0.3-3.0 equivalents, resulted in quenching of the luminescence intensity by approximately 20%. The most emissive state in solution was seen at approximately 0.3 equivalents of Tb(III), which is consistent with previously reported **btp**-Tb(III) systems, and is likely due to the existence of a stoichiometric species in which the Tb(III) ion is coordinatively saturated, and thus almost completely shielded from solvent quenching. Lifetime measurements obtained at 0.3 equivalents of Tb(III) gave a value of $\tau = 1.85$ ms, which is very close to the lifetime measured for the $[Tb(\mathbf{190})_3]^{3+}$ complex in Section 5.4, indicating the formation of a 1:3 assembly in solution. Again, these data were fit using non-linear regression analysis software and the results are discussed in Section 5.5.3.

5.6.3 Non-linear regression analysis of the experimental data for 190 with Tb(III)

As discussed in previous Chapters, the changes observed in the UV-visible absorption spectra and Tb(III)-centred emission spectra could be analysed with respect to established binding models. A global analysis method was used in order to provide a robust estimation of the species existing in solution and the stability constants corresponding to these species. Concentration profiles for each stoichiometric species in solution were also established. This analysis was completed with ReactLab EQUILIBRIA software.

Analysis of the UV-visible absorption data of **190** titrated with Tb(CF$_3$SO$_3$)$_3$ in CH$_3$CN solution pointed to the presence of three main species in solution (**190**, 3:1 metal:ligand and 1:1 metal:ligand ratios) with the distribution of these species estimated from this analysis. From 0.15 equivalents to the addition of 0.3 equivalents of metal solution, the ML$_3$ species was the most dominant in solution, reaching 97% abundance at 0.3 equivalents of Tb(III) (Figure 5.8). Subsequent additions of excess Tb(III) resulted in a dissociation of the ML$_3$ species and an increase in the abundance of the ML species. From
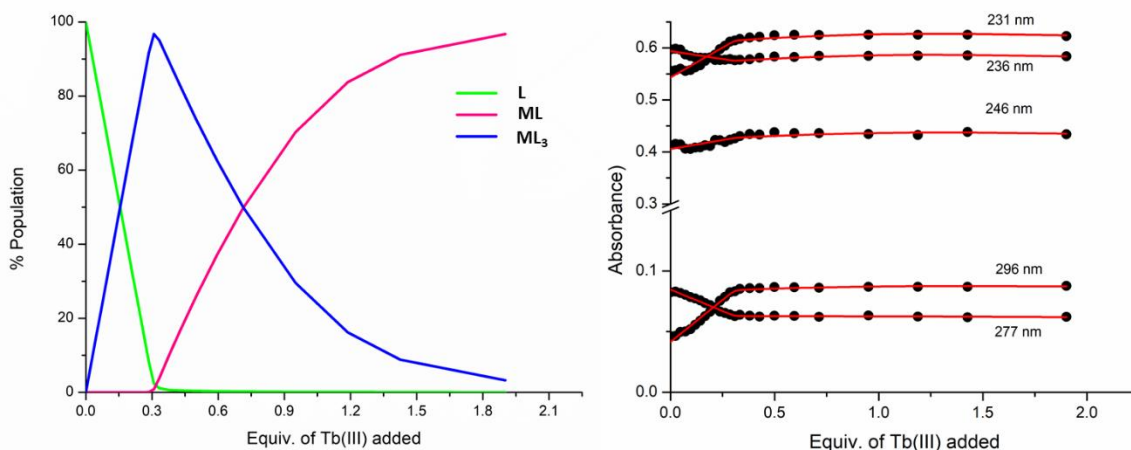
Figure 5.8 (Left) The speciation distribution diagram obtained from the fit of the UV-visible absorption titration data of ligand 190 against Tb(CF₃SO₃)₃ in CH₃CN. (Right) The fit of the experimental binding isotherms using non-linear regression analysis software ReactLab.

0.7 equivalents of Tb(III) the 1:1 metal:ligand species was the most prominent in solution, reaching 96% abundance at 2.0 equivalents of Tb(III) added. This indicates that the initial formation of the highly emissive ML_3 species in solution is followed by partial dissociation to the ML species upon addition of excess Tb(III). This data could not be fit acceptably if an intermediate ML_2 species was included in the model. While this is somewhat surprising, it is most likely due to the relatively small changes seen in the UV-visible absorption spectra at 298 nm with the main changes occurring at 230 nm. From the changes observed in the UV-visible absorption spectra throughout the titration, binding constants were estimated for each species.

The 1:3 metal:ligand assembly formed with $log\beta_{13} = 23.1\pm0.6$, which is in good agreement with binding constants reported for similar **btp** systems in the literature with Tb(III). The second species (1:1 metal:ligand) had a calculated binding constant of $log\beta_{11} = 8.3\pm0.2$, which is a value that is also in good agreement with previously reported Tb-**btp** assemblies.[177] The calculated and experimental binding isotherms are shown in Figure 5.8 and indicate an excellent fit of the calculated and experimental data.

Analysis of the changes observed in the Tb(III)-centred emission were also carried out (Figure 5.9) and indicated the presence of four main species in solution, (**190**, 3:1 metal:ligand, 2:1 metal:ligand and 1:1 metal:ligand species) which differs from the three species estimated from the UV-visible absorption data. From 0.15 equivalents to 0.3 equivalents of Tb(III), the ML_3 species was the most predominant in solution, reaching an abundance of 96% at 0.3 equivalents which is in agreement with the speciation estimated
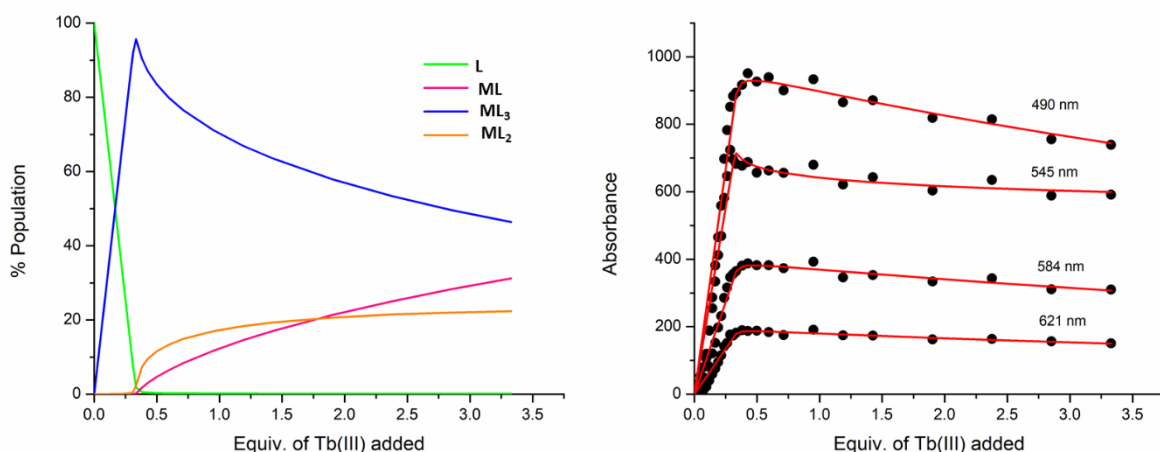
Figure 5.9 *(left) The speciation distribution diagram obtained from the fit of the Tb-centred phosphorescence titration data of ligand **190** against Tb(CF₃SO₃)₃ in CH₃CN. (right) the fit of the experimental binding isotherms using non-linear regression analysis software ReactLab.*

from the fitting of the UV-visible absorption data. Upon subsequent additions of Tb(III), an evolution of the 1:2 species was observed, which reaches 20% abundance at the addition of 1.5 equivalents of metal solution before reaching a plateau. The evolution of the 1:1 species occurred almost simultaneously with the 1:2 species; however, it is less predominant until the addition of 1.8 equivalents of Tb(III), after which point it continues to increase with a concomitant decreasing of the 1:3 species. From the changes observed in the phosphorescence spectra throughout the titration, binding constants were estimated for each species.

The 1:3 metal:ligand assembly formed with $\log\beta_{13}$ = 22.7, the second species (1:2 metal:ligand) had a calculated binding constant of $\log\beta_{12}$ = 14.5 ± 0.1, and the 1:1 metal:ligand species has a binding constant of $\log\beta_{11}$ = 7.0. The stability constants are roughly additive, suggesting that the binding process of each ligand to the metal centre was subject to a similar formation constant. The calculated and experimental binding isotherms were also in good agreement (Figure 5.9). The Tb(III)-centred emission data indicated the formation of the ML₃ species initially, which was the most emissive species in solution. This assembly then dissociated into the ML₂ species and subsequently the ML species upon addition of excess Tb(III). However, the speciation does not correlate well with the speciation estimated from the changes in the UV-visible absorption data. As mentioned above, no acceptable fit was obtained when the ML₂ species was included in the UV-visible absorption data model. The reliability of this fit should therefore be considered with caution. The changes in the UV-visible absorption spectra were not large and the resulting speciation

189

therefore may not be fully representative of the speciation in solution. The speciation obtained from the Tb(III)-centred emission spectral data, can be considered a more accurate representation of the likely speciation in solution.

5.6.4 Quantum Yield

The photoluminescence quantum yield (Φ_{tot}, %) was determined in CH_3CN using a relative method reported by Bünzli and co-workers using $Cs_3[Tb(\textbf{dpa})_3]\cdot 9H_2O$ as the standard.[78,79] The relative method for quantum yield determination is described in Chapter 4, equation 4.1. The quantum yield for this system was determined following self-assembly of the 1:3 species in solution at high concentration (1×10^{-4} M). The luminescence lifetime (τ_{obs}) of the assembly was determined to be monoexponential and highly similar to the lifetimes of the $[Tb(\textbf{190})_3]^{3+}$ complex determined in Section 5.5.1. The complex was stable over 48 hours. The relative quantum yield of a 1:3 assembly of compound **190** with $Tb(CF_3SO_3)_3$ was determined to be 72 % which is very close to relative quantum yields reported for other 1:3 Tb:**btp** compounds in CH_3CN.[176] The values obtained are an average of three measurements.

5.7 Formation of organogel 189 in CH₃CN

Before covalent attachment to the polymer matrix, the gelation ability of compound **189** was examined under a series of conditions. Compound **189** was suspended in a variety of solvents and subject to different gelation conditions including heating and sonication. Suspension of **189** in CH_3CN solution, followed by sonication, resulted in the formation of an off-white soft material almost immediately. Following this result, the optimum concentration for gelation was determined. Compound **189** (16 mg) was suspended in CH_3CN (1 mL) and sonicated for 60 seconds to yield an opaque gel that was robust to the naked eye. The inversion test was performed, and the gel supported its own weight over several hours. The thermoreversibility of the gel was investigated by heating the material to up to 60 ˚C. Upon heating the gel dissolved and, after standing at room temperature for 15 minutes, the gel reformed indicating that the gel formation was thermoreversible.

In order to investigate the wt% at which the gel forms, TGA was carried out on the material. TGA was carried out in the temperature range of 15 to 500 ˚C, and a loss in mass of 96.2 % was observed at 100 ˚C, indicating the gel was formed at 3.8 wt% of **189**. However, as the gel was prepared at 1.6 wt%, this experiment indicates that the gel does not retain all of the solvent in the sample. While inverting the gel upon formation did not result
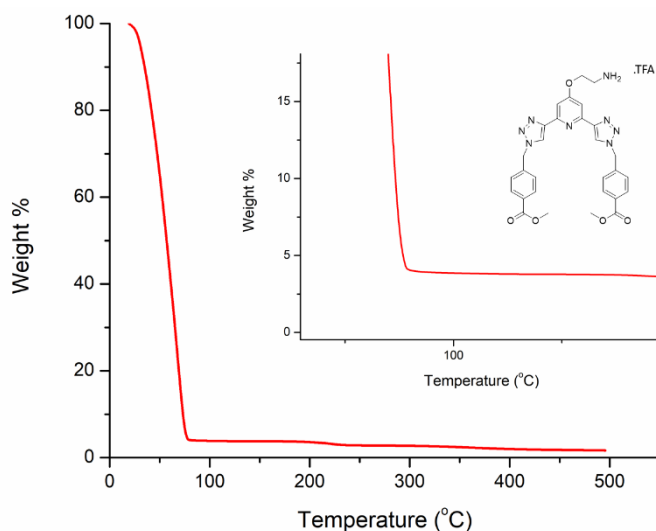
Figure 5.10 TGA thermograph of *189* gel showing weight loss of 96.2% before 100 ˚C.

in any loss of residual solvent, solvent was observed to be squeezed out of the material when the gel was disturbed by removal from the vial in which it was prepared.

A xerogel of compound **189** in CH₃CN was also generated by drying the sample under vacuum in order to study the morphology of the system by SEM. The SEM images (shown in Figure 5.11) show the fibrous, entangled nature of the gel structure. This morphology is typical of supramolecular gels in which non-covalent interactions are involved in forming cross-links within the structure immobilising the solvent. At higher wt% (Figure 5.11 right) white spots on the fibres were observed which are likely salt.

In order to examine the mechanical properties of the gel, rheological experiments were conducted in collaboration with Dr. Niamh Fox and Dr. Ronan Daly. The gel was generated at 3.8 wt% and an amplitude sweep was conducted in order to confirm the gel-like behaviour of the material. This experiment determines the deformation behaviour of the sample in the non-destructive deformation range as well as the upper limit for the strain applied to the sample. The strain on the sample was increased in a stepwise fashion, while
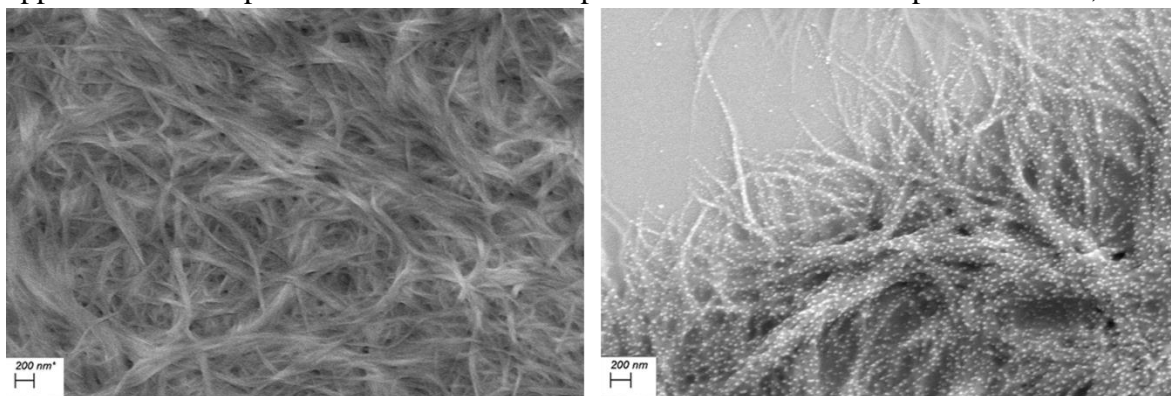
Figure 5.11 SEM images of *189* gel (scale bar 200 nm) showing fibrous structure of the material and salt on the surface of the fibres.
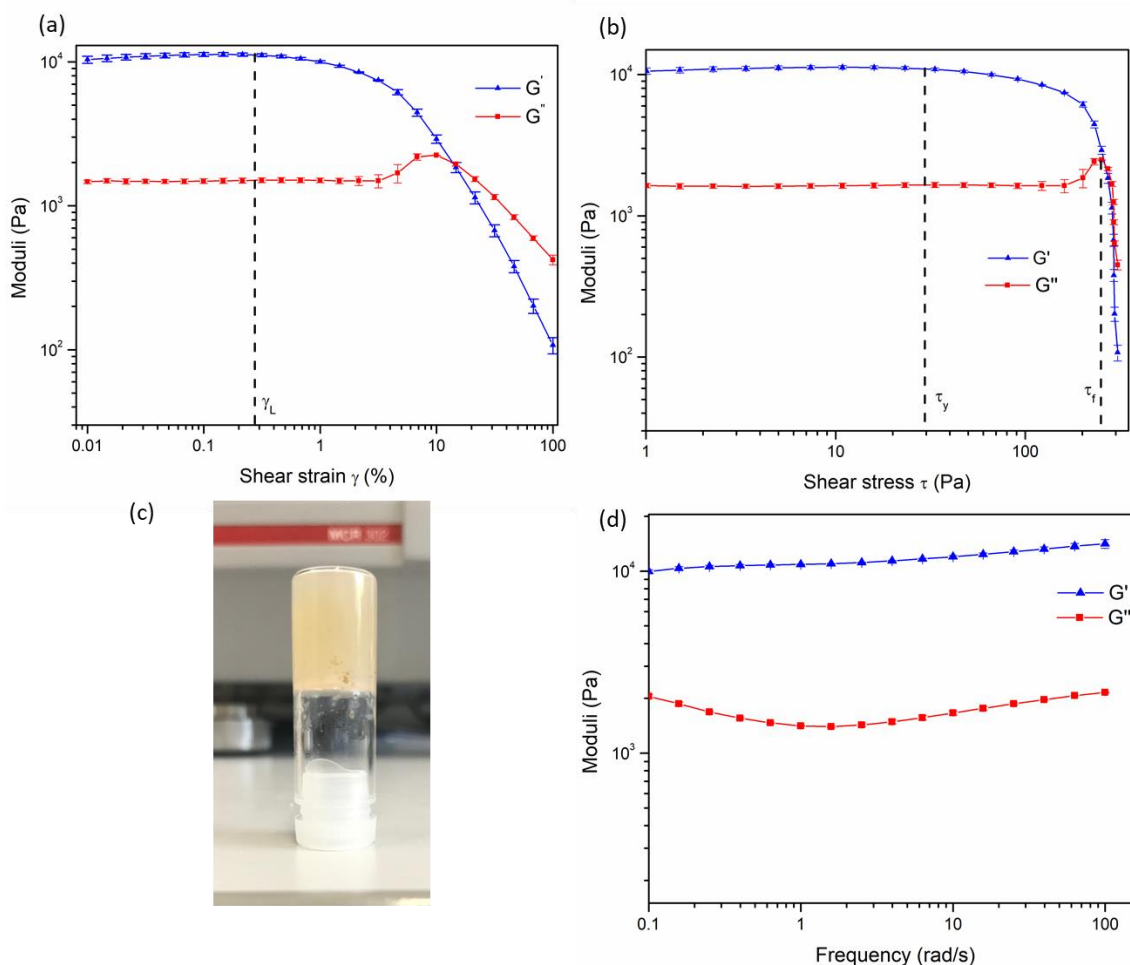
Figure 5.12 *(a) Amplitude (strain) sweep experiment of **189** gel showing the linear viscoelastic region (γ$_L$) and confirming the behaviour of the material as a gel. (b) Amplitude (stress) sweep showing yield point (τ$_y$) and flow point (τ$_f$) of the material (c) Image of the gel during inversion test (d) Frequency sweep experiment demonstrating that G' increases with increased frequency.*

the frequency was kept constant. In Figure 5.12 it can be seen that the storage modulus, G′ was larger than the loss modulus, G″, which indicates that the material can be classified as a gel or a viscoelastic solid material (G′ = 1.09 × 10^4 Pa and G″ = 1.46 × 10^3 Pa). The limit of the linear viscoelastic region (LVE, labelled γ$_L$ in Figure 5.12), which is the range in which further tests can be carried out on the sample without destruction of the sample, was determined to be 0.3% for this sample. After this point, G′ and G″ begin to converge and the material starts to flow. From the graph of G′ and G″ *vs* shear stress (t), in Figure 5.12, the yield point and flow point of the material can be determined. The yield point, τ$_y$, is value of shear stress at the limit of the LVE region. For this material its value was determined to be 28 Pa, and the flow point, τ$_f$, was observed to be 253 Pa. A frequency sweep experiment was also conducted to gain an insight into the long-term stability of the gel. Having determined

192
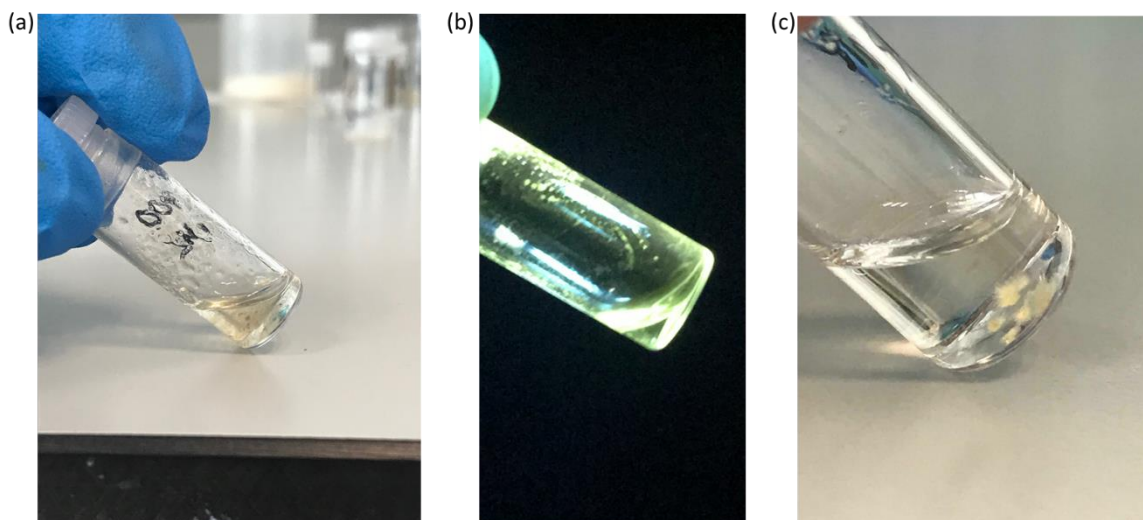
Figure 5.13 *(a) Image of the gel which solubilised upon addition of Tb(CF₃SO₃)₃ (b) green emission from the solution following addition of Tb(CF₃SO₃)₃ to* **189** *gel under UV-irradiation (λ_ex = 254 nm) (c) crystals of* **189** *formed from low wt% gel overnight.*

that the limit of the LVE region was 0.3%, the amplitude was set at 0.1%. As seen in Figure 5.12, $G' > G''$ over the entire frequency range, which indicates that the material has a cross-linked structure. Rheological tests were repeated three times with three gel samples to ensure reproducibility.

Having formed an organogel, the possibility of forming a supramolecular metallogel with Tb(III) was investigated. A solution of Tb(CF₃SO₃)₃ was added to the pre-formed organogel. Upon standing overnight, the gel dissolved to a solution, which emitted green light under UV-irradiation (λ_{exc} = 254 nm), as seen in Figure 5.13. This indicates the formation of a Tb(III) complex which, likely breaks-down the network of interactions which otherwise generate the supramolecular soft-material upon formation. Addition of Tb(III) salts to the compound **189** followed, by addition of CH₃CN, and sonication did not result in metallogel formation.

5.8 Crystal structure of 189

When the organogel was formed at low wt% (<1.5 wt%), a gel-to-sol transition occurred overnight, and yellow crystals were formed in a colourless solution. These crystals were examined by X-ray diffraction and were found to be crystals of **189**. This crystal structure was solved by June Lovitt. The structure was solved in the monoclinic $C2/c$ space group, with the asymmetric unit containing one complete molecule of **189**, as well as one TFA anion, and a molecule of CH₃CN. A hydrogen bonding interaction exists between the oxygen atom of the TFA molecule, O43 and the NH₃⁺ of compound **189**, with an N···O distance of
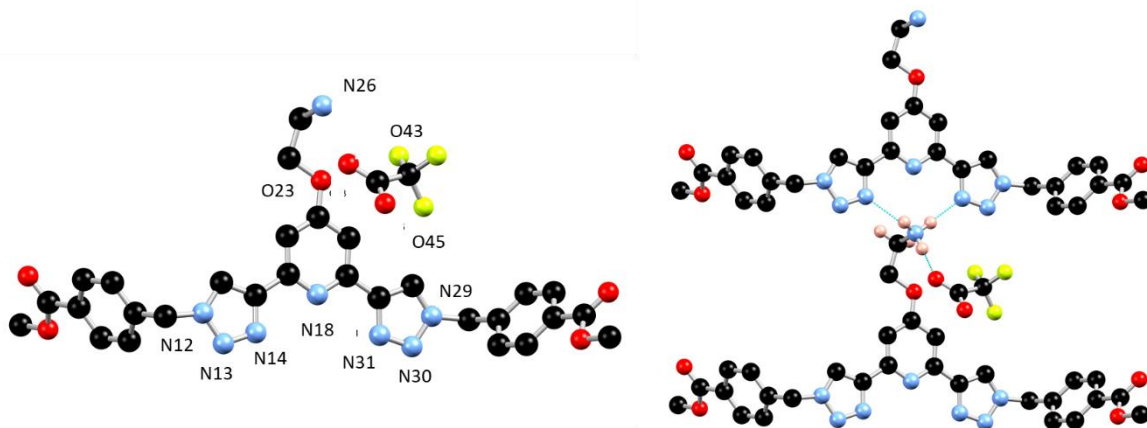
Figure 5.14 *(Left) Structure of one unique molecule of compound **189** with heteroatom labelling scheme and all hydrogen atoms omitted for clarity. (Right) Hydrogen bonding interaction between molecules. Selected hydrogen atoms omitted for clarity.*

2.793(5) Å and an N-H···O angle of 175.3(3)°. Unexpectedly, the triazoles in ligand **189** adopt a *syn-syn* conformation. **Btp** ligands have been most commonly reported in the *anti-anti* conformation, but in the presence of a cation such as a metal ion or a proton, the triazoles can adopt the *syn-syn* conformation.[40] In this case, the RNH_3^+ of one ligand molecule, and the triazole N14 and N31 nitrogen atoms of another ligand, form a hydrogen bonding interaction with an N···N distance of 2.998(6) and 2.885(6) Å, respectively, which causes the triazoles to adopt the *syn-syn* conformation.

5.9 Polymer Film

As described in the introduction to this chapter, previous work in the Gunnlaugsson group had focused on incorporating a **btp** Ln(III) complex $[Tb(\mathbf{140})_3]^{3+}$ into a polymer matrix. Combining this Tb(III) complex with a naphthyl-**dpa** Eu(III) complex, $[Eu(\mathbf{153})_3]^{3+}$ within a p(HEMA-*co*-MMA-*co*-EGDMA) polymer organogel, generated a [H⁺] and [F⁻] dual-responsive system. These ligands were selected due to their capacity to efficiently, and distinct sensitise Tb(III) or Eu(III). Indeed, the bis-(naphthyl-**dpa**) ligand has shown excellent Eu(III) emission sensitization abilities but it is less effective, however, at sensitising Tb(III). By contrast, **btp** derivatives can sensitise both Tb(III) and Eu(III), but the **btp** excited-state is significantly more efficient in the sensitisation of Tb(III) than Eu(III). These features meant that, upon non-covalent inclusion of $[Eu(\mathbf{153})_3]^{3+}$ and $[Tb(\mathbf{140})_3]^{3+}$ into a p(HEMA-*co*-MMA-*co*-EGDMA) organogel in CH_3OH, four logic states were possible which emitted with four distinct colours visible under UV irradiation. While this work showed promise in the first steps toward a robust molecular logic gate mimic using 4*f* ions

as outputs, limitations of this system nevertheless exist. In particular, this system was susceptible to leeching of compound **140** from the organogel under certain conditions, due to dissociation of the $[Tb(\mathbf{140})_3]^{3+}$ complex. In order to overcome this issue, covalently tethering the **btp** ligand to the polymer matrix was considered. Compound **189** was envisaged as a target for this purpose, wherein reaction with a methyacrylamide unit would generate a covalent bond between the polymer and the **btp** ligand while retaining the same analyte interactions as compound **140**.

5.9.1 Comparison of the photophysical properties of $[Tb(\mathbf{190})_3]^{3+}$ and $[Tb(\mathbf{140})_3]^{3+}$

Compound **190** was synthesised as an analogue of which would simulate the behaviour of compound **189** once it was covalently attached to the polymer backbone. Synthesis and characterisation of complex $[Tb(\mathbf{190})_3]^{3+}$ was as described in Section 5.3. Its photophysical properties were examined and are summarised.

The photophysical properties of compound **190** with $Tb(CF_3SO_3)_3$ were compared to those of compound **140** to confirm that compound **190** would be suitable for inclusion in the polymer to generate a logic gate mimic. The UV-visible absorption spectrum of **190** was recorded at $c = 1 \times 10^{-5}$ M in CH_3OH (Figure 5.15) and this spectrum was compared to the spectrum of **140** (Figure 5.15). The two spectra showed similar features, with two main bands observed at $\lambda = 230$ nm and $\lambda = 300$ nm. Coordination of the ligand **190** to Tb(III) resulted in a shift in the band at $\lambda = 230$ nm to 237 nm. The band at $\lambda = 300$ nm underwent a hyperchromic shift and concomitant redshift. In the case of compound **140** when complexed to Tb(III) both bands at $\lambda = 300$ nm and $\lambda = 230$ nm experienced a red shift and simultaneous increase in absorbance. The ligand fluorescence of compound **190** was found
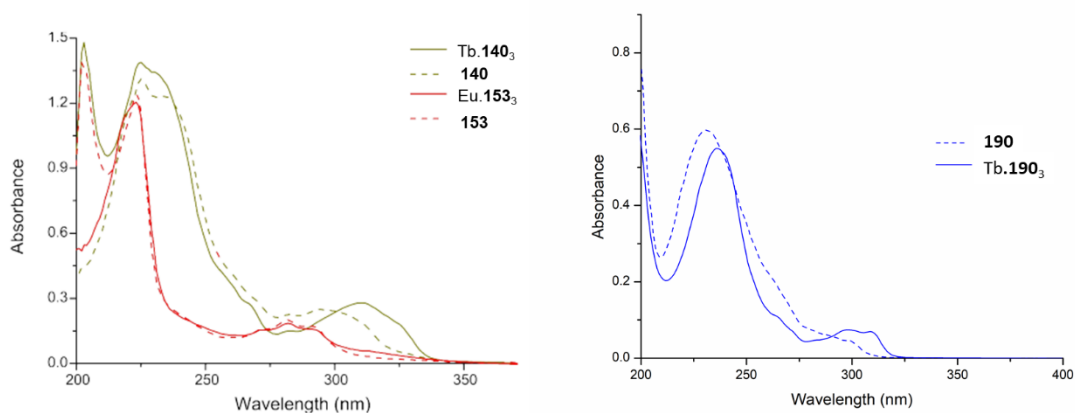
Figure 5.15 *(left) Overlaid UV-vis absorbance spectra of **140**, **153**, Tb.**140**₃ and Eu.**153**₃ recorded in CH₃OH and (right) UV-vis absorbance spectra of **190** and Tb.**190**₃ also recorded in CH₃OH showing a similar absorbance profile to that of **140** and Tb.**140**₃.*
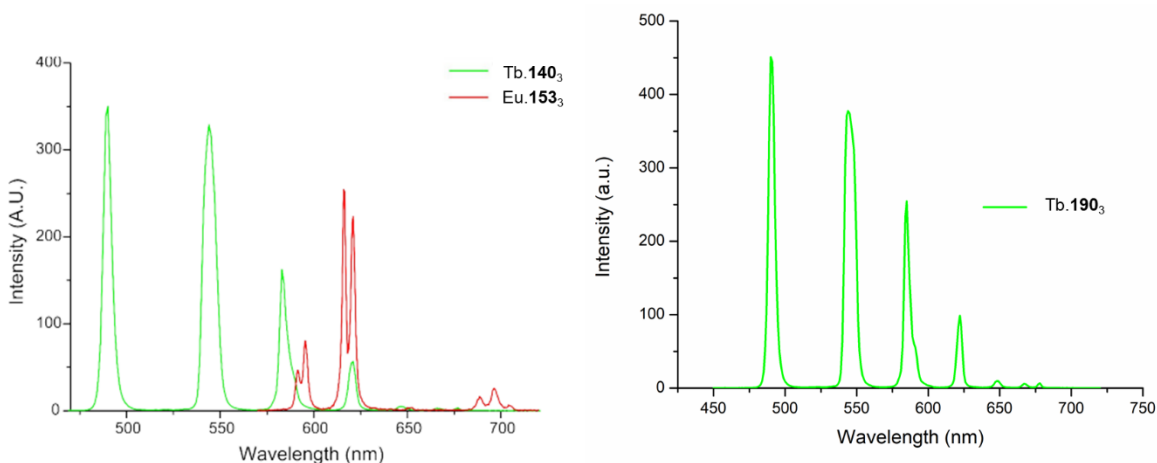
Figure 5.16 *(Left) overlaid phosphorescence spectra of Tb.**140**₃ and Eu.**153**₃ recorded in CH₃OH and (right) phosphorescence spectrum of Tb.**190**₃.*

to be blueshifted by 1985 cm^{-1} (20 nm) when compared to the ligand emission from compound **140** and in both cases the sensitisation of Tb(III) resulted in characteristic transitions resulting from $^5D_4 \rightarrow {}^7F_{6\text{-}2}$ as seen in Figure 5.16. Due to the similarities in the photophysical behaviour of $[\text{Tb}(\mathbf{190})_3]^{3+}$ and $[\text{Tb}(\mathbf{140})_3]^{3+}$, it was anticipated that compound **190** would be an excellent candidate for covalent inclusion in the gel matrix while also generating the same response to analytes as $[\text{Tb}(\mathbf{140})_3]^{3+}$.

5.9.2 Organogel inclusion

In the case of compound **140** previously, Tb(III) complex $[\text{Tb}(\mathbf{140})_3]^{3+}$ was generated and isolated before non-covalent inclusion in the gel matrix. However, in this case compound **189** was covalently attached to the polymer and the Ln(III) ions were introduced to the resulting hard polymer film through swelling in a solution of Tb(III) or Eu(III). Firstly, compound **189** was reacted with methacryloyl chloride for three hours in the presence of triethylamine, in order to install the amido-methacrylate moiety, and generate the monomer **199**. The reaction mixture was concentrated under reduced pressure and the crude product was extracted into CHCl₃. The compound was purified by column chromatography to yield compound **199** as a white solid in 63% yield. Formation of the desired product was confirmed by ^{1}H NMR spectroscopy (see Appendix Figure A5.12). Two singlet peaks at 5.68 and 5.34 ppm corresponding to the alkyne protons, and a peak at 1.85 ppm assigned to the CH₃ of the methacrylate moiety, confirm the presence of compound **199**. The appearance of a triplet at 8.17 ppm corresponding to the amide proton was also observed. Finally, a shift in the CH₂ protons which reside at 3.24 ppm in compound **189** to 3.56 ppm in compound

196
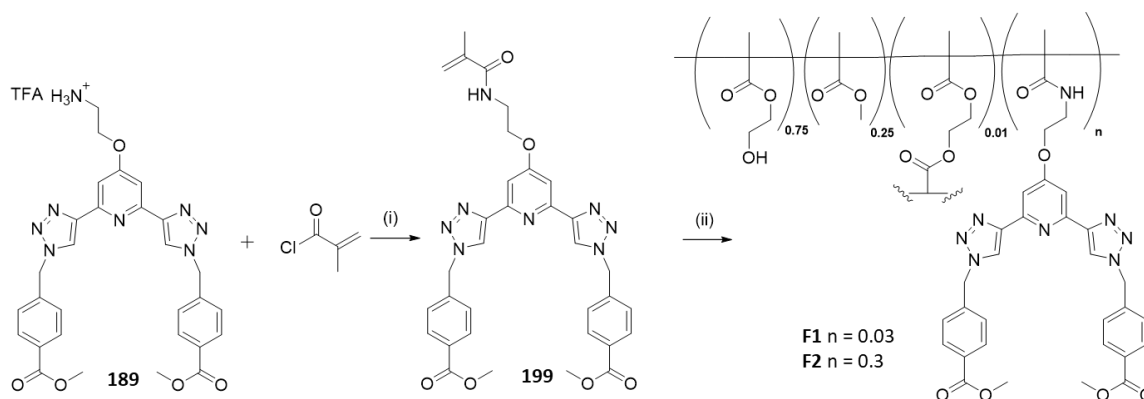
Scheme 5.4 *Synthesis and structure of compound **199**, **F1** and **F2**. Reagents and conditions: (i) NEt₃, CH₂Cl₂ (ii) 80 ˚C 6 hours.*

199 was also observed. The product was also characterised by $^{13}C\{^1H\}$ NMR spectroscopy, HRMS and IR spectroscopy (Appendix Figure A5.13).

The self-assembly of compound **199** with $Tb(CF_3SO_3)_3$ was also investigated in CH_3CN solution, as described above for compound **190** in Section 5.6. The changes to the UV-visible absorption, fluorescence, and time-gated emission spectra were very similar to those shown for compound **190** with Tb(III), and are thus shown in the Appendix (Figure A5.14-5.16). The data was fit using non-linear regression analysis, and four species were again estimated to be present in solution from this global analysis (**199**, 1:3 metal:ligand species, 1:2 metal:ligand species and 1:1 metal:ligand species), from which the binding constants could be estimated. The values were found to be in good agreement with those found for compound **190** with Tb(III). The 1:3 metal:ligand assembly formed with $\log\beta_{13} = 21.44 \pm 0.1$, the second species (1:2 metal:ligand) had a calculated binding constants of $\log\beta_{12} = 14.69 \pm 0.1$ and the 1:1 metal:ligand species had a binding constant of $\log\beta_{11} = 7.06 \pm 0.1$. The spectra, binding isotherms, and corresponding fit plots are shown in the Appendix Figure 5.14-5.16.

Having synthesised the monomer **199**, it was employed to generate two polymers at two different wt% of compound **199**. The first polymer film (**F1**) was synthesised at 0.3 wt% of compound **199**, while the second polymer film (**F2**) was formed at 0.03 wt%. The polymer films, **F1** and **F2**, were generated by suspending compound **199** (0.3 wt% or 0.03 wt%) in a mixture of 74% HEMA, 25% MMA (v/v) and 1 wt% ethylene glycol dimethacrylate (EGDMA). EGDMA acts as a cross-linker. The mixture solubilised over time with stirring and after solubilisation, Azobisisobutyronitrile (AIBN) at 1% w/w was added. The solution was transferred into a glass mould which was coated with a non-stick PE-based coating and thermal polymerisation was initiated at 80 ˚C in the oven. After 6 hours the material was

197

allowed to cool to room temperature and the hard material was released from the mould. The resulting monolith was transparent and hard, as shown in Figure 5.17, but when soaked in deionised water the polymer swelled and a soft, flexible material was obtained (Figure 5.17).

The monolith was soaked in deionised water over two days to remove any unreacted monomers and inhibitor. Examination of the supernatant by UV-visible absorption and fluorescence spectroscopy did not reveal the presence of any ligand monomer in the solution, indicating that the compound was not prone to leeching from the polymer material in water and it is likely that all of the monomer **199** was co-polymerised in the reaction. However, initial characterisation of the material by UV-visible absorption, ligand fluorescence, and time-gated luminescence spectroscopy revealed an absorption band at $\lambda_{abs} = 292$ nm and emission band at $\lambda_{em} = 565$ nm which could not be assigned to compound **199** or the HEMA-co-MMA-co-EGDMA polymer backbone. These bands were suspected to have arisen from the polymerisation of the inhibitor 4-methoxyphenol (MEHQ) which is present in the methacrylol chloride starting material at 200ppm. As soaking the polymer in water was not sufficient to remove this impurity, the hard polymer was soaked in CH_3OH overnight (Figure 5.18). This process was successful, removing the 4-methoxyphenol completely from the matrix, with no observation of leeching of the ligand monomer **199** from the polymer in the CH_3OH supernatant. Presence of the **btp** compound **199** in the polymer was confirmed by a fluorescence band centred at $\lambda_{em} = 323$ nm upon excitation at $\lambda_{ex} = 285$ nm which was at a very similar wavelength to the fluorescence band observed for the free compound **190** at $\lambda = 320$ nm. As the p(HEMA) matrix absorbs wavelengths up to 250 nm, UV-visible absorption spectroscopy was not a useful tool for the characterisation of the material.
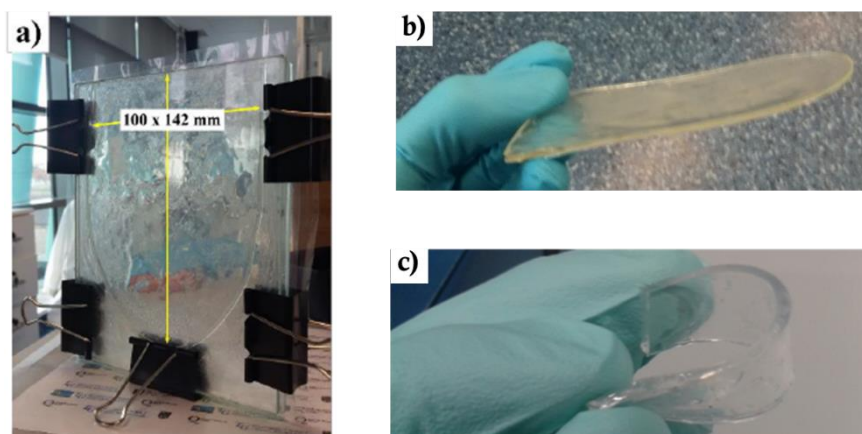
Figure 5.17 *(a) Photograph of cast used to fabricate polymer made from glass and lined with a nono-stick coating (b) Hard and transparent polymer monolith before soaking in solvent (c) Flexible and transparent polymer after soaking in solvent.*

Having confirmed the inclusion of the ligand **199** in the polymer matrix, the ability of the hard dehydrated polymer to uptake Ln(III) ions was investigated. The dry polymer was soaked in an aqueous solution of Tb(CF$_3$SO$_3$)$_3$ and after 10 minutes the resulting soft, flexible polymer was examined under UV-irradiation at λ_{exc} = 254 nm. The film exhibited bright green emission under UV-light, indicating that self-assembly of the monomer **199** with Tb(III) occurred, with sensitisation of the Tb(III) ion occuring either on the surface of the polymer or within the polymer film itself. Similarly, soaking the polymer in a Eu(CF$_3$SO$_3$)$_3$ solution resulted in the characteristic red emission of Eu(III) under UV-irradiation. While the colour changes appeared homogenous to the naked eye, further photophysical characterisation were carried out to determine the nature of the Tb(III) complexes formed *in situ,* whether the Tb(III) metal ions had diffused into the polymer matrix, and if so, whether the ions that were taken up into the polymer matrix had formed complexes of Tb.**199** which caused a "switching on" of the Tb(III)-centred emission.

5.9.3 Photophysical Studies of F1 and F2

In order to probe the uptake of Tb(III) or Eu(III) into the polymer film, the film **F1** was soaked in a Tb(CF$_3$SO$_3$)$_3$ solution and the film's ligand-centred fluorescence, as well as the Tb-centred emission, were monitored in water. Excitation of the polymer at λ = 285 nm in water resulted in a ligand fluorescence band at λ = 323 nm, and after continuous soaking of the polymer in a solution of Tb(CF$_3$SO$_3$)$_3$ and transferring to a water solution, little change to the ligand-centred emission was observed over two hours (Figure 5.18). The delayed Tb(III)-centred luminescence was also recorded upon excitation at λ = 285 nm, and the spectrum can be seen in Figure 5.19. Characteristic Tb(III)-centred luminescence was
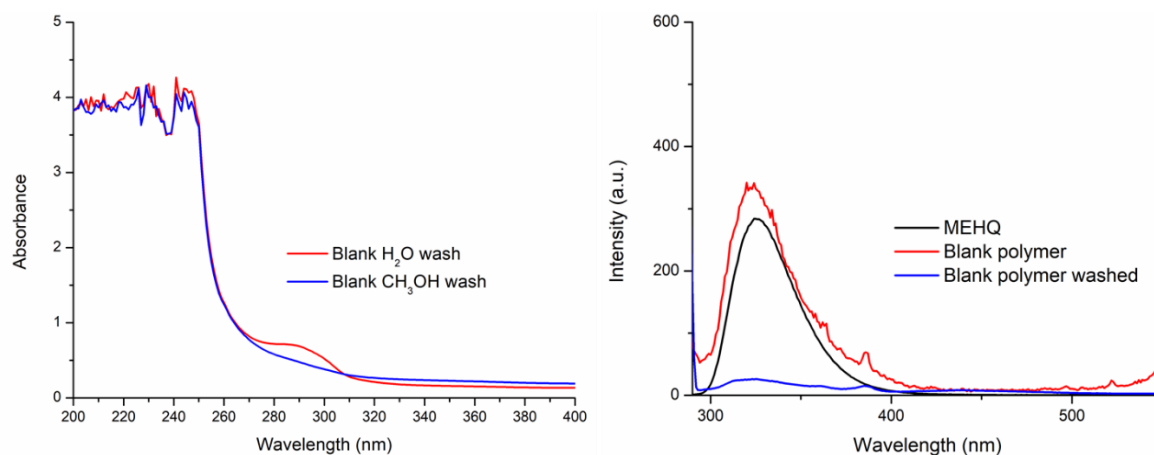
Figure 5.18 *(Left) UV-visible absorption spectrum of blank polymer before and after CH$_3$OH soak measured in H$_2$O (right) fluorescence spectrum of MEHQ, blank polymer before and after CH$_3$OH soak measured in H$_2$O.*

199
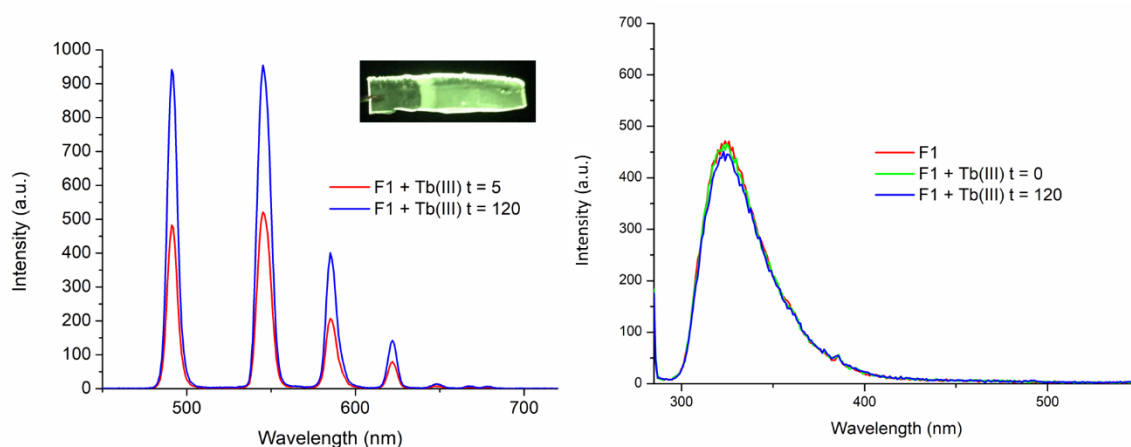
Figure 5.19 *(left) Tb(III)-centred phosphorescence spectra of **F1** over time measured in H_2O. (right) Fluorescence spectrum of **F1** over time measured in H_2O. Inset photograph of polymer following soaking in $Tb(CF_3SO_3)_3$ under UV-irradiation (λ_{exc} = 245 nm) showing green luminescence.*

observed upon soaking in $Tb(CF_3SO_3)_3$ for 5 minutes, and a gradual enhancement of the Tb(III)-centred luminescence occurred over 2 hours. Tb(III)-centred transitions at λ = 490, 545, 583, 620, 646, 665 and 675 nm, corresponding to deactivation from the $^5D_4$ excited states to the ^7F_J states (where J = 6 – 0) indicate sensitisation of the Tb(III) luminescence by the ligand monomer **199**. The films were stable in water, with no evidence of leeching of the monomer **199** from the polymer film into the supernatant, and no change in the intensity of the luminescence spectra was seen. This suggests that the Tb(III) ions underwent diffusion through the polymer film, and did not simply attach to the surface of the film. Thus, it is likely that self-assembly occurs within the polymer matrix, leading to the green luminescence observed.
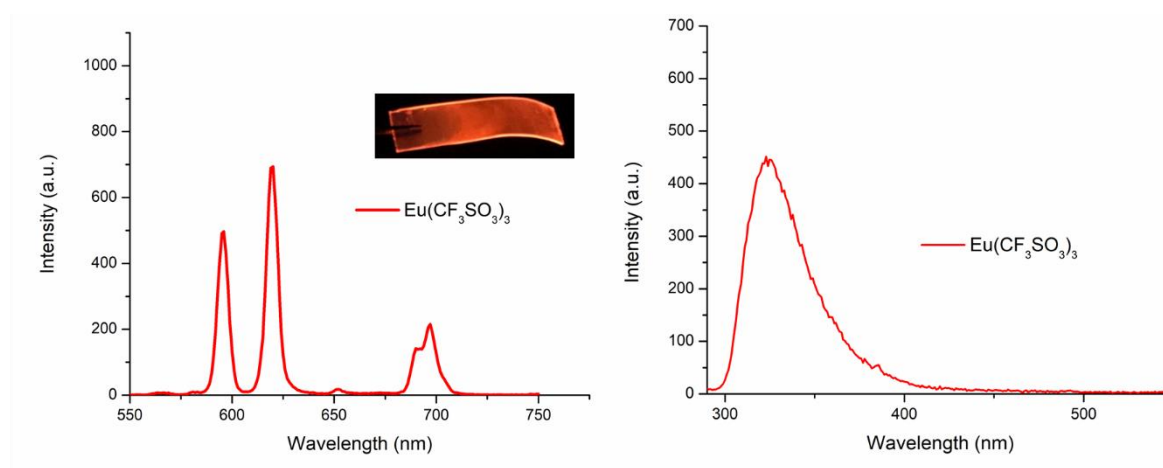
Figure 5.20 *(left) Eu(III)-centred phosphorescence spectrum of **F1** measured in H_2O. (right) Fluorescence spectrum of **F1** measured in H_2O. Inset photograph of polymer following soaking in $Eu(CF_3SO_3)_3$ under UV-irradiation showing red luminescence.*

200

Analogous experiments were repeated using $Eu(CF_3SO_3)_3$ under the same conditions, to confirm the uptake of Eu(III) into the polymer system, and its sensitisation by the monomer **199**. As before, the ligand-centred emission was not affected by the uptake of Eu(III) into the polymer matrix, and the fluorescence intensity remained the same over several hours. The delayed Eu(III)-centred luminescence was also recorded upon excitation at $\lambda = 285$ nm and the spectrum is shown in Figure 5.20. The Eu(III) luminescence was observed upon soaking the polymer in a solution of $Eu(CF_3SO_3)_3$ for 5 minutes, after continuous soaking of the polymer for 2 hours, an increase in the Eu(III)-centred emission was observed. Eu(III)-centred transitions appeared at $\lambda = 595$, 620, 652 and 695nm corresponding to the $^5D_0 \rightarrow {}^7F_J$ (J = 0 – 3) states characteristic of Eu(III) emission.

However, upon closer examination of the material it was found that the fluorescence and Ln(III)-centred luminescence intensities were not consistent across the polymer. Examination of different areas of the polymer film found that the intensities of Tb(III)-centred emission varied in different areas of the polymer. Covalent attachment of compound **199** to the polymer backbone was anticipated to generate a homogeneous film with HEMA, MMA, and EGDMA; however, dependence on convection for mixing of these viscous liquids during polymerisation to ensure a homogeneous dispersion of components throughout the film may not be adequate.

To examine the physical properties of the bulk material and analyse the distribution of the compound **199** throughout the material, the dry polymer was studied using differential scanning calorimetry (DSC). Using DSC, the glass transition temperature (T_g), and any phase-change behaviours of the polymer could be determined. Film **F2** and a blank HEMA-*co*-MMA-*co*-EGDMA polymer, which did not contain any of compound **199**, were analysed

Selected T_g values from 16 samples

Sample No. T_g temp	1	2	3 114 °C	4
	5	6 113 °C	7 117 °C	8
	9 114 °C	10	11 117 °C	12
	13	14	15 116 °C	16 116 °C
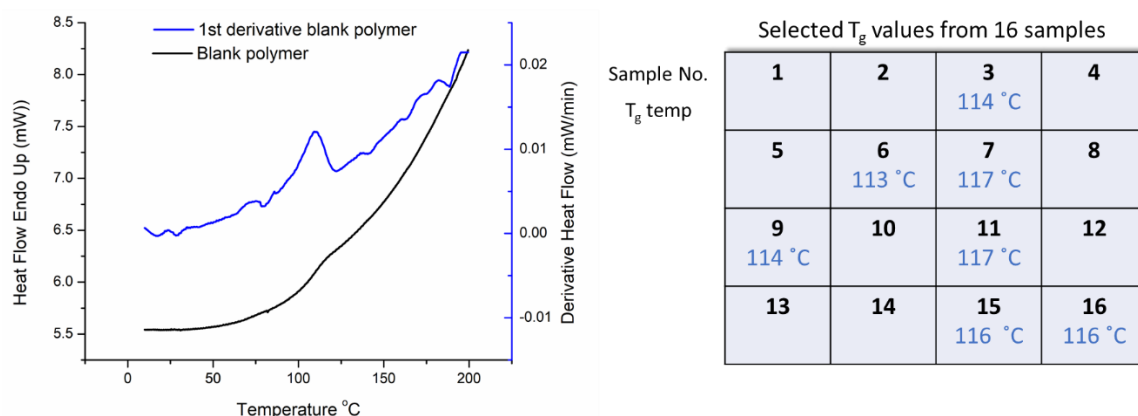
Figure 5.21 *(Left) Differential scanning calorimetry (DSC) curve recorded from solid samples of blank polymer (right) table of T_g temperatures from a selection of areas of polymer film **F1**. Each T_g temperature corresponds to the sample area in which it is located in the table.*

by heating in cycles from 10 to 200 ˚C. For the blank sample, a T_g was observed to occur at 109 ± 0.03 ˚C which was in close agreement with similar polymer systems reported in the literature.[271] To explore the homogeneity of the polymer samples, a section of the dry polymer **F2** was also selected and divided into 16 equal portions. A selection of these were analysed by DSC to examine the T_g values across the functionalised polymer. A table with the results is shown in Figure 5.21. No significant differences were observed in the T_g values across the polymer; however, the average value across the samples was found to be 116 ˚C, which is slightly higher than that of the blank polymer sample. Although there was no measurable variation in T_g across the samples which were measured, it is important to note that, while the glass transition temperature is reported as a single temperature, it is a region and so small changes to the T_g between samples may be difficult to determine. Also contributing to this is the low loading of **199** (0.3 wt%) at which this experiment was conducted. At higher loading variations in the T_g may be more easily measured. Unfortunately, while compound **199** was successfully co-polymerised with HEMA-co-MMA-co-EGDMA, and no leaching of the ligand from the polymer was observed, the irreproducibility of the photophysical measurements obtained from **F1** and **F2** rendered the outputs from this system unreliable and so it was not pursued further.

As discussed in Section 5.1 above, the most homogenous films were observed with more flexible matrices such as soft gel materials. For this reason, the next step was to covalently attach compound **189** to a commercially available polymer in solution for the generation of a viscous liquid or soft material as an alternative to the polymer films **F1** and **F2**.

5.10 Poly(ethylene-alt-maleic anhydride) grafted polymer

In an attempt to overcome the lack of homogeneity in films **F1** and **F2,** compound **189** was tethered to the polymer poly(ethylene-alt-maleic anhydride) (P(E-alt-MA)). The P(E-alt-MA) polymer is water soluble in moderate alkaline environments, as each anhydride moiety is converted into two carboxylate groups; however, an interesting application of this polymer is in rendering water soluble compounds insoluble for extraction from aqueous environments. The anhydride functionality of this polymer has been shown to react readily with even moderate nucleophiles, undergoing a variety of reactions including amidation, esterification, hydrolysis, thioesterification, and imidization,[272–277] generating a
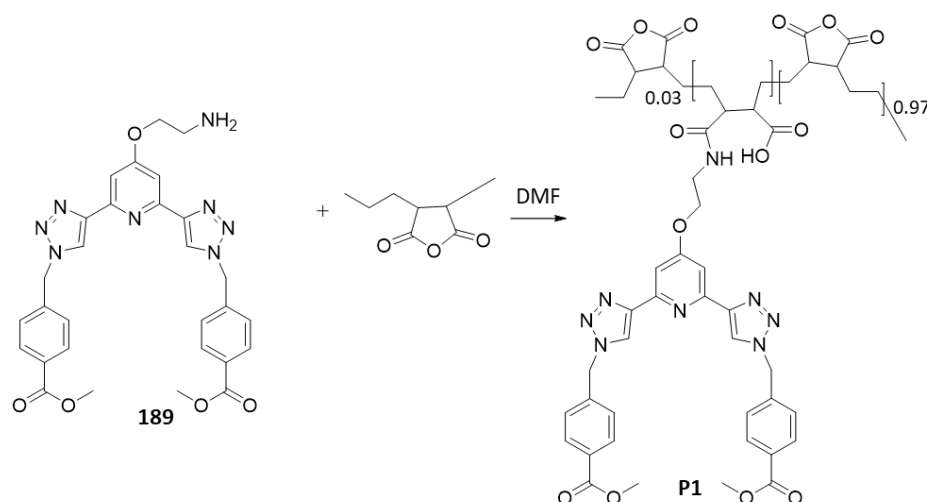
Scheme 5.5 *Synthesis and structure of **P1** conducted in anhydrous DMF.*

functionalised water-insoluble polymer. Applications for the functionalisation of the P(E-alt-MA) backbone include the formation of crosslinked polymer mixtures such as gate insulators for high performance thin film transistors,[278] water purification through functionalisation with sepia melanin,[279] and materials for pH controlled drug release.[280] With this in mind, compound **189** was reacted with poly(ethylene-alt-maleic anhydride) to generate polymers **P1** and **P2** with a low loading of compound **189**.

Poly(ethylene-alt-maleic anhydride) was dissolved in anhydrous DMF and to this 3 mol% of compound **1** was added dropwise. The reaction was complete after one hour and the polymer was isolated by dropping the reaction mixture into a 0.5M HCl solution in which a white precipitate formed. The substituted polymer **P1** was filtered and washed with water
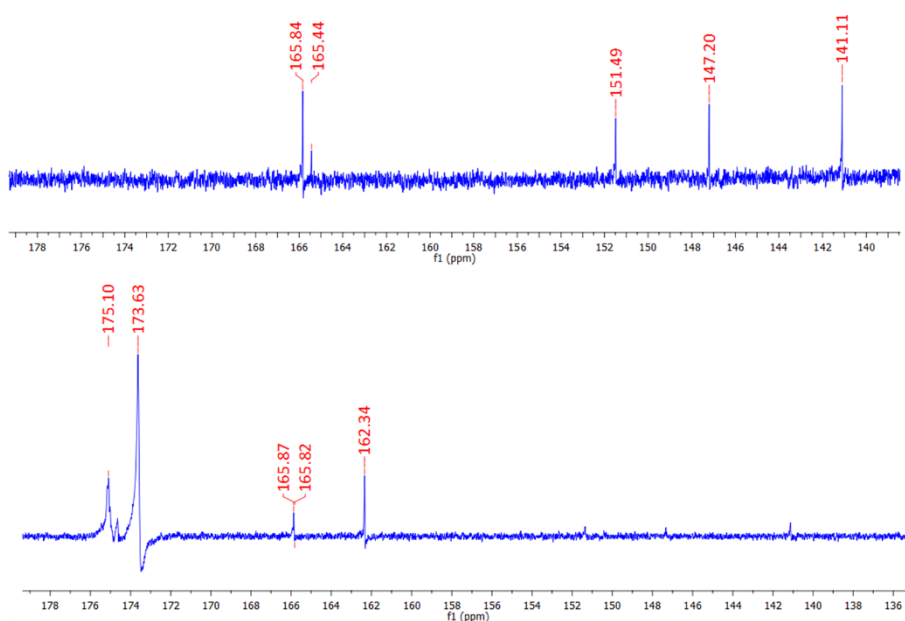
Figure 5.22 *^{1}H NMR spectrum (600 MHz, DMSO-d_6) of **P1**.*

203
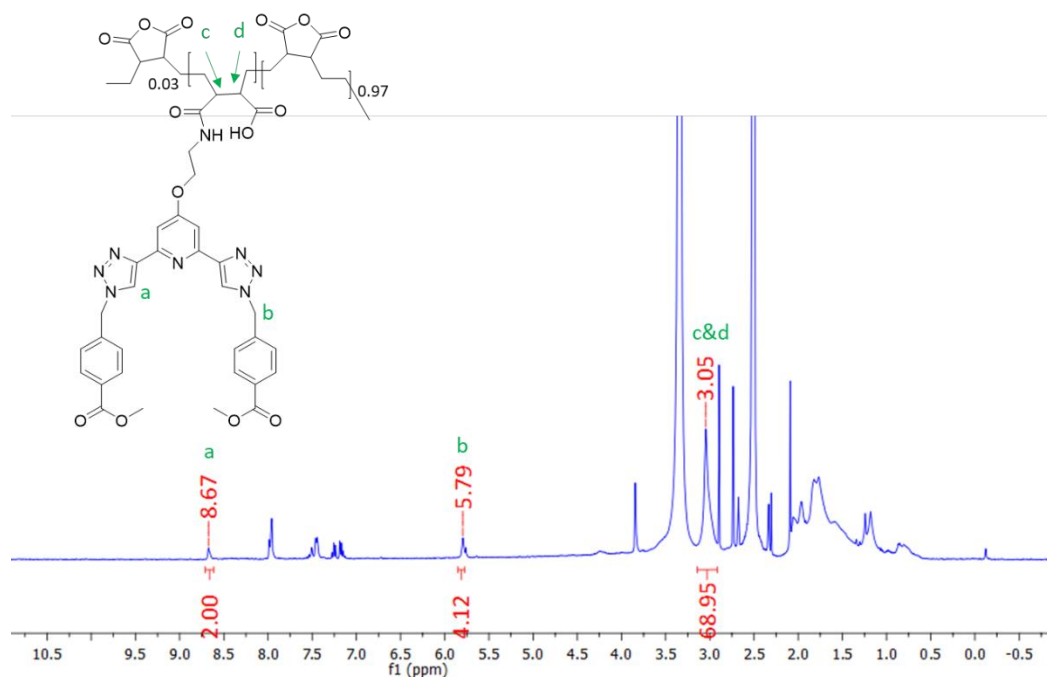
Figure 5.23 *^{13}C NMR spectrum (600 MHz, DMSO-d_6) of (top) **189** and (bottom) **P1**.*

to yield the pure product. This procedure was repeated to generate polymer **P2** at 6% loading and the polymers were characterised by NMR spectroscopies.

^{1}H NMR studies were used to confirm the formation of the grafted polymer **P1** (600 MHz, DMSO-d_6). The resonance corresponding to the triazole protons occurs at 8.67 ppm, which is at a similar resonance to the analogous proton in the free ligand **189**. The signal at 5.79 ppm can be assigned to the CH$_2$ protons of ligand **189**. The signal upfield at 3.05 ppm corresponds to the protons c and d of the polymer backbone while the remaining protons of the polymer chain resonate as a broad signal at approximately 0.85-1.96 ppm. Integration of the ^{1}H NMR peaks was used to confirming the loading of compound **189** onto the polymer backbone at approximately 3%. ^{13}C{^{1}H} NMR spectroscopy also confirmed the formation of the desired product **P1**. The appearance of two signals at 175.1 and 173.6 ppm in the polymer ^{13}C{^{1}H} NMR are indicative of the carbonyl carbons of the polymer backbone while the carbonyl carbon associated with the arms of ligand **189** is located at 165.9 ppm. The formation of **P2** was also confirmed by NMR spectroscopies (Appendix Figure A5.17).

5.11 Solution studies of the metal-directed self-assembly of P1 and P2

Polymer **P1** was readily soluble in water and CH$_3$OH, but **P2** which was soluble in CH$_3$OH required heating to 60 ˚C over several days was required to dissolve **P2** in water. Dissolving the polymers in water generated a colourless liquid in the case of **P1** and a more viscous and
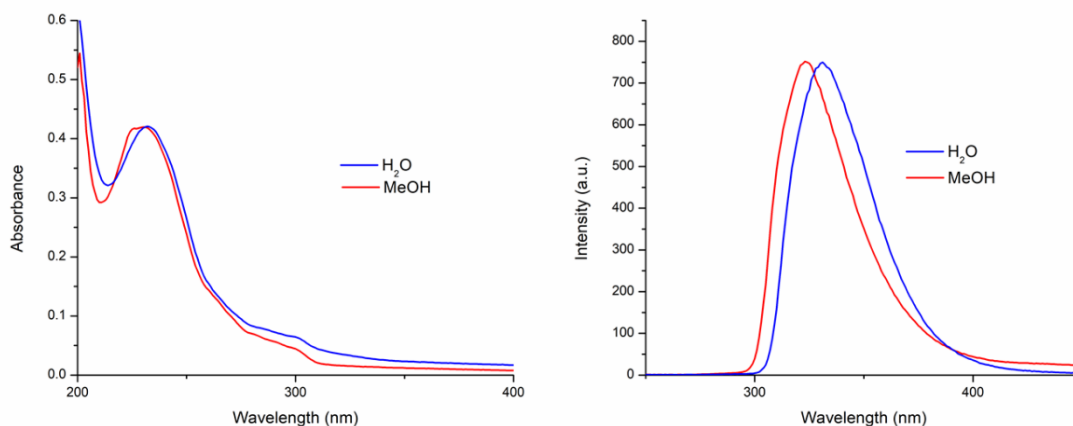
Figure 5.24 *(Left) Overlaid absorption spectra of **P1** in H₂O and CH₃OH and (right) fluorescence spectra of **P1** in H₂O and CH₃OH recorded at a concentration of approximately $c \sim 6 \times 10^{-6}$ M.*

white liquid in the case of **P2** while both polymers generated a colourless liquid when dissolved in CH₃OH.

The UV-visible absorption and fluorescence emission spectra of **P1** and **P2** were recorded in both H₂O and CH₃OH (Figure 5.24). In all cases there were two main bands observed in the UV-visible absorption spectrum at $\lambda_{max} = 231$ nm and $\lambda = 298$ nm. The features of the absorption spectrum resemble that of compound **189** described in Section 5.5, with only a slight loss of resolution in the band at $\lambda = 298$ nm, confirming that the poly(ethylene-alt-maleic) anhydride does not significantly interfere with the absorption profile of compound **189**, and thus providing a useful handle for monitoring the self-assembly of compound **189** within the polymer by UV-visible absorption spectroscopy. Upon excitation of the ligand **189** within the polymer at $\lambda = 240$ nm, ligand-centred fluorescence was observed at $\lambda = 323$ nm.

5.11.1 UV-visible absorption titration of P1 with Tb(III)

The self-assembly of the polymer **P1** with Tb(III) was then investigated in CH₃OH solution. The solution of **P1** was prepared so that the overall concentration of **189** within the solution was 1×10^{-5} M. This solution of **P1** was titrated against specific aliquots of Tb(CF₃SO₃)₃, and the changes to the UV-visible absorption, ligand fluorescence and time-gated luminescence spectra were analysed. The two main bands centred at $\lambda = 227$ nm and $\lambda = 298$ nm were affected by the addition of Tb(CF₃SO₃)₃ to the solution. The band at $\lambda = 227$ nm underwent a hypochromic and concomitant redshift up to the addition of 0.3 equivalents of Tb(III). From 0.3 equivalents to 0.5 equivalents of metal solution an increase in the
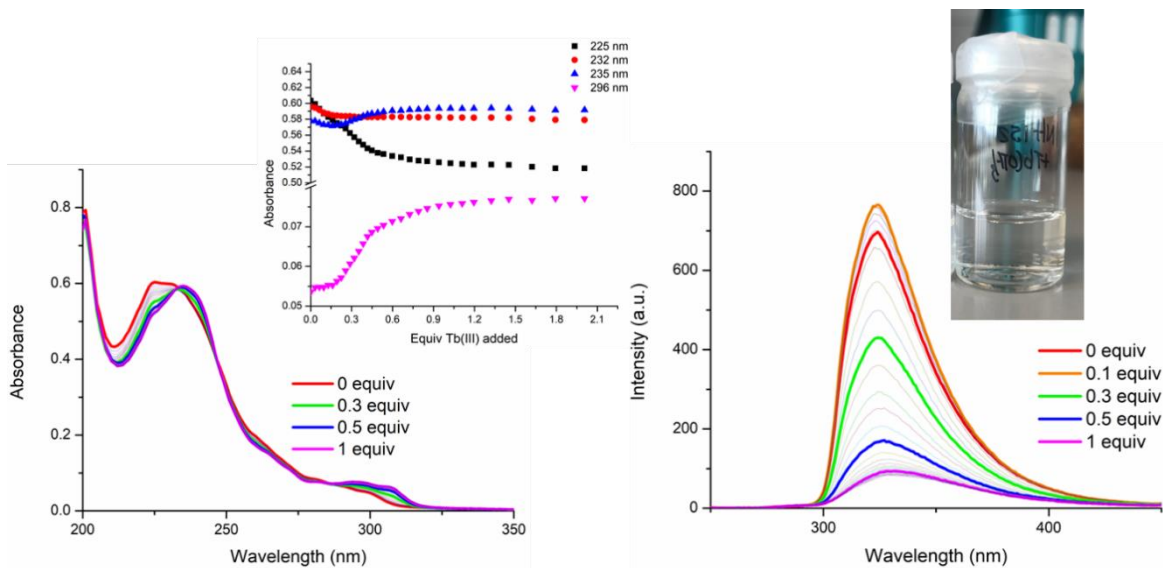
Figure 5.25 *The overall changes in the (left) UV-vis absorption spectra and (right) fluorescence spectra (λ_{exc} = 237 nm) upon titrating **P1** (**189** 1 × 10^{-5} M within **P1**) against Tb(CF$_3$SO$_3$)$_3$ (0→3 equiv.) in CH$_3$OH at RT. **Inset:** corresponding experimental binding isotherms of absorbance at λ = 325, 232, 235 and 295 nm and photograph of **P1** dissolved in H$_2$O.*

absorbance was observed and the band shifted to 236 nm, after which the changes reached a plateau. The band located at λ = 298 nm experienced a hyperchromic shift and this was accompanied by a deconvolution of the absorbance into two separate maxima at λ = 306 and 298 nm. These changes occurred up to the addition of 1 equivalent of Tb(III). Three isosbestic points at 232 nm, 247 nm and 286 nm were also observed, indicating the presence of two distinct species in solution.

5.11.2 Tb(III)-centred luminescence titrations (fluorescence and time-gated emission)

Upon excitation of the grafted polymer **P1** at λ = 237 nm, the ligand centred emission was observed at λ = 332 nm (Figure 5.25). Upon addition of the Tb(CF$_3$SO$_3$)$_3$ solution it was evident that the ligand luminescence was affected by the self-assembly of the substituted polymer with Tb(III). Up to the addition of 0.5 equivalents of Tb(III), a 79% reduction in the ligand emission was observed. At 1.0 equivalents of Tb(III), the emission reached a plateau at 10% of the initial ligand-centred emission. This can be attributed to an energy transfer process from compound **189** within the polymer to the Tb(III) metal centre upon self-assembly, giving rise to the characteristic Tb(III)-centred emission *via* indirect excitation of ligand **189**. Simultaneously, the evolution of the Tb(III)-centred emission was observed in the fluorescence spectra.
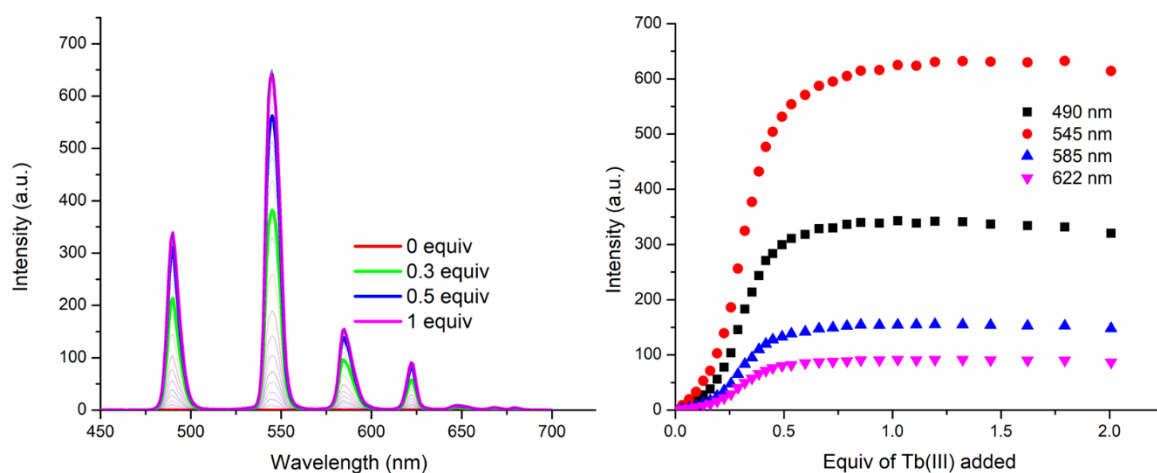
Figure 5.26 *The overall changes in the (left) Tb(III)-centred phosphorescence spectra (λ_{exc} = 237 nm) and (right) binding isotherms at λ = 490, 545, 585 and 622 nm upon titrating **P1** (1×10^{-5} M) against Tb(CF$_3$SO$_3$)$_3$ (0$\rightarrow$3 equiv.) in CH$_3$OH at RT.*

The delayed Tb(III)-centred luminescence was also recorded upon excitation at λ = 237 nm and the spectra and binding isotherms can be seen in Figure 5.26. A gradual enhancement of the Tb(III) luminescence was observed from 0 to 0.3 equivalents of Tb(III) added, after which a more rapid increase was observed up to approximately 0.5 equivalents. The characteristic Tb(III)-centred emission bands were observed at λ = 490, 545, 585, 622, 647, 667, and 675 nm. These transitions correspond to deactivation from the $^5D_4$ excited states to the ^7F_J states (where J = 6 – 0). Subsequent additions of Tb(III) from 0.5 to 3 equivalents resulted in no change to the luminescence intensity, indicating the formation of a stable metal:ligand stoichiometry which is also the most emissive species in solution.

Overall, the changes to the UV-visible absorption, florescence and Tb(III)-centred luminescence spectra indicate the formation of multiple metal:ligand stoichiometries in solution. Addition of Tb(III) after 0.5 equivalents does not appear to affect the absorption or emission spectra, indicating that the species formed at this stoichiometry are stable. The changes observed in this system are not the same as those described for compound **190** above with Tb(III). This can likely be attributed to restriction of the ligand's capacity to undergo metal coordination when grafted to the polymer backbone, which would thus prevent sole formation of the highly emissive ML$_3$ species. It is also important to note that the polymer backbone p(E-alt-MA) contains carbonyl groups, which are also capable of coordinating to the Tb(III) ion. Therefore, the speciation in solution has the potential to be quite complex, with the existence of multiple different species in solution. It is therefore not possible to confirm the presence of a 1:1 or 1:2 metal:ligand assembly in solution from the UV-visible and luminescence titration data. There is likely a mixture of species present in solution with

a variety of binding modes, coordinating the polymer backbone and also the btp ligand binding site. For this reason, and due to the restrictions, which the polymer **P1** places on the self-assembly process, the data from this titration was not fit using non-linear regression analysis. While future work would endeavour to determine the speciation in solution, the titration data indicates that at a 1:1 metal:ligand stoichiometry the system is most emissive and stable to the addition of excess Tb(III). At 1:1 metal:ligand stoichiometry, the assembly was also found to be stable over 24 hours.

5.11.3 Solution studies with polymer P2 and Tb(CF₃SO₃)₃

The solution studies were repeated with **P2** at the same concentration of compound **189** (1×10^{-5} M) in CH_3OH solution and again, changes to the UV-visible absorption, ligand fluorescence and time-gated luminescence spectra were analysed upon addition of $Tb(CF_3SO_3)_3$. In the absorption spectrum of the polymer **P2**, there were two main bands located at $\lambda = 231$ nm and $\lambda = 296$ nm. Upon addition of Tb(III), the higher energy band located at 231 nm experienced a redshift and concomitant decrease in absorbance up to the addition of 0.5 equivalents of Tb(III). Subsequently, this band increased up to 0.5 equivalents of the metal solution at $\lambda = 235$ nm. The lower energy band centred at $\lambda = 296$ nm experienced a hyperchromic shift along with a deconvolution of the absorbance into two separate maxima at $\lambda = 298$ nm and $\lambda = 307$ nm. These changes also occur up to the addition
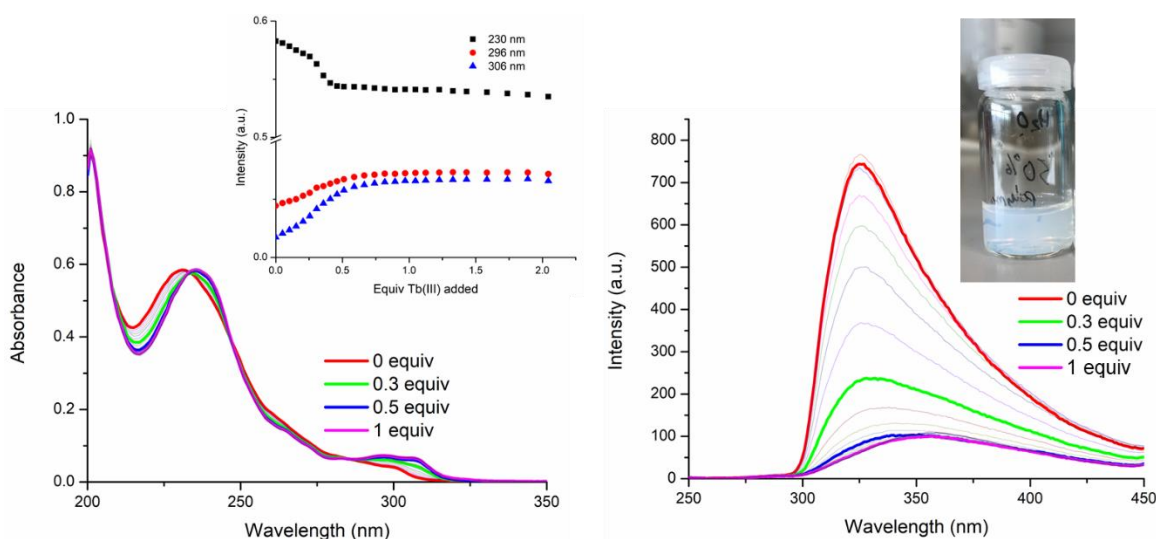
Figure 5.27 *The overall changes in the (left) UV-vis absorption spectra and (right) fluorescence emission spectra ($\lambda_{exc} = 237$ nm) upon titrating **P2** (1×10^{-5} M) against $Tb(CF_3SO_3)_3$ (0→3 equiv.) in CH_3OH at RT. **Inset**: corresponding experimental binding isotherms of absorbance at $\lambda = 230$, 295 and 306 nm and photograph of **P2** dissolved in H_2O.*

of 0.5 equivalents of Tb(III). Three isosbestic points at 233 nm, 246 nm and 287 nm were also observed.

5.11.4 Tb(III)-centred luminescence titrations (fluorescence and time-gated emission)

Upon excitation of the polymer **P2** at $\lambda = 237$ nm, the ligand centred emission band at $\lambda = 335$ nm was observed (Figure 5.27). It was evident upon addition of Tb(III) that the ligand fluorescence was affected by the self-assembly of the polymer with the metal ion. The fluorescence was gradually quenched by the addition of Tb(III), being reduced to 87% intensity at 0.5 equivalents of Tb(III), similarly to the previously observed results for **P1**. The energy transfer process responsible for the quenching of the ligand fluorescence is also responsible for the evolution of the Tb(III)-centred emission *via* indirect excitation of the ligand **189**.

Delayed Tb(III)-centred luminescence was observed upon excitation at 237 nm and is shown in Figure 5.28. A gradual enhancement in the Tb(III) luminescence was observed up to the addition of 0.5 equivalents of the metal, with characteristic Tb(III)-centred emission transitions appearing at $\lambda = 490, 545, 585, 622, 647, 667$, and 656 nm. Subsequent additions of Tb(III) did not result in any change in the luminescence intensity, which indicates the formation of stable emissive species in solution.

From the changes to the UV-visible absorption and luminescence spectra, it can be concluded that multiple species coexist in solution. As the most significant changes to the spectra occur up to the addition of 0.5 equivalents of Tb(III), it is likely that the more emissive ML_3 or ML_2 species are generated. The speciation above 0.5 equivalents does not
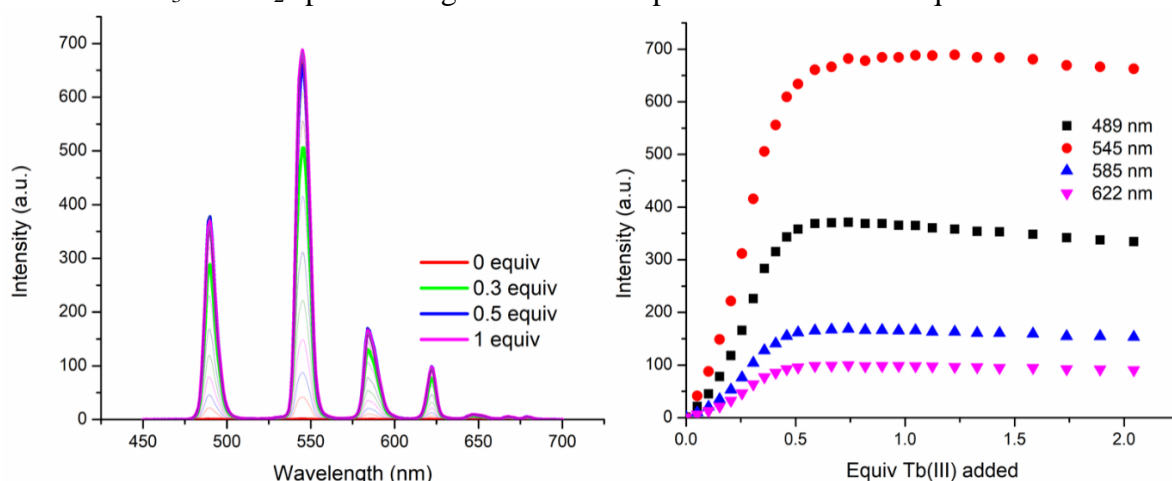
Figure 5.28 *The overall changes in the (left) Tb(III)-centred phosphorescence spectra and (right) binding isotherms at $\lambda = 490, 545, 585, 622, 647, 667$, and 656 nm upon titrating **P2** (1×10^{-5} M) against $Tb(CF_3SO_3)_3$ ($0 \rightarrow 3$ equiv.) in CH_3OH at RT.*

appear to undergo changes upon the addition of excess Tb(III), and thus suggests there is unlikely to be any dissociation to the less emissive ML species.

The changes to the UV-visible absorption and time-gated emission spectra of **P1** and **P2** when titrated with Tb(III) were similar; however, these changes reached a plateau at approximately 10. equivalents of Tb(III) in the case of **P1**, while in the case of **P2** this plateau was reached at approximately 0.5 equivalents of Tb(III), which indicates that the mol% loading of the polymer influences the self-assembly with Tb(III). While the concentration of compound **189** was the same (1×10^{-5} M) in each titration, the coordinating ligands appear more frequently on the polymer backbone in **P2** than in the case of **P1**, increasing the probability of forming higher order stoichiometric species such as ML_2 and ML_3. This indicates that subtle changes to the loading of the polymer p(E-alt-MA) can have a large influence on the self-assembly of the polymer with metal ions.

5.12 Future Work

Future work will explore the possibility of tuning the mechanical properties of the polymer, by probing the effects of polymer loading on the mechanical properties of the material, and how crosslinking interactions are induced by addition of *d*- or *f*-metals. Since the mechanical properties of soft materials are highly influenced by the crosslinking density within the polymer structure, it is feasible that the properties of the materials, such as **P1** and **P2** studied here, can be controlled by varying the cross-linking density, particularly *via* metal-centred crosslinks. Metal-centred crosslinks can be generated with *d*- and/or *f*-metals and can be tuned through a number of approaches, such as by varying the metal-dopant concentration. For example, with Tb(III), at appropriate metal concentrations it would be expected that saturated ML_3-type complexes would form where each metal ion cross-links three separate polymer chains. At higher metal concentrations, unsaturated ML_2-type complexes could form, which would result in less restricted cross-linked structures between only two polymer chains. Eventually, at high enough metal ion concentration ML-type structures would be the dominant coordination mode within the polymer, wherein little or no crosslinking would be present.

Aside from modulating the stoichiometry, the choice of metal ion would also exert significant influence over the mechanical properties of these systems, with transition metals tending to form stronger crosslinks, due to their higher charge densities and stronger coordination bonds when compared to f-metals.[281,282] While lanthanide-based crosslinks tend to be less robust, their luminescent properties nevertheless, makes them of interest, and

a number of examples of structural changes due to Eu(III)-based crosslinks have been reported.[121,266,283,284]

5.13 Conclusions

This chapter describes work aimed towards generating smart, luminescent, polymeric materials based on lanthanide complexes, formed through supramolecular crosslinking within the polymers. Novel **btp** ligands (**189** and **190**) were synthesised with a 4-pyridyl pendant amine chain, wherein **189** could be co-polymerised with other methacryl- species and **190** could act as a model compound to mirror the local environment of the polymer. These ligands were characterised fully using ^{1}H- and ^{13}C{^{1}H} NMR spectroscopies as well as IR spectroscopy and HRMS. The mononuclear tris complex [Tb(**190**)$_3$] was synthesised with Tb(CF$_3$SO$_3$)$_3$ and its photophysical properties were analysed using UV-visible absorption, fluorescence, and time-gated emission spectroscopy. The self-assembly of compound **190** with Tb(CF$_3$SO$_3$)$_3$ was then investigated using the same photophysical techniques to monitor the changes to the assembly upon successive additions of Tb(III) to the ligand solution. These changes to the data were fit using non-linear regression analysis and global stability constants were estimated from the analysis for each species in solution. Stability constants of logβ_{13} = 22.7 for the ML$_3$ species, logβ_{12} = 14.6 ± 0.1 for the ML$_2$ species, and logβ_{11} = 7.1 for the ML species were obtained. This analysis showed that the fully saturated and highly emissive ML$_3$ species was formed favourably under kinetic control at a 1:3 metal:ligand stoichiometry but was subject to a degree of dissociation to the less emissive ML$_2$ and ML species upon addition of excess Tb(III) to the system.

An organogel of **189** was formed upon sonication of compound **189** in CH$_3$CN solution and it was fully characterised by TGA, SEM, and rheological experiments to determine its mechanical properties. A crystal structure of **189** was also obtained from a low wt% gel sample which crystallised overnight. A hydrogen bonding interaction between the pendant amine of one ligand and the triazole nitrogen atoms of another causes the triazoles to adopt a *syn-syn* conformation and is likely a key interaction which is involved in the formation of a fibrous network in which the solvent was encapsulated to form the organogel.

Polymer matrices were then synthesised, copolymerising compound **199** with HEMA-*co*-MMA-*co*-EGDMA to form a hard and optically transparent film. The film was swelled in aqueous solution and upon uptake of water it became flexible and soft. The polymer was shown to be capable of the uptake of Ln(III) ions in aqueous solution; the

polymer exhibited red or green luminescence under UV-irradiation after soaking in a solution of Eu(III) or Tb(III), respectively. The photophysical properties of the film were measured and characteristic Tb(III)-centred emission bands were observed upon excitation of the ligand **199**, indicating that the ligand was capable of sensitising the metal centre to generate this luminescence. Covalently attaching compound **199** to the polymer prevented leeching of the monomer from the polymer matrix as expected; however, the luminescence of the polymer was not homogeneous throughout the film and this made the film unsuitable for use as a logic gate sensor. To overcome the lack of homogeneity in polymer films **F1** and **F2**, compound **189** was then incorporated into a commercially available polymer backbone p(E-alt-MA) to form **P1** and **P2**. Reaction of the amine of the **btp** ligand **189** with maleic anhydride resulted in a ring opening reaction wherein **189** was appended to the polymer at low loading to yield a white solid. This was confirmed by ^{1}H NMR spectroscopy and UV-visible absorption spectroscopy. The polymer was dissolved in aqueous solution successfully and self-assembly studies were carried out with the polymer and Tb(CF$_3$SO$_3$)$_3$ in CH$_3$OH to confirm the ability of compound **189** to sensitise the Tb(III)-centred luminescence within the polymer.

Future work will focus on studying this luminescent system in water to determine if the Tb(III)-assemblies are prone to dissociation in aqueous media in this particular case. . With a view to generating crosslinks which could make the solution more viscous, the introduction of *d*-metals to the polymer will also be explored. Increasing the loading of compound **1** will also be examined as a route to introducing further crosslinks, which could also modulate the structural properties of the material.

Lastly, there are a number of open questions still to be addressed. An improved understanding of the reason why the polymer films **F1** and **F2** were not homogeneous would be desirable. Techniques such as Raman spectroscopy and NIR spectroscopy could be employed to get a better picture of the distribution of compound **199** throughout the polymer film. Also, a map of Tb(III)-lifetimes across the polymer film would allow mapping of different self-assemblies, and potentially allow for better identification of smaller changes than the DSC measurements.

6. Conclusion

6.1 Final Summary and Conclusion

The aim of this project was to explore the coordination behavior of a new asymmetric chelating ligand **tzpa** with both *d-* and *f*-metals in the solid state and solution. The introduction provided an overview of symmetrical terdentate ligand motifs with a particular focus on **dpa** and **btp** as well as pyridine-centered, asymmetrical terdentate ligands. A review of recent literature on the coordination chemistry of these ligands with Ln(III) ions and also *d*-metals, describing the formation of metallosupramolecular assemblies and materials as well as their applications was provided.

Chapter 2 described the screening of chiral enantiomeric **tzpa** ligands **H₂157** and **H₂158** with various *d*-metals and the complexes in the crystalline state which were obtained. Tetrameric [2 × 2] grid structure [Cu₄(**H₂157**)₄](NO₃)₈ was obtained and interestingly, the chiral nature of the ligand had little effect on the metal coordination sites. By changing only the reaction solvent, an ML₂ assembly [Cu₂(**H₂157**)(NO₃)₄]CH₃CN was obtained and the ligand **H₂158** generated an analogous structure under the same conditions. Another tetranuclear grid [Cu₄(**H157**)₄](PF₆)₄ was obtained from reaction of the ligand **H₂157** with a Cu(I) salt which was oxidised to Cu(II) upon complexation. Linkage isomerism occurred at the metal centre, with each ligand singly deprotonated and coordinating through the deprotonated amide nitrogen. The self-assembly of these systems was examined by UV-visible absorption and fluorescence spectroscopy and the redox behaviour of [Cu₄(**H157**)₄](PF₆)₄ was also examined by CV.

Chapter 3 focused on derivatisation of the **tzpa** ligand with coordinating pyridyl arms in order to increase the opportunity for metal-ligand interactions. Ligand **162** was derivatized with a 3-pyridyl moiety replacing the chiral arms of ligands **H₂157** and **H₂158** and upon reaction with AgBF₄ in CH₃CN, formed a metallogel. A monotopic derivative of ligand **162**, ligand **166**, formed a 1D polymer with Ag(I) and the structural information obtained gave an insight into the metal-ligand interactions which likely contribute to the metallogel formation. The structural information obtained from these assemblies was then utilized to design derivatives **H169** and **H₂172** with a view to generate higher order structures. Ligand **H169**, a derivative of monotopic ligand **166** generated a 2D polymer [Cu₃(**169**)₂(CF₃SO₃)(OCH₃)₂]CF₃SO₃.H₂O where again, Cu(I) was oxidised to Cu(II) during the reaction under mild conditions and coordination to the Cu(II) centre occurred through

the deprotonated amide nitrogen atom. Methoxide ligands also coordinate the Cu(II) atom and due to the lack of a strong base, this observation is highly unusual. Ligand **H₂172**, a derivative of **162**, formed a tetranuclear grid structure [Cu₄(**H172**)₄](PF₆)₄ analogous to that described for ligand **H₂157** and again Cu(I) was oxidised to Cu(II) and coordination through the deprotonated amide nitrogen occurred. More profound changes to the ligand design, changing the linker moiety, resulted in drastic changes to the solubility and behavior of the compounds.

Chapter 4 described the synthesis of **tzpa** ligands **6** and **7**, functionalized with amino acid residues and their self-assembly with Tb(III) and Eu(III). Complexes of the ligands with Tb(III) and Eu(III) were generated and the **tzpa** ligands were found to sensitize Tb(III) more efficiently than Eu(III). These complexes were found to dissociate in aqueous solution, indicating that they are not suitable for biological applications. The self-assembly of these ligands with Tb(III) was investigated and it was found that a 1:2 metal:ligand species was formed more favorably than a 1:3 fully saturated metal:ligand complex at low concentration. Examination of the self-assembly of monotopic ligand **3** confirmed that this was not caused by a steric effect. Chiral, ditopic ligand **H₂157** was also titrated against Tb(III) to examine its self-assembly at low concentration and global analysis of the resulting data suggested the formation of an assembly M_2L_3 which could possibly take the form of a triple-stranded helicate.

The work described in Chapter 5 was aimed towards the formation of smart, luminescent, polymeric materials based on lanthanide complexes. **Btp** ligands were functionalized to enable co-polymerisation with HEMA-co-MMA-co-EGDMA forming a hard, optically transparent film which upon uptake of water became soft and flexible. The film was capable of uptake of Ln(III) ions in aqueous solution and the film emitted green or red luminescence under UV-irradiation. However, the luminescence of the polymer was not homogeneous. In order to overcome this lack of homogeneity, **btp** compound **H₂157** was incorporated into commercially available polymer backbone p(E-alt-MA) and this polymer was dissolved in aqueous solution as well as methanolic solution. Self-assembly studies were carried out with Tb(III) to confirm the ability of the polymer to sensitise the Tb(III)-centred luminescence. Future work would focus on this polymer system in aqueous solution and tuning the mechanical properties of the polymer through changing the crosslinking density.

7. Experimental Details

7.1 General methods and materials

All reagents and solvents were purchased from commercial sources and used without further purification. Solvents were of HPLC grade and used without further purification. Dry solvents were obtained from Solvent Purification System or prepared in accordance with standard procedures[285]. Flash chromatography was carried out using TeledyneIsco CombiFlash Rf 200 automated purification system and pre-packed normal phase silica cartridges were supplied by TeledyneIsco RediSep. Thin layer chromatography was conducted using MerckMillipore Kiesegel 60 F$_{254}$ silica plates and visualized under $\lambda = 254$ nm or using Ninhydrin. Melting points were obtained using Electrothermal IA900 digital apparatus. Infrared spectra were recorded using PerkinElmer Spectrum One FT-IR Spectrometer. Elemental analysis was carried out at Microanalytical Laboratory, School of Chemistry and Chemical Biology, University College Dublin or Chemistry Department, Maynooth University Kildare. Microwave assisted reactions carried out using a Biotage Initiator Eight EXP microwave reactor.

7.1.1 NMR spectroscopy

NMR spectra were recorded on a Bruker DPX-400 Avance spectrometer at frequencies of 400.13 MHz and 100.6 MHz for ^{1}H NMR and ^{13}C{^{1}H} NMR respectively or Bruker-AV-600 spectrometer at frequencies of 600.13 MHz and 150.2 MHz for ^{1}H NMR and ^{13}C{^{1}H} NMR respectively. All spectra were recorded in commercially available deuterated solvents and the residual proton signals of those solvents were used as a reference with chemical shifts expressed in parts per million (ppm).

7.1.2 Mass spectrometry

Mass spectrometry was carried out in the School of Chemistry, Trinity College Dublin. Electrospray mass spectra were measured ona Micromass LCT spectrometer calibrated against a leucine enkephaline standard and MALDI A-ToF mass spectra were obtained on a MALDI A-TOF Premier and high-resolution mass spectrometry was performed using Glu-Fib as an internal reference ($m/z = 1570.677$).

7.1.4 UV-visible absorption and luminescence spectroscopy

All photophysical measurements were taken using spectroscopic grade solvent and measured in quartz cells with path length 10 mm. UV-visible absorption spectra were recorded using a Varian Cary 50 spectrophotometer in a spectroscopic window of 400 – 200 nm. The blank used was a sample of the solvent in which the titration was carried out. Luminescence spectra

were measured using a Carian Cary Eclipse spectrometer and reported in arbitrary units and the luminescence data was collected between 450 and 700 nm for Tb(III) emission and 450 to 720 nm for Eu(III) emission. Time-gated emission spectra were recorded over an average integration time of 0.1 seconds.

7.1.5 Luminescence lifetime measurements

Luminescence lifetime measurements of Tb(III)-centered emission was recorded using Varian Cary Eclipse spectrophotometer as a time-resolved measurements at 298 K. All lifetimes were averaged from at least five measurements at different gate times between 0.02 – 0.045 ms. The decay curves were fitted to mono- or bi-exponential decay functions.

7.1.5 Circular dichroism

Circular dichroism (CD) spectra were recorded in solution on a Jasco J-810-150S spectropolarimeter in a 1.2 mL cell under a constant flow of nitrogen. Each spectrum was an average of three independent measurements with applied baseline correction.

7.1.6 Scanning electron microscopy

Microscopy analysis of gel samples was carried out in collaboration with Dr. Amy Lynes and Mr. Jason Delente from the Gunnlaugsson group at the Advanced Microscopy Laboratory (AML) in Trinity College Dublin. Samples were prepared using a drop-casting method onto silicon wafers and dried under high vacuum for 4 hours prior to imaging. Samples were coated with conductive Au layer in order to improve contrast and prevent static charge interfering with imaging.

7.1.7 X-ray powder diffraction

Powder diffraction patterns were measured on a Brucker D2 Phaser instrument using Cu Kα ($\lambda = 1.54178$ Å) radiation and a Lynxeye detector. Measurements were carried out at room temperature and samples were mounted on a zero-background silicon single crystal sample stage. X-ray powder diffraction patterns were also collected at 100 K on a Brucker APEX-II Duo duel-source instrument using microfocus Cu Kα ($\lambda = 1.54178$ A) which was maintained at 100 K using a cobra cryosystem. Patterns collected were compared to patterns simulated form the single crystal data collected at 100 K to establish phase purity.

7.1.8 X-ray Crystallography

Structural and refinement parameters are presented in the Appendix for each chapter. X-ray crystallographic data were collected by Dr. Chris Hawes, Dr. Hannah Dalton or Ms. June Lovitt using a Brucker APEX-II Duo dual-source instrument and using graphite-monochromated Mo K α (λ = 0.71073 A) or microfocus Cu Kα (λ = 1.54178 A) radiation. Datasets were collected using ω and φ scans and the samples were immersed in oil. Brucker APEX suite of programs were used to reduce and process the data.[286] Multi-scan absorption corrections were applied using SADABS.[287] The diffraction data were solved using SHELXT and refined by full-matrix least squares procedures using SHELXL-2015 within the OLEX-2 GUI.[288,289] The functions minimized were $\Sigma w(F^2_o - F^2_c)$, with $w = [\sigma^2(F^2_o) + aP^2 + bP]^{-1}$, where $P = [\max(F_o)^2 + 2F^2_c]/3$. All non-hydrogen atoms were refined with anisotropic displacement parameters. All hydrogen atoms were placed in calculated positions and refined with a riding model, with isotropic displacement parameters equal to either 1.2 or 1.5 times the isotropic equivalent of their carrier atoms. In cases where U_{ij} or position restraints were necessary, these were employed as sparingly as possible and only for the purpose of maintaining chemically sensible geometries and ADPs. Hirshfeld d_{norm} surface properties were mapped using CrystalExplorer package (Isovalue 0.5, property ranges 0.5 – 1.0).[290,291]

7.2 Synthesis

General Experimental Procedure 1

To a solution of halo-pyridine (5.10 mmol) in THF/NEt$_3$ stirring at 0 °C (4:1, 40 mL), CuI (0.2 mmol) and Pd(PPh$_3$)$_4$ (0.2 mmol) were added under an argon atmosphere. Ethynyltrimethylsilane (11.22 mmol) was added dropwise and left to stir at room temperature for 48 hrs. The resulting solution was concentrated under reduced pressure and filtered through a plug of celite with hexane or DCM where appropriate.

General Experimental Procedure 2

Halide precursor (4.3 mmol) and sodium azide (4.3 mmol) were added to a mixture of DMF/H$_2$O (4:1) (15 mL) and stirred for an hour. To the mixture CuSO$_4$.5H$_2$O (0.9 mmol), sodium ascorbate (1.7 mmol), and K$_2$CO$_3$ (4.3 mmol) were added and the mixture was degassed. Finally the relevant TMS protected alkyne (4.3 mmol) was added dissolved in DMF (2 ml). The reaction was stirred at r.t. under Ar for 48 hrs and dried under reduced

pressure. A solution of EDTA/NH4 (15 mL) was added and the product was extracted into DCM, washed with H$_2$O (3x30 mL) and dried over MgSO$_4$. The solution was concentrated under reduced pressure a and further purified if necessary.

In the case of a carboxylic acid precursor the product can be precipitate out from the EDTA/NH4 solution with 1M HCl followed by filtration to yield the final product.

General Experimental Procedure 3

To a solution of the relevant amine (0.64 mmol) in MeOH (1.7 mL) was added ImSO$_2$N$_3$.H$_2$SO$_4$ (0.71 mmol), K$_2$CO$_3$ (1.2 mmol) and CuSO$_4$.5H$_2$O (0.1 mmol). The solution turned lilac after 5 hours. Then sodium ascorbate (0.3 mmol) and K$_2$CO$_3$ (0.6 mmol) were added in H$_2$O (0.5 mL) along with ^{t}BuOH (0.75 mL). The mixture was degassed with argon. The TMS protected alkyne (0.64 mmol) was added dissolved in DMF (0.3 mL) and the reaction mixture was stirred at room temperature for 18 h. Reaction mixture was concentrated under reduced pressure and aqueous EDTA/NH$_4$OH (1:9, pH 9) solution was added. The product was extracted into CH$_2$Cl$_2$ and washed with H$_2$O (3 x 30 mL). The solution was dried over magnesium sulphate and the solvent was removed under reduced pressure.

General Experimental Procedure 4

A solution of the relevant amine (1 equivalent) in a DMF:DCM (4:1) mixture under argon was added HOBt (1 equivalent), NEt$_3$ (1.2 equivalents) and the relevant acid (1.1 equivalents). The reaction mixture was stirred for 30 mins and cooled to 0 °C. EDC·HCl (1.5 equivalents) was then added to the suspension and stirred at 0 °C for a further 30 mins. The mixture was then allowed to warm to room temperature and stirred for a further 48 hrs.

Experimental Details for Chapter Two
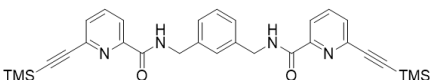
α,α'-m-Xylylenebis(N-(6-bromopicolinamide)) (160)
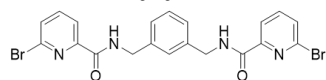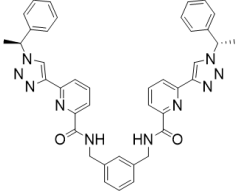
1,3-xylylenediamine (0.89 mL, 6.8 mmol) HOBt (1.80 g, 13.30 mmol) and NEt$_3$ (2.06 mL, 14.0 mmol) were added to a solution of 6-bromopyridine-2-carboxylic acid (3.00 g, 14.8 mmol) in DMF : DCM (4:1, 120 mL) under argon. The reaction mixture was stirred for 30 mins and cooled to 0 °C. EDCI·HCl (3.88 g, 20.3 mmol) was then added to the suspension and stirred at 0 °C for a further 30 mins. The mixture was then allowed to warm to room temperature and stirred for a further

48 hrs. The solvent was removed under reduced pressure and the resulting orange oil was taken up in DCM. The solution was washed with 1.0 M HCl (3 x 20 mL), sat. aq. NaHCO$_3$ (3 x 20 mL), H$_2$O and brine. The organic layer was dried over MgSO$_4$ and the solvent was removed under reduced pressure to yield a white solid. Yield (2.915 g, 5.78 mmol, 86%); m.p. 168 – 171 ºC; HRMS (*m/z*) (ESI+): C$_{20}$H$_{16}$N$_4$O$_2$Br$_2$Na $^+$ *m/z* = 524.9538 [M+Na]$^+$. Found *m/z* = 524.9531; ^{1}H NMR (400 MHz, CDCl$_3$): δ (ppm) = 8.18 (dd, 2H, pyridine H), 8.16 (br s, 2H, NH), 7.17 (t, , 2H, pyridine H), 7.60 (dd, 2H, pyridine H), 7.33-7.30 (m, 4H, benzyl H), 4.63 (d, 4H, CH$_2$); ^{13}C{^{1}H} NMR (150 MHz, DMSO-*d$_6$*): δ (ppm) = 162.5, 150.8, 140.5, 139.7, 138.4, 130.6, 129.1, 127.3, 127.2, 121.4, 43.4; IR ν$_{max}$ (cm^{-1}): 3061, 2959, 1671, 1564, 1517, 1442, 1248, 1171, 1077, 993, 841, 759, 700, 644.

α,α'-m-Xylenebis(N-(6-(trimethylsilylethynylpicolinamide)) (161)

Synthesised according to general procedure 1 from **160** (2.57 g, 5.10 mmol) and ethynyltrimethylsilane (1.6 mL, 11.22 mmol) to yield a brown solid which was purified by flash column chromatography (RediSep® 24g, gradient elution 0 → 50 % EtOAc in Hexane) to yield a brown solid. Yield (2.469 g, 4.59 mmol, 90%); m.p. 121 – 130 ºC; HRMS (*m/z*) (ESI+): C$_{20}$H$_{35}$N$_4$O$_2$Si$_2$ $^+$ *m/z* = 539.2299 [M+H]$^+$. Found *m/z* = 539.2311; ^{1}H NMR (400 MHz, CDCl$_3$): δ (ppm) = 8.36 (br s, 2H, NH), 8.17 (dd, 2H, *J* = 7.8, 1.0 Hz, pyridine H), 7.81 (t, 2H, *J* = 7.8 Hz, pyridine H), 7.57 (dd, 2H, *J* = 7.8, 1.0 Hz, pyridine H), 7.34 – 7.28 (m, 4H, benzyl H), 4.66 (d, 4H, *J* = 6.2 Hz, CH$_2$), 0.27 (s, 18H, 6 x CH$_3$); ^{13}C{^{1}H} NMR (150 MHz, CDCl$_3$): δ (ppm) = 163.8, 150.1, 141.7, 138.8, 137.7, 130.1, 129.2, 127.7, 127.2, 122.0, 103.2, 96.1, 43.5, 0.2; IR ν$_{max}$ (cm^{-1}): 3061, 2959, 1671, 1564, 1517, 1442, 1248, 1171, 1077, 993, 841, 759, 700, 644

N,N'-(1,3-phenylenebis(methylene))bis(6-(1-((S)-1-phenylethyl)-1H-1,2,3-triazol-4-yl)picolinamide) (157)

Synthesised according to general procedure 2 from s-α-methylbenzylamine (0.01 mmol) and **161** (0.02 mmol, 0.025 mL) to yield a white solid (48 mg, 0.012 mmol, 62%).; m.p. 118 – 123 ºC; HRMS (*m/z*) (ESI+): C$_{40}$H$_{37}$N$_{10}$O$_2$ $^+$ *m/z* = 689.3101 [M+H]$^+$. Found *m/z* = 689.3109; ^{1}H NMR (600 MHz, DMSO-*d$_6$*): δ (ppm) = 9.41 (t, 2H, NH), 8.98 (s, 2H, triazolyl H), 8.18 (dd, *J* = 7.8, 1.0 Hz, 2H, pyr CH-triazole), 8.02 (t, 2H, *ortho* pyr CH), 7.91 (dd, *J* = 7.7, 1.0 Hz, 2H, pyr CH-Ar), 7.45 – 7.09 (m, 14H, Ar CH), 6.05 (q, *J* = 7.1 Hz, 2H, *CH*-CH$_3$), 4.55 (d, *J* = 6.5 Hz, 4H, CH$_2$), 1.95 (d, *J* = 7.1 Hz, 6H, CH$_3$); ^{13}C{^{1}H} NMR (150

MHz, DMSO-d_6): δ (ppm) = 163.75, 149.53, 148.78, 146.79, 140.98, 139.59, 138.79, 128.82, 128.37, 128.05, 126.09, 125.61, 123.03, 121.57, 120.73, 64.90, 59.51, 42.28, 21.29; IR v_{max} (cm^{-1}): 3326, 2934, 2165, 1664, 1660, 1518, 1444, 1241, 1172, 1076, 995, 830, 765, 697.

Synthesis of [Cu₄(H₂157)₄] (NO₃)₈

To a solution of Cu(NO$_3$)$_2$ ·2.5H$_2$O (0.02 mmol, 3 mg) in CH$_3$OH (2 mL) was added a solution of **H₂157** (0.007 mmol, 5 mg) in CH$_3$OH (3 mL). Upon reaction together, a pale blue solution resulted and allowed to react in a closed vessel to yield blue crystals after one week. The crystals were isolated by filtration, washed with CH$_3$OH and allowed to air dry. Yield; (3 mg, 48%); m.p. (decomp) >280 °C; Elemental analysis for C$_{160}$H$_{144}$Cu$_4$N$_{48}$O$_{32}$·2CH$_3$OH Calculated: C 54.52 H 4.29 N 18.84; Found: C 54.22 H 3.90 N 19.13 %; IR v_{max} (cm^{-1}): 2931, 2850, 1659, 1609, 1563, 1523, 1437, 1382, 1302, 1251, 1105, 1041, 832, 756, 696.

Synthesis of [Cu₄(H157)₄](PF₆)₄

To a solution of [(MeCN)$_4$Cu]PF$_6$ (3 mg) in CH$_3$OH (2 mL) was added a solution of **H₂157** (0.007 mmol, 5 mg) in CH$_3$OH (3 mL). Upon reaction together a clear solution resulted which was subjected to vapour diffusion of toluene yielding blue crystals after one week. The crystals were isolated by filtration, washed with CH$_3$OH and allowed to air dry. Yield (2.6 mg, 40 %); m.p. (decomp) >280 °C; Elemental analysis for C$_{160}$H$_{140}$N$_{40}$O$_8$Cu$_4$P$_4$F$_{24}$·4PhMe·12H$_2$O Calculated: C 54.14 H 4.74 N 13.43; Found: C 54.29 H 4.21 N 13.55%; IR v_{max} (cm^{-1}): 2922, 1654, 1596, 1459, 1379, 1202, 1109, 832, 761, 734, 697, 594, 556.

Synthesis of [Cu₂(H₂157)(NO₃)₄]MeCN

To a solution of Cu(NO$_3$)$_2$ (4 mg) in MeCN (2 mL) was added a solution of **H₂157** (7.0 × 10^{-3} mmol, 5 mg) in MeCN (3 mL). Upon reaction together, a pale blue solution resulted which was reacted in a closed vial for 2 days to yield blue crystals. The crystals were isolated by filtration, washed with MeCN and allowed to air dry. Yield (4 mg, 52 %); m.p. (decomp) >280 °C; Elemental analysis for C$_{40}$H$_{36}$N$_{14}$O$_{14}$Cu$_2$·1.5 CH$_3$CN Calculated: C 45.89 H 3.63 N 19.29; Found: C 46.20 H 3.39 N 19.13%; IR v_{max} (cm^{-1}): 3093, 1638, 1605, 1552, 1489, 1393, 1327, 1285, 1211, 1041, 1008, 830, 763, 608.

Experimental Details for Chapter Three

N,N'-(1,3-phenylenebis(methylene))bis(6-(1-(pyridin-3-ylmethyl)-1H-1,2,3-triazol-4-yl)picolinamide) (162)
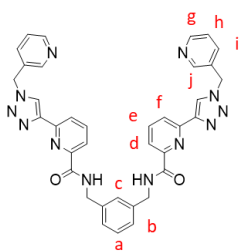
Synthesised according to general procedure 3 from 3-picolylamine (0.02 mL, 0.19 mmol) and **161** (50 mg, 0.09 mmol) to yield a white solid (49 mg, 0.07 mmol, 81%). m.p. 154 – 157 ℃; HRMS (*m/z*) (ESI+): $C_{36}H_{30}N_{12}O_2^+$ *m/z* = 663.2615 [M+H]$^+$. Found *m/z* = 663.2709; ^{1}H NMR (600 MHz, DMSO-*d$_6$*): δ (ppm) = 9.41 (t, 2H, NH), 8.94 (s, 2H, triazolyl H), 8.64 (br s, 2H, Hj), 8.56 (d, 2H, *J* = 7.9 Hz, Hg), 8.17 (d, 2H, *J* = 7.9, 1.0 Hz, Hf), 8.03 (t, 2H, *J* = 7.9 Hz, He), 7.91 (dd, 2H, J = 7.9, 1.0 Hz, Hd), 7.72 (d, *J* = 8.1 Hz, 2H, Hi), 7.45 – 7.39 (m, 2H, *J* = 7.9, 8.1 Hz, Hh), 7.27 (m, 2H, *J* = 7.8, 0.9 Hz, Ha & Hc), 7.22 (m, *J* = 7.8, 0.9 Hz, 2H, Hb), 5.78 (s, 4H, CH$_2$-triazole), 4.54 (d, *J* = 6.5 Hz, 4H, CH$_2$-NH). ^{13}C{^{1}H} NMR (150 MHz, DMSO-*d$_6$*): δ (ppm) = 164.2, 150.1, 150.0, 149.5, 149.1, 147.63, 140.1, 139.3, 136.2, 132.0, 128.9, 126.2, 126.1, 124.9, 124.4, 122.1, 121.3, 51.2, 42.8; IR ν$_{max}$ (cm^{-1}): 3353, 2706, 2131, 1678, 1520, 1419, 1232, 1028, 767, 830, 564.

N-benzyl-6-bromopicolinamide (167)
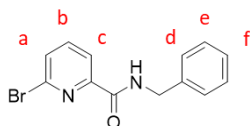
Synthesised according to general procedure 4 from 6-bromopyridine-2-carboxylic acid (2.0 g, 9.9 mmol) and benzylamine (1.1mL, 10.8 mmol). The product was dried under reduced pressure and taken up in CH$_2$Cl$_2$, washed with 1M HCl, sat. NaHCO$_3$ and H$_2$O, dried over magnesium sulfate and concentrated under reduced pressure to yield an orange oil. This resulting oil was dried to a solid by repeated evaporation under reduced pressure with toluene to give compound **166** in 69% yield.; m.p. 167 - 174 ℃; HRMS (*m/z*) (ESI+): $C_{13}H_{11}BrN_2O^+$ *m/z* = 291.0133 [M+H]$^+$. Found *m/z* = 291.0127; ^{1}H NMR (600 MHz, CDCl$_3$): δ (ppm) = 8.20 (d, *J* = 7.7 Hz, 1H, Ha), 8.14 (s, *J* = 6.2 Hz, 1H, NH), 7.72 (t, *J* = 7.7 Hz, 1H, Hb), 7.61 (d, *J* = 7.7 Hz, 1H, Hc), 7.36 (dd, *J* = 8.3, 5.5 Hz, 4H, Hd & He), 7.33 – 7.27 (m, 1H, *J* = 8.3, 5.5 Hz, Hf), 4.67 (d, *J* = 6.2 Hz, 2H, CH$_2$); ^{13}C{^{1}H} NMR (150 MHz, CDCl$_3$): δ (ppm) = 162.9, 151.1, 140.7, 139.8, 138.1, 130.9, 128.9, 128.1, 127.8, 121.6, 43.7; IR ν$_{max}$ (cm^{-1}): 3354, 3318, 3166, 3033, 2942, 1736, 1639, 1603, 1568, 1527, 1502, 1451, 1374, 1278, 1247, 1222, 1161, 1089, 1049, 972, 865, 819, 764, 743, 728, 687, 631, 606.

N-benzyl-6-((trimethylsilyl)ethynyl)picolinamide (168)
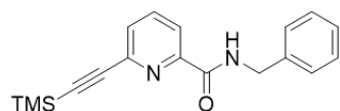
Synthesised according to general procedure 1 from **167** (1 g, 3.43 mmol) and ethynyltrimethylsilane (0.5 mL, 3.43 mmol) to yield a brown solid which was purified by flash column chromatography (RediSep® 24g, gradient elution 0 → 20 % EtOAc in Hexane) to yield a brown solid in 63% yield.; m.p. 187 - 191 ºC; HRMS (m/z) (ESI+): $C_{18}H_{21}N_2OSi^+$ m/z = 309.1418 [M+H]$^+$. Found m/z = 309.1418; ^{1}H NMR (600 MHz, DMSO-d_6): δ (ppm) = 9.22 (t, 1H, J = 6.4 Hz, NH), 8.02 (m, J = 7.5, 1.1 Hz, 2H, pyr H), 7.74 (dd, J = 7.5, 1.1 Hz, 1H, pyr H), 7.37 – 7.25 (m, 4H, Ar H), 7.27 – 7.18 (m, 1H, Ar H), 4.49 (d, J = 6.4 Hz, 2H, CH$_2$), 0.26 (s, 9H, CH$_3$-Si); ^{13}C{^{1}H} NMR (150 MHz, DMSO-d_6): δ (ppm) = 163.8, 151.0, 141.2, 139.9, 139.0, 130.6, 128.7, 127.9, 127.3, 122.5, 104.0, 95.7, 43.0, 0.1; IR ν$_{max}$ (cm^{-1}): 3371.0, 1674.1, 1520.7, 1442.9, 1248.4, 841.6, 762.4, 645.7, 610.3

N-benzyl-6-(1-(pyridin-3-ylmethyl)-1H-1,2,3-triazol-4-yl)picolinamide (166)
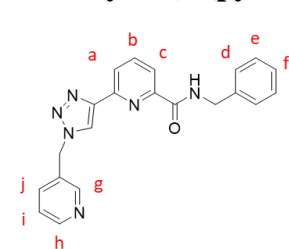
Synthesised according to general procedure 3 from 3-picolylamine (0.17 mL, 1.6 mmol) and **168** (0.5 g, 1.6 mmol) to yield a white solid in 72 % yield.; m.p. 156 - 163 ºC; HRMS (m/z) (ESI+): $C_{21}H_{19}N_6O^+$ m/z = 371.1615 [M+H]$^+$. Found m/z = 371.1614; ^{1}H NMR (600 MHz, DMSO-d_6): δ (ppm) = 9.44 (t, 1H, J = 6.5 Hz, NH), 8.99 (s, 1H, triazole H), 8.65 (s, 1H, J = 4.8 Hz, Hg), 8.56 (br d, 1H, J = 7.4 Hz, Hh), 8.21 (d, J = 7.8 Hz, 1H, Ha), 8.09 (t, J = 7.8, 1.1 Hz, 1H, Hb), 7.99 (d, J = 7.8 Hz, 1H, Hc), 7.73 (d, J = 7.9, 7.4 Hz, 1H, Hi), 7.43 (dd, J = 7.9, 4.8 Hz, 1H, Hj), 7.32 (d, J = 4.2. 3.6 Hz, 4H, Hd & He), 7.24 (d, J = 3.6 Hz, 1H, Hf), 5.80 (s, 2H, CH$_2$-triazole), 4.57 (d, J = 6.5 Hz, 2H, CH$_2$-NH). ^{13}C{^{1}H} NMR (150 MHz, DMSO-d_6): δ (ppm) = 163.8, 149.7, 149.6, 149.1, 148.8, 147.2, 139.5, 138.9, 135.7, 131.6, 128.4, 127.1, 126.8, 124.5, 124.0, 121.7, 120.9, 50.8, 42.3; IR ν$_{max}$ (cm^{-1}): 3350.3, 3065.8, 3030.2, 2164.5, 1977.6, 1667.4, 1599.3, 1521.9, 1478.4, 1430.1, 1361.0, 1282.0, 1255.2, 1235.9, 1168.9, 1077.3, 1046.0, 1028.6. 993.5, 849.6, 779.4, 764.8, 695.0, 627.1.

6-bromo-N-(pyridin-4-ylmethyl)picolinamide (170)
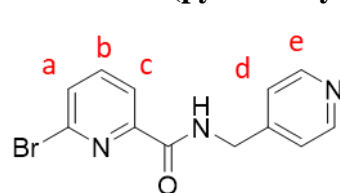
Synthesised according to general procedure 4 from 6-bromopyridine-2-carboxylic acid (1.0 g, 4.95 mmol) and 4-aminomethylpyridine (0.6 mL, 5.9 mmol) to give compound **170** in 52% yield.; HRMS (m/z) (ESI+): $C_{12}H_{10}BrN_3O^+$ m/z =

291.0007 [M+H]$^+$. Found m/z = 292.0080; ^{1}H NMR (400 MHz, DMSO-d_6): δ (ppm) = 9.36 (t, J = 6.2 Hz, 1H, NH), 8.49 (dd, J = 6.0 Hz, 1H, He), 8.06 (dd, J = 7.5, 0.9 Hz, 1H, Ha), 7.96 (t, J = 7.5 Hz, 1H, Hb), 7.88 (dd, J = 7.5, 0.9 Hz, 1H, Hc), 7.29 (d, J = 6.0 Hz, 1H, Hd), 4.50 (d, J = 6.3 Hz, 2H, CH$_2$). ^{13}C{^{1}H} NMR (150 MHz, DMSO-d_6): δ (ppm) = 163.5, 151.6, 150.0, 148.7, 141.5, 140.8, 131.6, 122.7, 122.2, 42.2; IR ν$_{max}$ (cm^{-1}): 3329, 3089, 1671, 1595, 1552, 1518, 1471, 1302, 1048, 1000, 794, 760, 641, 608.

N-(pyridin-4-ylmethyl)-6-((trimethylsilyl)ethynyl)picolinamide (171)
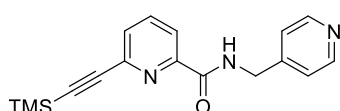
Synthesised according to general procedure 1 from **170** (0.65 g, 2.2 mmol) and ethynyltrimethylsilane (0.3 mL, 2.4 mmol) to yield a brown solid which was purified by flash column chromatography (RediSep® 12g, gradient elution 0 → 100 % EtOAc in Hexane) to yield a brown solid. Yield (0.462 g, 1.49 mmol, 68 %).; m.p. 155 - 158 ℃; HRMS (m/z) (ESI+): C$_{17}$H$_{20}$N$_3$OSi$^+$ m/z = 310.1376 [M+H]$^+$. Found m/z = 310.1356; ^{1}H NMR (600 MHz, CDCl$_3$): δ (ppm) = 8.57 (t, 1H, NH), 8.20 (d, J = 7.8, 0.9 Hz, 1H, pyr H), 7.88 (t, J = 7.8 Hz, 1H, pyr H), 7.70-7.69 (m, J = 0.9 Hz, 5H, pyr H), 4.77 (d, 2H, CH$_2$), 0.32 (s, 9H, TMS).; ^{13}C{^{1}H} NMR (150 MHz, DMSO-d_6): δ (ppm) = 161.1, 150.9, 149.8, 147.6 142.2, 137.1, 130.7, 122.4, 121.8, 112.7, 87.6, 42.1.

6-(1-(pyridin-3-ylmethyl)-1H-1,2,3-triazol-4-yl)-N-(pyridin-4-ylmethyl)picolinamide (H169)
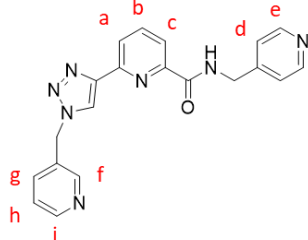
Synthesised according to general procedure 3 from 3-picolylamine (0.065 mL, 0.65 mmol) and **171** (0.2 g, 0.65 mmol) to yield a crude yellow oil which was purified by being dissolved in DCM followed by washing with 1M HCl. The remaining HCl solution was then basified with 1M NaOH to yield the pure product as a white precipitate in 52% yield; m.p. 162 - 169 ℃; HRMS (m/z) (ESI+): C$_{20}$H$_{17}$N$_7$O$^+$ m/z = 372.1573 [M+H]$^+$. Found m/z = 372.1573; ^{1}H NMR (600 MHz, DMSO-d_6): δ (ppm) = 9.53 (t, 1H, J = 6.3 Hz, NH), 8.97 (s, 1H, triazole H), 8.65 (d, 1H, Hf), 8.57 (d, J = 4.7 Hz, 1H, Hi), 8.50 (d, J = 5.7 Hz, 1H, He), 8.22 (dd, J = 7.8, 1.0 Hz, 1H, Ha), 8.10 (t, J = 7.8 Hz, 1H, Hb), 7.99 (dd, J = 7.8, 1.0 Hz, 1H, Hc), 7.73 (d, J = 8.0 Hz, 1H, Hg), 7.43 (dd, J = 8.0, 4.7 Hz, 1H, Hh), 7.31 (d, J = 5.7 Hz, 1H, Hd), 5.81 (s, 2H, *CH$_2$*-triazole), 4.58 (d, J = 6.3 Hz, 2H, *CH$_2$*-NH); ^{13}C{^{1}H} NMR (150 MHz, DMSO-d_6): δ (ppm) = 164.1, 149.6, 149.4, 149.4, 149.1, 148.8, 148.4, 147.2, 139.0, 135.7, 131.6, 124.5, 124.0, 122.1, 121.9,

121.0, 50.8, 41.5.; IR ν$_{max}$ (cm^{-1}): 3478, 3324, 3070, 1662, 1599, 1523, 1417, 1369, 1230, 1163, 1048, 995, 847, 789, 760, 663, 607.

N,N'-(1,3-phenylenebis(methylene))bis(6-(1-(pyridin-2-ylmethyl)-1H-1,2,3-triazol-4-yl)picolinamide) (H₂172)

Compound 133 was synthesised according to modified general procedure 2 with 2-(bromomethyl)pyridine hydrobromide (0.187 g, 0.74 mmol), compound **161** (0.20 mg, 0.3 mmol) using tris[(1-benzyl-1H-1,2,3-triazol-4-yl)methyl]amine (TBTA) (0.019 mg, 0.037 mmol) and [Cu(CH₃CN)₄]PF₆ (0.007 g, 0.018 mmol) in place of CuSO₄·5H₂O to give compound **H₂172** in 63 % yield.; m.p. 178 - 185 °C; HRMS (*m/z*) (ESI+): C₃₆H₃₀N₁₂O₂Na *m/z* = 685.2512 [M+Na]⁺ Found *m/z* = 685.2507; ¹H NMR (600 MHz, DMSO-*d₆*): δ (ppm) = 9.49 (d, *J* = 6.3 Hz, 2H, NH), 9.01 (s, 2H, triazole H), 8.52 (d, *J* = 4.4 Hz, 2H, Hd), 8.17 (d, *J* = 1.1, 7.7 Hz, 2H, Ha), 8.03 (t, *J* = 7.7 Hz, 2H, Hb), 7.92 (d, *J* = 1.1, 7.7 Hz, 2H, Hc), 7.83 (t, *J* = 7.7, 8.0 Hz, 2H, Hf), 7.36 (dd, *J* = 4.4, 7.7 Hz, 4H, He & Hg), 7.27 (d, *J* = 13.3 Hz, 2H, ArH), 7.21 (d, *J* = 13.3 Hz, 2H, Ar H), 5.81 (s, 4H, CH₂-pyr), 4.53 (d, *J* = 6.3 Hz, 4H, CH₂-NH); ¹³C{¹H} NMR (150 MHz, DMSO-*d₆*): δ (ppm) = 163.7, 154.7, 149.6, 149.4, 148.8, 146.9, 139.7, 138.8, 137.6, 128.3, 125.8, 125.7, 125.3, 123.4, 122.3, 121.5, 120.7, 54.7, 42.3; IR ν$_{max}$ (cm^{-1}): 3363, 3319, 3075, 2194, 2045, 1983, 1901, 1676, 1595, 1570, 1513, 1437,1412, 1355, 1271, 1226, 1177, 1077, 1010, 838, 751, 689, 636, 598.
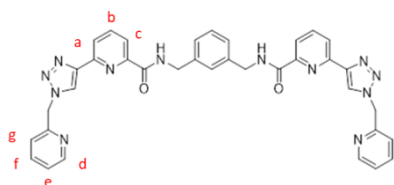
N,N'-(ethane-1,2-diyl)bis(6-bromopicolinamide) (174)
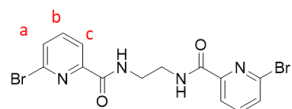
Synthesised according to the procedure for compound **161** from ethylenediamine (2.0 g, 6.75 mmol) and 6-bromopyridine-2-carboxylic acid (3.0 g, 14.8 mmol) to give compound **174** in 42% yield.; m.p. 149 - 158 °C; HRMS (*m/z*) (ESI+): C₁₄H₁₂N₄O₂Br₂Na *m/z* = 448.9225 [M+Na]⁺ Found *m/z* = 448.9219; ¹H NMR (600 MHz, DMSO-*d₆*): δ (ppm) = 8.83 (s, 2H, NH), 8.03 (d, *J* = 7.7 Hz, 2H, Ha), 7.93 (t, *J* = 7.7 Hz, 2H, Hb), 7.85 (d, *J* = 7.7 Hz, 2H, Hc), 3.53 – 3.49 (m, 4H, CH₂); ¹³C{¹H} NMR (150 MHz, DMSO-*d₆*): δ (ppm) = 163.4, 151.9, 141.4, 140.6, 131.3, 122.1, 39.4.; IR ν$_{max}$ (cm^{-1}): 3310, 3042, 2951, 2146, 1738, 1652, 1565, 1522, 1494, 1446, 1413, 1297, 1249, 1210, 1144, 1073, 990, 938, 895, 847, 818, 760, 712.

N,N'-(ethane-1,2-diyl)bis(6-((trimethylsilyl)ethynyl)picolinamide) (175)
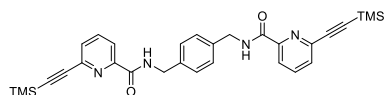
Synthesised with general procedure 1 from compound **174** (0.73 g, 1.7 mmol) and ethynyltrimethylsilane (0.5 mL, 3.8 mmol) to yield compound **175** in 82 % yield.; m.p. 163 - 169 ℃; HRMS (*m/z*) (ESI+): $C_{24}H_{30}N_4O_2Si_2Na$ *m/z* = 445.1805 [M+Na]$^+$ Found *m/z* = 445.1799; ^{1}H NMR (600 MHz, DMSO-*d$_6$*): δ (ppm) = 8.82 (s, 2H, NH), 8.04 – 7.95 (m, *J* = 7.2, 1.2 Hz, 4H, pyr H), 7.72 (dd, *J* = 7.2, 1.2 Hz, 2H, Pyr H-alkyne), 3.58 – 3.47 (m, 4H, CH$_2$), 0.26 (s, 18Hf, 3CH$_3$); ^{13}C{^{1}H} NMR (150 MHz, DMSO-*d$_6$*): δ (ppm) = 164.0, 151.1, 141.2, 138.9, 130.5, 122.4, 104.1, 95.6, 39.4, 0.1; IR ν_{max} (cm^{-1}): 3302, 2968, 2897, 2159, 1739, 1653, 1567, 1526, 1440, 1319, 1304, 1243, 1167, 1074, 995, 994, 826, 757, 676, 646, 585.

N,N'-(ethane-1,2-diyl)bis(6-(1-(pyridin-3-ylmethyl)-1H-1,2,3-triazol-4-yl)picolinamide) (173)

Synthesised according to general procedure 3 from 3-aminomethylpyridine (0.05 mL, 0.54 mmol) and compound **175** (0.25 g, 0.54 mmol) to give compound **173** in 65% yield.; m.p.
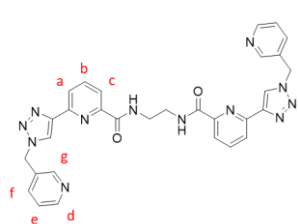
181 - 185 ℃; HRMS (*m/z*) (ESI+): Calculated for $C_{30}H_{26}N_{12}O_2^+$ *m/z* = 587.2380 [M+H]$^+$. Found *m/z* = 587.2374 ; ^{1}H NMR (600 MHz, DMSO-*d$_6$*): δ (ppm) = 9.18 (s, 2H, NH), 9.01 (s, 2H, triazole H), 8.66 (s, 2H, Hg), 8.57 (d, *J* = 8.1, 4.0 Hz, 2H, Hd), 8.19 (d, *J* = 7.7, 1.1 Hz, 2H, Ha), 8.04 (t, *J* = 7.7 Hz, 2H, Hb), 7.90 (d, *J* =

7.7, 1.1 Hz, 2H, Hc), 7.73 (d, *J* = 8.1 Hz, 2H, He), 7.43 (dd, *J* = 8.1, 4.0 Hz, 2H, Hf), 5.81 (s, 4H, CH$_2$-triazole), 3.61 – 3.49 (m, 4H, CH$_2$-NH); ^{13}C{^{1}H} NMR (150 MHz, DMSO-*d$_6$*): δ (ppm) = 164.3, 162.3, 149.6, 149.1, 148.7, 147.2, 138.9, 135.7, 131.5, 124.4, 123.9, 121.6, 120.5, 50.8, 35.8

Synthesis of coordination polymer {[Ag$_2$(166)$_2$](CF$_3$SO$_3$)$_2$}$_n$

To a solution of AgCF$_3$SO$_3$ (0.0134 mmol, 3 mg) in THF (2 mL) was added a solution of **166** (0.0134 mmol, 5 mg) in THF (3 mL). Upon reaction together, a colourless solution resulted and allowed to react in a closed vessel to yield yellow crystals after one week. The crystals were isolated by filtration, washed with THF and allowed to air dry. Yield; (3 mg, 48%); m.p. (decomp) >280 ℃; Elemental analysis for $C_{22}H_{18}N_6O_4F_3SAg$ Calculated: C 42.12 H 2.89 N 13.39; Found: C 42.62 H 2.79 N 13.43 %; IR ν_{max} (cm^{-1}): 3344, 3094, 2956, 2861, 2289, 1989, 1650, 1600, 1539, 1456, 1439, 1361, 1333, 1283, 1250, 1222, 1144, 1106, 994, 833, 761, 716, 639, 600.

Synthesis of [Cu₃(169)₂(CF₃SO₃)(OCH₃)₂]CF₃SO₃.H₂O

To a solution of [Cu(CH₃CN)₄](CF₃SO₃) (5 mg, 0.013 mmol) in CH₃OH (2 mL) was added a solution of **H169** (5 mg, 0.013 mmol) in CH₃OH (3 mL). Upon reaction together, a blue solution resulted and allowed to react in a closed vessel to yield blue crystals after several week. The crystals were isolated by filtration, washed with CH₃OH and allowed to air dry. Yield; (6 mg, 60%); m.p. (decomp) >280 ºC; IR ν_{max} (cm⁻¹): 3511, 3435, 3353, 3310, 2965, 2040, 1916, 1666, 1604, 1522, 1575, 1446, 1355, 1235, 1153, 1077, 1024, 828, 708, 631.

Synthesis of [Cu₄(H172)₄](PF₆)₄

To a solution of [Cu(CH₃CN)₄](PF₆) (0.0008 mmol, 3 mg) in CH₃OH (2 mL) was added a solution of **H₂172** (5 mg, (0.013 mmol) in CH₃OH (3 mL). Upon reaction together, a blue solution resulted and allowed to react in a closed vessel to yield blue crystals after several week. The crystals were isolated by filtration, washed with CH₃OH and allowed to air dry. Yield; (4 mg, 50%); m.p. (decomp) >280 ºC; IR ν_{max} (cm⁻¹):3389, 3250, 3067, 1661 1594, 1561, 1522, 1472, 1433, 1383, 1311, 1244, 1209, 1094, 1055, 994, 838, 750, 700, 588, 550.

Formation of 162.AgBF₄ gel

Reaction of ligand **1** (5 mg, 0.0075 mmol) with AgBF₄ (2 mg, 0.0075 mmol) in CH₃CN (2mL) in a closed vessel resulted in a gel material overnight.

Experimental Details for Chapter Four

Methyl-6-bromopicolinate (183)
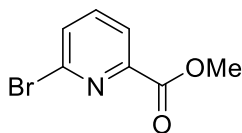
6-bromopicolinic acid (3.0 g, 14.85 mmol) was suspended in MeOH (5 mL) and 4 drops of sulfuric acid were added. The mixture was heated to reflux for four hours and quenched with NaHCO₃ in water. The product was extracted into DCM, washed with sodium hydrogen carbonate solution and dried over magnesium sulphate to yield a white solid (2.095 g, 9.65 mmol, 77%). The product decomposed over 91 °C. HRMS (*m/z*) (ESI+): Calculated for C₇H₇BrNO₂⁺ *m/z* = 215.9660 [M+H]⁺. Found *m/z* = 215.9654 ; ¹H NMR (400 MHz, CDCl₃-*d₆*): δ (ppm) = 8.10 (dd, *J* = 6.7, 1.8 Hz, 1H, 3-pyr H), 7.69 (t, *J* = 6.7, 2H, 4-pyr H),7.70 (dd, *J* = 6.7, 1.8 Hz, 1H, 5-pyr H), 4.00 (s, 3H, OCH₃). ¹³C{¹H} NMR (150 MHz, DMSO-*d₆*): δ (ppm) = 163.8,

148.1, 141.3, 140.9, 132.1, 124.5, 52.8 ; IR ν_{max} (cm^{-1}): 3106, 2968, 1718, 1556, 1437, 1422, 1310, 1246, 1132, 1113, 985, 955, 757, 732.

Methyl 6-((trimethylsilyl)ethynyl)picolinate (184)
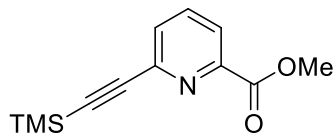
Synthesised according to general procedure from **183** (1.650 g, 7.60 mmol) and ethynyltrimethylsilane (1.1 mL, 7.60 mmol) to yield a brown solid which was purified by flash column chromatography (RediSep® 12g, gradient elution $0 \rightarrow 90$ % EtOAc in Hexane) to yield a brown solid. Yield (1.158 g, 4.94 mmol, 65 %). The product decomposes over 85 °C. HRMS (*m/z*) (ESI+): Calculated for C$_{12}$H$_{15}$NO$_2$Si$^+$ *m/z* = 234.0950 [M+H]$^+$. Found *m/z* = 234.0963; ^{1}H NMR (400 MHz, CDCl$_3$-*d6*): δ (ppm) = 8.06 (d, *J* = 7.6 Hz, 1H, 3-pyr H), 7.80 (t, *J* = 8.1, 7.6 Hz, 1H, 4-pyr H), 7.63 (d, *J* = 8.1 Hz, 1H, 5-pyr H), 4.00 (s, 3H, OCH$_3$), 0.26 (s, 9H, Si-(CH$_3$)$_3$). ^{13}C{^{1}H} NMR (150 MHz, DMSO-*d6*): δ (ppm) = 164.6, 147.8, 141.8, 138.5, 130.5, 124.6, 103.3, 95.1, 52.6, 0.4.; IR ν_{max} (cm^{-1}): 3106, 3082, 2092, 1864, 1736, 1577, 1437, 1251, 840, 764.

4-((4-(6-(methoxycarbonyl)pyridin-2-yl)-1H-1,2,3-triazol-1-yl)methyl)benzoic acid (185)
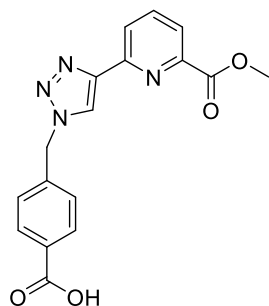
To a solution of 4-bromomethyl benzoic acid (1.418 g, 6.60 mmol) in 10 mL 4:1 DMF/water was added sodium azide (0.428 g, 6.60 mmol) and the reaction mixture was stirred for one hour to yield the azide intermediate which was not isolated and therefore used without further purification. To this solution was added ligand **184** (1.539 g, 6.560 mmol), CuSO$_4$·5H$_2$O (0.329 g, 1.32 mmol), sodium ascorbate (0.522 g, 2.64 mmol) and anhydrous K$_2$CO$_3$ (0.912 g, 6.60 mmol) and stirred at room temperature under argon atmosphere overnight. 1 M EDTA/NH$_4$OH solution was added to the mixture and the product was precipitated using 1M HCl and filtered to yield an off-white solid. The product was used without further purification. (1.562 g, 4.62 mmol, 70 %). HRMS (*m/z*) (ESI+): Calculated for C$_{17}$H$_{14}$N$_4$O$_4$H$^+$ *m/z* = 339.1093 [M+H]$^+$. Found *m/z* = 339.1087 ; ^{1}H NMR (400 MHz, DMSO-*d6*): δ (ppm) = 8.82 (s, 1H, triazole CH), 8.26 (dd, *J* = 7.8, 1.1 Hz, 1H, 5-pyr H), 8.10 (s, *J* = 7.8, 1H, 4-pyr *H*), 8.00 (dd, *J* = 7.8, 1.1 Hz, 1H, 3-pyr H), 7.95 (d, *J* = 8.4 Hz, 2H, Ar*H*-COOH), 7.47 (d, *J* = 8.4 Hz, 2H, Ar*H*-CH$_2$), 5.79 (s, 2H, C*H$_2$*-Ar), 3.90 (s, 3H, COO-*CH$_3$*). ^{13}C{^{1}H} NMR (150 MHz, DMSO-*d6*): δ (ppm) = 170.1, 165.6,

150.2, 147.6, 146.8, 137.2, 138.7, 135.3, 129.2, 128.1, 124.1, 123.9, 123.1, 52.7.; IR ν_{max} (cm^{-1}): 1725, 1612, 3215, 1282, 1126, 1011, 776, 707.

Methyl(R)-6-(1-(4-((1-methoxy-1-oxo-3-phenylpropan-2-yl)carbamoyl)benzyl)-1H-1,2,3-triazol-4-yl)picolinate (179)
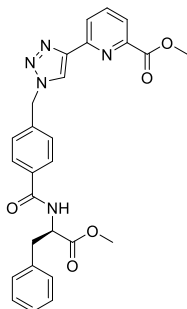
Synthesised according to general procedure 4 from phenylalanine hydrochloride (0.99 g, 4.91 mmol) and compound **185** (1.512g, 4.47 mmol) to yield a white solid. (1.611 g, 3.26 mmol, 72%). The product decomposes over 207 °C. HRMS (*m/z*) (ESI+): Calculated for C$_{27}$H$_{25}$N$_5$O$_5$Na$^+$ *m/z* = 522.1753 [M+Na]$^+$. Found *m/z* =522.1767; ^{1}H NMR (600 MHz, DMSO-*d$_6$*): δ (ppm) = 8.86 (d, *J* = 8.1 Hz, 1H, NH), 8.80 (s, 1H, triazole H), 8.26 (d, *J* = 1.1, 7.7 Hz, 1H, 5-pyr H), 8.10 (m, *J* = 1.1 Hz, 1H, 4-pyr *H*), 8.01 (d, *J* = 1.1, 7.7 Hz, 1H, 3-pyr H), 7.80 (d, *J* = 8.3 Hz, 2H, Ar *H*-C=O), 7.46 (d, *J* = 8.3 Hz, 2H, Ar *H*-CH$_2$), 7.28 (m, 4H, phe H), 7.19 (s, 1H, phe H), 5.76 (s, 2H, CH$_2$), 4.65 (s, *J* = 8.1 Hz, 1H, C*H*-NH), 3.91 (s, 3H, pyr-COOC*H$_3$*), 3.63 (s, 3H, COOCH$_3$), 3.23 – 2.97 (m, 2H, C*H$_2$*-Phe). ^{13}C{^{1}H} NMR (150 MHz, DMSO-*d$_6$*): δ (ppm) = 172.1, 165.9, 165.0, 150.1, 147.6, 146.7, 139.2, 138.7, 137.6, 133.5, 129.0, 128.2, 127.9, 127.9, 126.5, 124.1, 123.8, 122.9, 54.2, 52.6, 52.5, 51.9, 36.2; IR ν_{max} (cm^{-1}): 3314, 1732, 1719, 1637, 1600, 1539, 1438, 1349, 1246, 1135, 1221, 1006, 825, 776, 752, 706, 644.

methyl (R)-6-(1-(4-((3-(1H-indol-3-yl)-1-methoxy-1-oxopropan-2-yl)carbamoyl)benzyl)-1H-1,2,3-triazol-4-yl)picolinate (180)
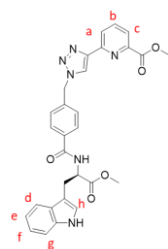
Synthesised according to general procedure 4 from tryptophan hydrochloride (0.15 g, 0.59 mmol) and compound **185** (0.20 g, 0.59 mmol) to yield compound **180** as a white solid (0.20 g, 63%);HRMS (*m/z*) (ESI+): C$_{29}$H$_{26}$N$_6$O$_5$$^+$ *m/z* = 538.1965 [M+H]$^+$. Found *m/z* = 539.2037; ^{1}H NMR (600 MHz, DMSO-*d$_6$*): δ (ppm) = 10.80 (s, 1H, NH), 8.81 (s, 1H, NH), 8.79 (s, 1H, triazole H), 8.26 (d, *J* = 7.9 Hz, 1H, Ha), 8.10 (t, *J* = 7.8 Hz, 1H, Hb), 8.00 (d, *J* = 7.7 Hz, 1H, Hc), 7.82 (d, *J* = 8.2 Hz, 2H, Phe-CH$_2$), 7.54 (d, *J* = 7.9 Hz, 1H, Hd), 7.46 (d, *J* = 8.2 Hz, 2H, Phe-C=O), 7.31 (d, *J* = 8.1 Hz, 1H, Hg), 7.18 (s, 1H, Hh), 7.05 (t, *J* = 7.5 Hz, 1H, Hg), 6.97 (t, *J* = 7.4 Hz, 1H, He), 5.75 (s, 2H, CH$_2$-triazole), 4.67 (d, *J* = 5.4 Hz, 1H, CH), 3.91 (s, 3H, CH$_3$-pyr), 3.62 (s, 3H, CH$_3$-Tryp), 3.24 (ddd, *J* = 23.9, 14.6, 7.3 Hz, 2H, CH$_2$-Tryp); ^{13}C{^{1}H} NMR (150 MHz, DMSO-*d$_6$*): δ (ppm) = 172.9, 166.5, 165.5, 150.6, 148.1, 147.1, 139.6, 139.2, 136.6, 134.1, 128.4, 124.6, 124.4, 124.1, 123.4, 121.4, 118.9,

118.5, 111.9, 110.4, 54.3, 53.1, 52.9, 52.4, 27.1; IR ν_{max} (cm^{-1}): 3403, 3297, 3150, 3049, 2948, 2923, 2841, 1739, 1627, 1602, 1531, 1450, 1369, 1253, 1217, 1147, 1055, 1010, 974, 772, 737, 696, 600.

(R)-6-(1-(4-((1-carboxy-2-phenylethyl)carbamoyl)benzyl)-1H-1,2,3-triazol-4-yl)picolinic acid (181)
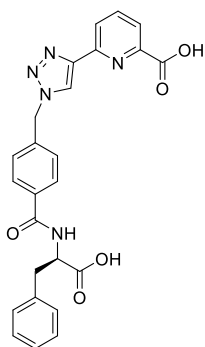
Compound **179** (1.611g, 3.23 mmol) was suspended in 1M NaOH and refluxed for 3 hours. The product was isolated by neutralization of the solution with acetic acid and filtration to yield a white solid. (1.278 g, 2.72 mmol, 84 %). HRMS (*m/z*) (ESI+): Calculated for $C_{25}H_{21}N_5O_5Na^+$ *m/z* = 494.1440 [M+Na]$^+$. Found *m/z* =494.1459; ^{1}H NMR (400 MHz, DMSO-*d6*): δ (ppm) = 8.77 (s, 1H, triazole H), 8.25 (s, 1H, NH), 8.00 (d, *J* = 8.1 Hz, 1H, 5-pyr H), 7.91 (m, *J* = 7.6, 8.1 Hz, 1H, 4-pyr H), 7.85 (d, *J* = 7.6 Hz, 1H, 3-pyr H), 7.73 (d, *J* = 8.2 Hz, 2H, Ar H-C=O), 7.42 (d, *J* = 8.2 Hz, 2H, Ar *H*-CH₂), 7.23 – 7.07 (m, 5H, phe H), 5.74 (s, 2H, CH₂), 4.33 (s, 1H, CH-N*H*), 3.04 (dd, 2H, C*H₂*-Ph).; ^{13}C{^{1}H} NMR (150 MHz, DMSO-*d6*): δ (ppm) = 173.10, 167.22, 165.79, 154.12, 149.30, 149.27, 147.75, 139.22, 139.13, 138.37, 134.84, 129.69, 128.40, 128.08, 126.48, 124.37, 123.41, 121.20, 55.29, 53.16, 37.24.; IR ν_{max} (cm^{-1}): 3355, 3059, 2436, 1960, 1736, 1634, 1535, 1503, 1381, 1180, 1052, 851, 812, 737.

N-benzyl-6-(1-benzyl-1H-1,2,3-triazol-4-yl)picolinamide (186)
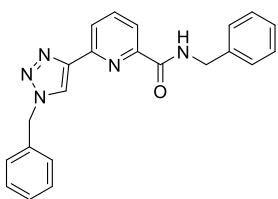
Synthesised according to general procedure from benzylbromide (0.13 mL, 1.135 mmol) and **188** (0.35 g, 1.13 mmol) to yield a white solid (85% yield) HRMS (*m/z*) (ESI+): $C_{22}H_{20}N_5O^+$ *m/z* = 370.1662 [M+H]$^+$. Found *m/z* = 370.1662; ^{1}H NMR (600 MHz, DMSO-*d6*): δ (ppm) = 9.47 (t, 1H, *J* = 6.5 Hz, NH), 8.98 (s, 1H, triazole H), 8.21 (d, *J* = 7.8, 0.6 Hz, 1H, pyr H), 8.09 (t, 1H, *J* = 7.8 Hz, pyr H), 7.99 (d, 1H, *J* = 7.8, 0.6 Hz, Pyr H), 7.39 – 7.23 (m, 10H, Ar H), 5.73 (s, 2H, CH₂-triazole), 4.56 (d, *J* = 6.5 Hz, 2H, CH₂-NH); ^{13}C{^{1}H} NMR (150 MHz, DMSO-*d6*): δ (ppm) = 163.8, 149.7, 148.8, 147.2, 139.5, 138.9, 135.9, 128.9, 128.3, 128.2, 127.7, 127.1, 126.8, 124.5, 121.7, 120.9, 53.2, 42.3; IR ν_{max} (cm^{-1}): 3322.8, 1654.9, 1601.8, 1571.5, 1521.9, 1545.6, 1420.3, 1354.1, 1257.3, 1232.6, 1168.8, 1042.9, 995.4, 977.0, 820.2, 750.7, 716.7, 696.3, 582.9;

Synthesis of [Tb(179)$_2$]$^{2+}$

Ligand **179** (10 mg, 0.02 mmol) was added to Tb(CF$_3$SO$_3$)$_3$ (5 mg, 0.007 mmol) in CH$_3$OH (5 mL) and heated at 70 ˚C under microwave irradiation for 15 minutes. The resultant solution was dried under vacuum to yield a colorless oil which was taken up in CH$_3$OH and dropped slowly into a large excess of swirling Et$_2$O to afford Tb.**179**$_2$ as a white solid in 56% yield. HRMS (*m/z*) (ESI+): C$_{56}$H$_{50}$N$_{10}$O$_{16}$F$_6$S$_2$Tb *m/z* = 1455.2005 [Tb(**179**)$_2$(CF$_3$SO$_3$)$_2$]$^+$. Found *m/z* = 1455.2075; IR ν_{max} (cm^{-1}): 3000, 1713, 1585, 1478, 1428, 1376, 1315, 1278, 1250, 1187, 1114, 996, 851, 767, 746, 697, 655.

Synthesis of [Tb(180)$_2$]$^{2+}$

Ligand **180** (10 mg, 0.02 mmol) was added to Tb(CF$_3$SO$_3$)$_3$ (5 mg, 0.007 mmol) in CH$_3$OH (5 mL) and heated at 70 ˚C under microwave irradiation for 15 minutes. The resultant solution was dried under vacuum to yield a colorless oil which was taken up in CH$_3$OH and dropped slowly into a large excess of swirling Et$_2$O to afford Tb.**180**$_2$ as a white solid in 43% yield. HRMS (*m/z*) (ESI+): C$_{60}$H$_{52}$N$_{12}$O$_{16}$F$_6$S$_2$Tb *m/z* = 1533.2223 [Tb(**180**)$_2$(CF$_3$SO$_3$)$_2$]$^-$. Found *m/z* = 1533.2262; IR ν_{max} (cm^{-1}): 1735, 1641, 1608, 1535, 1447, 1445, 1222, 1155, 1061, 1027, 836, 777, 744, 701, 660.

Synthesis of [Eu(179)$_2$]$^{2+}$

Ligand **179** (10 mg, 0.02 mmol) was added to Eu(CF$_3$SO$_3$)$_3$ (5 mg, 0.007 mmol) in CH$_3$OH (5 mL) and heated at 70 ˚C under microwave irradiation for 15 minutes. The resultant solution was dried under vacuum to yield a colorless oil which was taken up in CH$_3$OH and dropped slowly into a large excess of swirling Et$_2$O to afford Eu.**179**$_2$ as a white solid in 69 % yield. IR ν_{max} (cm^{-1}): 1721, 1636, 1530, 1501, 1449, 1242, 1166, 1046, 809, 729.

Experimental Details for Chapter 5

2,6-dibromopyridine 1-oxide (191)
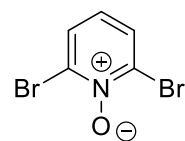
Synthesised according to literature procedure[292] from 2,6-dibromopyridine (2.0 g, 8.44 mmol) was dissolved in TFA (15 mL, 0.196 mmol) and hydrogen peroxide (2 mL) and the mixture was heated to reflux for 48 hours. The resulting solution was diluted in H$_2$O and stirred for one hour, after which the starting

material was filtered off as a pale pink solid. The yellow filtrate was extracted into CH_2Cl_2 (3 x 20 mL) and the organic layer was washed with K_2CO_3 (0.5 M, 3 x 10 mL). The organic layer was then dried over $MgSO_4$, and concentrated under reduced pressure to yield a pale yellow solid (1.533 g, 72%); m.p. 155 - 158 ºC; HRMS (*m/z*) (ESI+): $C_5H_3NOBr_2^+$ *m/z* = 250.8581 [M+H]$^+$. Found *m/z* = 251.8510; ^{1}H NMR (400 MHz, CDCl$_3$): δ (ppm) = 7.65 (d, *J* = 8.1 Hz, 2H, *meta*-H), 6.96-6.88 (t, *J* = 8.1 Hz, 1H, *ortho*-H); ^{13}C{^{1}H} NMR (150 MHz, DMSO-d_6): δ (ppm) = 132.8, 130.2, 125.9; IR ν_{max} (cm^{-1}): 3109, 3085, 2495, 1930, 1863, 1795, 1667, 1577, 1526, 1436, 1359, 1250, 1156, 1134, 1109, 1074, 836, 761, 744;

2,6-dibromo-4-nitropyridine 1-oxide (192)
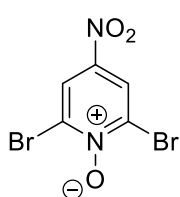
Synthesised according to literature procedure[293] from **191** (1.3g, 5.3 mmol) and concentrated H_2SO_4 (8.5 mL) in HNO_3 (3.5 mL). The mixture was stirred at 80 ˚C overnight and upon cooling to room temperature was poured onto ice. The mixture was neutralised with ammonium hydroxide and the product was filtered off as a pale yellow solid (1.216 g, 76%); m.p. 169 - 173 ºC; HRMS (*m/z*) (ESI+): $C_5H_3N_2O_3Br_2^+$ *m/z* = 295.8432 [M+H]$^+$. Found *m/z* = 296.8505; ^{1}H NMR (400 MHz, CDCl$_3$): δ (ppm) = 8.45 (s, 2H), ^{13}C{^{1}H} NMR (150 MHz, DMSO-d_6): δ (ppm) = 133.5, 123.9 ; IR ν_{max} (cm^{-1}): 3345, 2971, 1515, 1465, 1408, 1380, 1325, 1282, 1150, 1129, 1107, 948, 911, 884, 816, 761, 733, 709;

2,6-dibromo-4-nitropyridine (193)
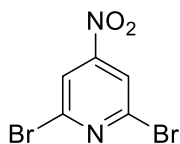
Synthesised according to literature procedure [294] from **192** (1.44 g, 4.8 mmol) in with acetic acid (40 mL, 69.0 mmol) and Fe filings (1.06 g, 19.0 mmol) to yield a light brown solid (0.82 g, 63%);HRMS (*m/z*) (ESI+): $C_5H_3N_2O_3Br_2^+$ *m/z* = 295.8432 [M+H]$^+$. Found *m/z* = 296.8505; ^{1}H NMR (400 MHz, CDCl$_3$): δ (ppm) = 8.19 (s, 2H), ^{13}C{^{1}H} NMR (150 MHz, CDCl$_3$): δ (ppm) = 142.5, 120.6; IR ν_{max} (cm^{-1}):3251, 3245, 2549, 1758, 1743, 1622, 1528, 1438, 1358, 1253, 1112, 1012, 1009, 943, 766, 748;

((((2,6-dibromopyridin-4-yl)oxy)ethyl)tert-butyl carbamate (195)
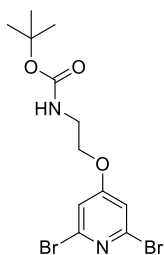
194 (1.38 g, 4.90 mmol) was dissolved in dry THF and sodium (0.176 g, 7.35 mmol) was added. The mixture was stirred under argon for 3 hours. Compound **193** was then dissolved in THF and added. The mixture was stirred at room temperature for 24 hours. The reaction was quenched with a saturated solution of ammonium chloride, diluted in 50 mL water and extracted into ethyl acetate. The solution was dried over magnesium sulphate and the solvent was removed under reduced pressure. The product was purified by flash column chromatography (Pet Ether: Ethyl Acetate; to 90:10) to yield an orange oil. (1.383 g, 3.49 mmol, 60 %). m.p. 163 - 168 °C; HRMS (m/z) (ES-): Calculated for $C_{12}H_{16}Br_2N_2O_3Cl^-$ m/z = 428.9216 [M+Cl]$^-$. Found m/z = 428.9228 ; ^{1}H NMR (400 MHz, CDCl$_3$):δ = 6.98 (s, 2H, pyr H), 4.89 (s, 1H, NH), 4.07 (t, J = 4.1 Hz, 2H, O-CH$_2$), 3.53 (q, J = 4.1 Hz, 2H, N-CH$_2$), 1.45 (s, 9H, t-butyl). ^{13}C{^{1}H} NMR (150 MHz, DMSO): δ = 166.6, 155.7, 141.2, 113.8, 80.0, 68.2, 39.6, 28.4.; IR ν$_{max}$ (cm^{-1}): 2976, 1695, 1569, 1532, 1366, 1280, 1235, 1151, 1067, 1041, 957, 760

tert-butyl (2((2,6-bis((trimethylsilyl)ethynyl)pyridine-4-yl)oxy)ethyl)carbamate (196)
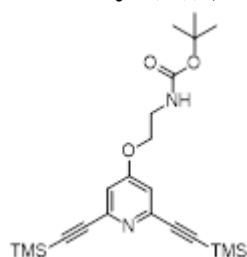
Ligand **195** (1.18 g, 2.98 mmol), Pd(PPh$_3$)$_2$Cl$_2$ (0.126 g, 0.18 mmol) and CuI (0.039 g, 0.36 mmol) were suspended in dry THF:NEt$_3$ under argon atmosphere over ice. Ethynyltrimethylsilane (1 mL, 7.45 mmol) was added dropwise and the reaction was stirred at room temperature for 48 hours. The reaction mixture was concentrated under reduced pressure and suspended in hexane. The suspension was filtered through celite and purified by flash chromatography (Pet Ether: Ethyl Acetate) to yield a brown oil. (0.834 g, 1.94 mmol, 65 %). m.p. 172 - 178 °C; HRMS (m/z) (ESI+): Calculated for $C_{22}H_{35}N_2O_3Si_2^+$ m/z = 431.2186 [M+H]$^+$. Found m/z = 431.2105 ; ^{1}H NMR (400 MHz, CDCl$_3$):δ = 6.93 (s, 2H, pyridine H), 4.89 (s, 1H, NH), 4.08 (t, J = 4.1 Hz ,2H, O-CH$_2$), 3.53 (q, J = 4.1 Hz, 2H, N-CH$_2$), 1.45 (s, 9H, O-(CCH$_3$)$_3$), 0.25 (s, 18H, TMS). ^{13}C{^{1}H} NMR (150 MHz, DMSO): δ = 165.2, 152.9, 144.0, 113.7, 102.4, 80.0, 67.8, 39.9, 29.9, 28.5, -0.3; IR ν$_{max}$ (cm^{-1}): 3821, 2963, 2166, 1693, 1580, 1530, 1339, 1272, 1245, 1153, 1048, 842, 759.

dimethyl 4,4'-(((4-(2-((tert-butoxycarbonyl)amino)ethoxy)pyridine-2,6-diyl)bis(1H-1,2,3-triazole-4,1-diyl))bis(methylene))dibenzoate (198)

To a solution of 4-bromomethyl benzoate (**197**) (0.954 g, 4.17 mmol) in 10 mL 4:1 DMF/water was added sodium azide (0.271 g, 4.17 mmol) and the reaction mixture was stirred for one hour to yield the azide intermediate which was not isolated and therefore used without further purification. To this solution was added **196** (0.897 g, 2.08 mmol), $CuSO_4.5H_2O$ (0.208 g, 0.83 mmol), sodium ascorbate (0.329 g, 1.67 mmol) and anhydrous K_2CO_3 (0.575 g, 4.16 mmol) and stirred at room temperature under argon atmosphere overnight. 1 M EDTA/NH_4OH solution was added to the mixture and the product was extracted into CH_2Cl_2. The organic layer was washed with water and dried over magnesium sulphate. The solvent was removed under reduced pressure to yield an off-white solid. (0.724 g, 1.08 mmol, 52 %). The product decomposed over 242 °C. HRMS (*m/z*) (ESI+): Calculated for $C_{34}H_{36}N_8O_8H^+$ *m/z* = 669.2785 [M+H]$^+$. Found *m/z* = 669.2785 ; ^{1}H NMR (600 MHz, DMSO) δ = 8.69 (s, 2H, triazole H), 7.98 (d, *J* = 8.2 Hz, 4H, Ar *H*-COOMe), 7.49 (s, 2H, pyr H), 7.45 (d, *J* = 8.2 Hz, 4H, Ar *H*-CH$_2$), 7.06 (s, 1H, NH), 5.80 (s, 4H, C*H*$_2$-Ar), 4.21 (t, *J* = 5.6 Hz, 2H, O-C*H*$_2$), 3.84 (s, 6H, O-CH$_3$), 3.37 (q, *J* = 5.6 Hz, 2H, C*H*$_2$-NH), 1.37 (s, 9H, O(CH$_3$)$_3$). ^{13}C{^{1}H} NMR (150 MHz, DMSO): δ = 170.3, 166.3,151.3, 146.6, 138.6, 130.5, 130.2, 129.0, 128.2, 128.1, 108.4, 77.2, 69.9, 54.2, 52.3, 39.5, 28.4.; IR ν$_{max}$ (cm^{-1}): 3099, 2952, 1689, 1563, 1536, 1499, 1396, 1270, 1171, 3099, 2236, 1717, 1407, 1368, 1110, 1046, 1022, 936, 850, 767, 725.
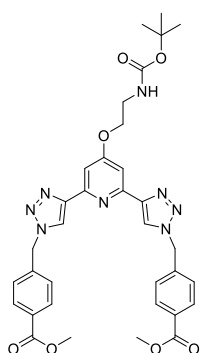
dimethyl 4,4'-(((4-(2-aminoethoxy)pyridine-2,6-diyl)bis(1H-1,2,3-triazole-4,1-diyl))bis(methylene))dibenzoate (189)

Ligand **198** was deprotected by stirring in neat TFA at room temperature for 30 mins. The resulting solution was neutralised with Na_2CO_3 and the product was filtered to yield a brown solid (0.493 g, 0.87 mmol, 80 %). The product decomposes over 182 °C. HRMS (*m/z*) (ESI+): Calculated for $C_{29}H_{29}N_8O_5H^+$ *m/z* = 569.2261 [M+H]$^+$. Found *m/z* = 569.2266 ; ^{1}H NMR (400 MHz, DMSO):δ = 8.70 (s, 2H, triazol H), 7.98 (d, *J* = 8.2 Hz, 4H, Ar *H*-COOMe), 7.54 (s, 2H, pyridine H), 7.46 (d, *J* = 8.2 Hz, 4H,Ar *H*-CH$_2$), 5.81 (s, 4H, CH$_2$), 4.31 (t, *J* = 4.3 Hz, 2H, O-CH$_2$), 3.84 (s, 6H, OCH$_3$), 3.15 (q, *J* = 4.3 Hz 2H, N-CH$_2$), ^{13}C{^{1}H} NMR (150 MHz, DMSO): δ = 165.8, 151.5, 147.2, 141.1, 129.7, 129.4, 128.5, 128.1, 124.1,
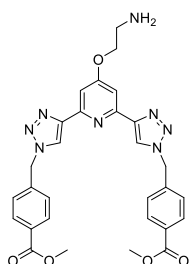
104.9, 64.7, 52.6, 52.2, 38.2. ; IR ν_{max} (cm^{-1}): 3112, 3088, 3086, 2955, 2478, 2203, 2091, 1933, 1865, 1796, 1714, 1685, 1610, 1281, 1174, 1041, 801.

dimethyl 4,4'-(((4-(2-acetamidoethoxy)pyridine-2,6-diyl)bis(1H-1,2,3-triazole-4,1-diyl))bis(methylene))dibenzoate (190)
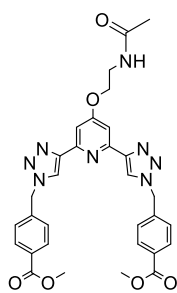
Ligand **189** (0.13 g, 0.02 mmol) was dissolved in dry DCM and triethylamine (0.01 mL, 0.07 mmol) was added. Acetic anhydride (0.003 mL, 0.03 mmol) was added to the mixture which was cooled over ice and the reaction was stirred at room temperature overnight. The solvent was removed under reduced pressure and the resulting solid was taken up in EtOAc and washed with brine. The solution was dried over MgSO$_4$ and the solvent was removed under reduced pressure to yield a brown solid. (0.077 g, 0.01 mmol, 55 %). m.p. 155 - 158 ºC; HRMS (*m/z*) (ESI+): Calculated for C$_{31}$H$_{30}$N$_8$O$_6$H$^+$ *m/z* = 611.2367 [M+H]$^+$. Found *m/z* = 611.2370. ^{1}H NMR (400 MHz, DMSO):δ = 8.69 (s, 2H, triazole H), 8.13 (s, 1H, NH), 7.98 (d, *J* = 8.3 Hz, 4H, Ar H-COOMe), 7.50 (s, 2H, pyridine H), 7.46 (d, *J* = 8.3 Hz, 4H, Ar *H*-CH$_2$), 5.80 (s, 4H, CH$_2$), 4.23 (s, 2H, O-CH$_2$), 3.48 (d, *J* = 5.4 Hz, 2H, *CH$_2$*-NH), 1.83 (s, 3H, CH$_3$). ^{13}C{^{1}H} NMR (150 MHz, DMSO): δ = 169.6, 165.9, 135.9, 151.4, 147.3, 141.2, 129.7, 129.4, 128.1, 124.1, 104.9, 66.9, 52.6, 52.3, 38.0, 22.6; IR ν_{max} (cm^{-1}): 3292, 3082, 2954, 1714, 1643, 1609, 1517, 1548, 1462, 1433, 1381, 1277, 1227, 1177, 1106, 1044, 1015, 982, 939, 801, 730, 668, 592.

dimethyl 4,4'-(((4-(2-methacrylamidoethoxy)pyridine-2,6-diyl)bis(1H-1,2,3-triazole-4,1-diyl))bis(methylene))dibenzoate (199)
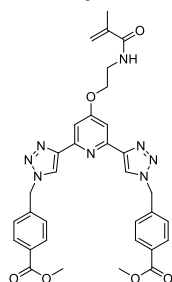
Ligand **189** (0.07 g, 1.23 mmol) was dissolved in a solution of CH$_2$Cl$_2$ (3 mL) with NEt$_3$ (0.017 mL, 1.29 mmol) in an ice bath. To this solution, methacryloyl chloride (0.012 mL, 1.29 mmol) was added dropwise in CH$_2$Cl$_2$ (5 mL). The mixture was stirred for 30 mins on ice and then allowed to stir at room temperature for two hours. The solution was then diluted in CH$_2$Cl$_2$, washed with dilute NaHCO$_3$ and H$_2$O and then dried over MgSO$_4$. The solution was dried under reduced pressure at 30 ˚C to yield colourless oil. The compound was purified by flash chromatography (CH$_2$Cl$_2$:CH$_3$OH gradient up to 5% CH$_3$OH) to yield a white solid (0.071 g, 64%).; m.p. 148 - 154 ºC; HRMS (*m/z*) (ESI+): Calculated for C$_{33}$H$_{32}$N$_8$O$_6$H$^+$ *m/z* = 637.2523 [M+H]$^+$. Found *m/z* = 637.2541. ^{1}H NMR (400 MHz,

DMSO):δ = 8.69 (s, 2H, triazole H), 8.17 (s, *J* = 5.7 Hz, 1H, NH), 7.98 (d, *J* = 8.4 Hz, 4H, Ar H-COOMe), 7.51 (s, 2H, pyridine H), 7.45 (d, *J* = 8.4 Hz, 4H, Ar *H*-CH$_2$), 5.80 (s, 4H, CH$_2$), 5.68 (s, 1H, alkene H), 5.34 (s, 1H, alkene H), 4.29 (s, *J* = 11.3, 2H, O-CH$_2$), 3.84 (s, 3H, 2CH$_3$), 3.56 (q, *J* = 11.3, 5.7 Hz, 2H, CH$_2$-NH), 1.85 (s, 3H, CH$_3$). ^{13}C{^{1}H} NMR (150 MHz, DMSO): δ = 151.9, 147.7, 141.6, 140.2, 130.2, 129.9, 128.5, 124.6, 119.8, 105.3, 66.9, 53.1, 52.7, 38.8, 19.1; IR ν$_{max}$ (cm^{-1}): 3434, 3289, 2514, 2094, 1711, 1612, 1588, 1493, 1279, 1203, 1184, 1010, 1000, 799, 726, 563.

Synthesis of Tb.190$_3$

Ligand **190** (0.01 g, 0.016 mmol) was added to Tb(CF$_3$SO$_3$)$_3$ (0.004 g, 0.0055 mmol) in CH$_3$OH (5 mL) and heated at 70 ˚C under microwave irradiation for 15 minutes. The resultant solution was dried under vaccum to yield a colorless oil which was taken up in CH$_3$OH and dropped slowly into a large excess of swirling Et$_2$O to afford Tb.**2**$_3$ as a white solid in 79% yield. m.p. (decomp) >280 ºC; Elemental analysis for C$_{93}$H$_{93}$N$_{24}$O$_{30}$Tb·3H$_2$O Calculated: C 46.27 H 3.88 N 13.48; Found: C 46.19 H 3.62 N 14.02 %; HRMS (*m/z*) (ESI+): C$_{64}$H$_{60}$N$_{16}$O$_{18}$F$_6$S$_2$Tb *m/z* = 1677.2871. Found *m/z* = 1677.2877; IR ν$_{max}$ (cm^{-1}): 3292, 2955, 1735, 1630, 1609, 1580, 1381, 1277, 1245, 1106, 982, 939, 744, 668.

Synthesis of F1 and F2

Polymer gels were generated by a modified procedure previously reported by Gunnlaugsson and McCoy.[295]

F1

199 (3 mg) was stirred in 2-hydroxyethyl methacrylate (HEMA, 7.5 mL), methylmethacrylate (MMA, 0.25 mL) and ethylene glycol dimethacrylate (EGDMA, 0.1 mL) at RT until compound **199** was completely dissolved. AIBN (100 mg) was added and the clear solution was injected into a non-stick mould. It was heated in the oven at 80 ˚C for 6 hours and after cooling to room temperature the material was released from the mould and cut into sections. The material was soaked in H$_2$O overnight followed by CH$_3$OH overnight to remove any remaining inhibitor or unreacted monomer.

F2

199 (0.3 mg) was stirred in 2-hydroxyethyl methacrylate (HEMA, 7.5 mL), methylmethacrylate (MMA, 0.25 mL) and ethylene glycol dimethacrylate (EGDMA, 0.1

mL) at RT until compound **199** was completely dissolved. AIBN (100 mg) was added and the clear solution was injected into a non-stick mould. It was heated in the oven at 80 ˚C for 6 hours and after cooling to room temperature the material was released from the mould and cut into sections. The material was soaked in H_2O overnight followed by CH_3OH overnight to remove any remaining inhibitor or unreacted monomer.

P1/ P2

Poly(ethylene-alt-maleic anhydride) (0.25 g, 0.006 mmol) was dissolved in anhydrous DMF (3 mL) under Ar and to this mixture, **189** (**P1**, 30 mg, 3mol%) (**P2**, 60 mg, 6mol%) was added dropwise dissolved in DMF (2 mL). The solution was stirred at RT for 1 hour. Addition of 0.5 M HCl dropwise resulted in a white precipitate which was filtered off as the pure product. (277 mg, 98%); ^{1}H NMR (600 MHz, DMSO):δ = 12.36 (s, OH), 8.67 (s, 2H, triazole H), 7.99 (m, 4H, Ar H-COOMe), 7.50 (s, 2H, pyr H), 7.46 (m, 4H, Ar H-CH$_2$), 5.79 (s, 4H, CH$_2$), 3.05(s, 69H, Hc and Hd), 085-1.96(br m, polymer backbone).

8. References

1. Lehn, J. M. *Pure Appl. Chem.* **2007**, *50*, 871–892.

2. Lehn, J. *Angew. Chem. Int. Ed.* **1988**, *27*, 89–112.

3. Lehn, J. *Supramolecular chemistry concepts and perspectives*; Wiley, **1995**.

4. Lehn, J.-M. *Science* **2002**, *295*, 2400–2403.

5. Lehn, J.-M. *Proc. Natl. Acad. Sci.* **2009**, *17*, 263–280.

6. Whitesides, G. M.; Mathias, J. P.; Seto, C. T. *Science* **1991**, *254*, 1312–1319.

7. Dietrich, B.; Sauvage, J.-P.; Lehn, J. *Tetrahedron Lett.* **1969**, *34*, 2889–2892.

8. Weber, E.; Vogtle, F. *Inorg Chim. Acta Lett.* **1980**, *45*, 65–67.

9. Pedersen, C. J. *J. Am. Chem. Soc.* **1967**, *89*, 7017–7036.

10. Sauvage, J.-P.; Christiane, D.-B. *Molecular Catenanes, Rotaxanes and Knots*; Sauvage, J.-P.; Christiane, D.-B., Eds.; Wiley_VCH, **1998**.

11. Beves, J. E.; Blight, B. A.; Campbell, C. J.; Leigh, D. A.; Mcburney, R. T. *Angew. Chem. Int. Ed.* **2011**, *50*, 9260–9327.

12. Cirulli, M.; Kaur, A.; Lewis, J. E. M.; Zhang, Z.; Kitchen, J. A.; Goldup, S. M.; Roessler, M. M. *J. Am. Chem. Soc.* **2019**, *141*, 879–889.

13. Byrne, J. P.; Blasco, S.; Aletti, A. B.; Hessman, G.; Gunnlaugsson, T. *Angew. Chem. Int. Ed.* **2016**, *55*, 8938–8943.

14. Lewis, J. E. M.; Modicom, F.; Goldup, S. M. *J. Am. Chem. Soc.* **2018**, *140*, 4787–4791.

15. Lynes, A. D.; Hawes, C. S.; Byrne, K.; Schmitt, W.; Gunnlaugsson, T. *Dalton Trans.* **2018**, *47*, 5259–5268.

16. Yang, B.; Zhang, H.; Peng, H.; Xu, Y.; Wu, B.; Weng, W.; Li, L. *Polym. Chem.* **2014**, *5*, 1945–1953.

17. Heinzmann, C.; Weder, C.; de Espinosa, L. M. *Chem. Soc. Rev.* **2015**, *342*, 342–358.

18. Weng, W.; Beck, J. B.; Jamieson, A. M.; Rowan, S. J. *J. Am. Chem. Soc.* **2006**, 11663–11672.

19. McCarney, E. P.; Hawes, C. S.; Kitchen, J. A.; Byrne, K.; Schmitt, W.; Gunnlaugsson, T. *Inorg. Chem.* **2018**, *57*, 3920–3930.

20. Kumar, P.; Gupta, R. *Dalton Trans.* **2016**, *45*, 18769–18783.

21. Ghosh, S. K.; Bharadwaj, P. K. *Inorg. Chem.* **2004**, *43*, 2293–2298.

22. Hofmeier, H.; Schubert, U. S. *Chem. Soc. Rev.* **2004**, *33*, 373–399.

23. Eliseeva, S. V; Bünzli, J.-C. G. *Chem. Soc. Rev.* **2010**, *39*, 189–227.

24. Gassner, A. L.; Duhot, C.; Bünzli, J. C. G.; Chauvin, A. S. *Inorg. Chem.* **2008**, *47*, 7802–7812.

25. Hua, K. T.; Xu, J.; Quiroz, E. E.; Lopez, S.; Ingram, A. J.; Johnson, V. A.; Tisch, A. R.; De Bettencourt-Dias, A.; Straus, D. A.; Muller, G. *Inorg. Chem.* **2012**, *51*, 647–660.

26. Wu, N.; Melan, C. F. C.; Stevenson, K. A.; Fleischel, O.; Guo, H.; Habib, F.; Holmberg, R. J.; Murugesu, M.; Mosey, N. J.; Nierengarten, H.; Petitjean, A. *Dalton Trans.* **2015**, *44*, 14991–15005.

27. Huang, C.; Bian, Z. *Rare Earth Coordination Chemistry: Fundamentals and Applications*; Huang, C., Ed.; Wiley, **2010**.

28. Parker, D.; Dickins, R. S.; Puschmann, H.; Crossland, C.; Howard, J. A. K. *Chem. Rev.* **2002**, *102*, 1977–2010.

29. Bunzli, J.-C. G. *Chem. Rev.* **2010**, *110*, 2729–2755.

30. De Bettencourt-Dias, A. *J. Chem. Soc. Dalt. Trans.* **2007**, 2229–2241.

31. Holliday B. J. and C. A. Mirkin *Angew. Chem. Int. Ed.* **2001**, *40*, 2022–2043.

32. Celestine, M.; Bullock, J.; Boodram, S.; Rambaran, V. *Rev. Inorg. Chem.* **2014**, *35*, 57–67.

33. Xiang, S.; Bao, D. X.; Wang, J.; Li, Y. C.; Zhao, X. Q. *J. Lumin.* **2017**, *186*, 273–282.

34. de Bettencourt-Dias, A.; Viswanathan, S.; Rollett, A. *J. Am. Chem. Soc.* **2007**, *129*, 15436–15437.

35. Halcrow, M. A. *Coord. Chem. Rev.* **2005**, *249*, 2880–2908.

36. Vos, J. G.; Kelly, J. M. *J. Chem. Soc. Dalt. Trans.* **2006**, 4869–4883.

37. Sauvage, J. P.; Collin, J. P.; Chambron, J. C.; Guillerez, S.; Coudret, C.; Balzani, V.; Barigelletti, F.; De Cola, L.; Flamigni, L. *Chem. Rev.* **1994**, *94*, 993–1019.

38. Nonat, A. M.; Harte, A. J.; Sénéchal-David, K.; Leonard, J. P.; Gunnlaugsson, T. *J. Chem. Soc. Dalt. Trans.* **2009**, 4703–4711.

39. Wang, P.; Li, Z.; Lv, G. C.; Zhou, H. P.; Hou, C.; Sun, W. Y.; Tian, Y. P. *Inorg. Chem. Commun.* **2012**, *18*, 87–91.

40. Byrne, J. P.; Kitchen, J. a; Gunnlaugsson, T. *Chem. Soc. Rev.* **2014**, *43*, 5302–5325.

41. Wang, H.; Zhang, B.; Yan, X.; Guo, S. *Dalton Trans.* **2018**, *47*, 528–537.

42. Bosmani, A.; Pujari, S. A.; Besnard, C.; Guénée, L.; Poblador-Bahamonde, A. I.; Lacour, J. *Chem. Eur. J.* **2017**, *23*, 8678–8684.

43. Hua, Y.; Flood, A. H. *Chem. Soc. Rev.* **2010**, *39*, 1262–1271.

44. Bradberry, S. J.; Savyasachi, A. J.; Martinez-Calvo, M.; Gunnlaugsson, T. *Coord. Chem. Rev.* **2014**, *273–274*, 226–241.

45. Cui, S. X.; Zhao, Y. L.; Li, B.; Zhang, J. P.; Liu, Q.; Zhang, Y. *Polyhedron* **2008**, *27*, 671–678.

46. Kirillova, M. V.; Kirillov, A. M.; Guedes da Silva, M. F. C.; Kopylovich, M. N.; Fraústo da Silva, J. J. R.; Pombeiro, A. J. L. *Inorg. Chim. Acta* **2008**, *361*, 1728–1737.

47. Zhao, B.; Yi, L.; Dai, Y.; Chen, X. Y.; Cheng, P.; Liao, D. Z.; Yan, S. P.; Jiang, Z. H. *Inorg. Chem.* **2005**, *44*, 911–920.

48. Hu, N. H.; Li, Z. G.; Xu, J. W.; Jia, H. Q.; Niu, J. J. *Cryst. Growth Des.* **2007**, *7*, 15–17.

49. Kirin, S. I.; Ohr, K.; Yennawar, H. P.; Morgan, C. M.; Levine, L. A.; Williams, M. E. *Inorg. Chem. Commun.* **2007**, *10*, 652–656.

50. Manna, S. C.; Ribas, J.; Zangrando, E.; Ray Chaudhuri, N. *Inorg. Chim. Acta* **2007**, *360*, 2589–2597.

51. Kirillova, M. V.; Guedes da Silva, M. F. C.; Kirillov, A. M.; Fraústo da Silva, J. J. R.; Pombeiro, A. J. L. *Inorg. Chim. Acta* **2007**, *360*, 506–512.

52. Cai, Y. P.; Su, C. Y.; Li, G. B.; Mao, Z. W.; Zhang, C.; Xu, A. W.; Kang, B. S. *Inorg. Chim. Acta* **2005**, *358*, 1298–1304.

53. Schmidt, B.; Jiricek, J.; Titz, A.; Ye, G.; Parang, K. *Bioorganic Med. Chem. Lett.* **2004**, *14*, 4203–4206.

54. Xu, Z.; Thompson, L. K.; Miller, D. O. *Polyhedron* **2002**, *21*, 1715–1720.

55. Milway, V. A.; Niel, V.; Abedin, T. S. M.; Xu, Z.; Thompson, L. K.; Grove, H.; Miller, D. O.; Parsons, S. R. *Inorg. Chem.* **2007**, *43*, 1874–1884.

56. MacDonald, J. C.; Dorrestein, P. C.; Pilley, M. M.; Foote, M. M.; Lundburg, J. L.; Henning, R. W.; Schultz, A. J.; Manson, J. L. *J. Am. Chem. Soc.* **2000**, *122*, 11692–11702.

57. Kirillova, M. V.; Kirillov, A. M.; Guedes Da Silva, M. F. C.; Pombeiro, A. J. L. *Eur. J. Inorg. Chem.* **2008**, 3423–3427.

58. Canty, A. J.; Lee, C. V. *Inorg. Chim. Acta* **1981**, *54*, L205–L206.

59. Chavez, F. A.; Olmstead, M. M.; Mascharak, P. K. *Inorg. Chem.* **2002**, *35*, 1410–1412.

60. Belford, R. L.; Calvin, M.; Belford, G. *J. Chem. Phys.* **1957**, *26*, 1165–1174.

61. Yano, T.; Tanaka, R.; Nishioka, T.; Kinoshita, I.; Isobe, K.; James, L.; Cambridge, R.; May, A.; Wright, J.; Collins, T. *Chem. Comm.* **2002**, *1*, 1396–1397.

62. Solomon, E. I.; Zhou, J.; Neese, F.; Pavel, E. G. *Chem. Biol.* **1997**, *4*, 795–808.

63. Chen, Z.; Yin, G. *Chem. Soc. Rev.* **2015**, *44*, 1083–1100.

64. Tehranchi, J.; Donoghue, P. J.; Cramer, C. J.; Tolman, W. B. *Eur. J. Inorg. Chem.* **2013**, 4077–4084.

65. Donoghue, P. J.; Tehranchi, J.; Cramer, C. J.; Sarangi, R.; Solomon, E. I.; Tolman, W. B. *J. Am. Chem. Soc.* **2011**, *133*, 17602–17605.

66. Halvagar, M. R.; Solntsev, P. V.; Lim, H.; Hedman, B.; Hodgson, K. O.; Solomon, E. I.; Cramer, C. J.; Tolman, W. B. *J. Am. Chem. Soc.* **2014**, *136*, 7269–7272.

67. Muller, F. C.; Muller, G.; Riehl, J. P. *Chirality* **2007**, *19*, 826.

68. Martinez-Calvo, M.; Kotova, O.; Mobius, M. E.; Bell, A. P.; McCabe, T.; Boland, J. J.; Gunnlaugsson, T. *J. Am. Chem. Soc.* **2015**, *137*, 1983–1992.

69. Chang, K. C.; Lin, J. L.; Shen, Y. T.; Hung, C. Y.; Chen, C. Y.; Sun, S. S. *Chem. Eur. J.* **2012**, *18*, 1312–1321.

70. Shen, Y. T.; Li, C. H.; Chang, K. C.; Chin, S. Y.; Lin, H. A.; Liu, Y. M.; Hung, C. Y.; Hsu, H. F.; Sun, S. S. *Langmuir* **2009**, *25*, 8714–8722.

71. Sondi, I.; Salopek-Sondi, B. *J. Colloid Interface Sci.* **2004**, *275*, 177–182.

72. Pan, L.; Woodlock, E. B.; Wang, X.; Lam, K. C.; Rheingold, A. L. *Chem. Commun.* **2001**, *1*, 1762–1763.

73. Cheng, P. Y.; Chen, C. Y.; Lee, H. M. *Inorg. Chim. Acta* **2009**, *362*, 1840–1846.

74. Zhao, B.; Zhao, X. Q.; Chen, Z.; Shi, W.; Cheng, P.; Yan, S. P.; Liao, D. Z. *CrystEngComm* **2008**, *10*, 1144–1146.

75. Surender, E. M.; Comby, S.; Cavanagh, B. L.; Brennan, O.; Lee, T. C.; Gunnlaugsson, T. *Chem* **2016**, *1*, 438–455.

76. Butler, S. J.; Lamarque, L.; Pal, R.; Parker, D. *Chem. Sci.* **2014**, *5*, 1750–1756.

77. Placide, V.; Pitrat, D.; Grichine, A.; Duperray, A.; Andraud, C.; Maury, O. *Tetrahedron Lett.* **2014**, *55*, 1357–1361.

78. Chauvin, A. S.; Gumy, F.; Imbert, D.; Bünzli, J. C. G. *Spectrosc. Lett.* **2004**, *37*, 517–532.

79. Chauvin, A. S.; Gumy, F.; Imbert, D.; Bünzli, J. C. G. *Spectrosc. Lett.* **2007**, *40*, 193.

80. George, M. R.; Golden, C. A.; Grossel, M. C.; Curry, R. J. *Inorg. Chem.* **2006**, *45*, 1739–1744.

81. Lamture, J. B.; Hong Zhou, Z.; Suresh Kumar, A.; Wensel, T. G. *Inorg. Chem.* **1995**, *34*, 864–869.

82. Debroye, E.; Ceulemans, M.; Vander Elst, L.; Laurent, S.; Muller, R. N.; Parac-Vogt,

T. N. *Inorg. Chem.* **2014**, *53*, 1257–1259.

83. Andres, J.; Hersch, R. D.; Moser, J. E.; Chauvin, A. S. *Adv. Funct. Mater.* **2014**, *24*, 5029–5036.

84. Chauvin, A. S.; Bünzli, J. C. G.; Bochud, F.; Scopelliti, R.; Froidevaux, P. *Chem. Eur. J.* **2006**, *12*, 6852–6864.

85. Muller, G. *Dalton Trans.* **2009**, 9692–9707.

86. Tsukube, H.; Shinoda, S. *Chem. Rev.* **2002**, *102*, 2389–2404.

87. Kirschner, S. *Pure Appl. Chem.* **1979**, *51*, 913–923.

88. Leonard, J. P.; Jensen, P.; McCabe, T.; O'Brien, J. E.; Peacock, R. D.; Kruger, P. E.; Gunnlaugsson, T. *J. Am. Chem. Soc.* **2007**, *129*, 10986–10987.

89. Bonsall, S. D.; Houcheime, M.; Straus, D. A.; Muller, G. *Chem. Commun.* **2007**, 3676–3678.

90. Yan, L.; Tan, C.; Zhang, G.; Zhou, L.; Sun, Q. *J. Am. Chem. Soc.* **2015**, *137*, 8550–8555.

91. Li, X. Z.; Zhou, L. P.; Yan, L. L.; Yuan, D. Q.; Lin, C. S.; Sun, Q. F. *J. Am. Chem. Soc.* **2017**, *139*, 8237–8244.

92. Li, X. Z.; Zhou, L. P.; Yan, L. L.; Dong, Y. M.; Bai, Z. L.; Sun, X. Q.; Diwu, J.; Wang, S.; Bünzli, J. C.; Sun, Q. F. *Nat. Commun.* **2018**, *9*.

93. Rostovtsev, V. V.; Green, L. G.; Fokin, V. V.; Sharpless, K. B. *Angew. Chem. Int. Ed.* **2002**, *41*, 2596–2599.

94. Tornøe, C. W.; Christensen, C.; Meldal, M. *J. Org. Chem.* **2002**, *67*, 3057–3064.

95. Meudtner, R. M.; Ostermeier, M.; Goddard, R.; Limberg, C.; Hecht, S. *Chem. Eur. J.* **2007**, *13*, 9834–9840.

96. Crowley, J. D.; Bandeen, P. H. *Dalton Trans.* **2010**, *39*, 329–336.

97. Himo, F.; Lovell, T.; Hilgraf, R.; Rostovtsev, V. V.; Noodleman, L.; Sharpless, K. B.; Fokin, V. V. *J. Am. Chem. Soc.* **2005**, *127*, 210–216.

98. Schulze, B.; Schubert, U. S. *Chem. Soc. Rev.* **2014**, *43*, 2522–71.

99. Bock, V. D.; Hiemstra, H.; Van Maarseveen, J. H. *Eur. J. Org. Chem.* **2006**, 51–68.

100. Mindt, T. L.; Struthers, H.; Brans, L.; Anguelov, T.; Schweinsberg, C.; Maes, V.; Tourwé, D.; Schibli, R. *J. Am. Chem. Soc.* **2006**, *128*, 15096–15097.

101. Chan, T. R.; Hilgraf, R.; Sharpless, K. B.; Fokin, V. V. *Org. Lett.* **2004**, *6*, 2853–2855.

102. Crowley, J. D.; Bandeen, P. H.; Hanton, L. R. *Polyhedron* **2010**, *29*, 70–83.

103. Zornik, D.; Meudtner, R. M.; Ela Malah, T.; Thiele, C. M.; Hecht, S. *Chem. Eur. J.* **2011**, *17*, 1473–1484.

104. Chandrasekhar, N.; Chandrasekar, R. *Angew. Chem. Int. Ed.* **2012**, *51*, 3556–3561.

105. Ostermeier, M.; Berlin, M. A.; Meudtner, R. M.; Demeshko, S.; Meyer, F.; Limberg, C.; Hecht, S. *Chem. Eur. J.* **2010**, *16*, 10202–10213.

106. Li, Y.; Huffman, J. C.; Flood, A. H. *Chem. Commun.* **2007**, *26*, 2692–2694.

107. Holloway, C. E.; Melnik, M.; Nevin, W. A.; Liu, W. *J. Coord. Chem.* **1995**, *35*, 85–178.

108. Danielraj, P.; Sankararaman, S. *Acta Crystallogr. Sect. C Cryst. Struct. Commun.* **2010**, *2701*, 366–370.

109. Allampally, N. K.; Daniliuc, C. G.; Strassert, C. A.; De Cola, L. *Inorg. Chem.* **2015**, *54*, 1588–1596.

110. Yam, V. W. *J. Am. Chem. Soc.* **2017**, *139*, 13858–13866.

111. Schulze, B.; Winter, A.; Friebe, C.; Birckner, E.; Schubert, U. S. *ACS Macro Lett.* **2017**, *6*, 181–184.

112. Preston, D.; Kruger, P. E. *Chem. Eur. J.* **2019**, *25*, 1781–1786.

113. Schmollinger, D.; Kraft, J.; Ewald, C.; Ziegler, T. *Tetrahedron Lett.* **2017**, *58*, 3643–3645.

114. Kraft, J.; Schmollinger, D.; Maudrich, J.; Ziegler, T. *Synthesis* **2015**, *47*, 199–208.

115. Boratyński, P. J.; Kowalczyk, R. *J. Org. Chem.* **2016**, *81*, 8029–8034.

116. Kowalczyk, R.; Lipke, K.; Czapor-irzabek, H.; Boratyn, P. J. **2017**, *121*, 1–8.

117. Gunnlaugsson, T.; Leonard, J. P. *Chem. Commun.* **2005**, *25*, 3114–3131.

118. Binnemans, K. *Chem. Rev.* **2009**, *109*, 4283–4374.

119. Gunnlaugsson, T.; Stomeo, F. *Org. Biomol. Chem.* **2007**, *5*, 1999–2009.

120. Chandrasekhar, N.; Chandrasekar, R. *J. Org. Chem.* **2010**, *75*, 4852–4855.

121. Yuan, J. C.; Fang, X. L.; Zhang, L. X.; Hong, G. N.; Lin, Y. J.; Zheng, Q. F.; Xu, Y. Z.; Ruan, Y. H.; Weng, W. G.; Xia, H. P.; Chen, G. H. *J. Mater. Chem.* **2012**, *22*, 11515–11522.

122. Bradberry, S. J.; Byrne, J. P.; McCoy, C. P.; Gunnlaugsson, T. *Chem. Commun.* **2015**, *51*, 16565–16568.

123. McCarney, E. P.; Byrne, J. P.; Twamley, B.; Martínez-Calvo, M.; Ryan, G.; Möbius, M. E.; Gunnlaugsson, T. *Chem. Commun. (Camb).* **2015**, *51*, 14123–14126.

124. Poinssot, C.; Bourg, S.; Ouvrier, N.; Combernoux, N.; Rostaing, C.; Vargas-Gonzalez, M.; Bruno, J. *Energy* **2014**, *69*, 199–211.

125. Diamond, R. M.; Street, K.; Seaborg, G. T. *J. Am. Chem. Soc.* **1954**, *76*, 1461–1469.

126. Hudson, M. J.; Harwood, L. M.; Laventine, D. M.; Lewis, F. W. *Inorg. Chem.* **2013**,

52, 3414–3428.

127. Macerata, E.; Mossini, E.; Scaravaggi, S.; Mariani, M.; Mele, A.; Panzeri, W.; Boubals, N.; Berthon, L.; Charbonnel, M. C.; Sansone, F.; Arduini, A.; Casnati, A. *J. Am. Chem. Soc.* **2016**, *138*, 7232–7235.

128. Wagner, C.; Mossini, E.; Macerata, E.; Mariani, M.; Arduini, A.; Casnati, A.; Geist, A.; Panak, P. J. *Inorg. Chem.* **2017**, *4*, 2135–2144.

129. Mossini, E.; Macerata, E.; Wilden, A.; Kaufholz, P.; Modolo, G.; Lotti, N.; Casnati, A.; Geist, A.; Mariani, M. *Solvent Extr. Ion Exch.* **2018**, *36*, 373–386.

130. Ossola, A.; Macerata, E.; Mossini, E.; Giola, M.; Chiara, M.; Casnati, A.; Mariani, M. *J. Radioanal. Nucl. Chem.* **2018**, *318*, 2013–2022.

131. Veliscek-Carolan, J.; Rawal, A. *Chem. Commun.* **2019**, *55*, 1168–1171.

132. Maiti, S.; Saha, P.; Das, T.; Bessi, I.; Schwalbe, H.; Dash, J. *Bioconjug. Chem.* **2018**, *29*, 1141–1154.

133. Liu, Y.; Parks, F. C.; Zhao, W.; Flood, A. H. *J. Am. Chem. Soc.* **2018**, *140*, 15477–15486.

134. Lewis, J. E. M.; Bordoli, R. J.; Denis, M.; Fletcher, C. J.; Galli, M.; Neal, E. A.; Rochette, E. M.; Goldup, S. M. *Chem. Sci.* **2016**, *7*, 3154–3161.

135. Kumar, P.; Gupta, R. *Dalton Trans.* **2016**, *45*, 18769–18783.

136. Fujita, M.; Ogura, K. Supramolecular Self-Assembly of Macrocycles, Catenanes, and Cages through Coordination of Pyridine-Based Ligands to Transition Metals. *Bull. Chem. Soc. Jpn.* **1996**, *69*, 1471–1482.

137. Chen, J. L.; Xiao, Y. L.; Xia, Y.; Qiu, L.; He, L. H.; Liu, S. J.; Wen, H. R. *Polyhedron* **2016**, *112*, 130–136.

138. Kratsch, J.; Beele, B. B.; Koke, C.; Denecke, M. A.; Geist, A.; Panak, P. J.; Roesky, P. W. *Inorg. Chem.* **2014**, *53*, 8949–8958.

139. Maiwald, M. M.; Wagner, A. T.; Kratsch, J.; Skerencak-Frech, A.; Trumm, M.; Geist, A.; Roesky, P. W.; Panak, P. J. *Dalton Trans.* **2017**, *46*, 9981–9994.

140. Chen, J. L.; Luo, Y. S.; Gao, G. P.; Zhao, J. L.; Qiu, L.; Liu, N.; He, L. H.; Liu, S. J.; Wen, H. R. *Polyhedron* **2016**, *117*, 388–393.

141. Kottas, G. S.; Mehlstäubl, M.; Fröhlich, R.; De Cola, L. *Eur. J. Inorg. Chem.* **2007**, *1*, 3465–3468.

142. Krinochkin, A. P.; Kopchuk, D. S.; Kozhevnikov, D. N. *Polyhedron* **2015**, *102*, 556–561.

143. Kopchuk, D. S.; Krinochkin, A. P.; Kozhevnikov, D. N.; Slepukhin, P. A. *Polyhedron*

2016, *118*, 30–36.

144. de Sa, G. F.; Malta, O. L.; de Mello Donega, C.; Simas, A. M.; Longo, R. L.; Anta-Cruz, P. A.; da Silva Jr, E. F. *Coord. Chem. Rev.* **2000**, *196*, 165–195.

145. Armelao, L.; Quici, S.; Barigelletti, F.; Accorsi, G.; Bottaro, G.; Cavazzini, M.; Tondello, E. *Coord. Chem. Rev.* **2010**, *254*, 487–505.

146. Bünzli, J. C. G.; Chauvin, A. S.; Kim, H. K.; Deiters, E.; Eliseeva, S. V. *Coord. Chem. Rev.* **2010**, *254*, 2623–2633.

147. Botelho, M. B. S.; Gálvez-Lõpez, M. D.; De Cola, L.; Albuquerque, R. Q.; De Camargo, A. S. S. *Eur. J. Inorg. Chem.* **2013**, 5064–5070.

148. Botelho, M. B. S.; De Queiroz, T. B.; Eckert, H.; De Camargo, A. S. S. *J. Lumin.* **2016**, *170*, 619–626.

149. Lv, B.; Wang, X.; Hu, H. M.; Zhao, Y. F.; Yang, M. L.; Xue, G. *Inorg. Chim. Acta* **2016**, *453*, 771–778.

150. Dalton, H. L.; Hawes, C. S.; Gunnlaugsson, T. *Cryst. Growth Des.* **2017**, *17*, 4365–4376.

151. Andreiadis, E. S.; Imbert, D.; Pécaut, J.; Demadrille, R.; Mazzanti, M. *Dalton Trans.* **2012**, *41*, 1268–1277.

152. Albertsson, J.; Nicholson, D. G.; Mukherjee, A. D.; Nilsson, K.; Nimmich, W. Structural Studies on the Rare Earth Carboxylates. 10. The Crystal and Molecular Structure of Monoclinic Trisodium Tris(pyridine-2,6-dicarboxylato)ytterbate(III) 13-Hydrate. *Acta Chem. Scand.* **2008**, *26*, 985–1004.

153. Brayshaw, P. A.; Bünzli, J. C.; Froidevaux, P.; Harrowfield, J. M.; Kim, Y.; Sobolev, A. N. *Inorg. Chem.* **1995**, *34*, 2068–2076.

154. Al-Rasbi, N. K.; Adams, H.; Harding, L. P.; Ward, M. D. *Eur. J. Inorg. Chem.* **2007**, 4770–4780.

155. van der Vlugt, J. I.; Demeshko, S.; Dechert, S.; Meyer, F. *Inorg. Chem.* **2008**, *47*, 1576–1585.

156. Singh, A. K.; Van Vlugt, J. I. Der; Demeshko, S.; Dechert, S.; Meyer, F. *Eur. J. Inorg. Chem.* **2009**, 3431–3439.

157. Schneider, B.; Demeshko, S.; Dechert, S.; Meyer, F. *Angew. Chem. Int. Ed.* **2010**, *49*, 9274–9277.

158. Steinert, M.; Schneider, B.; Dechert, S.; Demeshko, S.; Meyer, F. *Angew. Chem. Int. Ed.* **2014**, *53*, 6135–6139.

159. Kotova, O.; Kitchen, J. A.; Lincheneau, C.; Peacock, R. D.; Gunnlaugsson, T. *Chem.*

Eur. J. **2013**, *19*, 16181–16186.

160. Caffrey, D. F. No Title, Trinity College, The University of Dublin, **2013**.

161. Bradberry, S. J.; Savyasachi, A. J.; Peacock, R. D.; Gunnlaugsson, T. *Faraday Discuss.* **2015**, *185*, 413–431.

162. Comby, S.; Stomeo, F.; Mccoy, C. P.; Gunnlaugsson, T. *Helv. Chim. Acta* **2009**, *92*, 2461–2473.

163. Stomeo, F.; Lincheneau, C.; Leonard, J. P.; O'Brien, J. E.; Peacock, R. D.; McCoy, C. P.; Gunnlaugsson, T. *J. Am. Chem. Soc.* **2009**, *131*, 9636–9637.

164. Lincheneau, C.; Peacock, R. D.; Gunnlaugsson, T. *Chem. - An Asian J.* **2010**, *5*, 500–504.

165. Kotova, O.; Comby, S.; Pandurangan, K.; Stomeo, F.; O'Brien, J. E.; Feeney, M.; Peacock, R. D.; McCoy, C. P.; Gunnlaugsson, T. *Dalton Trans.* **2018**, *47*, 12308–12317.

166. Kotova, O.; Blasco, S.; Twamley, B.; O'Brien, J.; Peacock, R. D.; Kitchen, J. a.; Martínez-Calvo, M.; Gunnlaugsson, T. *Chem. Sci.* **2015**, *6*, 457–471.

167. Barry, D. E.; Kitchen, J. A.; Albrecht, M.; Faulkner, S.; Gunnlaugsson, T. *Langmuir* **2013**, *29*, 11506–11515.

168. Kitchen, J. A.; Barry, D. E.; Mercs, L.; Albrecht, M.; Peacock, R. D.; Gunnlaugsson, T. *Angew. Chem. Int. Ed.* **2012**, *1*, 704–708.

169. Galanti, A.; Kotova, O.; Blasco, S.; Johnson, C. J.; Peacock, R. D.; Mills, S.; Boland, J. J.; Albrecht, M.; Gunnlaugsson, T. *Chem. Eur. J.* **2016**, *22*, 9709–9723.

170. Gunnlaugsson, T.; Barry, D.; Kitchen, J.; Albrecht, M.; Peacock, R.; Mercs, L. *Dalton Trans.* **2019**, 11317–11325.

171. Wojtecki, R. J.; Meador, M. a; Rowan, S. J. *Nat. Mater.* **2011**, *10*, 14–27.

172. Piepenbrock, M. O. M.; Lloyd, G. O.; Clarke, N.; Steed, J. W. *Chem. Rev.* **2010**, *110*, 1960–2004.

173. Steed, J. W. *Chem. Commun.* **2011**, *47*, 1379–1383.

174. Kotova, O.; Daly, R.; Dos Santos, C. M. G.; Boese, M.; Kruger, P. E.; Boland, J. J.; Gunnlaugsson, T. *Angew. Chem. Int. Ed.* **2012**, *51*, 7208–7212.

175. Byrne, J. P.; Kitchen, J. a; Kotova, O.; Leigh, V.; Bell, A. P.; Boland, J. J.; Albrecht, M.; Gunnlaugsson, T. *Dalton Trans.* **2014**, *43*, 196–209.

176. Byrne, J. P.; Martínez-Calvo, M.; Peacock, R. D.; Gunnlaugsson, T. *Chem. Eur. J.* **2016**, *22*, 486–490.

177. Byrne, J. P.; Kitchen, J. A.; Obrien, J. E.; Peacock, R. D.; Gunnlaugsson, T. *Inorg.*

Chem. **2015**, *54*, 1426–1439.

178. Bradberry, S. J.; Byrne, J. P.; McCoy, C. P.; Gunnlaugsson, T. *Chem. Commun.* **2015**, *51*, 16565–16568.

179. Bradberry, S. J.; Dee, G.; Kotova, O.; McCoy, C. P.; Gunnlaugsson, T. *Chem. Commun.* **2019**, *55*, 1754–1757.

180. Barry, D.; Hawes, C. S.; Byrne, J. P.; la Cour Poulsen, B.; Ruether, M.; O'Brien, J. E.; Gunnlaugsson, T. *Dalton Trans.* **2017**, *46*, 6464–6472.

181. Yue, Q.; Guo, W. X.; Wang, Y. Y.; Hu, X. L.; Gao, E. Q. *Cryst. Growth Des.* **2019**, *19*, 2476–2484.

182. Yuan, J. C.; Fang, X.; Zhang, L.; Hong, G.; Lin, Y.; Zheng, Q.; Xu, Y.; Ruan, Y.; Weng, W.; Xia, H.; Chen, G. *J. Mater. Chem.* **2012**, *22*, 11515–11522.

183. Barry, D. E.; Hawes, C. S.; Byrne, J. P.; La Cour Poulsen, B.; Ruether, M.; O'Brien, J. E.; Gunnlaugsson, T. *Dalton Trans.* **2017**, *46*, 6464–6472.

184. Nitschke, J. R.; Hutin, M.; Bernardinelli, G. *Angew. Chem. Int. Ed.* **2004**, *43*, 6724–6727.

185. Klingele (née Hausmann), J.; Boas, J. F.; Pilbrow, J. R.; Moubaraki, B.; Murray, K. S.; Berry, K. J.; Hunter, K. A.; Jameson, G. B.; Boyd, P. D. W.; Brooker, S. *Dalton Trans.* **2006**, 633–645.

186. Vasdev, R. A. S.; Preston, D.; Crowley, J. D. *Dalton Trans.* **2017**, *46*, 2402–2414.

187. Spek, A. L. *Acta Crystallogr. Sect. C Cryst. Struct. Chem.* **2015**, *71*, 9–18.

188. N, B.; Nakanishi, K.; Woody, R. *Circular Dichroism: principles and applications*; John Wiley and Sons, **2000**.

189. Cárdenas, D. J.; Livoreil, A.; Sauvage, J. P. *J. Am. Chem. Soc.* **1996**, *118*, 11980–11981.

190. Coronado, E.; Gaviña, P.; Ponce, J.; Tatay, S. *Chem. Eur. J.* **2014**, *20*, 6939–6950.

191. Flory, P. J. *Faraday Discuss. Chem. Soc.* **1974**, *57*, 7.

192. Dastidar, P. *Chem. Soc. Rev.* **2008**, *37*, 2699–2715.

193. Buerkle, L. E.; Rowan, S. J. *Chem. Soc. Rev.* **2012**, *41*, 6089–6102.

194. Yagai, S.; Nakajima, T.; Kishikawa, K.; Kohmoto, S.; Karatsu, T.; Kitamura, A. *J. Am. Chem. Soc.* **2005**, *127*, 11134–11139.

195. Sugiyasu, K.; Fujita, N.; Takeuchi, M.; Shinkai, S. *Org. Biomol. Chem.* **2003**, *1*, 895–900.

196. Beck, J. B.; Rowan, S. J. *J. Am. Chem. Soc.* **2003**, *125*, 13922–13923.

197. De Jong, J. J. D.; Lucas, L. N.; Kellogg, R. M.; Van Esch, J. H.; Feringa, B. L. *Science*

2004, *304*, 278–281.

198. Webber, M. J.; Langer, R. *Chem. Soc. Rev.* **2017**, *46*, 6600–6620.

199. Puigmartí-Luis, J.; Laukhin, V.; Pérez Del Pino, Á.; Vidal-Gancedo, J.; Rovira, C.; Laukhina, E.; Amabilino, D. B. *Angew. Chem. Int. Ed.* **2007**, *46*, 238–241.

200. Häring, M.; Díaz, D. D. *Chem. Commun.* **2016**, *52*, 13068–13081.

201. Zhao, H.; Shi, Q.; Xiao, H.; Li, X. *J. Porous Mater.* **2014**, *21*, 691–697.

202. Metherell, A. J.; Ward, M. D. *Chem. Sci.* **2016**, *7*, 910–915.

203. Liu, C.; Zhang, R.; Lin, C.; Zhou, L.; Cai, L.; Kong, J.; Yang, S.; Han, K.; Sun, Q. *J. Am. Chem. Soc.* **2017**, *139*, 12474–12479.

204. Wang, Z.; Zhou, L. P.; Zhao, T. H.; Cai, L. X.; Guo, X. Q.; Duan, P. F.; Sun, Q. F. *Inorg. Chem.* **2018**, *57*, 7982–7992.

205. Wu, W. P.; Wang, Y. Y.; Wang, C. J.; Wu, Y. P.; Liu, P.; Shi, Q. Z. *Inorg. Chem. Commun.* **2006**, *9*, 645–648.

206. Kuppler, R. J.; Timmons, D. J.; Fang, Q. R.; Li, J. R.; Makal, T. A.; Young, M. D.; Yuan, D.; Zhao, D.; Zhuang, W.; Zhou, H. C. *Coord. Chem. Rev.* **2009**, *253*, 3042–3066.

207. Burchell, T. J.; Eisler, D. J.; Puddephatt, R. J. *Chem. Commun.* **2004**, *4*, 944–945.

208. Ross, D. A. W.; Preston, D.; Crowley, J. D. *Molecules* **2017**, *22*, 1–13.

209. Braga, D.; D'Agostino, S.; D'Amen, E.; Grepioni, F. *Chem. Commun.* **2011**, *47*, 5154–5156.

210. Guo, Y.-P.; Li, D.-Y.; Li, G.-T. *Acta Crystallogr. Sect. C Cryst. Struct. Commun.* **2012**, *68*, m284–m286.

211. Abdul-Kadir, M.; Clements, P. R.; Hanton, L. R.; Hollis, C. A.; Sumby, C. J. *Supramol. Chem.* **2012**, *24*, 627–640.

212. Energy dispersive X-ray spectroscopy. https://www.mee-inc.com/hamm/energy-dispersive-x-ray-spectroscopyeds/ (accessed August 7, 2019).

213. Barnes, H. A. *A Handbook of elementary rheology*; University of Wales Institute of Non-Newtonian Fluid Mechanics, **2000**.

214. Liu, Q.; Wang, Y.; Li, W.; Wu, L. *Langmuir* **2007**, *23*, 8217–8223.

215. Xue, M.; Lü, Y.; Sun, Q.; Liu, K.; Liu, Z.; Sun, P. *Cryst. Growth Des.* **2015**, *15*, 5360–5367.

216. Nelson, K. J.; Guzei, I. A.; Lund, G. S.; Mcgaff, R. W. *Polyhedron* **2002**, *21*, 2017–2020.

217. Basak, S.; Nandi, N.; Banerjee, A. *Chem. Commun.* **2014**, *50*, 6917–6919.

218. Sambri, L.; Cucinotta, F.; De Paoli, G.; Stagni, S.; De Cola, L. *New J. Chem.* **2010**, *34*, 2093–2096.

219. Bünzli, J. C. G.; Piguet, C. *Chem. Soc. Rev.* **2005**, *34*, 1048–1077.

220. Bünzli, J. C. G. *J. Coord. Chem.* **2014**, *67*, 3706–3733.

221. Parker, D.; Williams, J. A. G. *J. Chem. Soc. Dalt. Trans.* **1996**, 3613.

222. Bünzli, J. C. G. *Acc. Chem. Res.* **2006**, *39*, 53–61.

223. Macdonald, M. R.; Bates, J. E.; Ziller, J. W.; Furche, F.; Evans, W. J. *J. Am. Chem. Soc.* **2013**, *135*, 9857–9868.

224. Evans, W. J. *Organometallics* **2016**, *35*, 3088–3100.

225. Cotton, S. *Lanthanide and Actinide Chemistry*; Wiley, **2006**.

226. Liu, G.; Jacquier, K.; Eds, B. *Spectroscopic Properties of Rare Earths in Optical Materials*; Springer, Berlin, Heidelberg, **2005**.

227. Mei, Y.; Yan, B. *Inorg. Chem. Commun.* **2014**, *40*, 39–42.

228. Bünzli, J. C. G.; Eliseeva, S. V. *Lanthanide Luminescence*; Springer, Berlin, Heidelberg, **2011**.

229. Ward, M. D. *Coord. Chem. Rev.* **2007**, *251*, 1663–1677.

230. D'Aléo, A.; Pointillart, F.; Ouahab, L.; Andraud, C.; Maury, O. *Coord. Chem. Rev.* **2012**, *256*, 1604–1620.

231. Ward, M. D. *Coord. Chem. Rev.* **2010**, *254*, 2634–2642.

232. Forster, T. *Discuss. Faraday Soc.* **1959**, *27*, 7–17.

233. Heffern, M. C.; Matosziuk, L. M.; Meade, T. J. *Chem. Rev.* **2014**, *114*, 4496–4539.

234. Plush, S. E.; Clear, N. A.; Leonard, J. P.; Fanning, A. M.; Gunnlaugsson, T. *Dalton Trans.* **2010**, *39*, 3644–3652.

235. McMahon, B. K.; Mauer, P.; McCoy, C. P.; Lee, T. C.; Gunnlaugsson, T. *Aust. J. Chem.* **2011**, *64*, 600–603.

236. Lincheneau, C.; Stomeo, F.; Comby, S.; Gunnlaugsson, T. *Aust. J. Chem.* **2011**, *64*, 1315–1326.

237. Dos Santos, C. M. G.; Fernández, P. B.; Plush, S. E.; Leonard, J. P.; Gunnlaugsson, T. *Chem. Commun.* **2007**, 3389–3391.

238. Kotova, O.; Comby, S.; Gunnlaugsson, T. *Chem. Commun.* **2011**, *47*, 6810–6812.

239. Kitchen, J. A.; Gunnlaugsson, T. *The Rare Earth Elements: Fundamentals and Applications*; Wiley, **2015**.

240. Bünzli, J.-C. G.; Piguet, C.; Bunzli, J. G.; Piguet, C. *Chem. Rev.* **2002**, *102*, 1897–1928.

241. Barry, D. E.; Caffrey, D. F.; Gunnlaugsson, T. *Chem. Soc. Rev.* **2016**, *45*, 3244–3274.

242. Vickers, M. S.; Beer, P. D. *Chem. Soc. Rev.* **2007**, *36*, 211–225.

243. Lincheneau, C.; Destribats, C.; Barry, D. E.; Kitchen, J. A.; Peacock, R. D.; Gunnlaugsson, T. *Dalton Trans.* **2011**, *40*, 12056–12059.

244. Oshovsky, G. V.; Reinhoudt, D. N.; Verboom, W. *Angew. Chem. Int. Ed.* **2007**, *46*, 2366–2393.

245. Song, B.; Vandevyver, C. D. B.; Chauvin, A. S.; Bünzli, J. C. G. *Org. Biomol. Chem.* **2008**, *6*, 4125–4233.

246. Aarons, R. J.; Notta, J. K.; Meloni, M. M.; Feng, J.; Vidyasagar, R.; Narvainen, J.; Allan, S.; Spencer, N.; Kauppinen, R. A.; Snaith, J. S.; Faulkner, S. *Chem. Commun.* **2006**, 909–911.

247. Binnemans, K.; Görller-Walrand, C. Application of the Eu3+ Ion for site symmetry determination. *J. Rare Earths* **1996**, *14*, 179–180.

248. Lincheneau, C.; Leonard, J. P.; McCabe, T.; Gunnlaugsson, T. *Chem. Commun. (Camb).* **2011**, *47*, 7119–7121.

249. Nitz, M.; Franz, K. J.; Maglathlin, R. L.; Imperiali, B. *ChemBioChem* **2003**, *4*, 272–276.

250. MacManus, J. P.; Hogue, C. W.; Marsden, B. J.; Sikorska, M.; Szabo, A. G. *J. Biol. Chem.* **1990**, *265*, 10358–10366.

251. Bonnet, S.; Devocelle, M.; Gunnlaugsson, T. *Chem. Commun.* **2008**, 4552–4554.

252. Carubelli, C. R.; Massabni, A. M. G.; Leite, S. R. D. A. *J. Braz. Chem. Soc.* **1997**, *8*, 597–602.

253. Canard, G.; Koeller, S.; Bernardinelli, G.; Piguet, C. *J. Am. Chem. Soc.* **2008**, *130*, 1025–1040.

254. Piguet, C.; Bernardinelli, G.; Hopfgartner, G. *Chem. Rev.* **1997**, *97*, 2005–2062.

255. Lehn, J. M.; Rigault, A.; Siegel, J.; Harrowfield, J.; Chevrier, B.; Moras, D. *Proc. Natl. Acad. Sci. U. S. A.* **1987**, *84*, 2565–2569.

256. Chauvin, A. S.; Comby, S.; Song, B.; Vandevyver, C. D. B.; Thomas, F.; Bünzli, J. C. G. *Chem. Eur. J.* **2007**, *13*, 9515–9526.

257. Vandevyver, C. D. B.; Chauvin, A. S.; Comby, S.; Bünzli, J. C. G. *Chem. Commun.* **2007**, 1716–1718.

258. Yakimanskii, A. V.; Goikhman, M. Y.; Podeshvo, I. V.; Anan'eva, T. D.; Nekrasova, T. N.; Smyslov, R. Y. *Polym. Sci. Ser. A* **2012**, *54*, 921–941.

259. Hasegawa, Y.; Sogabe, K.; Wada, Y.; Kitamura, T.; Nakashima, N.; Yanagida, S.

Chem. Lett. **1999**, *28*, 35–37.

260. Zhang, H.; Fan, R.; Wang, P.; Wang, X.; Gao, S.; Dong, Y.; Wang, Y.; Yang, Y. *RSC Adv.* **2015**, *5*, 38254–38263.

261. Kai, J.; Felinto, M. C. F. C.; Nunes, L. A. O.; Malta, O. L.; Brito, H. F. *J. Mater. Chem.* **2011**, *21*, 3796–3802.

262. Jiu, H.; Zhang, L.; Liu, G.; Fan, T. *J. Lumin.* **2009**, *129*, 317–319.

263. Hsu, S. H.; Hung, K. C.; Chen, C. W. *J. Mater. Chem. B* **2016**, *4*, 7493–7505.

264. Alves, R.; Ravaro, L. P.; Pawlicka, A.; Silva, M. M.; Camargo, A. S. S. De **2015**, *26*, 2590–2597.

265. Lenaerts, P.; Driesen, K.; Van Deun, R.; Binnemans, K. *Chem. Mater.* **2005**, *17*, 2148–2154.

266. Yuan, J.; Zhang, H.; Hong, G.; Chen, Y.; Chen, G.; Xu, Y.; Weng, W. *J. Mater. Chem. B* **2013**, *1*, 4809–4818.

267. Yang, B.; Zhang, H.; Peng, H.; Xu, Y.; Wu, B.; Weng, W.; Li, L. *Polym. Chem.* **2014**, *5*, 1945.

268. Raatikainen, K.; Rissanen, K. *CrystEngComm* **2009**, *11*, 750–752.

269. Garden, S. J.; Da Cunha, F. R.; Wardell, J. L.; Skakle, J. M. S.; Low, J. N.; Glidewell, C. *Acta Crystallogr. Sect. C Cryst. Struct. Commun.* **2002**, *58*, o463–o466.

270. Beeby, A.; Clarkson, I. M.; Dickins, R. S.; Faulkner, S.; Parker, D.; Royle, L.; De Sousa, A. S.; Williams, J. A. G.; Woods, M. *J. Chem. Soc. Perkin Trans. 2* **1999**, *2*, 493–503.

271. Sailaja, G.; Parameswar, R.; Varma, H. *J. Appl. Polym. Sci.* **2011**, *121*, 3509–35115.

272. Hu, G. H.; Lindt, J. T. *Polym. Bull.* **1992**, *29*, 357–363.

273. Bergbreiter, D. E.; Liu, Y. S. *Tetrahedron Lett.* **1997**, *38*, 3703–3706.

274. Stoilova, O.; Ignatova, M.; Manolova, N.; Godjevargova, T.; Mita, D. G.; Rashkov, I. *Eur. Polym. J.* **2010**, *46*, 1966–1974.

275. Russell, G. S.; Pelesko, J. D. Hydrolysed or esterified maleic anhydride-methyl vinyl ether copolymer composition as pressure sensitive adhesives **1991**.

276. Stamm, W. Thiol derivatives of olefin-maleic anhydride copolymers **1971**.

277. Morduchowitz, A. Bonding utilizing imide ester derivatives of ethene maleic anhydride copolymers **1976**.

278. Choe, Y. S.; Yi, M. H.; Kim, J. H.; Ryu, G. S.; Noh, Y. Y.; Kim, Y. H.; Jang, K. S. *Org. Electron. physics, Mater. Appl.* **2016**, *36*, 171–176.

279. Panzarasa, G.; Osypova, A.; Consolati, G.; Quasso, F.; Soliveri, G.; Ribera, J.;

Schwarze, F. W. M. R. *Nanomaterials* **2018**, *8*.

280. Kenawy, E.-R.; Abdel-Hay, F.; El-Newehy, M.; M, O. R. *Polym. Int* **2008**, *57*, 85–91.

281. Yang, Y.; Urban, M. W. *Chem. Soc. Rev.* **2013**, *42*, 7446–67.

282. Chiper, M.; Fournier, D.; Hoogenboom, R.; Schubert, U. S. *Macromol. Rapid Commun.* **2008**, *29*, 1640–1647.

283. Weng, W.; Beck, J. B.; Jamieson, A. M.; Rowan, S. J.; Benjamin Beck, J.; Jamieson, A. M.; Rowan, S. J. *J. Am. Chem. Soc.* **2006**, *128*, 11663–11672.

284. Yang, B.; Zhang, H.; Peng, H.; Xu, Y.; Wu, B.; Weng, W.; Li, L.; Zu, Y.; Wu, B.; Weng, W.; Li, L. *Polym. Chem.* **2014**, *5*, 1945.

285. Armarego, W. L. F.; Chai, C. C. . *Purification of Laboratory Chemicals (Sixth Edition)*; Oxford, B.-H., Ed.; **2009**.

286. APEX-3, Brucker-AXS Inc **2016**.

287. SADABS, Brucker-AXS Inc **2016**.

288. Dolomanov, O. V; Bourhis, L. J.; Gildea, R. J.; Howard, J. A. K.; Puschmann, H. *Appl. Crystallogr.* **209AD**, *42*, 339–341.

289. Sheldrick, G. *Acta Crystallogr. Sect. C Struct Chem* **2015**, *71*, 3–8.

290. McKinnon, J. .; Jayatilaka, D.; Spackman, M. A. *Chem. Comm.* **2007**, 3814–3816.

291. Spackman, M. A.; Jayatilaka, D. *CrystEngComm* **2009**, *11*, 19–32.

292. Nettekoven, M.; Jenny, C. *Org. Process Res. Dev.* **2003**, *7*, 38–43.

293. Deria, P.; Li, S.; Zhang, H.; Snurr, R. Q.; Hupp, J. T.; Farha, O. K. *Chem. Commun.* **2015**, *51*, 12478–12481.

294. Shetty, R.; Nguyen, D.; Flubacher, D.; Ruggle, F.; Schumacher, A.; Kellya, M.; Michelotti, E. *Tetrahedron Lett.* **2006**, 113–117.

295. McCoy, C. P.; Stomeo, F.; Plush, S. E.; Gunnlaugsson, T. *Chem. Mater.* **2006**, *18*, 4336–4343.

Appendices

Appendix Two
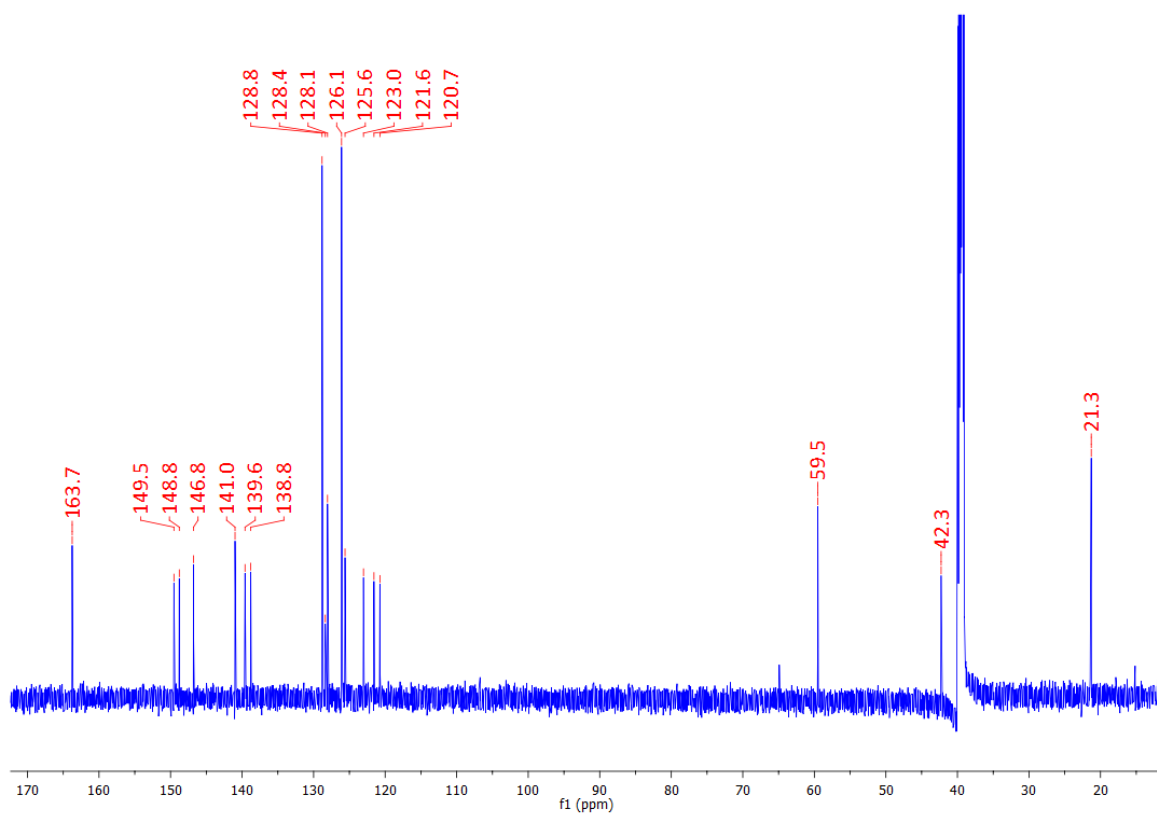
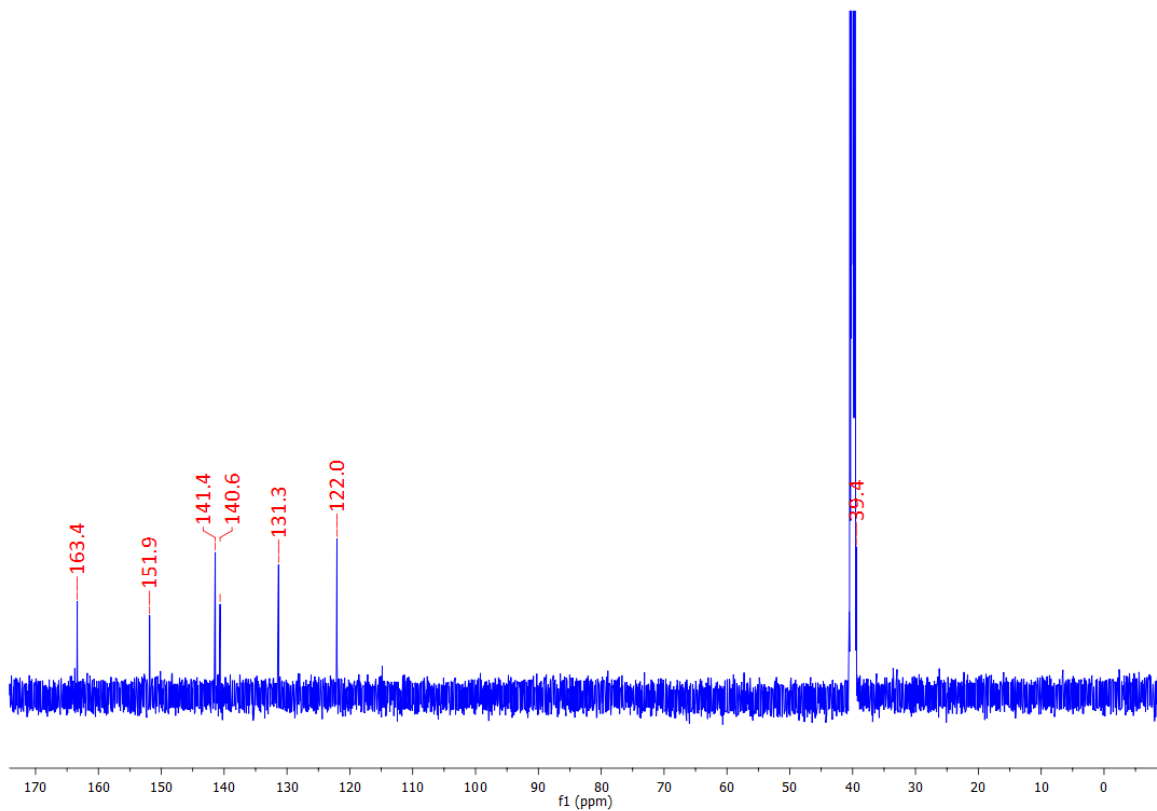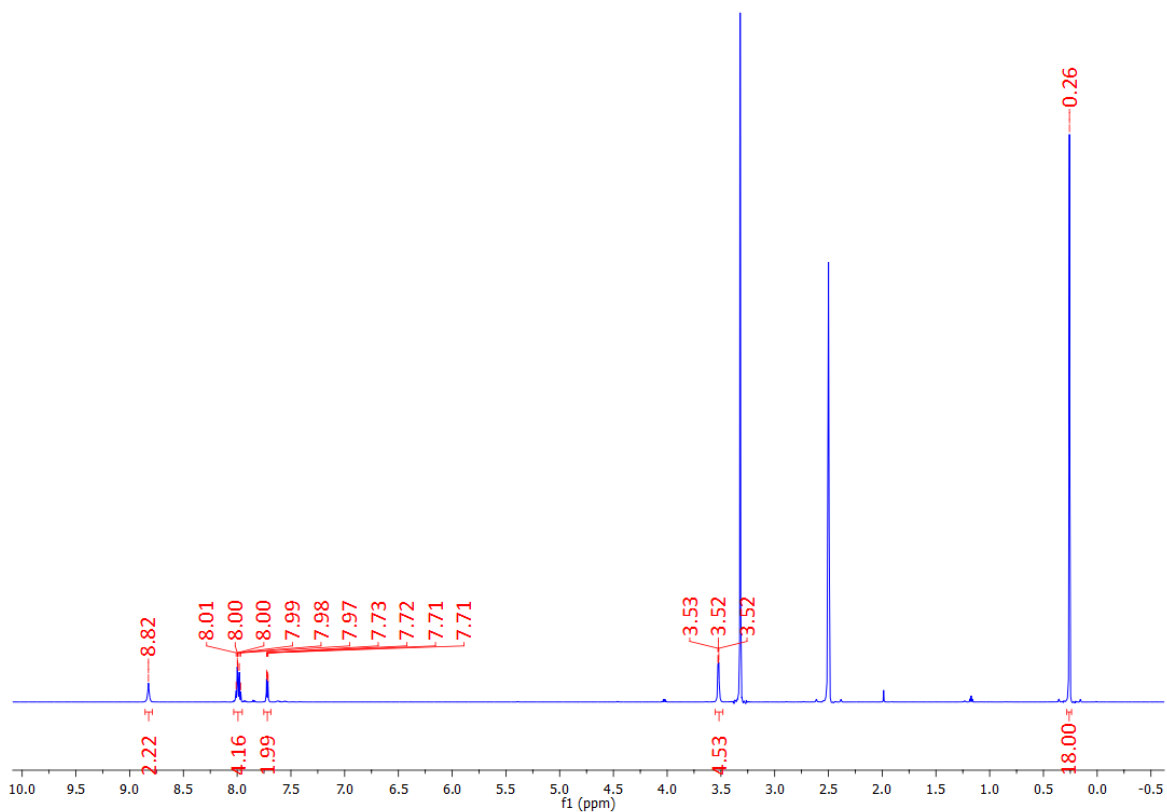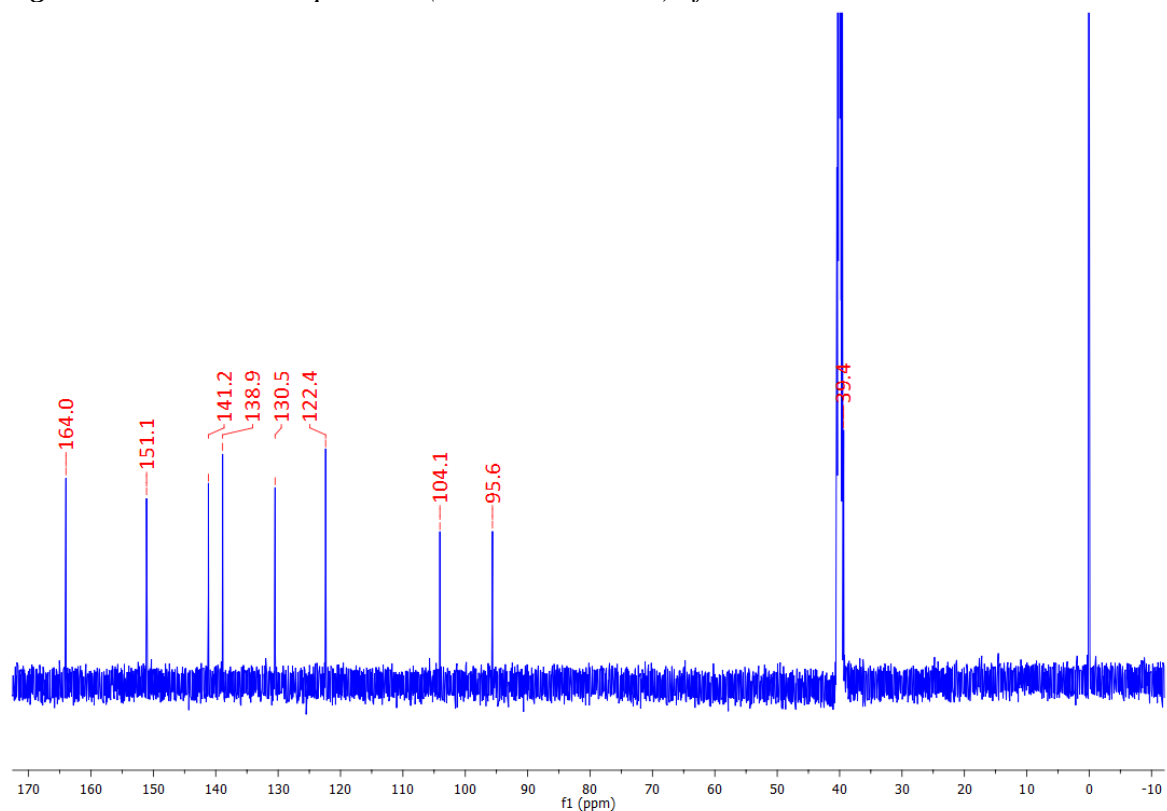**Figure A2.1** ^{13}C NMR spectrum (150 MHz, DMSO) of **H₂157**.
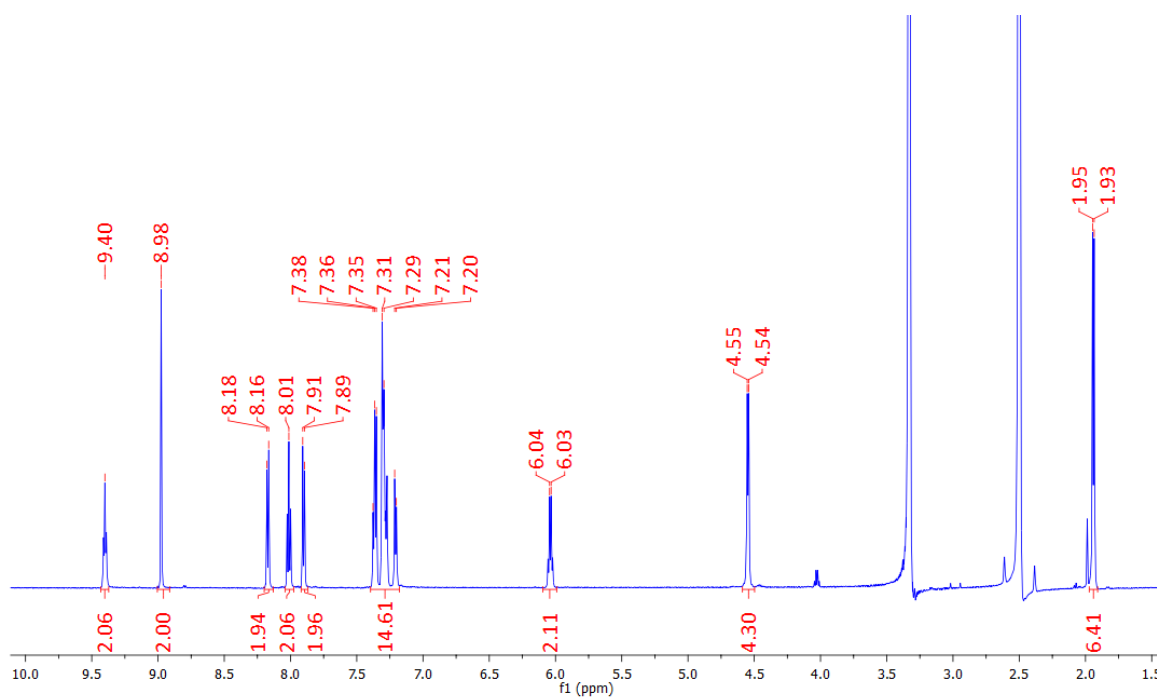
**Figure A2.2** ^{1}H NMR spectrum (600 MHz, DMSO) of **H₂158**.
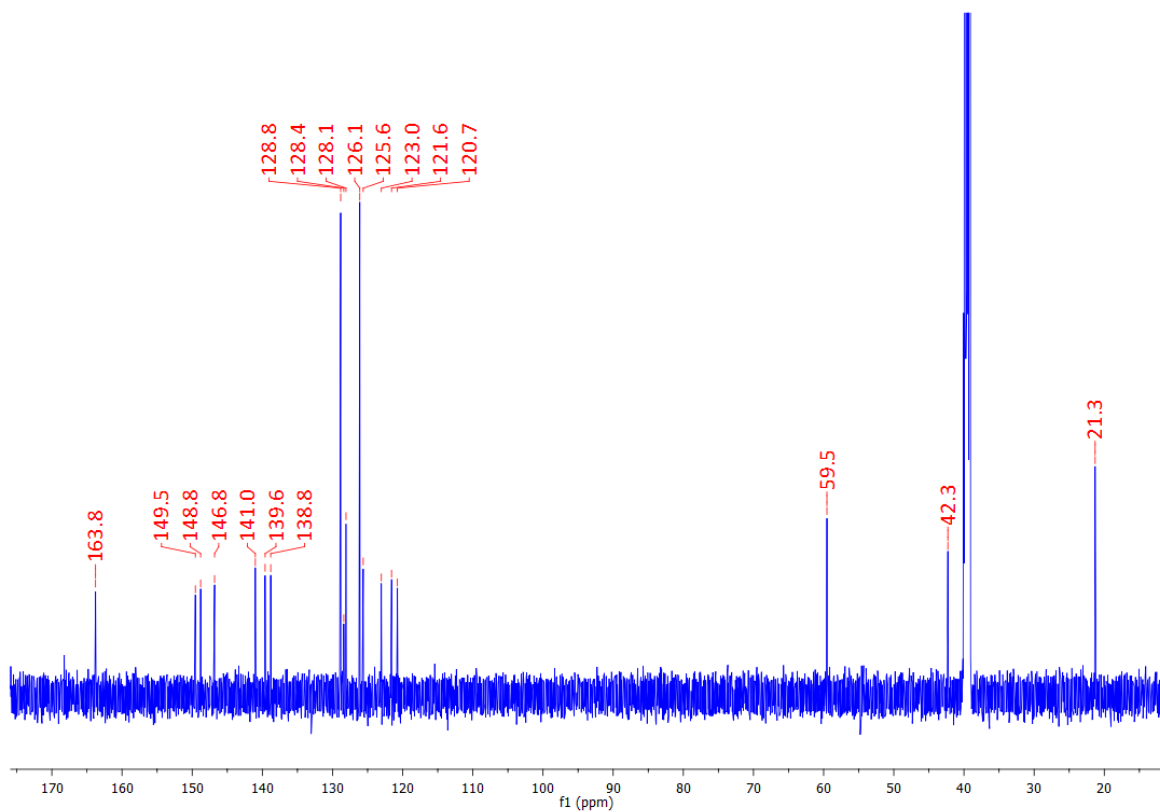
Figure A2.3 *¹³C NMR spectrum (150 MHz, DMSO) of **H₂158**.*
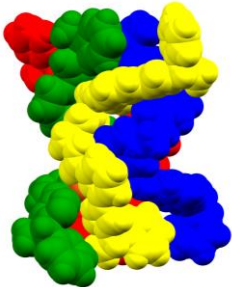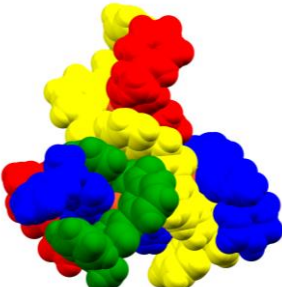
Table A2.1 *Crystal and refinement paramaters for all structures in Chapter 2.*

Identification code	[Cu$_4$(**H$_2$157**)$_4$](NO$_3$)$_8$	[Cu$_4$(**H157**)$_4$](PF$_6$)$_4$	**161**	[Cu$_2$**H$_2$157**(NO$_3$)$_4$]MeCN
Empirical formula	C$_{160}$H$_{146}$Cu$_4$N$_{48}$O$_{33}$	C$_{188}$H$_{172}$Cu$_4$F$_{24}$N$_{40}$O$_8$P$_4$	C$_{60}$H$_{68}$N$_8$O$_4$Si$_4$	C$_{42}$H$_{39}$Cu$_2$N$_{15}$O$_{14}$
Formula weight	3523.4	3953.69	1077.58	1104.96
Temperature/K	100(2)	100(2)	100(2)	100(2)
Crystal system	tetragonal	monoclinic	triclinic	monoclinic
Space group	$P4_3$	$C2$	P-1	$P2_1/c$
a/Å	23.6571(7)	36.3689(12)	11.7552(4)	24.6908(16)
b/Å	23.6571(7)	30.0761(11)	13.6950(4)	12.2647(6)
c/Å	31.1834(11)	26.1089(9)	20.8774(6)	15.4847(8)
α/°	90	90	102.4020(10)	90
β/°	90	131.776(2)	98.165(2)	97.288(5)
γ/°	90	90	106.5800(10)	90
Volume/Å^3	17452.1(12)	21297.9(14)	3070.98(17)	4651.3(5)
Z	4	4	2	4
ρ$_{calc}$g/cm^3	1.341	1.233	1.165	1.578
μ/mm^{-1}	1.254	1.422	1.297	1.857
F(000)	7288	8144	1144	2264
Crystal size/mm^3	0.18 × 0.16 × 0.06	0.24 × 0.14 × 0.1	0.6 × 0.12 × 0.04	0.14 × 0.08 × 0.03
Radiation	CuKα (λ = 1.54178)	CuKα (λ = 1.54178)	CuKα (λ = 1.54178)	CuKα (λ = 1.54178)
2Θ range for data collection/°	6.79 to 136.834	6.518 to 136.874	4.44 to 139.826	3.608 to 113.816
Index ranges	-27 ≤ h ≤ 27, -28 ≤ k ≤ 27, -37 ≤ l ≤ 37	-43 ≤ h ≤ 43, -35 ≤ k ≤ 36, -31 ≤ l ≤ 31	-14 ≤ h ≤ 14, -16 ≤ k ≤ 16, -24 ≤ l ≤ 25	-26 ≤ h ≤ 26, -13 ≤ k ≤ 13, -15 ≤ l ≤ 16
Reflections collected	88981	114816	35417	49115
Independent reflections	31736 [R$_{int}$ = 0.0576, R$_{sigma}$ = 0.0686]	38707 [R$_{int}$ = 0.0481, R$_{sigma}$ = 0.0544]	11490 [R$_{int}$ = 0.0515, R$_{sigma}$ = 0.0505]	6255 [R$_{int}$ = 0.2490, R$_{sigma}$ = 0.1285]
Reflections Observed [I>=2σ (I)]	22806	33716	10172	3859
Data/restraints/parameters	31736/112/2083	38707/412/2551	11490/0/697	6255/264/635
Goodness-of-fit on F^2	1.011	1.033	1.054	1.049
Final R indexes [I>=2σ (I)]	R$_1$ = 0.0752, wR$_2$ = 0.2006	R$_1$ = 0.0671, wR$_2$ = 0.1880	R$_1$ = 0.0571, wR$_2$ = 0.1572	R$_1$ = 0.1298, wR$_2$ = 0.2913

Final R indexes [all data]	R$_1$ = 0.1002, wR$_2$ = 0.2343	R$_1$ = 0.0747, wR$_2$ = 0.1998	R$_1$ = 0.0616, wR$_2$ = 0.1640	R$_1$ = 0.1847, wR$_2$ = 0.3186
Largest diff. peak/hole / e Å^{-3}	0.62/-0.71	0.81/-0.38	0.92/-0.46	1.04/-0.63
Flack Parameter	-0.008(18)	0.012(7)	n/a	n/a
CCDC No.	1905243	1905244	1905245	1905246

Table A2.2 *Comparison of the geometric parameters for [Cu$_4$(**H$_2$157**)$_4$](NO$_3$)$_8$ and [Cu$_4$(**H157**)$_4$](PF$_6$)$_4$*

[Cu$_4$(**H$_2$157**)$_4$](NO$_3$)$_8$	Compound	[Cu$_4$(**H157**)$_4$](PF$_6$)$_4$
10.83	d_{avg}Cu-Cu (Intrastrand, Å)	8.77
8.20	d_{avg}Cu-Cu (interstrand, Å)	10.33
2310	Molecular Volume (Å^3)	2292
102	Cu$_4$ tetrahedral volume (Å^3)	86
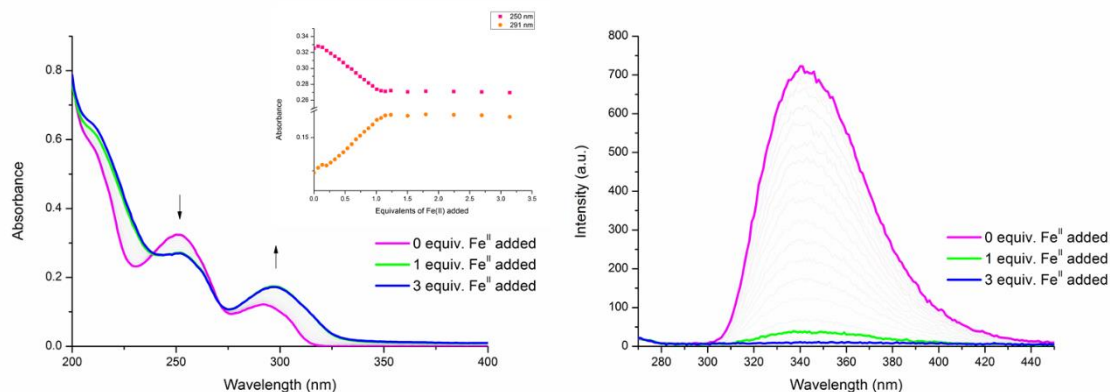
Figure A2.4 *The overall changes in the (left) UV-vis absorption spectra and (right) fluorescence emission spectra upon titrating* ***H$_2$157*** *(1×10^{-5} M) against Fe(ClO$_4$)$_2$ (0→3 equiv.) in CH$_3$CN at RT.* ***Inset****: corresponding experimental binding isotherms of absorbance*
.
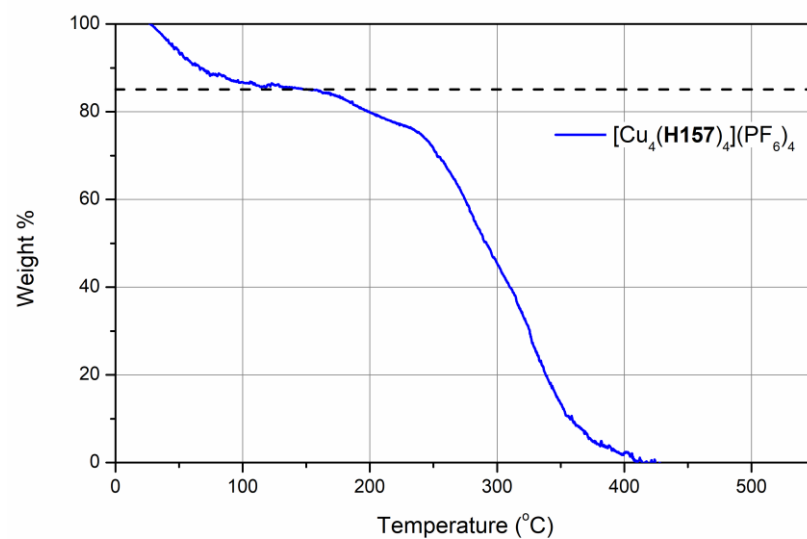
Figure A2.5 *TGA showing loss in mass of 14.4% of [Cu₄(**H157**)₄](PF₆)₄ at 85 ˚C.*
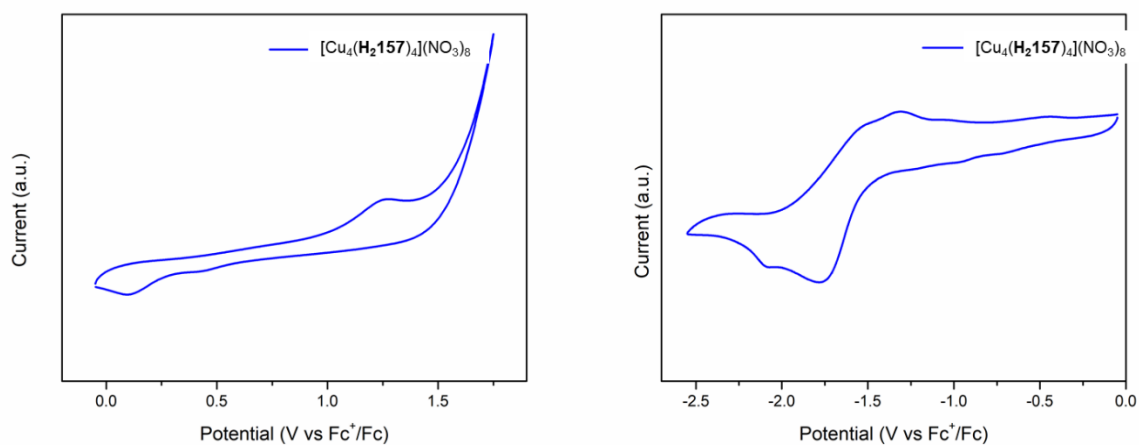
Figure A2.6 *Cyclic voltammetry of (left) cathodic and (right) anodic traces of [Cu₄(**H₂157**)₄](NO₃)₈ recorded in deaerated acetonitrile; supporting electrolyte TBAPF₆ 0.1 M. The Fc⁺/Fc couple was used as an internal standard. Scan rates were at 100 mV s⁻¹.*
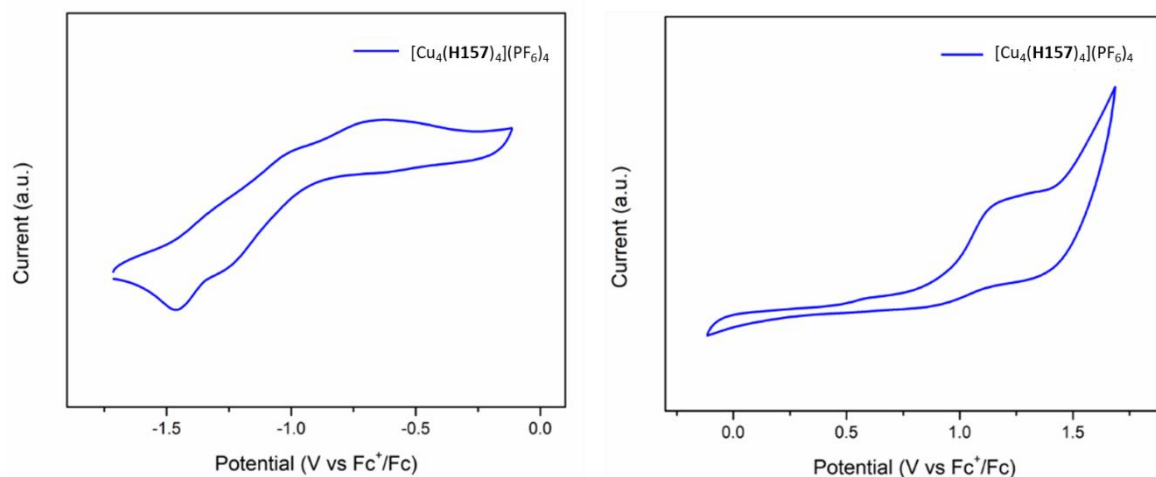
Figure A2.7 *Cyclic voltammetry of (left) anodic and (right) cathodic traces of [Cu$_4$(**H157**)$_4$](PF$_6$)$_4$ recorded in deaerated acetonitrile; supporting electrolyte TBAPF$_6$ 0.1 M. The Fc$^+$/Fc couple was used as an internal standard. Scan rates were at 100 mV s^{-1}.*
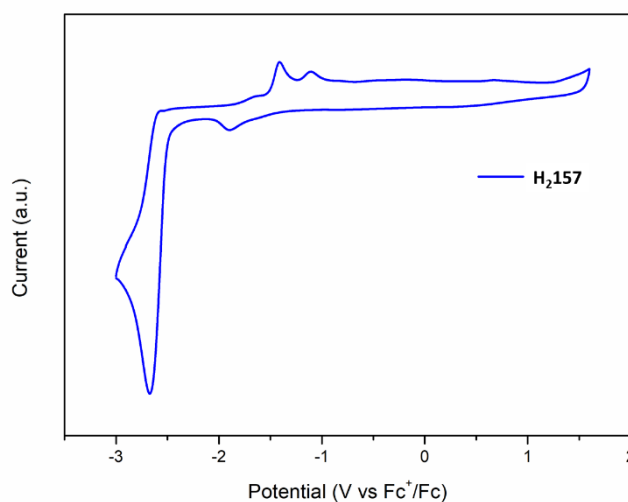
Figure A2.8 *Cyclic voltammetry of **H$_2$157** recorded in deaerated acetonitrile; supporting electrolyte TBAPF$_6$ 0.1 M. The Fc$^+$/Fc couple was used as an internal standard. Scan rate was at 100 mV s^{-1} in the negative direction.*
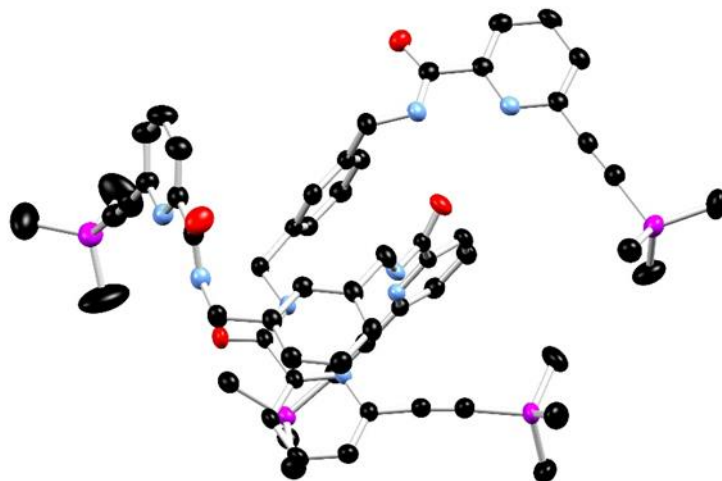
Figure A2.9 *Elipsoid plot of the asymmetric unit of ligand **161**. Ellipsoids rendered at 50% probability.*
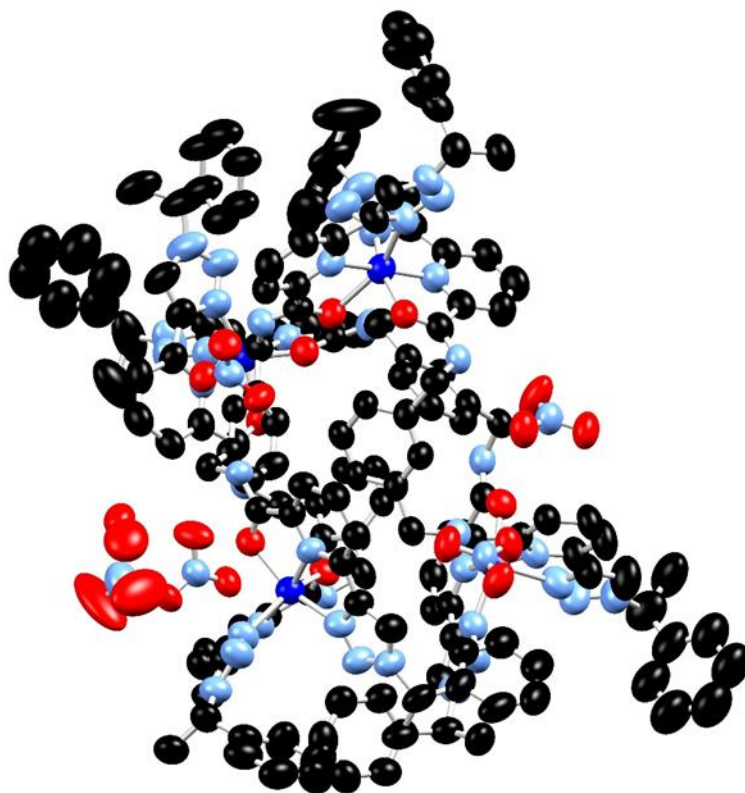
Figure A2.10 *Ellipsoid plot of asymmetric unit of [Cu₄(**H₂157**)₄](NO₃)₈. Ellipsoids rendered at 50% probability.*
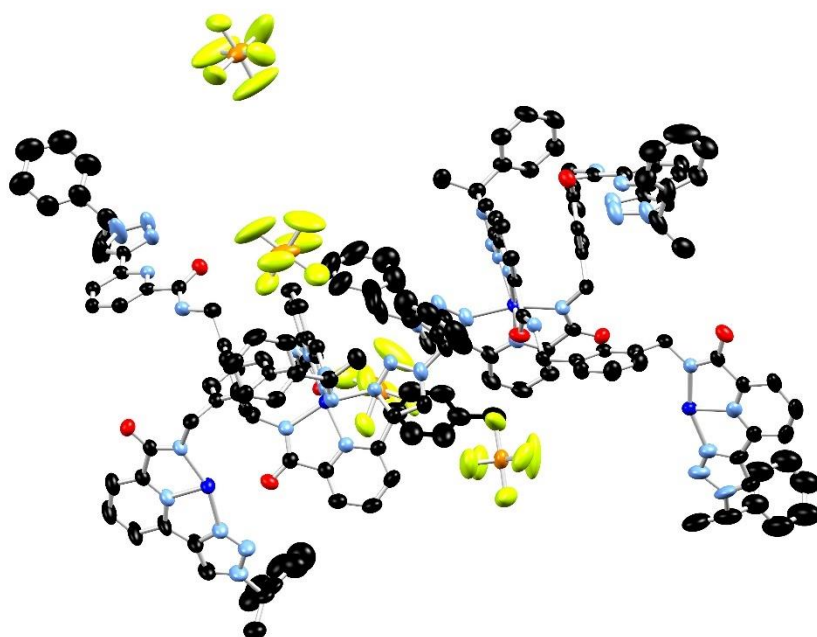
Figure A2.11 *Ellipsoid plot of asymmetric unit of [Cu₄(**H157**)₄](PF₆)₄. Ellipsoids rendered at 50% probability.*
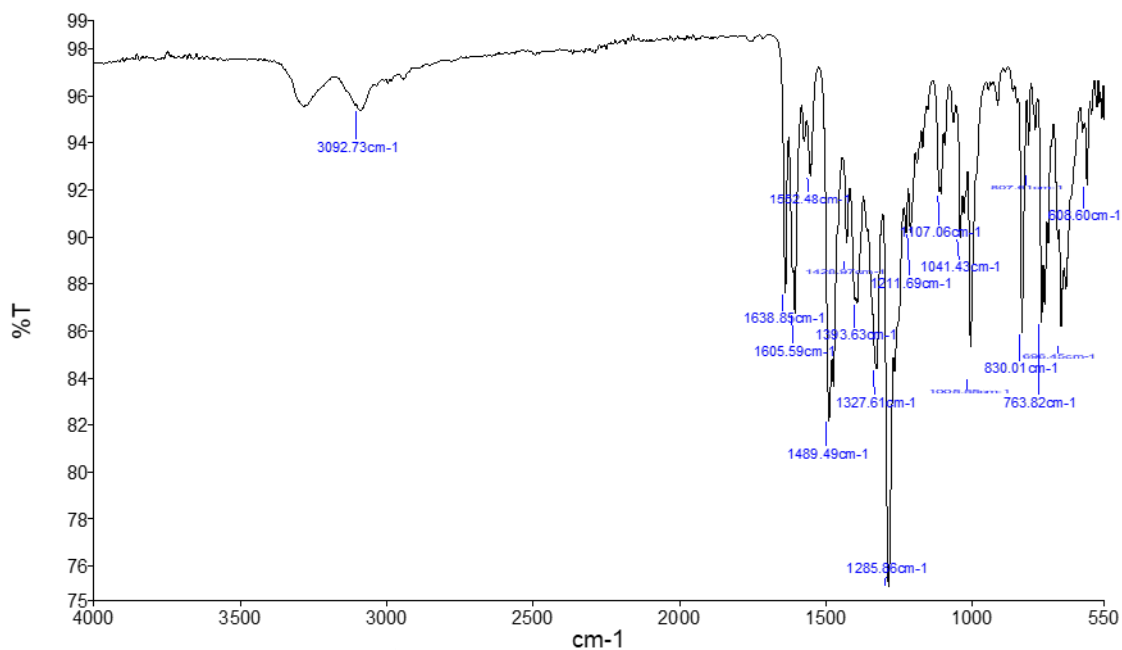
Figure A2.12 *Infrared spectrum of [Cu₄(**H₂157**)₄](NO₃)₈*
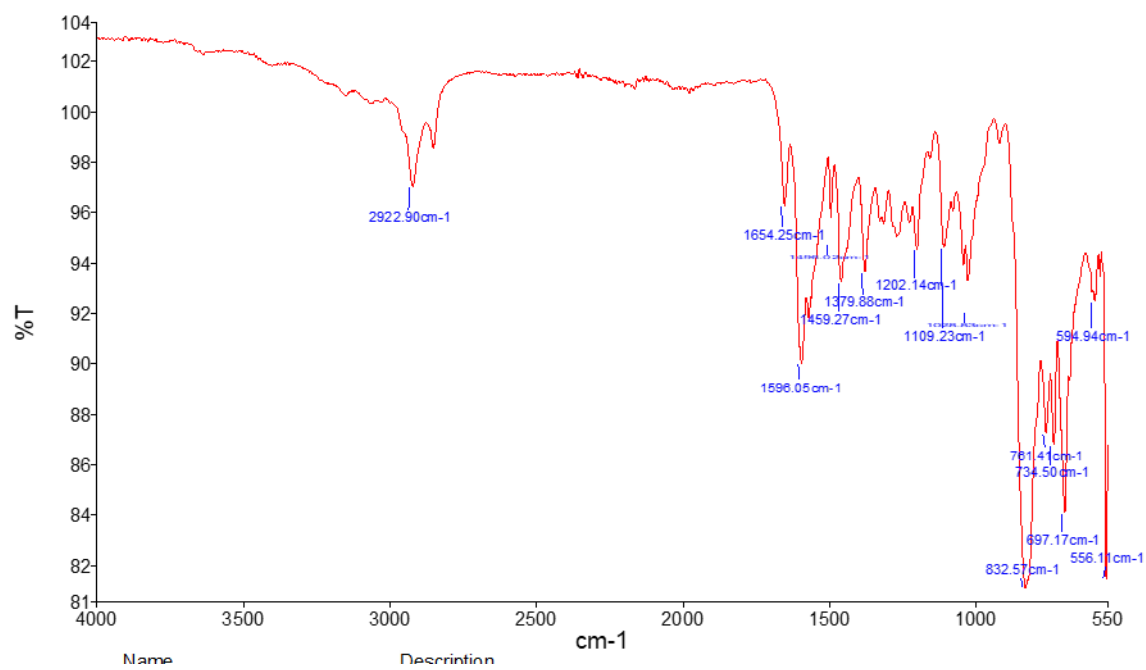
Figure A2.13 *Infrared spectrum of [Cu₄(**H157**)₄](PF₆)₄.*

Appendix Three
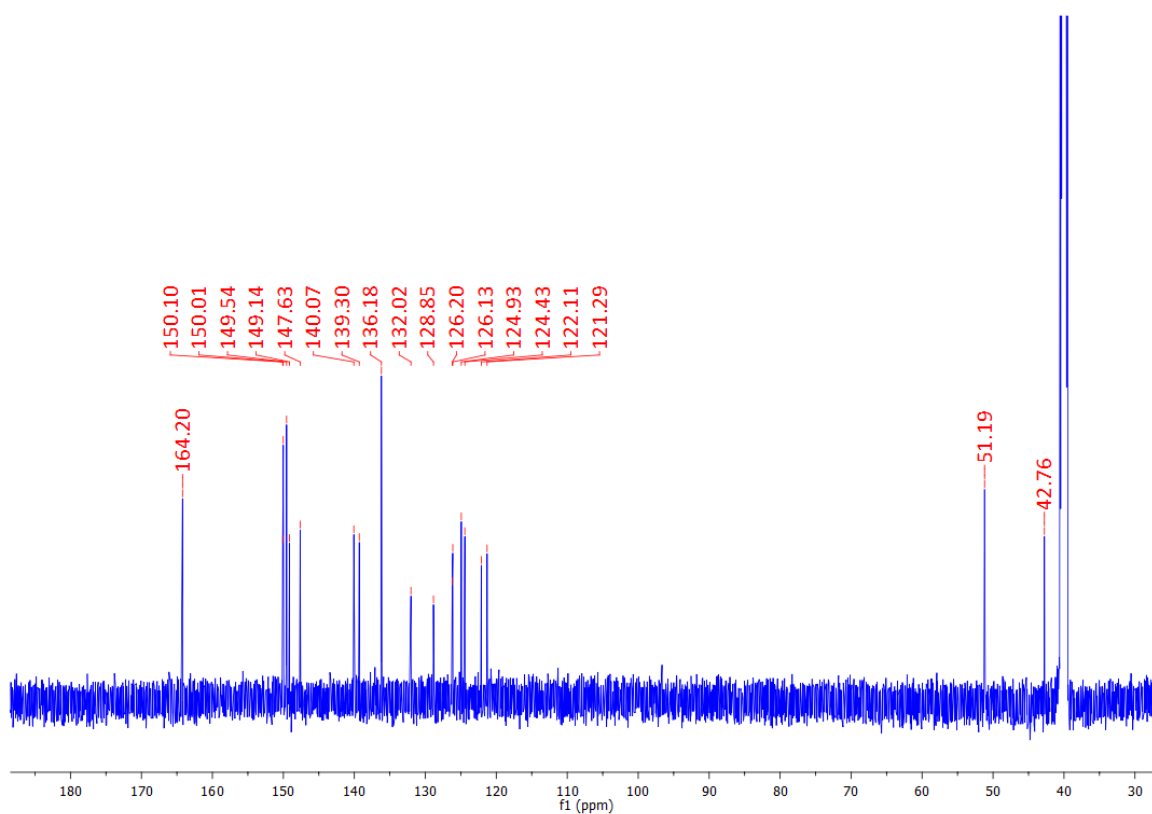
Figure A3.1 ^{13}C NMR spectrum (150 MHz, DMSO) of **162**.
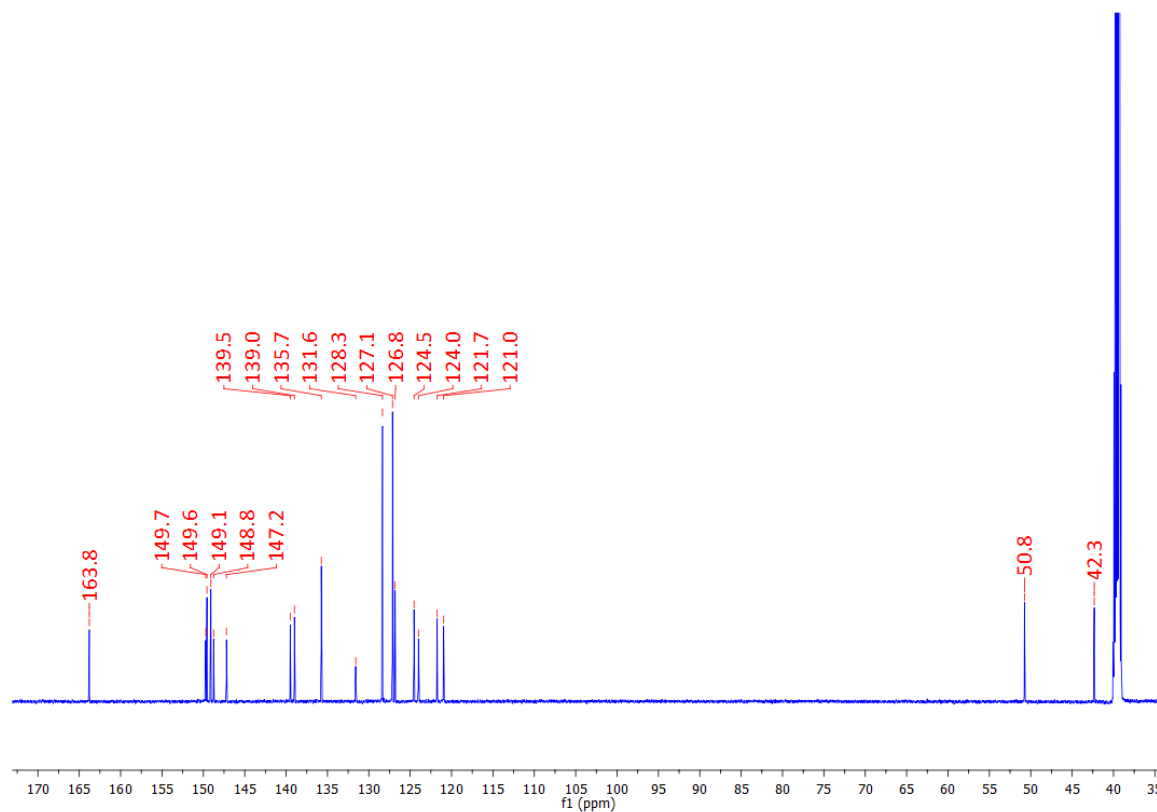
Figure A3.2 ^{13}C NMR spectrum (150 MHz, DMSO) of **166**.
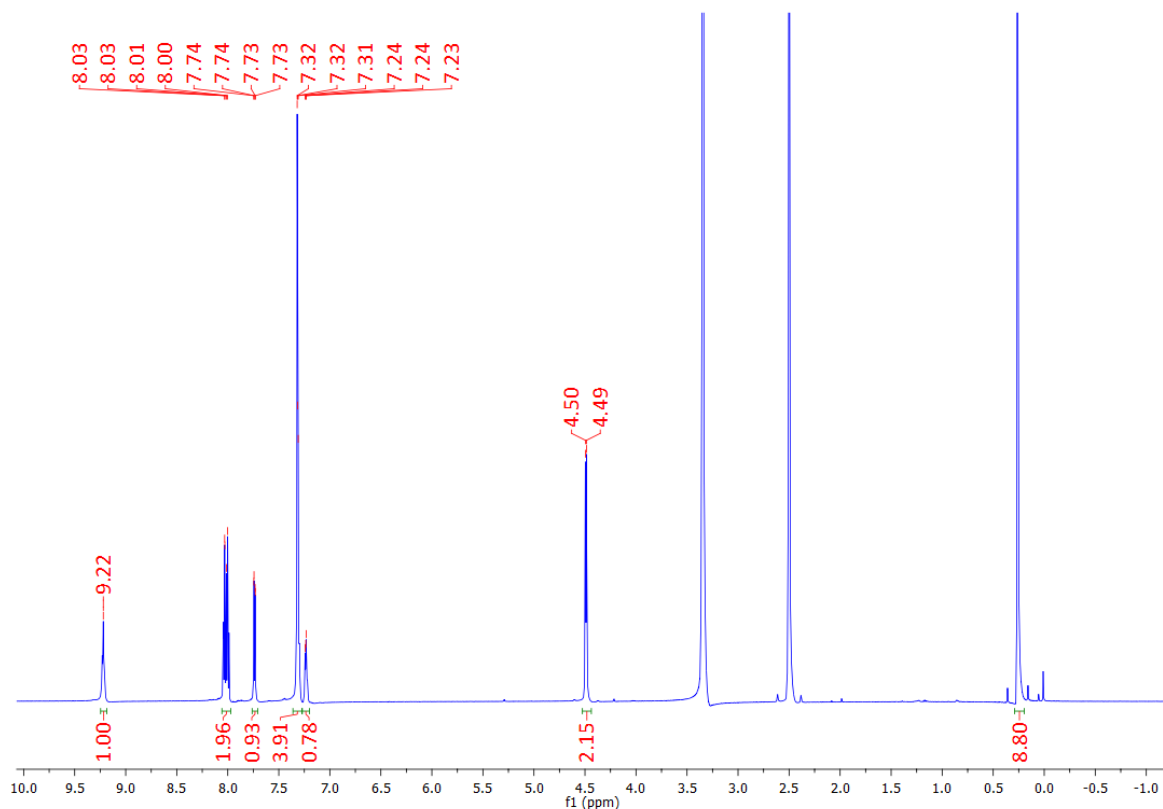
Figure A3.3 *^{1}H NMR spectrum (600 MHz, DMSO) of **168**.*
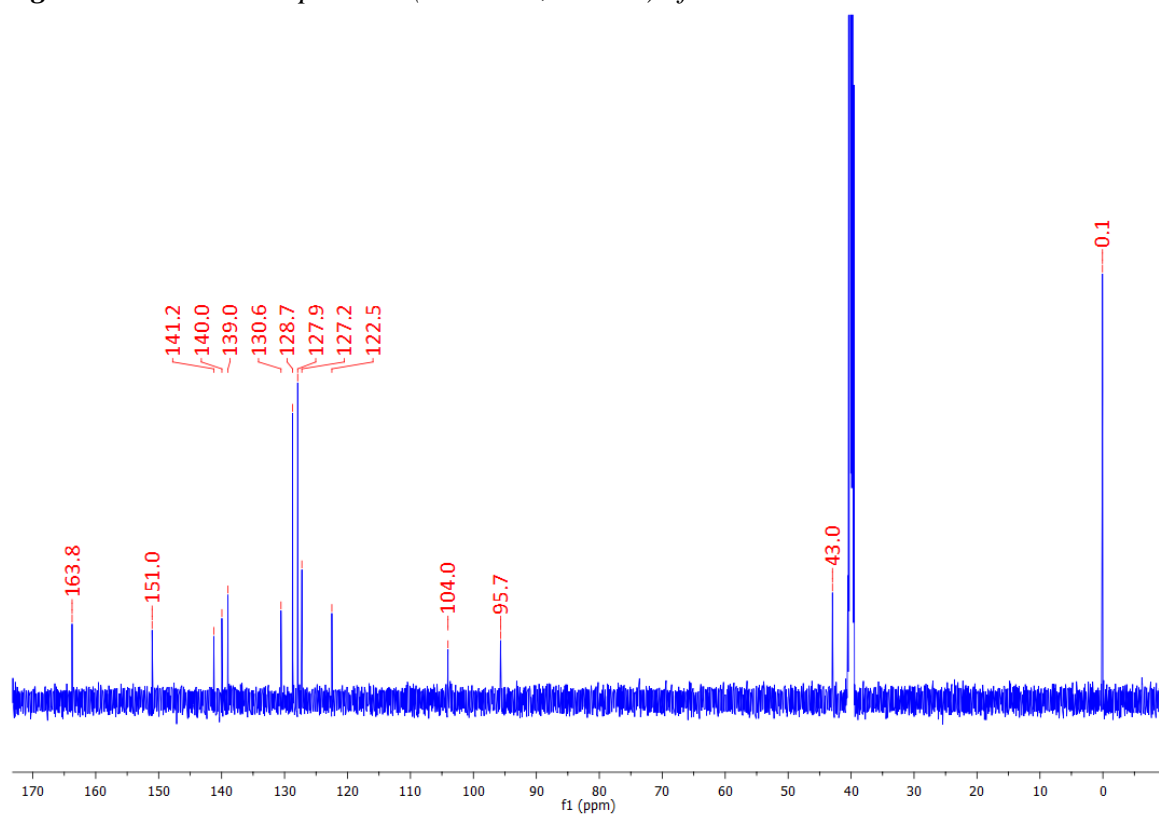
Figure A3.4 *^{13}C NMR spectrum (150 MHz, DMSO) of **168**.*

*A2.1 Crystal and refinement parameters for structures **168**, **166** and {[Ag₂(**166**)₂](CF₃SO₃)₂}ₙ in Chapter 3.*

Identification code	**168**	**166**	{[Ag$_2$(**166**)$_2$](CF$_3$SO$_3$)$_2$}$_n$
Empirical formula	C$_{18}$H$_{20}$N$_2$OSi	C$_{21}$H$_{18}$N$_6$O	C$_{22}$H$_{18}$AgF$_3$N$_6$O$_4$S
Formula weight	308.45	370.41	627.35
Temperature/K	100(2)	100(2)	100(2)
Crystal system	triclinic	orthorhombic	monoclinic
Space group	*P*-1	*P*2$_1$2$_1$2	*P*2$_1$/n
a/Å	5.8838(2)	14.781(2)	17.0839(18)
b/Å	11.1708(4)	19.903(2)	9.8330(11)
c/Å	13.3912(5)	6.1151(6)	27.626(3)
α/°	84.6200(10)	90	90
β/°	80.2820(10)	90	92.821(2)
γ/°	77.1310(10)	90	90
Volume/Å^3	844.29(5)	1798.9(4)	4635.1(9)
Z	2	4	8
ρ$_{calc}$g/cm^3	1.213	1.368	1.798
μ/mm^{-1}	0.142	0.721	1.028
F(000)	328.0	776.0	2512.0
Crystal size/mm^3	0.28 × 0.2 × 0.07	0.22 × 0.06 × 0.05	0.4 × 0.07 × 0.06
Radiation	MoKα (λ = 0.71073)	CuKα (λ = 1.54178)	MoKα (λ = 0.71073)
2Θ range for data collection/°	3.746 to 55.302	10.718 to 136.618	2.744 to 52.186
Index ranges	-7 ≤ h ≤ 7, -14 ≤ k ≤ 14, -17 ≤ l ≤ 17	-16 ≤ h ≤ 17, -22 ≤ k ≤ 23, -7 ≤ l ≤ 5	-16 ≤ h ≤ 21, -12 ≤ k ≤ 12, -34 ≤ l ≤ 34
Reflections collected	10456	10412	39534
Independent reflections	3925 [R$_{int}$ = 0.0194, R$_{sigma}$ = 0.0219]	3248 [R$_{int}$ = 0.1015, R$_{sigma}$ = 0.0898]	9198 [R$_{int}$ = 0.0647, R$_{sigma}$ = 0.0607]
Data/restraints/parameters	3925/0/202	3248/65/320	9198/2/673
Goodness-of-fit on F^2	1.038	1.056	1.009
Final R indexes [I>=2σ (I)]	R$_1$ = 0.0317, wR$_2$ = 0.0776	R$_1$ = 0.0823, wR$_2$ = 0.2140	R$_1$ = 0.0545, wR$_2$ = 0.1191
Final R indexes [all data]	R$_1$ = 0.0392, wR$_2$ = 0.0817	R$_1$ = 0.1011, wR$_2$ = 0.2264	R$_1$ = 0.0918, wR$_2$ = 0.1355
Largest diff. peak/hole / e Å^{-3}	0.31/-0.24	0.23/-0.25	2.01/-0.88
Flack parameter		0.1(12)	

Table A2.2 *Crystal and refinement parameters for structures in Chapter 3.*

Identification code	[Cu₃**H169**₂(CF₃SO₃)(OCH₃)₂(H₂O)](CF₃SO₃)₂	[Cu₄(**H172**)₄](PF₆)₄
Empirical formula	$C_{45.5}H_{44}Cu_3F_9N_{14}O_{15.25}S_3$	$C_{576}H_{529.82}Cu_{16}F_{94.84}N_{192}O_{61.07}P_{15.02}$
Formula weight	1488.74	14402.60
Temperature/K	100(2)	100(2)
Crystal system	triclinic	triclinic
Space group	*P*-1	*P*-1
a/Å	15.1820(5)	19.0862(5)
b/Å	15.3531(5)	22.0482(6)
c/Å	15.9147(5)	37.3685(11)
α/°	66.598(2)	91.542(2)
β/°	79.019(2)	92.366(2)
γ/°	61.486(2)	98.0920(10)
Volume/Å³	2991.47(18)	15546.9(7)
Z	2	1
ρ_{calc}g/cm³	1.653	1.538
μ/mm⁻¹	3.141	1.910
F(000)	1506.0	7361.0
Crystal size/mm³	0.06 × 0.04 × 0.02	0.08× 0.31 × 0.02
Radiation	CuKα (λ = 1.54178)	CuKα (λ = 1.54178)
2Θ range for data collection/°	6.052 to 118.044	2.368 to 120
Index ranges	-16 ≤ h ≤ 16, -17 ≤ k ≤ 17, -17 ≤ l ≤ 17	-21 ≤ h ≤ 21, -24 ≤ k ≤ 24, -41 ≤ l ≤ 41
Reflections collected	25058	107137
Independent reflections	8566 [R$_{int}$ = 0.0421, R$_{sigma}$ = 0.0443]	43799 [R$_{int}$ = 0.0512, R$_{sigma}$ = 0.0635]
Data/restraints/parameters	8566/90/875	43799/2514/4783
Goodness-of-fit on F²	1.040	1.092
Final R indexes [I>=2σ (I)]	R₁ = 0.0718, wR₂ = 0.2017	R₁ = 0.0916, wR₂ = 0.2523
Final R indexes [all data]	R₁ = 0.0821, wR₂ = 0.2130	R₁ = 0.1251, wR₂ = 0.2797
Largest diff. peak/hole / e Å⁻³	1.96/-1.26	1.14/-1.92
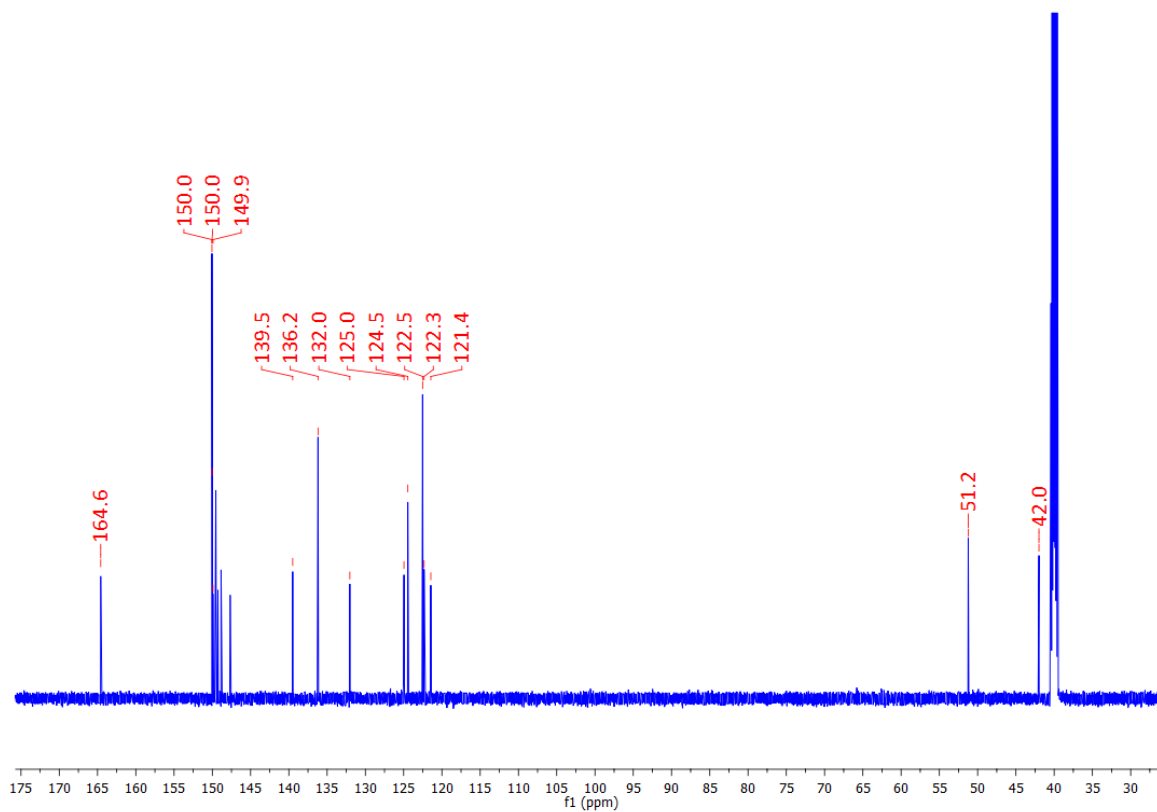
Figure A3.5 *^{13}C NMR spectrum (150 MHz, DMSO) of **169**.*
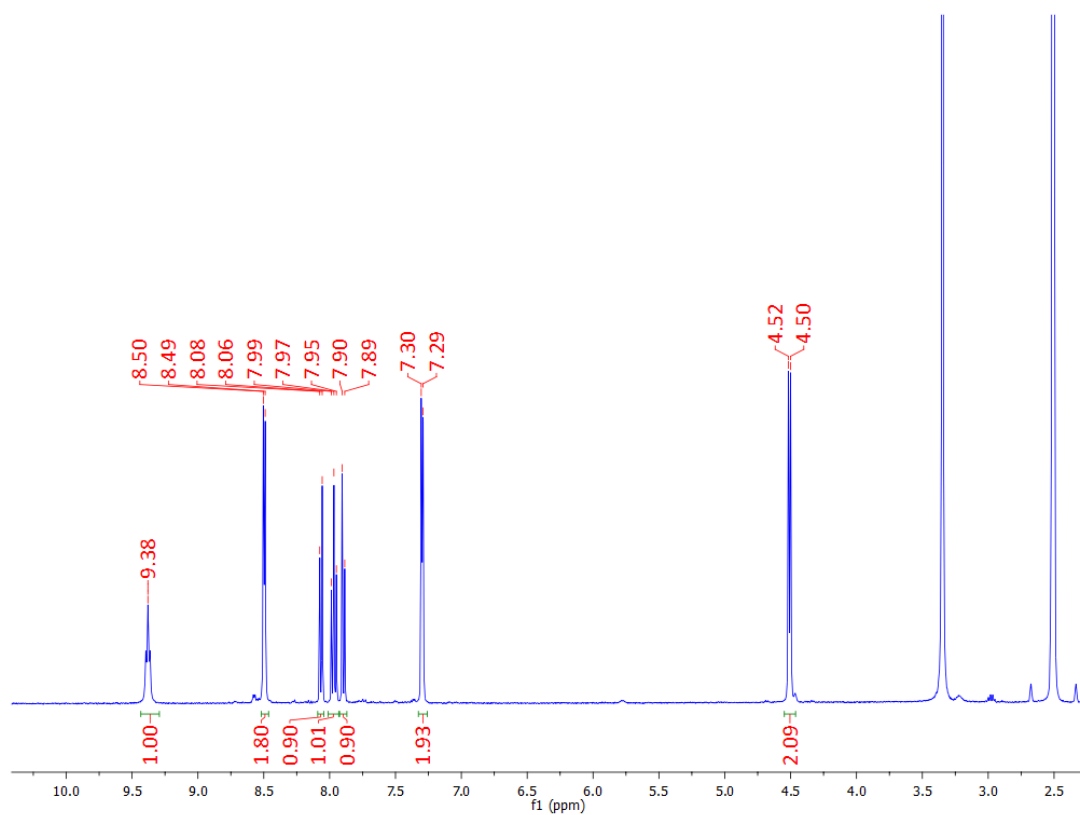
Figure A3.6 *^{1}H NMR spectrum (600 MHz, DMSO) of **167**.*
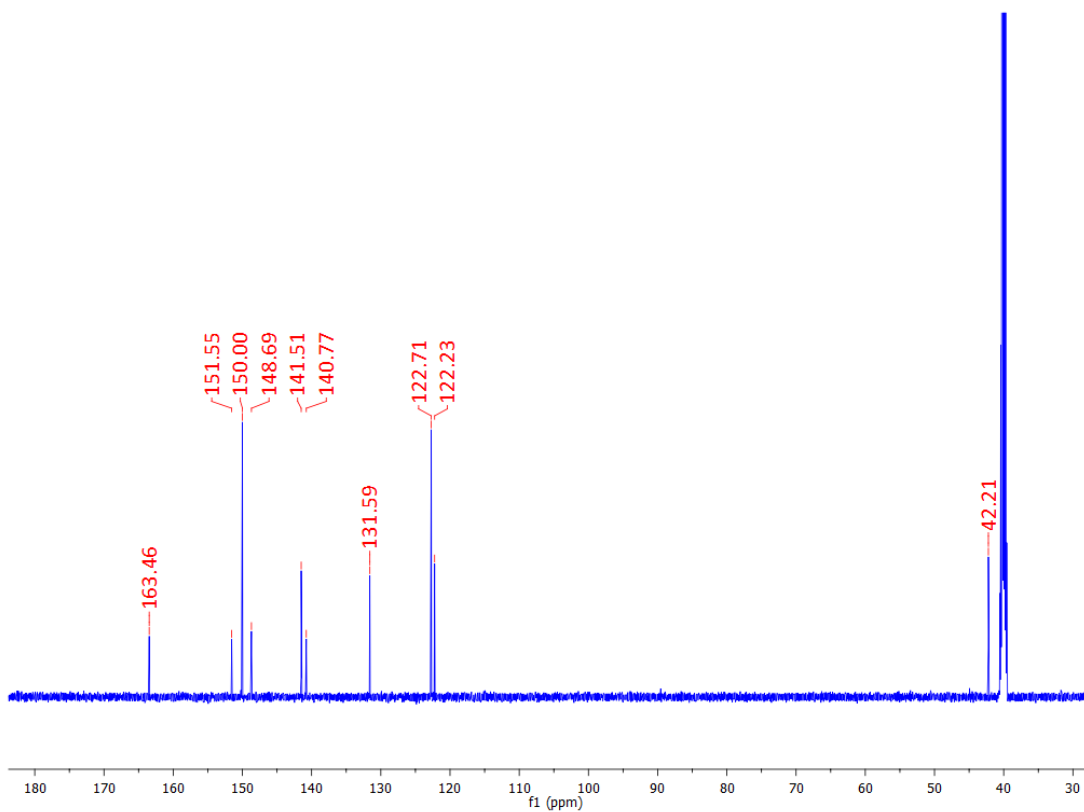
Figure A3.7 ^{13}C *NMR spectrum (150 MHz, DMSO) of* **167***.*
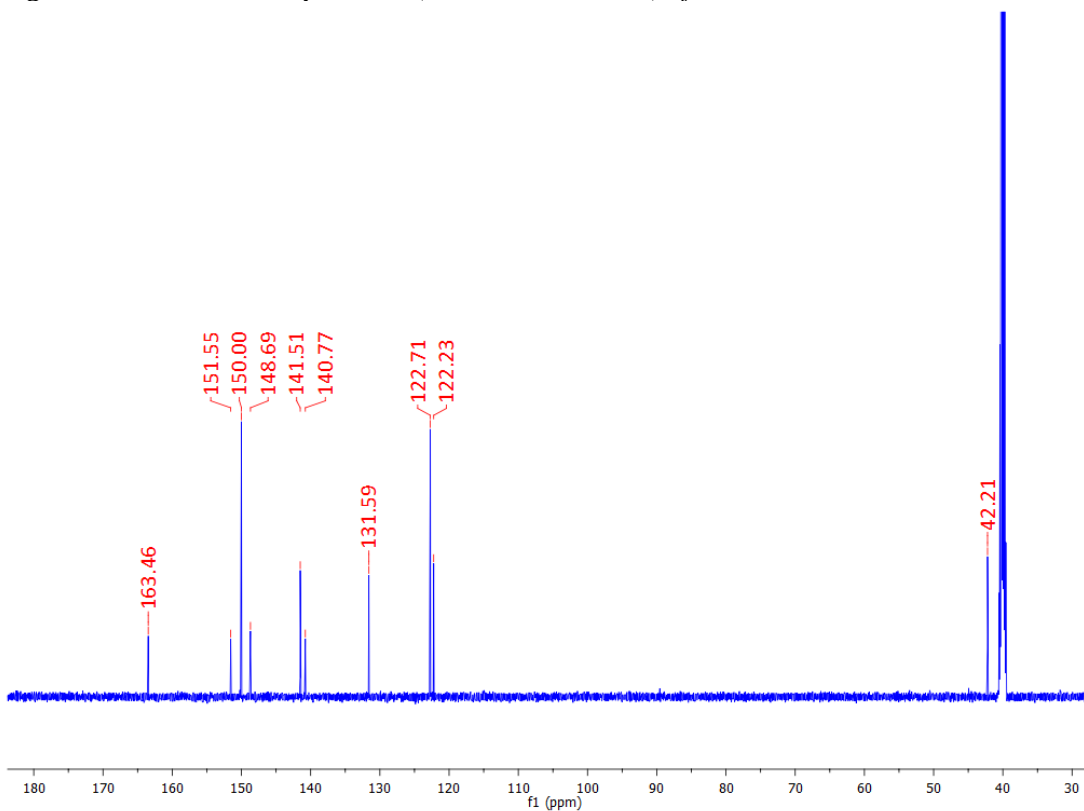
Figure A3.8 ^{13}C *NMR spectrum (150 MHz, DMSO) of* **172***.*
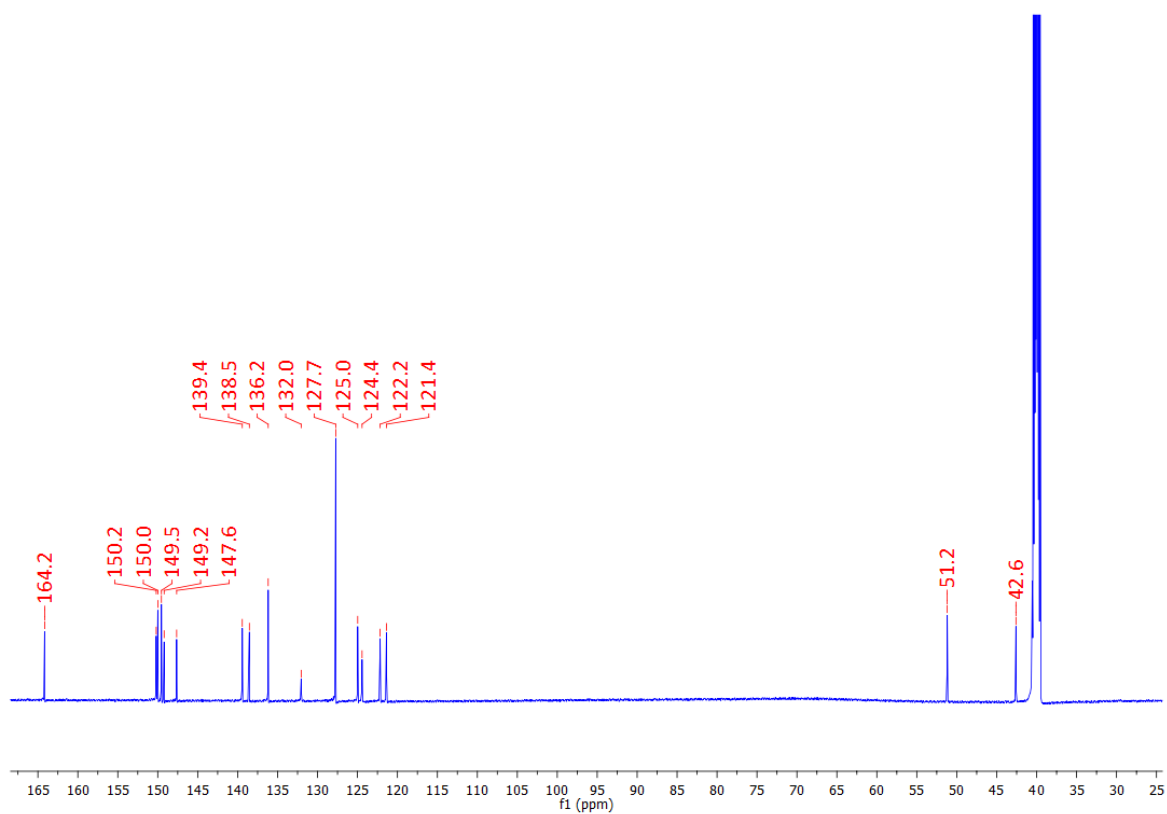
Figure A3.9 *^{13}C NMR spectrum (150 MHz, DMSO) of* **173**.
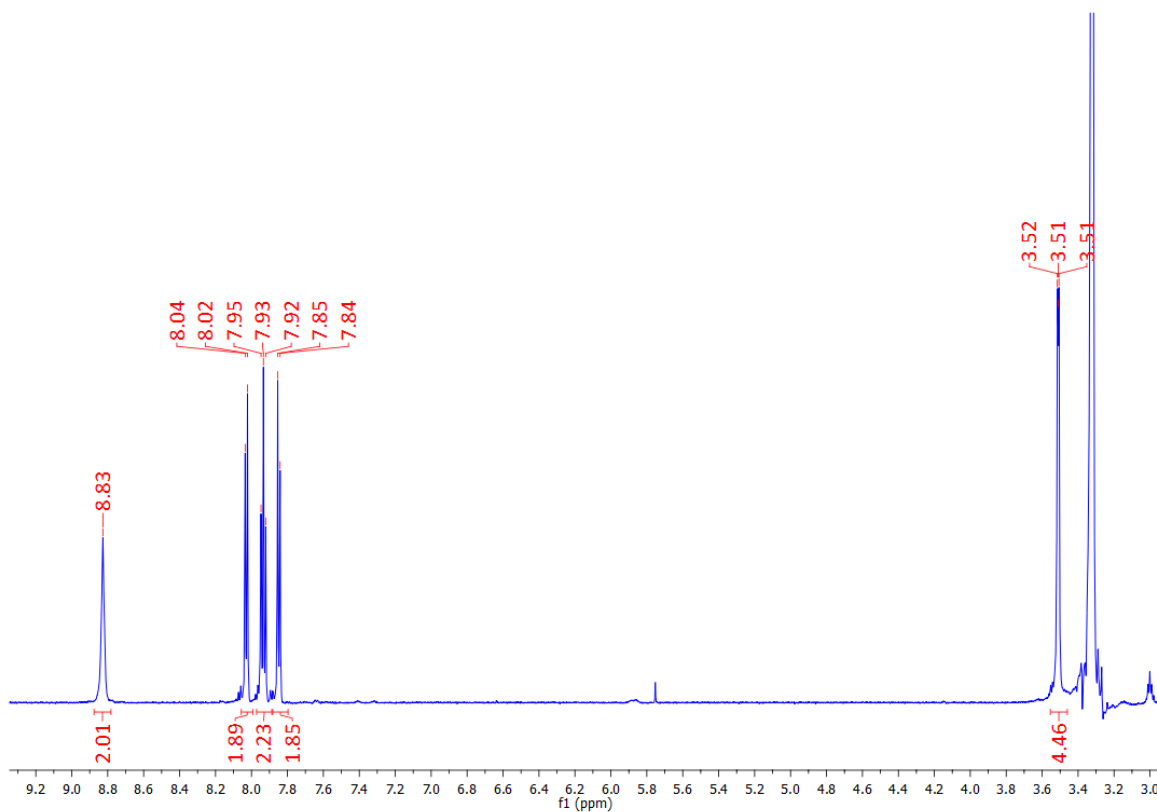
Figure A3.12 *¹H NMR spectrum (600 MHz, DMSO) of **177**.*

Figure A3.13 *¹³C NMR spectrum (150 MHz, DMSO) of **177**.*

Figure A3.14 ^{1}H NMR spectrum (600 MHz, DMSO) of **178**.

Figure A3.15 ^{13}C NMR spectrum (150 MHz, DMSO) of **178**
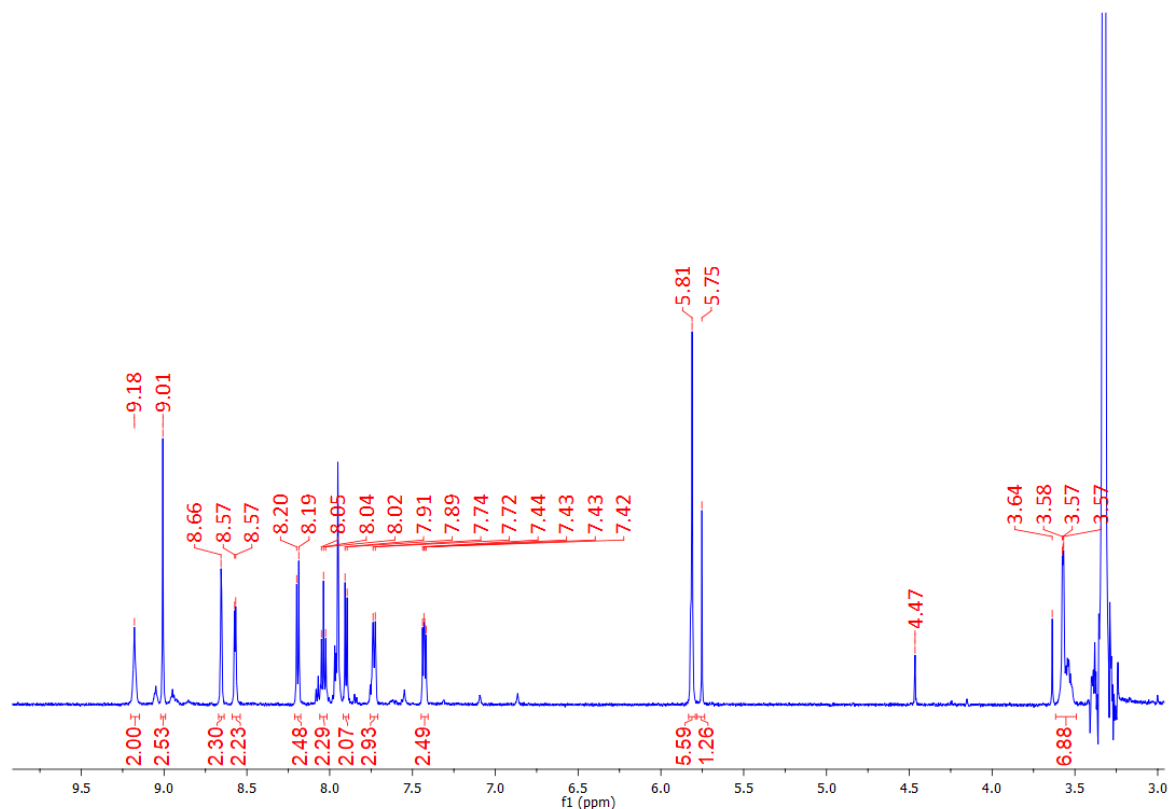
Figure A3.10 *^{1}H NMR spectrum (600 MHz, DMSO) of* ***176***.
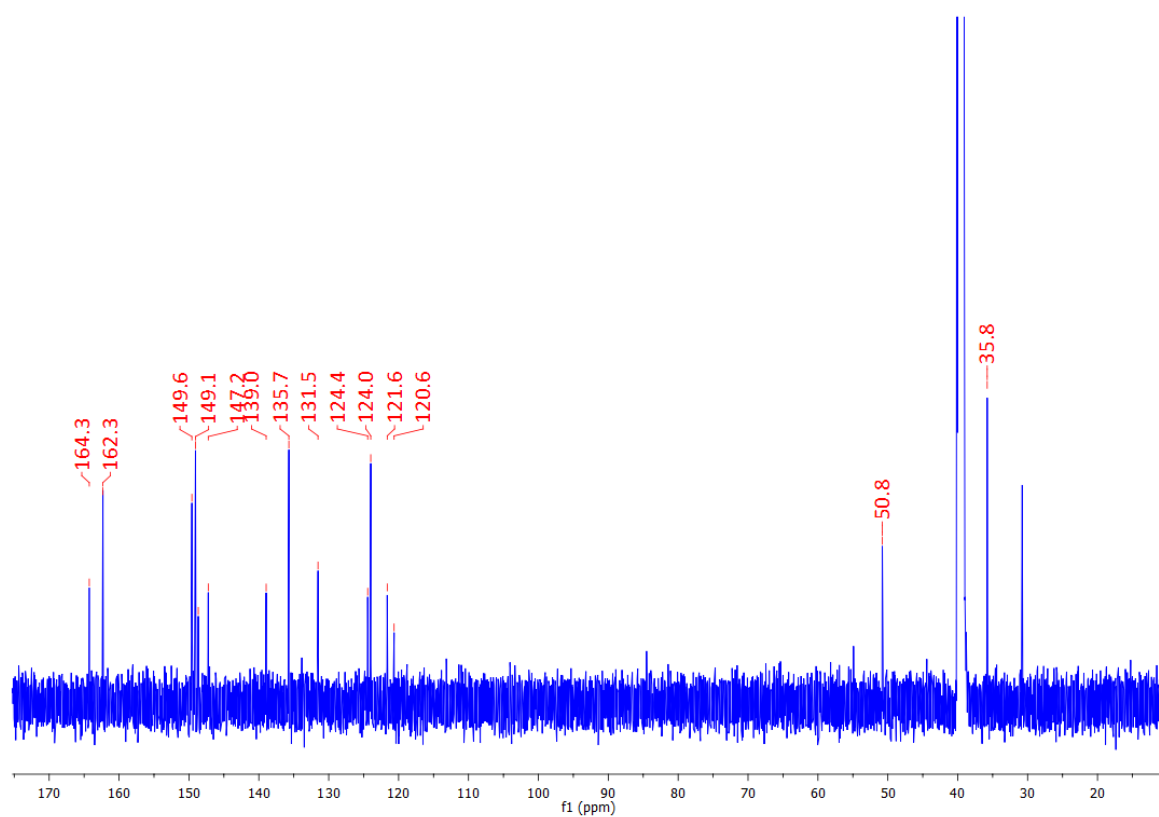
Figure A3.11 *^{13}C NMR spectrum (150 MHz, DMSO) of* ***176***.
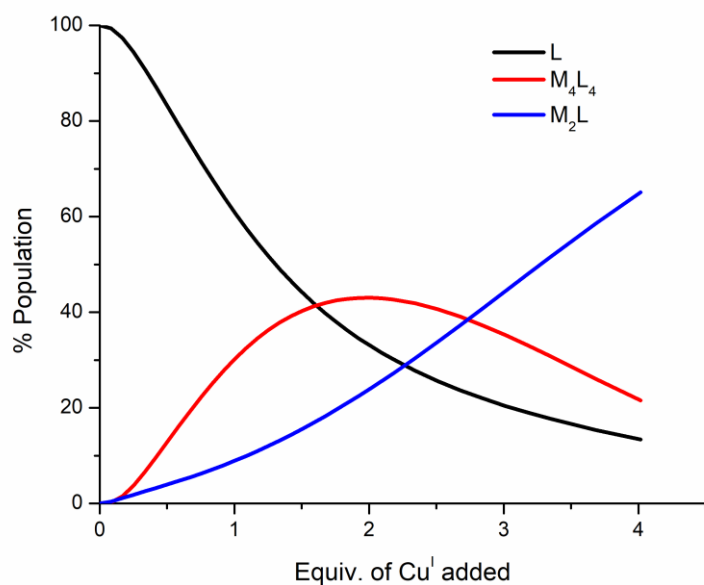
Figure A3.12 *The speciation distribution diagram obtained from the fit of the UV-vis absorption titration data of ligand* ***176*** *against [Cu(CH₃CN)₄]PF₆ in CH₃OH.*
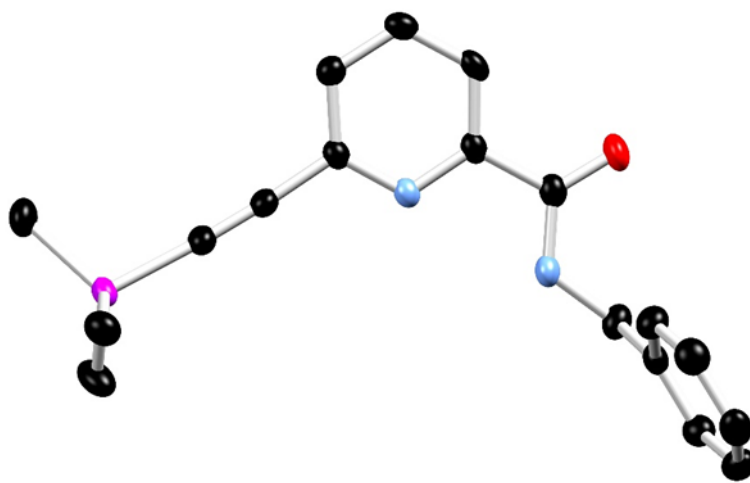
Figure A3.13 *Ellipsoid plot of asymmetric unit of ligand* ***168*** *with ellipsoids shown at 50% probability.*
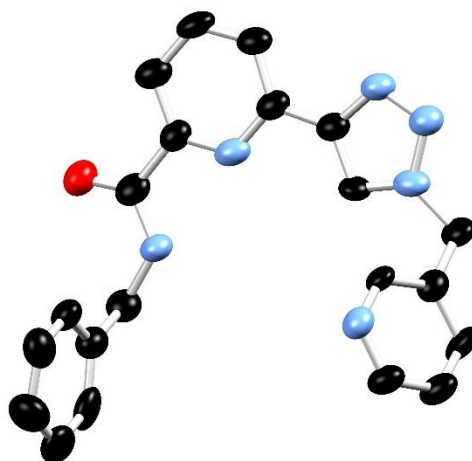
Figure A3.14 *Ellipsoid plot of asymmetric unit of ligand **166** with ellipsoids shown at 50% probability.*
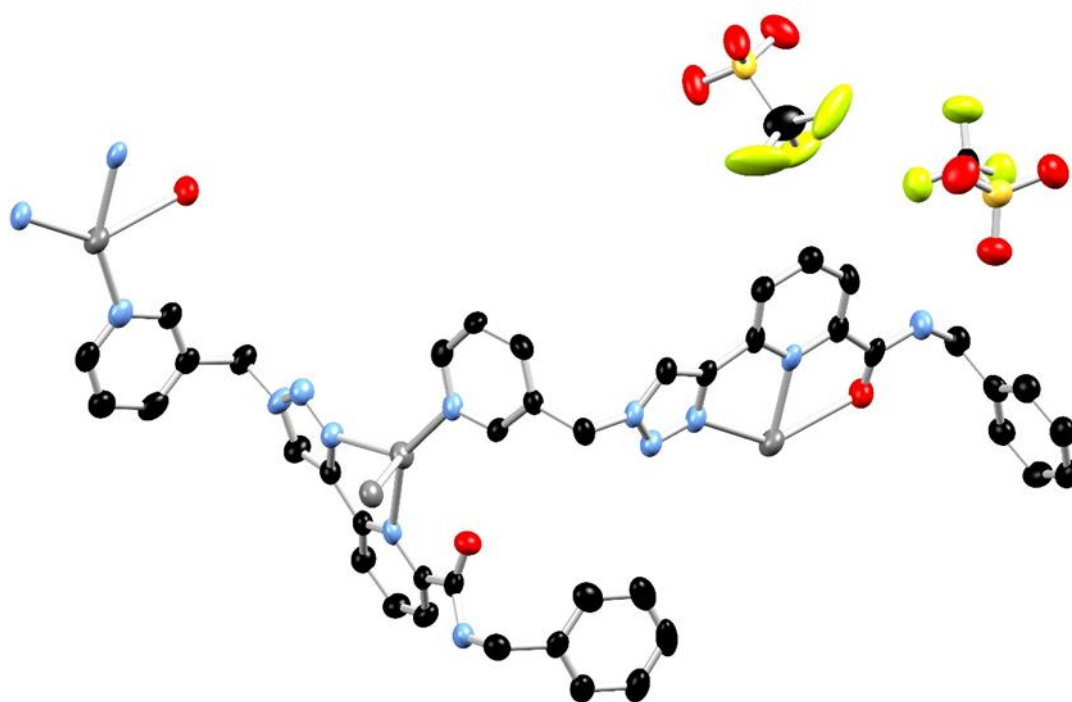
Figure A3.15 *Ellipsoid plot of asymmetric unit of {[Ag$_2$(**166**)$_2$](CF$_3$SO$_3$)$_2$}$_n$ with ellipsoids shown at 50% probability.*
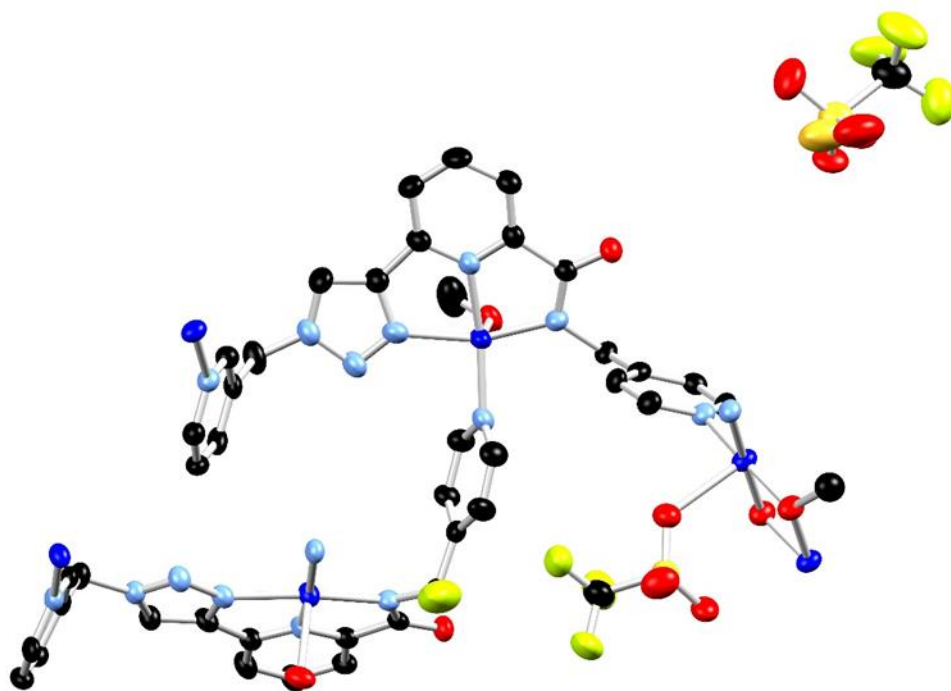
Figure ***A3.15*** *Ellipsoid* *plot* *of* *asymmetric* *unit* *of* *[Cu$_3$(**H169**)$_2$(CF$_3$SO$_3$)(OCH$_3$)$_2$(H$_2$O)](CF$_3$SO$_3$)$_2$. with ellipsoids shown at 50% probability.*
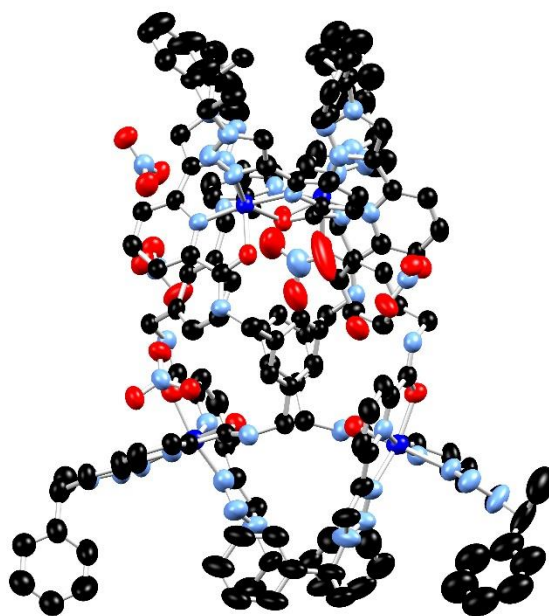
Figure A3.15 *Ellipsoid plot of asymmetric unit of [Cu$_4$(**H172**)$_4$](PF$_6$)$_4$ with ellipsoids shown at 50% probability.*

278
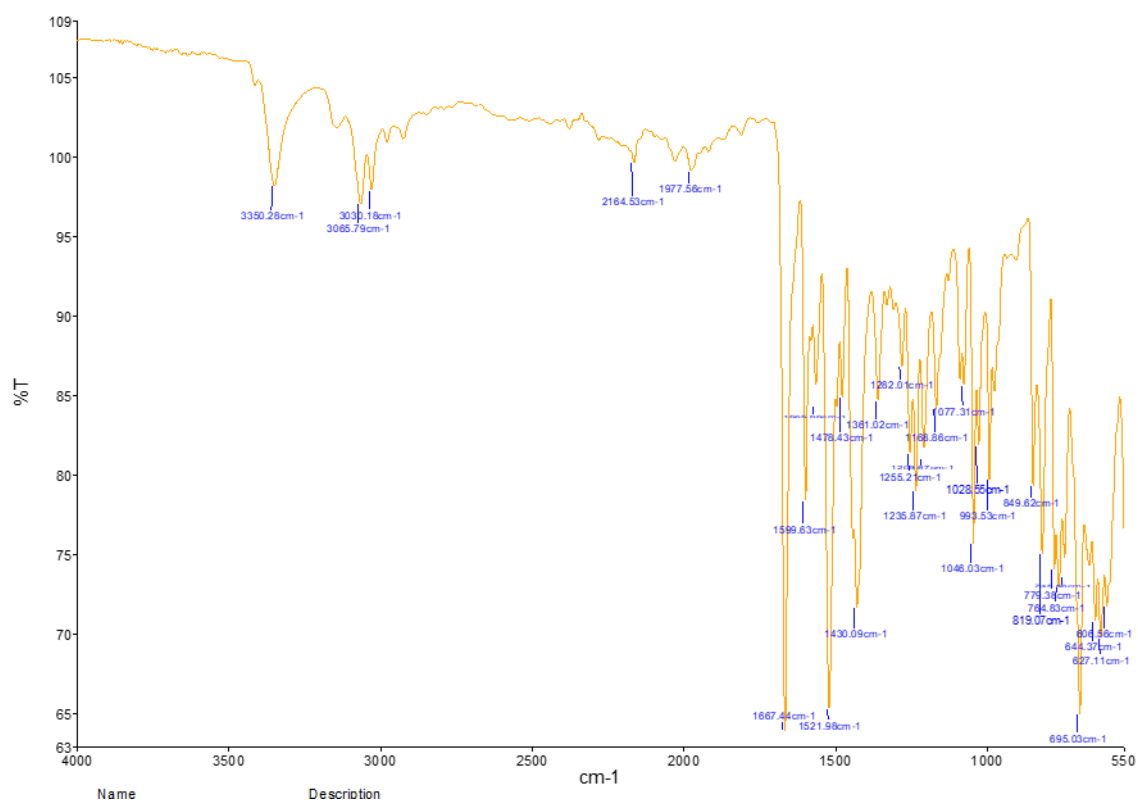
Figure A3.16 *Infrared spectrum of ligand **166**.*
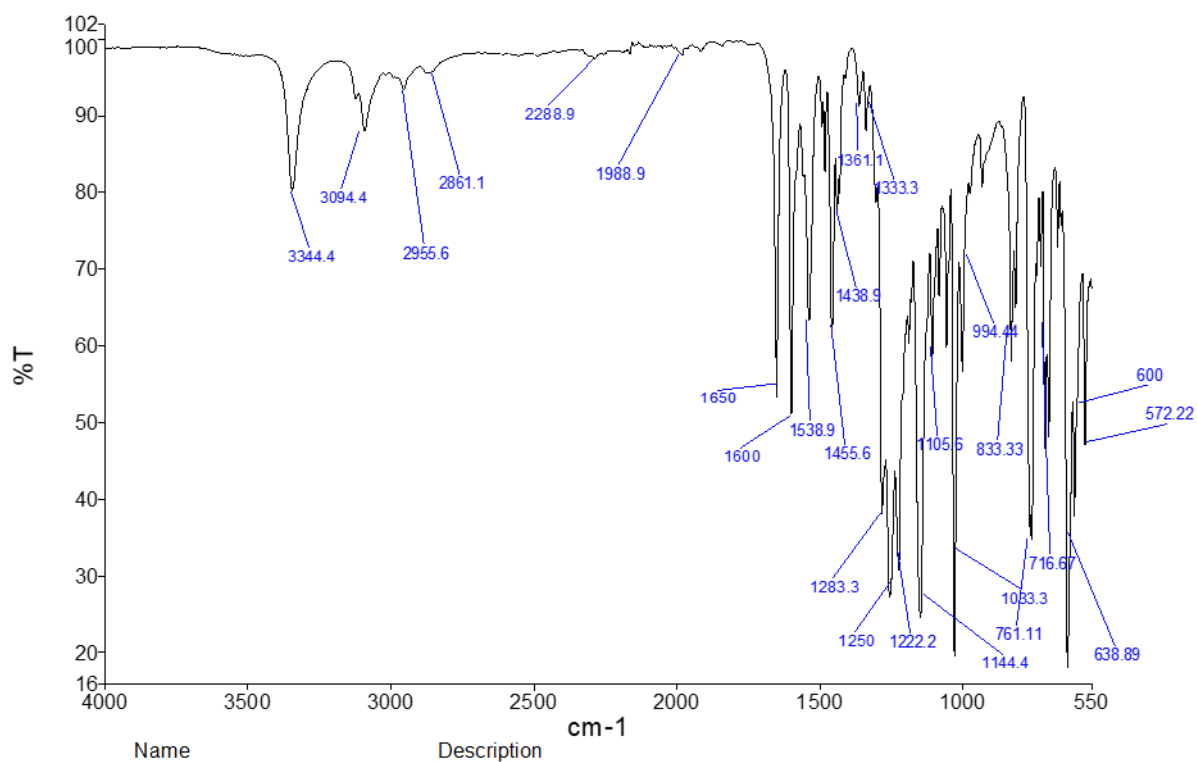
Figure A3.17 *Infrared spectrum of {[Ag₂(**166**)₂](CF₃SO₃)₂}ₙ*
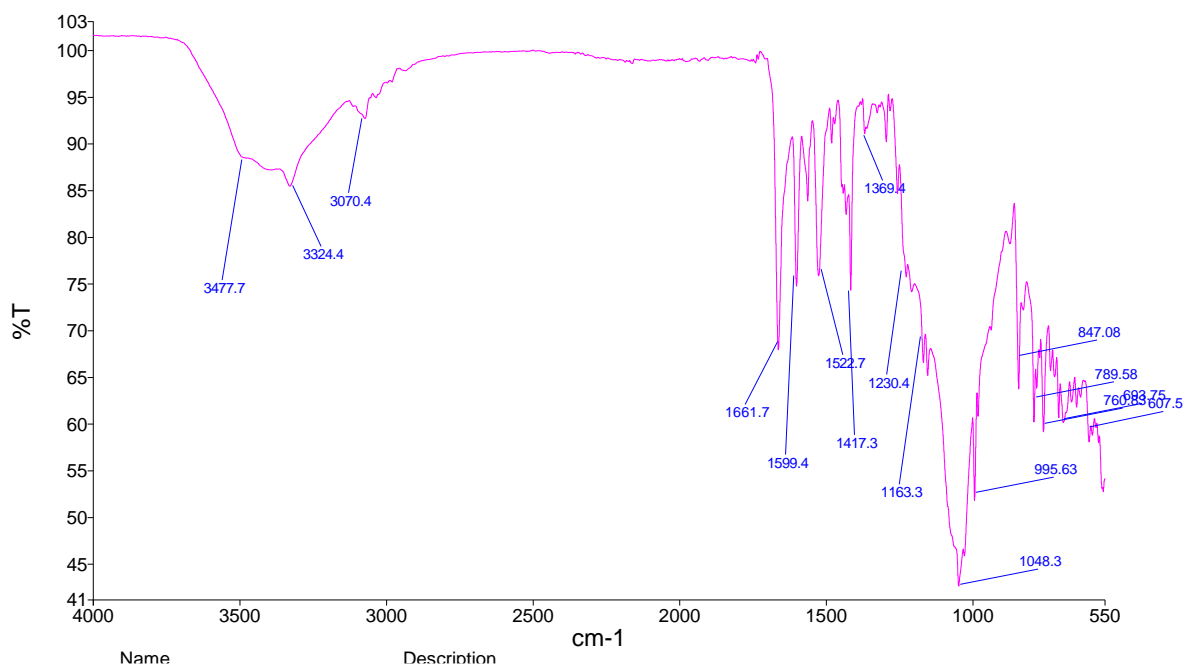
Figure A3.18 *Infrared spectrum of ligand H₂169*
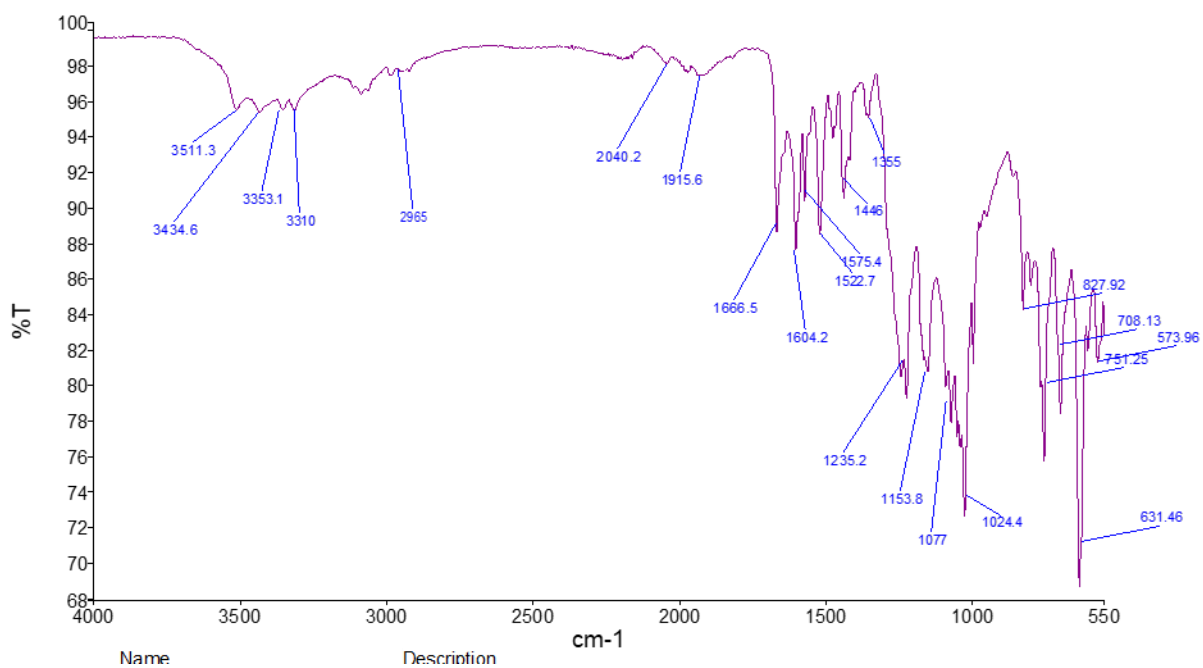
Figure A3.19 Infrared spectrum of [Cu₃(H169)₂(CF₃SO₃)(OCH₃)₂(H₂O)](CF₃SO₃)₂.
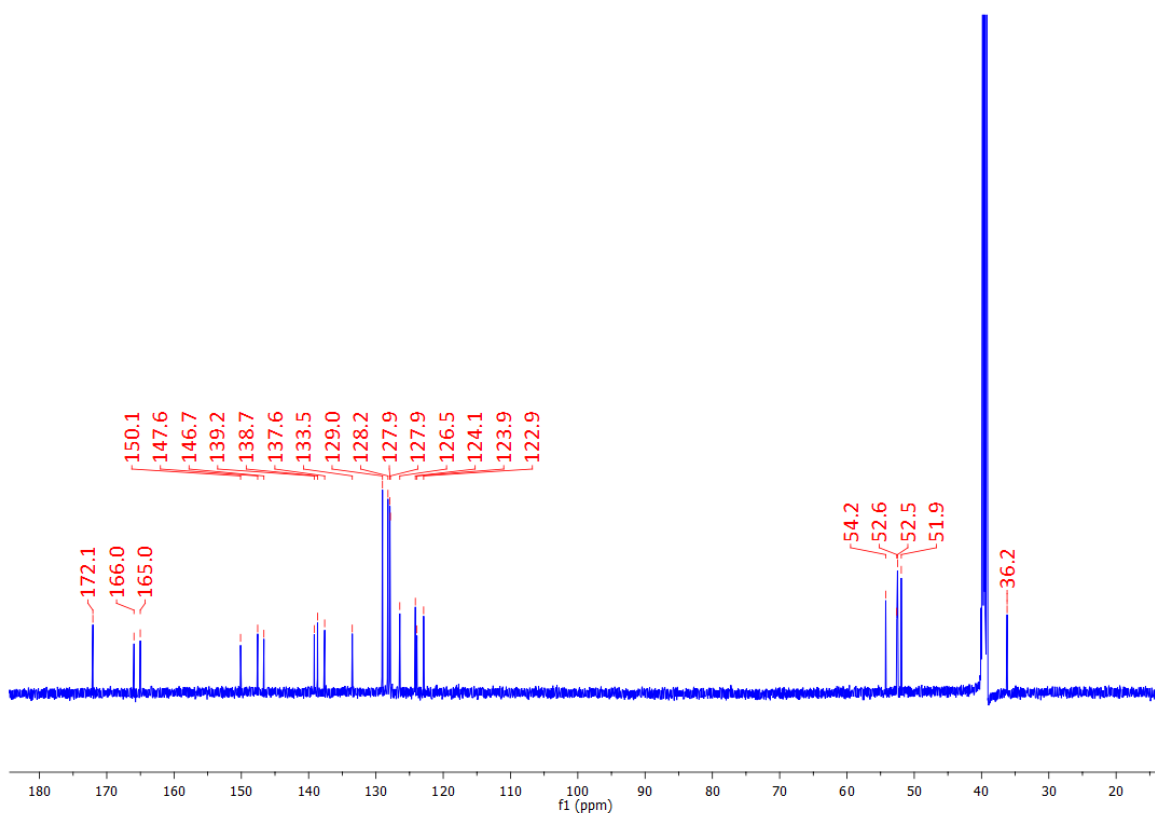
Figure A4.1 *¹³ C NMR spectrum (150 MHz, DMSO) of **179**.*
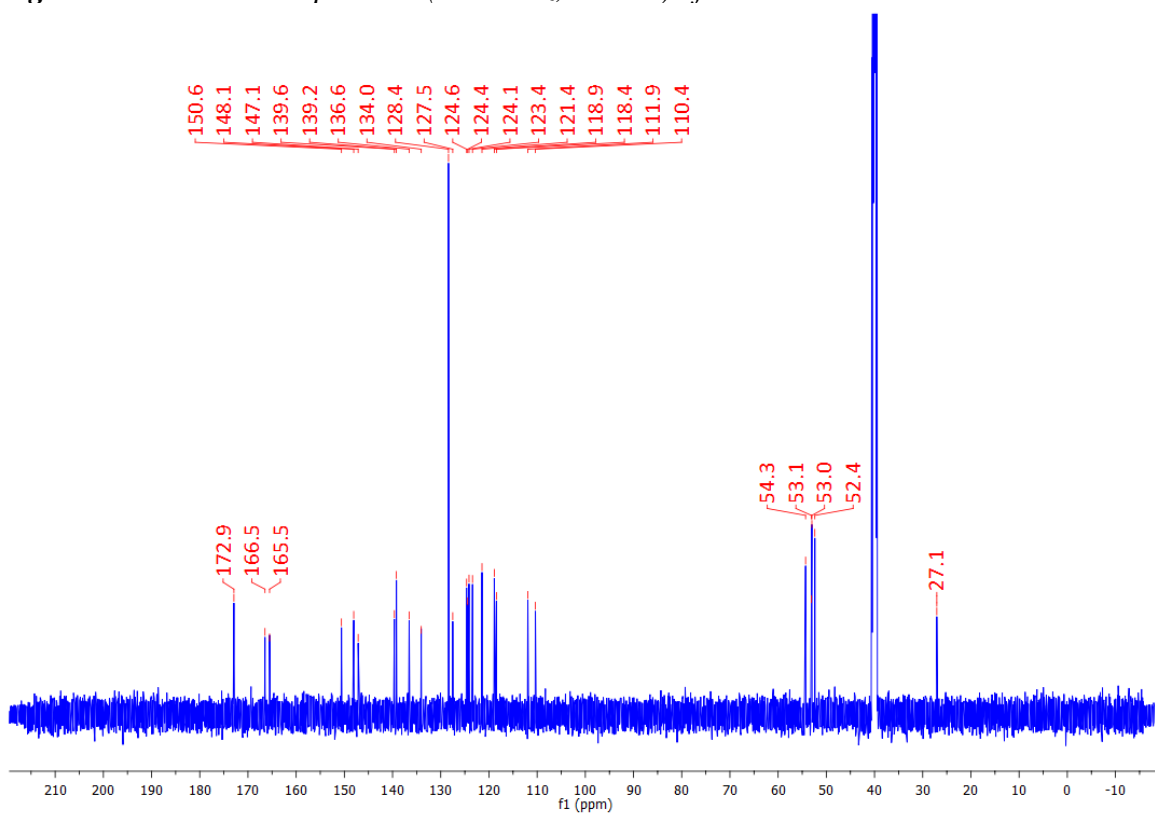
Figure A4.2 *¹³C NMR spectrum (150 MHz, DMSO) of **180**.*
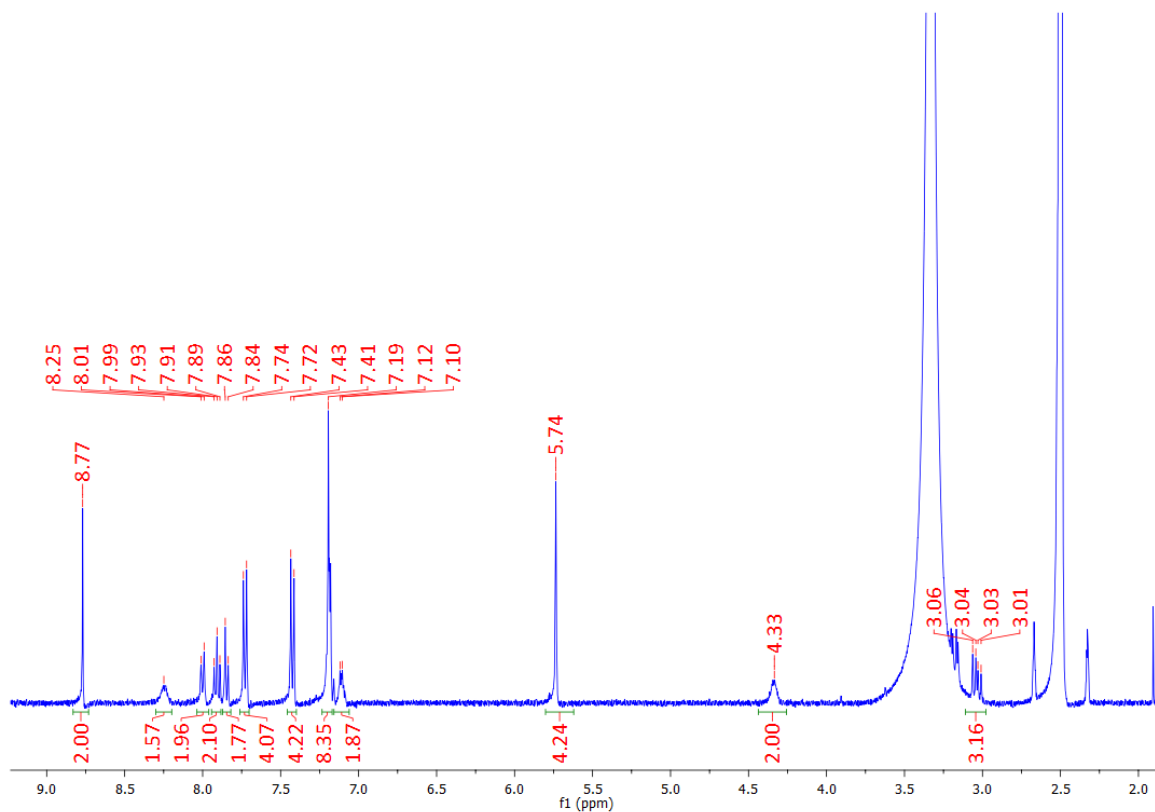
Figure A4.3 *¹H NMR spectrum (600 MHz, DMSO) of **181**.*
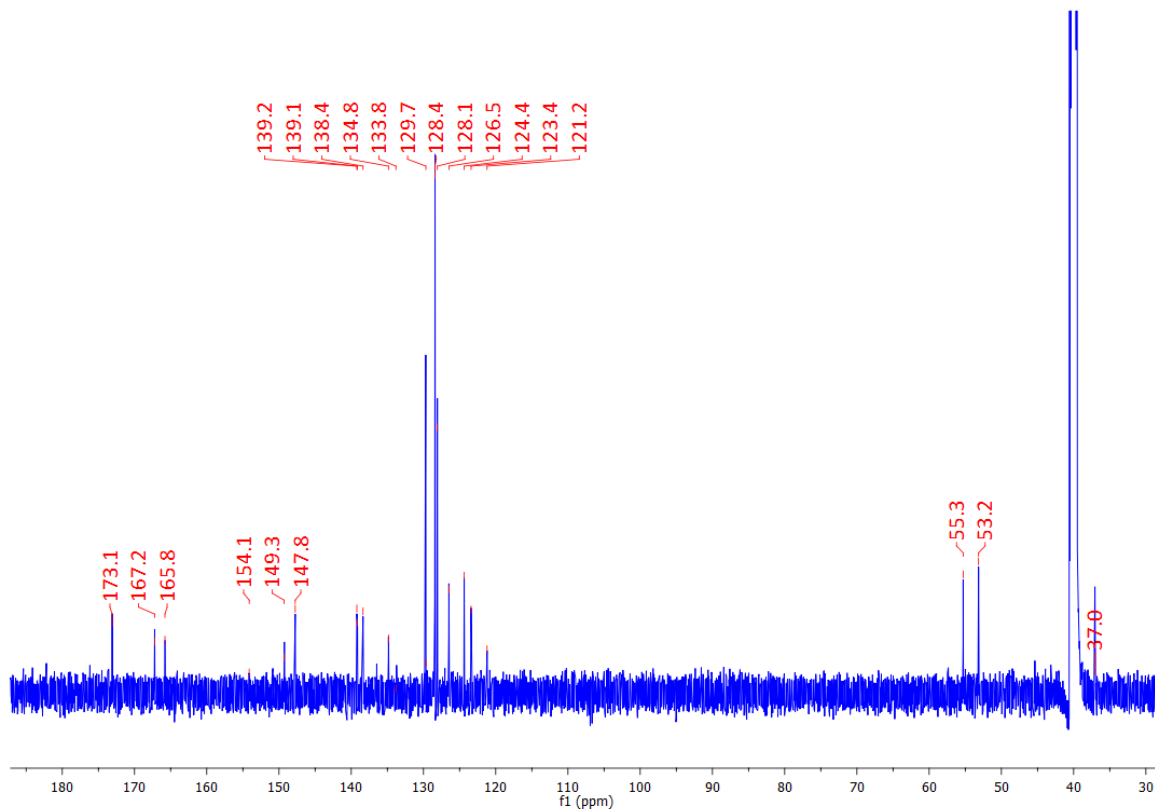
Figure A4.4 *¹³C NMR spectrum (150 MHz, DMSO) of **181**.*

Table A4.1 *Crystal and refinement parameters for structures **179** in Chapter 4.*

Identification code	**179**
Empirical formula	$C_{27}H_{25}N_5O_5$
Formula weight	499.52
Temperature/K	100(2)
Crystal system	monoclinic
Space group	$P2_1$
a/Å	9.9204(3)
b/Å	9.6670(3)
c/Å	13.2315(4)
α/°	90
β/°	106.3690(10)
γ/°	90
Volume/Å^3	1217.47(6)
Z	2
ρ_{calc}g/cm^3	1.363
μ/mm^{-1}	0.793
F(000)	524.0
Crystal size/mm^3	$0.14 \times 0.13 \times 0.1$
Radiation	CuKα (λ = 1.54178)
2Θ range for data collection/°	9.29 to 136.496
Index ranges	$-11 \leq h \leq 11$, $-11 \leq k \leq 11$, $-15 \leq l \leq 15$
Reflections collected	12684
Independent reflections	4398 [R_{int} = 0.0369, R_{sigma} = 0.0383]
Data/restraints/parameters	4398/1/336
Goodness-of-fit on F^2	1.021
Final R indexes [I>=2σ (I)]	R_1 = 0.0275, wR_2 = 0.0716
Final R indexes [all data]	R_1 = 0.0281, wR_2 = 0.0722
Largest diff. peak/hole / e Å^{-3}	0.13/-0.14
Flack parameter	0.04(7)
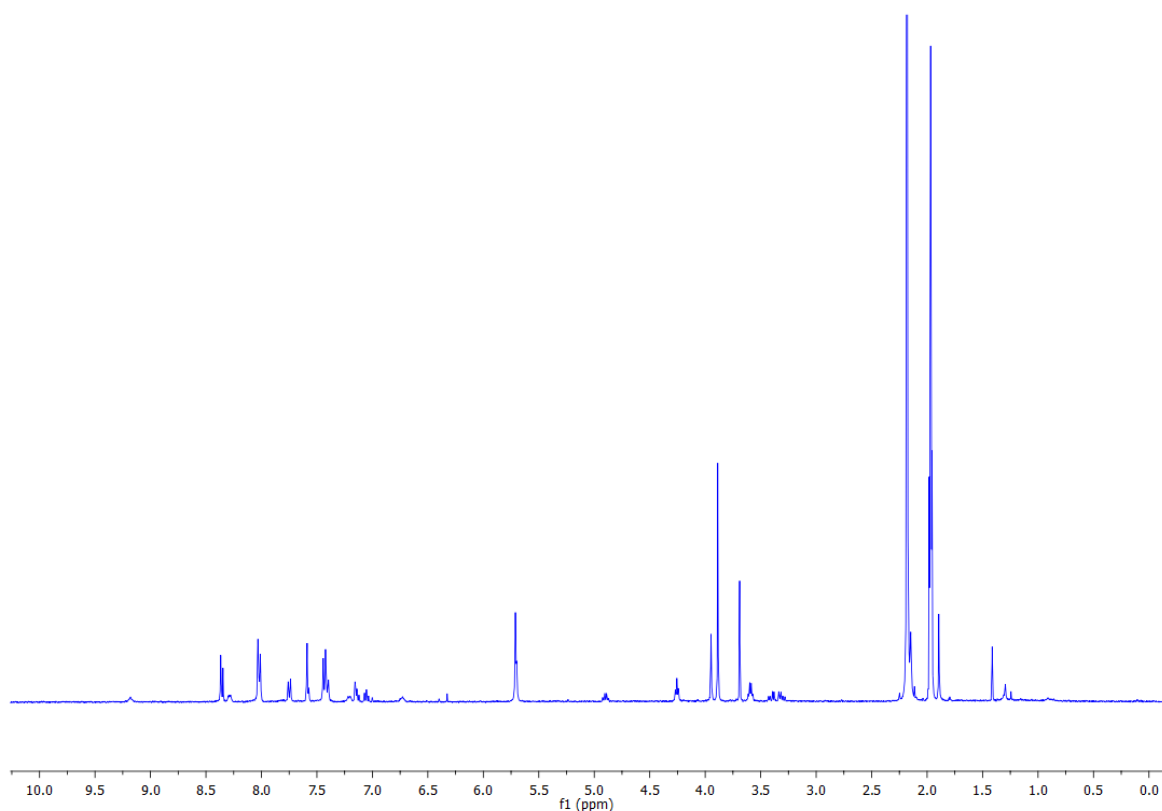
Figure A4.5 *¹H NMR spectrum (400 MHz, CD₃CN) of Tb.**180**₃.*
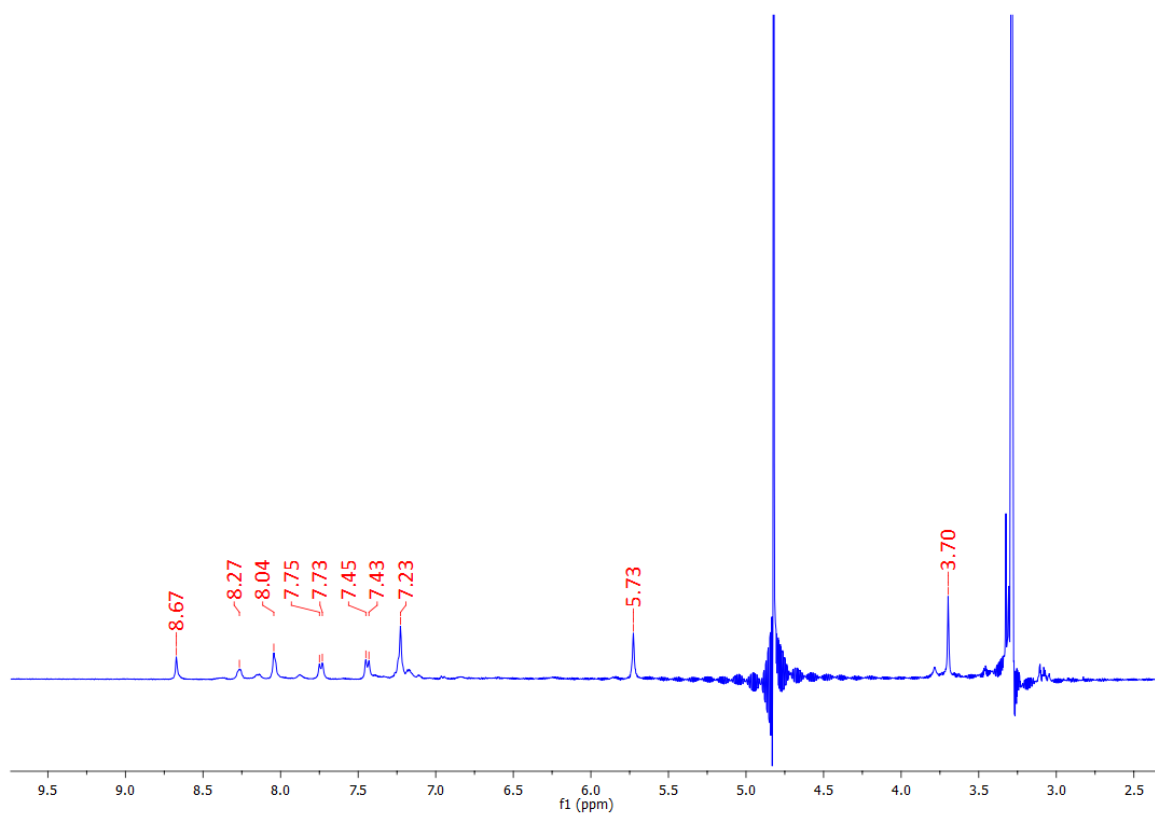
Figure A4.6 *¹H NMR spectrum (400 MHz, CD₃OD) of Eu**179**₃*
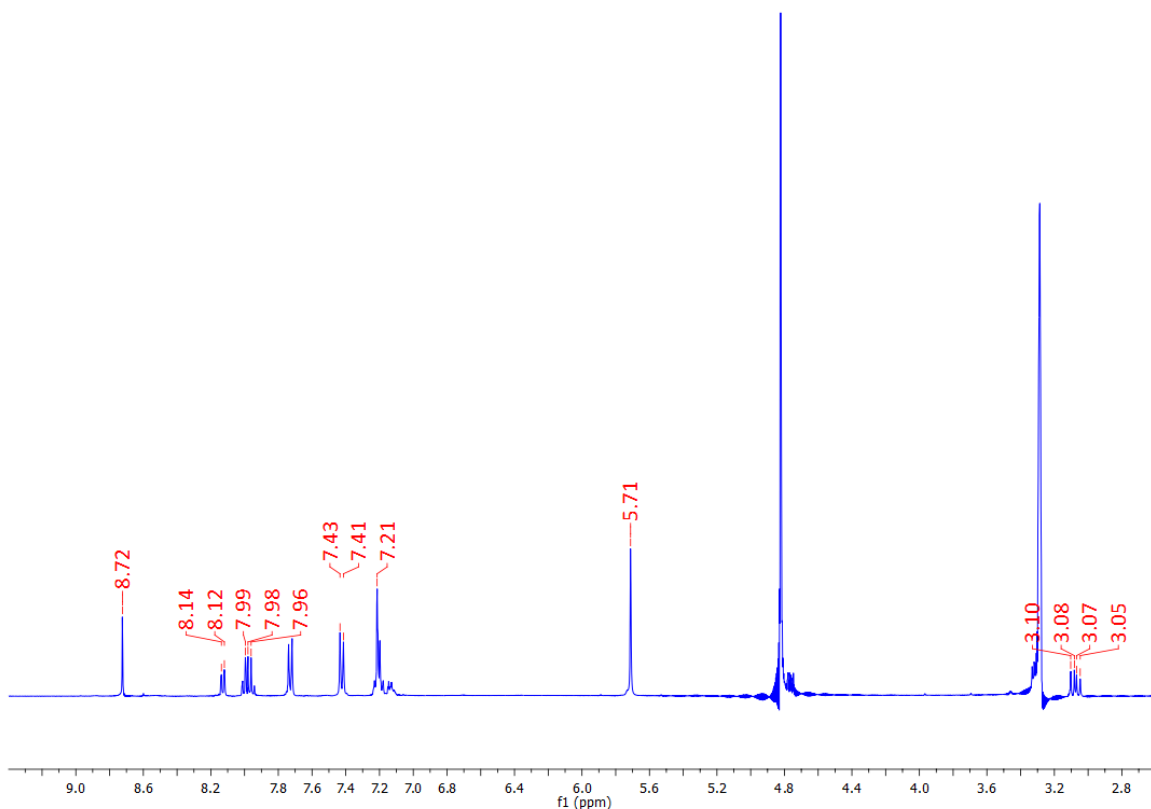
Figure A4.7 *¹H NMR spectrum (400 MHz, CD₃OD) of Tb**181**₃*
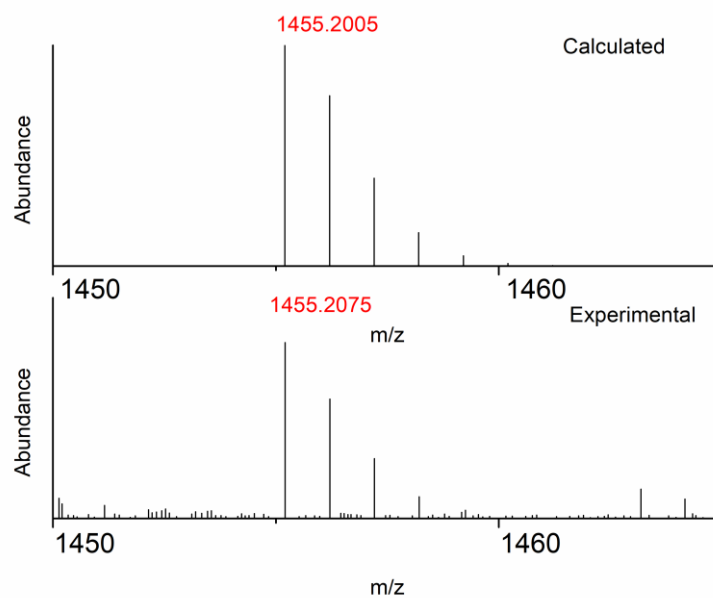
Figure A4.8 *The calculated and experimental isotopic distribution patterns for Tb.**179**₂ showing the 1:2 metal:ligand stoichiometric pattern for a molecular species of the formula [Tb(**179**)₂](CF₃SO₃)₂⁺*
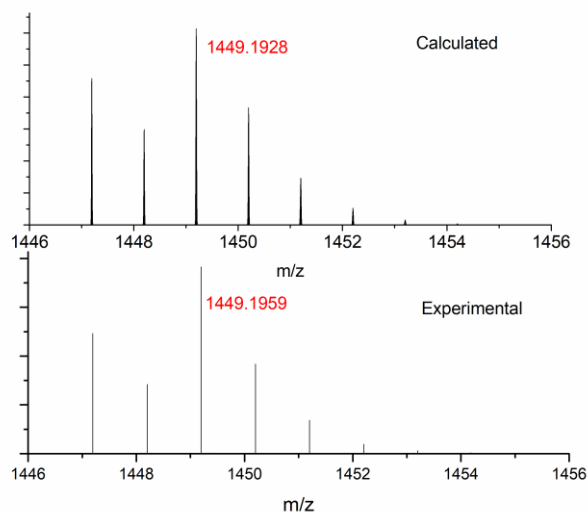
Figure A4.9 The calculated and experimental isotopic distribution patterns for Eu.179₂ showing the 1:2 metal:ligand stoichiometric pattern for a molecular species of the formula [Eu(179)₂](CF₃SO₃)₂⁺
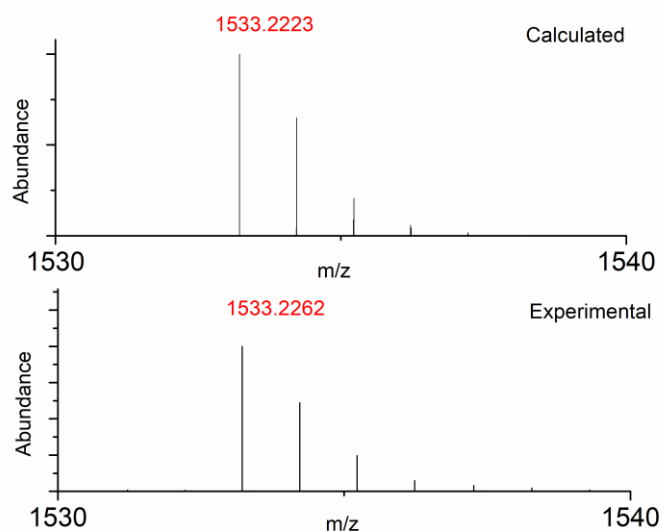

***Figure A4.10** The calculated and experimental isotopic distribution patterns for Tb.180₂ showing the 1:2 metal:ligand stoichiometric pattern for a molecular species of the formula [Tb(180)₂](CF₃SO₃)₂⁺*
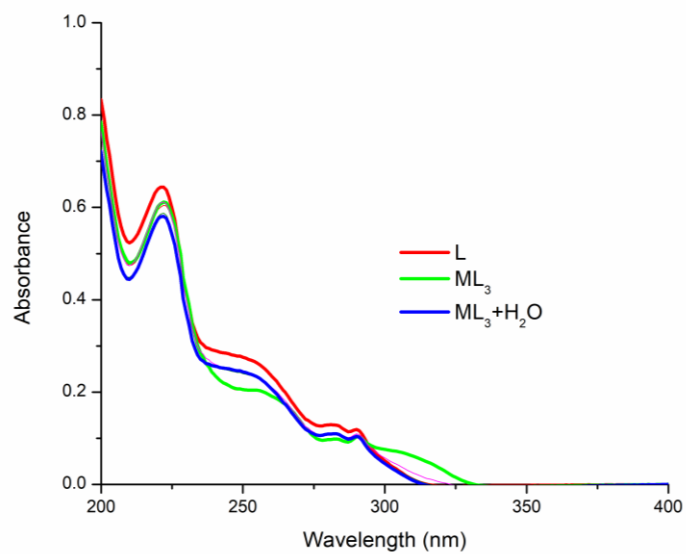
Figure A4.11 *Absorbance spectra of ligand **182** and Tb.**182**$_3$ upon addition of H_2O showing dissociation of the tris complex.*
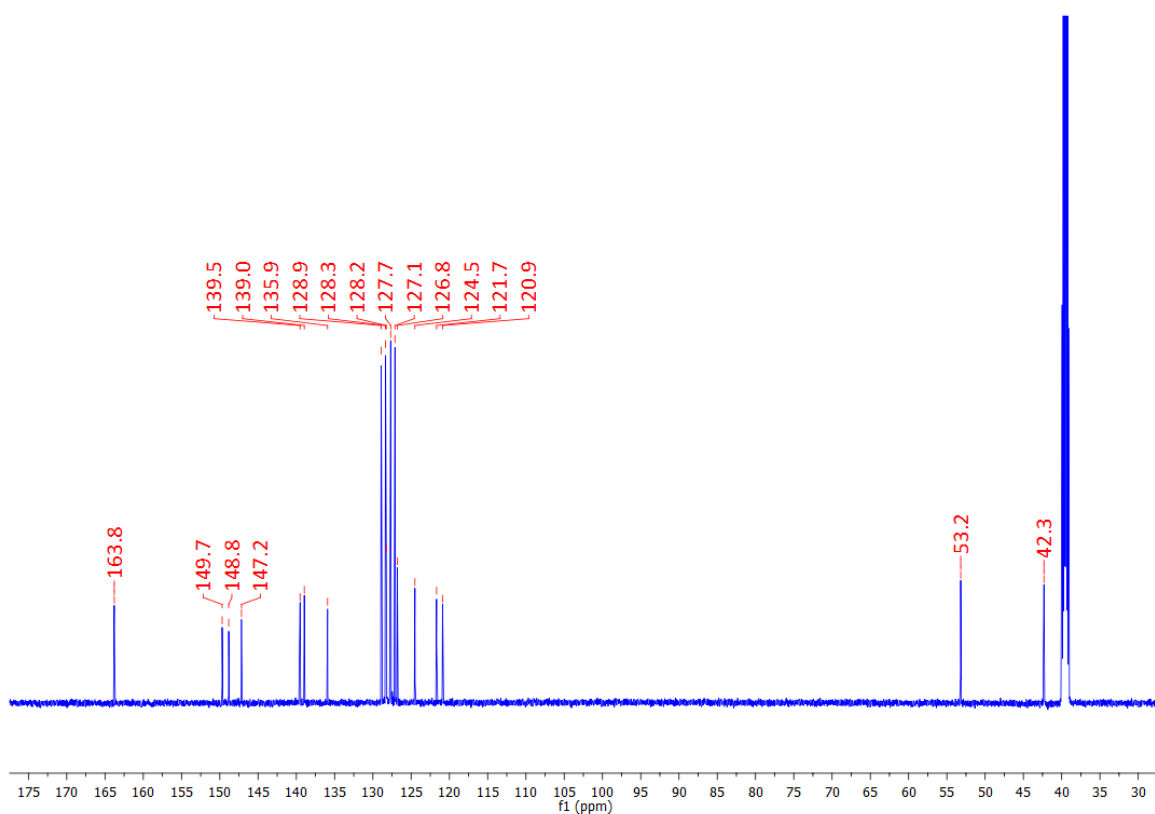
Figure A4.12 ^{13}C *NMR spectrum (150 MHz, DMSO) of **186**.*
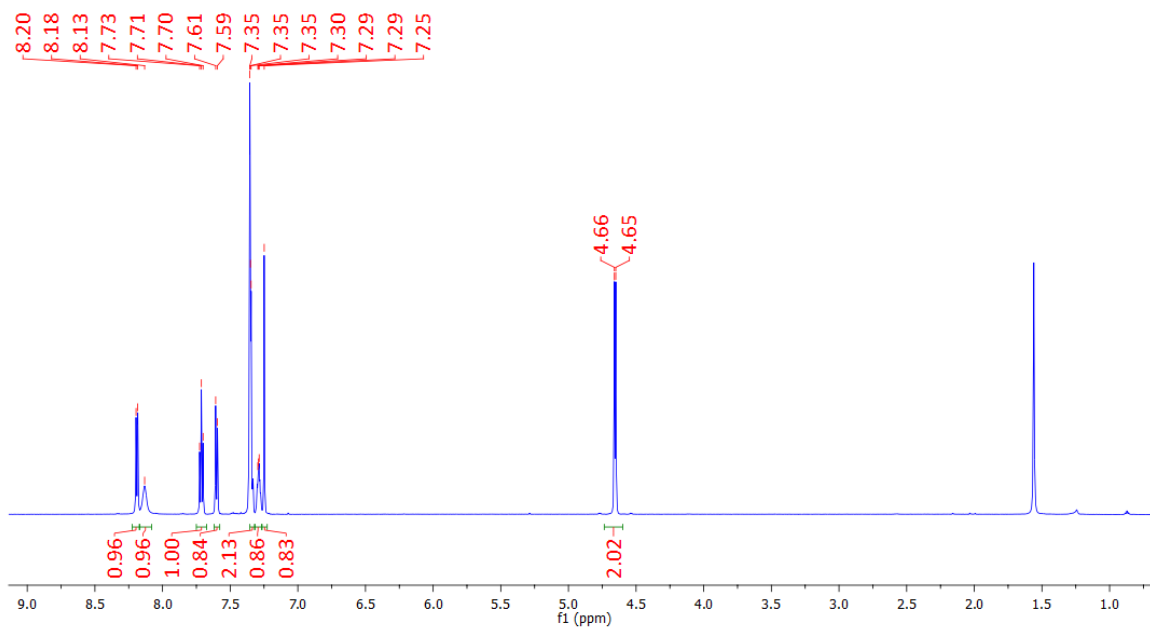
Figure A4.13 *^{1}H NMR spectrum (600 MHz, CDCl$_3$) of **187**.*
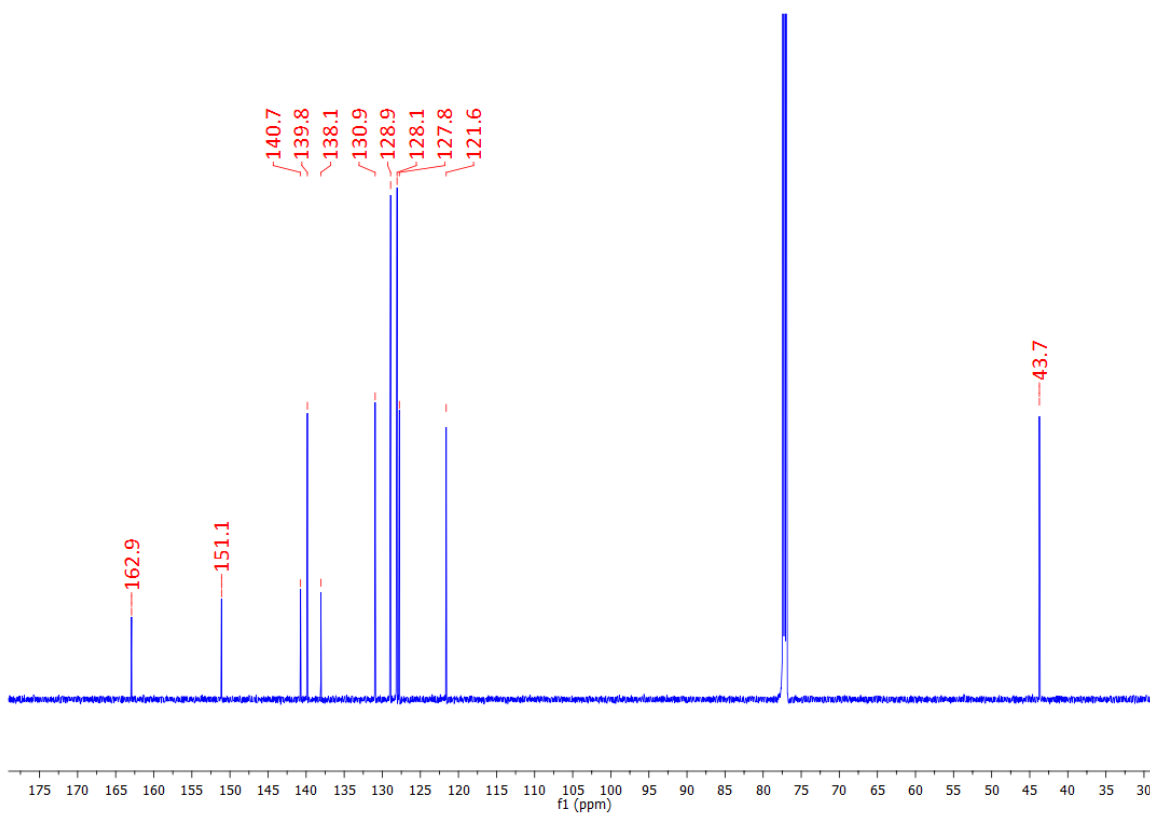
Figure A4.14 *^{13}C NMR spectrum (150 MHz, CDCl$_3$) of **187**.*
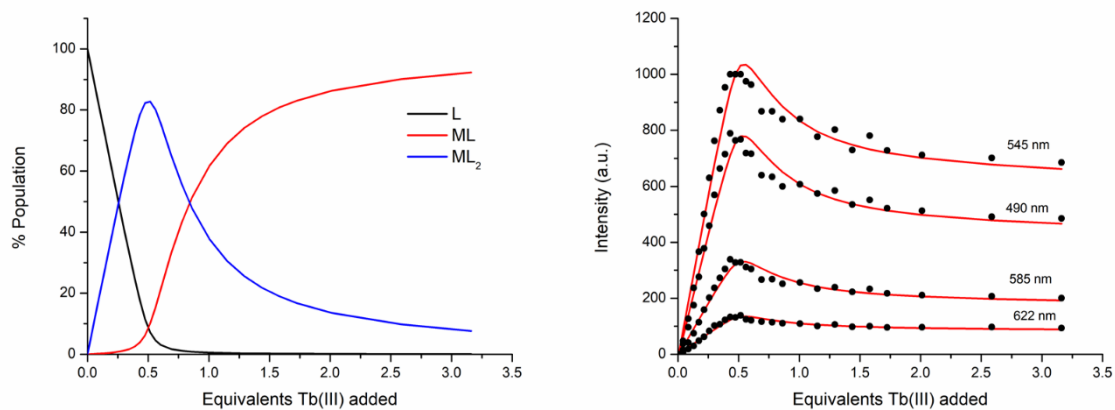
Figure A4.15 *(left) The speciation distribution diagram obtained from the fit of the time-gated luminescence titration data of ligand **186** against Tb($CF_3SO_3)_3$ in CH_3CN. (right) the fit of the experimental binding isotherms using non-linear regression analysis software ReactLab.*
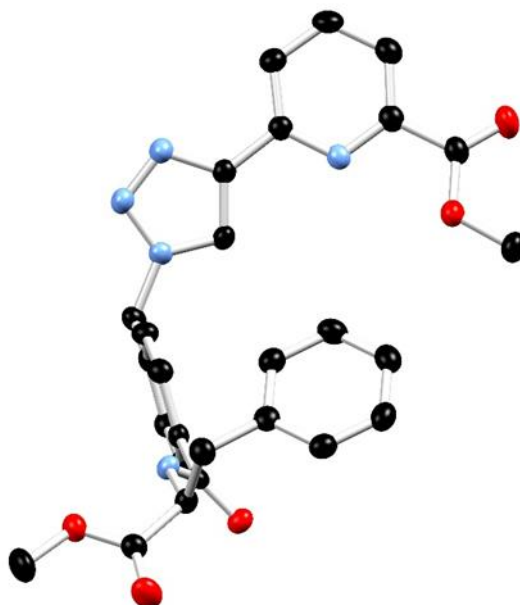
Figure A4.16 *Ellipsoid plot of asymmetric unit of ligand **179**. Ellipsoids shown at 50% probability*
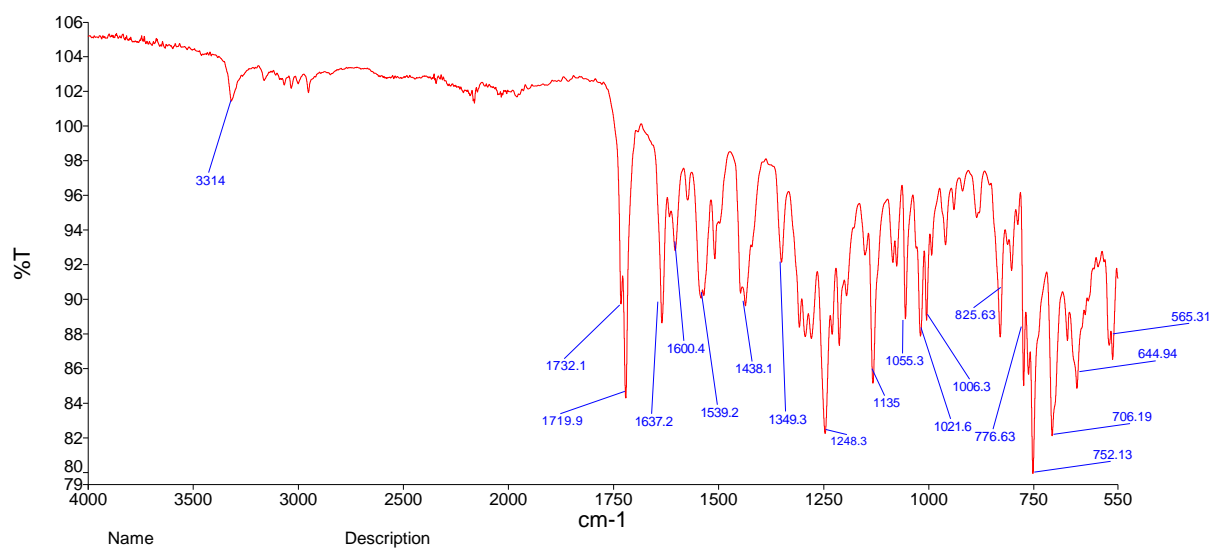
Figure A4.17 *Infrared spectrum of ligand **179**.*
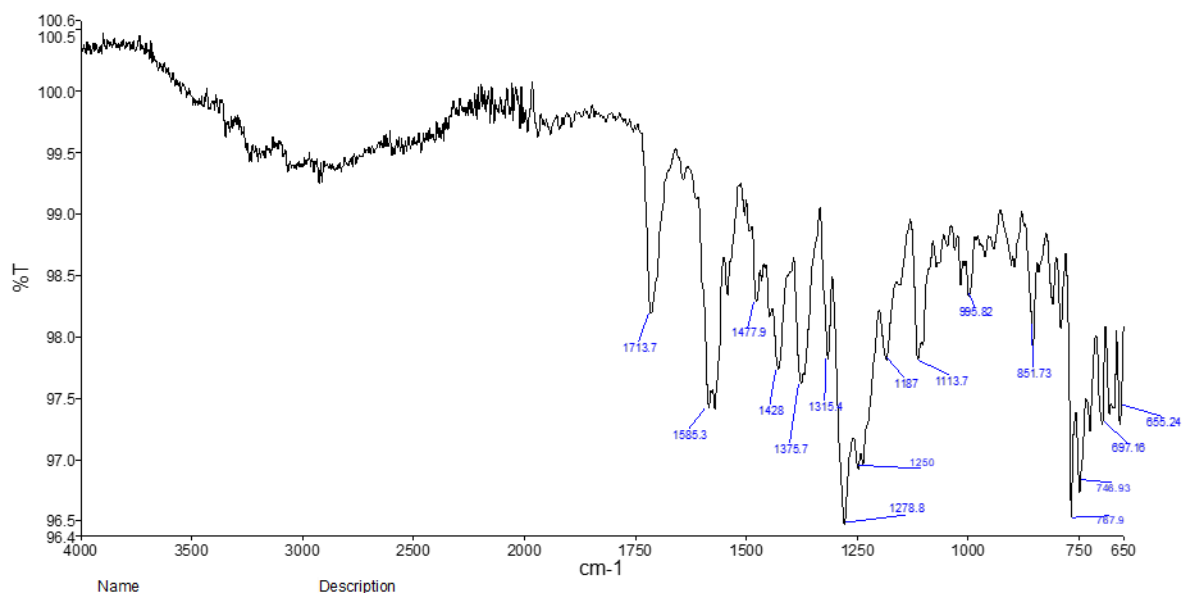
Figure A4. *18 Infrared spectrum of [Tb(**179**)₂](CF₃SO₃)₂*
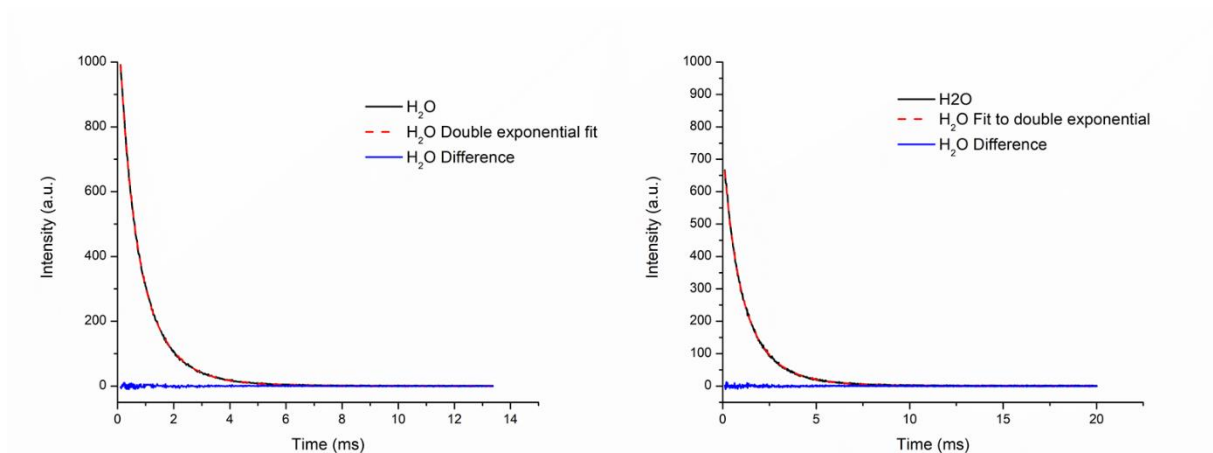
***Figure* A4.19** *Lifetime spectra of [Tb(**179**)₂]²⁺ fit to double exponential curve recorded in H₂O*
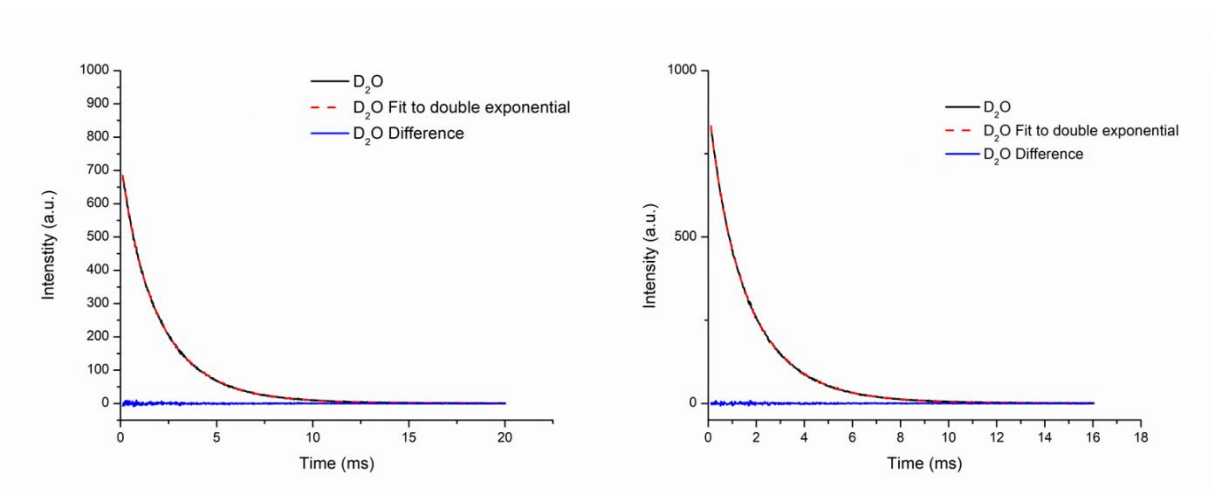
***Figure* A4.20** *Lifetime spectra of [Tb(**179**)₂]²⁺ fit to double exponential curve recorded in D₂O*
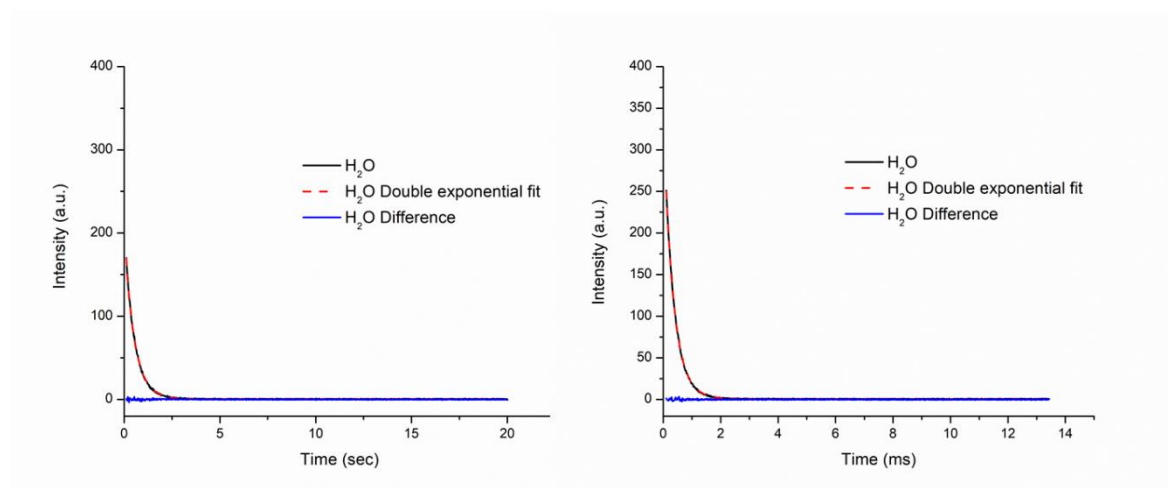
***Figure* A4.21** *Lifetime spectra of [Tb(**180**)₂]²⁺ fit to double exponential curve recorded in H₂O*
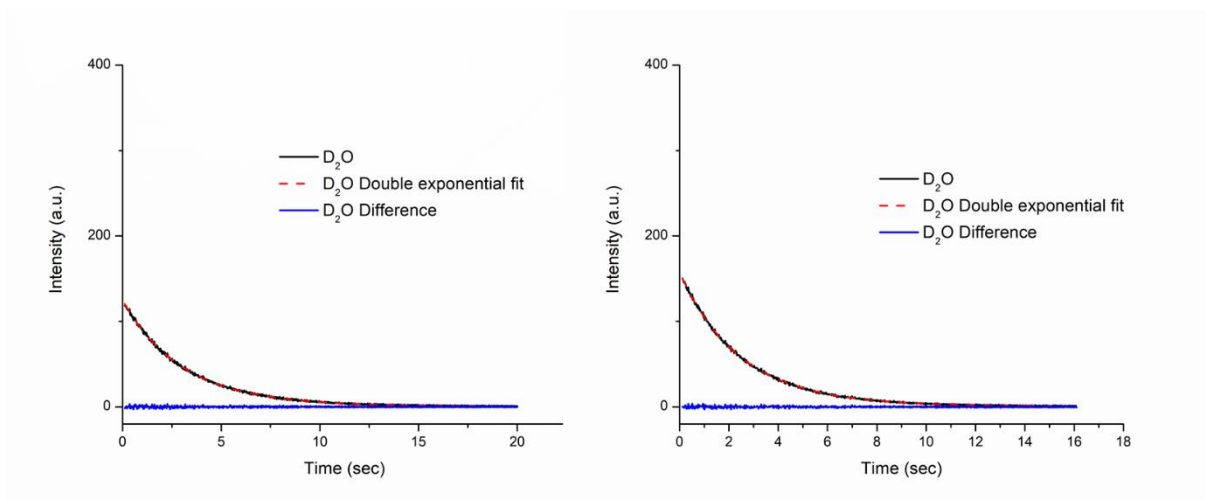
Figure A4.22 *Lifetime spectra of [Tb(**180**)₂]²⁺ fit to double exponential curve recorded in D₂O*

Appendix Five
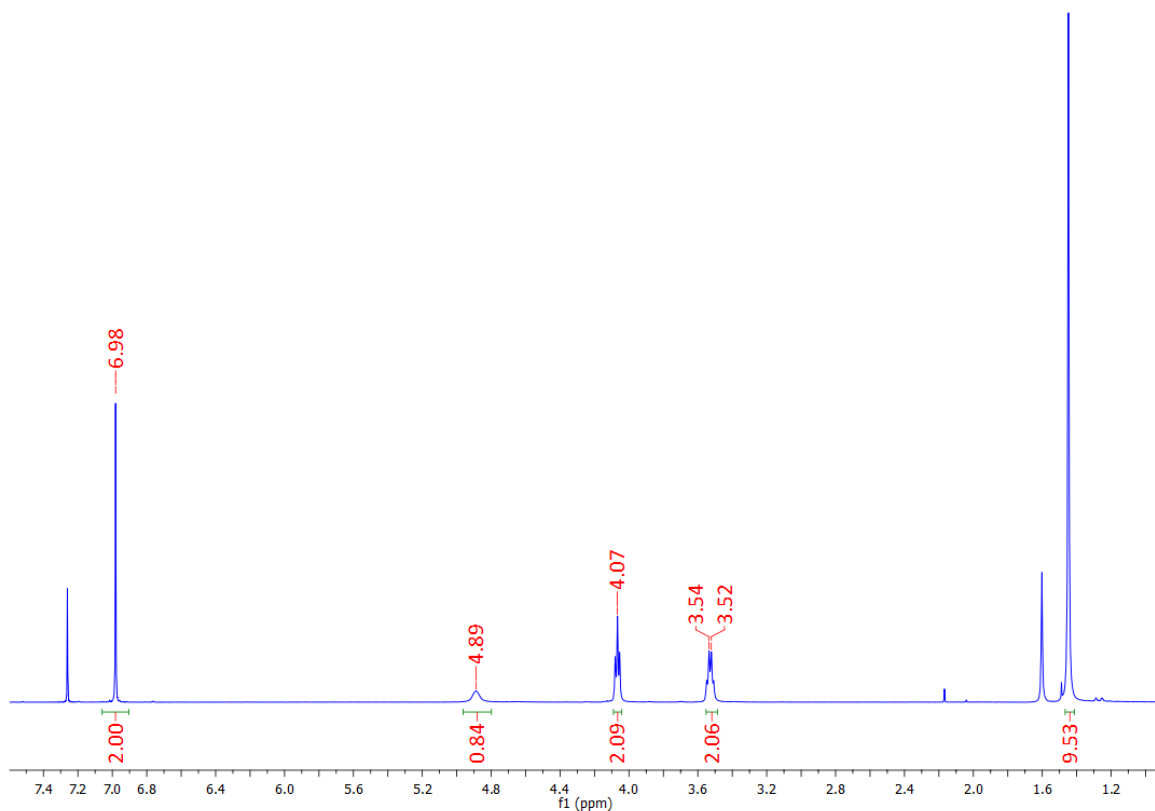
Figure A5.1 *^1H NMR spectrum (400 MHz, CDCl$_3$) of **195**.*
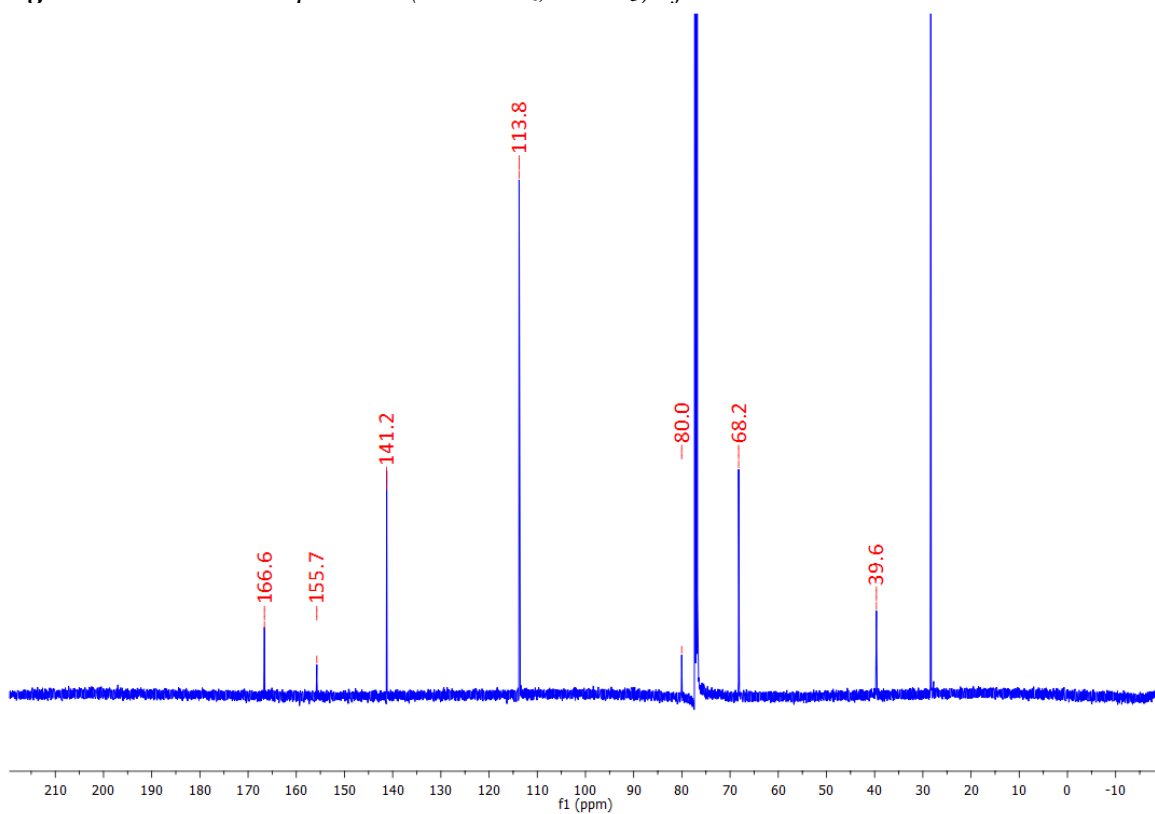
Figure A5.2 *^{13}C NMR spectrum (150 MHz, CDCl$_3$) of **197**.*
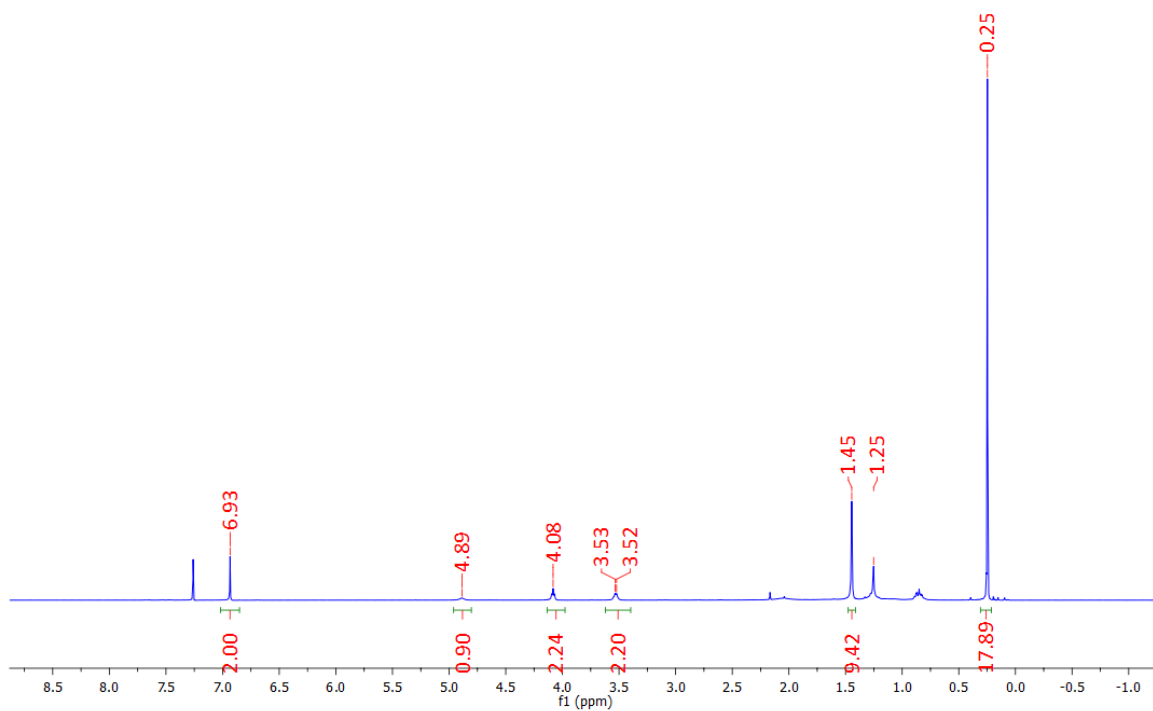
Figure A5.3 *^{1}H NMR spectrum (400 MHz, CDCl$_3$) of* **196**.
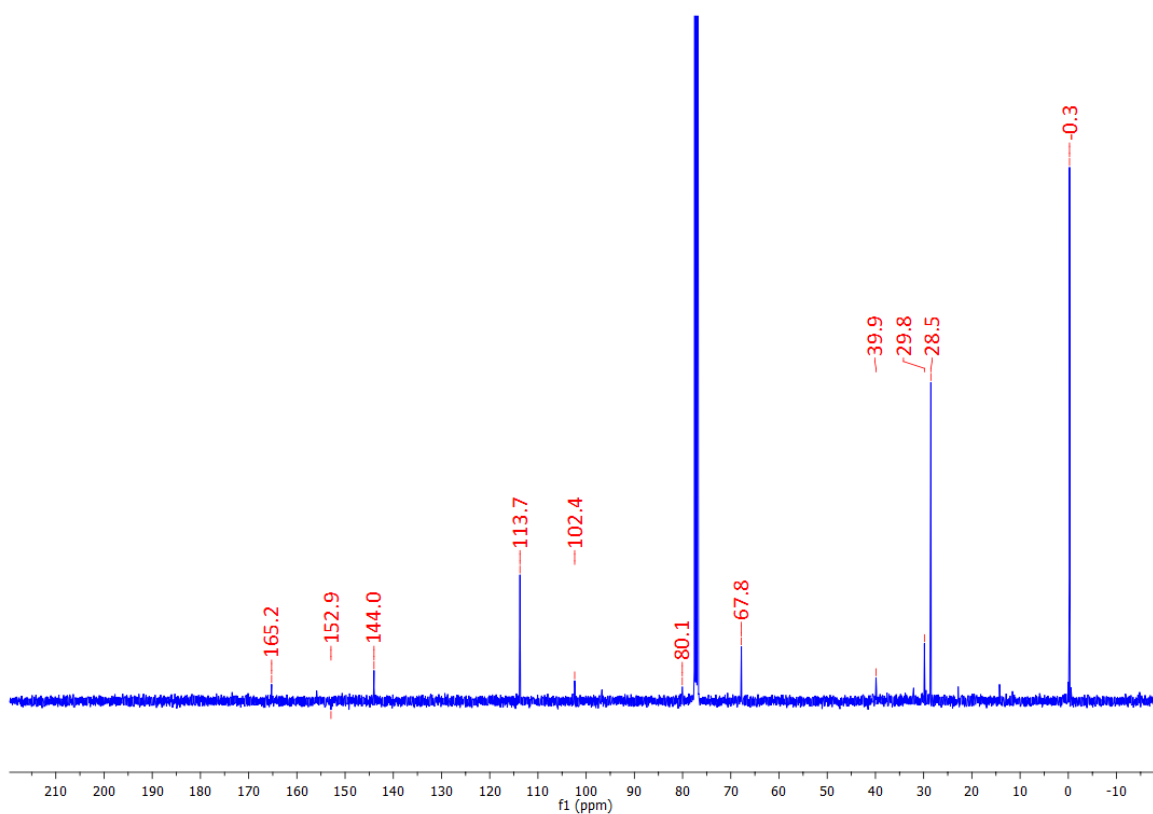
Figure A5.4 *^{13}C NMR spectrum (150 MHz, CDCl$_3$) of* **196**.
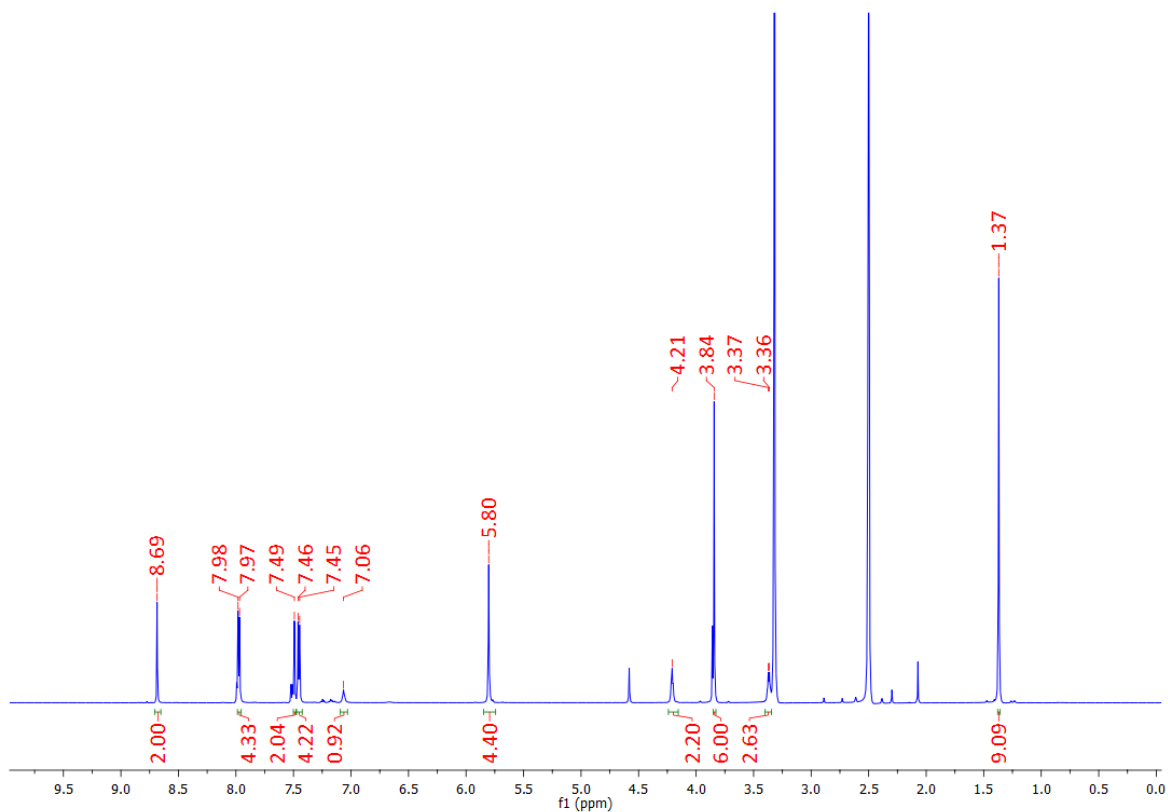
Figure A5.5 *^{1}H NMR spectrum 6400 MHz, DMSO) of* **198**.
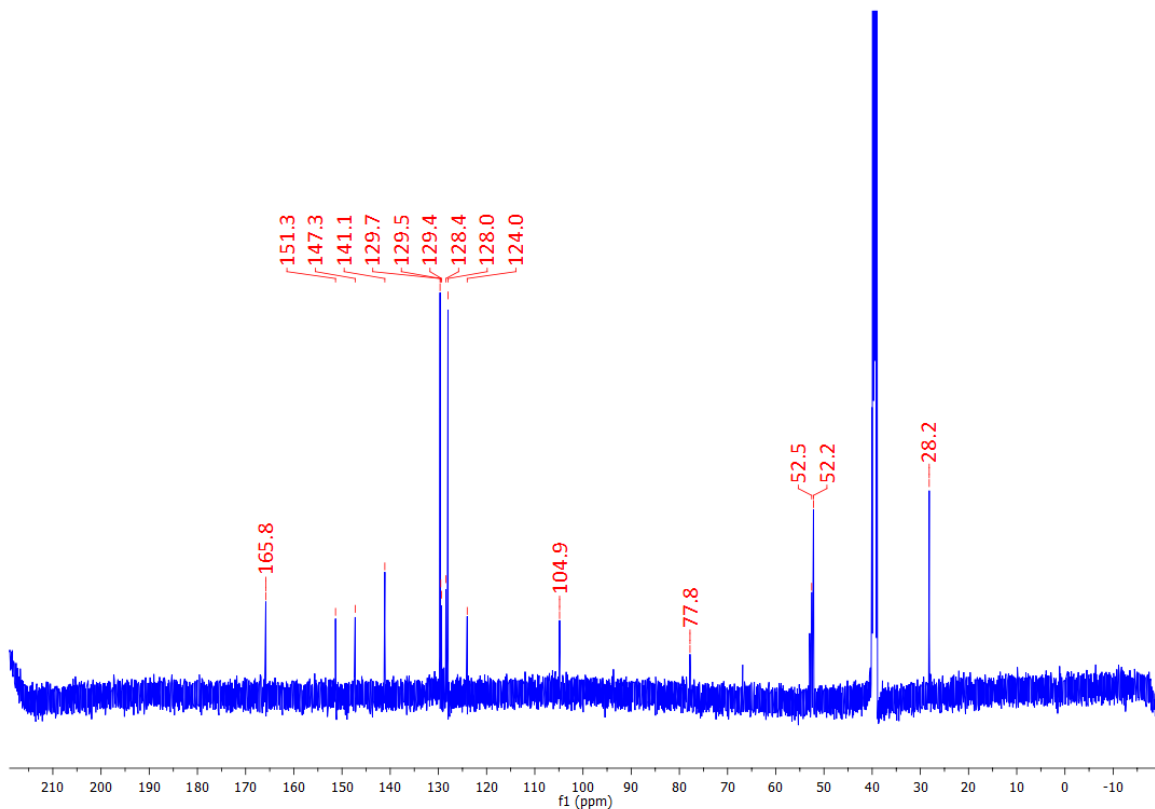
Figure A5.6 *^{13}C NMR spectrum (150 MHz, DMSO) of* **198**.
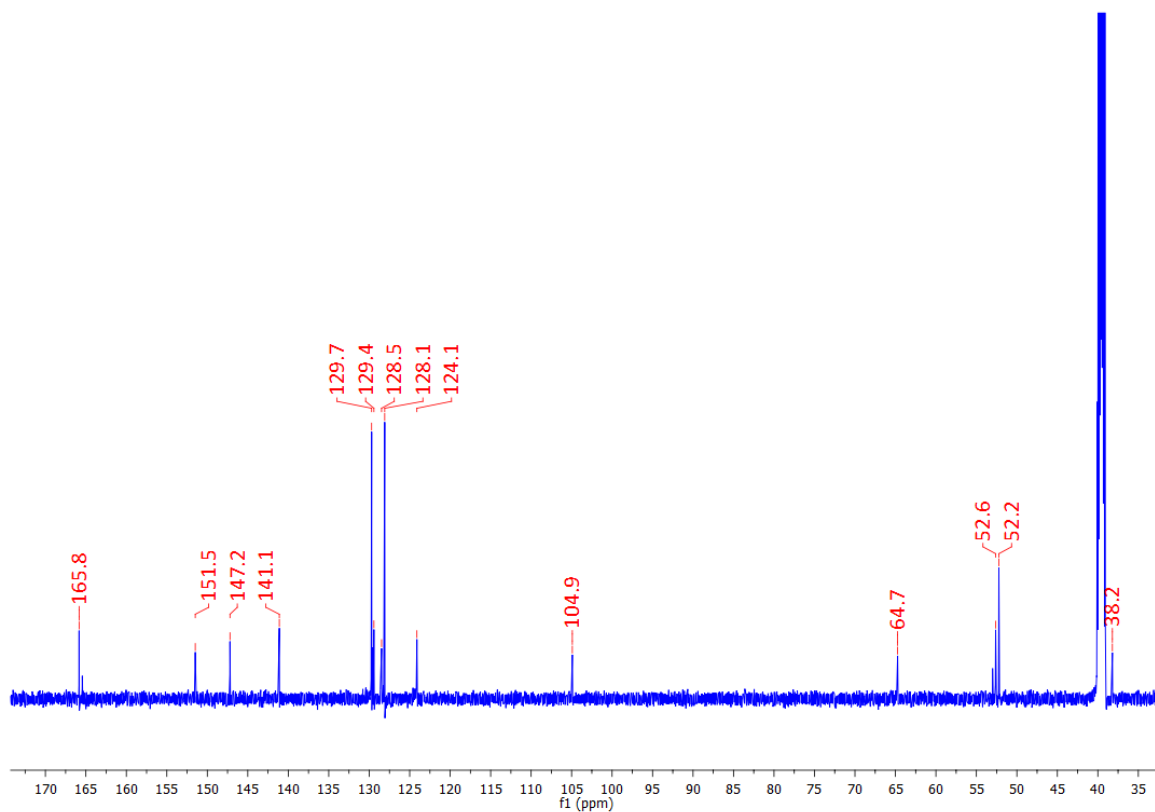
Figure A5.7 *¹³C NMR spectrum (150MHz, DMSO) of* **189**.
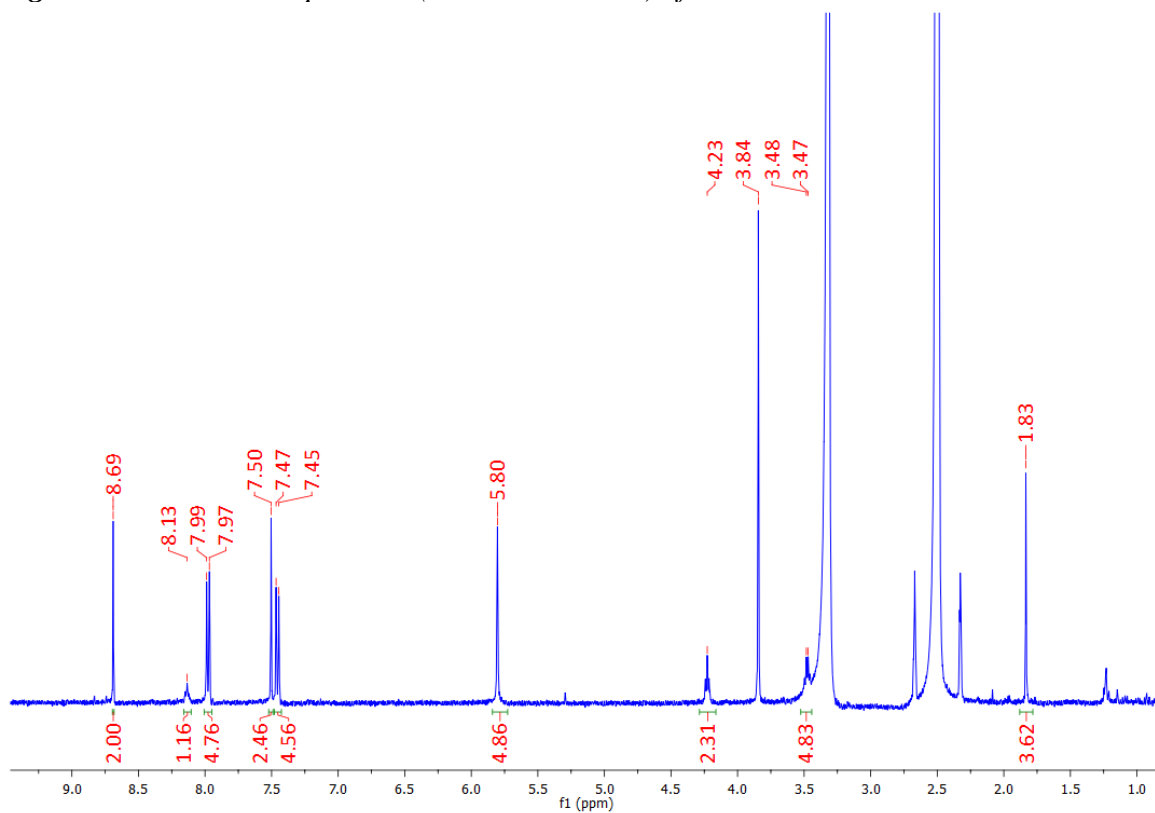
Figure A5.8 *¹H NMR spectrum (600 MHz, DMSO) of* **190**.
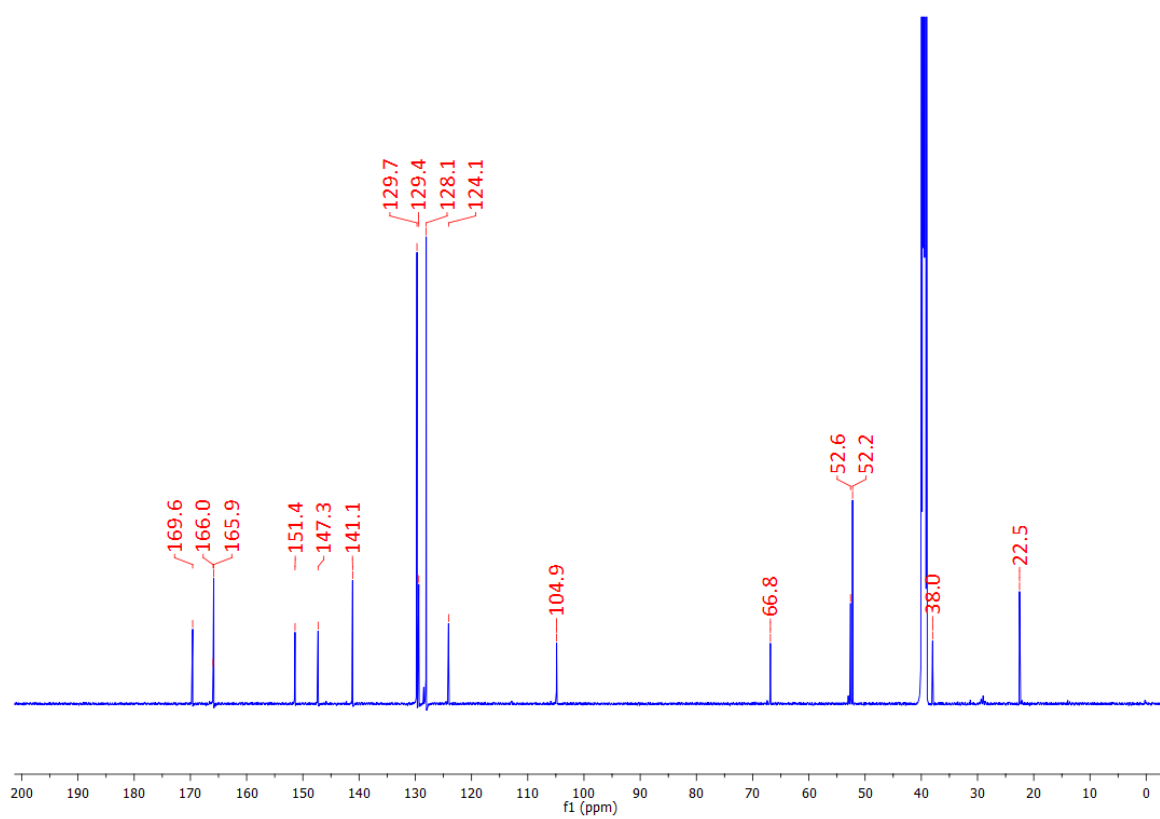
Figure A5.9 *¹³C NMR spectrum (150 MHz, DMSO) of* **190**.
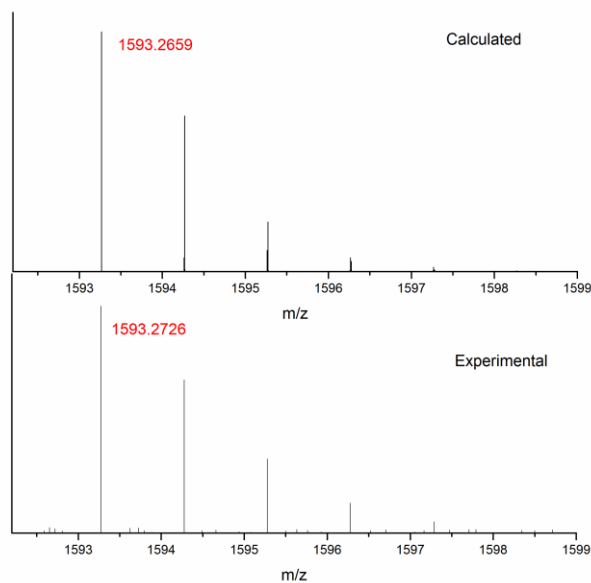
Figure A5.10 *The calculated and experimental isotopic distribution patterns for Tb.**189**$_2$ showing the 1:2 metal:ligand stoichiometric pattern for a molecular species of the formula [Tb(**189**)$_2$](CF$_3$SO$_3$)$_2^+$*
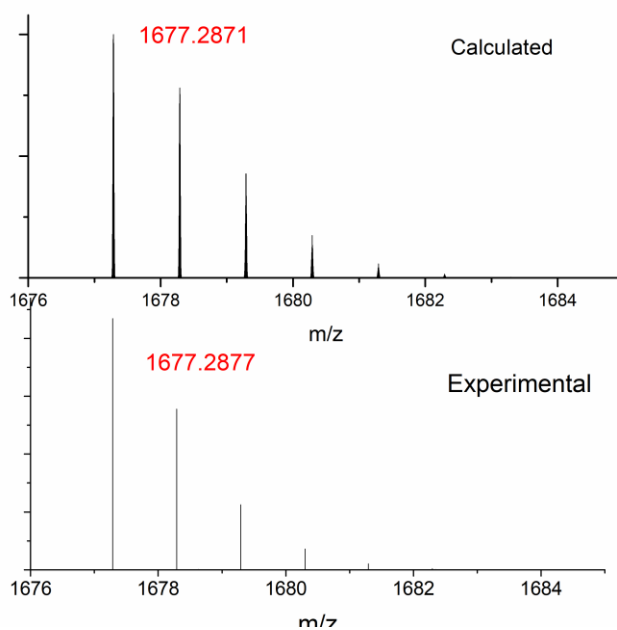
Figure A5.11 *The calculated and experimental isotopic distribution patterns for Tb.**189**$_2$ showing the 1:2 metal:ligand stoichiometric pattern for a molecular species of the formula [Tb(**189**)$_2$](CF$_3$SO$_3$)$_2^+$*
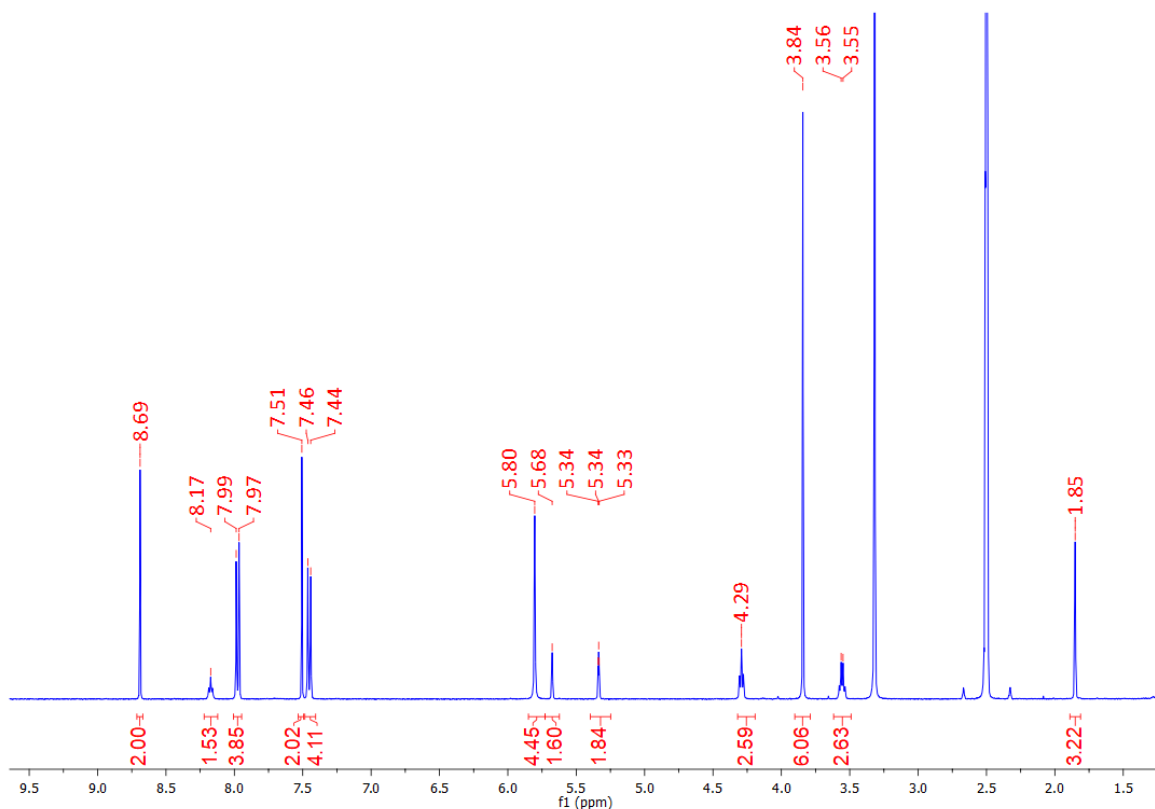
Figure A5.12 ^1H NMR spectrum (600 MHz, DMSO) of **199**.
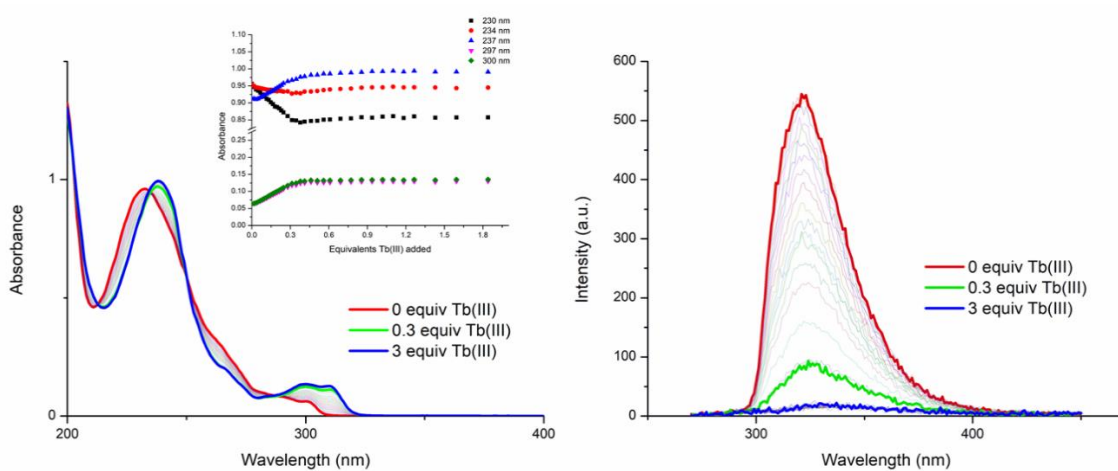
Figure A5.14 *The overall changes in the (left) UV-visible absorption spectra and (right) fluorescence emission spectra (excitation wavelength λ = 237 nm) upon titrating **199** (1×10^{-5} M) against Tb(CF$_3$SO$_3$)$_3$ ($0\rightarrow3$ equiv.) in CH$_3$CN at 22°C. **Inset**: corresponding experimental binding isotherms of absorbance at λ = 230, 234, 237, 297 and 300 nm.*
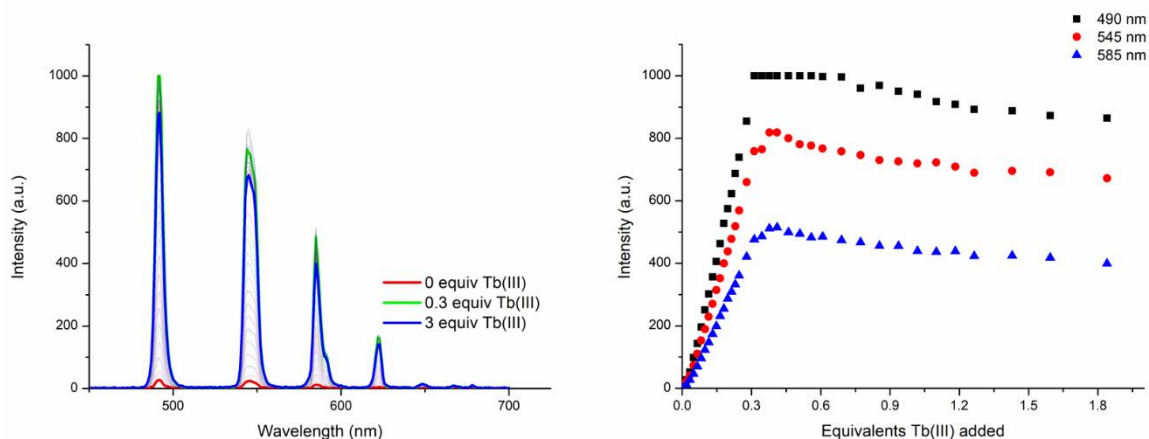
Figure A5.15 *(Left) The overall changes to the Tb(III)-centred phosphorescence spectra upon titrating **199** (1×10^{-5} M) against Tb(CF$_3$SO$_3$)$_3$ (0$\rightarrow$3 equiv.) in CH$_3$CN at 22 ˚C. (right) corresponding experimental binding isotherms of phosphorescence at λ = 490, 545 and 585 nm.*
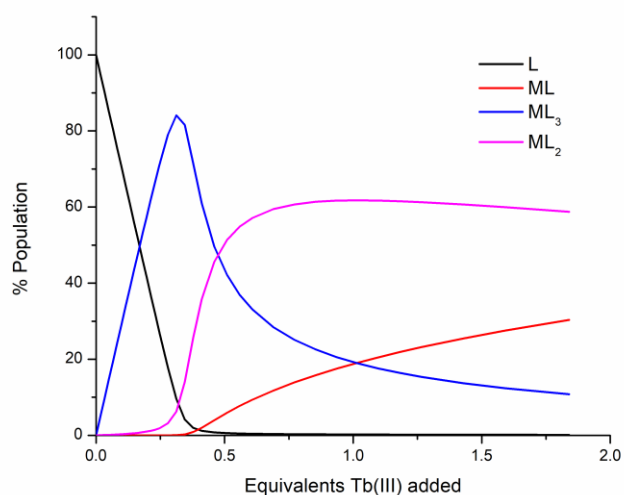
Figure A5.16 *Speciation distribution diagram obtained from the fit of the UV-visible absorption titration data of ligand **199** against Tb(CF$_3$SO$_3$)$_3$ in CH$_3$CN.*
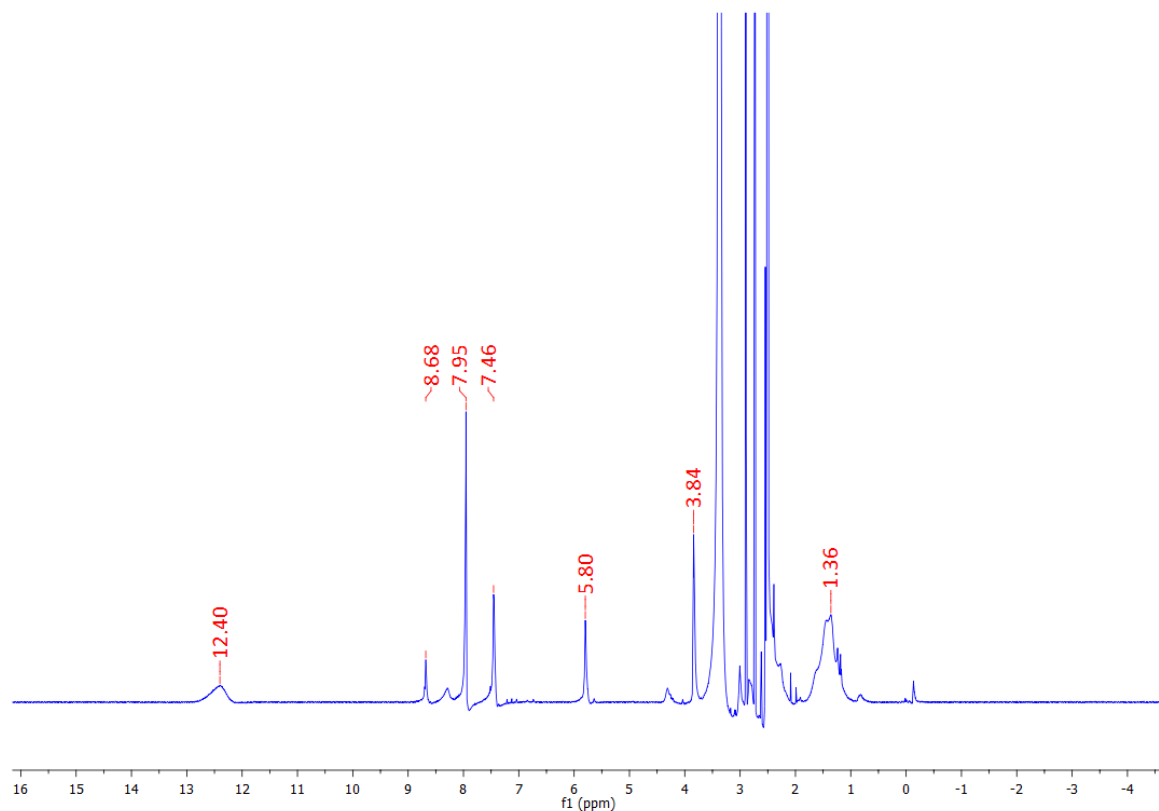
Figure A5.17 *^{1}H NMR spectrum (600 MHz, DMSO) of **P2**.*

Table A5.1 *Crystal and refinement parameters for structures **193** and **189** in Chapter 5.*

Identification code	193	189
Empirical formula	$C_5H_2Br_2N_2O_2$	$C_{33}H_{32}F_3N_9O_7$
Formula weight	281.91	723.67
Temperature/K	100(2)	99.98
Crystal system	orthorhombic	monoclinic
Space group	$P2_12_12_1$	C2/c
a/Å	5.3120(2)	37.042(7)
b/Å	7.5807(2)	9.974(2)
c/Å	19.3315(6)	18.080(4)
α/°	90	90
β/°	90	96.40(3)
γ/°	90	90
Volume/Å^3	778.45(4)	6638(2)
Z	4	8
ρ_{calc}g/cm^3	2.405	1.448
μ/mm^{-1}	10.361	0.984
F(000)	528.0	3008.0
Crystal size/mm^3	$0.14 \times 0.05 \times 0.04$	$0.29 \times 0.19 \times 0.05$
Radiation	MoKα (λ = 0.71073)	CuKα (λ = 1.54178)
2Θ range for data collection/°	4.214 to 66.536	4.8 to 117.862

Index ranges	$-7 \leq h \leq 8$, $-11 \leq k \leq 11$, $-29 \leq l \leq 29$	$-40 \leq h \leq 39$, $-11 \leq k \leq 11$, $-15 \leq l \leq 19$
Reflections collected	18543	13925
Independent reflections	2983 [R_{int} = 0.0441, R_{sigma} = 0.0347]	4650 [R_{int} = 0.0780, R_{sigma} = 0.0881]
Data/restraints/parameters	2983/0/100	4650/0/473
Goodness-of-fit on F^2	1.072	0.965
Final R indexes [I>=2σ (I)]	R_1 = 0.0336, wR_2 = 0.0680	R_1 = 0.0703, wR_2 = 0.1784
Final R indexes [all data]	R_1 = 0.0434, wR_2 = 0.0707	R_1 = 0.1271, wR_2 = 0.2143
Largest diff. peak/hole / e Å^{-3}	0.99/-0.96	0.29/-0.30
Flack parameter	0.040(7)	

Compound Reference Guide
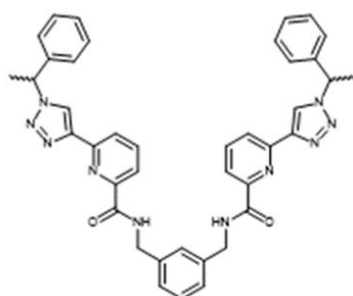
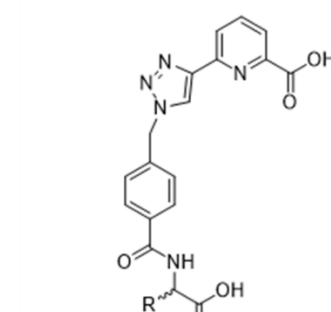**H₂157** (R,R)
H₂158 (S,S)

162
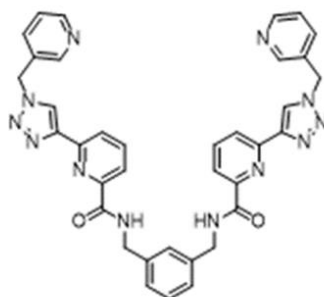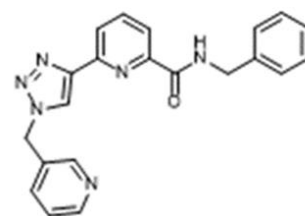
166
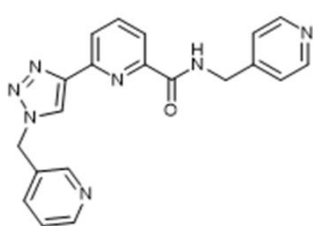
H169
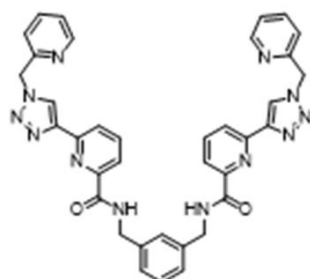
H₂172
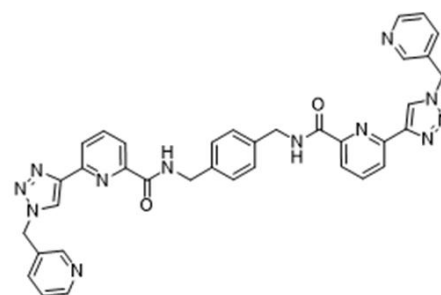
173
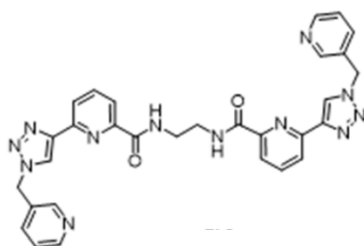
176
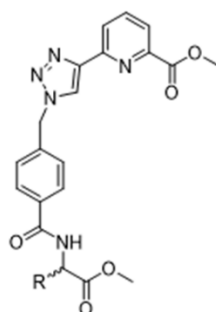
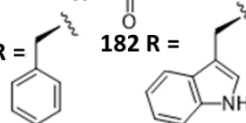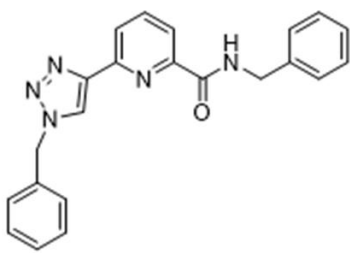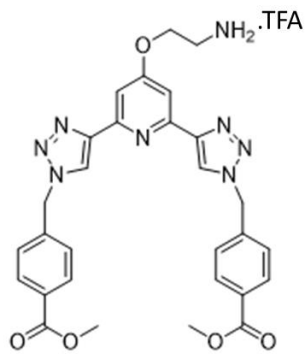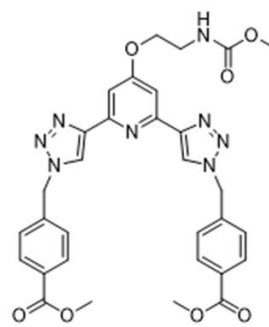**179 R =**
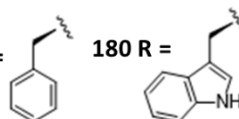
180 R =

181 R =

182 R =

186

189

190

304